



Kent Academic Repository

Shrine, Nicholas Robert George (1999) *Laboratory investigation of oblique hypervelocity impacts with relevance to in situ meteoroid and space debris detectors*. Doctor of Philosophy (PhD) thesis, University of Kent.

Downloaded from

<https://kar.kent.ac.uk/86111/> The University of Kent's Academic Repository KAR

The version of record is available from

<https://doi.org/10.22024/UniKent/01.02.86111>

This document version

UNSPECIFIED

DOI for this version

Licence for this version

CC BY-NC-ND (Attribution-NonCommercial-NoDerivatives)

Additional information

This thesis has been digitised by EThOS, the British Library digitisation service, for purposes of preservation and dissemination. It was uploaded to KAR on 09 February 2021 in order to hold its content and record within University of Kent systems. It is available Open Access using a Creative Commons Attribution, Non-commercial, No Derivatives (<https://creativecommons.org/licenses/by-nc-nd/4.0/>) licence so that the thesis and its author, can benefit from opportunities for increased readership and citation. This was done in line with University of Kent policies (<https://www.kent.ac.uk/is/strategy/docs/Kent%20Open%20Access%20policy.pdf>). If y...

Versions of research works

Versions of Record

If this version is the version of record, it is the same as the published version available on the publisher's web site. Cite as the published version.

Author Accepted Manuscripts

If this document is identified as the Author Accepted Manuscript it is the version after peer review but before type setting, copy editing or publisher branding. Cite as Surname, Initial. (Year) 'Title of article'. To be published in *Title of Journal*, Volume and issue numbers [peer-reviewed accepted version]. Available at: DOI or URL (Accessed: date).

Enquiries

If you have questions about this document contact ResearchSupport@kent.ac.uk. Please include the URL of the record in KAR. If you believe that your, or a third party's rights have been compromised through this document please see our [Take Down policy](https://www.kent.ac.uk/guides/kar-the-kent-academic-repository#policies) (available from <https://www.kent.ac.uk/guides/kar-the-kent-academic-repository#policies>).

**Laboratory Investigation of Oblique
Hypervelocity Impacts with Relevance to
In situ Meteoroid and Space Debris
Detectors**

by

Nicholas Robert George Shrine

Thesis submitted for the degree of Doctor of Philosophy

November 1999

Unit for Space Sciences and Astrophysics
School of Physical Sciences
University of Kent at Canterbury
UK

Abstract

Inferring the properties of the near-Earth meteoroid and space debris environments as sampled by *in situ* detectors and retrieved spacecraft surfaces requires understanding of the hypervelocity impact process. To infer the nature of an impact after the event, we need to establish relationships between the relevant impact parameters and the resulting impact features. This task is performed in the laboratory by controlled hypervelocity impact experiments using various acceleration techniques. A facet of understanding impact processes in space is the investigation of behaviour under impact from an oblique angle. Despite the fact that impacts normal to the target surface are the exception under real conditions, impact angle studies are often given low priority in investigation of a material's response to hypervelocity impact, with other parameters such as projectile size, velocity and density being initially studied at normal incidence. The author has identified, in his analysis of space-flown surfaces and previous applications of empirical relationships to space data, two areas where oblique impact studies are lacking leading to an uncertain interpretation of the near-Earth environment.

The first of these areas is oblique penetration of thin aluminium targets as observed on capture cell detectors such as the EURECA-TICCE experiment. An experimental programme was performed using the University of Kent's light-gas gun to fire steel and aluminium ball bearings through aluminium plates, covering more angles and target thicknesses than similar previous studies. It is found that the method by which an empirical equation derived from normal impact studies has been modified for application to space data using an *assumed* angle dependence does not predict the laboratory data well. An alternative method of applying the same laboratory-derived equation is presented that more closely reproduces the oblique experimental data. This new method is shown to give a significantly different estimation of the size distribution of meteoroids and debris when applied to the EURECA-TICCE penetration record.

The second area is oblique impacts on solar cells as observed on the EURECA and HST solar arrays. A second experimental programme using the light-gas gun was performed firing 50 μm soda-lime glass beads at solar cell samples over a range of impact angles from 0-75° from normal. It is found that, of impact crater features previously used as a guide to impact angle, only the *pit circularity* is primarily related to impact angle. It is also found that the conchoidal diameter, previously believed to have a power law dependence on impact angle, is insensitive to impact angle for angles less than 45° from normal and decreases in size linearly with the cosine of the impact angle for angles greater than 45° from normal. This experimental programme was extended to determine the survivability of the glass beads to launch in the light-gas gun and it was found that although it is likely that soda-lime glass beads reach the target intact, other commonly used small projectiles such as meteorite-analogue mineral powders do not.

Acknowledgements

I must thank the Unit for Space Sciences and Astrophysics at the University of Kent at Canterbury, especially the head of the Unit Prof. Tony McDonnell and my PGRA supervisor Dr. Mark Burchell, for allowing me to incorporate research for this thesis into the schedule of my research post. This work was funded by the Particle Physics and Astronomy Research Council (PPARC).

I acknowledge the early collaboration of the TICCE team: David Gardner, Hajime Yano and especially Ian Collier whose broadcasts on “radio clean room” helped stave off crater madness. I acknowledge Mike Cole for consistently providing rapid solutions for problems that arose on the light-gas gun, especially the ones that were my fault; also Mark Burchell for running the accelerator lab so productively. Discussions with Emma Taylor and Neil McBride were appreciated, not least for sometimes making me realise that I didn’t really understand things as well as I thought I did! I am also grateful to them for proof reading. I acknowledge the excellent *stats-desk* service run by the Institute of Mathematics and Statistics and particularly thank Prof. Donald Preece and Dr. Eryl Bassett for their time spent clarifying statistics concepts and helping me to identify some appropriate analyses for my data. Thanks to Margaret Fowler for help over the years with office and admin stuff and Jo Dunn for dealing with the PhD red tape.

People who helped me through the time when doing this thesis seemed like *Groundhog Day* include the occupants of Rm. 164: Jon Marchant, for never boring me by saying anything that made any sense whatsoever, funny, after a few years he started making sense and everybody else stopped, what no *magic-midget-wolfman-elvis* poppadoms? James Garry, for his quaintly British penchant for polished metal and for not removing the dashboard; Andrew Ball for being “like someone’s dad” as far as taste goes and for mastering the fine art of skimming the sink scum; Mike Foster for being nothing but a cockney and Ralph Lorenz for those early deathmatches.

Emma Taylor deserves thanks for supplying encouragement, chocolate, crepes, herbal tea bags and more chocolate, none of which she ever ate herself of course. Beyond the lab (a place that seemed inaccessible to me at times), people who are thanked for putting up with me at No. 62 are Mary and Eleanor - for being fun and tolerant housemates and for sending long-distance encouragement after they left -, Kneale, Chris (honorary), and Nav. People who made Friday nights an oasis of beer and curry in this desert of toil include Richard “*gaspers*” Miller, Mark “*Vindaloo-hot-sir?*” Price, Martin “*big-curved-axe*” Towner and Dave “*big-curved-belly*” Wallis.

I thank my parents for their constant support and I dedicate this thesis to them.

Contents

1. Introduction.....	1
1.1. The process of <i>in situ</i> detection of meteoroids.....	2
1.1.1. Step 1: Exposure and retrieval.....	2
1.1.2. Step 2: Data collection.....	3
1.1.3. Step 3: Data reduction.....	3
1.1.4. Step 4: Simulation.....	4
1.1.5. Step 5: Analysis and modelling.....	6
1.2. Hypervelocity impacts.....	8
1.2.1. The hypervelocity impact process.....	9
1.2.2. Thick targets.....	10
1.2.3. Thin targets.....	10
1.2.4. Oblique impacts.....	11
1.2.5. Brittle materials.....	12
1.3. Recent <i>in situ</i> detectors.....	13
1.3.1. EURECA and TICCE.....	14
1.3.2. HST.....	16
1.3.3. Euromir.....	17
1.4. The UKC light-gas gun.....	17
1.5. Thesis overview.....	21
2. The Timeband Capture Cell Experiment.....	23
2.1. Description of the Experiment.....	24
2.1.1. Mechanical configuration.....	24
2.2. Data collection.....	25
2.2.1. Scanning procedure.....	25
2.2.2. Hole diameters.....	26
2.2.3. Calibration of the SEM.....	27
2.2.4. Foil thickness.....	34
2.3. Hole-shape analysis.....	37
2.3.1. Morphological classifications.....	39
2.3.2. Quantitative shape analysis.....	41
2.3.3. Correcting the TICCE data.....	46
2.3.4. Hole circularity.....	49
2.3.5. Hole shape.....	53
2.4. Summary.....	55
3. Oblique hypervelocity penetration of thin metal targets.....	56
3.1. Introduction.....	56
3.1.1. Previous studies.....	56
3.1.2. Experimental aims and rationale.....	59
3.2. Experimental procedure.....	60
3.2.1. Measuring the independent parameters.....	61
3.3. Experimental results.....	64
3.3.1. Measurement procedure.....	69
3.4. Analysis.....	74
3.4.1. Multiple regression analysis.....	80
3.4.2. Evaluation of the fitted models.....	97
3.4.3. Material effects.....	99
3.5. Discussion.....	100
3.5.1. Comparison with previous work.....	100
3.5.2. Summary.....	107
4. Oblique impacts on EURECA and HST solar cells.....	110
4.1. Solar cell impact scanning.....	110

4.1.1. EURECA and HST commercial scanning	111
4.1.2. Definition of crater parameters	113
4.1.3. Scanning of the Unit's HST samples	115
4.2. Oblique impact analysis.....	119
4.2.1. Impact azimuth angle	120
4.2.2. Impact elevation angle	129
4.2.3. Correlation of crater size with location.....	130
4.3. Discussion	131
4.3.1. Distributions and correlations of "oblique impact" parameters.....	132
4.3.2. Impact experiments	133
5. Oblique impact experiments on solar cells	134
5.1. Introduction	134
5.1.1. Previous studies.....	134
5.1.2. Experimental aims and rationale.....	135
5.2. Experimental procedure.....	135
5.2.1. Targets and Projectiles	136
5.2.2. Experimental procedure	136
5.2.3. Velocity variation	139
5.3. Experimental results	143
5.3.1. Measurement procedures	144
5.3.2. Processing the raw data	146
5.4. Analysis.....	150
5.4.1. Morphological observations.....	150
5.4.2. Comparison of glass and solar cell craters	152
5.4.3. Regression analysis	154
5.5. Discussion	166
5.5.1. Dependence of solar cell crater parameters on impact angle.....	166
5.5.2. Comparison with aluminium craters.....	167
5.5.3. Comparison with space impacts.....	168
5.5.4. Comparison with previous work.....	169
5.5.5. Summary.....	169
5.5.6. Follow-up experiments.....	170
6. Survivability of buckshot projectiles upon launch in the light-gas gun	173
6.1. Experimental method.....	174
6.1.1. Targets	174
6.1.2. Projectiles	175
6.1.3. Experimental method	182
6.2. Results	182
6.3. Analysis.....	191
6.3.1. Collecting the shape data	191
6.3.2. Size distributions	194
6.3.3. Aspect-ratio distributions.....	202
6.3.4. Shape distributions	204
6.4. Discussion	206
6.4.1. Summary of main results	206
6.4.2. Comparison with previous similar studies.....	207
6.4.3. Implications for previous, current and future studies.....	207
6.4.4. Future recommendations	208
7. Discussion: Interpreting space data	209
7.1. Statistical analysis of flux distributions	209
7.1.1. Previous analyses of flux distributions	210
7.1.2. A formal numerical approach	212
7.1.3. Parametric tests.....	213

7.2. Thin metal target penetrations	214
7.3. Solar cells	216
7.3.1. Applying laboratory calibration to space data.....	216
7.3.2. Space calibration	217
8. Summary	220
8.1. Oblique impacts in space	220
8.1.1. TICCE.....	220
8.1.2. EURECA and HST.....	220
8.2. Oblique impacts in the laboratory	221
8.2.1. Oblique penetration of metal targets.....	221
8.2.2. Oblique impacts on solar cells	221
8.2.3. The light-gas gun buckshot technique	222
8.3. Other work by the author	222
8.3.1. 3D stereo analysis: a new technique for measuring craters	222
8.3.2. ESEF-Euromir '95: Dustwatch-P	223
8.3.3. The Van de Graaff top-terminal monitor.....	224
8.4. Future recommendations	224

References

Appendix A – Regression Theory

Appendix B – TICCE perforations

Appendix C - Oblique solar cell impact programme: images and data

Appendix D - Images of Van de Graaff glass impacts

Appendix E – Program Listings

1. Introduction

Hypervelocity impact features on spacecraft surfaces bear witness to the fact that the near-Earth environment is populated with particles moving at high relative velocities. These particles are of two primary origins, namely natural cosmic dust and man-made space debris. Natural particles are of interest to space scientists as they confer information about their parent bodies, namely asteroids and comets. These bodies are representative of the prevailing conditions at the dawn of the solar system some 4.6 billion years ago as they have been not been significantly modified since that time. In contrast, the larger planetary bodies of the solar system have undergone aeons of geological processing. The effect that high velocity encounters with both natural and man-made particles have on spacecraft structures is of vital concern to spacecraft engineers, due to the destructive potential of a hypervelocity impact. Consequently, the spacecraft engineer is concerned with the rate of degradation of materials under hypervelocity impact conditions and the projectile-size-to-impact-probability relationship. The space scientist, however, is keen to extract as much information as possible about the impacting particles from hypervelocity impact features in order to study the natural particulate environment of the solar system.

In order to either predict the effects of a hypervelocity impact, or conversely to infer the nature of an impact after the event, we need to establish relationships between the relevant impact parameters and the resulting impact features. Before embarking on a discussion of these relationships, it is important to distinguish what sort of phenomena we are concerned with, namely those impacts that count as “hypervelocity” (covered in section 1.2). The evolution of a hypervelocity impact is complex. The interaction of shock waves in the impact region is inherently non-linear such that the material dynamics cannot be derived analytically and must be studied numerically (Melosh, 1989). Consequently, most established relationships between impact feature and impactor are purely empirical. Occasionally generalised energy-volume relationships are formulated but the most rigorous semi-theoretical treatments involve brute-force hydrodynamic computer simulations. Some of these “hydrocodes” have elaborations such as material strength models, the most recent of which include models to reproduce fracturing of brittle targets.

The most common empirical studies involve impact experiments using novel acceleration techniques. However, the field of ground-based simulations of space impacts is dogged by the fact that with currently available acceleration techniques we can only just touch upon the edges of the mass-velocity regime encountered in near-Earth space. For some highly sensitive instruments this is not the case such as the plasma type detectors flown on interplanetary missions. For these instruments we can achieve good coverage of the mass-velocity regime for all but the fastest interstellar particles that may be encountered ($> 200 \text{ km s}^{-1}$) using electrostatic acceleration techniques. This is because the particles these detectors are designed to record are small ($\sim 1 \mu\text{m}$). However, it is still not possible, even with the most highly tuned guns and electrostatic accelerators, to simulate typical impacts by cometary and asteroidal grains on spacecraft surfaces.

Consequently, interpretation of such impacts almost invariably relies on extrapolating empirical relationships beyond the limits of the data from which they were derived.

A facet of understanding impact processes in space is the investigation of behaviour under impact from an oblique angle. Impact angle studies are often given low priority in investigation of a material's response to hypervelocity impact with other parameters such as projectile size, velocity and density being initially studied. In this respect some empirical laboratory relationships have been applied to decoding space cratering records with insufficient or no consideration of the effect of impact angle. The author has identified, in his analysis of space-flown surfaces and in literature concerning the application of empirical relationships to space data, two areas where oblique impact studies are lacking. These are penetration of aluminium foils and impacts on solar cells. This thesis reports the observation of these phenomena on space-flown materials and the results of experiments performed in order to gain a new understanding of oblique hypervelocity impacts in these two scenarios.

1.1. The process of *in situ* detection of meteoroids

The process of *in situ* detection of meteoroids (and space debris) is as follows:

1. Spacecraft surface or dedicated detector is returned from Low Earth Orbit (LEO).
2. The retrieved surface is scanned for impact features.
3. The size distribution of impact features thus acquired characterises this exposure.
4. Impact experiments are performed to relate the desired impactor parameters - usually size - to the impact feature dimensions.
5. The distribution of impact features is converted to a distribution of inferred impactors.

The aim is to infer from the *sample* the parameters of the meteoroid and debris *populations*. The previous sentence is, of course, the definition of *statistics*. Thus, *in situ* detection of meteoroids and space debris is an intrinsically statistical subject where we want to infer what we can about the population being sampled; compare new samples with old ones and with theoretical distributions; look for *significant* differences and determine how *confident* we are about our knowledge of the population. However, in the author's opinion, formal statistical analyses of impact distributions are lacking in the field. Accordingly, some recommendations as to how to quantitatively analyse impact flux data are given in the discussion section of this thesis (section 7.1).

1.1.1. Step 1: Exposure and retrieval

This has only been possible since the start of the space shuttle era and later was also viable through *Mir-Soyuz*. Previous to this, surfaces exposed in space were not available for inspection post-flight, with a few exceptions such as retrieved lunar rock samples and Gemini and Apollo re-entry capsule surfaces. Detectors in the pre-shuttle era relied on making *in situ* measurements of impact events with subsequent down-link of the data.

Some of the first *in situ* techniques included rupture of thin wires on satellites 1958 α and 1958 γ and abrasion of an optically thick coating on *Vanguard III* (1961). However, the first reliable measurement of the meteoroid flux was made using the penetration sensors on *Explorer XVI* and *Explorer XXIII* (1963). The *Explorer* sensors consisted of pressurised beryllium-copper containers or “beer cans”, containing pressure transducers that registered a penetration of the 25 μm and 50 μm thick walls. The *Pegasus* series of satellites improved upon the *Explorer* measurements, using a capacitance discharge technique to detect penetrations (sensing surface of 200 m^2). The *Ariel II* detector used an optical transmission technique to detect penetration, extending the sensitivity to smaller sizes than *Explorer* and *Pegasus*. Another significant early experiment was the *Meteoroid Technology Satellite* (MTS), which employed a capacitance discharge sensor to give sensitivity comparable to 1 μm thick foil. In addition to these dedicated detectors, early incidental witness surfaces were available from *Gemini 9* and *Gemini 12*.

Lunar rock samples have been examined in an attempt to calculate the meteoroid flux over a long period. Fluxes measured on lunar rocks vary between different investigators over several orders of magnitude, reflecting both the different exposure conditions of the samples and the different dating techniques employed (Ashworth, 1978).

1.1.2. Step 2: Data collection

The author has experience with this procedure for two of the Unit’s recent space-deployed meteoroid/space-debris detectors. It involves laborious microscopic inspection of the retrieved surface for generally micron scale impact features. The man-hours required for this process has been greatly reduced in the Unit thanks to the in-house construction of an automated scanning facility (Paley, 1995), an enhancement of which is presented in this thesis. Once impact features have been located they must be accurately measured. Occasionally chemical analysis of any impactor residues is also possible

1.1.3. Step 3: Data reduction

Step 3 usually involves the plotting of the *cumulative size flux distribution*. The *cumulative* size distribution is invariably used for historical reasons because early spacecraft detectors were *threshold* detectors in that they only recorded the cumulative number of events occurring above a certain threshold: usually the ballistic limit of a metal foil. Also, where there is a paucity of data it is not always possible to group the data thus the cumulative distribution must be used. However, in the author’s opinion the differential distribution should be used whenever appropriate as it is more intuitively interpreted than the cumulative distribution and statistical tests for differential distributions are more abundant and simpler than those for cumulative distributions. Furthermore, fitting a functional form to a differential distribution is simpler than for a cumulative distribution where the application of *least-squares* is dubious (section 7.1). Methods for working with distributions are discussed in section 7.1. Figure 1.1 shows the results from these early detectors in the context of a currently used meteoroid model, derived by Grün *et al.* (1985). The *Explorer* data

remains a relatively reliable source: it is within a factor of 2-4 of the Grün meteoroid model. The close agreement of the *Pegasus* data and the Grün model follows from the fact that the model uses the *Pegasus* data for its absolute flux magnitude. The MTS data from the longer exposure shows good agreement at small sizes. The *Ariel II* and *Gemini* data, in recording either none or a maximum of 1 impact, can only give an upper limit to the flux (McDonnell, 1978).

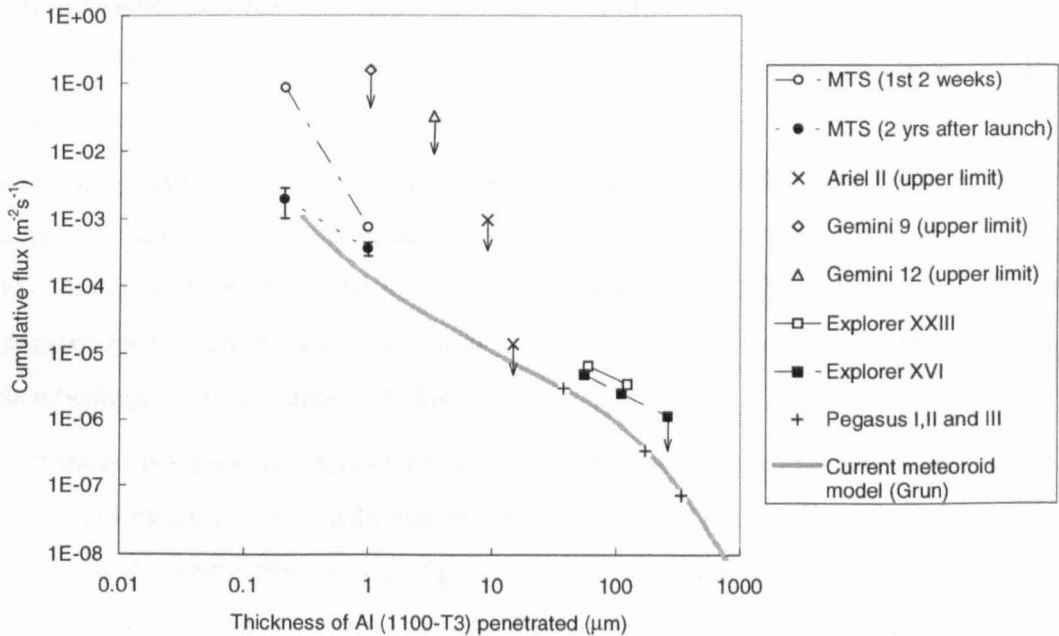


Figure 1.1 – Results from early spacecraft detectors (McDonnell, 1978) compared to a current meteoroid model (Grün *et al.*, 1985)

1.1.4. Step 4: Simulation

Step 4 requires the ability to produce impacts in the laboratory under controlled conditions such that the projectile parameters are tightly constrained. Currently available techniques for producing hypervelocity impacts in the laboratory are of the following types:

- **Explosive** – An explosive charge accelerates the projectile. This often disrupts the projectile and produces unwanted debris. A variation of this technique accelerates the target plate, which impacts a stationary projectile. Another type is the *shaped charge accelerator*, which although is capable of velocities up to 16 km s^{-1} requires determination of the projectile size and shape in-flight.
- **Light Gas Gun** – The Light Gas Gun is a modified version of a conventional gun. The thermal velocity of the expanding gas (gunpowder) limits the speed of conventional guns to around 1 km s^{-1} . Therefore, in a light gas gun, a conventional gunpowder charge is used to compress a light gas (helium or hydrogen) which has a higher mean molecular speed. Upon release of pressure the projectile is accelerated to up to several km s^{-1} .
- **Electrostatic** – Charged particles are accelerated through a large potential difference; the most common type is based on a *Van de Graaff* arrangement. High velocity and particle size resolution is possible, as undesired particles can be electrically deflected from the beam. This

technique provides the highest recorded velocities in the laboratory (over 100 km s^{-1}), but is limited to micron scale particles.

- **Plasma drag** – To raise the temperature of an accelerating gas above what can be achieved by chemical energy (such as in the Light Gas Gun), the gas can be heated by an electrical discharge. A plasma drag accelerator discharges a large capacitor through a gas or metal creating plasma that has a velocity of some $30\text{-}50 \text{ km s}^{-1}$ that subsequently accelerates the projectile by aerodynamic drag. However, such drastic heating can result in projectile disruption.
- **Electromagnetic** – An accelerator employing electromagnetic interaction is the parallel electric *rail gun*. A conducting projectile is placed in sliding contact with two parallel rails and when the current flows from rail 1 through the projectile to rail 2, the interaction of the current and the magnetic field produces velocities of up to 6 km s^{-1} ; though, the current technology has little advantage over the Light Gas Gun.

Figure 1.2 shows the projectile diameter and velocity regimes covered by these various accelerator technologies compared to the distribution of interplanetary and interstellar dust and orbital debris. It can be seen that only the *Van de Graaff* gives adequate coverage of meteoroid velocities and then only at the micrometre scale. The Light Gas Gun is suitable for simulating impacts of orbital particles over a relatively large size range such that the effect of impacts by untrackable debris (*National Research Council, 1995*) at mm sizes can be investigated. A review of laboratory simulation techniques is given by Fechtig *et al.* (1978).

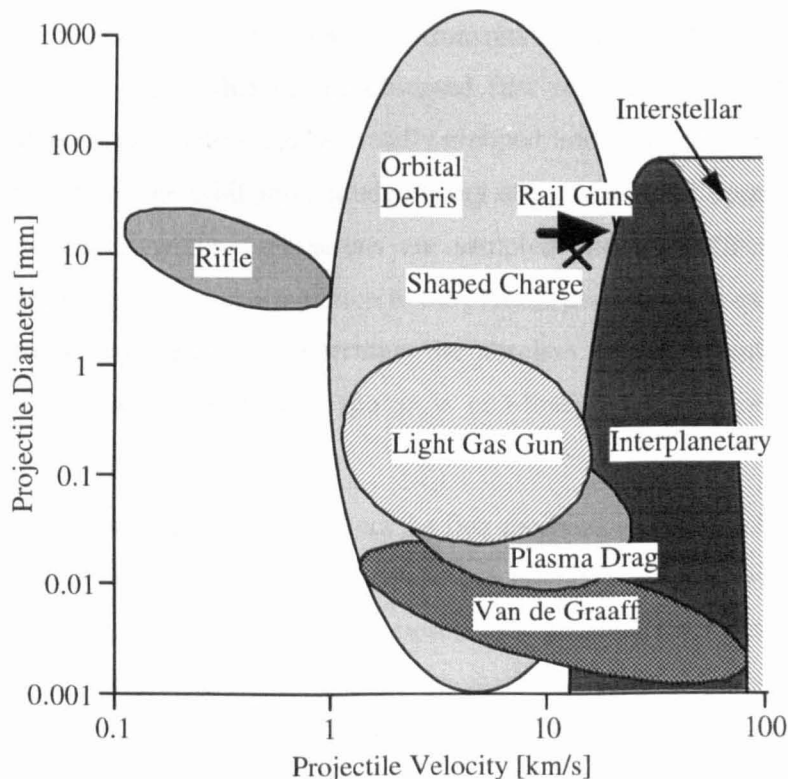


Figure 1.2 – Particle diameter-velocity regimes covered by laboratory accelerators

To extend the data set beyond what can be achieved by laboratory simulations, computer codes that simulate the impact process can be used. The most commonly used codes model primarily the hydrodynamic phase of crater formation, where the pressures are higher than the material strength, and are thus known as *hydrocodes*. The codes incorporate two models: (i) an equation of state (EOS), which describes the thermodynamic state of the material; (ii) a strength model that determines the material's resistance to distortion. The models used are usually derived from laboratory simulation results and the behaviour is extrapolated to regimes unattainable in the laboratory. Figure 1.3 shows stages in crater formation using a hydrocode, giving an interesting insight into the intermediate crater morphologies.

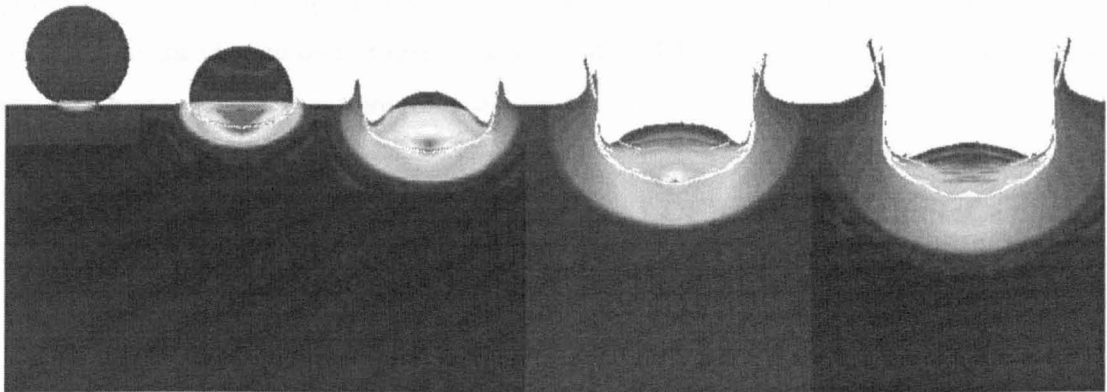


Figure 1.3 – Computer simulation of an iron sphere impacting a copper surface at 10 km s^{-1} using Century Dynamics' *Autodyn-2D*TM hydrocode

1.1.5. Step 5: Analysis and modelling

The ultimate aim of *in situ* detection of meteoroids and space debris is to learn what we can about their sources and evolution. Data from different instruments has to be reduced to take into account differences between them that influence the observed flux such that they can be appropriately compared. *In situ* detector parameters can be broadly grouped into two types: (i) Orbital parameters and (ii) material properties. The orbit and attitude history of the spacecraft upon which the detector is mounted will determine which populations are sampled and will effect the flux received dependent on the relative motion and orientation to the particle population in question. The detector material and corresponding signal will determine the abscissa of each event recorded and thus effects the “location” – and shape if the response is non-linear – of the distribution of impacts recorded.

The velocity of the detector will, of course, effect the flux received, as the flux is the spatial density of particles multiplied by the relative velocity. There are effects associated with proximity to the Earth that must be considered when comparing impact rates in near-Earth space. The first of these is *gravitational enhancement*, whereby the Earth's gravitational well has the effect of accelerating particles and focussing their trajectories, increasing both the velocity and the spatial density and therefore the flux. The second effect is *Earth shielding*, whereby a proportion of the viewing solid angle of the detector is masked off by the Earth. McDonnell *et al.*, (1998) give the appropriate formulation of the correction required for these two factors. For comparing the data from two

different detectors, the relationship between the “signal” recorded on each detector must be known or for comparison to a meteoroid model, for example, the relationship between the signal and the particle parameters.

The current effort in modelling meteoroid and space debris is to include directional dependence in what were previously isotropic models. McBride *et al.*, (1999) show how comparison of fluxes encountered by LDEF and EURECA can lead to an understanding of the relative contributions of orbital debris and sporadic and stream meteoroids. Figure 1.4 taken from McBride *et al.* (1999) illustrates how flux differences between LDEF and EURECA can be modelled in terms of different sampling of meteoroids and space debris due to their different stabilisation: gravity gradient and sun-pointing respectively. The higher flux on LDEF’s Earth-orbital ram face at small sizes is attributed to enhanced sampling of orbital debris and EURECA’s enhancement at larger sizes can be explained by favourable exposure to stream meteoroids.

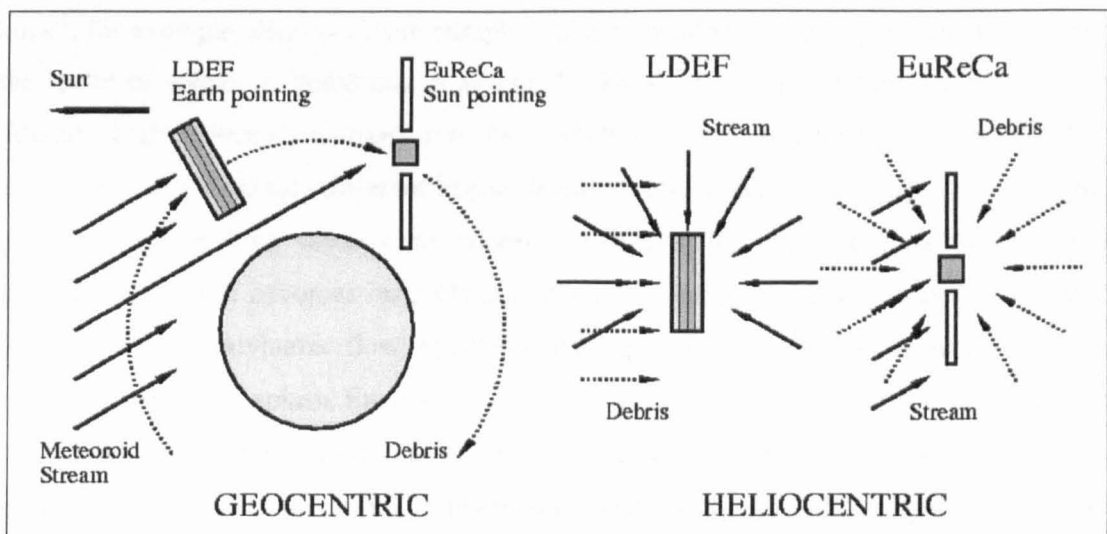


Figure 1.4 – Different sampling of meteoroids and space debris for two differently stabilised spacecraft (source: McBride *et al.*, 1999).

This demonstrates one way of investigating anisotropy by comparing differently oriented detectors. Another way is to determine particle trajectories from impact feature morphology. The extent to which this can be achieved for two types of exposed surface is investigated in this thesis.

McBride *et al.* (1999) also demonstrate how a meteoroid model derived from measurements away from the Earth, comprising lunar microcrater fluxes and heliocentric spacecraft measurements (HEOS II and Pegasus) at 1 AU from the Sun, can be used to model the flux on a spacecraft in near-Earth space, namely LDEF. They take the mass distribution model of Grün *et al.* (1985) and the meteoroid velocity distribution of Taylor (1995) and using the appropriate gravitational enhancement and Earth shielding factors “transform” the flux from 1 AU away from the Earth to LDEF’s altitude (a vertical shift of the flux distribution ordinates). Using empirical impact equations they transform the flux distribution from particle masses to the relevant detector signal (a horizontal shift of the flux distribution abscissas), in the case of LDEF the aluminium ballistic limit. The results show that the fluxes recorded on LDEF’s “space” zenith-pointing face agree “well” with the model and accordingly conclude that the space face is dominated by meteoroids.

They note that LDEF's "East" Earth-orbital ram face shows a "striking excess" above the meteoroid model prediction at small sizes ($< 30 \mu\text{m } F_{\text{max}}$) and accordingly attribute this excess to orbital debris. However, the empirical impact equations used were derived from laboratory impacts with impact trajectories normal to the target surface *only*. The ballistic limit calculation for angles away from the normal is performed using an *assumed* $\cos\theta$ dependence, unsupported by any experimental results. This thesis investigates the penetration behaviour of aluminium with impact angle and relative plate thickness and is thus able to evaluate the accuracy of this assumed dependence.

1.2. Hypervelocity impacts

The most commonly used definition of a hypervelocity impact is one where the impact speed exceeds the speed of sound in the target and projectile (Fechtig *et al.*, 1978). This is by no means rigorous though. In the author's experience impacts of aluminium on aluminium at around 4.5 km s^{-1} , for example, display all the paraphernalia associated with a "hypervelocity" impact and yet the speed of sound in aluminium is around 5.1 km s^{-1} . Impacts at lower velocities – but still considered "high velocity" in most spheres – such as those produced by high-velocity rifles ($\sim 1 \text{ km s}^{-1}$) produce strikingly different impact features. The reason for the disparity in morphology is that at sufficiently high velocity the energy imparted at the point of impact is such that the strength of the material becomes insignificant. When this happens the displacement of material is characterised by hydrodynamic flow; hypervelocity impact features in most common metal targets resemble a frozen liquid splash. Energy is also released in an electromagnetic pulse, often visible as a flash of light, and in shock waves induced in both the projectile and target. Although the material strength plays little part in the initial hydrodynamic phase of the impact process, in some cases the key characteristics associated with the final morphology of the impact feature result from the material's response to the induced shock waves and the resistance of material further away from the point of impact to the pressures induced by the hydrodynamic flow. This is the case for impacts in brittle targets such as glass and rock.

The 4th edition (1989) of the McGraw-Hill *Dictionary of Scientific and Technical Terms* defines hypervelocity as the muzzle velocity of an artillery/small-arms projectile that exceeds around $1\text{-}1.5 \text{ km s}^{-1}$. However, this definition from the sphere of military ballistics is not what is widely accepted in the space science field as hypervelocity, where velocities much higher than this are at the lower end of the velocity range commonly encountered. Fechtig *et al.* (1978) provide a good definition of what is commonly accepted as "hypervelocity" and give a brief summary of the hypervelocity impact phenomenon:

"Collisions in interplanetary space generally occur at hypervelocity speeds, i.e. impact speeds which exceed the speed of sound in both colliding bodies (above approximately 5 km s^{-1}). In this case shock waves propagate from the interface between the colliding bodies into both of them, compressing and heating up the

affected material. If they reach free surfaces, rarefaction waves start to propagate in the opposite direction, unloading the compressed material. As a result of these shock and rarefaction waves the material will fragment, melt and even evaporate. Light is emitted from the hot vapour and ionisation takes place. In the remaining solid material, decaying shock waves become elastic waves travelling at the speed of sound.”

1.2.1. The hypervelocity impact process

The process described above results in a characteristic crater shape in metallic, ductile targets as shown in Figure 1.5. The characteristics are a smooth, bowl-shaped crater with “lips” round the edge indicating outward flow of molten material.

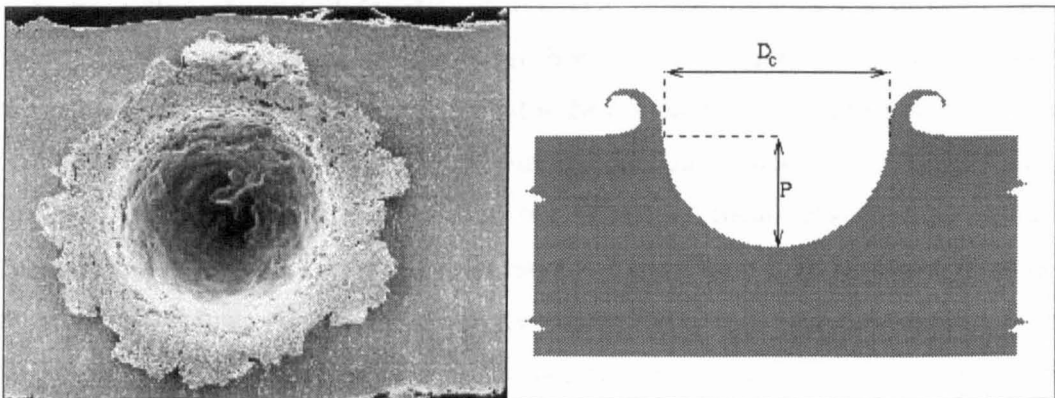


Figure 1.5 – A hypervelocity impact crater in a “thick” target and simplified profile showing characteristic measurements (source: Gardner *et al.*, 1997b)

Figure 1.5 also shows the approximate crater profile and the characteristic measurements that are normally taken, namely the diameter measured in the plane of the original surface (D_c) and the depth from the original surface to the bottom of the crater (P). Gardner (1995) gives another useful summary of phenomena associated with hypervelocity impact (chiefly describing metallic targets):

1. *The projectile has sufficient energy to cause its own disruption, often by melting or vaporisation. It is rare for the crater formed in the target material to contain more than a trace of the projectile material.*
2. *The impact velocity is sufficiently high (and hence the process over so quickly) that the energy of the impactor cannot be dissipated throughout the target and effectively confined to a small volume of the target material.*
3. *Pressures caused by the impact are such that the strengths of the impactor and target materials are negligible in the early stages of the impact.*
4. *The shock-induced heating is sufficient to produce phase changes in the material. Depending on the impact velocity and materials concerned, these may include melting, vaporisation and impact plasma production.*
5. *Lips are formed on the front of the target and if it is penetrated then they also form on the rear, as shown in Figure 1.6*

6. Whilst the formation of a shock-wave requires the impactor to exceed the target's sound speed, no sudden transition is observed in the final crater shape as impact velocity is increased through this point.

In the author's experience the presence of lips round the rim of the crater, as shown in Figure 1.5, are enough for a crater to be classified by the investigators as "hypervelocity". Non-hypervelocity craters, often referred to as "bullet speed" as such craters are most likely formed at speeds within the range attained by conventional firearms, include craters that appear as dents with no lips or as scratches in the surface.

For space flown hypervelocity impact detectors there are two key impact regimes: (i) the target is thick enough so that the impact behaviour is indistinguishable from a hypothetical semi-infinite target (i.e. an infinite expanse of material on one side of the plane of the surface); (ii) effects associated with the rear surface of the target become significant. For first investigation of hypervelocity impacts all impacts are considered to be normal to the target surface. Consideration of behaviour at impact angles away from the normal (*oblique impacts*) is of course required to interpret "real" impact phenomena. The behaviour of ductile, metal targets under hypervelocity impact is relatively simple (all craters, more or less resemble Figure 1.5). However, there is a large cratering record from lunar rock samples and materials displaying *brittle* impact phenomena such as retrieved solar cells. Impact phenomena associated with brittle targets are far more complex and variable than for ductile targets.

1.2.2. Thick targets

Craters in thick targets are usually characterised by their depth-to-diameter ratio (P/D_c), which gives an indication of projectile velocity and density. Craters formed in the hypervelocity regime generally become shallower with increasing velocity and decreasing density. As a first approximation in the process of relating the crater size and shape to impactor parameters, the crater is usually approximated to be hemispherical with its volume being proportional to the kinetic energy of the impactor. This leads to the crater depth being proportional to the $2/3$ power of the impact velocity, but experiments show this to be only an approximation over a wider parameter range (Cour-Palais, 1987).

1.2.3. Thin targets

Thin targets (usually foils) are used in space detectors, primarily to provide a simple count of the number of particles with sufficient energy to penetrate the target. However, much can be learned about particle size, shape and other parameters by study of individual craters and penetration holes. A key parameter in the consideration of thin target impacts is the target thickness f . There are several impact regimes defined by the ratio of the particle size to the thickness of the target at which changes in crater/hole size vary in different ways. Gardner *et al.* (1997a) have defined these different hole-growth regions with respect to Figure 1.6:

1. $D_h = 0$ (Figure 1.5): *cratering; the target is sufficiently thick that perforation does not occur.*
2. $0 < D_h < D_c$ (Figure 1.6a): *marginal perforation; the target is perforated, but this is due to late-stage tearing of the rear surface. Rapid growth occurs in this region ($\partial D_h / \partial d_p \gg 1$) and spall rather than “hypervelocity” lips form on the rear surface.*
3. $D_c \approx D_h \gg d_p$ (Figure 1.6b): *near-marginal perforation. In this region the rapid growth slows but $\partial D_h / \partial d_p$ is still greater than 1. The formation of rear-surface lips characterises this region, though they may not be fully developed.*
4. $D_h > d_p > f$ (Figure 1.6c), $\partial D_h / \partial d_p < 1$: *penetration; characteristic lips are fully developed on the rear surface. Although the impact is usually sufficient to vaporise or melt the particle, the damage to the projectile decreases as the hole diameter becomes closer to the particle size.*
5. $D_h \approx d_p \gg f$ (Figure 1.6d): *undisturbed penetration; the particle is not significantly damaged by the foil and effectively punches out its cross section.*

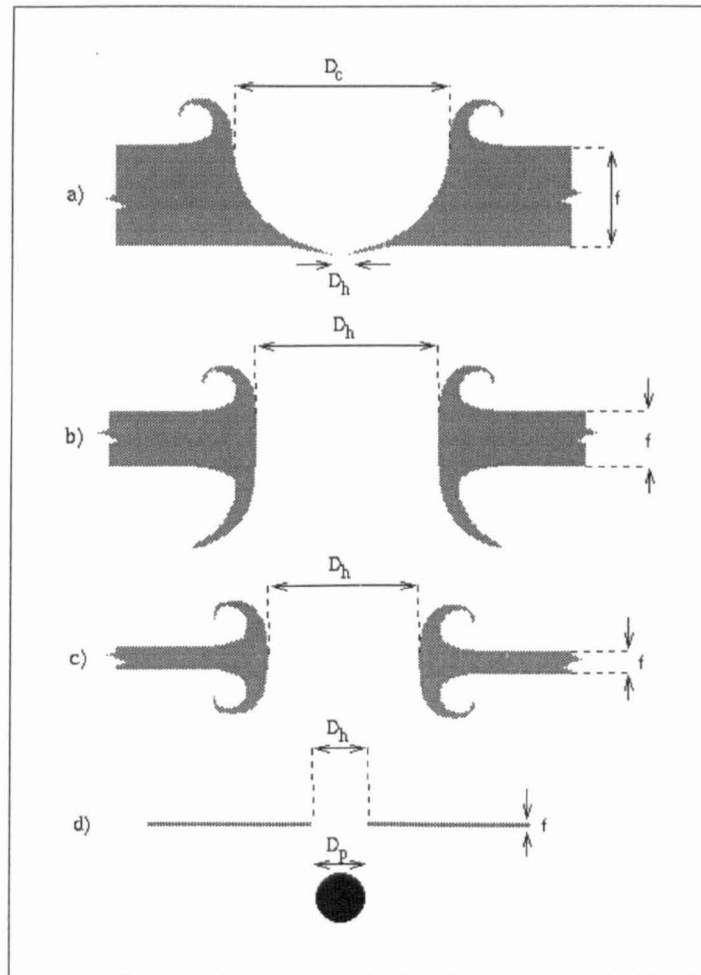


Figure 1.6 – Hole growth regions for thin target hypervelocity impacts
(source: Gardner, 1995)

1.2.4. Oblique impacts

Impacts from angles sufficiently far from the normal to the surface result in characteristic changes in crater shape (Figure 1.7): the crater becomes elongated along the line of flight, resulting in an elliptical or egg shaped plan view; the crater becomes shallower and the crater profile becomes

asymmetric, the forward wall becoming steeper than the rear wall; the lips on the forward edge become smaller or disappear altogether, whilst on the down-range side they become larger.

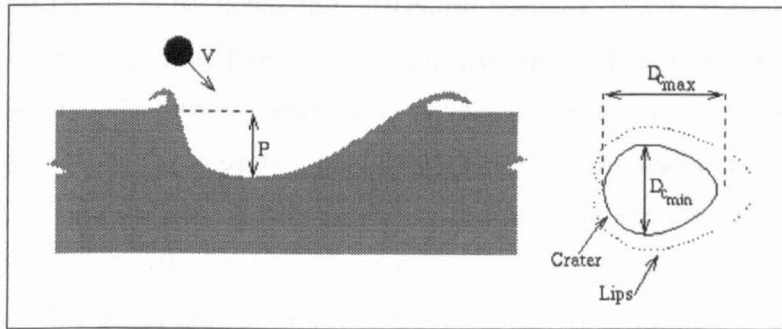


Figure 1.7 – Schematic of an oblique hypervelocity impact (source: Gardner, 1995)

For thick targets the depth, P , is measured as before. The crater or hole “diameter” parameter is most commonly defined as the geometric mean of the maximum and minimum diameters (Figure 1.7) i.e. $D_{c\ or\ h} = (D_{max} \times D_{min})^{1/2}$, which is equal to the diameter of a circle with equal area to that of the ellipse with axes D_{max} and D_{min} . The eccentricity or the simply the ratio of the maximum and minimum diameters are used as parameters for reconstructing the impact angle. Although this behaviour for thick targets has been well characterised, the behaviour of thin targets under oblique impact has received relatively little attention in comparison. It is fairly intuitive that for a sufficiently thin target the projectile will simply punch out its projection in the plane of the target, but what how does the transition from thick target to thin target behaviour take place? This is one of the questions to be addressed in this thesis.

1.2.5. Brittle materials

Features resulting from fracture and cracking, rather than hydrodynamic flow and plastic deformation, dominate brittle material crater shape. Brittle materials retrieved from space upon which hypervelocity impact features have been studied include lunar rocks, spacecraft windows and solar cells. Figure 1.8 shows a typical crater formed in glass. The damage to the surface extends over a much wider region than for the equivalent crater in a ductile target for the same impact conditions.

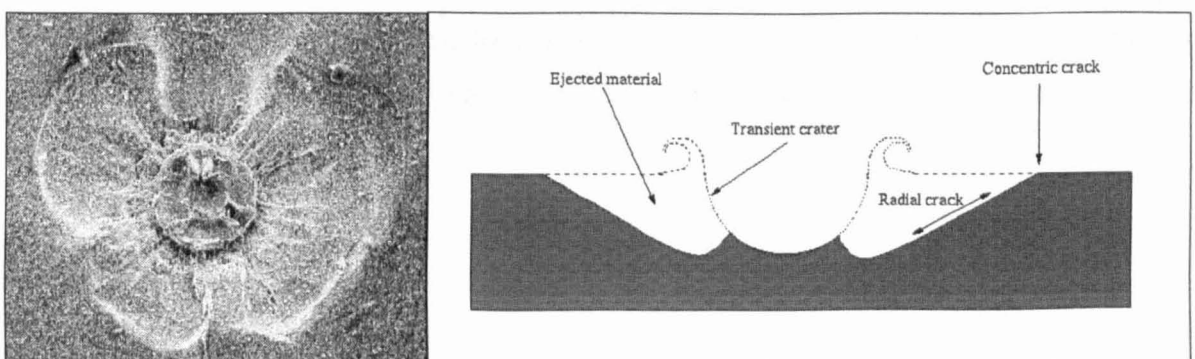


Figure 1.8 – Hypervelocity impact crater in glass and schematic of typical crater shape in brittle materials

The two main features of an impact crater in a brittle material are a central pit, surrounded by a *spalled* zone. The diameters of these features are usually used as characteristic parameters.

Formation of a crater such as that shown in Figure 1.8 begins in much the same way as a crater in a ductile target. However, stresses induced in the surrounding material by the expansion of the initial crater, in its molten phase, cause radial and concentric cracking. Where these cracks join up, the material bounded by them and the free surface is ejected, often taking most of the *transient* crater with it. Cour-Palais (1987) gives a description of the processes involved. As a result of this complex behaviour, relating the impacting particle parameters to the final crater parameters is more difficult than for metallic targets. However, due to the fact that the damage is much larger for brittle materials, their sensitivity for detecting impacts extends to smaller sizes. As with thin metal target penetrations, this thesis aims to improve the relatively poor understanding of how impact angle effects brittle target morphology: specifically, solar cells.

1.3. Recent *in situ* detectors

Some recent *in situ* measurements of near-Earth microparticle fluxes include the Space shuttle *Microabrasion Foil Experiment* (McDonnell *et al.*, 1984), the *Solar Maximum Mission* satellite (Warren *et al.*, 1989) and the *Mir-Aragatz* mission (Mandeville, 1990). By far the most important being NASA's *Long Duration Exposure Facility* (LDEF), which was a dodecagonal prism shaped satellite, 9.1 m long by 4.3 m wide, designed to study the exposure of materials to the space environment in Earth orbit. LDEF was deployed in April 1984 at 477 km altitude and 28.5° inclination by STS 41-C; it was planned to be retrieved a year later, but due to Shuttle manifesting problems, followed by the *Challenger* explosion, retrieval was delayed until January 1990, when it was retrieved at an altitude of 377 km by STS-32 (O'Neal and Lightner, 1991). This unprecedented exposure of 69 months resulted in the largest area-time product of any space-retrieved surface. Consequently, at the time of writing, LDEF is the most important previous data source for understanding the near-Earth particle environment and is the "baseline" against which subsequent experiments are often compared.

Figure 1.9 shows LDEF's gravity gradient stabilisation whereby the Earth face (Ea) is always Earth pointing and the space face (Sp) is always pointing 1.1° from zenith. The east face (E) is aligned 8° from the Earth-orbital ram direction and the north face (N) points to the north celestial pole (McBride *et al.*, 1999). As was described in section 1.1.5, this stabilisation results in different sampling of Earth-orbital particles on each face with exposure to meteoroid streams being generally randomised.

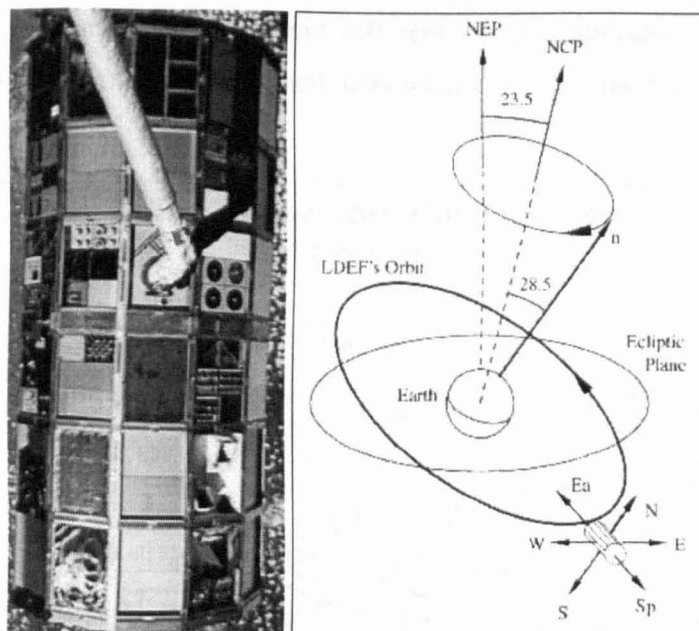


Figure 1.9 – The long duration exposure facility (LDEF) and orbital schematic (source: McBride *et al.*, 1999)

The missions since LDEF, relevant to this thesis, are introduced in the rest of this section.

1.3.1. EURECA and TICCE

ESA's European Retrievable Carrier (EURECA) is a reusable orbital platform, primarily for microgravity experiments. EURECA made its first (and, at the time of writing, only) flight during 1992/3. A diagram of EURECA and its orbital stabilisation strategy are shown in Figure 1.10. EURECA was released by STS-46 *Atlantis* on 2 August 1992 at 425 km altitude. It reached its operational orbit of 508×502 km and 28.5° inclination using its on-board thrusters on 7 August. It reached the end of its operational phase on 20 May 1993 at an orbit of 510×465 km. It then descended to an altitude of 481×470 km for retrieval by STS-57 *Endeavour* on 24 June with subsequent return to Earth on 1 July; thus giving a total exposure of 326 days.

With reference to Figure 1.10, the solar arrays and the +Z face of the spacecraft were Sun-pointing with an accuracy of $\pm 1^\circ$. The solar arrays did not rotate relative to the spacecraft body. The spacecraft +Y-axis pointed generally in the Earth apex direction, apart from during certain periods in April and May 1993 when rotations about the Z-axis were performed for experimental purposes. With this stabilisation, the flux of Earth-orbital particles will be averaged mainly over the +Z, -Z, +Y and -Y faces, with some access to the +X and -X faces. However, relative impact rates on EURECA's faces should bear a record of significant anisotropy of the interplanetary population.

EURECA-1 carried the Unit's *Timeband Capture Cell Experiment* (TICCE), a passive dust detector that was designed to additionally give time of impact information (Figure 1.11). TICCE was mounted so that that its normal vector was 45° between the +Y and +Z faces (Figure 1.10). In addition to TICCE, information about the particle flux encountered by EURECA was available in the form of a post flight analysis of EURECA's external surfaces, which included multilayer insulation blankets, aluminium signs and scuff plates and the solar array wings. Due to EURECA's

similar altitude and inclination to LDEF, but different orbital stabilisation (sun synchronous as opposed to gravity-gradient), the directional dependence of the particle environment can be investigated.

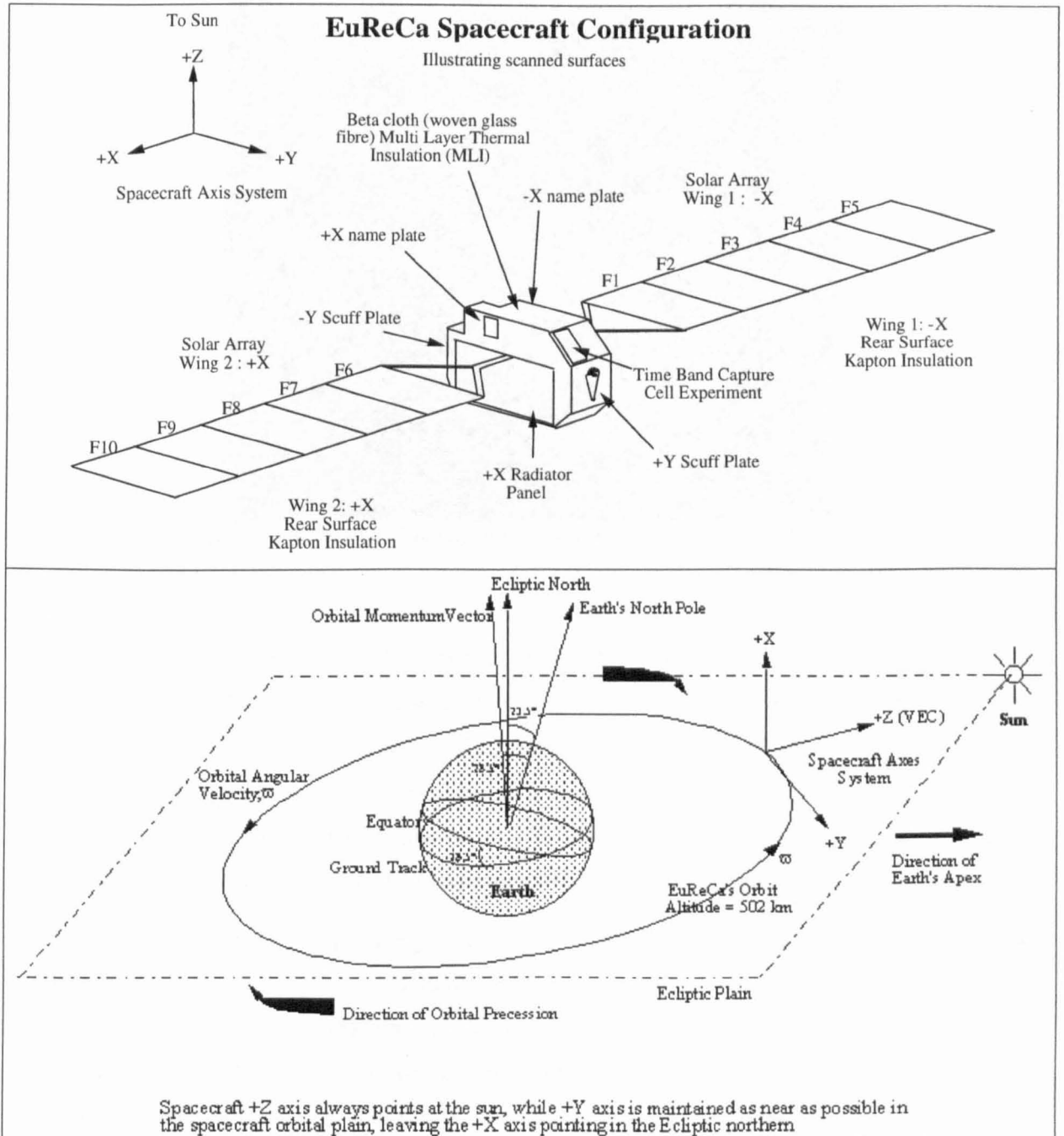


Figure 1.10 – EURECA configuration and orbital parameters (source: Unispace Kent)

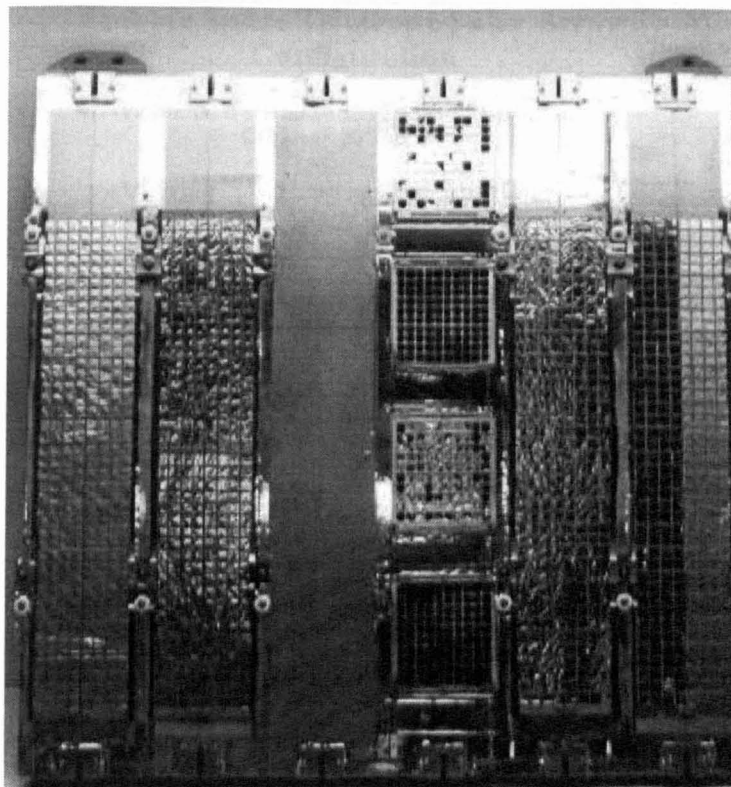


Figure 1.11 – The *Timeband Capture Cell Experiment (TICCE)*

1.3.2. HST

The Hubble Space Telescope (HST), NASA's (15% ESA) orbiting observatory, was deployed in its operational orbit of 614 km altitude and 28.5° inclination by STS-31 *Discovery* during 24-29 April 1990. During the first servicing mission (2-13 December 1993; STS-61 *Endeavor*) the -V2 solar array wing (Figure 1.12) was retrieved. The other wing could not be stowed due to a mechanical fault and was discarded in orbit to subsequently re-enter and burnt up. The retrieved 20.73 m^2 of solar array had been exposed to the LEO environment for almost $3\frac{3}{4}$ years.

The HST solar arrays were primarily maintained in a sun-pointing attitude. However, unlike EURECA the spacecraft body could rotate 360° about its attachment to the solar array wings. Consequently, the amount of shielding of the arrays offered by the spacecraft body was variable; similarly the potential for secondary impact production. Furthermore, HST was not maintained in a fixed attitude like EURECA, in that it is re-oriented to track different astronomical targets, and so has almost total freedom of pointing within the constraint that the telescope aperture is never Sun or Earth pointing. Accordingly we do not expect the directional signatures of individual impacts to divulge the source direction of impactors with respect to celestial or geocentric frames. Nevertheless, impact directions relative to the spacecraft axes might indicate the fraction of secondary impacts. This *quasi-random* orientation (arrays mainly sun pointing, but free to rotate) is expected to provide a telling comparison with the impact record from the approximately statically oriented EURECA solar arrays.

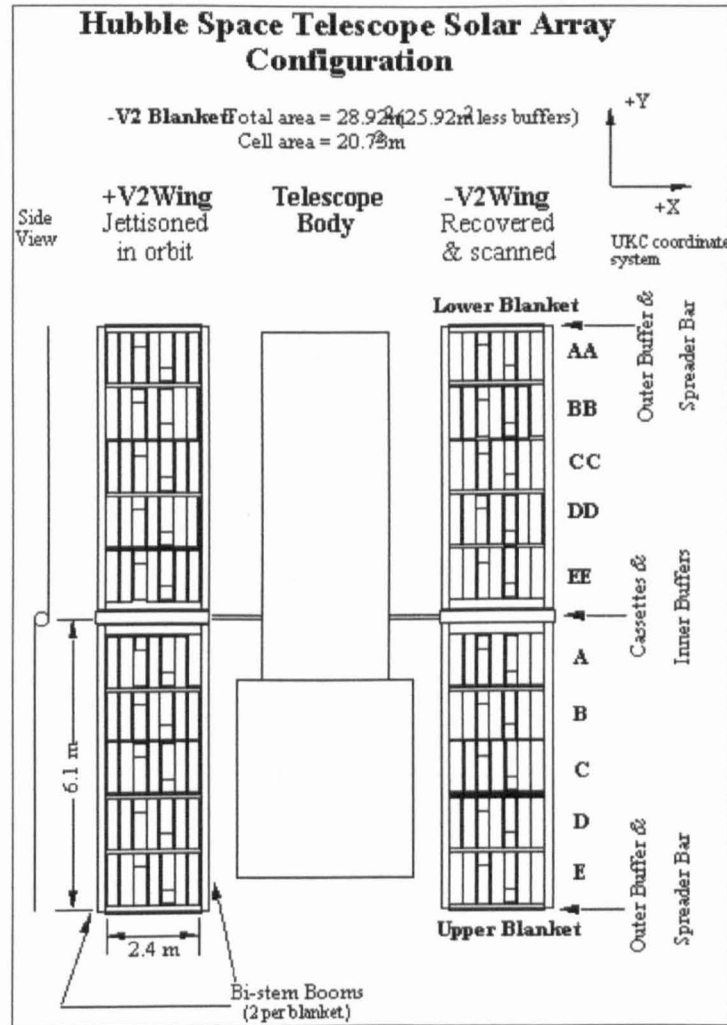


Figure 1.12 – HST configuration (source: Unispace Kent)

1.3.3. Euromir

As part of the ESA-Russian *Euromir '95* mission, a suite of passive and active detectors were flown by several institutes on a platform called *The European Space Exposure Facility* (ESEF). The USSA's contribution (*Dustwatch-P*) consisted of aerogel intact capture modules and thin foil capture cells. The author was responsible for the post-flight analysis these detectors. As these results are not of direct relevance to the primary line of investigation of this thesis they are not presented here. Although, oblique impact phenomena were identified and interpreted as ejecta from a large as-of-yet undiscovered impact site (Shrine *et al.*, 1997). It was found that the impact rate was compatible with LDEF.

1.4. The UKC light-gas gun

As the experiments in this thesis were performed using the Unit's light-gas gun, an introduction to this facility is now given.

The Unit for Space Sciences and Astrophysics at the University of Kent possesses a two stage light-gas gun that is capable of accelerating particles up to 3 mm in diameter to velocities of around 5 km s⁻¹; the current highest velocity achieved is 7.5 km s⁻¹. A piston driven by a powder charge compresses a volume of hydrogen gas, which upon attaining a sufficient pressure breaks an aluminium *burst disk* with subsequent release of the hydrogen into the adjacent *launch tube*

containing the projectile mounted in a nylon *sabot* flush with the burst disk. The expanding hydrogen accelerates the sabot down the launch tube, which is rifled, giving the sabot a rotational component. The sabot is pre-cut along its length into four quadrants so that as it leaves the launch tube it flies apart and is intercepted by an aperture through which the projectile, still travelling on axis, continues to the target. Before reaching the target the projectile passes through 2 laser curtains in order to record the velocity. During firing the range is evacuated to < 0.2 mb pressure to minimise deceleration of the particle in flight. A detailed description of the facility is given by Burchell *et al.* (1999). A photograph and schematic of the light-gas gun are shown in Figure 1.13; the photograph has been mirrored to correspond with the schematic.

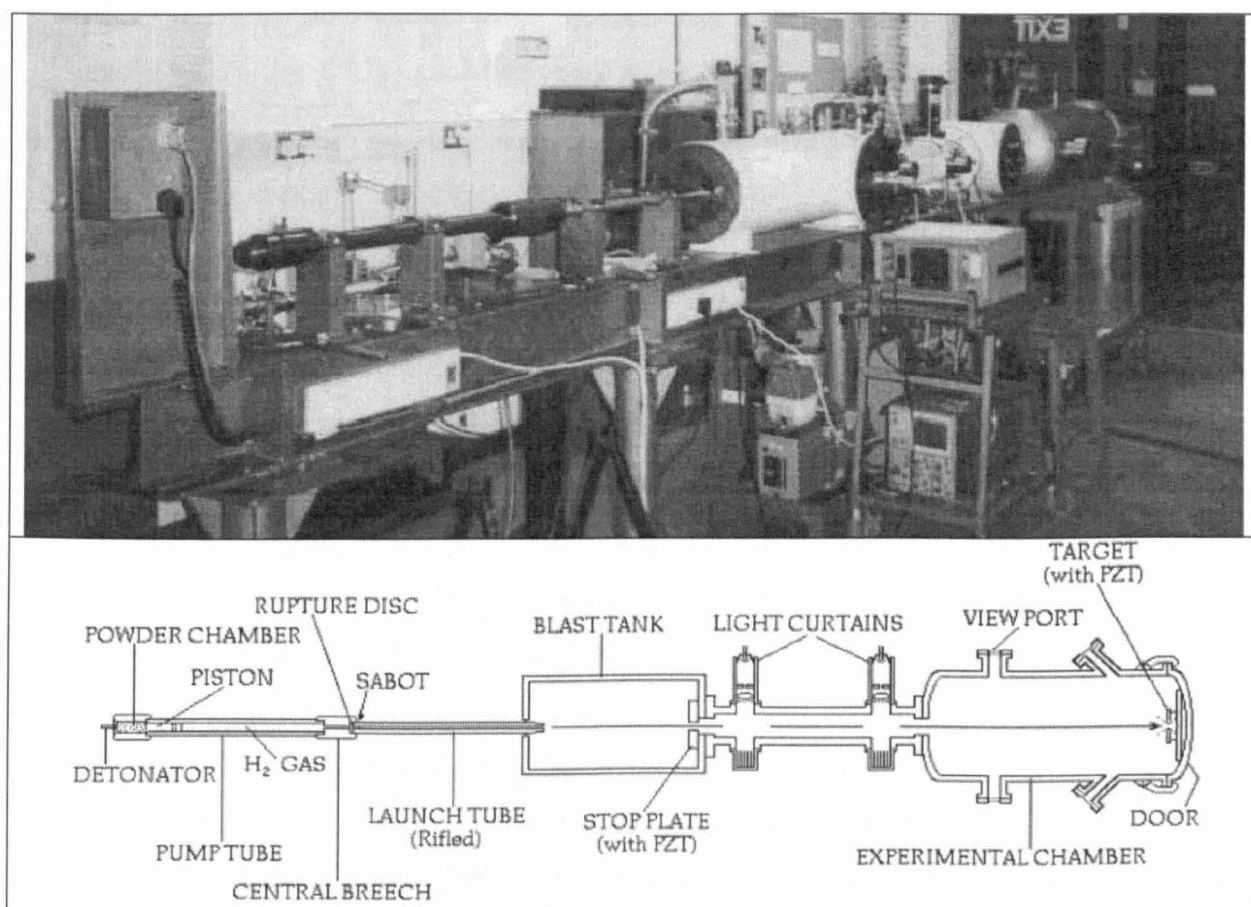


Figure 1.13 – The UKC light-gas gun

Firing procedure

The operation of the light gas gun is as follows:

1. The projectiles are loaded into a cylindrical nylon container (*sabot*) assembled from 4 quadrants, as shown in Figure 1.14. If the sabot is being loaded with a large number of small projectiles, as is the case for the experiments in section 5, the open end of the sabot is usually sealed with a steel ball bearing.

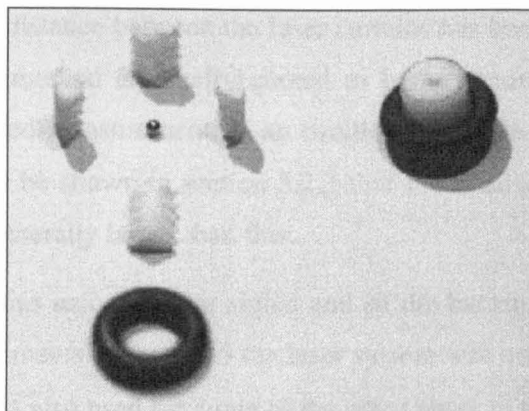


Figure 1.14 – A four-way split-sabot

2. The target is mounted in the target chamber and a piezoelectric crystal (PZT) is usually attached to the target to give a timing signal when the target is struck.
3. The sabot is placed in the launch tube, which is sealed with a burst disc. The range is now air tight and is evacuated to < 0.2 mb.
4. The central breech and pump tube are fastened to the launch tube. The pump tube is sealed at one end by the burst disc and at the other by a nylon piston. The pump tube is filled with hydrogen, normally to 45 bars; the velocity can be altered according to the initial pressure in the pump tube. A shotgun cartridge is loaded behind the piston. The gun is now ready for firing.
5. The shotgun cartridge is detonated which forces the piston along the pump tube compressing the hydrogen. When the hydrogen reaches the critical pressure, the burst disc ruptures and the sabot is propelled down the launch tube by the release of pressure in the pump tube.
6. The sabot enters the blast tank, spinning due to the rifling of the launch tube, travelling at several km s^{-1} . The quadrants of the sabot fly apart and impact the stop plate inducing an electrical pulse from a PZT attached to the stop plate giving the first timing signal. The projectiles contained in the sabot proceed through the aperture in the stop plate towards the target.
7. The projectiles pass through 2 laser curtains to give a velocity measurement, they then enter the experimental chamber and impact the target, to which is attached a second PZT to give the second timing signal.

Velocity measurement

The light-gas gun has two velocity measurement systems, the laser curtains and the PZT detectors. The laser curtains are focussed onto photodiodes the current from which is monitored by a digital oscilloscope. When obscuration of the beam occurs as projectiles pass through the laser curtains the output from the photodiode circuit rises. The time of flight between the curtains is usually measured between a point halfway up the leading edge of each of the two pulses from the first and second laser curtains. Using a sharply rising part of the pulse in this way minimises the uncertainty in position on the horizontal timebase axis. Some example oscilloscope traces are shown in

sections 5.2.3 and 6.2. The distance between the laser curtains has been measured as 499 mm. The velocity calculated by this method is usually quoted as being accurate to $\pm 50 \text{ m s}^{-1}$ (1%). The author has found by repeated measurement of an oscilloscope trace that this can be reduced to $\pm 30 \text{ m s}^{-1}$ (0.6%), but it will be shown in section 5.2.3 that 1% is adequate given that the velocity variation *between* shots is generally larger than this.

Occasionally the laser curtains record a poor signal and so the backup system has to be used. For the first 8 shots of the experiments in section 5 the laser system was not operational and so the PZT system had to be used. It was also used for some of the other shots in the experiments in this thesis when the laser curtain signals were unclear or not available. The time between the signals from the PZT on the stop plate and the target corresponds to the time of flight between them plus the time it takes the acoustic wave to traverse the material from the point of impact to the PZT. Thus the velocity is given by:

$$V = \frac{s}{t - x_1/c_1 - x_2/c_2}$$

where c_1 and c_2 are the speed of sound in the stop plate (mild steel) and target materials, respectively, and x_1 and x_2 are the distances from the closest impact to the PZT. s is the distance between the stop plate and the target and t is the time interval between the two pulses from each PZT. Figure 1.15 shows a stop plate after firing and the distance x_1 that is measured. The accuracy of this method is around 4% (Burchell *et al.*, 1999).

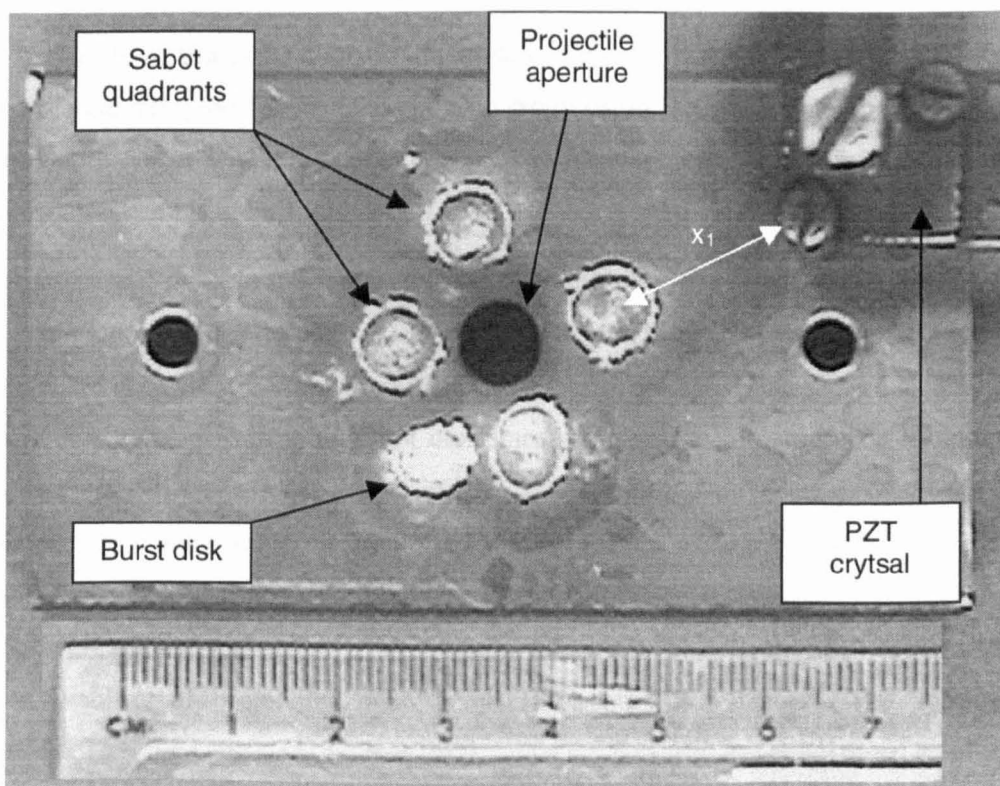


Figure 1.15 – Blast tank exit aperture (“stop plate”) after firing

1.5. Thesis overview

An overview of each section of this thesis is as follows:

1. An introduction of why *in situ* detection of meteoroids is important and what the key stages of the data collection and analysis process is given. An introduction to the hypervelocity impact process is given and a review of the results from recently flown detectors. Areas that require further investigation for interpreting oblique impacts in space data are highlighted.
2. The widely employed data set from the Unit's TICCE experiment is examined and previously unconsidered uncertainties are evaluated leading to corrections in the hole-size data, due to a previously unreported astigmatism of the SEM system, and the foil thicknesses, due to a more precise measurement. A new method of automatically measuring perforation images is presented, which facilitates the analysis of hole *shape* distributions. The hole-shape data suggests that experimental investigation of oblique hypervelocity penetration phenomena is required for its interpretation.
3. An experimental programme to study the effects of impact angle and relative target thickness on hypervelocity perforation of aluminium plates is presented for two different projectile materials at constant velocity. Previous empirical penetration equations are compared to the data in this section, in particular the accuracy of the GMC equation (Gardner *et al.*, 1997a) is evaluated. This equation has been employed in the past for oblique penetrations and yet was derived from normal impact data only.
4. The distributions and correlations of features of solar cell craters in the EURECA and HST solar cells are analysed for evidence of anisotropy of the ambient meteoroid and space debris environment. Accordingly, the requirement of experimental investigation of oblique solar cell impact phenomena is identified.
5. An experimental programme is presented that investigates the effect of impact angle on solar cell crater morphology. Solar cells, thick glass and aluminium targets were impacted simultaneously to give a comparison of the response of these materials. Calculations of the velocity dispersion within a buckshot cloud are made and a new approach to analysing data from buckshot light-gas gun experiments is presented. The features that are primarily influenced by impact angle are identified and the effect of impact angle, as is relevant for empirical conchoidal diameter equations, is shown. Previous interpretations of space-flown solar cell craters are scrutinised in the light of this work. The requirement for investigation of the survivability of projectiles upon launch in a buckshot firing of the light-gas gun is identified.
6. Experiments to determine the survivability of buckshot projectiles to launch in the light-gas gun are presented. Various typical buckshots were fired through thin foils and the hole size and shape distributions are analysed to determine the survival rate. The tool developed in section 2

is employed for automatic acquisition of hole perforation perimeter co-ordinates. Modelling of the effect of randomised projectile orientation upon impact is also presented.

7. The application of empirical equations derived by regression to laboratory impact equations is discussed. Noting the previous lack of formalism in comparisons of impact distributions the author describes how established statistical tests can be applied to impact flux data. The validity of the application of laboratory relationships to space data is discussed and, where appropriate, the experimental investigations in this thesis are used to evaluate the accuracy of previous interpretations of space data.
8. A summary of the results of the research presented in this thesis is given. An addendum of other work the author has contributed to the field is included, not encompassed by the primary aims of this thesis. Future recommendations for follow-up studies are finally made.

2. The Timeband Capture Cell Experiment

The Time-band Capture Cell experiment (TICCE) is a simple but effective modification of the well established “capture cell” technique, used most successfully on LDEF. In addition to measuring a penetration flux and capturing particle residues, TICCE is also designed to record information about the time at which the impacts occurred. Thus, instead of simply an integrated flux for the entire exposure, the flux may be resolved into *timebands*. Coupled with particle chemistry and orbital history, this can give important clues to particle sources. TICCE was a payload on the first flight of the European Retrievable Carrier (EURECA-1), ESA's reusable platform for microgravity experiments.

On joining the Unit, the author was assigned to the post flight analysis of the TICCE experiment. At the time of joining the analysis team, one of the foil carriers had already been scanned by D.J. Gardner using the LOSS system and the co-ordinates of holes located were recorded. A piece of the foil carrier was cut off, approximately 1/5 the total area of the foil, and the holes located by Gardner in this piece were imaged in the Unit's SEM by H. Yano. Gardner and Yano had previous experience of these procedures, as they were part of the LDEF-MAP scanning team. The author and I. Collier were subsequently trained in the use of the LOSS system and the SEM by Gardner and Yano and the rest of the scanning (the remaining 4/5 of the first foil carrier and the other two foil carriers) was performed by them with occasional assistance from Gardner and Yano. The data collection proceeded in alternating shifts over a 6 month period except for certain operations where the procedure required two operators. The data collected by the author and I. Collier was added to that already taken by Gardner and Yano to produce a final data set comprising hole and crater dimensions and EDX spectra of chemical composition of residues.

The first presentation of the impact flux data appears in Gardner *et al* (1996) and the first presentation of the chemistry data in Yano *et al.* (1996), with an expanded analysis of these two areas in their respective theses (Gardner, 1995 and Yano, 1995). A detailed description of the de-integration and scanning procedures is given by Collier in his thesis (Collier, 1995) and a similar expansion on the flux and chemical analyses of the first two papers. The flux data from the TICCE foils now frequently appears in papers from the Unit discussing fluxes in LEO and constitutes the most important flux measurement since LDEF. However, the author uncovered a previously unknown astigmatism in the SEM system that was used for measuring the TICCE perforations and for collecting the LDEF data before that. Therefore, an investigation of the astigmatism and its implications for data taken with the SEM is presented here. Previously published TICCE data is not corrected for this astigmatism.

In addition to working on the analysis required for the first two publications, the author's own analysis of the TICCE data focuses on the hole shape distribution. Thus, the investigation of the

astigmatism is vital to this study. To this end the author developed a tool for extracting the polar co-ordinates of the edge of a hole with the centre of the hole as the origin. Previous to this the only information recorded about the shapes of holes was the ratio of the major and minor axes - these axes being estimated by eye. The analysis of hole shapes led to the specification of an experimental programme to investigate the influences on hole shape under controlled impact conditions.

2.1. Description of the Experiment

The standard passive capture cell technique acquires an integrated flux for the total exposure time. With a mechanical modification of this arrangement it is possible to record the time of individual impacts to a resolution of a few days. This time resolution is sufficient to monitor the contribution from meteor showers, which have duration of a similar time-scale. This would be an important scientific result as it is still uncertain how the total flux encountered in LEO is partitioned between meteor showers and the sporadic meteoritic background.

TICCE was designed to achieve its time resolution by moving the top foil over the substrate in discrete steps, each step being the length of one cell of foil (1 cm) and being separated by a few days. During the post-flight scanning phase, when a perforation in the top foil is located, the distance to its corresponding debris on the second surface in units of foil steps gives the *timeband* of the impact (Figure 2.1). Thus the impacts are binned by epoch, each bin being a few days wide, giving a temporal distribution of impacts for the exposure. Stevenson (1988), the designer, gives a comprehensive summary of the rationale of TICCE.

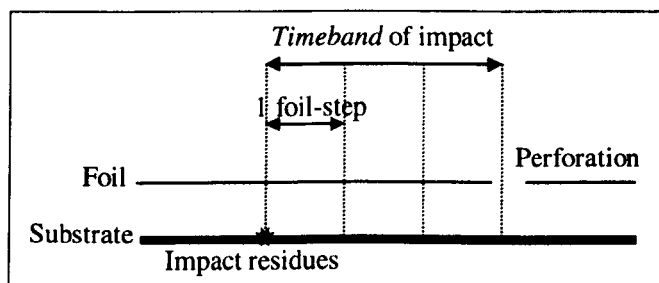


Figure 2.1 – Schematic of TICCE operation

2.1.1. Mechanical configuration

The configuration of TICCE is shown in Figure 2.2 (compare with Figure 1.11, page 16). The platform for the various impact detection and particle collection devices is a 690×690 mm, 15 mm thick, aluminium honeycomb base-plate. The primary impact detectors are 4 *capture cell* devices, each comprised of a 490×100 mm aluminium mesh with a matrix of 41 by 8 10×10 mm aluminium foil cells. Each mesh carries a foil of different thickness to measure different regimes of the penetration flux. One of the foils, a $5 \mu\text{m}$ foil mounted above an aluminium substrate, belongs to *CERT-ONERA/DERTS*, France (Mandeville and Berthoud, 1995). The 3 *USSA/UKC* foils are mounted above gold substrates to provide an inert background for chemical analyses, in that we do not expect to find gold in space, and were nominally $0.85 \mu\text{m}$, $1.85 \mu\text{m}$ and $5 \mu\text{m}$ thick. The foils move across the substrates (from bottom to top in the diagram) in steps of length equal to that of a

capture cell (10 mm). In addition to the 4 foil carriers, the remainder of the surface area of the TICCE platform was occupied by additional contributed experiments. These were mainly focussed on *intact capture*, comprising collection materials such as aerogel and micropore foam (Maag *et al.*, 1993).

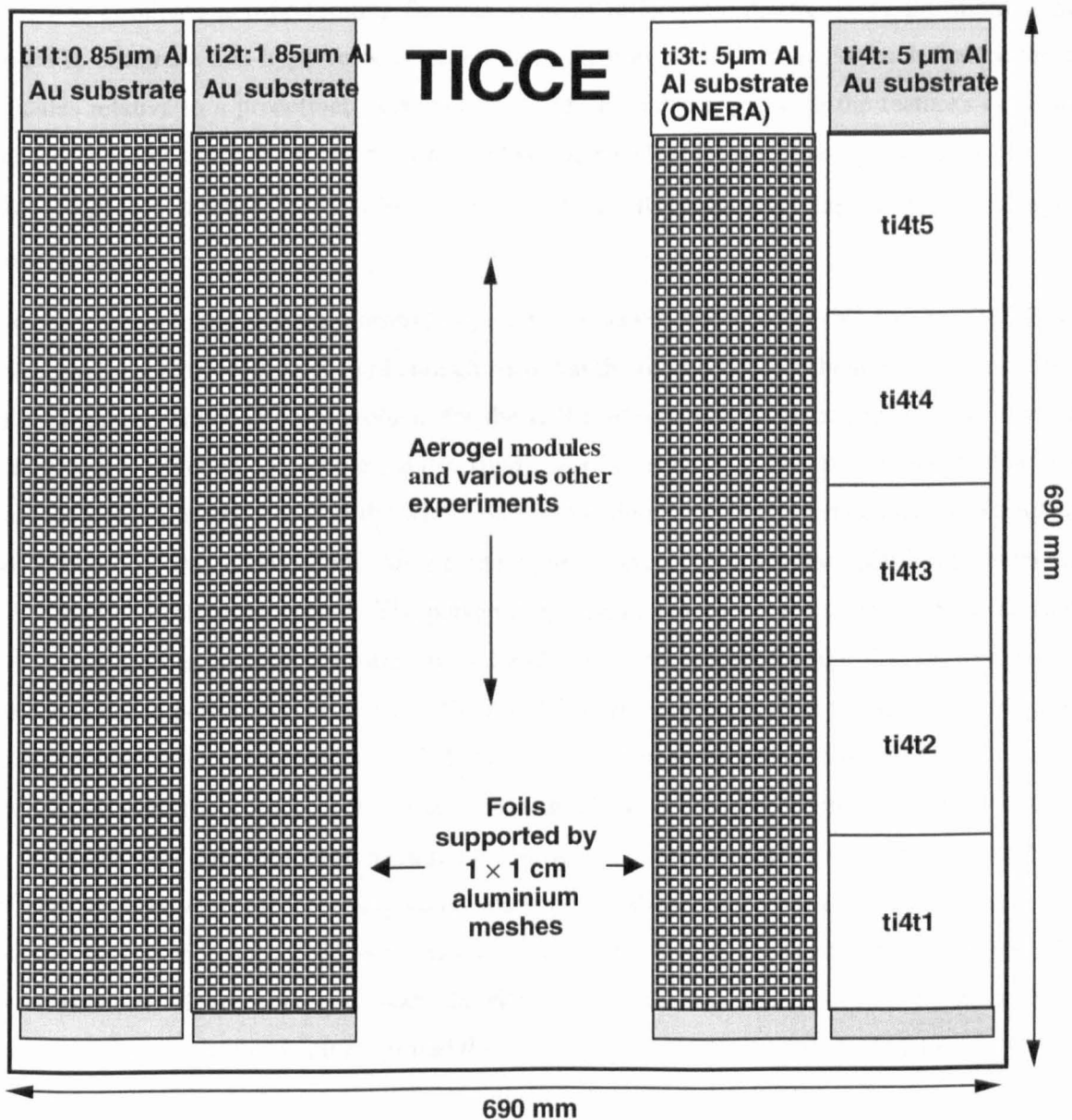


Figure 2.2 – Configuration of TICCE

2.2. Data collection

2.2.1. Scanning procedure

The TICCE foils were scanned for perforations by the author and I. Collier using the Unit's *Large Optical Scanning System (LOSS)*, designed by Paley (1995) to automate the scanning of LDEF-MAP foils. Using this system, a sample of up to 100 by 40 cm is placed on a stage, which can be moved with a positional accuracy of better than 50 μm. The sample is illuminated from the rear and perforations, visible as points of light from the front side, are located by means of a long focal length stereo microscope and 2 colour CCD cameras. The microscope has 5 fixed magnifications, of 6.4, 10, 16, 25 and 40×. These give field widths from 13 × 9 mm to 1.9 × 1.4 mm. In "autoscan"

mode the computer moves the stage such that an optimal scan over any polygonal object can be performed. Each time the stage stops all features, which match the selection criteria, are automatically recorded in a file. The scan pattern has adjustable overlaps so as not to miss features at the edge of the field of view. Features are recorded above an adjustable brightness threshold, chosen to eliminate non-perforating features such as reflections. A circularity threshold is also chosen to eliminate non-hypervelocity perforations such as rips in a foil. For each feature the co-ordinates relative to a predefined, arbitrary origin are recorded along with the feature's circularity and area in terms of pixels. It has been found that the smallest features that can be reliably located with LOSS are around $3\ \mu\text{m}$, which corresponds to the area of a single pixel at highest magnification.

However, it was found that the automatic operation of LOSS was not feasible for the TICCE foils in that the foil carriers were not rigid enough such that the foil was always held in the focal plane of the microscope. This was not a problem for the LDEF-MAP foils, for which LOSS was designed, as they were mounted on smaller, more rigid meshes. Therefore, the author and Collier took alternate approximately 1 hour shifts where one person donned the appropriate clean-room apparel and worked in the clean room, whilst the other person operated the LOSS computer and microscope controls from outside. The person in the clean room moved the stage under the LOSS microscope, until a point of light was spotted and then went to higher magnification to determine whether it was a perforation or a tear in the foil. This was extremely time consuming as the focus controls for the microscope were outside the clean room and so the person inside had to shout “up” and “down” until the foil was in focus at each magnification. Once a candidate site was identified the person outside the clean room recorded the position of the stage. After scanning with LOSS the foil carriers were cut into 5 roughly equal sections and then transferred to the SEM for detailed analysis. The co-ordinates of perforations recorded by LOSS were used to locate sites in the SEM. If confirmed as a hypervelocity impact, the site was imaged and measured. Preliminary chemical analysis was performed of features around the crater suspected to be impactor residues.

2.2.2. Hole diameters

The parameter D_h was defined to be the geometric mean of 2 perpendicular measurements of the hole diameter, D_{max} and D_{min} :

$$D_h = \sqrt{D_{max} \times D_{min}}$$

Thus D_h is the diameter of a circle with area equal to that of an ellipse with major and minor axes equal to D_{max} and D_{min} respectively. Although it should be noted that not all perforations are suitably approximated by an elliptical shape. For approximately circular holes the 2 diameters chosen were simply the vertical and horizontal diameters as the hole appeared on the imaging display. For elliptical craters the orientation of the major axis was estimated and used. Often this would also be defined as the line of flight if the hole showed signs of impact from an oblique angle. The features measured are shown in Figure 2.3. Note the lack of lips at one end indicating that this

is the *up-range* side of the crater. A consistent definition of the impact angle θ was used with respect to the captured image, although the angle had to be corrected for consistency relative to the spacecraft axes as the samples were scanned at different orientations in the SEM. Also shown in Figure 2.3 by the black arrows are the 4 measurements made of the lip thickness along the axes defined by the 2 diameter parameters.

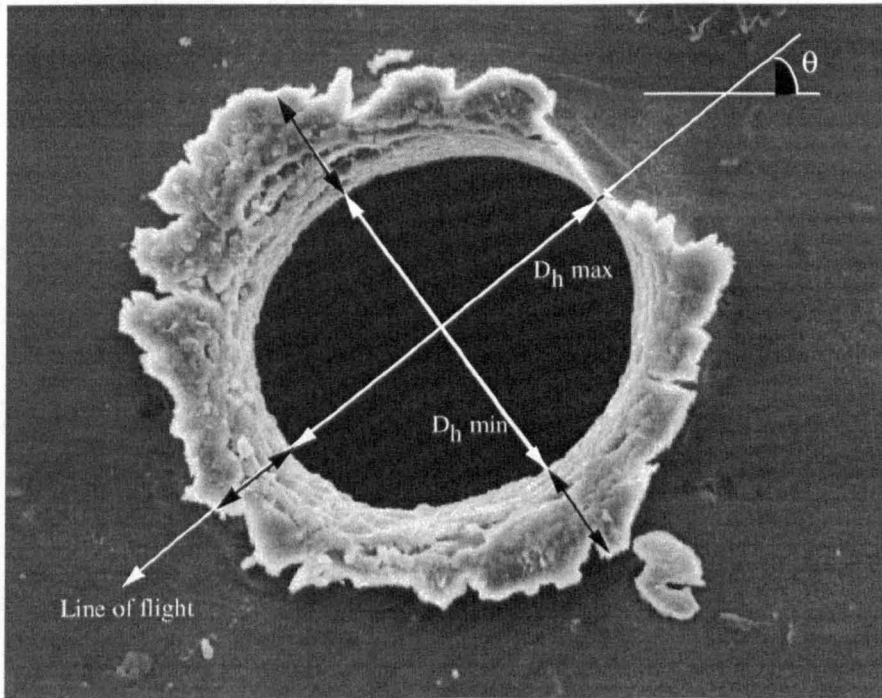


Figure 2.3 – Definition of hole measurements

When performing measurements of metal craters for the experimental programme in section 5 the author noticed that craters were invariably wider horizontally than they were vertically, irrespective of orientation of the sample. This can *only* be attributed to astigmatism of the SEM system. The author is not aware of any previous knowledge of this astigmatism inherent in the SEM imaging system. It was never mentioned during his training in the use of the system and no mention is made in publications of data taken with the Unit's SEM. Consequently the author embarked on a study to quantify this astigmatism and to check the calibration of the SEM against calibration samples.

2.2.3. Calibration of the SEM

The first most obvious way to check the astigmatism of the SEM is to measure something oriented horizontally and then measure the same feature oriented vertically. Thus an aluminium sheet mounted on an SEM stub was imaged in the SEM. The aluminium had been impacted with micron sized dust particles at several km/s in the Unit's 2MV Van de Graaff accelerator as part of the experimental programme in section 5.5.6 and so was expected to have features suitable for measuring. However, it was found that, at lower magnification, the distance between bits of dirt and dust on the surface was a more suitable measurement. Measurements were made at 3 magnifications: 101 \times , 1010 \times and 10,000 \times . The measurements for 101 \times and 10,000 \times are shown in Figure 2.4. The image on the right in each case was taken after the SEM stage was rotated 90° clockwise. For the "horizontal" measurements, firstly two features were chosen roughly the same

vertical distance from the bottom (or top) of the image. Next two vertical lines were drawn that just touched the inside edge of each feature (the side nearest the other feature), then these two vertical lines were joined by a horizontal line thus recording the horizontal distance between them. The SEM stage was then rotated 90° clockwise; the SEM has a rotation readout that displays the rotation to the nearest degree. The procedure was then repeated only this time drawing two horizontal lines to mark the edges of the features and connecting these lines with a vertical line. A reasonable estimate of the uncertainty in the line lengths is 1 pixel based on the author's confidence in positioning at the edge of the features. The results for the three chosen magnifications are shown in Table 2.1.

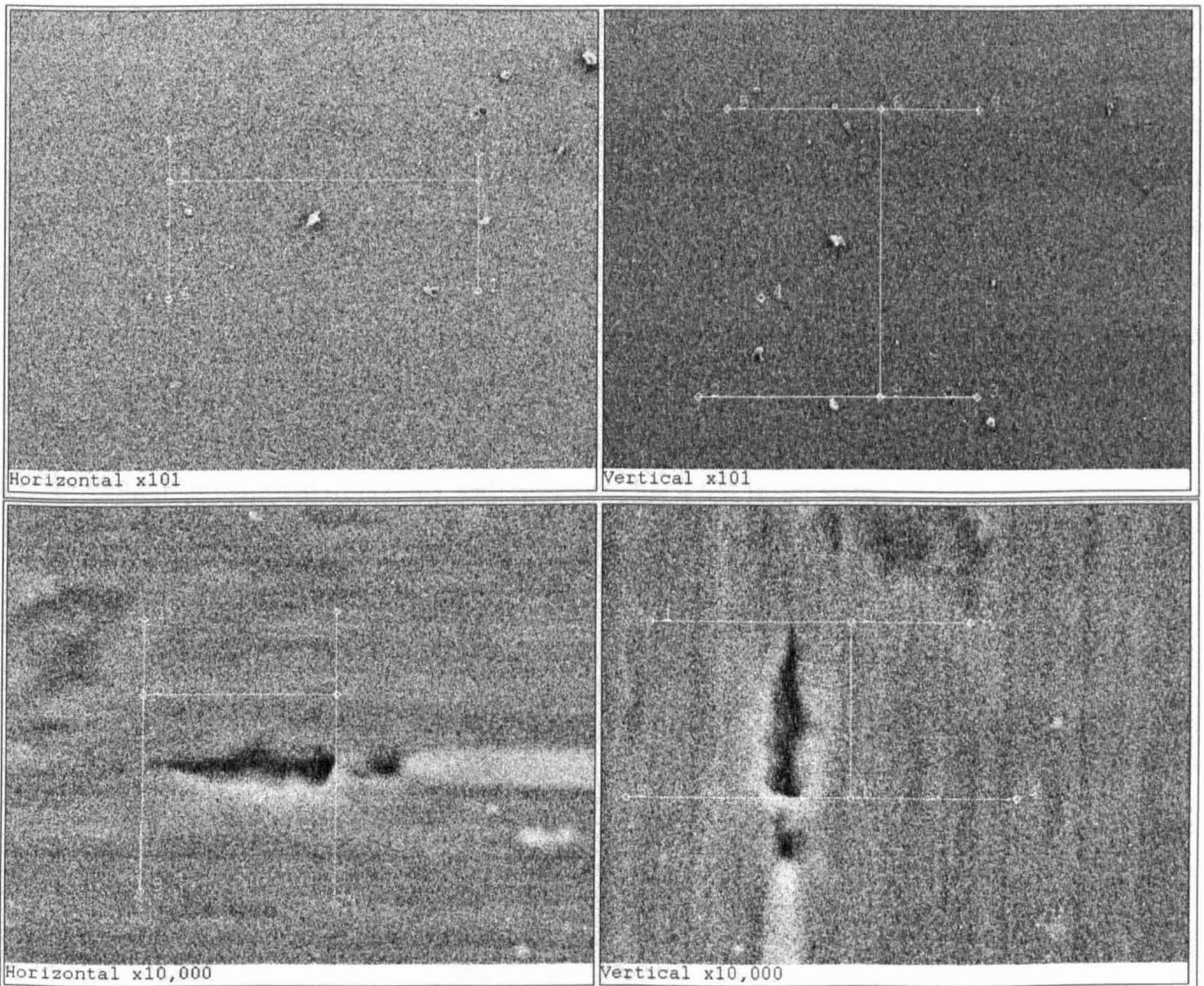


Figure 2.4 – Repeat measurements of features after rotating through 90°

Table 2.1 – Astigmatism measurements

Magnification	Horizontal (pixels)	Vertical (pixels)	Aspect ratio (H/V)
101×	541 ± 1	502 ± 1	0.923 ± 0.003
1010×	546 ± 1	514 ± 1	0.941 ± 0.003
10000×	335 ± 1	330 ± 1	0.985 ± 0.004

It can be seen that there is a significant astigmatism of around 8% for 101×, 6% for 1010× and 1 to 2% for 10,000×. Thus, these first results suggest that the astigmatism improves with increasing magnification. This would seem to follow if the astigmatism is due to a problem with the focussing

system in that one would expect that more parallel electron beams (i.e. those focussed on a smaller area) would be relatively less affected by the error than those with a wider angular separation focussed over a larger area.

To further investigate this phenomenon the author imaged screw holes in the SEM stage. One would expect these holes to be highly circular - at least to better than 1%. 5 screw holes round the periphery of the stage were imaged and then the central hole where stubs are mounted was imaged twice: the second time with the stage rotated 90° clockwise. A tool developed by the author, described in section 2.3.2 was used to analyse these images. This software allows the recording of the co-ordinates of the edge of the holes to be recorded and then an ellipse is fitted to the hole shapes. Table 2.2 shows the results of the ellipse fits in terms of the major and minor axes of the fitted ellipses and the orientation of the major axis relative to the vertical. The aspect ratio is also shown. Individual uncertainties for the aspect ratios are not shown as the mean and of all the measurements and its standard deviation are used to characterise the astigmatism. The orientation of the major axis shows in which direction the image is most greatly magnified. The fact that this angle is significantly different from 90° means that the distortion maybe more complicated than a simple horizontal-vertical aspect ratio. The close fit to an elliptical shape suggests that the distortion is a simple aspect ratio problem rather than a more complex angular dependence, but that the perpendicular maximum and minimum lengths may not be oriented exactly corresponding to the horizontal and vertical directions with respect to the SEM raster scan.

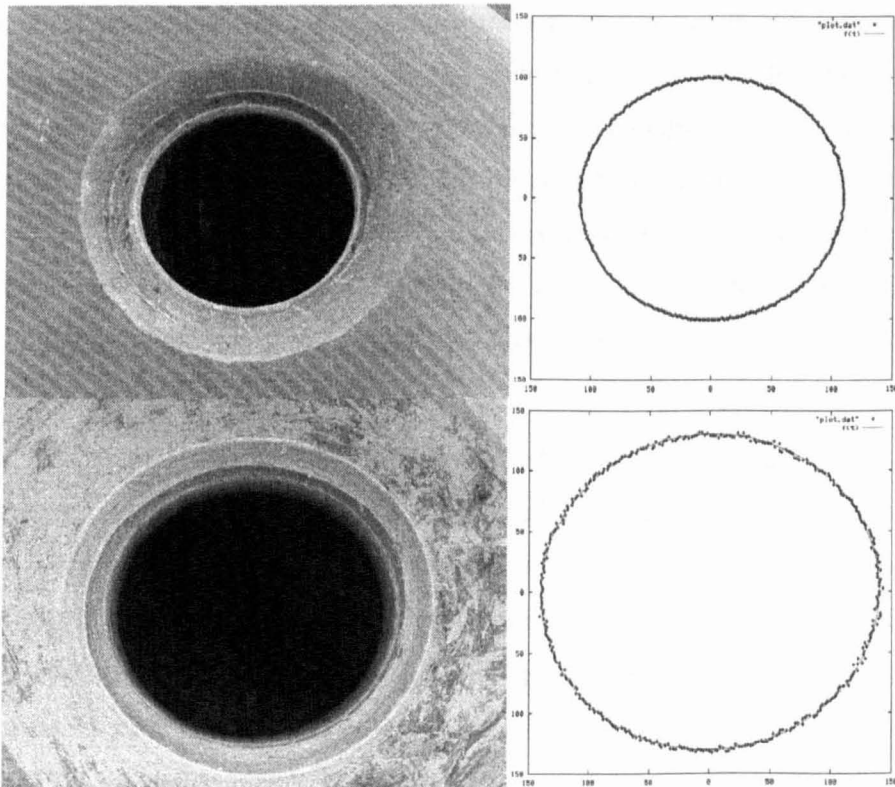


Figure 2.5 – Ellipse fitting of screw hole images to test for unusual distortion

An important observation that was made during the imaging of the circular screw hole features was that the image appeared circular when the SEM was in “TV” mode, but became obviously elliptical, when viewed in immediate comparison, when the SEM was switched to “line” mode. In

TV mode the SEM scans in a fast (presumably about as fast as a TV) raster scan, fast enough so that the image relays, to all intents and purposes, in real-time what is in the field of view so that the stage can be moved and the area of interest can be positioned. In “line” mode, various scan speeds can be chosen, with the back-scattered electron signal being proportional to the dwell time and thus the quality of image improves with decreasing scan speed. This mode is used for collecting images once the region of interest has been positioned in the field of view and focussed. This could mean that the problem lies in the scanning system rather than the focussing.

Table 2.2 – Results of ellipse fits to screw holes

ID	Major axis (pixels)	Minor axis (pixels)	Orientation of major axis (°)	Aspect ratio (minor/major)
c1	100.46 ± 0.05	109.28 ± 0.06	85.4 ± 0.3	0.919
c2	101.46 ± 0.11	109.18 ± 0.12	77.0 ± 0.7	0.929
c3	101.02 ± 0.05	108.61 ± 0.06	83.9 ± 0.3	0.930
c4	101.11 ± 0.05	108.96 ± 0.06	86.5 ± 0.3	0.928
c5	104.71 ± 0.06	114.10 ± 0.06	86.9 ± 0.3	0.918
c0	130.30 ± 0.13	139.82 ± 0.14	84.1 ± 0.7	0.932
c90	129.08 ± 0.12	138.08 ± 0.13	86.3 ± 0.7	0.935
		Mean	84.3	0.927
		Standard deviation	3.4	0.006

The next question to be answered is which axis, horizontal or vertical, is the “correct” length, or are they both wrong? More generally, how well is the SEM imaging system calibrated? It is possible to make a calibration of the system before making measurements, but in the following study the calibration used will be that that was used for the collection of the TICCE data. For information this is the calibration file named “SEM 10kV”. It should also be noted that it is possible to specify an aspect ratio for the imaging software to use. This suggests that the authors of the software (PGT) are aware that SEM systems can have inherent astigmatism that needs to be compensated for. If the astigmatism uncovered by the author had been known about at the time of the TICCE scanning, then possibly the appropriate aspect ratio value could have been used to give properly proportioned images and thus measurements.

To determine the accuracy of the SEM calibration, SEM calibration stubs that have a certain number of lines per mm etched on them were imaged and measured by the author. The Unit possesses two such stubs, one labelled as having “19.7 lines/mm”, the other labelled “2160 lines/mm”. The 19.7 lines mm⁻¹ stub was imaged at magnifications of 101× and 1010×; the 2160 lines mm⁻¹ one at 20,000×. Even though the stubs had both horizontal and vertical lines etched on them, two images for each combination of stub were taken, the second time with the stage rotated 90° clockwise. Thus the determination of the aspect ratio will not be affected if the accuracy of the etching is different for the horizontal and vertical lines.

For each image measurements were taken of both the distance between the horizontal and vertical lines. The labelling convention for the measurements taken is defined in Figure 2.6. Calling one

distance between lines on the stub a and the corresponding perpendicular measurement of the same number of lines b , the lengths in the first image are labelled a_v and b_h with the subscript specifying the direction of measurement, horizontal or vertical respectively. After rotation through 90° (the right hand diagram in Figure 2.6) the length a is now re-measured horizontally and b vertically. Thus as well as checking the calibration, another check of the astigmatism can be made. The results are shown in Table 2.3, where the value shown is the mean of 10 parallel measurements and the error is the standard deviation.

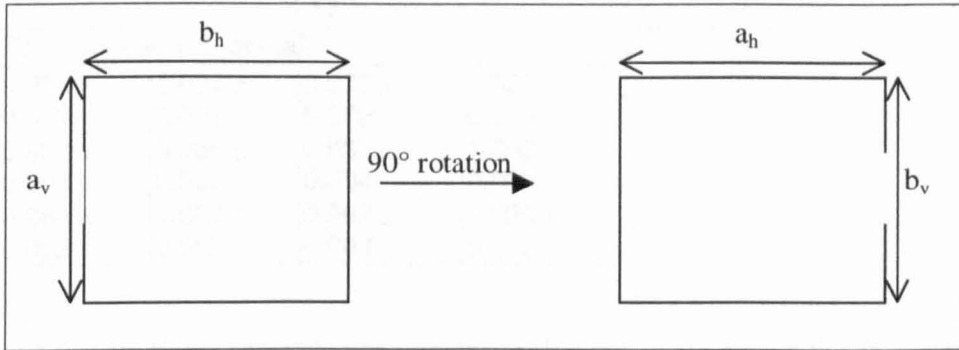


Figure 2.6 – Definition of measurements made for checking calibration

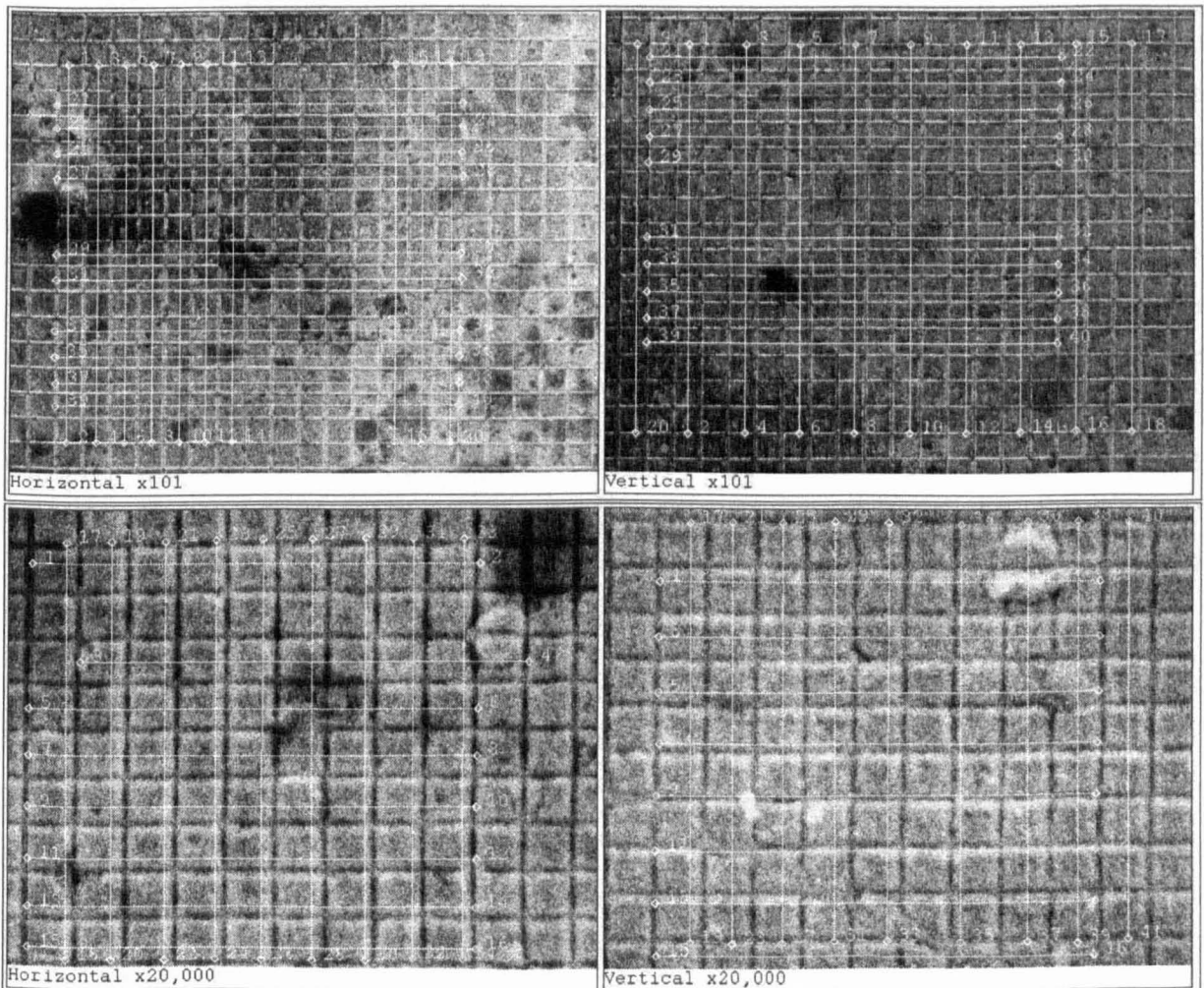


Figure 2.7 – Calibration measurements

Table 2.3 – Summary of calibration measurements

Mag.	a_v (μm)	a_h (μm)	b_v (μm)	b_h (μm)	Aspect ratio (a_v/a_h)	Aspect ratio (b_v/b_h)
101×	723 ± 1	790 ± 1	741 ± 2	777 ± 2	0.916 ± 0.002	0.954 ± 0.004
<i>101×</i>	<i>660</i>	<i>703</i>	<i>652</i>	<i>704</i>	<i>0.939</i>	<i>0.926</i>
1010×	47.2 ± 0.2	50.1 ± 0.2	47.4 ± 0.2	50.9 ± 0.2	0.943 ± 0.006	0.931 ± 0.005
20,000×	4.02 ± 0.01	4.20 ± 0.01	4.01 ± 0.01	4.27 ± 0.01	0.957 ± 0.003	0.938 ± 0.004
	Actual length (μm) calculated from \rightarrow				# of lines	lines mm^{-1}
101×	761				15	19.7
1010×	50.8				1	19.7
20,000×	4.17				9	2160
	Ratio (measured / actual)					
101×	0.950 ± 0.001	1.037 ± 0.001	0.973 ± 0.002	1.020 ± 0.003		
1010×	0.930 ± 0.003	0.986 ± 0.005	0.935 ± 0.004	1.003 ± 0.003		
20,000×	0.964 ± 0.002	1.007 ± 0.002	0.962 ± 0.003	1.025 ± 0.002		

The results of this study are somewhat anomalous in that we would expect the aspect ratios of the perpendicular line spacings a and b to be the same. That is to say, the ratio of two measurements of any length made with the stage rotated 90° between measurements should be the same for the same magnification, unless the astigmatism is varying in some other way. Sometimes the parts of the grid measured horizontally were widely separated from the part used for the vertical measurement as the measurements were not made at the centre of rotation of the stage due to the most clearly defined parts of the grid not coinciding with the centre of rotation. Therefore the discrepancies could arise from the accuracy of the etching of the grid varying over its surface. Nevertheless, it is seen that the astigmatism is always such that horizontal measurements are larger and the astigmatism generally improves (gets closer to 1:1) with increased magnification. The measurements made at 101× magnification were repeated (shown in italics) as an aspect ratio of 0.95 seemed unusually high for this magnification when compared to the other measurements (Table 2.1). It can be seen that the horizontal measurements are more accurate than the vertical measurements, which consistently give shorter measurements than the calibration specimen.

A final line of investigation followed by the author as regards the astigmatism of the SEM was to test the effect of the “stigmator” control used for improving the focus at high magnification. The effect of the stigmator control is shown in Figure 2.8. With the stigmator set incorrectly the image is distended along perpendicular axes either side of focus - by rotating the focus control clockwise and anticlockwise away from the best possible focus. With adjustment of the stigmator control this effect can be removed so that the blurring of the image either side of focus is circularly symmetric and the best possible focus is greatly improved. The stigmator control has no noticeable effect at low magnifications; the effect only becomes significant at several 1000× magnification. To see if this control effected the aspect ratio of the images as well as just their focus, the author imaged the calibration grid, firstly with the stigmator set to the best and then with it at a worse setting, but not so bad that the grid could no longer be made out (Figure 2.9).

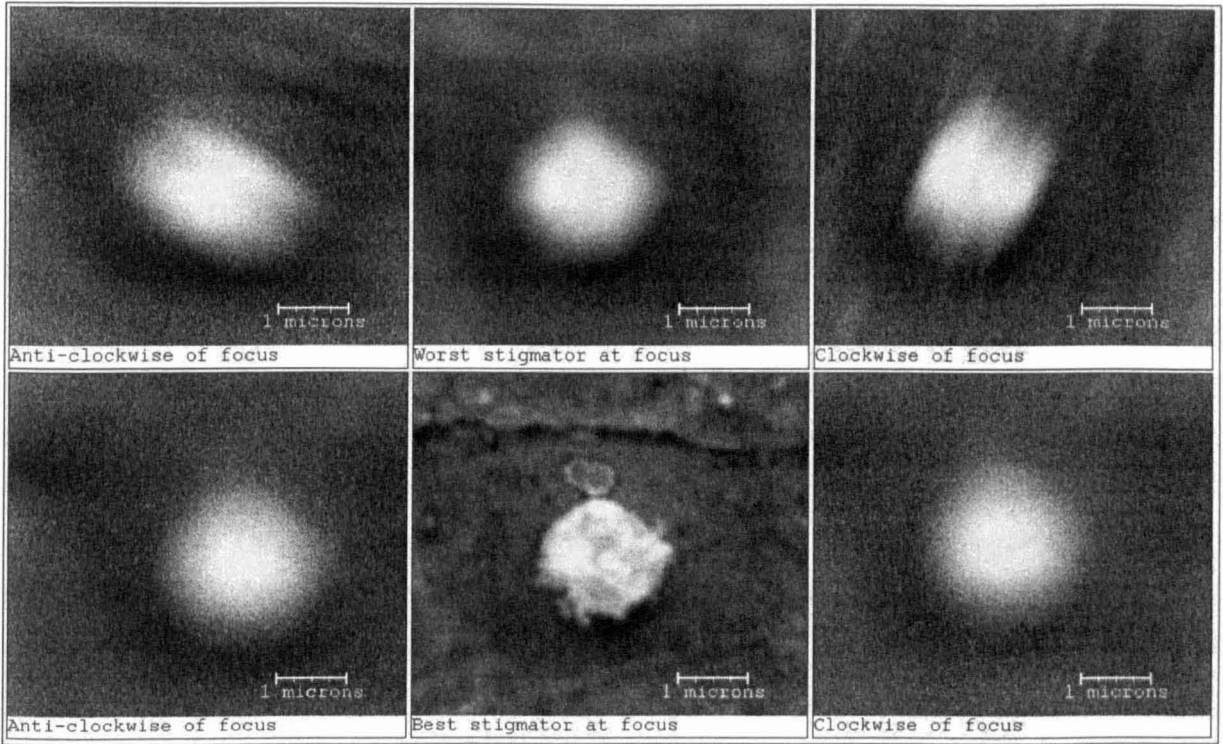


Figure 2.8 – The effect of the “stigmator” control

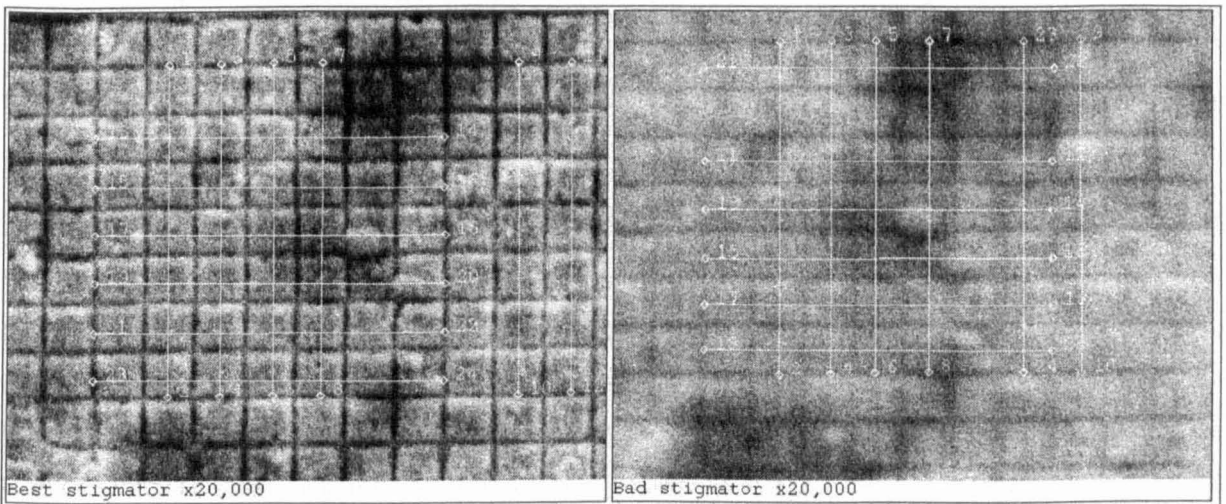


Figure 2.9 – Calibration at different stigmator settings

A *t*-test for sample means (Hugill, 1985) between the mean lengths obtained at “best” and “bad” stigmator returns a 20% probability that they are identical and therefore it is concluded that the stigmator control has no significant effect on the aspect ratio.

Summary

In all the tests the vertical-to-horizontal aspect ratio is less than 1. Although, there appears to be a trend towards a 1:1 aspect ratio with increasing magnification, there is not a strong enough correlation to assign the appropriate aspect ratio for a given magnification. Therefore, for the purposes of this thesis, where it is the hole shapes that are being analysed and thus an accurate aspect ratio is required, it was decided to take the average aspect ratio as a suitable approximate correction factor. The horizontal calibration is accurate to on average 1%, whereas the vertical calibration is systematically gives lengths that are around 5% too short (Table 2.3). Therefore, in

order to correct the TICCE hole sizes the horizontal dimensions were not modified, but the vertical dimensions of all holes were increased by 5%.

2.2.4. Foil thickness

Although the 3 USSA/UKC foils were manufactured to be 0.85 μm , 1.85 μm and 5 μm thick, it was found, after weighing selected areas of each foil, that they were respectively, $2.5 \pm 0.13 \mu\text{m}$, $3.2 \pm 0.16 \mu\text{m}$ and $9.2 \pm 0.20 \mu\text{m}$ thick. This apparent gross error in the foil thickness is suggested by the TICCE principle investigator to be a result of inaccuracy or miscalibration of the manufacturer's production processes (McDonnell, personal communication, 1998); no explanation, further investigation, or any further comment is offered in any previous presentation of the TICCE perforation data. The author is not aware that the thickness of the foil owned by *ONERA-CERTS/DERT* has been checked – it is not mentioned by Mandeville and Berthoud (1995) - and thus any publication of their data is called into question. It was believed that the variation in foil thickness with position would be small compared to the offset from the requested foil thickness due to the nature of the rolling process (McDonnell, personal communication, 1998). In the original weighing 4 squares of foil found to be free from perforations were weighed by the author and Collier and the total weight was divided by the product of the area and the density of aluminium (2780 kg m^{-3}). Thus no information about the variability of the foil thickness with position can be extracted from these measurements.

As the author's analysis is concerned with the effect of foil thickness on perforation shapes it was decided to check the foil thicknesses and variation in the thickness at different locations on a foil. Accordingly, the author cut 3 squares of foil, free from (located) impacts, from four of the five pieces that the ti4 foil carrier was cut into and weighed these separately. Thus the variability of the foil thickness across the length of the foil carrier over 4 discrete length increments could be studied. For the other two foils (ti2t and ti1t) samples of 10 and 16 pieces from widely spaced intervals of the length of the carriers and recorded the total weight. The total weight was taken rather than separate weights for different positions along the foil carriers, firstly because a larger number of squares of foil was required to register a weight significantly larger than the random fluctuations of the last digit on the balance; secondly, taking a large number of squares from several locations would have destroyed too much of the detector area. As the samples for the two thinner foils were taken from widely spaced areas the calculated uncertainty of the foil thickness will reflect the variability of the foil thickness over a large area; it is only for the thickest foil that any correlation of thickness with position was analysed.

The foils were cut from the TICCE mesh in the clean room using a scalpel and placed in sealed containers for removal from the clean room. A section of the ti4t foil carrier, ti4t2, could not be located; it had most probably been dissected for other studies. Consequently, only samples from 4 of the 5 sections of this foil carrier were available. The 6 samples of foil (4 samples each of 3 squares cut from ti4t1, ti4t3, ti4t4 and ti4t5 respectively; 1 sample of 10 squares from ti2t; 1 sample

of 16 squares from tilt) were weighed using a *Sartorius* balance, accurate to 0.1 mg. Each weighing was repeated 5 times to give an estimate of the uncertainty in the recorded weight. The procedure for the weighing was to zero the balance, open the glass door that shielded the balance from air currents, place the pieces of foil on the balance, close the door and wait until the reading on the balance was stable for a count of 5 seconds. The foils were then removed from the balance and the procedure was repeated, thus recording sets of *replicate* measurements from which an estimate of the true weight and a confidence for this estimate could be calculated.

Area measurement

The area of the pieces of foil that were weighed was calculated firstly by flattening the foils and smoothing out any creases. This was difficult for the thinnest foils because the slightest tension had a tendency to tear the foil. The foils were then placed on a flatbed scanner and flattened against the glass (the focal plane of the scanner) by covering them with a microscope slide, which was held in place by closing the scanner lid and piling books on it. A microscope graticule was also scanned to calibrate the images. An image captured in this way is shown in Figure 2.10.

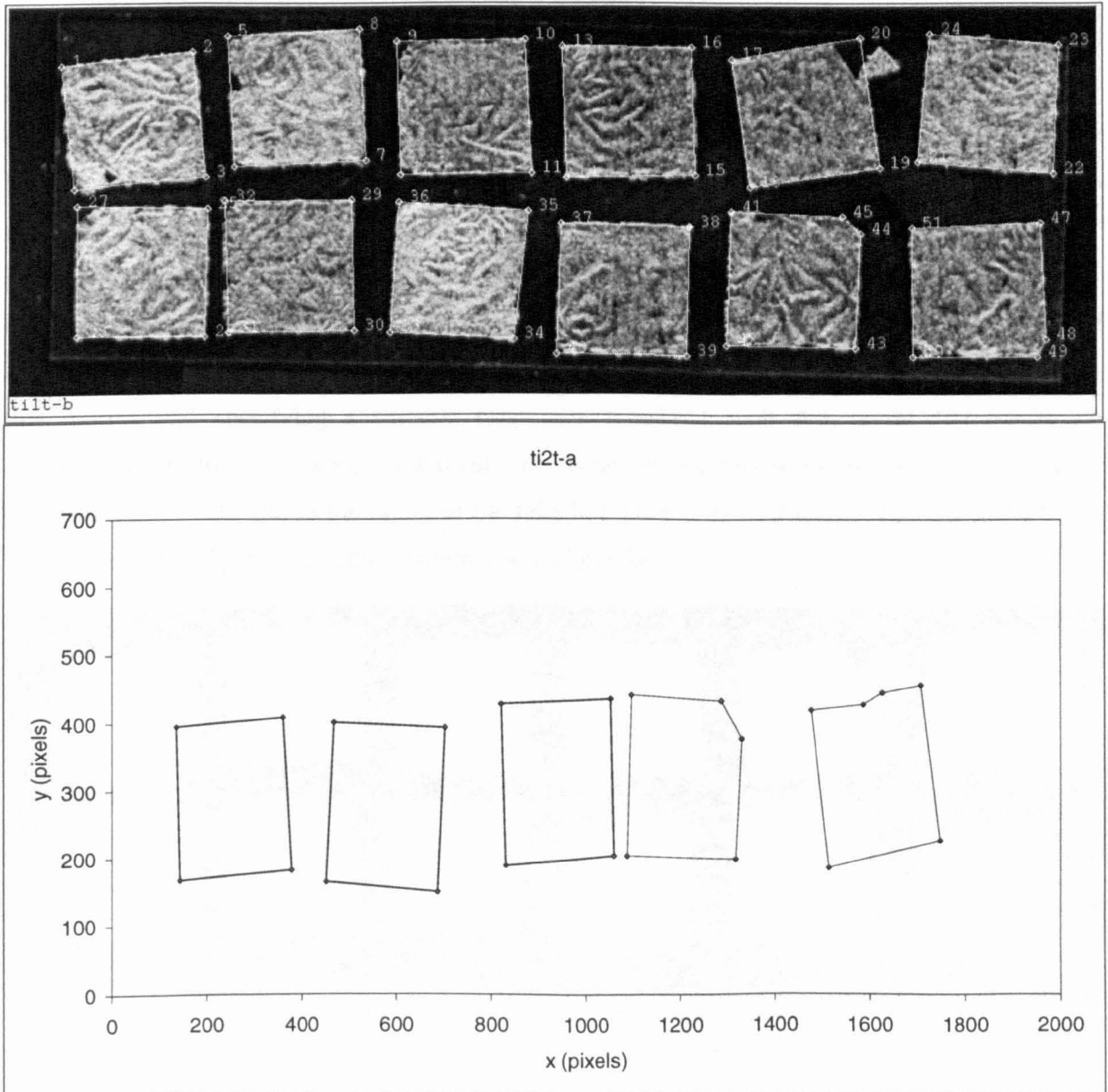


Figure 2.10 – Area measurement of a sample of the TICCE foil

Using software usually used for taking measurements from SEM micrographs (the same software as used for measuring TICCE holes) it was possible to select points on the image and read off the co-ordinates. The calibration was performed by selecting a line on the image of the graticule that connected the “0” and “10” graduations and thus corresponded to a length of 10 mm. This length was recorded for all three images to be 237 pixels, giving a calibration for the images of 23.7 pixels mm^{-1} , noting that the limiting accuracy, corresponding to a single pixel, is 42 μm . Once cartesian co-ordinates for the vertices of the pieces of foil had been recorded (Figure 2.10), the area A in pixels² could be calculated using the formula for the area of a polygon:

$$2A = \sum_{i=0}^{n-1} (x_i y_{i+1} - y_i x_{i+1})$$

The area in pixels² could then be converted to cm^2 using the graticule calibration. For the first piece of foil the author repeated the selection of the vertices 6 times, thus giving 6 area measurements, the fractional standard deviation of which was used as the error for all subsequent foil area measurements.

A secondary measurement of the foil area was additionally made making use of some of the LOSS software. The “*getcoord*” routine (Paley, 1995) starts by locating pixels in an image above a user-specified brightness threshold and then proceeds to find adjacent pixels that are also above the brightness threshold. This process proceeds following the commonly-used (in computer graphics rendering) *seed-fill* algorithm (Glassner, 1990) until it can find no more adjacent “interesting” pixels i.e. it has found all pixels bounded by “uninteresting” – in this case approximately black - pixels. It then records this set of adjacent pixels as a “feature”, also recording the area in pixels of the feature before moving on to look for interesting pixels elsewhere. Inputting the foil images into this routine and specifying a suitable brightness threshold such that bright foil pixels are distinguished from dark background pixels, the areas of the pieces of foil in pixels could be acquired. Figure 2.11 shows the image of the foils in Figure 2.10 after it has been thresholded into white “interesting” pixels and black “uninteresting” pixels.

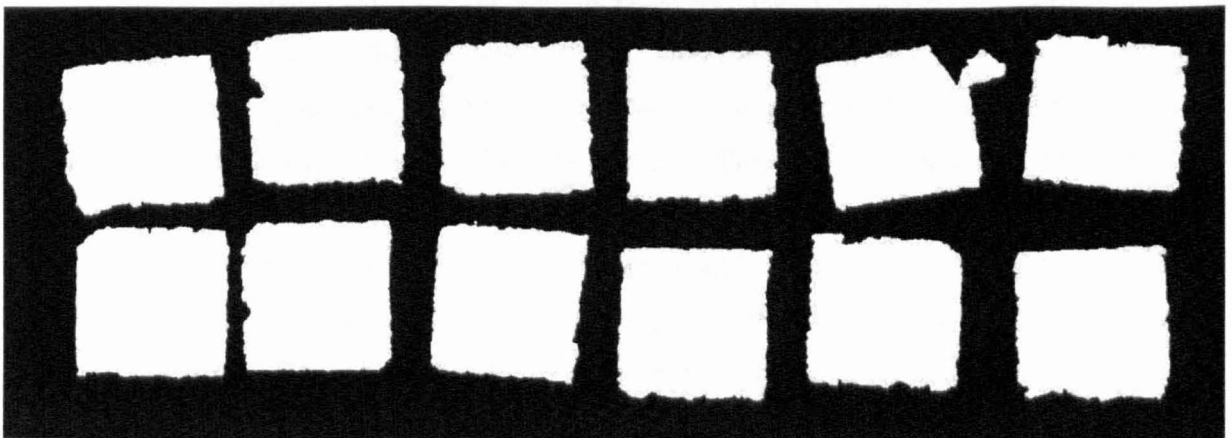


Figure 2.11 – Area measurement using pixel counts

Table 2.4 – Data used for foil thickness calculation

Foil ID	ti4t1	ti4t3	ti4t4	ti4t5	ti2t	ti1t
# of pieces of foil	3	3	3	3	10	16
Repeat weighing #	Weight (mg)					
1	7.7	7.8	7.4	7.5	5.5	7.7
2	7.3	7.7	7.5	7.5	5.4	7.4
3	7.8	7.5	7.2	7.3	6.0	7.5
4	7.6	7.6	7.0	7.6	5.7	7.6
5	7.6	7.3	7.5	7.5	5.5	7.5
Mean ± standard error	7.60 ± 0.08	7.58 ± 0.09	7.32 ± 0.10	7.48 ± 0.05	5.62 ± 0.11	7.54 ± 0.05
	Area (×10 ⁵ pixels)					
Calculated from coordinates of vertices	1.643 ± 0.011	1.637 ± 0.011	1.618 ± 0.011	1.670 ± 0.011	5.407 ± 0.035	8.800 ± 0.058
From <i>getcoord</i> pixel count	1.647	-	-	-	-	8.849
	Area (cm ²)					
	2.924 ± 0.019	2.915 ± 0.019	2.880 ± 0.019	2.973 ± 0.019	9.627 ± 0.063	15.666 ± 0.103
	Thickness (µm)					
	9.35 ± 0.12	9.35 ± 0.12	9.14 ± 0.14	9.05 ± 0.08	2.10 ± 0.04	1.73 ± 0.02

Table 2.4 shows the results of the weighing and area measurements. It can be seen without formal significance testing that the areas calculated by the two methods agree. For the ti4t foil a two-sample *t*-test for means (Cooper, 1969) between the highest (9.35 ± 0.12) and lowest (9.05 ± 0.08) thickness shows that they are not significantly different at the 5% level.

Summary

It is concluded that the appropriate value to used for the thickness of the ti4t foil is the mean of $9.22 \mu\text{m}$ with the uncertainty given by the standard deviation which is $0.15 \mu\text{m}$. This is not significantly different from the value of $9.2 \pm 0.2 \mu\text{m}$ recorded in the original calculation. Thus, publications and databases using the original thickness fortunately do not require correction in the light of this study. However, the thickness of the ti2t and ti1t foils calculated here are significantly different from the original calculations: $2.10 \pm 0.04 \mu\text{m}$ compared to $3.20 \pm 0.16 \mu\text{m}$ for ti2t and $1.73 \pm 0.02 \mu\text{m}$ compared to $2.50 \pm 0.13 \mu\text{m}$ for ti1t. The new measurements of these foil thicknesses are closer to the manufacturers nominal thicknesses of 1.85 and $0.85 \mu\text{m}$ respectively. Any publications and databases of the TICCE data should be accordingly amended to use these new values for the ti2t and ti1t thicknesses as they are based on a larger area of foil than the original calculations (2× and 4× respectively) and a more precise area calculation.

2.3. Hole-shape analysis

Figure 2.12 shows some typical morphologies observed for perforations of the TICCE foils. The ratio of hole diameter to foil thickness is shown to give a guide to the scale. For the top row of

images - the largest holes relative to the foil thickness - it can be seen that there are a variety of complicated shapes, most likely a reflection of the shape of the impacting particle. It could be argued that such irregular morphologies, particularly the ones with re-entrant features and obtuse internal angles such as the hole at the top-right of Figure 2.12 could be due to a double impact. That is a perforation is made by a particle with a perimeter that intersects that of one made by a previous impact. However, the total perforated area of foil is less than 5×10^{-6} of the total detector area so this is highly unlikely.

It appears that, as the hole becomes smaller relative to the thickness of the foil, the shape becomes more elliptical or circular. Intuition suggests that a large particle will not be disrupted when intercepting a relatively thin foil and will to a certain extent punch out its cross-section. However, for a relatively thick foil/small particle the particle will be disrupted and the behaviour will be more like an impact into a semi-infinite target. Hydrocode simulations allow the motion of projectile and target material during a hypervelocity impact to be observed and for the case of a semi-infinite metal target they reveal that the projectile flattens upon impact, becomes vaporised or molten with material jetting radially outward from the point of impact resulting in a radially symmetric morphology with little if any of the original particle shape being recorded in the final crater shape (Melosh, 1989).

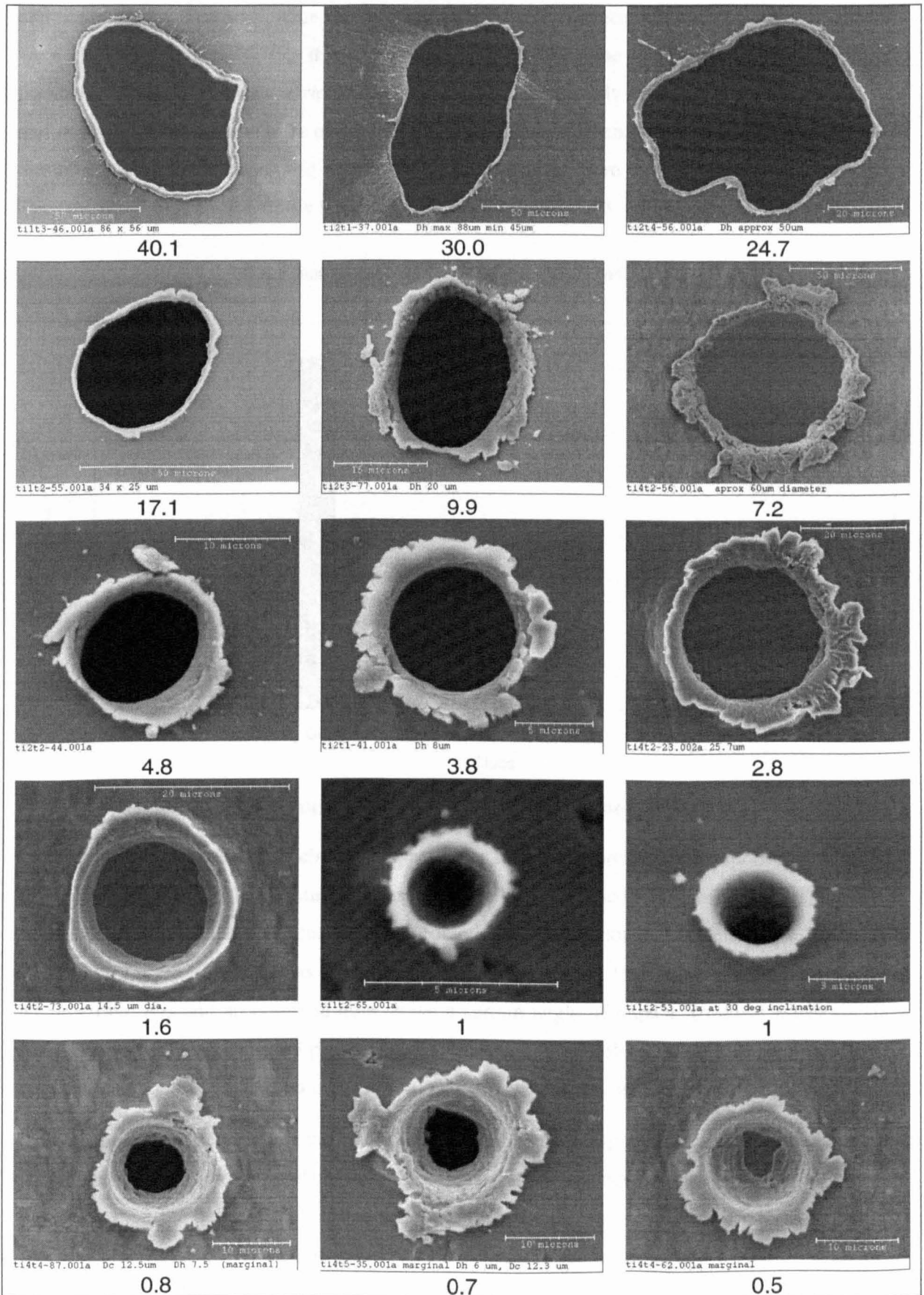


Figure 2.12 – TICCE hole shapes with D_h/f values shown

2.3.1. Morphological classifications

Whilst scanning the TICCE foils the author defined a taxonomic classification scheme based on the observed perforation morphologies. The classifications were based on two factors: the hole shape

and the lip shape. The holes were classified as *circular* (C), *elliptical* (E) and *irregular* (I). The lips were classified as *regular* (R) if the lips were roughly the same width at all points around the perimeter of the hole; *asymmetrical* (A) if the lips were obviously thicker on one side of the hole and *irregular* (I) if the lips were of varying thickness. Thus with each perforation being assigned to one of the three hole classes and one of the three lip classes there were 9 possible classifications. The frequency distribution of the 9 classes is shown in Figure 2.13.

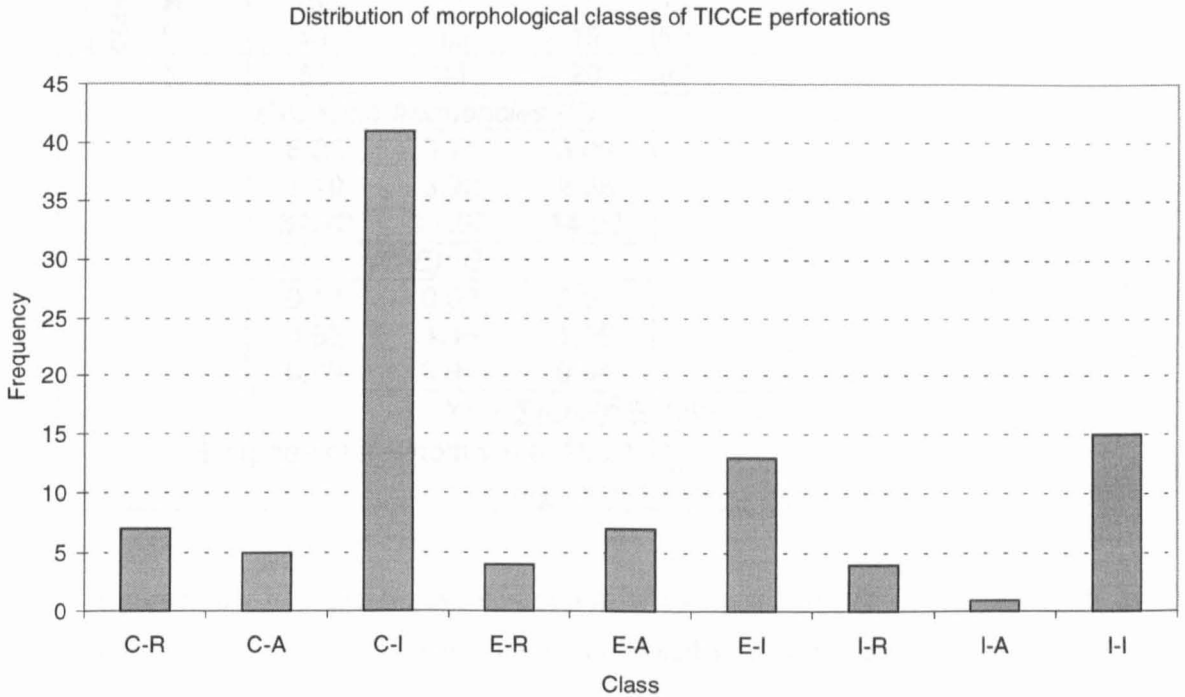


Figure 2.13 – Frequency distribution of 9 TICCE morphological classes

Circular holes could be due to circular impactors or to fragile particles that vaporise upon impact. The author cannot think of an intuitive cause of irregular as opposed to symmetrical lips, but it may be related to impact speed, impactor density or relative foil thickness. Asymmetrical lips usually signify an oblique impact. It has been observed for thick targets that an oblique impact produces asymmetrical lips and an elliptical hole above a certain angle of impact. Irregular holes are most likely due to irregularly shaped projectiles. The fact that most holes are circular suggests that the meteoroid and debris population is comprised primarily of low aspect ratio particles.

To see if holes of a certain type are likely to have lips of a corresponding type a contingency table of hole and lip types was compiled (Table 2.5). If the hole type does not determine the lip type and vice-versa then the perforations of a certain hole type should be evenly distributed amongst the 3 lip types and vice-versa. Thus, for example, the 53 “circular” holes should have lip types in the ratio 15:13:69 as there were 15, 13 and 69 occurrences of the lip types “regular”, “asymmetrical” and “irregular” respectively. In this way the corresponding table of expected frequencies of each type is compiled and compared to the observed frequencies to give the appropriate Pearson’s statistic (X^2 in Table 2.5), which has a χ^2 distribution with degrees of freedom equal to $(r - 1)(c - 1)$, where r and c are the number of rows and columns in the contingency table, respectively. Since the

χ^2 probability in this case is 10% it is not highly unlikely that these frequencies of hole and lip classes would be observed if they are independent of each other.

Table 2.5 – Contingency of TICCE hole and lip shape classes

		<i>Observed frequencies (O)</i>			$\Sigma \downarrow$
		Hole class			
		C	E	I	
Lip class	R	7	4	4	15
	A	5	7	1	13
	I	41	13	15	69
$\Sigma \rightarrow$		53	24	20	97
		<i>Expected frequencies (E)</i>			
		8.20	3.71	3.09	
		7.10	3.22	2.68	
		37.70	17.07	14.23	
		<i>(O-E)²/E</i>			
		0.17	0.02	0.27	
		0.62	4.45	1.05	
		0.29	0.97	0.04	
		$\chi^2 = \Sigma(O-E)^2/E$			7.89
		Degrees of freedom $\nu = (r-1)(c-1)$			4
		$P(\chi^2_{\nu} \geq \chi^2)$			10%

What is required now is a quantitative description of the qualitative classifications made in this section. Since the classifications were based on whether a hole appeared to be “circular”, “elliptical” or “irregular” then it makes sense to determine exactly how circular, elliptical or irregular the holes are. Accordingly the author decided to fit an ellipse to the hole shapes, with the eccentricity - actually the ratio of minor to major axis was used - giving a measure of how elliptical or circular the holes are and the quality of fit to an ellipse giving a measure of the irregularity.

2.3.2. Quantitative shape analysis

To fit an ellipse to a hole shape, the co-ordinates of the edge of the hole is required. This could have been done using the SEM imaging software that was used for measuring the diameters of the holes, but would have been prohibitively time consuming in that for a meaningful fit to be obtained, the co-ordinates of several tens, if not hundreds of points around the perimeter of each of around 100 holes would have to be “manually” recorded. Consequently, the author decided to see if an automatic technique could be developed. The software for use with the Unit’s optical scanning system (Paley, 1995) was already capable of taking an image and then locating “features” in the field of view that are above a certain brightness threshold. In the case of back-lit foils the perforations show up as bright pixels in the image. The software could also record the centre of a feature and its circularity. Thus some of the of the required processing functionality was already implemented and it was a trivial matter for the author to modify the existing software to be used with SEM images, rather than images from the LOSS system. Therefore, as it stood an SEM image could be (i) thresholded into dark, “interesting” hole pixels and lighter “uninteresting” foil pixels

and (ii) the co-ordinates of the centre of the hole could be found by taking the average x and y values of the interesting pixels. What was now required was a way of recording the co-ordinates of the hole perimeter. The author thus wrote an additional routine called “radar” (the radar C code and other relevant routines are given in appendix E) as the algorithm is reminiscent of the way a radar sweeps round in a circle locating features at some radial distance from the centre of rotation.

After thresholding the image into interesting and uninteresting pixels, the image is loaded into an array of size equal to the size of the image i.e. a 800×600 image would be loaded into an array of 800 by 600 elements, each element being set to either 255 (an interesting hole pixel) or 0 (an uninteresting foil pixel). The routine starts with an x and y variable set to the co-ordinates of the centre of the hole and then increments these variables so that the location of the pixel under scrutiny moves radially outwards from the centre. At each location the value of the array element (x,y) is looked up and if it is still “interesting” the co-ordinates carry on being incremented until an “uninteresting” pixel is reached i.e. the edge of the hole. The co-ordinates of this location are recorded and “it” (i.e. the point specified by the x and y variables) returns to the centre. The angle at which the scan moves radially outwards from the centre is then incremented by a user defined interval and the scan once again moves radially outwards until a dark (value 0) pixel is intercepted. This procedure is repeated until a full revolution has been performed and the perimeter of the hole has been recorded in terms of polar co-ordinates with the origin at the centre of the hole - recall that this is the average of all the x and y co-ordinates of the pixels that comprise the image of the hole. The accuracy to which the perimeter is recorded depends on the increment specified by the user, the limiting accuracy being when such a small increment is used that the same pixel on the perimeter of the hole is recorded by two or more subsequent radial scans. The author also included the facility to specify an averaging factor whereby a moving average would be calculated so that the hole perimeter could be smoothed if required (smooth.c appendix E), for example if the irregularities were present due to poor imaging quality. This smoothing was not required however for the author’s analysis but may be of use to future users of the system.

Figure 2.14 shows the results for an example SEM image of a hole (1) that is first thresholded at an appropriate brightness (2). It doesn’t matter if some of the foil pixels are below the threshold brightness and are recorded as “interesting” as can be seen in image 2 because the seed-fill algorithm always starts at the centre of the image, so as long as the boundary of the hole comprises only black pixels then only the hole will be filled and marked as interesting. Part 3 of Figure 2.14 shows the data plotted with the best-fit ellipse. The fitting was performed using the widely used plotting program *Gnuplot*, which is freely available on the World Wide Web. The program’s non-linear least squares fitting routine was used, which implements the *Levenberg-Marquandt* algorithm - the most widely used non-linear least squares algorithm (appendix A). A sample of the fits obtained by *Gnuplot* were checked against fits obtained using the commercial data analysis package *Microcal Origin*TM, which also uses the *Levenberg-Marquandt* algorithm as specified by (Press, 1992), and also against a non-linear least squares routine implemented by the author using

Microsoft *Excel*'s "solver". The author decided that it was not necessary to perform weighted fits as there was no apparent reason that would give rise to dissimilar uncertainties in the hole perimeter co-ordinates. The minimum uncertainty in the hole perimeter would be the distance corresponding to a single pixel of the image.

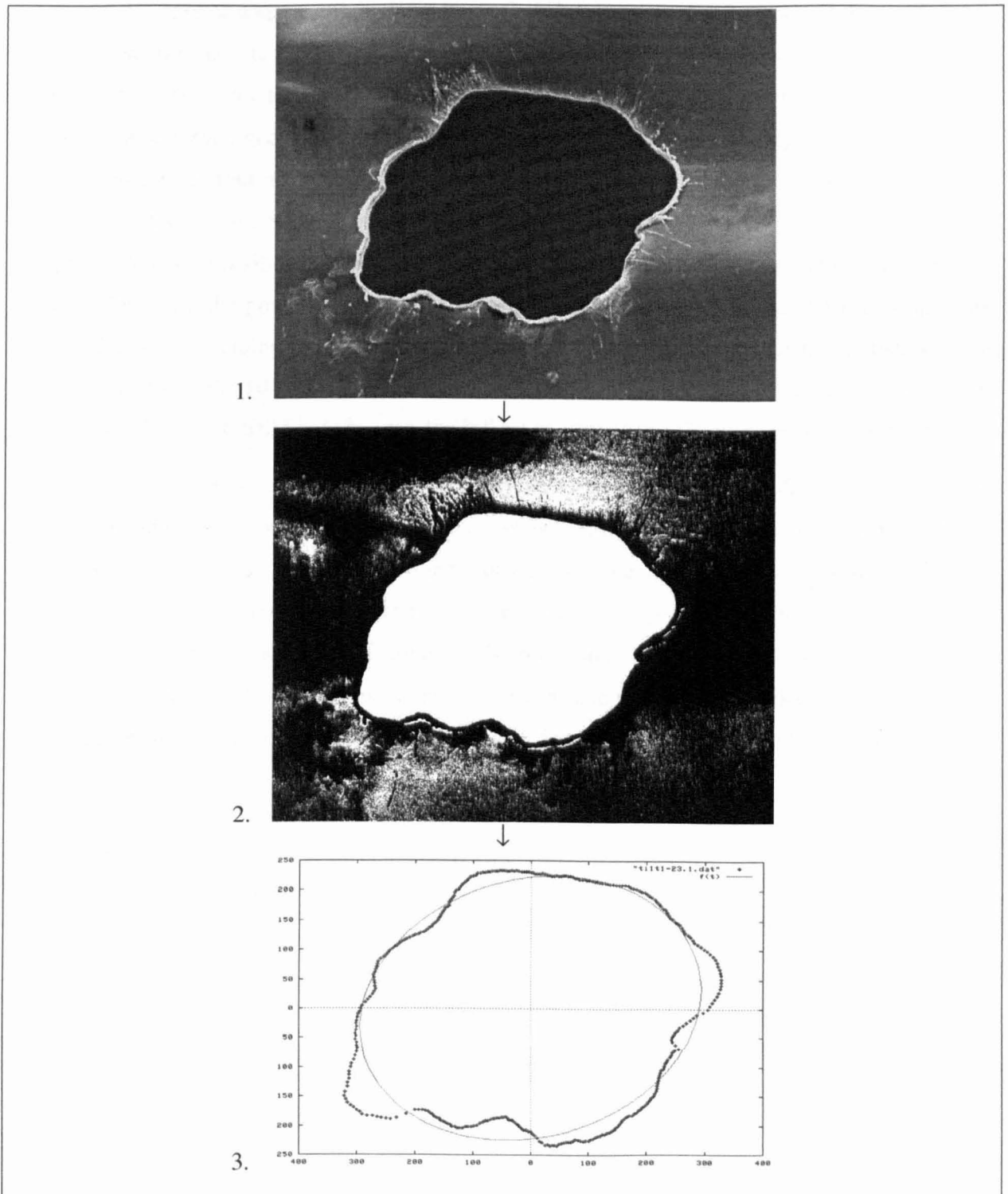


Figure 2.14 – Steps in obtaining an ellipse fit for a TICCE perforation

The equation fitted was the equation of an ellipse in polar co-ordinates such that the radial distance r is fitted against the angle θ :

$$r = \frac{ab}{\sqrt{a^2 \sin^2(\theta + \phi) + b^2 \cos^2(\theta + \phi)}}$$

where the fitting parameters a , b and ϕ are the semi-major axis, semi-minor axis and orientation of the major axis with respect to $\theta = 0$, respectively. The process of obtaining fits could for the most part be run in “batch mode”, that is to say the SEM image file is piped into the thresholding/filling routine, the output of which is then piped into the radar scan/perimeter co-ordinate recording routine, the output of which is finally piped into *Gnuplot* giving as the final output the coefficients and statistics for the fitted ellipse. However, for some poor-quality, low-contrast SEM images the author had to first adjust the brightness and contrast in an image processing software package - in a few cases it was even necessary to manually paint some black around the edge of the hole for the thresholding/filling routine to successfully mark the correct region as the hole. This should not be necessary if in future the SEM operator is aware that a high contrast image is required with the hole being as dark as possible if these routines are going to be used for subsequent processing. Nevertheless once the poorer images (only around 10-20 of the total 104) had been enhanced the entire process of obtaining the co-ordinates of the hole perimeters, coefficients and statistics of the best fit ellipses for the 104 TICCE holes took less than 5 minutes. Figure 2.15 shows the results for some example TICCE SEM hole images, the full set of images and fits is given in appendix B.

The fitting routine was not infallible however. Figure 2.16 shows two examples where the routine has converged on the wrong solution. In both cases the routine has converged on a minimum in the sum of squared residuals with the major and minor axes perpendicular to the *best* possible fit. The fact that there exists more than one minima in the parameter space meant that the author had to check each plot and if the wrong solution had been obtained, as is obvious in the cases in Figure 2.16, then the initial values of the major and minor axes had to be altered so that the routine would converge on the correct solution. This only had to be done for about 5-7 of the total number.

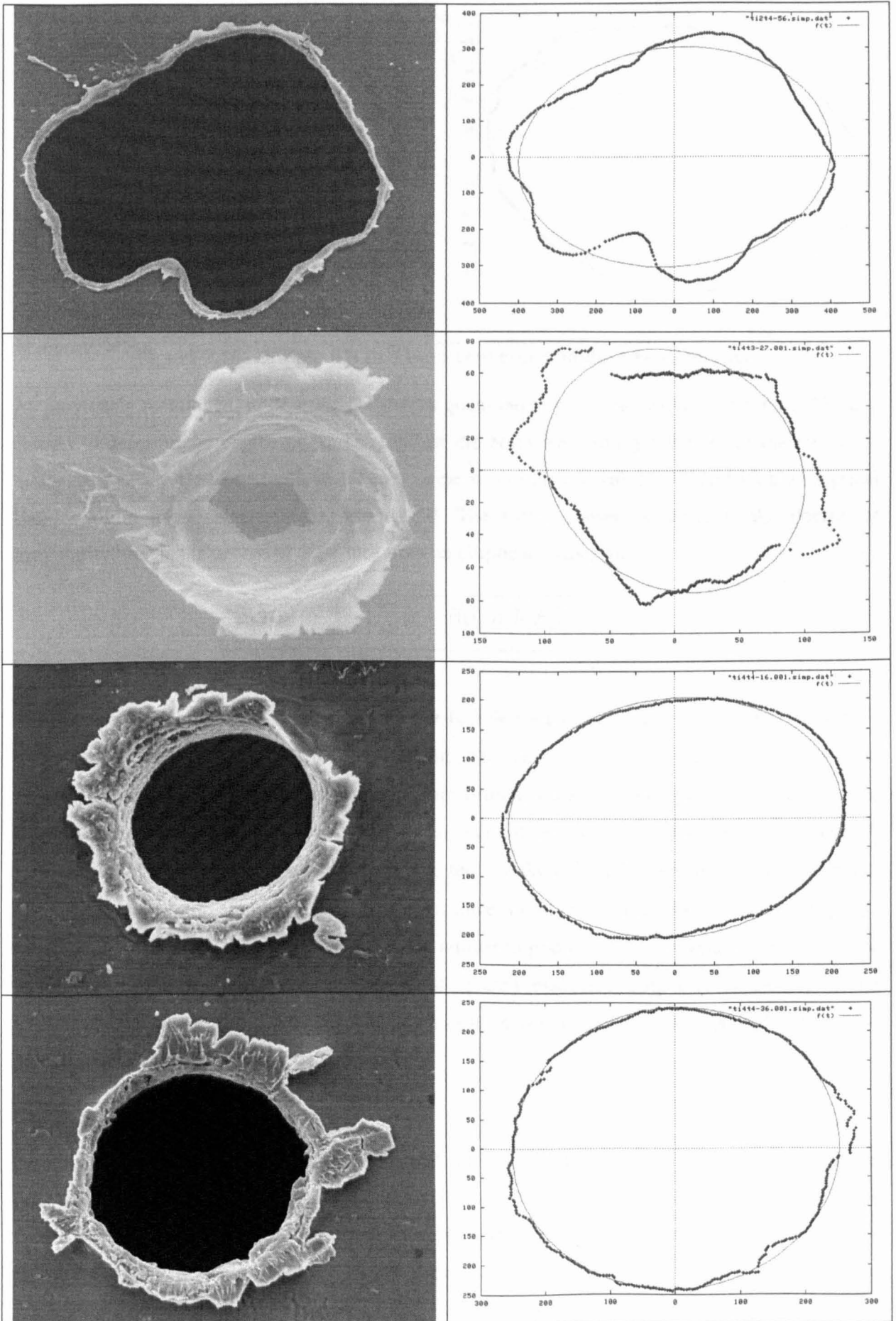


Figure 2.15 – Example holes and fits

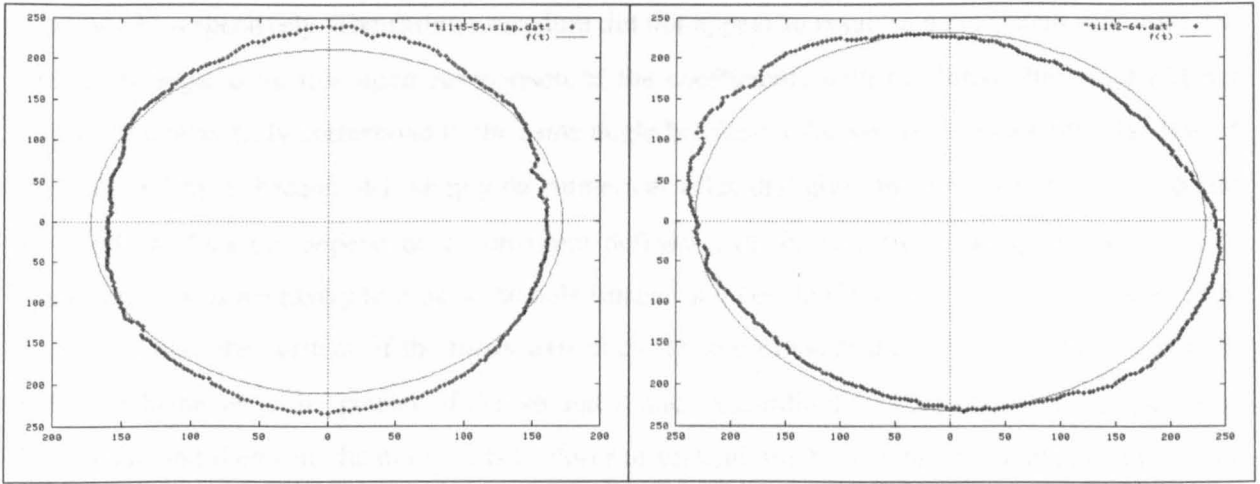


Figure 2.16 – Ellipse fits that have converged on the wrong solution

As previously mentioned, to describe the shapes quantitatively two factors were required. The one chosen to describe the degree of “circularity” of the holes was simply the ratio of the minor-to-major axes of the best-fitted ellipse. Thus a circle would have a value of 1 and highly elliptical shapes would have values tending towards 0. The factor chosen to describe the degree of irregularity, that is the degree of departure from an elliptical shape, was:

$$S = \sqrt{\frac{\sum_i (r_i - \hat{r}(\theta_i; a, b, \phi))^2}{ab}}$$

Thus giving a dimensionless “shape factor” that is independent of scale i.e. the same *shape* hole will give the same value regardless of its absolute size. This value will be 0 for a perfect fit to an ellipse and will increase with increasing departure from an elliptical shape. It can be seen that the shape factor S is the root sum of squared residuals normalised by the geometric mean diameter. A more generalised factor may have been to use the standard deviation normalised by the mean diameter, which would simply be S/\sqrt{n} . However, since for all the analyses in this thesis 360 points were used, it was found that not dividing by the number of points gave a numerically “tidier” shape factor that varied in the range 0 to 10. The sum of squared residuals is output by the *Gnuplot* fitting routine. The value was once again checked against the values computed by *Microcal Origin* and the author’s calculations using *Microsoft Excel*.

2.3.3. Correcting the TICCE data

Now that we have the major and minor axes of the best-fit ellipses to the TICCE holes *and* the orientation of the major/minor axes it is possible to correct the major-to-minor axis aspect ratios for the SEM astigmatism discussed earlier. This is more important for this study, where we are investigating the circularity, than for previous studies where the geometric mean diameter was the variable of interest. Figure 2.17 shows a fitted ellipse with the vertical and horizontal components of the semi-major (A) and semi-minor (B) axes. It was decided in section 2.2.3 that only the vertical calibration of the SEM images needed correcting by a factor of 0.95. Therefore the corrected vertical components of the semi-major and semi-minor axes are $A \sin \phi / 0.95$ and

$B\cos\phi/0.95$ respectively. The fitting procedure did not appear to result in a consistent definition for the offset angle ϕ , in that upon comparison of the coefficients with the fitted ellipses, ϕ did not appear to consistently correspond to the same angle between a the x-y axis and a particular axis of the ellipse. This is because ϕ is simply the numerical value that gives the best fit based on $\cos\phi$ and $\sin\phi$, which does not depend on a consistent definition of the direction corresponding to $\phi=0$. Therefore, it was necessary to look at the hole images and decide if the major axis was closer to the horizontal than the vertical. If the major axis is closer to horizontal then its horizontal component will be whichever is the greater of $A\cos\phi$ and $A\sin\phi$. Accordingly, if the major axis is closer to horizontal, and therefore the minor axis is closer to vertical, the horizontal component of the minor axis will be whichever is the smaller of $B\cos\phi$ and $B\sin\phi$.

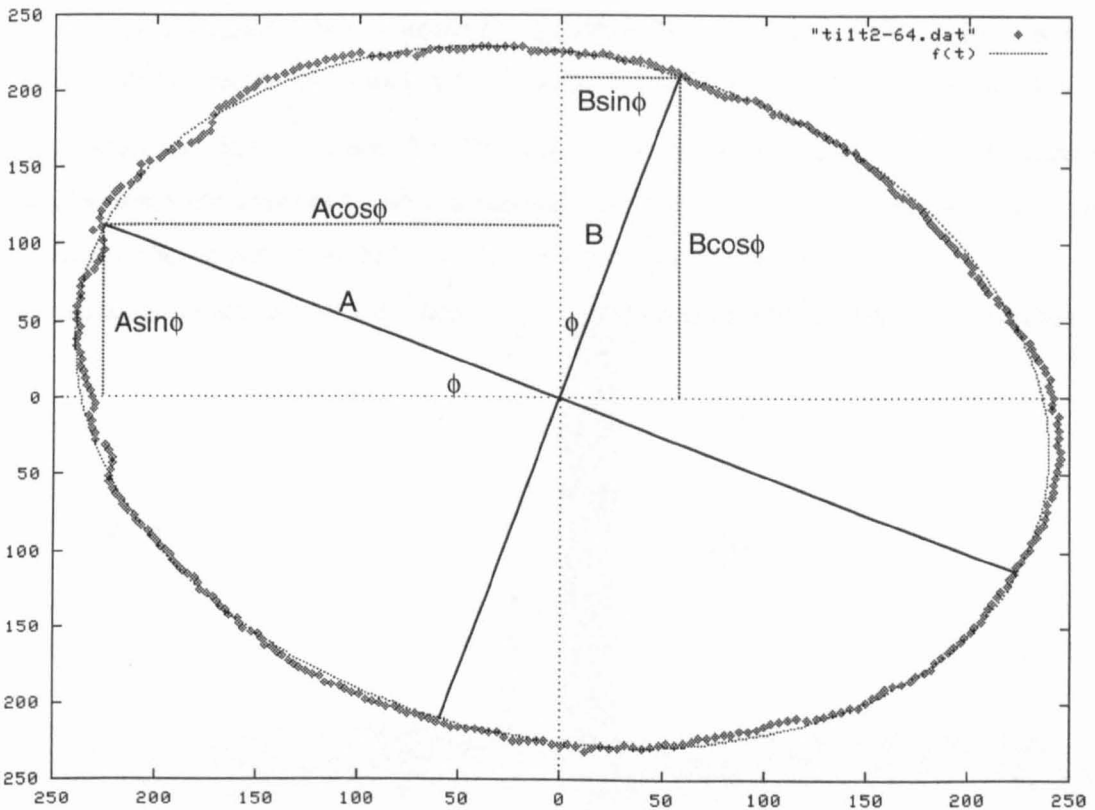


Figure 2.17 – Correcting the aspect ratio

For the example shown in Figure 2.17 the corrected major (a) and minor axes (b) are given by:

$$a = 2\sqrt{(A\cos\phi)^2 + \left(\frac{A\sin\phi}{0.95}\right)^2}$$

$$b = 2\sqrt{\left(\frac{B\cos\phi}{0.95}\right)^2 + (B\sin\phi)^2}$$

For some highly circular holes it could be that the author incorrectly identified the horizontal axes as being the major axis when in fact the vertical dimension was larger. This error would be largest when the major and minor axes are aligned with the x-y axes i.e. when $\phi=0$, which would lead to the horizontal axis being increased by 5% instead of the vertical axis, thus giving a 10% error in aspect ratio. This error is believed to have a negligible effect on the overall distribution of

circularities in that even if the author was biased such that roughly circular craters were more often assigned as being larger in the horizontal dimension it is unlikely that a significant proportion of them would *actually* be vertically larger. In other words this is likely to be a random error as it is unlikely that holes would be *consistently* have the wrong orientation attributed to them, thus constituting a systematic error. Therefore, this error may *widen* the distribution to some extent but it is not believed that it would bias the location of the “centre” of the distribution. It was found by comparing the corrected circularities to the crater images that holes that were horizontally larger had their circularities increased and those that were vertically larger had their circularities decreased as expected. For the case of a hole that is larger in the vertical direction the circularity should decrease upon correction but if the hole is mistakenly identified as being horizontally larger the circularity will be increased. For the case of a mistake for a horizontally larger hole the circularity will be decreased when it should be increased. Thus, the *signs* of the two possible errors are opposite and thus, as already stated, the error is more likely to be random than systematic.

For future reference, the corrected TICCE data set is given in appendix B. The percentage difference between the corrected and original data is shown in Figure 2.18; the vertical stalks simply illustrate the relative magnitudes of shifts from original to corrected values.

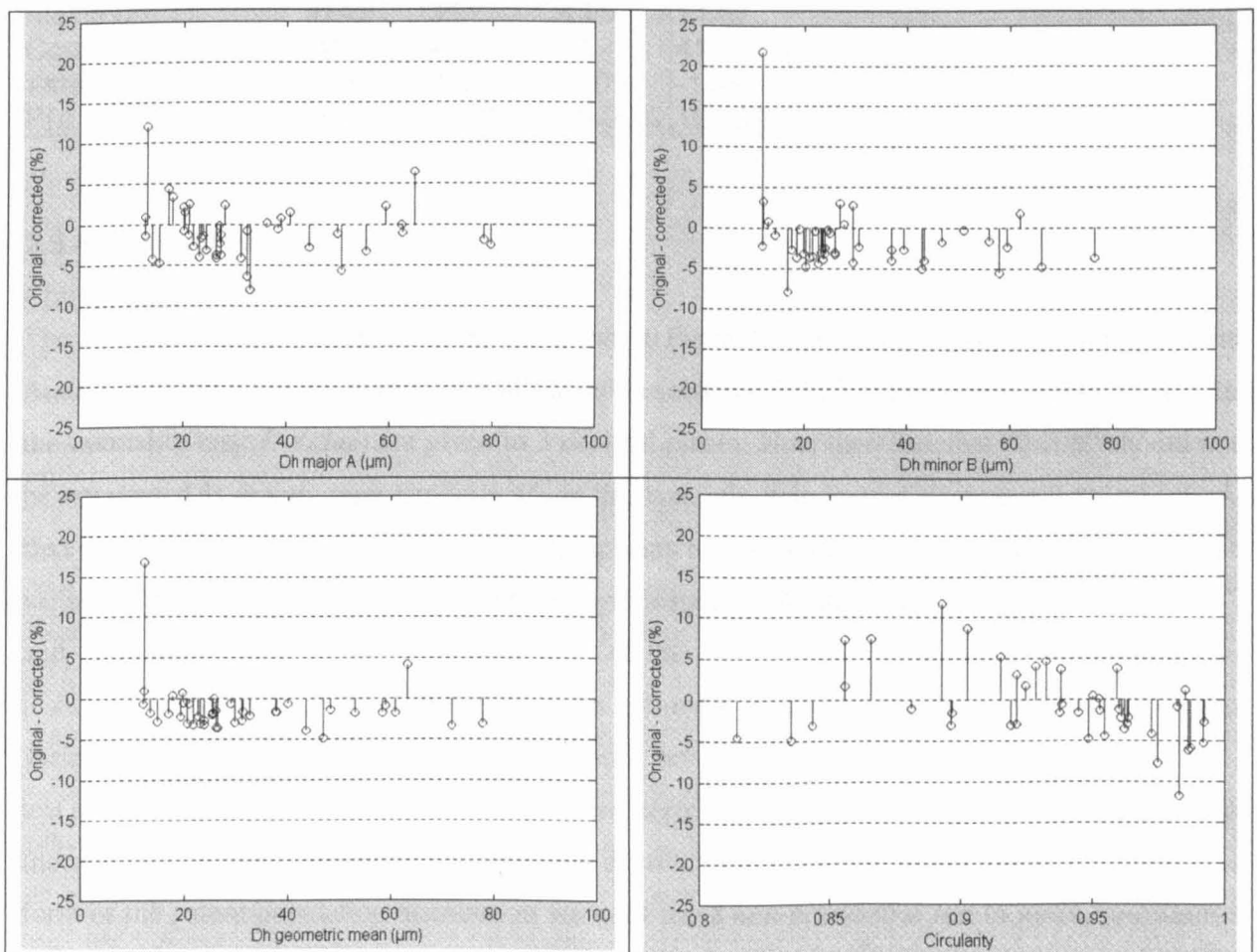


Figure 2.18 – Difference between corrected and original data

There is one hole where the minor axis was measured much more imprecisely in the original data collection than the rest of the craters. This is easily visible in Figure 2.18. This impact was excluded as an anomalous measurement when studying the overall trend in the error between the

corrected and original data. Table 2.6 shows the summary statistics for this percentage error. The *t*-statistic is the number of standard deviations the mean is from 0, where the standard deviation of the mean is the standard error. The probability associated with this value (from the *Student's t*-distribution with $n - 1$ degrees of freedom) is the probability that the mean percentage error is 0. It can be seen that there is only a reasonably acceptable probability of this being true for the circularity (B/A). For the other parameters the astigmatism – and possibly some operator bias that is eliminated by using the automatic ellipse fitting – introduces a *systematic* error into the measurements with the hole measurements being systematically too small. The astigmatism will introduce more of a random error into the circularity tending to widen the distribution rather than shifting the abscissa of the mean.

Table 2.6 – Summary statistics for differences between corrected and original data

Error (%)	A	B	\sqrt{AB}	B/A
Mean	-1.20	-2.24	-1.75	-0.94
Standard Error	0.47	0.38	0.25	0.70
Median	-1.27	-2.66	-1.75	-1.54
Standard Deviation	3.00	2.40	1.58	4.48
Range	14.33	11.07	8.96	23.40
Minimum	-7.91	-7.80	-4.87	-11.73
Maximum	6.42	3.27	4.09	11.67
Count	41	41	41	41
<i>t</i> -statistic	-2.56	-5.97	-7.09	-1.34
P(<i>t</i>)	1.42%	<0.00%	<0.00%	18.76%

2.3.4. Hole circularity

Circularity distribution

The circularity frequency distributions are shown in Figure 2.19 with a normal probability plot (the Anderson-Darling test for normality is discussed in section 6.1.2). The probabilities associated with the normality test (*P-Value*) are given to 3 decimal places. Note therefore that “0.000” should not be interpreted as *exactly* zero; similarly where this type of output is used elsewhere in this thesis. A first observation is that the thickest foil (ti4t) appears to have more circular impacts with a smaller variation in circularity. Formal tests for the significance of the difference between the “location” and “spread” depend on the functional form of the distribution. For a normal distribution the location or “average” of the distribution is the arithmetic mean and the measure of spread is the variance. The corresponding tests for comparisons between sample means and variances are the *t*-test and *F*-test, respectively. These are *parametric tests* as they are based on *parameters* of a known (normal) population distribution function. For distributions where we do not know the functional form of the parent population distribution we must use a *non-parametric test* to make quantitative comparisons between distributions. For distributions of unknown functional form the appropriate measure of the location or “central tendency” of the distribution is the median. A description of tests for medians follows as they are used throughout this thesis.

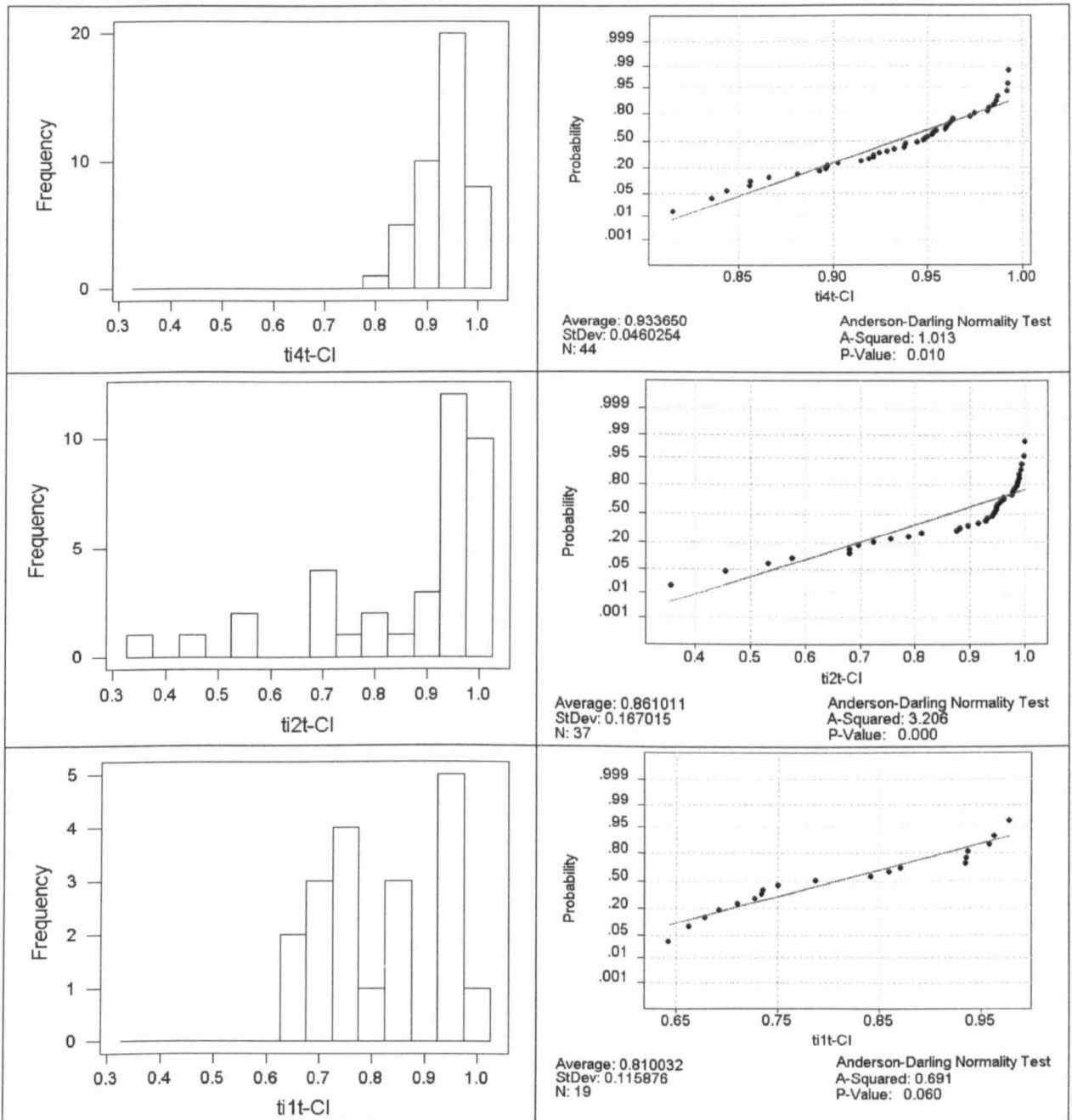


Figure 2.19 – Distribution of TICCE hole circularities

A simple test for medians is the *sign test* (Hugill, 1985), which is simply based on the fact that we expect to find half the values in the distribution on either side of the median (by definition). To test if the sample is likely to come from a population with median X the *sign* of the difference between each datum and X is taken. The probability that the population median is X is given by the binomial probability of the number of positive signs occurring for N trials (where N is the number of data points) with a probability of $\frac{1}{2}$ i.e. the probability of a value being greater than the median. However, the sign test for medians is rather crude in that it only counts the number of values on either side of the median and thus does not take into account the *magnitude* of deviations from the median. A related test, which takes magnitudes into account is the *Wilcoxon rank-sum test* (Hugill, 1985), which is based on the idea that if two distributions are the same they should be balanced around the same median. Thus if the values from both of the two samples to be compared are placed in rank order, the sum of the *ranks* from each sample should be equal. The *Mann-Whitney*

formulation (Cooper, 1969) of the Wilcoxon rank-sum test is implemented in the statistical package *Minitab*; this software is used for analysing the distributions presented here. The Mann-Whitney test is the non-parametric equivalent to the t -test for sample means from a normal population and gives the same result when applied to a normal distribution.

Table 2.7 shows the summary statistics for the circularity data and Table 2.8 shows the results of Mann-Whitney and t -tests between the sample medians and means, respectively. The tests indicate that the two thickest foils (ti4t and ti2t) do not have significantly different average circularities but that the thinnest foil has holes that are significantly less circular than the thicker foils. The thinner ti2t foil does have a significantly different distribution to the thickest foil despite having a similar median, the means are significantly different and the thinner foil has a much wider spread of circularities.

Table 2.7 – Summary statistics for TICCE hole circularity data

	ti4t	ti2t	ti1t
Mean	0.934	0.861	0.810
Standard Error	0.007	0.027	0.027
Median	0.946	0.942	0.787
Standard Deviation	0.046	0.167	0.116
Kurtosis	0.054	1.759	-1.603
Skewness	-0.858	-1.571	0.120
Range	0.178	0.644	0.335
Minimum	0.815	0.354	0.642
Maximum	0.993	0.998	0.977
Count	44	37	19

Table 2.8 – Tests for differences between circularity distributions

Hypothesis	ti4t = ti2t	ti4t = ti1t	ti2t = ti1t
Mann-Whitney test for medians	36%	0.01%	3.3%
2 sample t -test for means	1.4%	0.02%	19%

The results here are somewhat anomalous in that we would expect the 2.1 μm and 1.73 μm ti2t and ti1t foils to have distributions more in common with each other than the thicker 9.2 μm ti4t foil. They both have a larger spread of circularities than the thicker foil with more higher aspect ratio holes, but the ti2t foil has a closer median to the ti4t foil. The assumption that the *only* influence on the circularity distributions is the foil thickness may not be valid for such small samples of holes. It could be that that significant differences in average shape and trajectory of the impacting particles on each foil has a comparable effect to the foil thickness. However, the general observation that the holes in the thickest foil are more circular is sensible in that it is known that for an infinitely thick target holes are mostly circular and for a thin target the particle's cross-sectional shape will be retained to some extent.

Correlation of circularity with hole size

The correlation of circularity with size is plotted in Figure 2.20. If we define “significant correlation” as the probability of the observed correlation coefficient arising by chance, $P(F)$, being less than 5% (the F -statistic is described in appendix A), then for the thickest foil (ti4t) the correlation of circularity with size is insignificant, but is significant for the two other foils.

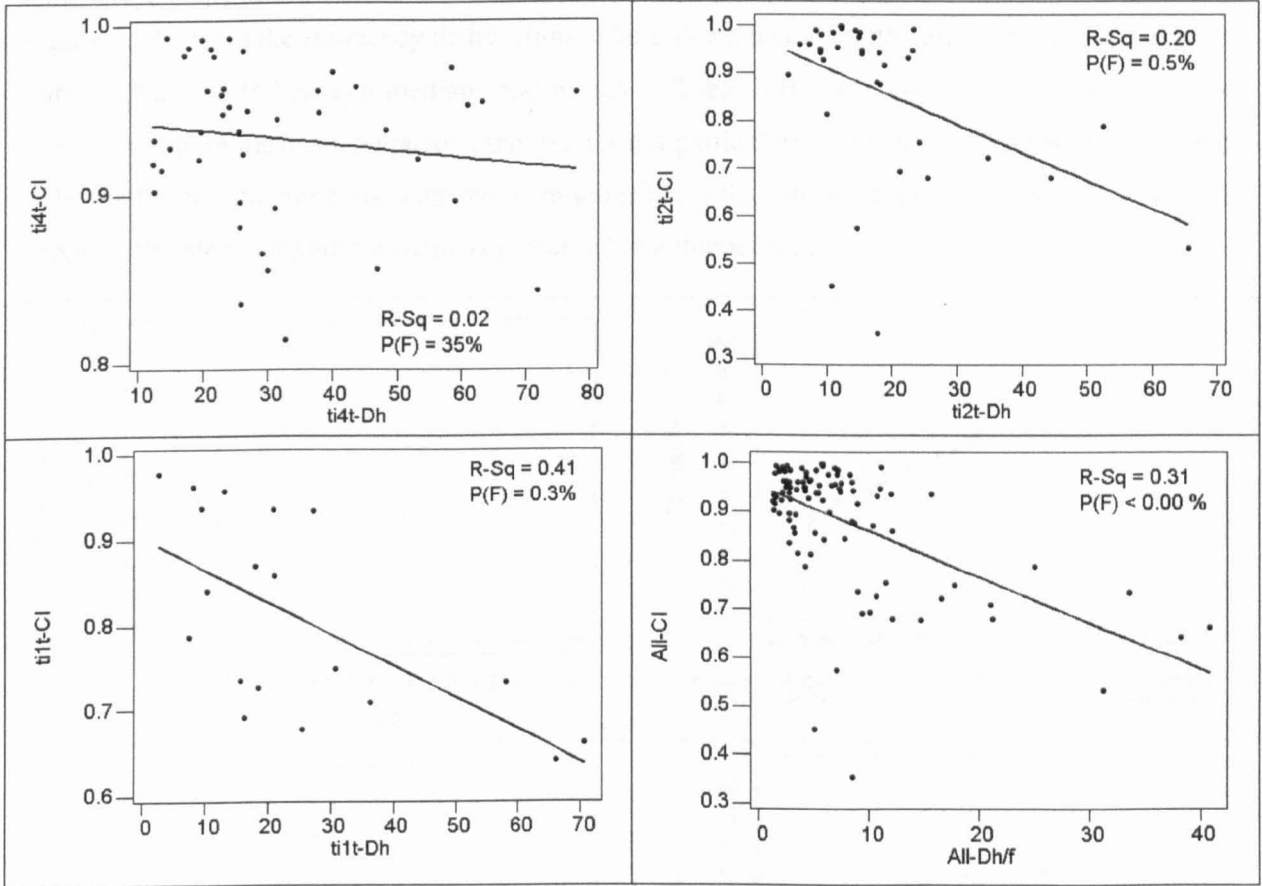


Figure 2.20 – Correlation of circularity with size

However, as the data for the ti2t and ti1t foils appears somewhat sparse, it could be that a single outlier is solely responsible for the apparent correlation. Therefore, for these two data sets the F -test for significant correlation was recalculated with each data point excluded in turn to study the effect of removing a single point. For the ti2t foil it was found that the maximum $P(F)$ of 5.1%, corresponding to the *least* significant correlation, was attained when the largest hole was excluded. For the ti1t foil the maximum was 1.2% with the second-largest hole excluded. Thus, for the thinnest foil the correlation is still significant whichever possible “outlier” is removed and for the second-thinnest foil (ti2t) the probability has only just exceeded our subjective* 5% significance threshold. Therefore, the author feels that there is still reasonable evidence that the correlation of circularity with hole size becomes stronger with decreasing foil thickness.

The data from all 3 foils was normalised by the foil thickness (d_h/f) and plotted together in the bottom-right pane of Figure 2.20. The highly significant ($P(F) < 0.00\%$) correlation of circularity with *normalised* hole size suggests that either smaller particles are more circular and/or particle

* The decision as to what probability demarks the boundary between “significant” and “insignificant” is invariably subjective, although 5% is the most widely employed value (Hugill, 1985 or Cooper, 1969).

shape is preserved to a greater extent in thinner foils. This may explain why the ti2t circularity distribution is closer to that of ti4t than to ti1t that has almost the same foil thickness. The ti2t mean hole size is 18 μm , but the ti1t mean is 25 μm so the foil is *relatively* thicker for the ti2t holes.

2.3.5. Hole shape

Hole shape distribution

Figure 2.21 shows the frequency distribution of hole shape factors, with summary statistics given in Table 2.9 and tests between medians and means in Table 2.10. Although the holes in the thinner foils have higher mean shape factors, the trend is not particularly significant. The variation in shape is larger for the thinner foils with more irregular holes than in the thicker foil, which once again supports the idea that particle shape is preserved in a thinner foil.

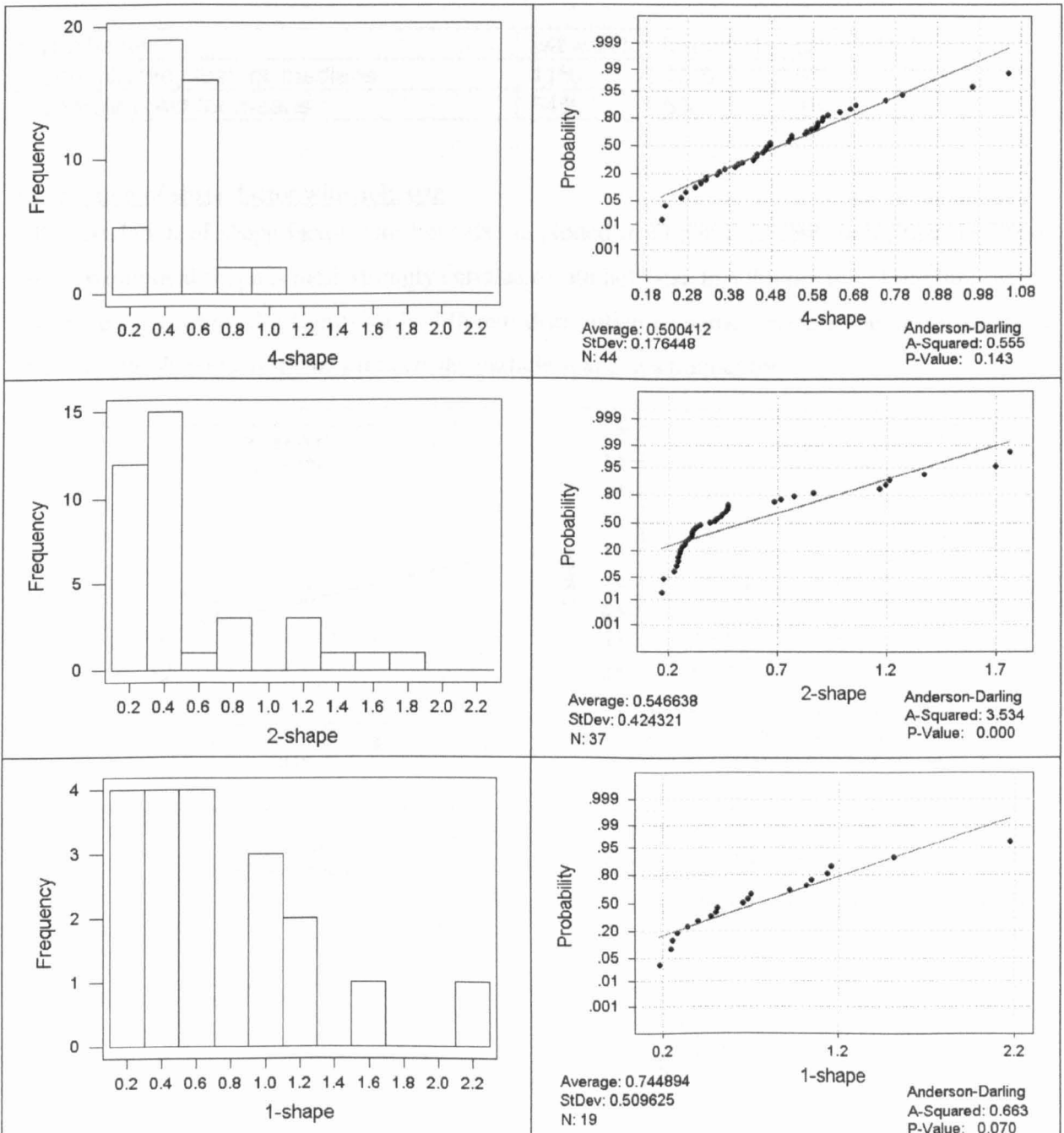


Figure 2.21 – Distributions of TICCE hole shape factors

Table 2.9 – Statistics for TICCE shape factor data

	ti4t	ti2t	ti1t
Mean	0.500	0.547	0.745
Standard Error	0.027	0.070	0.117
Median	0.472	0.388	0.654
Standard Deviation	0.176	0.424	0.510
Kurtosis	1.620	1.863	2.072
Skewness	0.964	1.652	1.343
Range	0.832	1.594	1.995
Minimum	0.217	0.169	0.178
Maximum	1.049	1.762	2.173
Count	44	37	19

Table 2.10 – Tests for differences between shape factor distributions

Hypothesis	ti4t = ti2t	ti4t = ti1t	ti2t = ti1t
Mann-Whitney test for medians	11%	13%	9%
2 sample t-test for means	54%	6%	16%

Correlation of shape factor with hole size

The correlation of shape factor with hole size is plotted in Figure 2.22 and shows that departure from an elliptical shape is more strongly correlated with hole size in a thinner foil. Therefore unless the three foils received a significantly different distribution of particle shapes this result suggests that the hole shape more closely reflects the particle shape in a thinner foil.

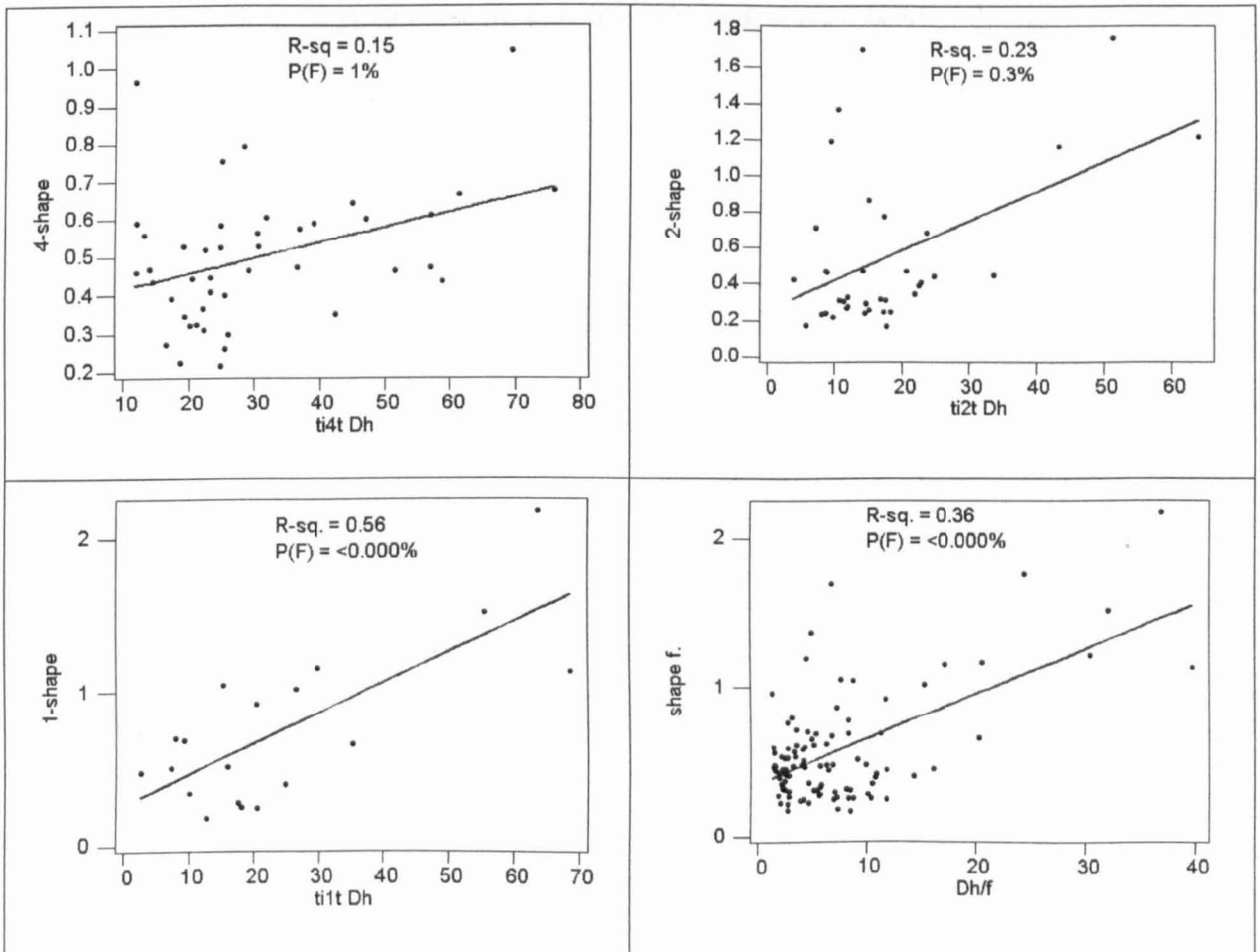


Figure 2.22 – Correlation of shape factor with size

2.4. Summary

The data collected by the TICCE scanning team has been re-evaluated to take into consideration factors that were not adequately addressed in previous publications. It is important that this data set is reliable in that it represents the most important measurement of the near-Earth meteoroid flux by a dedicated capture cell device since LDEF. Areas addressed were:

- Uncertainties in hole diameter measurements and correction of the measured hole diameters for the previously unknown astigmatism of the Unit's SEM system.
- Precise re-calculation of the foil thicknesses and its variation with position.

In order to perform an analysis of the distribution of hole shapes an extension of the LOSS system was implemented adding the capability to automatically measure perforations by a method that is free from operator bias and records more information about a perforation than was previously possible. Specifically, the polar co-ordinates of each hole perimeter.

The analysis of the hole shape distribution showed that for foils exposed to a statistically identical flux that a different distribution of shapes is observed depending on foil thickness. Therefore, any interpretation of hole circularity in terms of impact trajectory must take foil thickness into account. Previous analyses have not done so (e.g. Gardner, 1995). In order to interpret the significance of hole circularity and shape, the response of hole shape to projectile trajectory and shape for different target thicknesses must be investigated. In view of the lack of adequate previous investigation in this area an experimental programme to study this behaviour was initiated by the author.

3. Oblique hypervelocity penetration of thin metal targets

The analysis of the TICCE perforation data in the previous chapter highlighted the need for an understanding of the oblique hypervelocity penetration process. It is intuitively obvious that a sufficiently thin plate will simply record the projection of the particle shape onto the plane of the target as a penetration feature. In contrast, it has been shown that semi-infinite target response to oblique hypervelocity impacts is insensitive to impact angle up to a certain “critical angle”, usually $> 60^\circ$ (Gardner and Burchell, 1997). It is the intermediate regime where the transition from “thin” to “thick” behaviour takes place that will be investigated in this thesis. This progression of *hole growth* with target thickness has been investigated for normal impacts using progressively larger particle to plate thickness combinations and functional forms have been fitted to describe the behaviour, notably by Gardner *et al.* (1997a). However no term for impact angle has as of yet been included in these equations. Nevertheless these relationships established purely from normal impacts have been used to decode space impact data (Gardner *et al.*, 1997b and McBride *et al.*, 1999) by replacing the velocity term with $V\cos\theta$ and the hole diameter with the geometric mean of the maximum and minimum hole diameters. There has been no experimental support for these modifications.

The author initiated a series of impact experiments using Unit’s light gas gun, firing steel and aluminium spheres at aluminium alloy plates at $\sim 5 \text{ km s}^{-1}$, covering impact angles of 0° , 15° , 30° , 45° , 60° and 72° for particle-diameter-to-plate-thickness ratios of 0.67, 1.04, 1.42, 2.63 and 3.50. Thus the effect of impact angle and relative plate thickness (relative to the projectile size) on the size and shape of hypervelocity perforation features could be studied leading to a better understanding of the impact angle dependence relevant to decoding data from space-flown detectors.

3.1. Introduction

3.1.1. Previous studies

Hypervelocity penetration of thin metal plates or foils is a phenomenon almost entirely limited to impacts in space. The primary interest in this area is concerned with the performance of spacecraft *bumper shields*, whereby a stand-off plate is used to disrupt an incoming meteoroid or space debris particle before it impacts the spacecraft main wall (McDonnell, 1978). Another scenario is the thin foil *capture cell* (McDonnell *et al.*, 1984) whereby a thin, usually aluminium, foil is mounted above a stop plate with the aim of decoding the impacting particle diameter from the foil perforation and capturing particle residues for chemical analysis on the second, or occasionally third, surface. Such impacts in space occur at speeds of over 7 km s^{-1} for man-made space debris, around 20 km s^{-1} for meteoroids, occasionally as high as 70 km s^{-1} but rarely below 3 km s^{-1} (McDonnell, 1999).

The study of *hypervelocity* penetration phenomena has mostly been limited to impacts normal to the target surface; normal impacts are, of course, the exception under real conditions. Additionally, the majority of literature addressing *oblique* penetration is limited to *sub-hypervelocity* speeds (rarely exceeding 1 km s^{-1}), chiefly driven by military concerns such as the effectiveness of tank armour. At these speeds phenomena associated with the hypervelocity regime do not come into play such as strong shock waves and hydrodynamic flow (Melosh, 1989). Oblique hypervelocity impacts in semi-infinite targets has received much attention, however there has been little experimental study of oblique hypervelocity *penetration*, covering a wide enough range of particle-diameter-to-target-thickness ratios (d_p/f), to confidently establish empirical relationships or to thoroughly test (semi) analytically derived ones.

Herrmann and Wilbeck (1987) give a review of hypervelocity penetration theories but only mention previous investigations of oblique impacts in *semi-infinite* targets, indicating a lack of investigation up to that point. Most of the work investigating hypervelocity oblique penetration is concerned with the effect of the “debris cloud” (the disrupted projectile after penetration) on a second surface as the investigation is aimed at testing the effectiveness of a bumper shield in protecting a spacecraft surface e.g. Ari and Wilbeck (1993). It is the second scenario described above, namely the capture cell, that is the concern of this work where the primary goals are determination of particle size and trajectory rather than the effects on surfaces behind the target.

Schonberg and Taylor (1989), in addition to studying debris cloud effects, derive a relationships between the major and minor hole diameters and the impact angle, projectile diameter, plate thickness and velocity through “regression analysis”. As their experimental programme comprised only 22 shots it is unlikely that they actually have enough data to give a meaningful fit against 3 (or 4, depending on whether particle sizes and plate thicknesses are combined as a single variable) independent regressors. Statistical texts recommend that the number of data points required in multiple regression is at least 10 times the number of regressors (Ryan, 1997). The author is not satisfied with the regression analysis they present particularly when they appear to compare a fit to an equation with 5 parameters to 5 data points. Another general criticism is that no mention of any uncertainties in any of the experimental parameters is made. The mean percentage “error” and its standard deviation are quoted when comparing data to equation predictions. Interpretation of the significance of these “statistics” is not obvious. If by “error” they mean the arithmetic difference between the fitted and actual value then the average of this should be approximately 0 depending on how good their regression algorithm is and how closely its associated assumptions are met. If they mean the squared residual then how can the negative values that are quoted occur? Qualitative statements like “*the equations were found to predict the minimum hole dimension under oblique impact rather well*” and “*it can be seen that the equations are a fairly good fit to the data*” presumably appeal to the readers own judgement of the raw data, but with no uncertainties in the data presented no judgement can be made as to how well the equations model the data. To quote Lyons’ (1991) undergraduate text: “*Without error estimates it is impossible to judge consistency*”

with anything". In the table of raw data given the authors neglect to specify the plate thicknesses used and so their data, unfortunately, cannot be compared to the experimental results of this thesis.

Baker and Persechino (1993) announce the construction of an analytical model that computes both the major and minor diameters of oblique hypervelocity impact holes for *all* target thicknesses up to the ballistic limit. However, they note that "*more data is needed to properly validate the model over the full range of target thicknesses*"; the model was only tested for 2 target thicknesses. They present no uncertainties in the data used – it was someone else's data – and no quantitative evaluation of their regression, merely stating that the parameters of the regression were found by "*trial and error*". It is questionable that their model is actually "analytical" in that the equations were simply chosen to give the best fit to the data. They try to persuade us by adding "*It should therefore be recognised that, while these equations were not obtained by pure deduction from fundamental first principles of physics, nevertheless the physics of the impact process is inherent in the data itself and is therefore contained in the analytical model.*" Surely this is so for any experimental data and hence it is not clear where their distinction between "empirical" and "analytical" lies.

Christiansen *et al.* (1993) performed a series of experiments firing aluminium projectiles at thin aluminium plates for a single particle-diameter-to-plate-thickness ratio (d_p/f) of 7.2 at angles from 0-88° from normal at $\sim 6 \text{ km s}^{-1}$. They do not present any quantitative empirical relationship between the hole dimensions and the impact angle, but simply note that above a certain angle the hole becomes irregular and multiple cratering occurs. They subsequently present hydrocode simulations that predict the onset of particle disruption at a *critical angle* of incidence. It will be shown later that this is a pertinent result for the analysis of the experimental data presented here.

Grady and Kipp (1994) performed experiments at 3-5 km s^{-1} , firing copper spheres through steel plates at $d_p/f = 1.1$ at angles of 0° and 30.8°. The primary result of this work was a comparison of the observed debris cloud dynamics with a hydrocode model.

Farenthold (1995) simulated a single 23° impact of a aluminium sphere on an aluminium plate at $d_p/f = 3.7$ at 7.1 km s^{-1} using a hydrocode, again to study debris effects.

Other vaguely relevant literature the author located was either concerned with sub-hypervelocity penetration of rod shaped projectiles - plainly tank armour simulations - or only addressed the effect of the debris cloud on the second surface of a *Whipple* bumper arrangement.

Figure 3.1 shows the coverage of the angle- d_p/f parameter space in previous literature found by the author compared to that for this work.

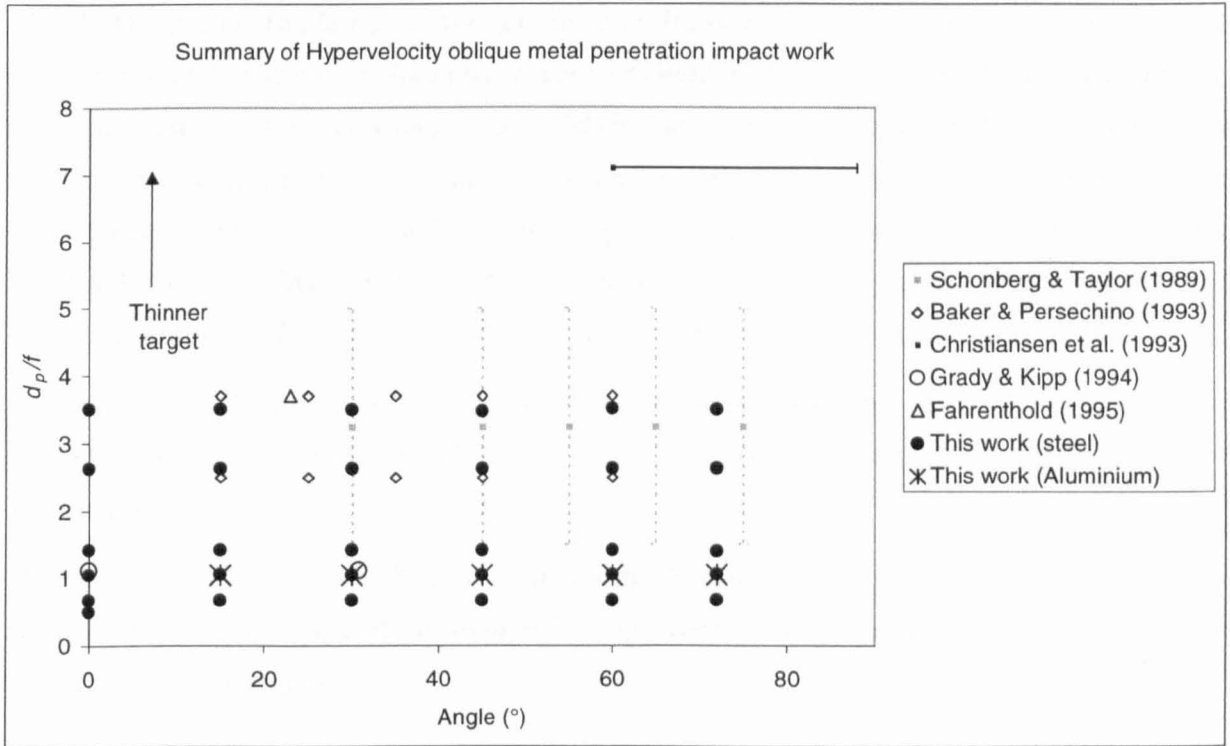


Figure 3.1 – Previous oblique penetration experiments

It can be seen that the author's coverage of the parameter space is unrivalled by previous studies mentioned here and of those is the only data set to which meaningful fits against both d_p/f and impact angle can be made, with the exception of possibly Schonberg and Taylor's data, which has to be shown in Figure 3.1 as upper and lower bounds only since the target thicknesses used are unavailable.

3.1.2. Experimental aims and rationale

The aim of this experimental programme is to derive relationships between the impact angle and hole major and minor axes over a range of relative plate thicknesses so as to determine how the hole-circularity-to-impact-angle relationship depends on target thickness. All other parameters will be held constant – or as near constant as is possible with the apparatus available. Thus, unlike some previous studies, no velocity dependence will be investigated. As can be seen in Figure 3.1 for each relative plate thickness there is data for at least 6 impact angles, thus a functional fit with 2 or possibly 3 parameters can be made with impact angle as the regressor and the other parameters held constant. Conversely fits with the relative plate thickness as the regressor and the impact angle held constant can be also made with 3 to 4 degrees of freedom. Fitting to each regressor with the others held constant is desirable for *multiple regression* (Ryan, 1997), where the dependent variables (hole size and shape) depend on more than one independent variable (plate thickness and impact angle). One set of experiments was repeated with identical conditions but using aluminium projectiles instead of steel to give a preliminary indication of the effect of projectile composition.

The projectiles chosen were steel ball bearings. The reasons being: (i) they are readily available; (ii) they are highly circular and have a small size variation; (iii) they have a higher success rate – i.e. actually staying on axis and reaching the target - than glass or aluminium projectiles in the

UKC light gas gun. The last point was an important factor as there were strict time constraints on this experimental programme. Admittedly, glass or aluminium projectiles may be closer in density to average densities of meteoroids and space debris, but this first investigation of this phenomena is not concerned with density dependence and will not go as far as refining a comprehensive tool for thorough decoding of space data. There are proposals that the effects of higher velocities can be simulated – as is required to simulate the LEO environment – by using denser projectiles at lower velocities (Mullin *et al.*, 1995), but the author has yet to be convinced of the validity of this.

The targets were aluminium HE30 alloy, which was chosen primarily because it is readily available in the laboratory in a wide variety of thicknesses and because it is widely used in previous impact experiments.

The velocity was chosen to be 5 km s^{-1} as this is the “standard” velocity of the UKC light gas gun and is the most easily repeatable, bearing in mind that for this experimental programme the velocity was required to be constant.

3.2. Experimental procedure

The projectiles used were stainless steel and 2014 aluminium alloy ball bearings nominally 0.8, 1 and 2 mm in diameter. The targets used were 0.57, 0.70, 0.96 and 1.49 mm thick aluminium alloy sheets, 140 mm square. The targets were mounted in a target holder borrowed from a commercial space consultancy company that frequently uses the University’s light gas gun. Figure 3.2 shows the configuration of the target assembly. The target holder allowed the mounting of several plates in a parallel arrangement separated by spacers and also plates perpendicular to the front target surface to intercept ricochet fragments.

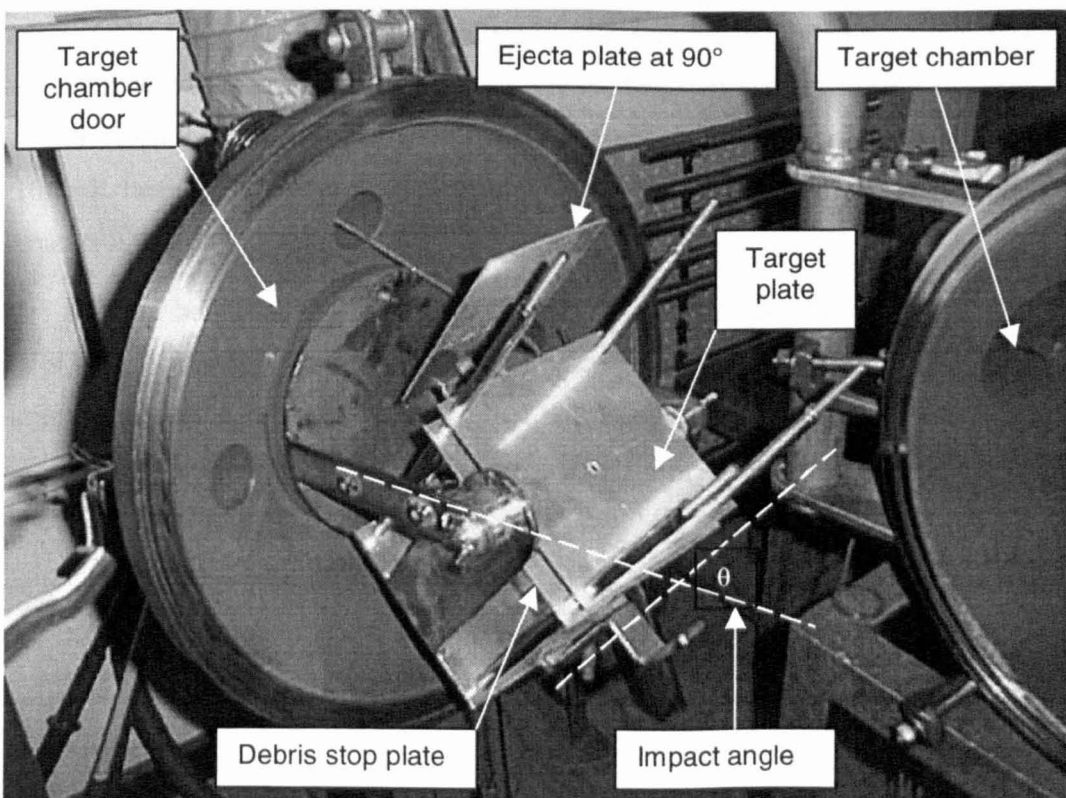


Figure 3.2 – Target holder arrangement

The entire arrangement could be rotated in the target chamber and secured so that the target plate was at the desired angle to the line of flight of the projectile. The axis of rotation approximately passed through the plane of the front target plate so that the impact was never more than a millimetre or so from the centre of the plate. A second aluminium plate was placed a few cm behind the target plate to protect the target holder from the high velocity debris exiting the rear side of the target. Another plate was also placed on the downrange side of the target at right angles to the surface to catch any ricochet ejecta. These plates were generally re-used to save time but a few were kept that had only been impacted from one individual shot for possible later extension of this study to rear-surface and ejecta phenomena.

3.2.1. Measuring the independent parameters

Target thickness

The thickness of the aluminium plates used for the experimental programme was measured using a digital micrometer that reads to the nearest micron. For each plate around 12 measurements of the thickness were made at fairly evenly distributed points on the surface of the plate; the results are shown in Table 3.1. The author chose the *standard deviation* as the “±” error term when quoting the plate thicknesses as this represents the 1σ ($\approx 68\%$ confidence) uncertainty in the thickness of a point on the plate chosen at random, whereas the *standard error* is the uncertainty in the *mean* thickness of the entire plate and will decrease with more measurements.

Ball bearing diameters

The diameters of the ball bearings used for the shots were measured using the digital micrometer again. The surface of the micrometer jaws was smeared with some grease to stop the ball bearing rolling away whilst the jaws were being closed. The jaws were closed after a ball bearing had been measured to see if the layer of grease added significantly to the measured diameter. It was found that when the greased jaws were closed that the zero reading only fluctuated by 2 to 3 μm . For four types of ball bearing used (0.8 mm, 1 mm and 2 mm stainless steel and 1 mm aluminium 2017 alloy) 10 ball bearings were chosen at random from the stock of each. A summary of the measurements is shown in Table 3.2.

It appears that the ball bearings are all systematically smaller than their nominal size, but the diameter of the stock is only quoted to 1 decimal place anyway and so is most likely in agreement with the manufacturer’s tolerance. 1.5 mm steel ball bearings were also used and for these it is assumed that they are made to the same accuracy as the 1 mm and 2 mm stocks i.e. to within 0.5% of their nominal diameter.

Table 3.1 – Summary of plate thickness measurements in mm

Shot #	1	2	3	4	5	6	7	8	9	10	11	12	13	17	19	25	26
Mean	1.491	0.703	1.489	0.703	1.489	0.960	0.958	0.574	0.569	0.568	0.569	1.492	0.569	1.491	0.568	0.703	0.704
Standard Error	0.001	0.001	0.001	0.001	0.001	0.003	0.001	0.002	0.001	0.001	0.001	0.001	0.001	0.001	0.000	0.000	0.000
Median	1.490	0.702	1.488	0.702	1.489	0.958	0.958	0.572	0.568	0.566	0.569	1.491	0.569	1.491	0.568	0.703	0.703
Mode	1.490	0.702	1.488	0.702	1.488	0.959	0.958	0.579	0.567	0.566	0.571	1.490	0.569	1.488	0.569	0.703	0.703
Standard Deviation	0.004	0.003	0.002	0.003	0.004	0.009	0.003	0.006	0.004	0.003	0.003	0.002	0.003	0.003	0.002	0.001	0.001
Range	0.011	0.013	0.007	0.014	0.016	0.034	0.011	0.019	0.014	0.012	0.010	0.006	0.011	0.013	0.007	0.004	0.004
Minimum	1.486	0.699	1.486	0.698	1.484	0.951	0.954	0.567	0.564	0.564	0.565	1.490	0.562	1.486	0.564	0.702	0.702
Maximum	1.497	0.712	1.493	0.712	1.500	0.985	0.965	0.586	0.578	0.576	0.575	1.496	0.573	1.499	0.571	0.706	0.706
Count	12	12	12	12	12	12	12	13	11	13	11	12	12	13	13	8	8
Confidence (95.0%)	0.002	0.002	0.001	0.002	0.003	0.006	0.002	0.003	0.002	0.002	0.002	0.001	0.002	0.002	0.001	0.001	0.001

Table 3.2 – Statistics for ball bearing diameters

Diameters in mm	0.8 mm steel	1 mm steel	2 mm steel	1 mm Al
Mean	0.791	0.995	1.991	0.992
Standard Error	1.80E-04	2.13E-04	2.13E-04	0.002
Median	0.791	0.995	1.991	0.996
Mode	0.791	0.995	1.991	0.996
Standard Deviation	0.001	0.001	0.001	0.007
Range	0.002	0.002	0.002	0.018
Minimum	0.790	0.994	1.990	0.980
Maximum	0.792	0.996	1.992	0.998
Count	10	10	10	10
Confidence Level(95.0%)	4.06E-04	4.83E-04	4.83E-04	0.005
% of nominal diameter	98.9%	99.5%	99.5%	99.2%

Impact angle

The target holder had graduations marked on it at 0°, 15°, 30°, 45° and 60°. These graduations were used for setting the target at the respective angles. The accuracy of each setting was subsequently checked with a spirit-level style inclinometer after the target holder was removed from the target chamber and was found to be good to $\pm 1^\circ$. Due to time constraints, a setting of 70° was estimated whilst the target holder was mounted in the target chamber and a graduation was marked for this setting. Subsequent measurement of the inclination when the target holder was set at this estimated “70°” graduation showed that it in fact corresponded to $72 \pm 1^\circ$. The impact point of the ball bearing was estimated to be within a 1 cm diameter region on each target. Since the muzzle-to-target distance is around 3 m this variation in trajectory contributes approximately $\pm \tan^{-1}(0.5/300)$ to the uncertainty in impact angle, which is $\pm 0.1^\circ$ and therefore negligible.

Velocity

The velocity was maintained as far as possible at 5 km s^{-1} although various random, uncontrollable factors such as friction in the pump and launch tubes, efficiency of the powder burn and compression of the gas lead to a substantial deviation in velocity from one shot to the next for apparently identical firing conditions. This is a fact of life that experimenters using the UKC light gas gun have to deal with. With experiments performed on the light gas gun it is usually the velocity that introduces the greatest variability into the independent parameters of an experiment, the velocity usually being required to be constant. In the case of this work the small uncertainty in plate thickness and ball bearing diameter will most likely contribute insignificantly to the observed variability of the dependent parameters (hole size and shape) compared to that introduced by the variability in velocity. The term “variability” is used for the velocity rather than “uncertainty” as the *uncertainty* in the velocity for a particular shot is small, usually around $\pm 0.05 \text{ km s}^{-1}$ i.e. 1% for 5 km s^{-1} . However for an investigation such as this one where the velocity is required to be constant as the effect of a different parameter is being studied, the variation in velocity will be significantly large. Assuming that the variation in velocity isn’t negligible it is desirable that the variation be random, thus having the effect of a introducing an additional random error into the experiment rather than a systematic one. A test for normality of the distribution of velocities achieved in this

experimental programme is given in Figure 3.3. It appears that the velocity is random (24%), but we also require it to be uncorrelated with the other parameters, namely impact angle and particle-diameter-to-plate-thickness ratio. This is addressed in section 5.2.3. Table 3.3 shows the statistics for the velocities attained for this shot programme.

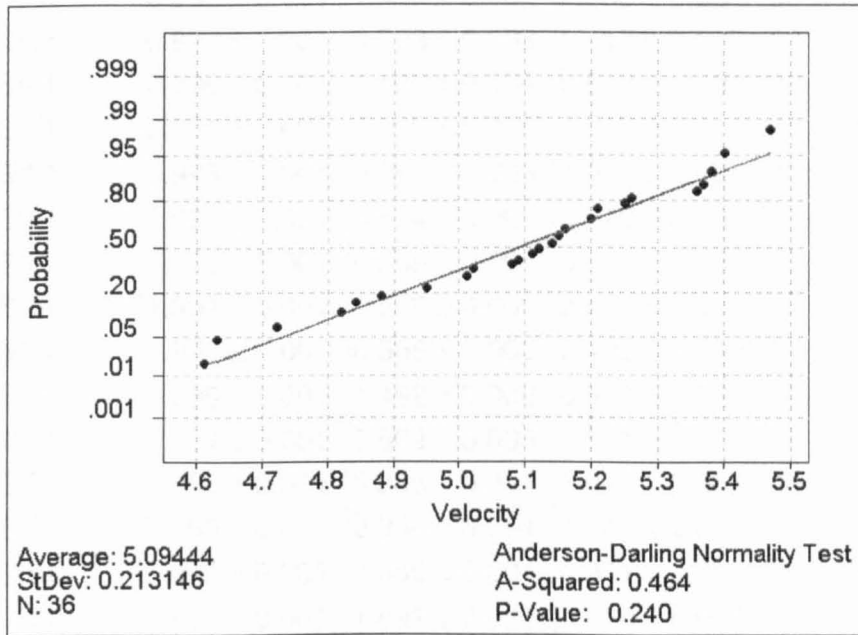


Figure 3.3 – Test for normality of velocity distribution

Table 3.3 – Velocity statistics for shot programme

	V (km s ⁻¹)
Mean	5.09
Standard Error	0.04
Median	5.13
Mode	5.20
Standard Deviation	0.21
Range	0.86
Minimum	4.61
Maximum	5.47
Count	36

The following regression analysis ideally requires that the variability in velocity is negligible but as can be seen the standard deviation is some 4% of the mean velocity with the difference of 860 m s⁻¹ between the fastest and slowest shot. The implications of this variability are discussed in section 5.2.3.

3.3. Experimental results

Projectile and target combinations were chosen from the available stock so as to cover the widest range of particle-diameter-to-plate-thickness ratios (d_p/f). A summary of the shots performed is given in Table 3.4.

Table 3.4 – Summary of independent variables for shot programme

ID	Target	Projectile	d_p (mm)	f (mm)	d_p/f	θ°	V (km s ⁻¹)
1	AlAl	StSt	0.995 ± 0.001	1.491 ± 0.004	0.668 ± 0.002	45 ± 1	5.25 ± 0.05
2	AlAl	StSt	0.995 ± 0.001	0.703 ± 0.003	1.416 ± 0.007	45 ± 1	5.20 ± 0.05
3	AlAl	StSt	0.995 ± 0.001	1.489 ± 0.002	0.669 ± 0.001	60 ± 1	5.20 ± 0.05
4	AlAl	StSt	0.995 ± 0.001	0.703 ± 0.003	1.417 ± 0.007	60 ± 1	4.95 ± 0.05
5	AlAl	StSt	0.995 ± 0.001	1.489 ± 0.004	0.668 ± 0.002	30 ± 1	5.20 ± 0.05
6	AlAl	StSt	0.995 ± 0.001	0.960 ± 0.009	1.037 ± 0.010	30 ± 1	5.11 ± 0.05
7	AlAl	StSt	0.995 ± 0.001	0.958 ± 0.003	1.039 ± 0.004	45 ± 1	5.38 ± 0.05
8	AlAl	StSt	1.991 ± 0.001	0.574 ± 0.006	3.470 ± 0.039	45 ± 1	4.88 ± 0.05
9	AlAl	StSt	1.991 ± 0.001	0.569 ± 0.004	3.497 ± 0.025	30 ± 1	4.72 ± 0.05
10	AlAl	StSt	1.991 ± 0.001	0.568 ± 0.003	3.508 ± 0.020	60 ± 1	4.82 ± 0.05
11	AlAl	StSt	1.991 ± 0.001	0.569 ± 0.003	3.496 ± 0.018	72 ± 1	4.61 ± 0.05
12	AlAl	StSt	0.995 ± 0.001	1.492 ± 0.002	0.667 ± 0.001	72 ± 1	4.82 ± 0.05
13	AlAl	StSt	1.991 ± 0.001	0.569 ± 0.003	3.501 ± 0.018	15 ± 1	5.12 ± 0.05
14	AlAl	StSt	0.995 ± 0.001	0.956 ± 0.004	1.041 ± 0.004	60 ± 1	5.47 ± 0.05
15	AlAl	StSt	0.995 ± 0.001	0.956 ± 0.004	1.041 ± 0.004	72 ± 1	5.21 ± 0.05
16	AlAl	StSt	0.995 ± 0.001	0.956 ± 0.004	1.041 ± 0.004	15 ± 1	5.01 ± 0.05
17	AlAl	StSt	0.995 ± 0.001	1.491 ± 0.003	0.668 ± 0.002	15 ± 1	5.16 ± 0.05
18	AlAl	StSt	0.791 ± 0.001	1.579 ± 0.006	0.501 ± 0.002	0 ± 1	5.15 ± 0.05
19	AlAl	StSt	0.791 ± 0.001	0.568 ± 0.002	1.394 ± 0.004	72 ± 1	5.15 ± 0.05
20	AlAl	Al 2017	0.992 ± 0.007	0.956 ± 0.004	1.038 ± 0.008	45 ± 1	5.11 ± 0.05
21	AlAl	Al 2017	0.992 ± 0.007	0.956 ± 0.004	1.038 ± 0.008	60 ± 1	5.40 ± 0.05
22	AlAl	Al 2017	0.992 ± 0.007	0.956 ± 0.004	1.038 ± 0.008	72 ± 1	5.38 ± 0.05
23	AlAl	Al 2017	0.992 ± 0.007	0.956 ± 0.004	1.038 ± 0.008	30 ± 1	5.26 ± 0.05
24	AlAl	Al 2017	0.992 ± 0.007	0.956 ± 0.004	1.038 ± 0.008	15 ± 1	5.36 ± 0.05
25	AlAl	StSt	0.995 ± 0.001	0.703 ± 0.003	1.417 ± 0.007	30 ± 1	5.09 ± 0.05
26	AlAl	StSt	0.995 ± 0.001	0.703 ± 0.003	1.417 ± 0.007	15 ± 1	5.01 ± 0.05
27	AlAl	StSt	1.50 ± 0.01	0.569 ± 0.003	2.635 ± 0.013	15 ± 1	5.14 ± 0.05
28	AlAl	StSt	1.50 ± 0.01	0.569 ± 0.003	2.635 ± 0.013	30 ± 1	5.02 ± 0.05
29	AlAl	StSt	1.50 ± 0.01	0.569 ± 0.003	2.635 ± 0.013	45 ± 1	5.01 ± 0.05
30	AlAl	StSt	1.50 ± 0.01	0.569 ± 0.003	2.635 ± 0.013	60 ± 1	4.95 ± 0.05
31	AlAl	StSt	1.50 ± 0.01	0.569 ± 0.003	2.635 ± 0.013	72 ± 1	5.08 ± 0.05
32	AlAl	StSt	0.995 ± 0.001	0.956 ± 0.004	1.041 ± 0.004	0 ± 1	5.20 ± 0.05
33	AlAl	StSt	0.995 ± 0.001	1.492 ± 0.002	0.667 ± 0.001	0 ± 1	5.14 ± 0.05
34	AlAl	StSt	0.995 ± 0.001	0.703 ± 0.003	1.416 ± 0.007	0 ± 1	5.37 ± 0.05
35	AlAl	StSt	1.50 ± 0.01	0.574 ± 0.006	2.614 ± 0.029	0 ± 1	4.84 ± 0.05
36	AlAl	StSt	1.991 ± 0.001	0.568 ± 0.003	3.508 ± 0.020	0 ± 1	4.63 ± 0.05

Figure 3.4 shows images of the holes recorded for the 25 of the 31 steel-projectile shots (normal incidence shots not shown) and Figure 3.5 shows the 5 aluminium-projectile shots. It should be noted when comparing the sizes of the holes that the 15° and 30° images in the $d_p/f = 1.42$ column are at roughly twice the magnification of the other images. Also the projectiles used for the $d_p/f = 2.63$ and 3.50 shots are one and a half and twice the diameter of the other shots respectively.

The large hole next to the hole made by the projectile in the 15° aluminium shot was made by the burst disk, which can occasionally travel on axis after leaving the launch tube and reach the target. Notable first observations are:

- *Hole size* – It can be seen that the hole size decreases as the target becomes thinner. Also the holes made by the aluminium projectile are smaller than those made by the steel projectile for the same particle size and plate thickness. For the 72° aluminium shot the projectile has failed to penetrate forming a crater instead.
- *Hole circularity* – Comparing the first and last columns it can be seen that holes become more rapidly elliptical with increasing obliquity in the thinner target than in the relatively thicker one.
- *Lip size* – It can be seen that the lips surrounding holes in thicker targets are relatively larger than those in thinner targets.
- *Lip symmetry* – For the highest obliquity shots (60° and 72°) the lips on the uprange end of the crater (the direction from which the impactor came: the bottom in all images) are smaller than the lips elsewhere. There also appears to be a slight reduction in the downrange end lips, with the “side” lips being the largest, particularly for the 2 thinnest plates on the right.

The same trends are observed for the shots using aluminium projectiles (Figure 3.5) apart from the shot at 72° has failed to penetrate due to the lower impact energy of the less dense aluminium.

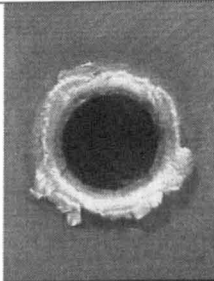
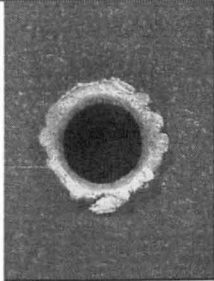
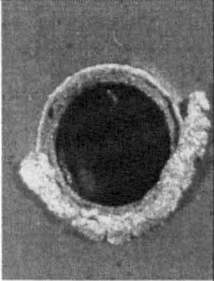
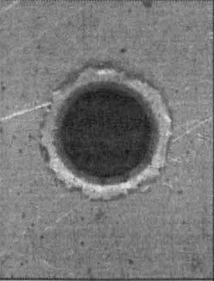
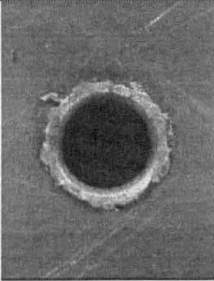
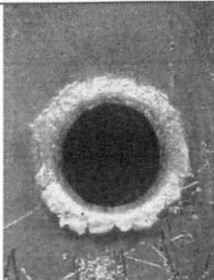
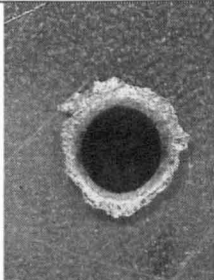
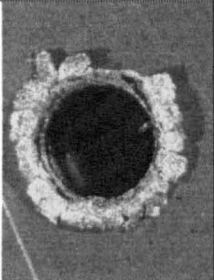
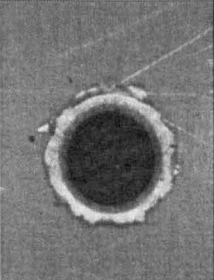
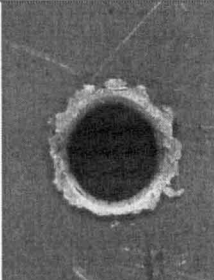
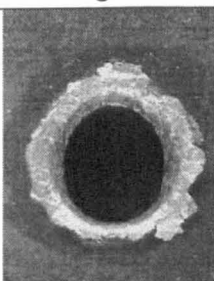
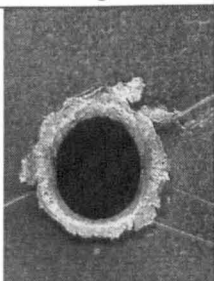
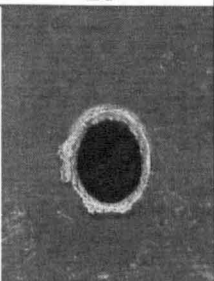
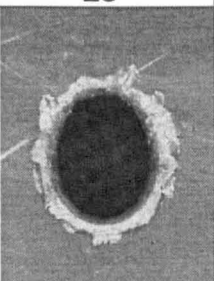
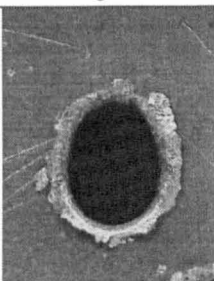
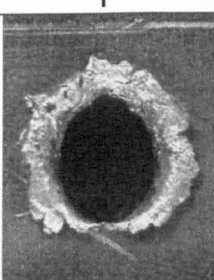
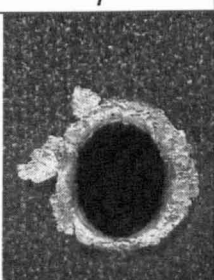
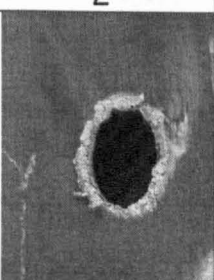
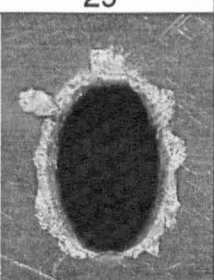
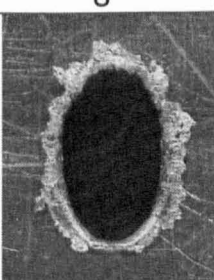
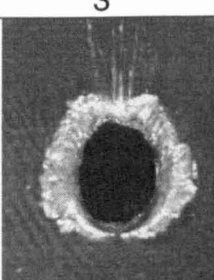
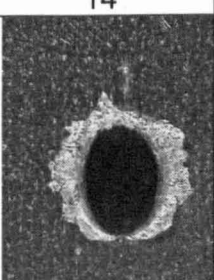
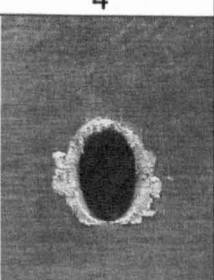

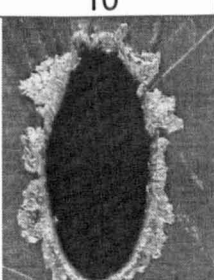
$d_p: f$	1.00: 1.49	1.00: 0.96	1.00 :0.70	1.50: 0.57	2.00: 0.57
d_p/f	0.67	1.04	1.42	2.63	3.50
15°	 17	 16	 26	 27	 13
30°	 5	 6	 25	 28	 9
45°	 1	 7	 2	 29	 8
60°	 3	 14	 4	 30	 10
72°	 12	 15	 19	 31	 11

Figure 3.4 – Images of holes categorised by impact angle and d_p/f

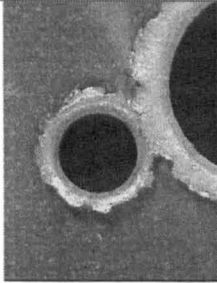
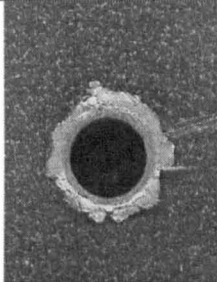
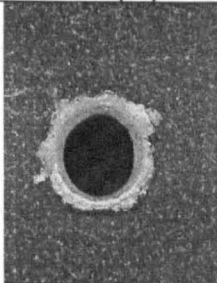
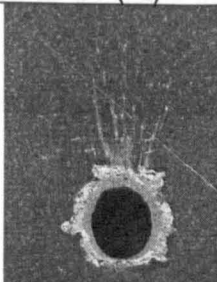

$d_p: f$	1.00: 0.96
d_p/f	1.04
15°	 24 (Al)
30°	 23 (Al)
45°	 20 (Al)
60°	 21 (Al)
72°	 22 (Al)

Figure 3.5 – Images of impact features using aluminium projectiles

Figure 3.6 shows some of the various rear-side morphologies observed. The progression in morphology is clearly illustrated from thick targets to thin targets. Although the target is thinner for shot 22 than for shot 12 and 1, the less dense aluminium projectile (shot 22) does not have enough energy to penetrate the target. Note that the resulting crater will be deeper than if the target were semi-infinite. The projectile has just enough energy to penetrate for shot 12 and the rear side shows “necking”, the hole diameter is somewhat smaller than the crater diameter at the original surface of

the target. For shots 1 and 11 the rear side morphology is indistinguishable from the front surface morphology.

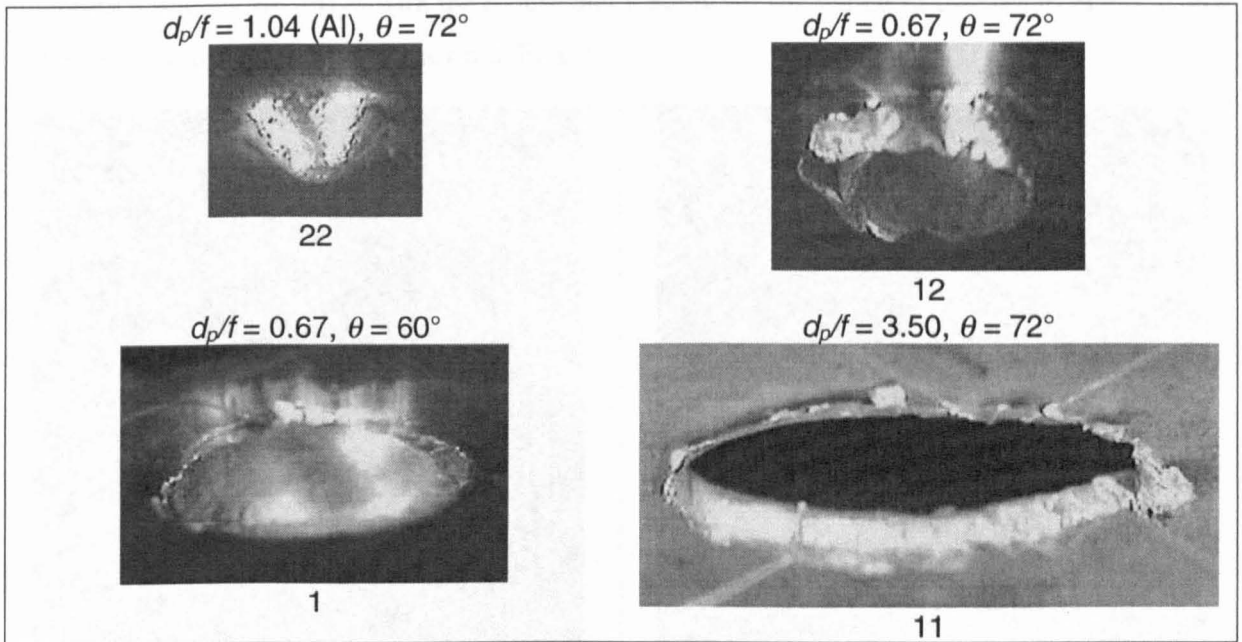


Figure 3.6 – Rear side morphologies

3.3.1. Measurement procedure

After firing, the targets were imaged using a CCD camera and various zoom lenses. The camera system used was originally used by commercial contractors for scanning the EURECA solar arrays. After completion of the contract the system became available for general use and the author set up the system in the gas gun area for use by experimenters wishing to image targets immediately after firing. The author arranged for the purchase of the necessary adapters so that a variety of standard 35 mm camera lenses could also be used with the system. The author also designed an adapter so that a CCD camera could be attached in the correct position for a focussed image to an existing microscope that did not have a CCD mounting (top-left Figure 3.7). This system has been in use by many experimenters for several years now.

Calibration of camera system

The images were calibrated in terms of pixels per mm by imaging microscope graticules. The graticules were imaged both vertically and horizontally to check for any astigmatism in the system. Since the imaging system was in use by other experimenters in-between the authors experimental sessions the camera was re-focussed and repositioned such that *precisely* the same optical configuration could not be maintained for all the hole images. Setting up the camera to take an image involved selecting the appropriate lens and then adjusting the height of the camera above the target until the target surface appeared to be at the best focus. This could potentially introduce some error in the calibration if the judgement of the best-focus height was not consistent. Accordingly, several calibration images were taken with the graticule positioned at different heights above the table surface so that the camera had to be repositioned to focus on the surface. In this way the tolerance of the calibration to repositioning of the target/camera could be evaluated.

Software normally used for taking measurements from SEM micrographs – the same software used for measuring the TICCE holes - was used to make measurements from the images. This involved dragging a line on the image with the mouse and reading off the length of the line in pixels. Some example calibration images are shown in Figure 3.8.

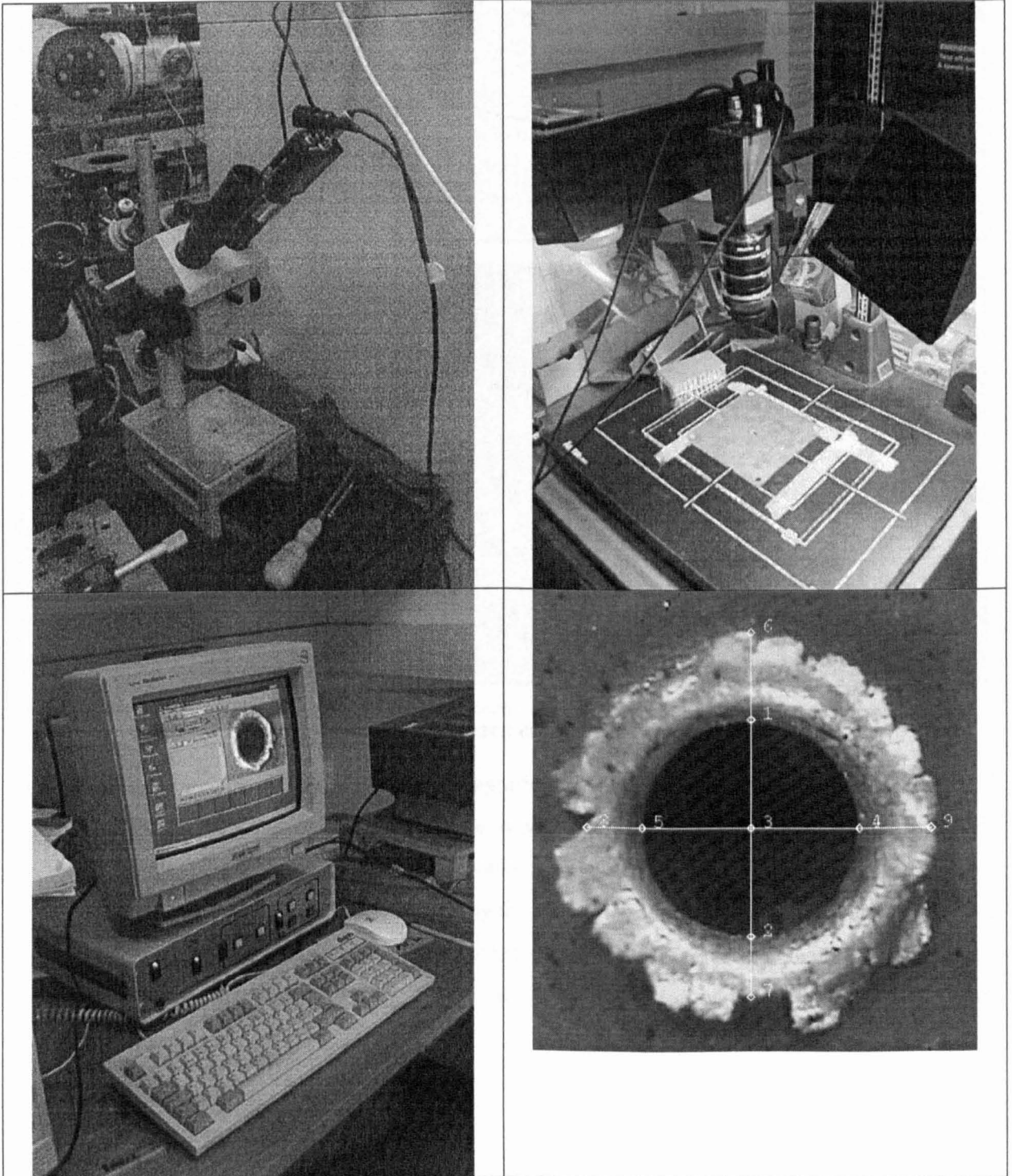


Figure 3.7 – Scanning equipment and example of crater measurements

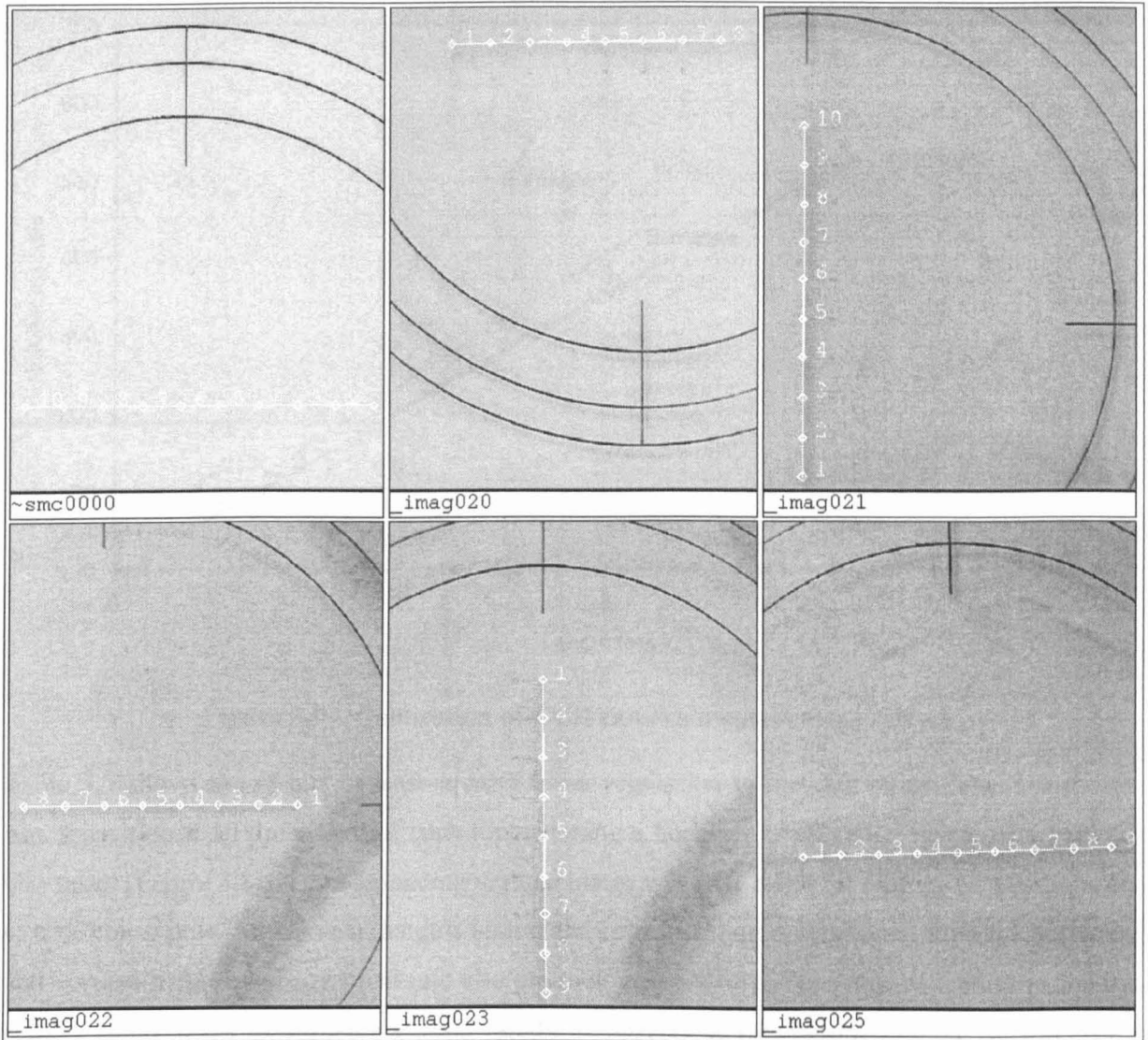


Figure 3.8 – Camera calibration images

As this was done with the image greatly magnified so that a hole of a few mm filled a 17" computer display, measurements could be made to within a pixel accuracy. Measurements in pixels of the graticule divisions were made, as shown in Figure 3.8, and then linear least squares regression with the length in mm as specified by the graticule scale as the independent variable and the length as recorded in pixels as the dependent variable was performed with the fits forced through the origin for simplicity. Figure 3.9 shows the calibration of the system for 3 different magnifications.

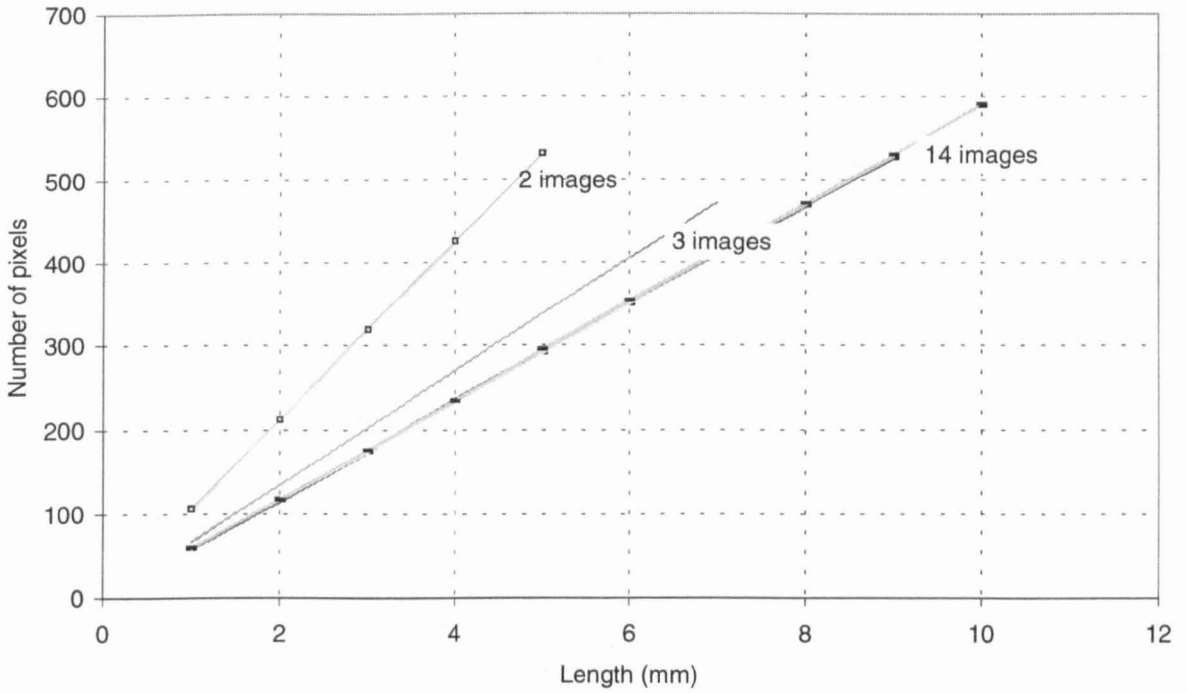


Figure 3.9 – Calibration of CCD camera measurement system

Table 3.5 shows the results of least-squares linear regression to the calibration data. The camera was repositioned 10 times and for each repositioning a horizontal calibration image of a graticule was taken (Figure 3.8). A corresponding vertical image was only taken for 6 of the 10 positions due to time constraints. All the data (lengths in mm and corresponding pixel counts) from the horizontal and vertical images were grouped into two data sets respectively. Thus any variability in the two respective linear fits would represent the variability introduced by repositioning the camera. The σ column is the resulting estimate of the standard deviation of a length measured in pixels (except for the last row) and corresponds to the composite variability due to both the author's ability to position the mouse accurately and due to repositioning the camera. It can be seen without need for a formal significance test that the horizontal and vertical calibrations are different, which means that there is a slight astigmatism in the system. However, as the difference is so small – but indeed significant – it was decided to use a fit to the whole data set and accept the resulting slight loss in accuracy. The fits were initially performed with the length in pixels (dependent variable) regressed against the “true” length in mm (independent variable). However, we require the length in mm for a length measured in pixels. We could just take the inverse of the *forward* regression, but if we perform an *inverse* regression, where we plot the independent variable against the dependent variable we will readily obtain the statistics from the regression required to compute uncertainties for our calculated lengths in mm (see discussion section 3.4). Specifically, $(1-\alpha)\%$ confidence intervals for a length in mm calculated from a length in pixels using the regression are given by (Cooper, 1969):

$$Y_i \pm t_{\alpha/2, v} \sqrt{\frac{n+1}{n} \sigma^2 + (x_i - \bar{x})^2 \text{var}(\hat{b})} \quad (3.1)$$

where Y_i is the length in mm, x_i is the length in pixels and \bar{x} is the mean value of the data from which the regression was calculated. $t_{\alpha/2, \nu}$ is the *Student's t*-distribution corresponding to a confidence of $\alpha/2$ with $\nu = N-2$ degrees of freedom. σ is the standard deviation specified in Table 3.5, the derivation of which is explained in appendix A. $\text{Var}(b)$ is the variance of the fitted gradient equal to the square of the "Error" in Table 3.5. Thus it can be seen, as we would intuitively expect, that the confidence in any measurement is proportional to how far from the centre of the calibration data the value lies and inversely proportional to the amount of data from which the calibration was derived. It should be noted that *inverse* regression performed in this way violates the assumptions upon which least squares is founded (see section 3.4) i.e. that the dependent variable is random and not pre-selected, but for highly correlated data such as this the approximation is good. In this case the gradient calculated by inverse regression is no different (to at least 4 decimal places) from the reciprocal of the forward-regression gradient.

Table 3.5 – Calibration data for CCD camera system

ID	Gradient	Error	R^2	σ (mm)	# positions	N
Horizontal	58.40 pixel mm ⁻¹	0.03	1.000	1.35	10	64
Vertical	58.90 pixel mm ⁻¹	0.02	1.000	0.85	6	55
All	58.67 pixel mm ⁻¹	0.03	1.000	1.78	16	119
Inverse	0.0170 mm pixel ⁻¹	8.73E-06	1.000	0.030	16	119

For the case in hand with 117 degrees of freedom, the *Student's t*-distribution is approximately gaussian, therefore $t_{68.3\%/2, 117} \approx 1$; with $n=119$, $n+1/n \approx 1$; additionally, the size of the holes being measured are close enough to the centre of the calibration data such that $(x - \bar{x})^2 \cdot \text{var}(b) \approx 0$. Therefore 68.3% confidence intervals calculated using equation 3.1 are not significantly different from $\pm\sigma$ in Table 3.5 i.e. 0.03 mm. Therefore, the calculated accuracy of all hole measurements is 30 μm , which seems reasonable for the equipment used.

A summary of the dependent variables measured is given in Table 3.6.

Table 3.6 – Dependent variables

Shot ID	d_p (mm)	angle (°)	f (mm)	a (pixels)	b (pixels)	Calibration (mm pixel ⁻¹)	a (mm)	b (mm)
1	1.00	45	1.49	297	262	0.017	5.07 ± 0.03	4.47 ± 0.03
2	1.00	45	0.70	211	168	0.017	3.60 ± 0.03	2.87 ± 0.03
3	1.00	60	1.49	336	245	0.017	5.73 ± 0.03	4.18 ± 0.03
4	1.00	60	0.70	253	170	0.017	4.32 ± 0.03	2.90 ± 0.03
5	1.00	30	1.49	270	255	0.017	4.61 ± 0.03	4.35 ± 0.03
6	1.00	30	0.96	228	211	0.017	3.89 ± 0.03	3.60 ± 0.03
7	1.00	45	0.96	264	225	0.017	4.50 ± 0.03	3.84 ± 0.03
8	1.99	45	0.57	312	236	0.017	5.32 ± 0.03	4.03 ± 0.03
9	1.99	30	0.57	254	229	0.017	4.33 ± 0.03	3.91 ± 0.03
10	1.99	60	0.57	453	259	0.017	7.73 ± 0.03	4.42 ± 0.03
11	1.99	72	0.57	611	267	0.017	10.42 ± 0.03	4.56 ± 0.03
12	1.00	72	1.49	284	201	0.017	4.85 ± 0.03	3.43 ± 0.03
13	1.99	15	0.57	237	226	0.017	4.04 ± 0.03	3.86 ± 0.03
14	1.00	60	0.96	305	230	0.017	5.20 ± 0.03	3.92 ± 0.03
15	1.00	72	0.96	287	191	0.017	4.90 ± 0.03	3.26 ± 0.03
16	1.00	15	0.96	214	208	0.017	3.65 ± 0.02	3.55 ± 0.03
17	1.00	15	1.49	253	245	0.017	4.32 ± 0.03	4.18 ± 0.03
18	0.79	0	1.58	208	207	0.017	3.55 ± 0.03	3.53 ± 0.03
19	0.79	72	0.57	242	145	0.017	4.13 ± 0.03	2.47 ± 0.03
20	0.99	45	0.96	212	184	0.017	3.62 ± 0.03	3.14 ± 0.03
21	0.99	60	0.96	190	158	0.017	3.24 ± 0.03	2.70 ± 0.03
22	0.99	72	0.96	-	-	0.017	-	-
23	0.99	30	0.96	210	201	0.017	3.58 ± 0.03	3.43 ± 0.03
24	0.99	15	0.96	208	205	0.017	3.55 ± 0.03	3.50 ± 0.03
25	1.00	30	0.70	332	306	0.009	3.12 ± 0.03	2.88 ± 0.03
26	1.00	15	0.70	296	289	0.009	2.78 ± 0.03	2.72 ± 0.03
27	1.50	15	0.57	236	228	0.015	3.57 ± 0.03	3.45 ± 0.03
28	1.50	30	0.57	249	224	0.015	3.77 ± 0.03	3.39 ± 0.03
29	1.50	45	0.57	312	234	0.015	4.72 ± 0.03	3.54 ± 0.03
30	1.50	60	0.57	433	259	0.015	6.56 ± 0.03	3.92 ± 0.03
31	1.50	72	0.57	503	258	0.015	7.62 ± 0.03	3.91 ± 0.03
32	0.99	0	0.96	241	243	0.015	3.55 ± 0.03	3.58 ± 0.03
33	0.99	0	1.49	286	286	0.015	4.21 ± 0.03	4.21 ± 0.03
34	0.99	0	0.70	194	193	0.015	2.85 ± 0.03	2.84 ± 0.03
35	1.50	0	0.57	226	227	0.015	3.33 ± 0.03	3.34 ± 0.03
36	1.99	0	0.57	260	259	0.015	3.83 ± 0.03	3.81 ± 0.03

3.4. Analysis

Choice of parameters for regression analysis

The methodology adopted for this analysis is to express the hole size and particle size in terms of the plate thickness, D_H/f and d_p/f respectively. Publications in this field almost invariably adopt this

approach. The hole diameter is usually expressed as a dimensionless ratio by “normalising” i.e. dividing either by the particle diameter (Schonberg and Taylor, 1989; Baker and Persechino, 1993) or the target thickness (Hörz *et al.*, 1993; Gardner *et al.*, 1997a). In this way the derived relationships will be independent of the choice of units and any self-consistent set of units can be used. For this analysis the author chose to follow Hörz *et al.*, (1993) and Gardner *et al.*, (1997a) and express the hole and particle diameters as multiples of the target thickness. This approach is suitable for performing calibration work aimed at interpreting space data in that the particle diameter will be unknown and so normalising by the target thickness (a known parameter) is more appropriate.

The data used in the following regression analyses is given in Table 3.7; the uncertainties of the independent parameters are not shown as they are given in Table 3.4.

Table 3.7 – Data used for regression analyses

Shot ID	angle (°)	dp/f	a/f	b/f	b/a
1	45	0.67	3.40 ± 0.02	3.00 ± 0.02	0.882 ± 0.003
2	45	1.42	5.12 ± 0.04	4.08 ± 0.03	0.796 ± 0.004
3	60	0.67	3.85 ± 0.02	2.81 ± 0.02	0.729 ± 0.003
4	60	1.42	6.14 ± 0.05	4.13 ± 0.03	0.672 ± 0.003
5	30	0.67	3.09 ± 0.02	2.92 ± 0.02	0.944 ± 0.004
6	30	1.04	4.05 ± 0.05	3.75 ± 0.04	0.925 ± 0.004
7	45	1.04	4.70 ± 0.03	4.01 ± 0.03	0.852 ± 0.004
8	45	3.47	9.28 ± 0.12	7.02 ± 0.09	0.756 ± 0.003
9	30	3.50	7.61 ± 0.07	6.86 ± 0.07	0.902 ± 0.004
10	60	3.51	13.62 ± 0.11	7.79 ± 0.07	0.572 ± 0.002
11	72	3.50	18.31 ± 0.14	8.00 ± 0.06	0.437 ± 0.001
12	72	0.67	3.25 ± 0.02	2.30 ± 0.02	0.708 ± 0.003
13	15	3.50	7.11 ± 0.06	6.78 ± 0.06	0.954 ± 0.004
14	60	1.04	5.44 ± 0.04	4.10 ± 0.03	0.754 ± 0.003
15	72	1.04	5.12 ± 0.04	3.41 ± 0.03	0.666 ± 0.003
16	15	1.04	3.82 ± 0.03	3.71 ± 0.03	0.972 ± 0.005
17	15	0.67	2.90 ± 0.02	2.80 ± 0.02	0.968 ± 0.004
18	0	0.50	2.25 ± 0.02	2.24 ± 0.02	0.995 ± 0.005
19	72	1.39	7.27 ± 0.05	4.36 ± 0.03	0.599 ± 0.004
20	45	1.04	3.78 ± 0.03	3.28 ± 0.03	0.868 ± 0.005
21	60	1.04	3.39 ± 0.03	2.82 ± 0.02	0.832 ± 0.005
22	72	1.04	-	-	-
23	30	1.04	3.75 ± 0.03	3.59 ± 0.03	0.957 ± 0.005
24	15	1.04	3.71 ± 0.03	3.66 ± 0.03	0.986 ± 0.005
25	30	1.42	4.44 ± 0.02	4.10 ± 0.02	0.922 ± 0.003
26	15	1.42	3.96 ± 0.02	3.87 ± 0.02	0.976 ± 0.003
27	15	2.63	6.28 ± 0.04	6.06 ± 0.04	0.966 ± 0.004
28	30	2.63	6.62 ± 0.04	5.96 ± 0.04	0.900 ± 0.004
29	45	2.63	8.30 ± 0.05	6.22 ± 0.04	0.750 ± 0.003
30	60	2.64	11.54 ± 0.06	6.90 ± 0.04	0.598 ± 0.002
31	72	2.63	13.38 ± 0.07	6.86 ± 0.04	0.513 ± 0.002
32	0	0.67	3.71 ± 0.02	3.74 ± 0.02	1.008 ± 0.004
33	0	1.04	2.82 ± 0.02	2.82 ± 0.02	1.000 ± 0.009
34	0	1.41	4.06 ± 0.06	4.04 ± 0.06	0.995 ± 0.020
35	0	2.61	5.80 ± 0.12	5.82 ± 0.12	1.004 ± 0.023
36	0	3.50	6.74 ± 0.13	6.72 ± 0.13	0.996 ± 0.026

In order to find a suitable functional form for the regression equations the dependent parameters (*variates*) b/f , a/f and b/a are plotted against each of the independent parameters (*regressors*) in Figures Figure 3.10 to Figure 3.15. Measurement errors are not shown in the plots as they are smaller than the points representing the data.

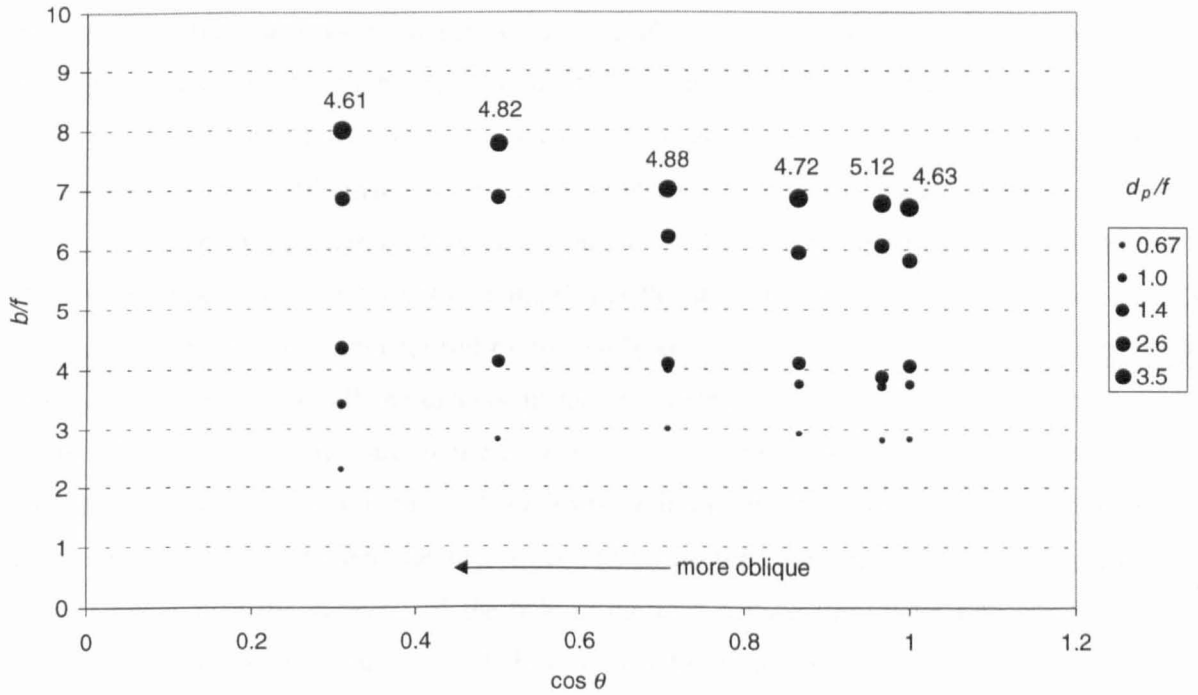


Figure 3.10 – Variation of minor axis with impact angle

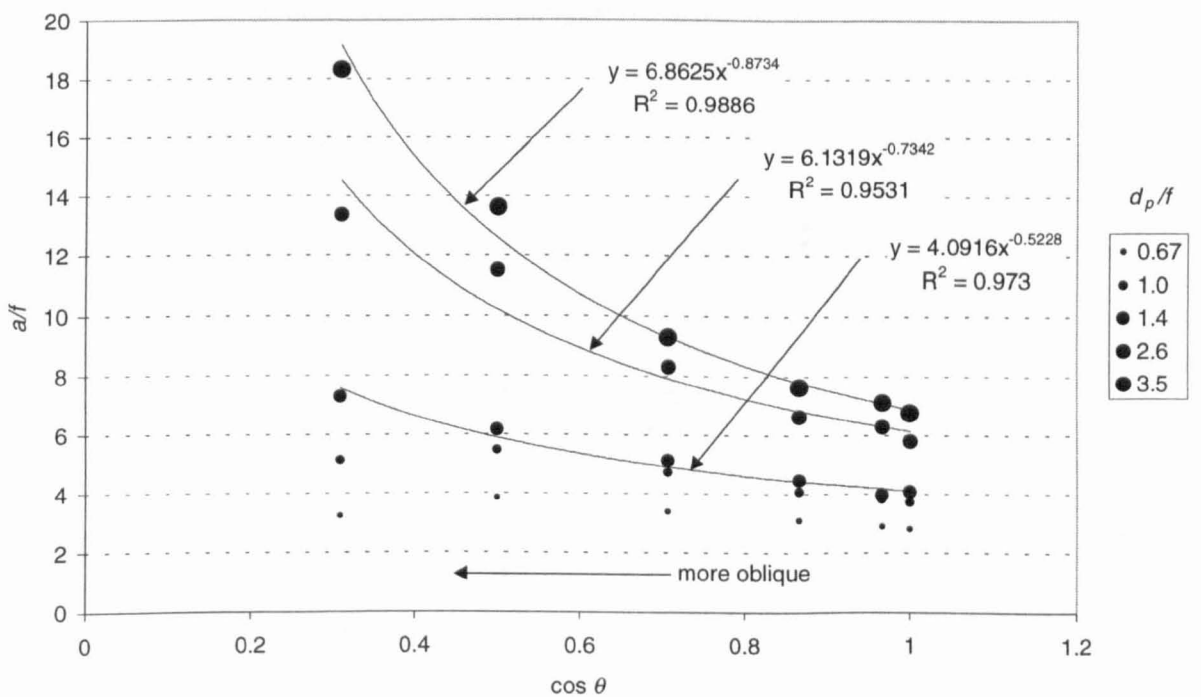


Figure 3.11 – Variation of major axis with impact angle

In Figure 3.10 it can be seen that the minor axis is relatively insensitive to impact angle, but for the thinnest plates there is a significant increase in the minor diameter with increasing obliquity. The velocities of the shots for the thinnest plates ($d_p/f = 3.50$) are marked on Figure 3.10 and the

increase in minor axis does not appear to be due to the velocity, the largest values occurring at the lower velocities. The author suspects that this increase in minor axis is primarily due to the fact that the particle is being presented with a greater depth of target to pass through – greater by a factor of $1/\cos \theta$ – along its line-of-flight; it has long been known that hole size increases with target thickness for impacts well above the ballistic limit. For the thickest targets ($d_p/f = 0.67$) there appears to be a slight decrease in minor axis at the highest obliquity. Inspection of the morphology of the highest obliquity shot in the thickest target shows that the hole is starting to close up. As can be seen in Figure 3.6 the rear surface does not show any hypervelocity lips, but a “neck” of material where the projectile material – probably molten – has only just opened up the rear surface. This regime has been characterised by empirical fits to data for normal impacts by Hörz *et al.*, (1993) and Gardner *et al.*, (1997a). It is found that as the target becomes significantly thick there is a transition from a regime characterised by relatively slow hole growth to a regime of rapid hole shrinkage for relatively small increments in target thickness. However, if rather than the hole diameter, the diameter of the crater in the plane of the target surface is used it is found that there is a much simpler progression in diameter from holes in thin targets to craters in semi-infinite targets (Sawle, 1969). With this in mind the author decided to use the diameter of the hole in the plane of the target rather than the diameter of the hole at the rear surface (the distinction can be seen in Figure 3.4). Modelling the rear-surface behaviour would require a lot of data to be taken in the *marginal perforation* region where rapid changes in the rate of growth/shrinkage of the hole diameter take place. Also the definitions of the major and minor axis of the hole in this region becomes ambiguous as holes become increasingly irregular as d_p/f becomes small (Figure 2.12, page 39).

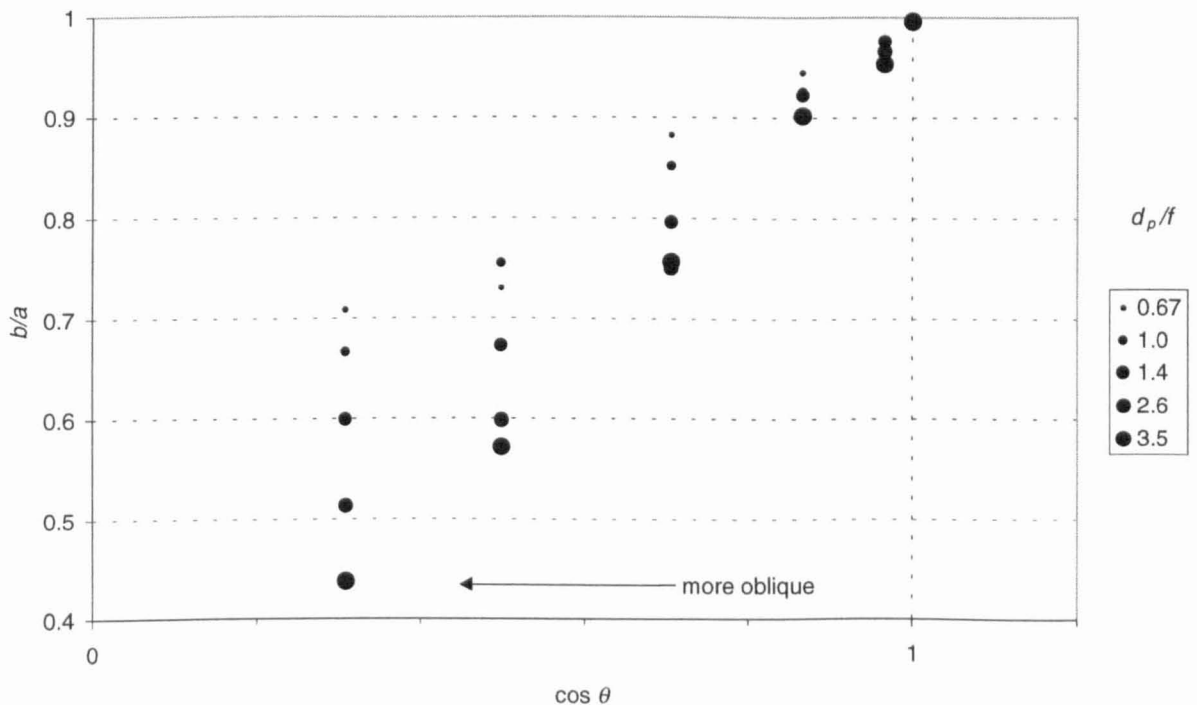


Figure 3.12 – Variation of circularity with impact angle

The major axis appears to display a simple power law relationship with $\cos \theta$, with a progression in gradient and intercept (in log-log space) with the relative target thickness. Power law fits for the three thinnest targets are shown in Figure 3.11 to illustrate the suitability of this functional form.

The circularity appears to show a linear relationship with impact angle with the gradient showing a relatively straightforward progression from thick to thin targets. The minor and major axes and circularity are next plotted against d_p/f .

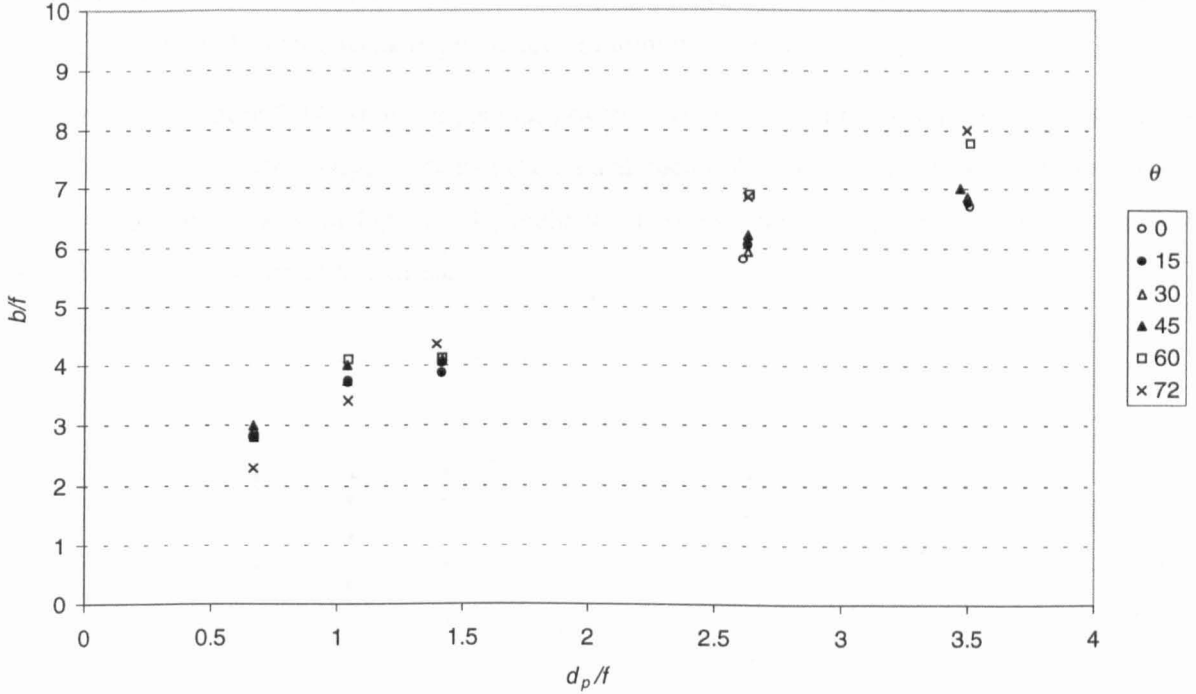


Figure 3.13 Variation of minor axis with dp/f

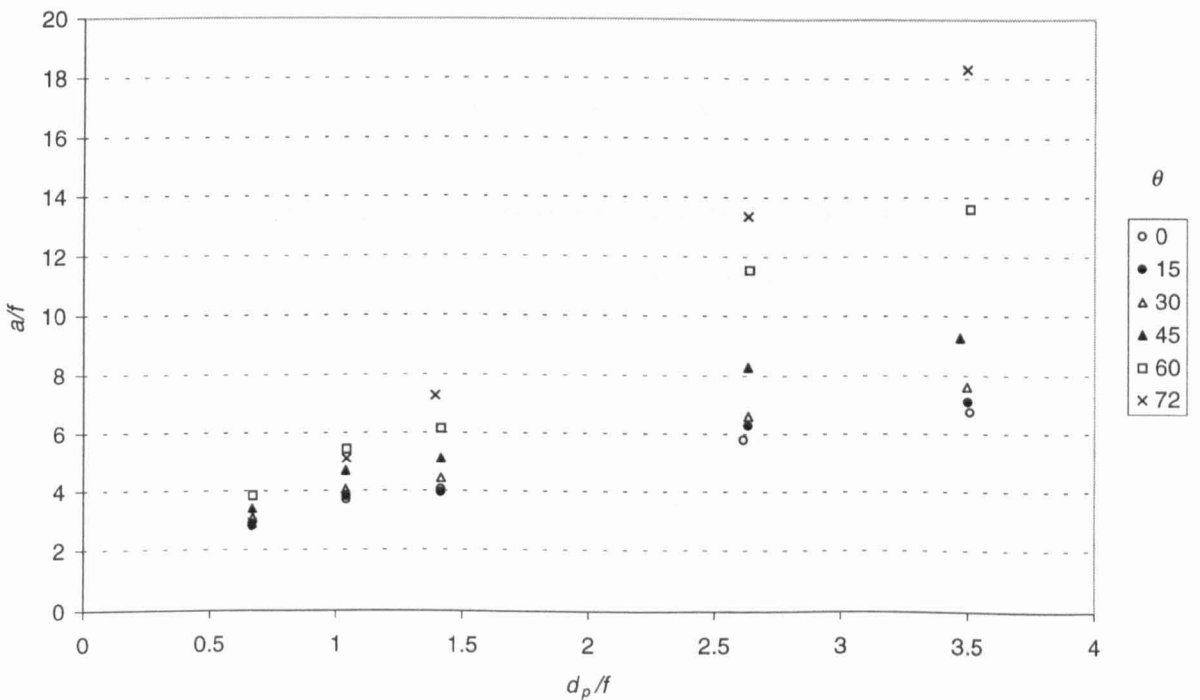


Figure 3.14 – Variation of major axis with dp/f

The minor axis (Figure 3.13) appears to show a simple power law relationship with relative target thickness. The relationship between hole diameter and target thickness for normal impacts has often been expressed as a power law in the past (Maiden *et al.*, 1963 and Nysmith and Denardo, 1969). Gardner *et al.*, (1997a) have pointed out that a more complicated function is required to describe the progression of hole growth with relative target thickness: the hole opens up rapidly for relatively thick targets, subsequently the growth then slows down until the hole diameter tends towards the projectile diameter for very thin targets. However a simple power law may be suitable as a predictive tool over a restricted parameter range. The apparently small scatter of the data about the “by-eye” line reflects the weak dependence of minor axis on impact angle.

The major axis (Figure 3.14) shows a general positive correlation with decreasing target thickness (increasing d_p/f) but with a large scatter of the data at each d_p/f value that increases with increasing d_p/f . This when coupled with Figure 3.11 indicates a strong relationship between major axis and both impact angle and target thickness.

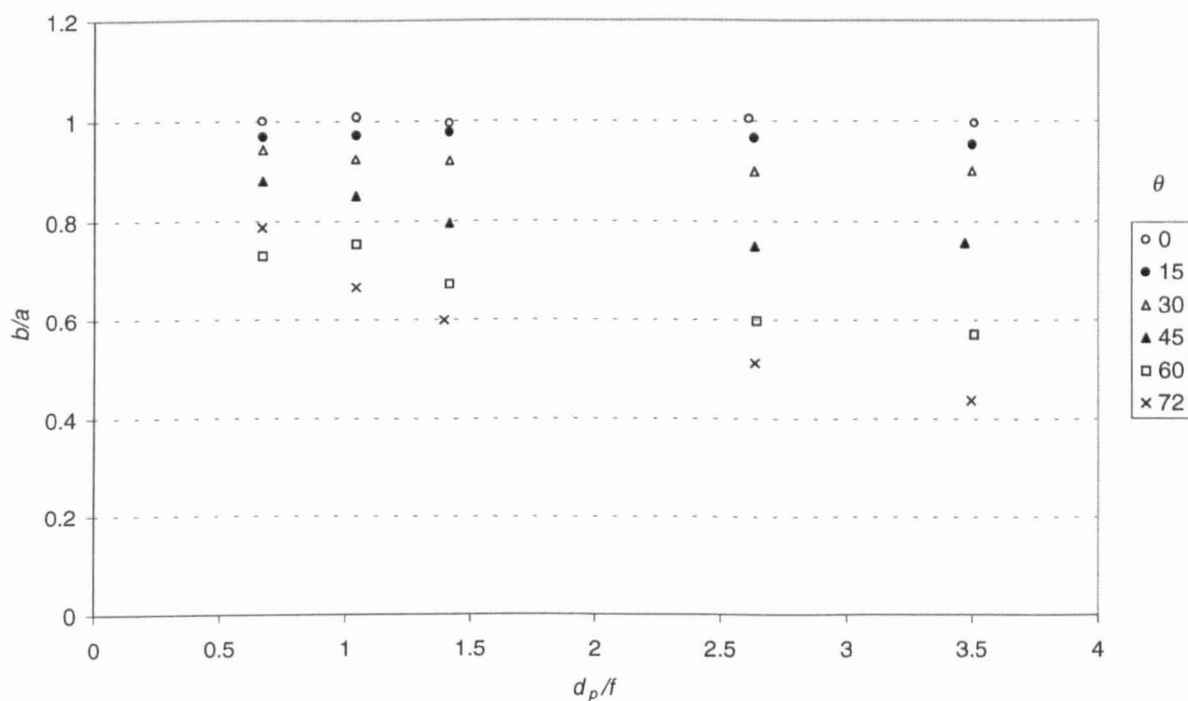


Figure 3.15 – Variation of circularity with d_p/f

The variation of circularity (Figure 3.15) appears to be less influenced by target thickness than by impact angle.

Types of regression

Before embarking on a formal regression analysis of this data it is worth reviewing the aims of the analysis. These experiments are “calibration” experiments rather than “control” experiments, to use the accepted terminology in regression texts. That is to say rather than trying to find out what the size and shape of a hole will be if we fire a particle with a certain size-to-target thickness ratio at a certain angle, we want to find out what particle parameters gave rise to the holes we observed in our space-flown capture cell. This is not invariably the case however. For example, a spacecraft

engineer might want to know what sort of holes can be expected for a given particle population, *before* the spacecraft flies. The analysis to be performed in the former case is *inverse regression* and since we have more than one independent variable, the regression is also *multiple*.

There are two approaches to inverse regression. Firstly, to regress Y on X as with classical regression, where Y is the dependent, random variable and X is the independent, controlled variable and then to rearrange the resulting regression equation such that X is the subject. Alternatively X can be regressed on Y . It can be easily shown, by trying a simple example, that the two methods will result in different coefficients for the regression. If the correlation between X and Y is high then the coefficients obtained by the two methods will usually be sufficiently close to make no difference. However, Ryan (1997) reports the controversy surrounding the second method (regressing X on Y) in that having a non-random *dependent* variable violates the assumptions upon which methods such as *least-squares* are founded. With these caveats in mind the author feels that where this type of *inverse* regression is used (e.g. Gardner *et al.*, 1997a) and low correlation coefficients are obtained, researchers using the regression equation should be aware that there may be some significant *systematic* error in the fitted coefficients.

The author required an accepted formal regression method that would give the required coefficients and associated statistics, such that confidence intervals for the coefficients, and thus in turn, for values predicted by the fitted regression equation can be computed. This is a highly desirable result in the author's opinion – apparently not in the opinion of other researchers in the field - as it tells you the confidence of any values predicted by the equation. Thus, rather than telling a spacecraft engineer that he can expect a hole 2 mm wide and then you shrug when he asks “are you sure?” we can tell him, for example, that we are 99.7% confident that it will be no larger than 2.35 mm wide.

There are widely published methods for *normal* multiple regression as opposed to *inverse* multiple regression and many implementations of these methods in popular spreadsheet and mathematical software (the relevant regression theory is given in appendix A). Thus, the author feels that it is appropriate to proceed along these lines and then to subsequently consider how the regression should be applied to the case where it is the dependent variable that we know (the hole size and shape) and we are trying to determine the independent variables (particle diameters); this is discussed in section 3.5.2.

3.4.1. Multiple regression analysis

Choosing a model

Figure 3.16 shows a 3D plot of the major axis data to be fitted. By trying several intuitive functional forms the author found that a power law function in $\cos \theta$ and d_p/f gave a reasonable description of the data. Other more complicated functions were tried, but these only gave a marginal improvement in the fit at the expense of added complexity.

The model chosen for the major and minor axes is:

$$Y = \beta_0 \left(\frac{d_p}{f} \right)^{\beta_1} \cos^{\beta_2} \theta \quad (3.2)$$

where Y is either the major or minor axis normalised by the target thickness, a/f and b/f respectively, and β_i are the regression coefficients. Before proceeding it is worth evaluating the validity of the chosen model in terms of the *qualitative* requirements that we believe it should fulfil. Firstly, for normal impacts one would expect the hole to be circular and thus the major and minor axes to be equal. As can be seen the $\cos \theta$ term will be 1 for a normal impact and therefore we would require the coefficients β_0 and β_1 to be the same for each equation. The coefficient β_2 can be different for the equations for the major and minor axis and the plots presented so far certainly indicate that the two diameters have a different dependence on impact angle. It could be argued that the equation does not have the correct form as the minor and major axes should approach d_p and $d_p/\cos\theta$ respectively as dp/f becomes very large i.e. the particle merely punches out its cross section in the plane of the target for a very thin target. However, the author feels that to model such behaviour – including turning points in the regression – would be over-stretching the data and that a simple predictive relationship for the regime being investigated is more suitable, with limitations on feasible extrapolation being clearly stated.

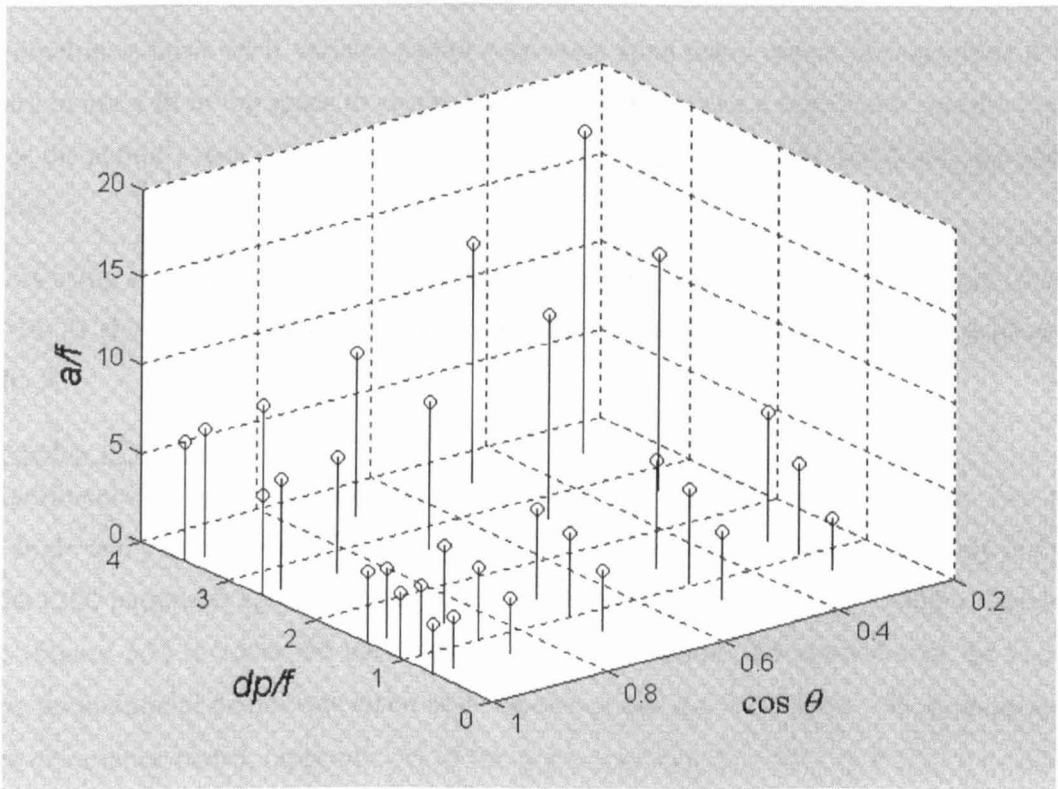


Figure 3.16 – 3D plot of major axis data

Choosing a regression method

Transforming the model by taking logs gives a linear multiple regression model (see appendix A):

$$\log Y = \log \beta_0 + \beta_1 \log \left(\frac{d_p}{f} \right) + \beta_2 \log(\cos \theta) + \varepsilon \quad (3.3)$$

where ε is the error term. However, although power law fits are very often performed by transforming to linear regression by taking logs, this approach raises some problems when analysing the relative contributions of measurement errors and lack-of-fit to the error term ε . Looking at the linear multiple regression model (equation 3.3) it can be seen that when this is transformed back to a power law that the error term becomes *multiplicative* rather than *additive* thus:

$$Y = \left[\beta_0 \left(\frac{d_p}{f} \right)^{\beta_1} \cos^{\beta_2} \theta \right] \varepsilon$$

Now it is not clear how a multiplicative error could arise; errors are invariably quoted as $\pm s$, where s is our estimator of the standard deviation of observations about the “true” value. Other problems that arise are that least-squares regression requires the errors to be normally distributed, which in the case of a power law transformed to a linear model would require $\log(\varepsilon)$ to be normally distributed, requiring a rather unlikely skewed distribution of errors. Least-squares weights positive and negative errors equally, but it makes no sense to weight positive and negative equally from a skewed distribution and to do so will not result in the best fit being obtained. Consequently, regression texts usually tackle power-law fitting using *non-linear* regression with an *additive* error term. Sometimes, however if variates and/or regressors span many orders of magnitude it may be necessary to use a fit in log space to ensure that small values make a significant contribution to the fit. Since the author’s data only covers a single order of magnitude it was decided to use non-linear regression.

The shots using steel projectiles impacting aluminium alloy plates were analysed first (shots 1-19 and 25-36; 31 shots in total). The method used for the non-linear multiple regression is described in appendix A.

Orthogonality of regressors

The experimental programme followed a fairly methodical design, in that for the two factors, impact angle and particle-to-plate-thickness ratio, 6 and 5 different values respectively are used to cover the (2D) parameter space making a total of 30 possible combinations. Using a “rectangular” scheme (Figure 3.1) to cover the parameter space should ensure independence of the regressors. However an additional datum was taken at 0° incidence and $d_p/f = 0.5$ (shot 18). Consequently the variance-covariance matrix (appendix A) of the regressors d_p/f (X_{1i}) and $\cos \theta$ (X_{2i}) was calculated with and without shot 18 included; 31 and 30 data points respectively:

$$\text{var-cov}(X_{n=31}) = \begin{bmatrix} 2.292 & -0.081 \\ -0.081 & 1.017 \end{bmatrix} \quad \text{var-cov}(X_{n=30}) = \begin{bmatrix} 2.059 & 0.002 \\ 0.002 & 0.988 \end{bmatrix}$$

It can be seen that the set of regressors with the shot 18 datum excluded is more closely orthogonal and thus this data set will be used comprising 30 data points. Statistical texts vary in their recommendations of how many data points are required for multiple regression to be meaningful,

but Ryan (1997) suggests at least 10 times the number of regressors, thus in this case 20 is the minimum. The small residual covariance of the regressors reflects the small variation between nominally identical d_p/f shots; note the third decimal place of d_p/f for shots 2 and 4 and 6 and 7 in Table 3.4. This is smaller than the accuracy of the measurements and so this covariance is most likely insignificant; in fact an F test shows that the regressors have insignificant correlation (0.45% confidence).

A prime example of experiments where the regressors are not orthogonal (i.e. they are correlated) are those performed using the UKC Van de Graaff where particle velocity is a strong function of mass. In fact almost all hypervelocity calibration work, where velocity is one of the regressors, suffers from this problem. Another example is when light gas gun data (slow, large particles) is amalgamated with electrostatic accelerator data (fast, small particles). The author has yet to find a publication in the field that addresses this issue. Ryan (1997) notes that correlated regressors “...make the analysis of regression data difficult.” and he devotes a section of his book to methods for interpreting the results of such. It is intuitively obvious why we want uncorrelated regressors. If our regressors are correlated then the value of each regressor’s coefficient will be influenced to some extent by the other regressors. Thus, if different experimenters have different degrees of correlation of their regressors, for example different performance accelerators, they will derive *systematically* different regression coefficients for the same model.

Regression results

Figure 3.17 shows the non-linear fit to the major axis, for the model:

$$Y = \beta_0 \left(\frac{d_p}{f} \right)^{\beta_1} \cos^{\beta_2} \theta + \epsilon$$

The fitting was performed using the *Levenburg-Marquadt* non-linear least-squares routine in *Microcal Origin*. The “x” shows the location of each datum and the dot “.” shows the location of the vertical projection of the datum onto the regression surface. A linear fit in log-log space did not give as good a fit as the non-linear fit, R^2 of 0.93* compared to 0.95, and was weighted towards smaller values such that the regression systematically under-predicted the data to a worsening degree with increasing regressor value. The major-axis fit is re-plotted in Figure 3.18, rotated 90° about the vertical axis with 95% prediction limits shown. The fitted coefficients and statistics for the non-linear fit to the major and minor axes are shown in Table 3.8 and Table 3.9, respectively. The definition of the parameters in the tables is given in appendix A. Example predictions using the regression are shown in Table 3.10 and Table 3.11.

* It should be noted that when performing a power law fit by linear regression in log-log space that the correlation coefficient (R^2) returned by the fit is not relevant. The data must be converted back to their non-logged values and the correlation coefficient recomputed.

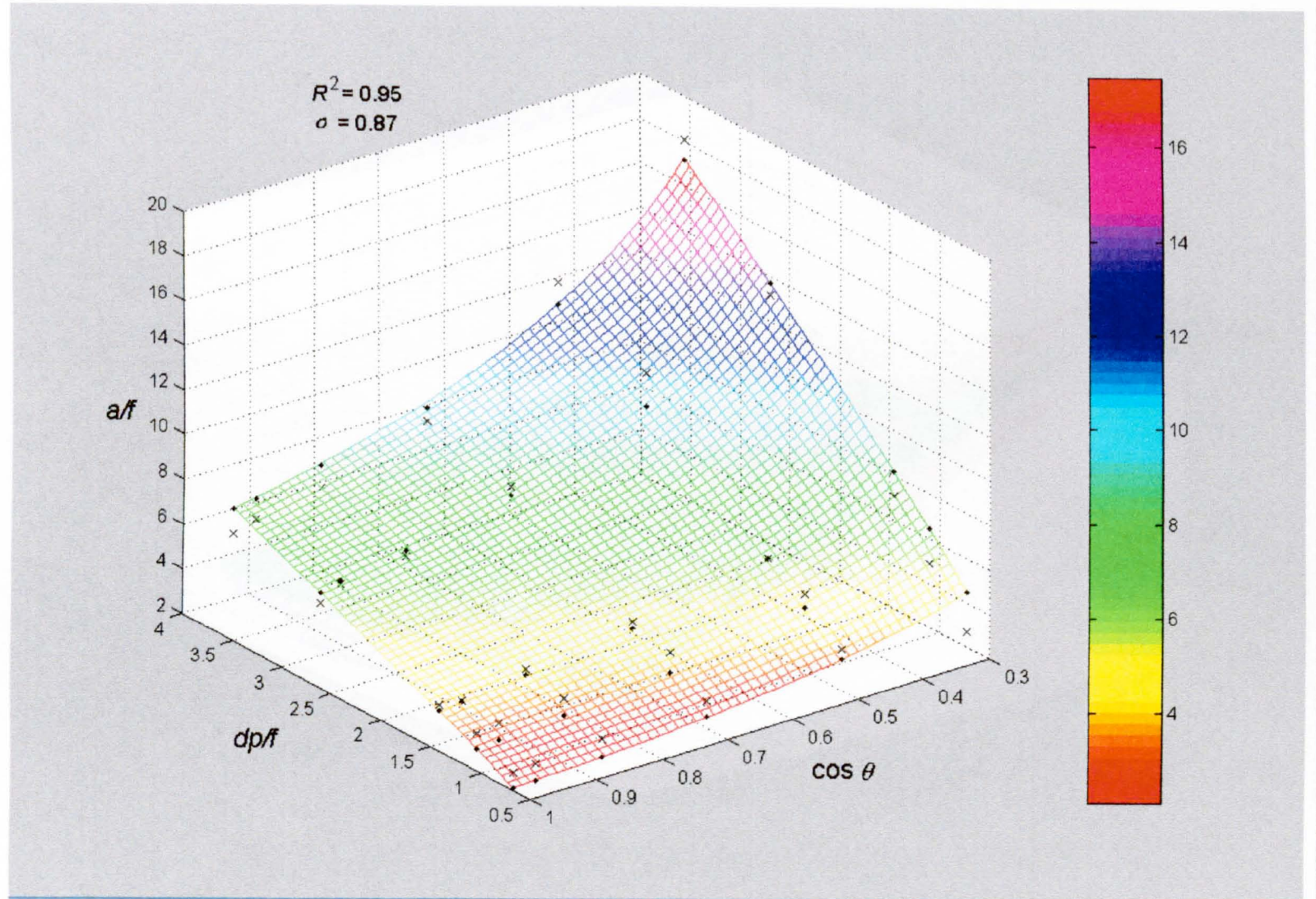


Figure 3.17 - Non-linear fit to major axis data

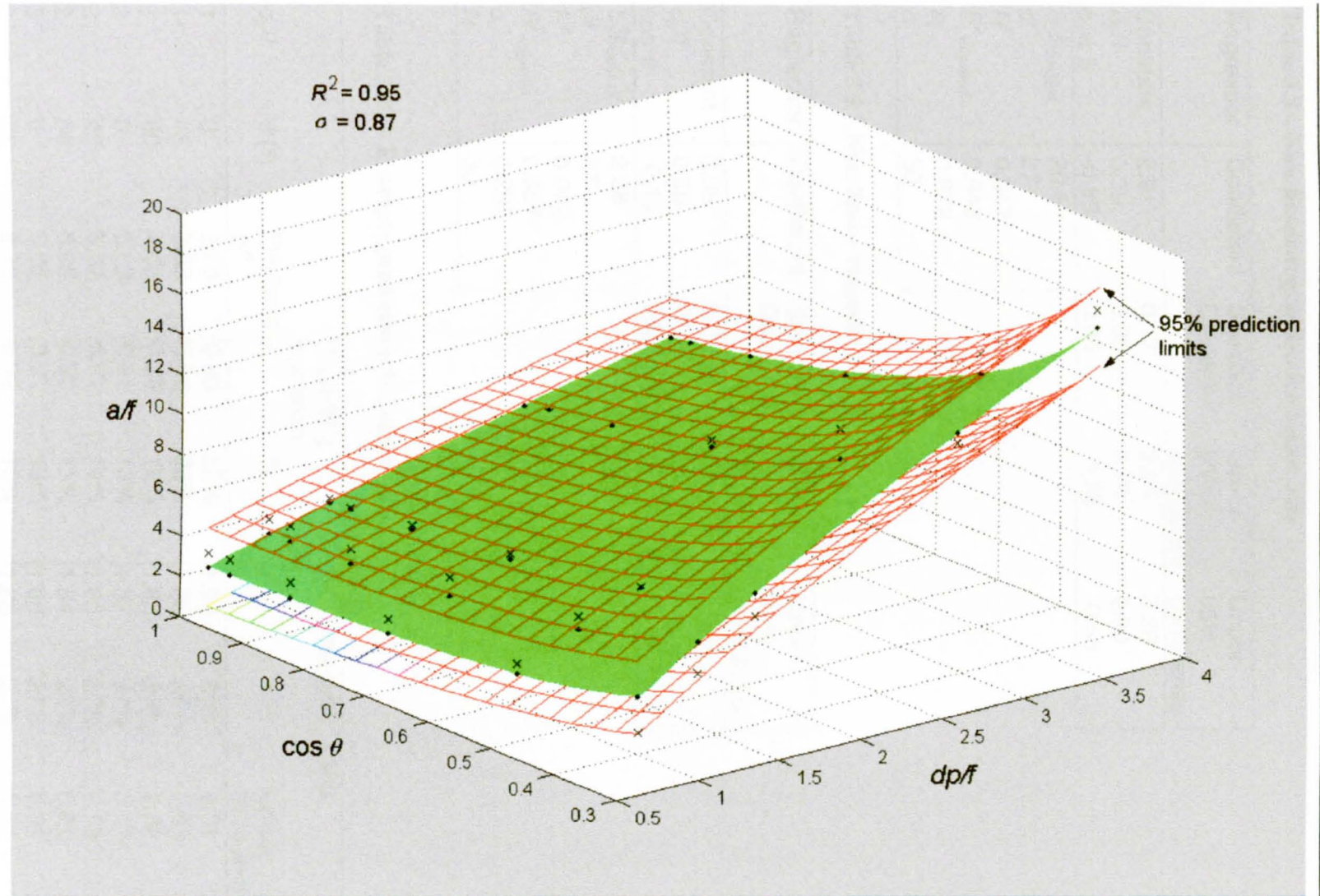


Figure 3.18 - Prediction limits for non-linear fit to major axis

Table 3.8 – Non-linear regression for major axis

Regressor	Coefficient	Standard Deviation	Lower 95% confidence	Upper 95% confidence
Constant	2.91	0.17	2.55	3.28
d_p/f	0.79	0.05	0.70	0.90
$\cos \theta$	-0.68	0.05	-0.78	-0.58
$SS_{residual}$	20.5			
df	27			
R^2	0.947			
$R^2_{adjusted}$	0.943			
s_ε	0.872			
N	30			

Table 3.9 – Non-linear regression for minor axis

Regressor	Coefficient	Standard Deviation	Lower 95% confidence	Upper 95% confidence
Constant	3.38	0.08	3.22	3.54
d_p/f	0.58	0.02	0.54	0.62
$\cos \theta$	-0.10	0.02	-0.15	-0.05
$SS_{residual}$	2.38			
df	27			
R^2	0.972			
$R^2_{adjusted}$	0.957			
s_ε	0.297			
N	30			

Table 3.10 – Example predictions for major axis

d_p/f	θ (°)	Predicted a/f	1 σ (68%) prediction		95% prediction limits			
			\pm	%	\pm	%	Lower 95% limit	Upper 95% limit
1	0	2.90	0.93	32%	1.90	65%	1.01	4.80
1	45	3.68	0.90	25%	1.85	50%	1.83	5.53
1	60	4.65	0.89	19%	1.83	39%	2.82	6.48
2	0	5.03	0.91	18%	1.87	37%	3.17	6.90
2	45	6.37	0.90	14%	1.85	29%	4.53	8.22
2	60	8.06	0.90	11%	1.84	23%	6.22	9.91
3	0	6.95	0.91	13%	1.88	27%	5.07	8.82
3	45	8.79	0.92	10%	1.88	21%	6.91	10.67
3	60	11.12	0.92	8%	1.90	17%	9.22	13.02

Table 3.11 – Example predictions for minor axis

d_p/f	θ (°)	Predicted b/f	1 σ (68%) prediction		95% prediction limits			
			\pm	%	\pm	%	Lower 95% limit	Upper 95% limit
1	0	3.38	0.32	9%	0.65	19%	2.73	4.03
1	45	3.51	0.31	9%	0.63	18%	2.87	4.14
1	60	3.63	0.30	8%	0.62	17%	3.01	4.26
2	0	5.04	0.31	6%	0.64	13%	4.41	5.68
2	45	5.23	0.31	6%	0.63	12%	4.60	5.86
2	60	5.42	0.31	6%	0.63	12%	4.79	6.05
3	0	6.37	0.31	5%	0.64	10%	5.74	7.01
3	45	6.61	0.31	5%	0.64	10%	5.97	7.25
3	60	6.85	0.32	5%	0.65	9%	6.21	7.50

Excluding the 72° data

The author found, however, that a significant improvement in the fits occurred when the data for the 72° shots was excluded. This may seem at first a rather arbitrary rejection of data for no other reason than that it makes things work better, but the author believes there are good grounds for not including the 72° data in the final regression analysis. It has been severally reported, most notably by Christiansen *et al.* (1993) that for oblique hypervelocity impact phenomena there exists a *critical angle* that signifies the boundary between different impact mechanisms. The reason for this is that, if the impact is sufficiently oblique, the shock wave induced in the projectile at the first point of contact with the target will have reached the free surface at the opposite side of the projectile before it has completely engaged the target. This results in fragmentation of the projectile and thus significant alteration of the impact feature (crater or hole) morphology. Accordingly, the critical angle is a function of the impact velocity.

Christiansen *et al.* (1993) used an *Eulerian* hydrocode to perform oblique impact simulations and thus were able to monitor the simulated pressures within the projectile upon impact. They derived a “theoretical” - remember that a hydrocode only approximates the physical processes of a hypervelocity impact (Melosh, 1989) - relationship between the impact velocity and the critical angle. The hydrocode predicts a critical angle of around 60° for aluminium spheres impacting at 5 km s⁻¹. Their experimental data shows the onset, at angles of 65° and above, of phenomena associated with exceeding the critical angle, such as multiple craters and irregular holes. Since the speed of sound in steel is lower than in aluminium (5.0 km s⁻¹ compared to 5.1 km s⁻¹) it may take significantly longer for the shock wave to traverse a steel projectile thus increasing the critical angle. Therefore the author suspects that his 60° data is marginally below the critical angle.

To study this phenomenon the tool developed in section 2.3.2 was applied to the perforation data such that the influence of impact angle and target thickness on the shape as expressed as the *shape factor* (defined in section 2.3.2) could be examined.

The fit and prediction limits for the major axis with the 72° data excluded are shown in Figure 3.19 and Figure 3.20 and in Figure 3.21 and Figure 3.22 for the minor axis. The coefficients, statistics and example predictions are given in Table 3.12 through Table 3.15.

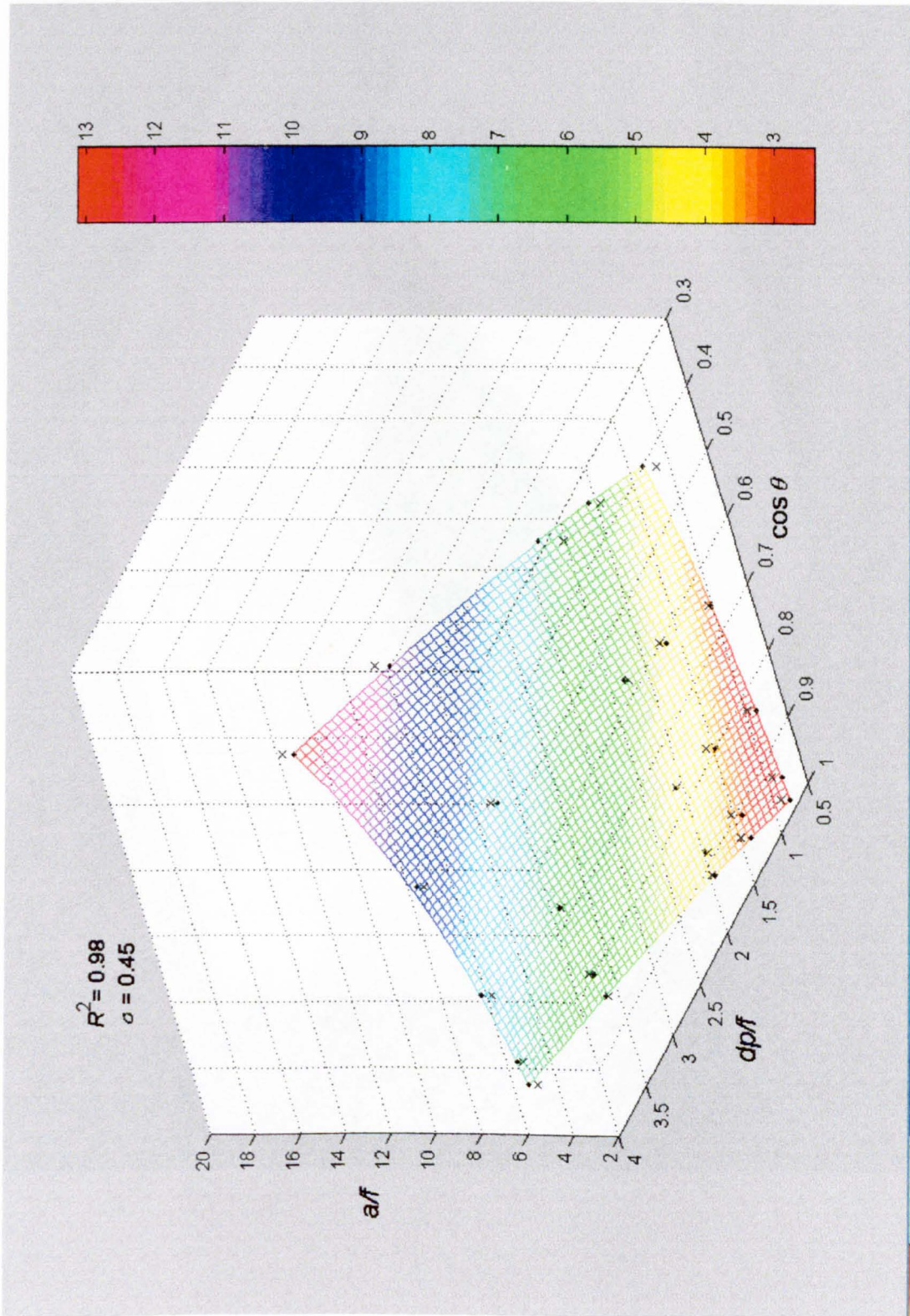


Figure 3.19 - Non-linear fit to major axis data with 72° data excluded

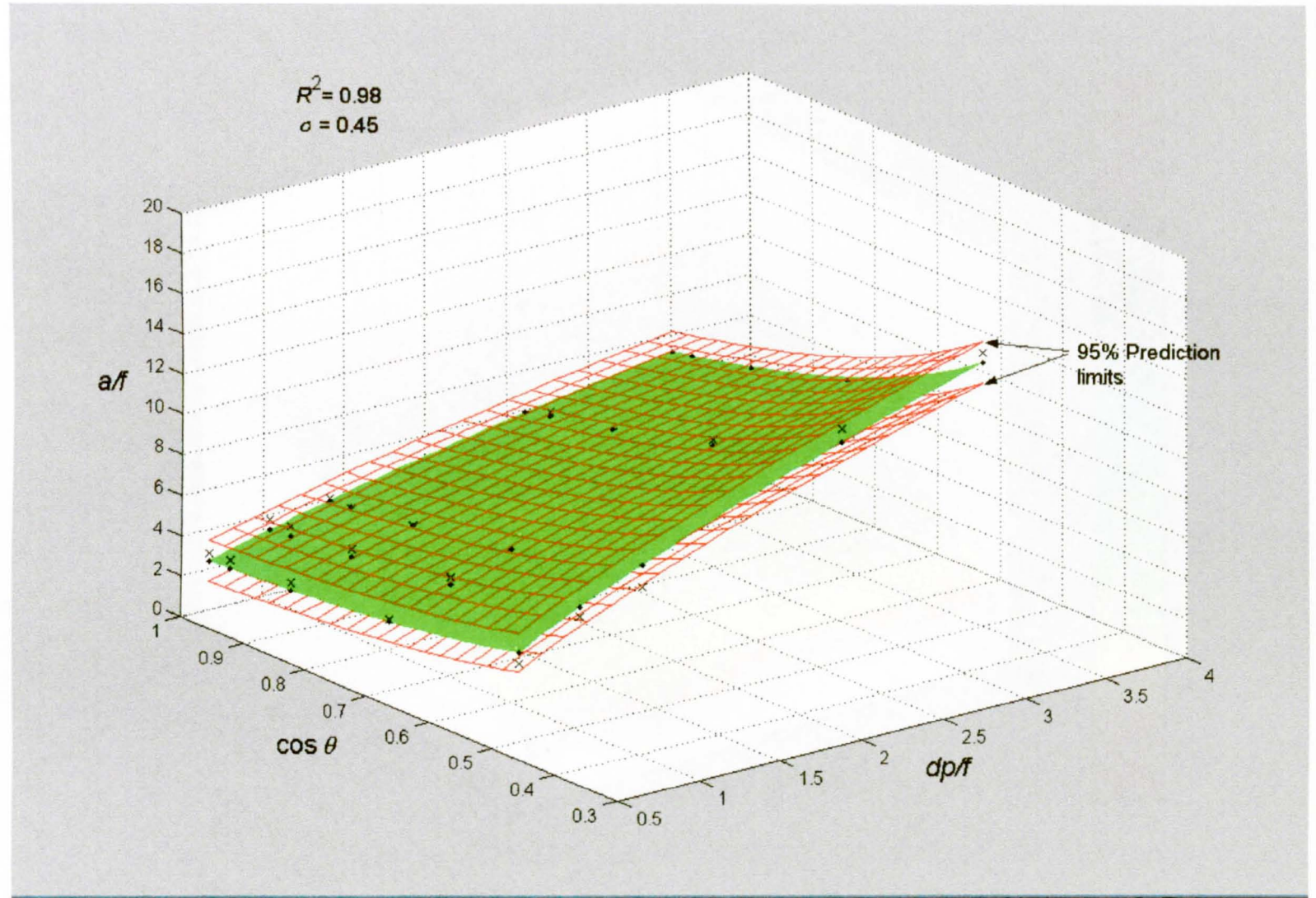


Figure 3.20 - Prediction limits for non-linear fit to major axis with 72° data excluded

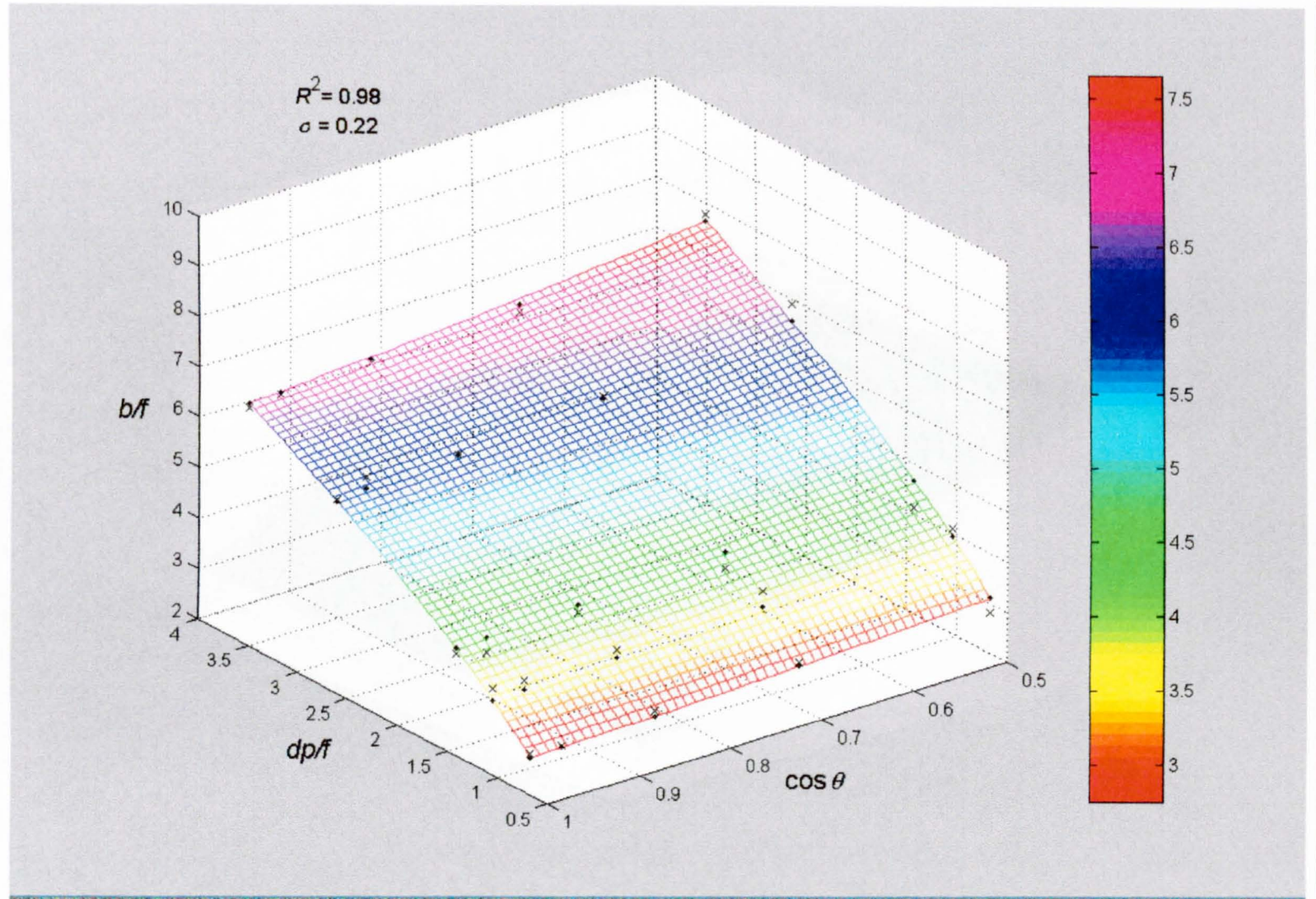


Figure 3.21 - Non-linear fit to minor axis with 72° data excluded

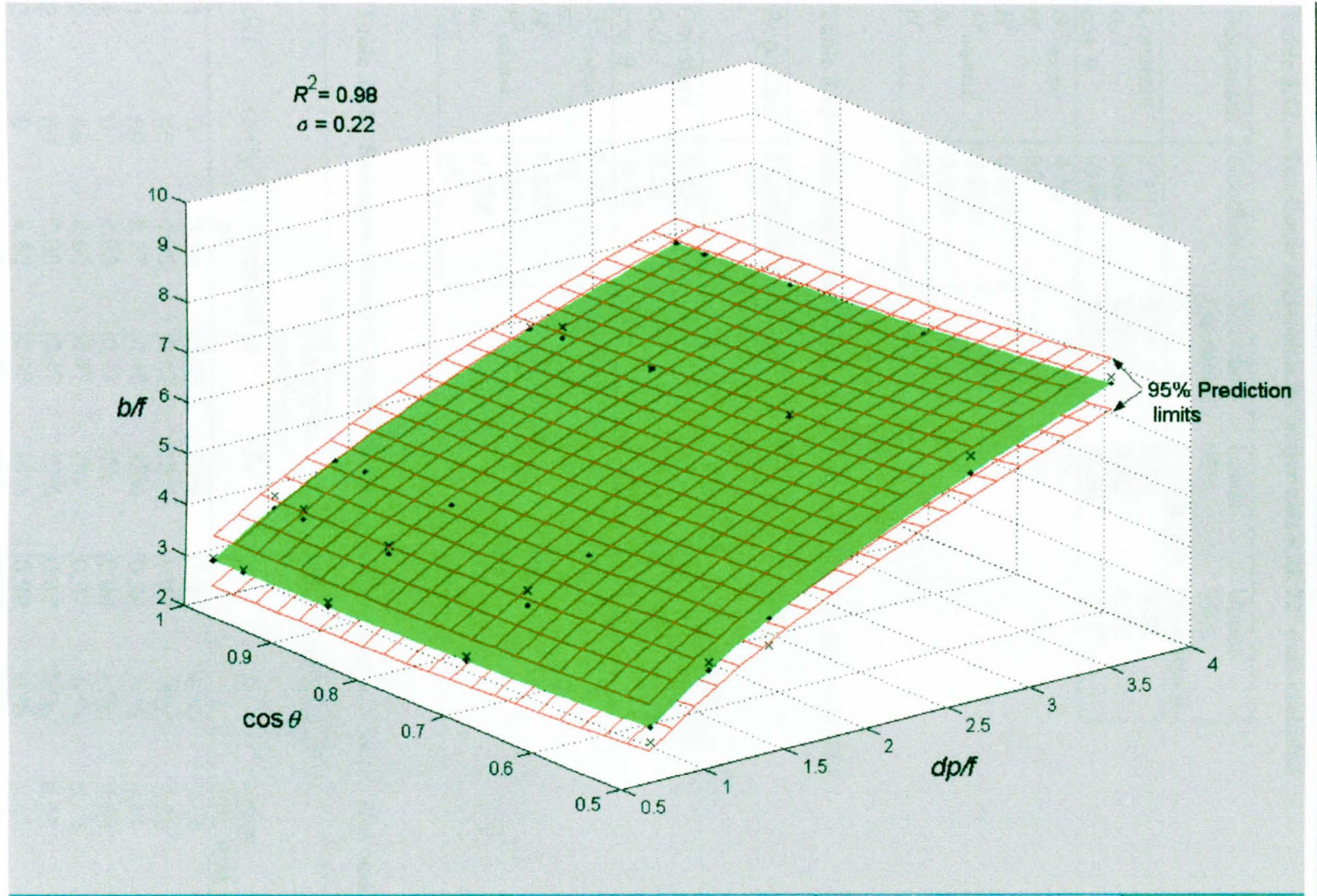


Figure 3.22 - Prediction limits for non-linear fit to minor axis with 72° data excluded

Table 3.12 – Non-linear regression for major axis with 72° data excluded

Regressor	Coefficient	Standard Deviation	Lower 95% confidence	Upper 95% confidence
Constant	3.13	0.11	2.91	3.36
d_p/f	0.65	0.03	0.60	0.72
$\cos \theta$	-0.88	0.05	-0.98	-0.77
$SS_{residual}$	4.45			
df	22			
R^2	0.975			
$R^2_{adjusted}$	0.972			
s_ϵ	0.449			
N	25			

Table 3.13 – Non-linear regression for minor axis with 72° data excluded

Regressor	Coefficient	Standard Deviation	Lower 95% confidence	Upper 95% confidence
Constant	3.43	0.06	3.30	3.56
d_p/f	0.55	0.02	0.51	0.58
$\cos \theta$	-0.17	0.03	-0.24	-0.10
$SS_{residual}$	1.08			
df	22			
R^2	0.983			
$R^2_{adjusted}$	0.981			
s_ϵ	0.222			
N	25			

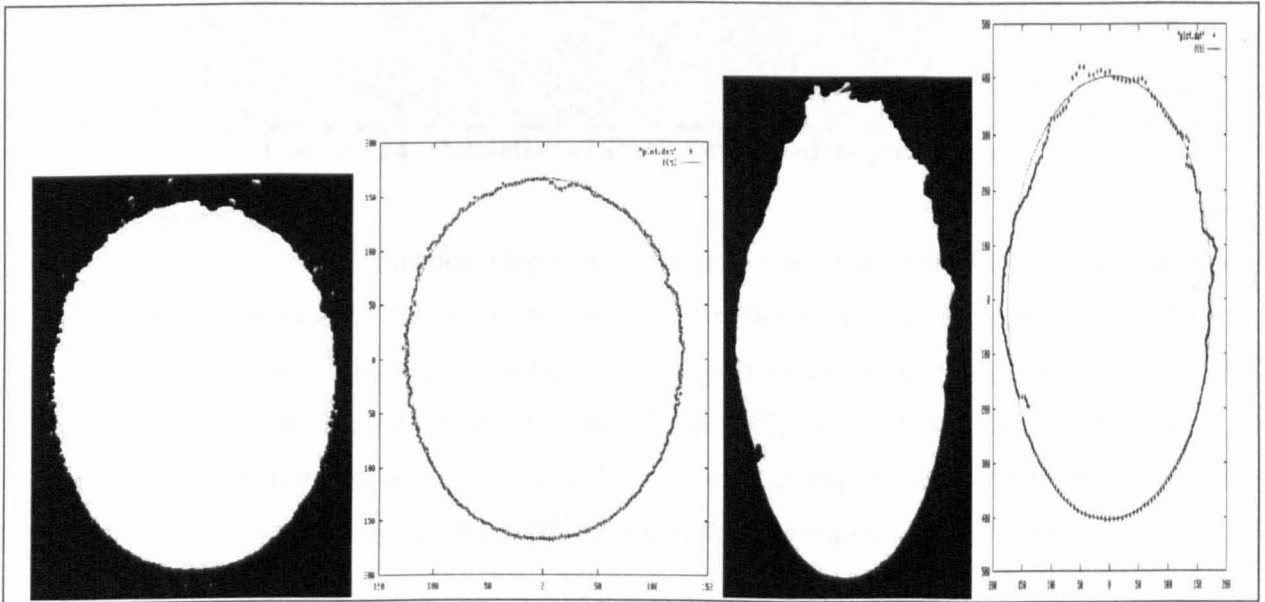
Table 3.14 – Examples of major axis predictions using regression with 72° data excluded

d_p/f	θ (°)	Predicted a/f	1 σ (68%) prediction		95% prediction limits			
			\pm	%	\pm	%	Lower 95% limit	Upper 95% limit
1	0	3.13	0.48	20%	1.00	41%	2.14	4.13
1	45	4.25	0.47	15%	0.97	30%	3.28	5.22
1	60	5.77	0.46	12%	0.96	24%	4.81	6.72
2	0	4.93	0.47	8%	0.98	17%	3.96	5.91
2	45	6.69	0.47	7%	0.97	14%	5.73	7.66
2	60	9.08	0.47	19%	0.97	39%	8.11	10.05
3	0	6.43	0.48	14%	0.99	30%	5.45	7.42
3	45	8.73	0.48	12%	0.99	24%	7.73	9.72
3	60	11.84	0.49	8%	1.01	17%	10.83	12.85

Table 3.15 – Examples of minor axis predictions using regression with 72° data excluded

d_p/f	θ (°)	Predicted b/f	1 σ (68%) prediction		95% prediction limits			
			\pm	%	\pm	%	Lower 95% limit	Upper 95% limit
1	0	3.43	0.24	7%	0.49	14%	2.93	3.92
1	45	3.64	0.23	6%	0.48	13%	3.16	4.12
1	60	3.86	0.23	6%	0.47	12%	3.39	4.33
2	0	5.00	0.23	5%	0.48	10%	4.52	5.48
2	45	5.31	0.23	4%	0.48	9%	4.83	5.79
2	60	5.64	0.23	4%	0.48	8%	5.16	6.11
3	0	6.24	0.23	4%	0.49	8%	5.75	6.73
3	45	6.62	0.24	4%	0.49	7%	6.13	7.11
3	60	7.03	0.24	3%	0.50	7%	6.53	7.53

Example ellipse fits to the target holes using the tool developed in section 2.3.2 are shown in Figure 3.23.

**Figure 3.23 – Picture of example holes and ellipse fits**

The variation of shape factor with impact angle and relative target thickness is shown in Figure 3.24. The shape factor does indeed increase with impact angle, although there does not appear to be any clear discontinuity or abrupt transition. The 72° impact in the relatively thickest target has the largest shape factor (i.e. the most irregular hole) for reasons already discussed, namely that the rear surface has only just opened up resulting in a highly irregular morphology. For this reason the hole diameter is measured in the plane of the original surface rather than at the bottom of the crater.

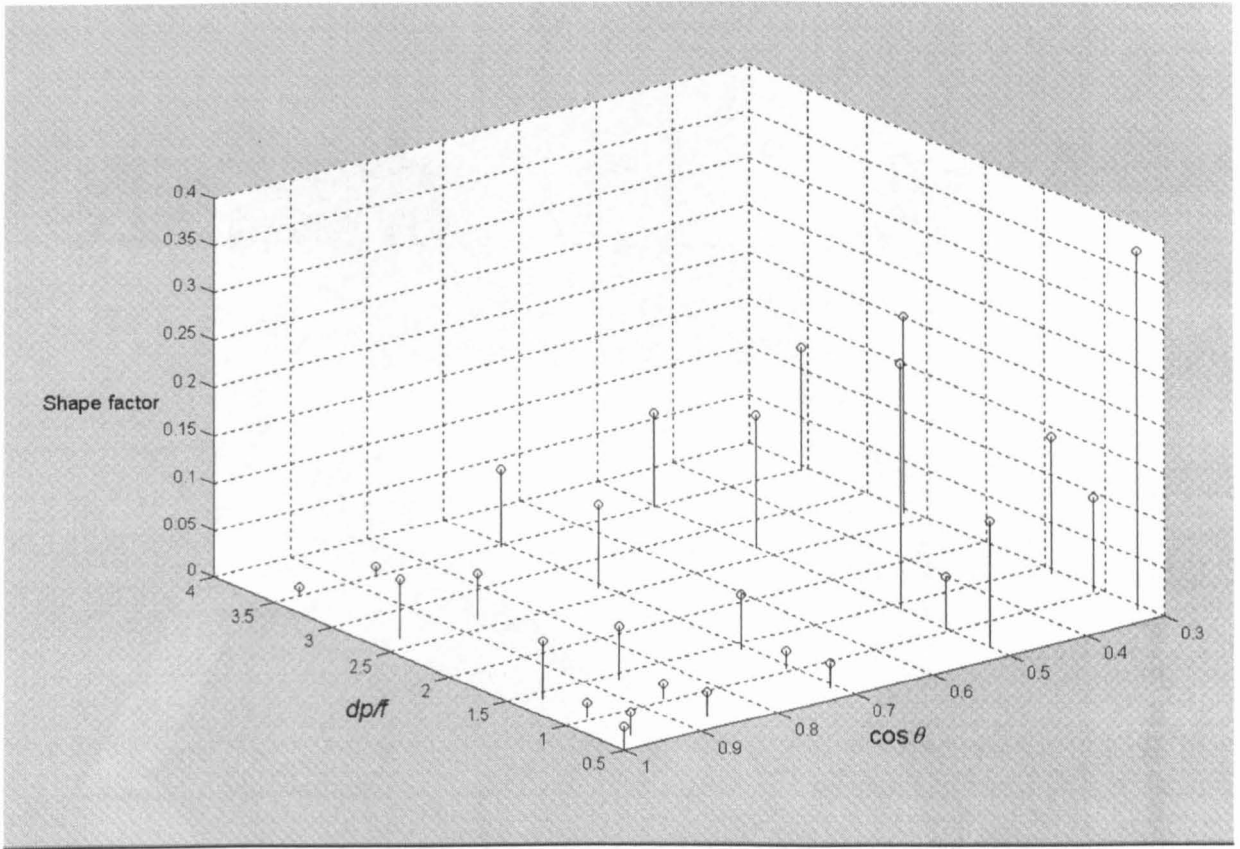


Figure 3.24 – Variation of shape factor with impact angle

Fits to circularity data

At first it may seem that the functional form of the circularity b/a has already been suitably defined by the regression analysis of the major and minor axis separately. However just dividing the minor axis equation by the major axis equation would give a relationship that depends only on $\cos \theta$. This is in apparent contradiction with Figure 3.12 and Figure 3.15, which suggest that b/a depends to a seemingly significant extent on *both* $\cos \theta$ and d_p/f . The following function was found to suitably model the data, whilst at the same time fulfilling the qualitative requirements of the relationship.

$$\frac{b}{a} = \cos \theta + \beta_0 \left(\frac{d_p}{f} \right)^{\beta_1} (1 - \cos \theta) \quad (3.4)$$

It can be seen that for normal impacts ($\cos \theta = 1$) the second term will disappear and the circularity index will be 1, as we require. Also, for a negative β_1 the second term will tend towards zero as d_p/f becomes large thus fulfilling the requirement that as the relative target thickness becomes small the circularity approaches $\cos \theta$ i.e. the particle simply punches out its projection onto the plane.

The non-linear fit to the circularity data is shown in Figure 3.25, with prediction limits shown in Figure 3.26. The coefficients and statistics are given in Table 3.16, with example predictions given in Table 3.17.

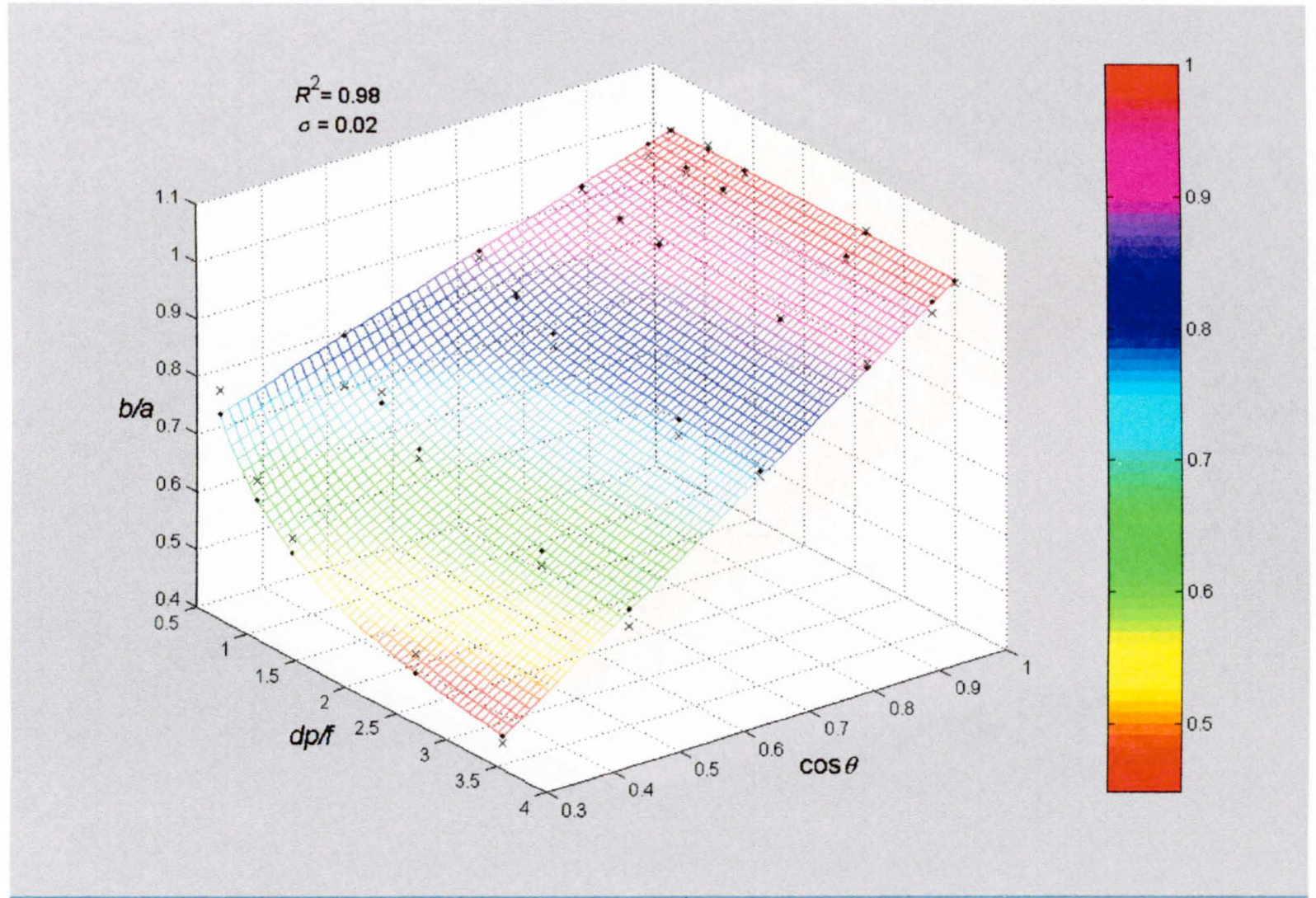


Figure 3.25 - Non-linear fit to circularity data

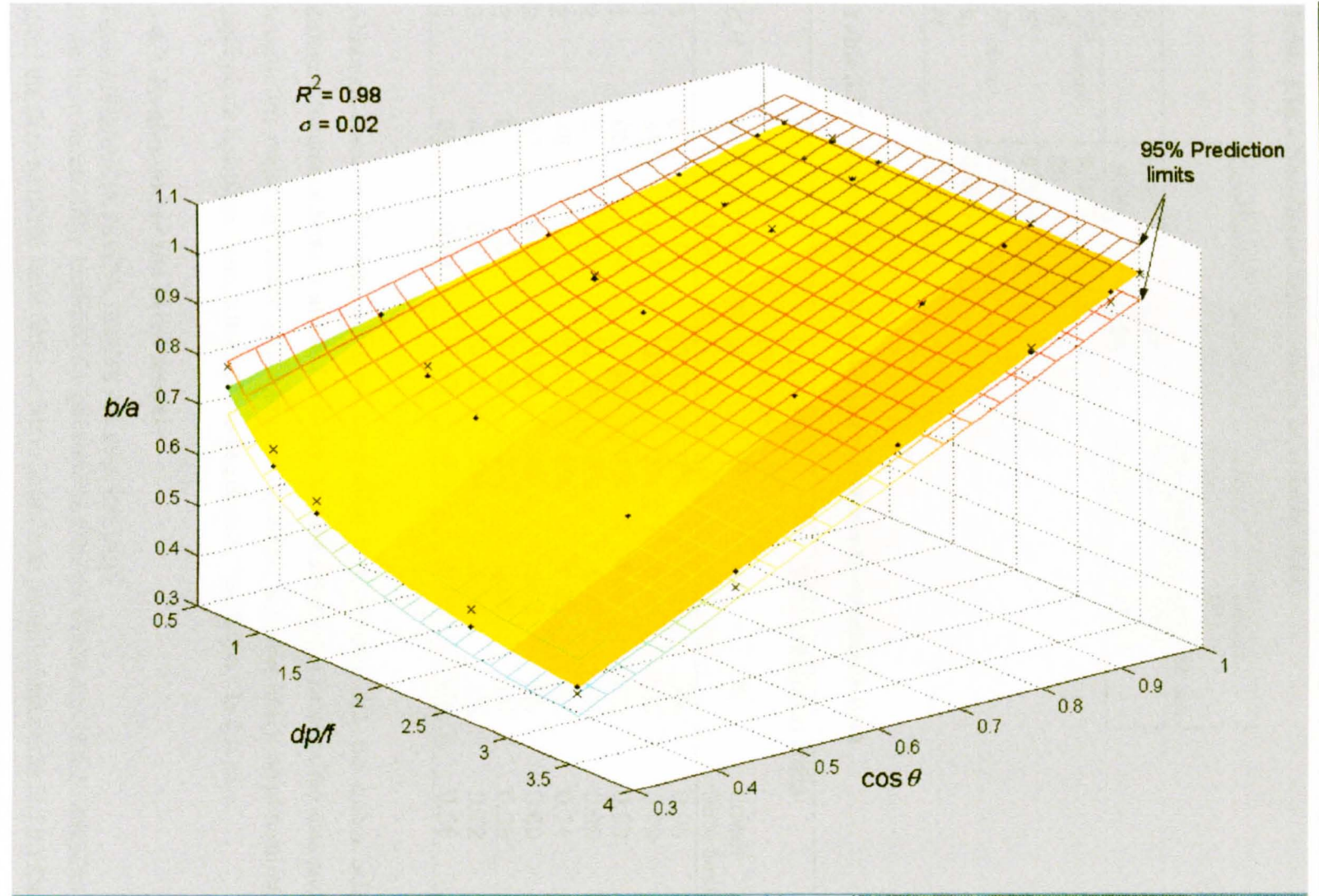


Figure 3.26 - Prediction limits for non-linear fit to circularity data

Table 3.16 – Non-linear regression for circularity data

	Coefficient	Standard Deviation	Lower 95% confidence	Upper 95% confidence
β_0	0.48	0.01	0.45	0.51
β_1	-0.69	0.06	-0.81	-0.57
$SS_{residual}$	0.017			
df	28			
R^2	0.978			
$R^2_{adjusted}$	0.977			
s_ϵ	0.025			
N	30			

Table 3.17 – Example predictions using regression to circularity data

d_p/f	θ (°)	Predicted b/a	1 σ (68%) prediction		95% prediction limits			
			\pm	%	\pm	%	Lower 95% limit	Upper 95% limit
1	0	1.00	0.03	3%	0.05	5%	0.95	1.05
1	45	0.85	0.03	3%	0.05	6%	0.79	0.90
1	60	0.74	0.03	4%	0.05	7%	0.69	0.79
2	0	1.00	0.03	3%	0.05	5%	0.95	1.05
2	45	0.79	0.03	3%	0.05	7%	0.74	0.85
2	60	0.65	0.03	4%	0.05	8%	0.60	0.70
3	0	1.00	0.03	3%	0.05	5%	0.95	1.05
3	45	0.77	0.03	3%	0.05	7%	0.72	0.83
3	60	0.61	0.03	4%	0.05	9%	0.56	0.67

Although equation 3.4 may not seem compatible with equation 3.3, the author believes that a different functional form is justified both by the high correlation between the data and the fit and because the major and minor axis regression equations are most likely simplifications of a more appropriate functional form, but are felt to be adequate “predictors” in this case.

3.4.2. Evaluation of the fitted models

Further diagnostics: residual variance and goodness-of-fit

If we have successfully modelled the phenomena then we would expect the variability of the data about the fit to be of the same order as our experimental measurement errors and the formal tests of this are the χ^2 -test or the F -test (appendix A). It can be seen from Table 3.12, Table 3.13 and Table 3.7 that the standard deviation of the error term in the model is significantly larger than the uncertainty to which the data was measured. For the best fit using non-linear regression applied to the data from 0-60° the estimated error standard deviation is around 5% of the minor axis values and around 10-20% for the major axis, yet the measurement errors are around 1%. For the case of the fits presented here $\chi^2/\nu = 33, 150$ and 92 for the minor axis, major axis and circularity respectively. Thus assuming that the errors on our measured values are an accurate – and the author is confident that they are (section 3.3.1) – we would conclude from a χ^2 -test that our model is

wrong. But it is not the purpose of this thesis to construct an equation that comprehensively models the physics of an oblique hypervelocity penetration in a metal target. It has already been highlighted that the model presented here is a simplified, primarily *predictive* tool and it was known at the start that there was at least one missing regressor in the model, namely the velocity. Thus in this case a goodness-of-fit test is of little value as we are not concerned with whether we have accurately modelled the phenomena merely with whether we can predict future events to a satisfactory precision. To quote Cooper (1969):

“We may calculate the function at a number of points and use the method of least squares to fit a simpler function such as a polynomial. In this situation the ultimate goodness-of-fit criterion is whether, or not, the fitted function produces values close enough to those of the original function. The statistical tests of goodness-of-fit are of little interest in this situation.”

In probably *all* hypervelocity impact research statistical goodness-of-fit tests based purely on measurement errors are of little, if any, interest, which may explain why the author has only ever seen one χ^2 test in relevant literature* and that was calculated incorrectly giving a false “good fit”. However, “error” can be defined as *“the variability that cannot be reduced by improving the model”* (Ryan, 1997). In the case of hypervelocity impact research if an experiment is repeated many times with exactly the same impact conditions – as exact as we can make them with the apparatus – then a distribution of impact features will arise, the spread of which will be due to the process’ sensitivity to slight, unavoidable variations in impact conditions and will most likely be significantly larger than the accuracy to which the features can be measured. Thus, this variability (which cannot be reduced) would make a suitable substitute for the measurement precision as an “error” variance in statistical tests of empirical models. In this sense we are using a limiting intrinsic random variability, which is essentially what measurement errors are. This is the approach adopted in section 5.

Velocity variation

We can start to investigate the effect of the undesirable, yet unavoidable velocity variation over the experimental programme by looking at the correlation of velocity with the other regressors (Table 3.18).

Table 3.18 – Correlation coefficients R^2 of regressors

	d_p/f	$\cos \theta$	V
d_p/f	1	0.000	0.461
$\cos \theta$	0.000	1	0.001
V	0.461	0.001	1

* The only experimental hypervelocity impact study that the author could find that employs any statistical analysis of regression was that of Mog *et al.* (1993) who use ANOVA and the F -statistic.

It can be seen that d_p/f and $\cos \theta$ are uncorrelated, as has already been shown. $\cos \theta$ and velocity V have insignificant correlation and so regression against these two regressors would be valid for constant d_p/f . However V shows significant correlation ($P(\rho=0) = 0.001\%$) with d_p/f , where ρ is the population correlation coefficient (Hugill, 1985 describes the significance test for correlation coefficients), as larger particles go slower. Therefore, in the previous regression analysis the d_p/f exponents will contain some measure of the influence of velocity on the dependent parameters, assuming velocity significantly effects the dependent parameters over the range of velocities covered here. If the variation in velocity is responsible for the lack of fit observed then we might expect the residuals about the fitted function to show some degree of correlation with velocity.

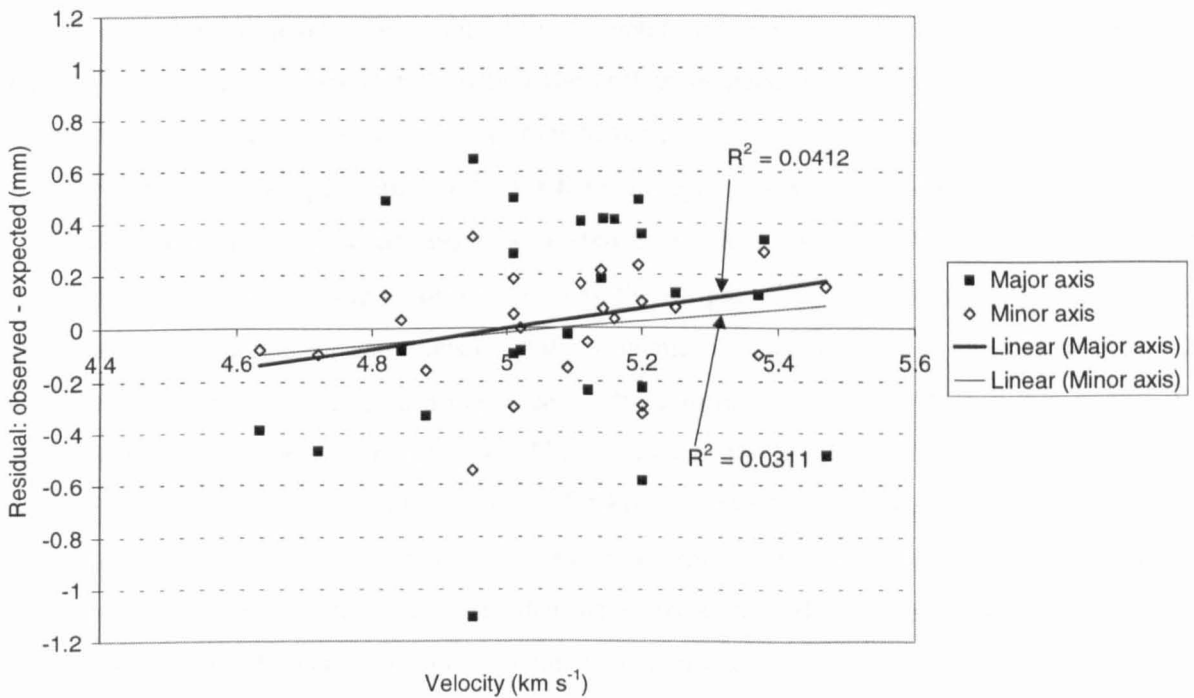


Figure 3.27 – Variation of residuals with velocity

It can be seen that the deviation of the data from the function fitted to d_p/f and $\cos \theta$ shows insignificant correlation with velocity for the major and minor axis fits: $P(\rho=0) = 40\%$ and 33% respectively. Thus it is not evident that the velocity variation accounts for the observed lack of fit, at least not in a simple way. Most previous research (for normal impacts only) incorporates a velocity exponent of $2/3$, which over the range of velocities used here would give rise to an approximately 12% increase in hole diameter. However, the standard deviation estimates for the regression to the major and minor axes are 0.2 and 0.04 respectively, which is $<10\%$ of the smallest a/f and b/f values of around 2.8.

3.4.3. Material effects

There is not enough data using the aluminium projectiles to perform a similar multiple regression analysis with which to compare to the regression using steel projectiles. However, we can see if the observed aluminium perforations are compatible with the values predicted by the regression to the steel projectile data. Table 3.19 shows the predicted major and minor axes compared to those

observed in aluminium for the 4 different angles at which we have aluminium perforation data, calculated at $d_p/f = 1.04$ at which the aluminium data was taken.

Table 3.19 – Aluminium projectile data compared to steel projectile equation predictions

θ	b/f predicted	b/f 95% confidence interval	b/f Al. projectile	a/f predicted	a/f 95% confidence interval	a/f Al. projectile
15°	3.52	3.03, 4.01	3.66	3.31	2.32, 4.31	3.71
30°	3.59	3.10, 4.07	3.58	3.65	2.67, 4.63	3.74
45°	3.72	3.24, 4.19	3.28	4.36	3.39, 5.33	3.78
60°	3.94	3.47, 4.42	2.82	5.92	4.96, 6.87	3.39

The observed aluminium diameters are only incompatible at 60° impact angle with the steel regression (at the 5% level). The aluminium diameters are significantly smaller than would be expected for steel projectiles at 60°, which the author suspects is due to the lower penetrating power of the aluminium projectiles due to their lower density and thus kinetic energy. It could be that at 60° the aluminium projectiles only just have enough energy to penetrate $f \cos \theta$ thickness of target and perhaps some projectile material is starting to ricochet rather than penetrate. Another factor is that the speed of sound in aluminium is slightly higher than in steel so it could be that 60° is above the critical angle for aluminium and the projectile is starting to break up (section 3.4.1). It can be seen that material is strewn downrange for the aluminium 60° shot (Figure 3.5) unlike the steel 60° shot at the same d_p/f (Figure 3.4). The velocity of the aluminium shots (5.1 – 5.4 km s⁻¹) was generally higher than the steel shots (4.6 – 5.4 km s⁻¹), which may explain the slightly larger – but not particularly significant – than predicted diameters for the 15° shots. Remember that the prediction intervals include the variability that arises from the velocity spread of the steel shots. Since the aluminium diameters become smaller than predicted at 45° and that the 60° was faster than the 45° shot (5.4 compared to 5.1 km s⁻¹) suggests that the factors already described have a larger effect than the velocity variation.

3.5. Discussion

3.5.1. Comparison with previous work

GMC - Gardner et al. (1997a)

The first impact equation that should be scrutinised in the light of this work is that of Gardner *et al.* (1997a), commonly referred to within the Unit as “GMC”. This has been extensively employed in the Unit for reducing hypervelocity perforation data from space-flown instruments. This equation was derived from purely normal impact data, but has been applied to holes resulting from non-normal impacts. The form of the equation is:

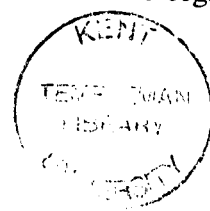
$$\frac{d_p}{f} = A \left(\frac{10}{9 - \exp(D'_h/B)} \right) + D'_h (1 - \exp(-D'_h/B)) \quad (3.5)$$

where $D'_h = D_h/f$. A and B are functions of velocity: $A = A1(V)^{A2}$ and $B = B1 + B2(V)$, where $A1$, $A2$, $B1$ and $B2$ are the best fit values for different target and projectile material combinations. The

factor A is also presented in a generalised form as a function of velocity, projectile density, target density and yield strength. This relationship was derived by *inverse* regression, regressing the independent variable d_p/f against the dependent variable D_h/f . Gardner *et al.* (1997a) give the reason for this that it results in a more useful equation for decoding space impact data in that it is the particle size that one is trying to determine from observed hole sizes. The method used for application to space data (Gardner *et al.*, 1997b) is to insert the *geometric* mean of the largest and smallest diameter of a perforation as D_h and the velocity with its component normal to the surface i.e. $V \cos \theta$. Furthermore, to approximate the input of an isotropic flux a constant average elevation angle of 45° is used with a single representative mean velocity. Thus it is assumed *a-priori* with *no* experimental justification that an oblique impact will be equivalent to a normal impact with a diameter equal to the geometric mean of the major and minor axes of the oblique perforation and with a velocity equal to the normal component of the oblique velocity.

It can be seen from equation 3.5, that it is not trivial to rearrange GMC so that predicted hole sizes can be obtained for a given impacting particle diameter. The author could have input the geometric mean of the hole axes of his experimental data into GMC and compared the predicted particle sizes to those actually fired, but it is the validity of using the geometric mean that is under scrutiny. Consequently, the author used a numerical method to calculate the hole diameter GMC requires to yield a particle size equal to the one fired. The “Solver” in Microsoft Excel was used whereby the residual sum of squares between the actual particle size and that predicted by GMC is minimised for trial values of hole diameter. Values of D_h/f could be found that corresponded to values of d_p/f essentially identical to the actual values used i.e. to within many more decimal places than the accuracy of the actual values. Firstly the D_h/f “predicted” by GMC using values of A and B specified as being appropriate for the materials in question and using $V \cos \theta$ were compared to the observed geometric mean hole diameters; essentially using GMC as it has been used for application to space data. The percentage difference between the observed and predicted values is shown in the following plots to readily illustrate the extent of any inaccuracy.

It can be seen in Figure 3.28 that GMC systematically under-predicts the hole diameters to a worsening degree with increasing impact angle. This simple first comparison of the equation’s predictions with oblique impact data immediately calls into question the methodology with which it has been applied in the past to space data. The fact that the equation always *under*-predicts the normal impact data, to which it should be applicable, could possibly be either due to the coefficients A and B not being entirely appropriate due to an inexact correspondence between the materials used here and those used to derive the equation or due to the inversion of the regression. It may be that the correlation between the equation and data from which it was derived is not sufficiently high enough so that using GMC “inversely” to predict D_h rather than to predict d_p does not introduce a significant systematic error (see earlier discussion on inverse regression; section 3.4). The comparison is next made against d_p/f (Figure 3.29).



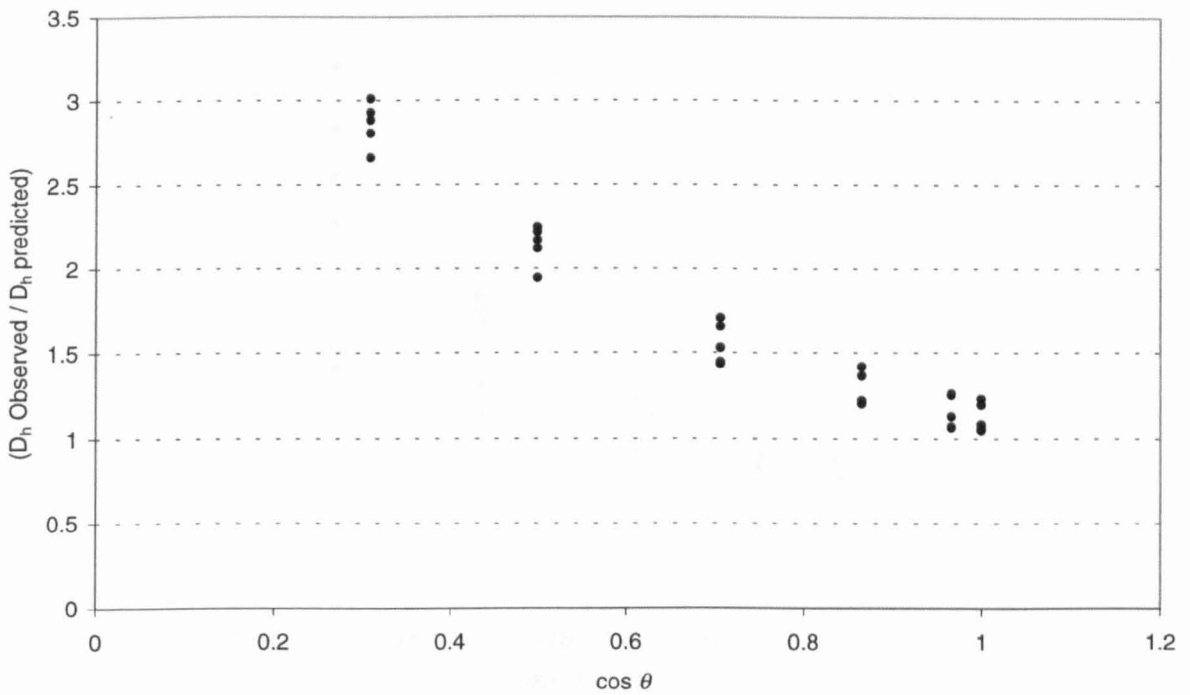


Figure 3.28 – Performance of GMC for oblique impact prediction against impact angle

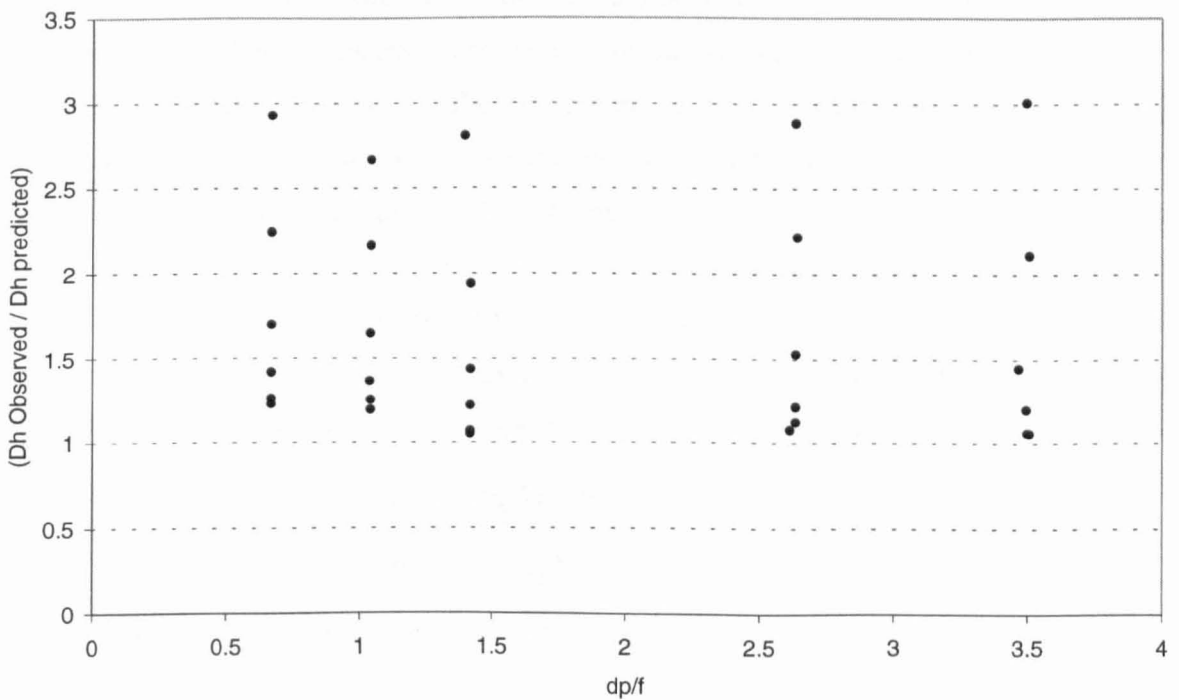


Figure 3.29 – Performance of GMC for oblique impacts against d_p/f

It can be seen in Figure 3.29 that the inaccuracy is uncorrelated with d_p/f and thus it would appear that the lack of an appropriate relationship with impact angle is the prime cause of the inaccuracy. The predicted hole diameters are next compared to the major and minor axes separately (Figure 3.30).

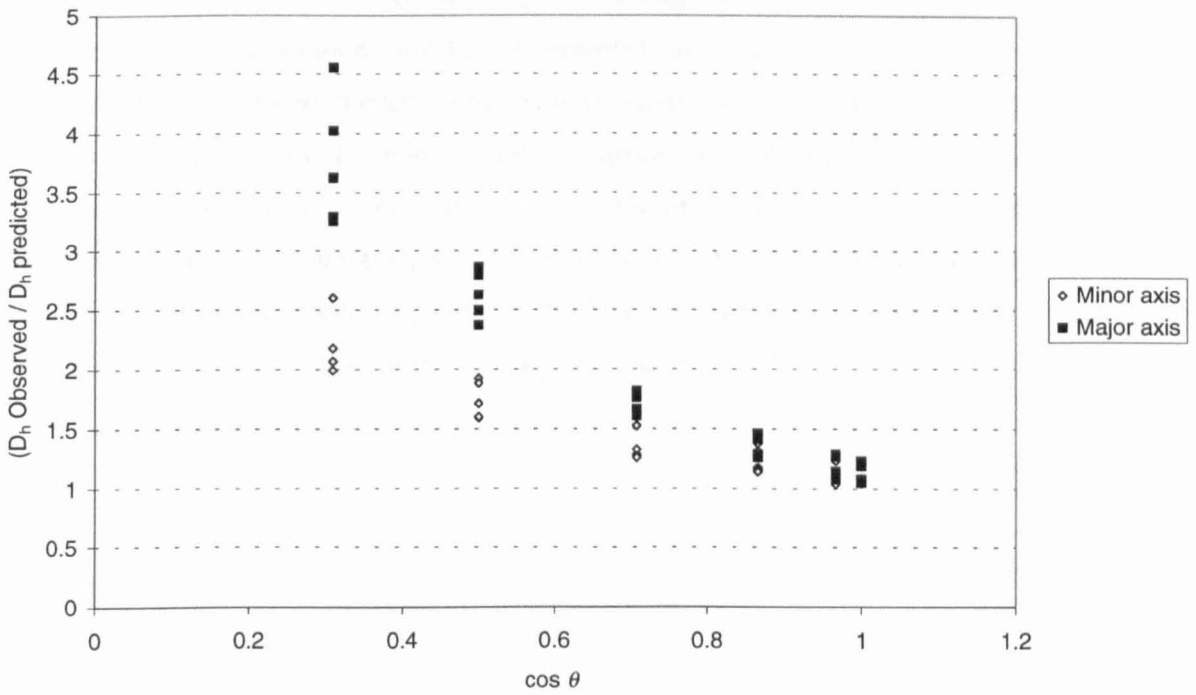


Figure 3.30 – Performance of GMC for major and minor axes

Table 3.20 shows R^2 and the estimator of the standard deviation $s_\epsilon = (SS_{residual}/df)^{1/2}$. We do not lose any degrees of freedom in this case because none of the parameters are being estimated from the data and GMC is being used “as-is”. The first column (d_p/f) is not particularly interesting, but just shows that the values of d_p/f arising from using the corresponding D_p/f are insignificantly different from the actual independent value used in the experiments. The standard deviation estimate s_ϵ should be of the same order as our measurement errors if the model is correct and thus this value gives us a rough guide to goodness-of-fit in the absence of carefully calculated/estimated errors. For a large data set s_ϵ will also correspond approximately to 68% prediction limits for values predicted by the equation and so in this respect also gives us a guide to the regression’s usefulness.

Table 3.20 – Performance of GMC using $V\cos\theta$

	d_p/f	D_p/f	b/f	a/f
R^2	1.000	0.367	0.675	0.181
$SS_{residual}$	0.000	223.034	77.564	558.974
N	30	30	30	30
df	30	30	30	30
s_ϵ	0.000	2.727	1.608	4.317

Although the minor axis is more closely predicted than the major axis there is still a systematic increase with impact angle. The author suspects that the inaccuracy is, in part, due to the use of $V\cos\theta$ as the impact velocity. The author has never been happy with the often-used simple replacement of V with $V\cos\theta$ when impact equations derived from normal impacts are applied to oblique impacts. Although, for parameters such as the depth of a crater in a thick target it may seem to follow intuitively that the normal component of the velocity will be the “deciding factor”, the author does not believe that this is always the case. If we think about the case for a thin target, once

the projectile has engaged the target, it still passes through the material at a speed V – ignoring for the time being any deceleration - not $V\cos\theta$, regardless of its angle to the top surface of the target. In a hypervelocity perforation event as the particle passes through the plane of the target it pushes material radially away from the point of impact causing the molten perimeter of the hole to “flow back” and eventually freeze forming lips. The amount of hole-growth beyond the diameter of the object that penetrated the target is proportional to the velocity. An analogy that springs to mind is the speed of a car going through a puddle determines how much water is splashed out to the sides. GMC was thus applied using V for the velocity rather than $V\cos\theta$.

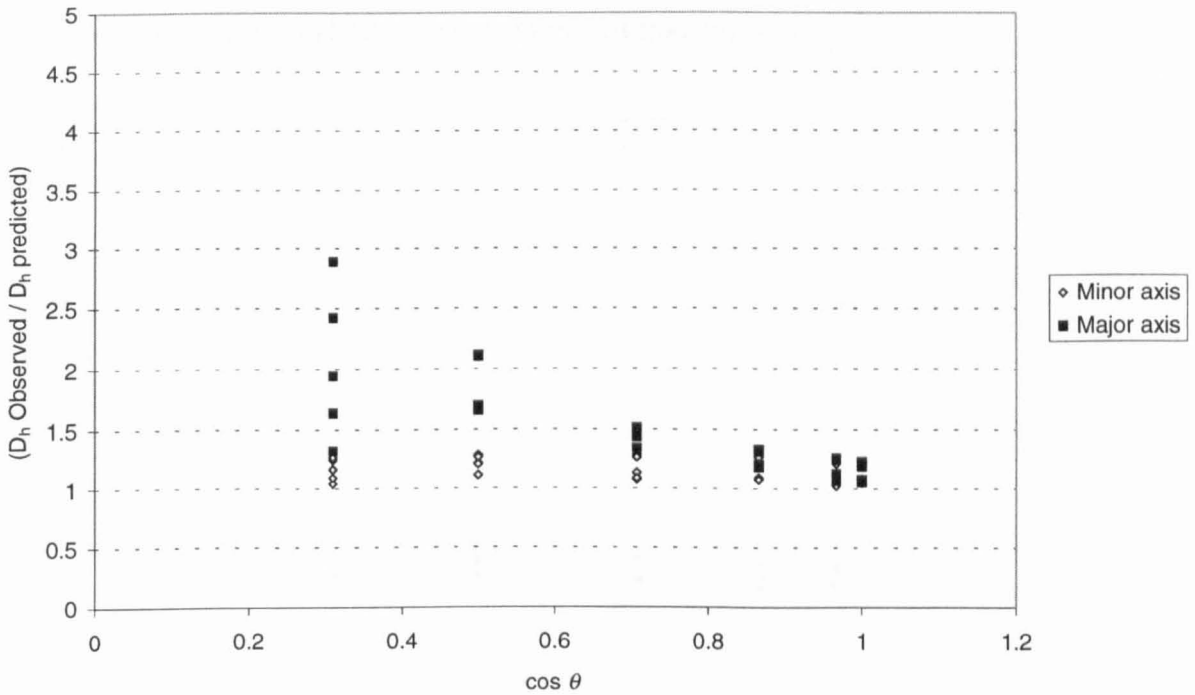


Figure 3.31 – GMC prediction using V

Table 3.21 - Performance of GMC using V

	d_p/f	D_h/f	b/f	a/f
R^2	1.000	0.762	0.954	0.561
SS_{residual}	0.000	99.329	15.477	351.568
N	30	30	30	30
df	30	30	30	30
s_e	0.000	1.820	0.718	3.423

It can be seen from the graph and the associated statistics that using V instead of $V\cos\theta$ improves the performance of GMC. Thus, this simple test already suggests a change in the way GMC should be applied to spacecraft data. Although the observed minor axis values are now to within 50% of the predicted values, the performance for the major axis is still poor. Consequently, this study suggests that the minor axis of a hole witnessed space would be a better guide to the particle size than the geometric mean diameter.

Modelling of the major axis may be improved by thinking of GMC as predicting the amount of *extra* hole growth that occurs beyond the diameter of the hole punched out by the particle. Thus we

can think of the process as a particle punching out a hole equal in diameter to d_p/f that expands an additional amount, given by GMC, that is proportional to the impact velocity and the relative target thickness. For an oblique impact the particle punches out $d_p/f \cos \theta$, the perimeter of which then may flow back by the same amount. Accordingly the amount of hole growth ($D_h/f - d_p/f$) was calculated using GMC for the d_p/f values and velocities used in the experimental programme and the predicted major axis was calculated by adding this amount to $d_p/f \cos \theta$. First, however, the parameters A and B were re-evaluated by performing a fit to the minor axis data. Thus, we retain the functional form of GMC but choose our own material-specific parameters – possibly not purely material-dependent depending on the correlation with other regressors. Consequently, we lose 4 degrees of freedom as 4 parameters, $A1$, $A2$, $B1$ and $B2$, are being estimated from the data.

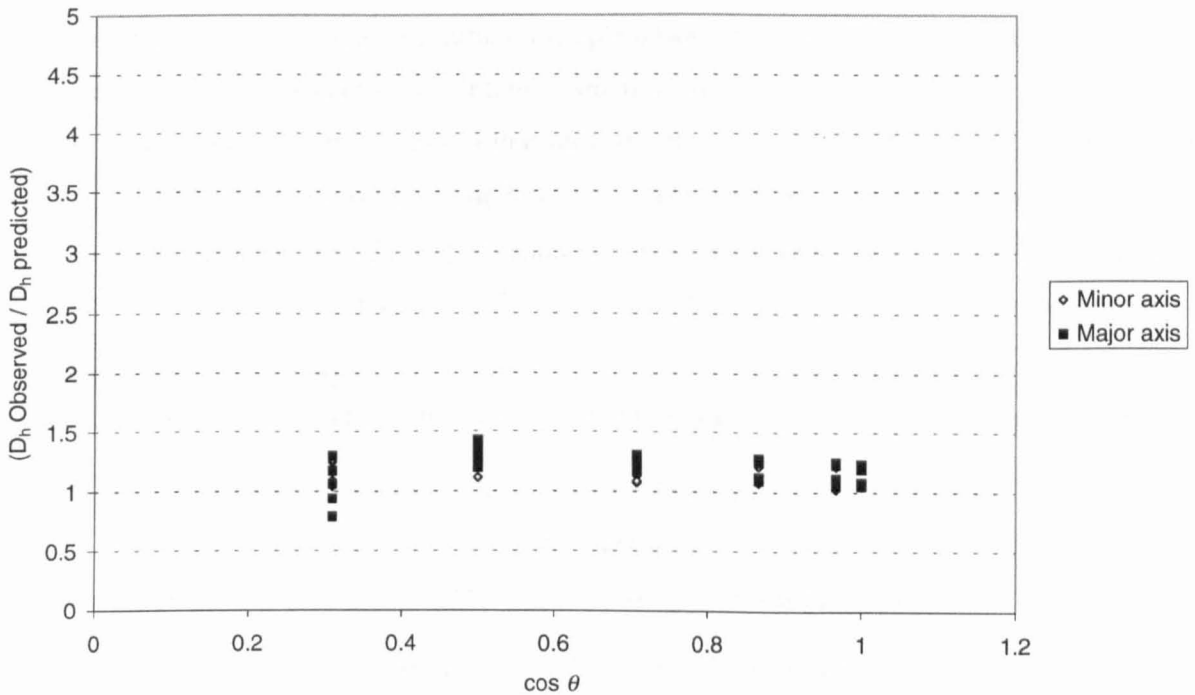


Figure 3.32 – Predictions using GMC predicted hole growth added to $d_p/f \cos \theta$.

Table 3.22 shows the performance of GMC using the new fitted parameters. The d_p/f column this time shows the statistics for the fit of d_p/f against the observed minor axes data used to derive the new coefficients. The far right “ a/f mod.” column is the modified calculation of a/f using the hole growth added to $d_p/f \cos \theta$.

Table 3.22 - Performance of GMC using new parameter estimates.

	d_p/f	D_r/f	b/f	a/f	a/f mod.
R^2	0.943	0.761	0.953	0.560	0.952
SS_{residual}	1.916	57.836	4.401	269.995	32.315
N	30	30	30	30	30
df	26	26	26	26	26
s_e	0.271	1.491	0.411	3.222	1.115

There is an improvement in the fit using the new parameters and for the modified calculation of the major axis there is approximately a three-fold decrease in the lack-of-fit. It should be noted that

although in many papers in the field R^2 is the only statistic quoted, this should not be solely relied upon and certainly does not indicate goodness of fit. It is entirely possible to have highly correlated predicted and observed values but for there to be *systematically* orders of magnitude difference between them.

Schonberg and Taylor (1989)

Schonberg and Taylor's equations are as follows:

$$\begin{aligned} \frac{D_{\min}}{d_p} &= 2.974 \left(\frac{V}{C}\right)^{0.962} \left(\frac{f}{d_p}\right)^{0.895} + 1.120 & 30 < \theta < 65 \text{ deg} \\ \frac{D_{\max}}{d_p} &= 3.841 \left(\frac{V}{C}\right)^{0.415} \sin^{1.468} \theta \left(\frac{f}{d_p}\right)^{0.519} + 1.530 & 30 < \theta < 75 \text{ deg} \end{aligned} \quad (3.6)$$

Although far more complex than the author's simple power law relationships, they do not appear to give as good a fit to their data as the author's equations do to the data in this study. Additionally they are more limited in applicability in that they are obviously invalid for normal impacts when $\sin \theta$ will be zero*. What is most puzzling however is that when the author applies equation 3.6 for the independent parameters of this experimental programme the predicted values give a seemingly better fit to this data than to Schonberg and Taylor's data from which the relationship was derived.

Baker and Persechino (1993)

Baker and Persechino's model for the major and minor diameters of an elliptical hole are given by:

$$\begin{aligned} D_{\text{minor}}/d &= (\alpha + \sigma v)\beta_L \\ D_{\text{major}}/d &= \phi D_{\text{minor}}/d \end{aligned}$$

where d is the projectile diameter, v is the impact velocity and α is given by:

$$\alpha = \alpha_n + \alpha_5(1 - e^{-\alpha_6(90^\circ - \theta)/\theta}) + (1 - 1/\sin^n(90^\circ/35^\circ))$$

where $n = e^{1.13t/d} - 1$ and this time θ is the angle from the plane of the target. α_n is the parameter used for normal impacts given by:

$$\begin{aligned} \alpha_n &= 1 + \alpha_1(1 - e^{-\alpha_2 t/d}) & \text{for } t/d \leq 0.70 \\ \alpha_n &= 1 + \alpha_1 - (\alpha_3 + \alpha_4(t/d - 0.07))(t/d - 0.07) & \text{for } t/d \geq 0.70 \end{aligned}$$

where t is the plate thickness and α_1 through α_6 are fitting constants. σ is given by:

$$\sigma = \sigma_n(1 - e^{-\sigma_5\theta/(\sigma_6 - \theta)})$$

and σ_n is given by an equally complex function to α_n with 4 fitting parameters. β_L is the ballistic limit parameter that is 0 for velocities below the ballistic limit, rising gradually to 1 with velocity.

The author did not attempt to compute this function for the data in this work but read the points corresponding to the angles covered in this work from the plot of the function in their paper. Figure 3.33 shows some of the data from this work compared to Baker and Persechino's model (B and P)

*Note that in some publications (e.g. Baker and Persechino, 1993) θ is defined as the angle from the plane of the target, however, in this case θ is the angle from the normal as in this thesis.

for aluminium on aluminium impacts; the t/d ratio for each data set is shown in brackets. The aluminium data from this work shows the same general trend as their model with a decrease in major axis with increasing impact angle. However, the steel data shows a faster growth in major axis with impact angle suggesting that the data Baker and Persechino fitted to was taken near the ballistic limit, thus their model is somewhat limited in relevance to oblique hypervelocity penetration.

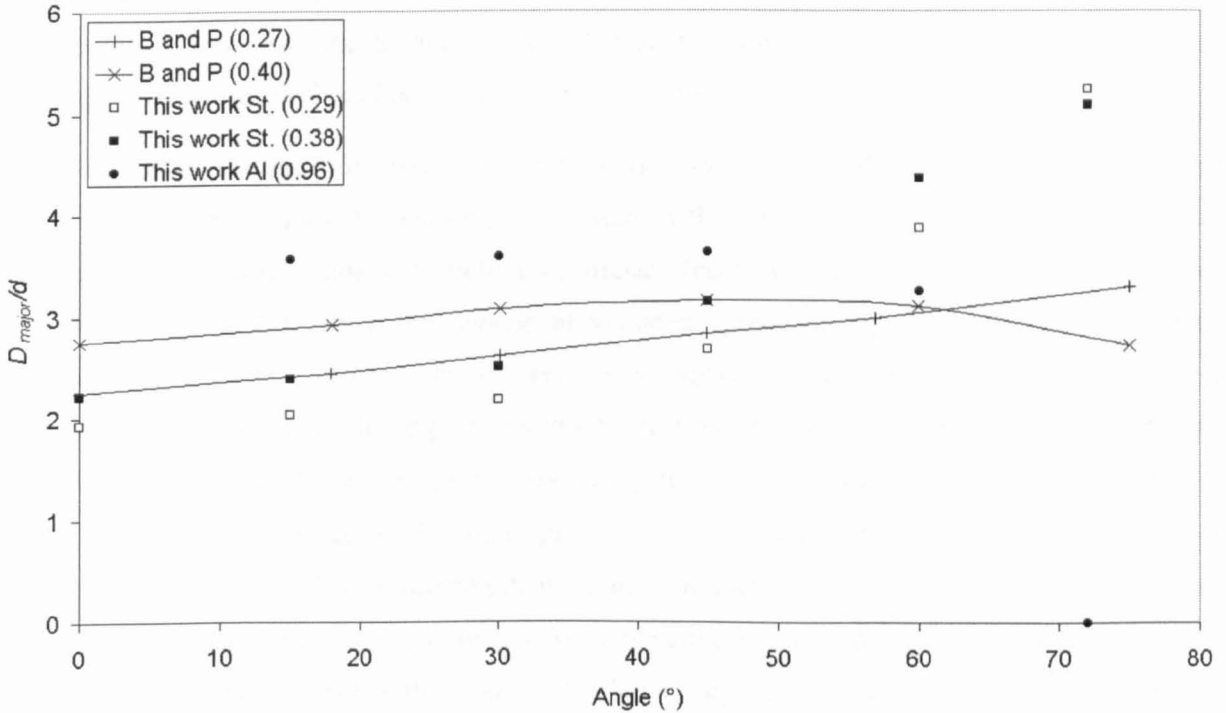


Figure 3.33 – Comparison with Baker and Persechino’s model; t/d ratios shown in brackets

3.5.2. Summary

The experimental programme presented in this chapter produced a data set giving a more complete coverage of the parameter space than any previous study the author was able to locate. This orthogonal coverage of the parameter space permitted unambiguous multiple regression of the hole major and minor axes and circularity against the impact angle and projectile-diameter-to-target-thickness ratio. It was shown that the method in which the GMC equation of Gardner *et al.* (1997a) has been applied to space data does not predict the laboratory data as well as an alternative approach. In this approach the velocity term of GMC is *not* replaced with its normal component and the extra *hole growth* is calculated and added to the projection of the particle’s cross-section onto the plane of the target.

Application of the regression

It was discussed that these experiments were intended to be *calibration* experiments where we want to determine the independent variables (impact angle and particle size) from the dependent variables (hole size and shape) rather than vice-versa. This could be achieved by rearranging the *forward* multiple regression equations derived here to make the variables of interest the subject; as there is more than one parameter that we are trying to “decode” we would require simultaneous equations: possibly the equation for the major axis and the minor axis. However, it is not clear how

the statistics and confidence intervals would propagate through this procedure. Forward multiple regression was used as it is not clear how to proceed with *inverse* multiple regression where we would have to regress the independent variables against the dependent variables, either choosing each independent variable as the variate in turn or performing *multivariate* regression where more than one variate is used in the regression. The author could not find any relevant literature that was within the author's capacity to adequately digest and apply with sufficient confidence within a reasonable time-scale regarding the statistical procedures for topics such as *inverse multivariate regression*. In any case, the author believes that such techniques are unnecessary and that the technique that was used should be applied in the following way.

A method that is frequently used when interpreting meteoroid and space debris fluxes using laboratory-derived empirical equations is to start with a mass and velocity distribution and determine the corresponding distribution of impact features (e.g. McDonnell *et al.*, 1998 or McBride *et al.*, 1999). Thus, the dependent variables, predicted by incorporating the model-specified independent variables into the regression equation, are compared with the observed impact features rather than the impact features being used to determine the projectile parameters via inverse regression. However, the regression equation is invariably treated as the "theoretical model prediction" and therefore infinitely precise and only uncertainties in the observed impact features are considered when comparing them to those predicted by the regression. The author does not believe that this is the correct approach. What we are effectively doing is comparing one set of observations (space craters) with another set (laboratory craters), only the laboratory data is represented by an empirical regression equation, which in most cases has no theoretical basis. The "true" values of the coefficients – i.e. what theory dictates they should be – are not known and we only have an estimate of them from our fit to the data. The estimated coefficients have corresponding uncertainties and it is shown in section 3.3.1 (and appendix A) how these uncertainties, coupled with the distance from the regression data that the prediction is being made, contribute to a final uncertainty in any value predicted by the regression. Therefore the appropriate *t*-statistic for evaluating the significance of the difference between a predicted and an observed value, rather than being:

$$t = \frac{Y - \hat{Y}}{\sigma_Y} \quad \text{should be} \quad t = \frac{Y - \hat{Y}}{\sqrt{\sigma_Y^2 + \sigma_{\hat{Y}}^2}}$$

where the denominator in the second case is the uncertainty in the observed and predicted values added in quadrature. The uncertainty in the predicted value is given by equation 3.1. For quick graphical comparisons the error bars of the observed data should be compared to the prediction limits of the regression equation rather than solely to the regression line itself.

Dimensional scaling

It should be noted that a weak dimensional scaling effect has been severally observed such that the depth-to-diameter ratio of thick target craters scales with the $^{19/18}$ power of projectile diameter

(Cour-Palais, 1987). Gardner et al. (1997a) incorporated this same index such that a scaling of hole diameter with target thickness to the same power was found to be compatible with their data, specifically: $D_p/f = f(d_p/f)f^{0.053}$, where f is in μm . This effect was not investigated in this study, but attention should be drawn to this if the results of this work are to be extrapolated to smaller scales, as would be the case for application to spacecraft data.

4. Oblique impacts on EURECA and HST solar cells

The analyses of the impact records from the EURECA and HST solar arrays were performed as part of ESA contracts 10522/93/NL/JG and 10830/94/NL/JG; prime contractors Unispace Kent and SAS Belgium respectively. The scanning and imaging of craters was performed by a team from Mare Crisium UK. The measurement of impact features was performed by J.A.M. McDonnell of Unispace Kent and J.C. Mandeville of ONERA-CERTS/DERT. In both cases the analysis of the data collected by the various co-contractors was performed by a team of PhD students and staff at the University of Kent.

The analysis was divided up in the following manner:

EURECA analysis

- A. Griffiths – impact flux and spatial distribution.
- L. Kay – size distribution.
- N. Shrine – directional distribution.

HST analysis

- A. Griffiths – impact flux.
- H. Yano – database management and morphological classification.
- N. Shrine – spatial and directional distributions.

Since the initial contract the spatial distribution of impacts on each spacecraft has been thoroughly analysed by an international team of researchers for a subsequent ESA contract (Unispace *et al.*, 1998). The conclusions of this contract were in agreement with the author's initial analysis of the HST spatial distribution in that the pattern of impacts across the solar arrays is non-random and cannot easily be explained by shielding or secondary impact effects. Therefore, it is concluded that the scanning of the HST solar array was inconsistent. Accordingly, no further presentation of the spatial distribution analysis is required here.

The author's initial analysis of the distribution of inferred impact directions, in addition to the ESA contract reports, appears in Yano (1995), Griffiths (1997) and Drolshagen *et al.* (1996). However, this analysis made conclusions about the distribution of impact directions unsupported by any statistical analysis. Therefore the appropriate statistical analysis will be presented here and represents a significant upgrade to any previous publication. A scan by the author of HST solar cells donated to the Unit for impact experiments is also presented here.

4.1. Solar cell impact scanning

The scanning of the EURECA solar arrays was performed at *Fokker* in the Netherlands, where they were deployed in a clean room and the scanning team performed a detailed survey of impact sites

during which a library of images of was compiled. Crater measurements could subsequently be taken from the images in this archive.

The retrieved HST solar array was first transported to British Aerospace (now Matra-Marconi Space), Bristol for initial inspection and subsequently moved to a scanning facility housed in a clean room at ESA's *ESTEC* establishment in the Netherlands. The scanning, performed during summer 1994, was co-ordinated by the same team as the EURECA solar array scanning (hence continuity of rationale is to be expected), with the output, once again, consisting of a set of photographs and digitised images of impact sites.

Scanning of both the EURECA solar array wings and the HST SCA wing was performed at two levels of resolution to make the most of the limited man-hours available. For one survey, small areas were scanned in detail with every crater visible to the naked eye being located and photographed. For the other survey a cut-off size was decided upon such that all craters above this size limit over the entire surface could be located and imaged. This means that the flux of impacts above this size limit is reliable.

4.1.1. EURECA and HST commercial scanning

EURECA

After retrieval by STS-57, the EURECA spacecraft was transported to the *Astrotech* facility, Florida for payload de-integration. Subsequently, the solar arrays were transported to *Fokker* in the Netherlands where they were deployed and hung vertically (Figure 4.1). A scanning rig was brought up to the arrays, which supported cameras and a CCD microscope system. A technical description of the apparatus is given by Drolshagen *et al.* (1996).

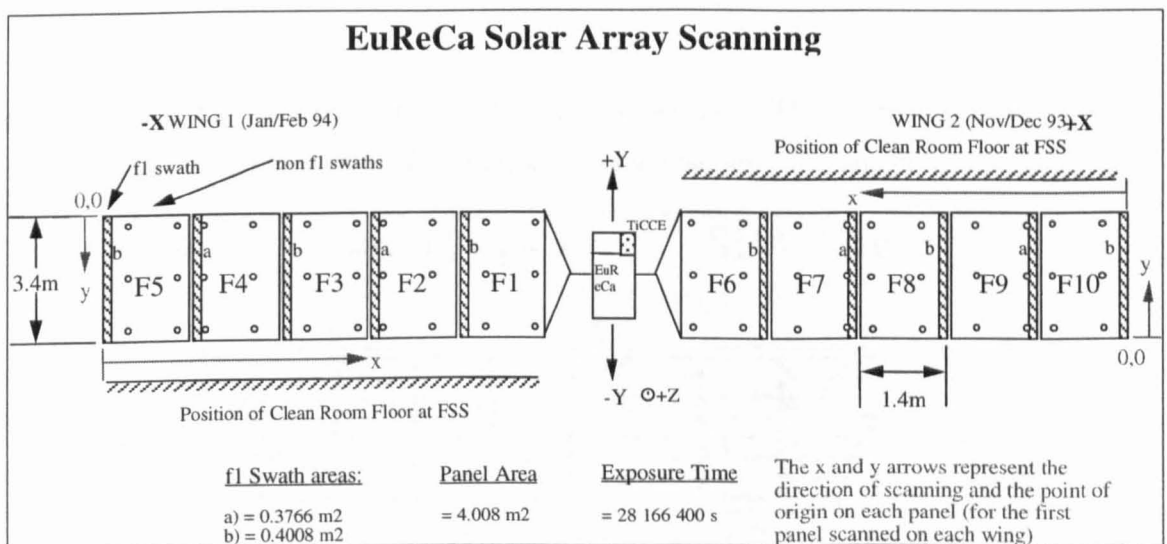


Figure 4.1 – EURECA solar array scanned sections (source: Unispace Kent)

For each of the 10 EURECA solar array panels the scanning proceeded by moving the camera a fixed vertical distance after each exposure, thus creating a series of pictures called a *swath*. Using a fixed horizontal displacement between each swath, a mosaic of pictures covering the entire surface of the array was built up. There were 10 swaths per panel: one high resolution one (*fl swath*) and nine low resolution ones (*f2-f10* or *non-fl swaths*). The following criteria were applied:

- *fl swaths* - Every impact feature that could be located with the naked eye under optimal illumination was recorded. It is estimated that this survey provided a complete record of all features larger than 300-400 μm , although it did include some features as small as 100 μm . The area covered by this scan was 4.008 m^2 .
- *non-fl swaths* - Every feature with diameter larger than half the solar cell electrode spacing was recorded: features approximately larger than 650 μm . By comparison with the *fl swaths* it was found that 50% of craters are captured by the *non-fl swaths* at 700 μm . The entire 40.08 m^2 of the solar arrays were covered in this scan.

Figure 4.1 shows the location and areas of the swaths. The location of the *fl swaths* was chosen to monitor spatial variation of the flux across the wings, at small sizes.

HST

The HST solar array wing was unfurled on a scanning table at *ESA-ESTEC* over which a motion rig was moved equipped with imaging apparatus similar to that used for EPFA (the equipment is described by Space Application Services *et al.*, 1995). A similar scanning strategy to EPFA was employed for the HST SCA wing. This time the high-resolution scan was called the *catch-all* (CA) survey (equivalent to EURECA *fl swaths*) and the low-resolution scan was simply called the (*main*) survey (equivalent to EURECA *non-fl swaths*). The following criteria were applied:

- *Catch-all* - Every impact feature that could be located with the naked eye under optimal illumination was recorded, giving an estimated resolution of 100 μm . The area covered by this scan was 0.582 m^2 .
- *Survey* - Every feature larger than 1.2 mm was recorded over the entire 20.73 m^2 of solar cells on the -V2 wing.

Figure 4.2 shows the location of the *catch-all* and *survey* areas. The catch all regions were chosen to monitor the spatial distribution of small impacts along the long axis and perpendicular to it.

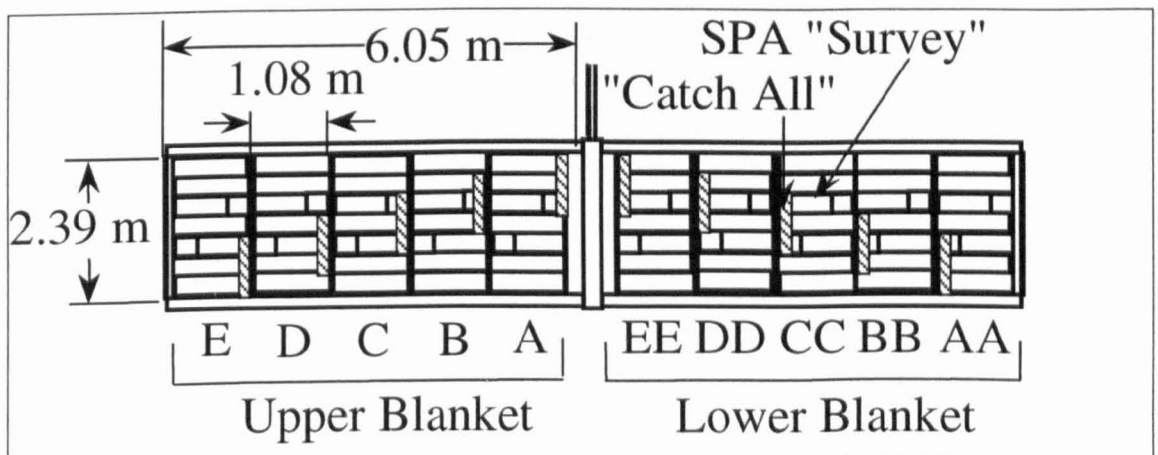


Figure 4.2 – HST solar array scanned sections (source: Unispace Kent)

Results of commercial scanning

Table 4.1 shows the number of impacts found in each survey and the percentage of impact sites showing signs of oblique incidence.

Table 4.1 – Summary of PFA scanning

	Exposed Area	Exposure Time	Cut-off size	# impacts Survey ratio CA / main	Total	% oblique Survey ratio CA/main	Mean % oblique
EURECA	40.08 m ²	2.82×10 ⁷ s	650 μm	168 / 535	703	37.5 / 30.28	32.01
HST	20.73 m ²	1.14×10 ⁸ s	1200 μm	137 / 696	841	26.2 / 15.1	17.3

The morphology of craters in *brittle* targets is markedly different from ductile targets and is, on the whole, more complex. A set of characteristic features for measurement need to be defined in order to effect a quantitative analysis of the impact record.

4.1.2. Definition of crater parameters

The definitions of the defining parameters of solar cell craters were made during the EURECA and HST post-flight analyses (PFAs). These definitions are adopted for consistency in this section of this thesis and for the experimental programme in section 5.

Symmetrical “normal” craters

The PFA team identified repetitively observed, easily identifiable regions of the solar cell craters. These parameters were most commonly diameters of successive, concentric regions of damage. The key features of solar cell craters used in the PFAs are shown in Figure 4.3.

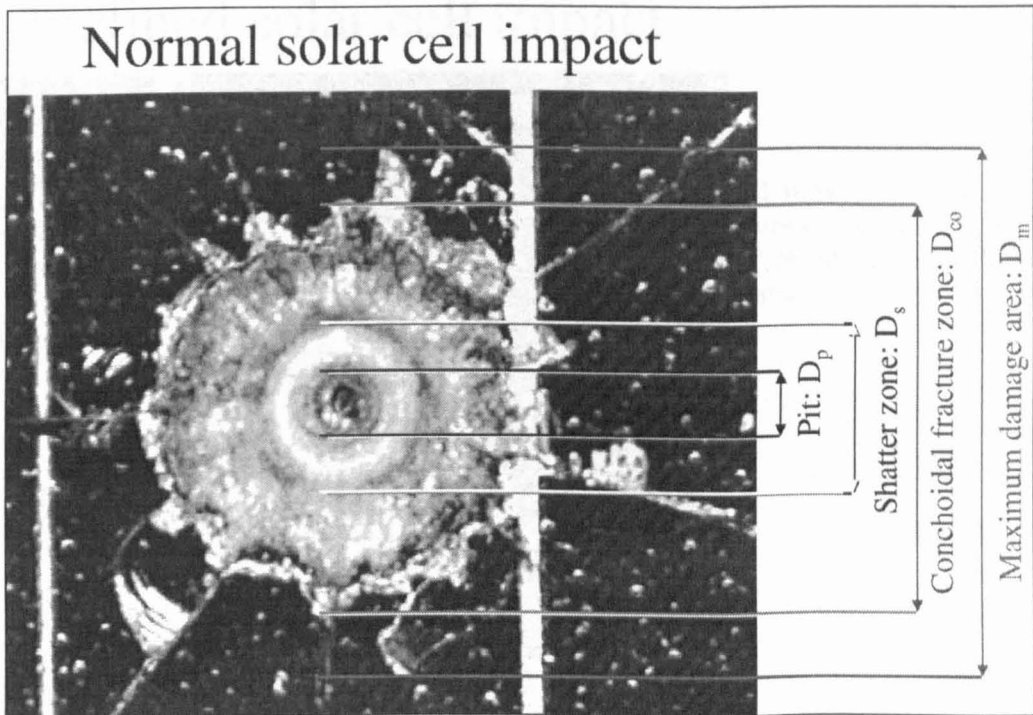


Figure 4.3 – Definition of characteristic features of solar cell crater

The features identified during EPFA are:

- *Central pit: diameter D_{pit} or D_p* - believed to be formed early in the impact process in a similar way to hypervelocity craters in ductile targets.
- *Shatter zone: diameter D_{sh} or D_s* - a region of highly shocked powdered glass surrounding the pit.
- *Conchoidal spallation zone: diameter D_{co}* - This region is formed by fracturing and subsequent ejection of the surrounding material due to stresses induced by the expansion of the central pit.
- *Diameter D_{max} or D_m* - the maximum extent of damage (not including radial cracks).

The main difference between impacts on EURECA and HST solar arrays is that the HST solar array is thin enough for impacts on the rear face to cause damage to the front face and vice versa.

Asymmetrical “oblique-impact” craters

A typical crater deemed to be due to an inclined impact is shown in Figure 4.4 with the measurements made for such an impact. Two measurements are made of each of the parameters D_p , D_s , D_{co} & D_m (Figure 4.3): one along the inferred line of flight, usually the larger diameter, (D_{max}) and one perpendicular to this, usually smaller (D_{min}).

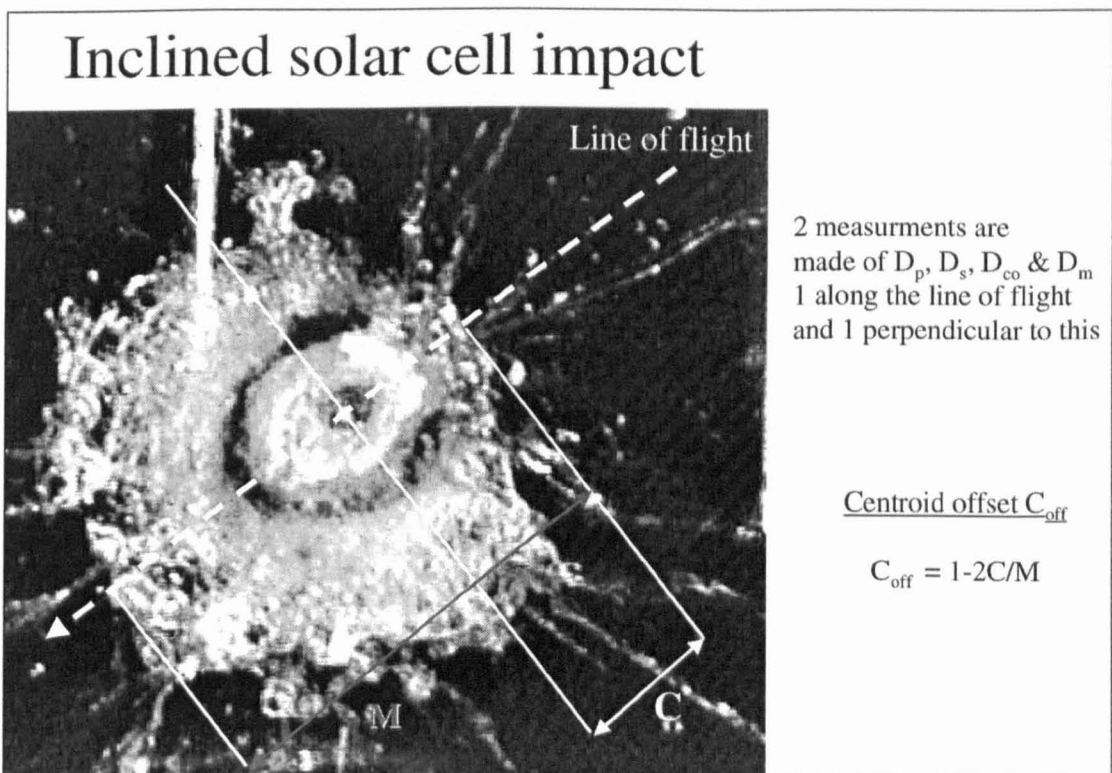


Figure 4.4 - Definition of measurements made for an oblique impact

An additional measurement, C , is made, which is the distance from the edge of the crater from which the impact is suspected to have come to the centre of the pit. A parameter is defined, which is a measure of the asymmetry of the crater, corresponding to the offset of the centre of the pit from the centre of damage, referred to as the *centroid offset* (C_{off}), defined as:

$$C_{off} = 1 - \frac{2C}{M} \quad (4.1)$$

This value will be zero for circularly symmetrical craters.

An asymmetrical morphology that was frequently observed on EURECA was labelled “butterfly” morphology in that the spallation was symmetrical about an axis passing through the centre of the crater forming butterfly-wing type features, with cracks emanating from each end of the central elliptical “body” forming “antennae”. These were assumed to be formed by an oblique impact although there was often a 180° ambiguity in impact direction as it is not intuitively obvious which is the uprange end of the crater. Some examples are shown in Figure 4.5.

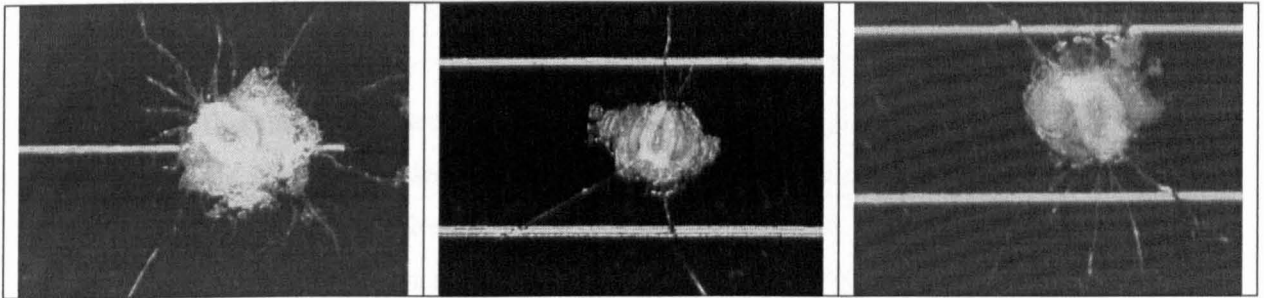


Figure 4.5 – Examples of butterfly morphology

4.1.3. Scanning of the Unit’s HST samples

After the post-flight analysis contracts, samples of space-flown HST solar cells were made available to the Unit by ESA. The author used these solar cells in for the experimental programme in section 5. However, small 50 μm projectiles were going to be used in the experimental programme, yet there were few impacts recorded smaller than a few hundred microns in the post-flight analyses due to the low scanning resolution used. Therefore, the author decided to scan the HST solar cell samples at a higher resolution than had been used in the first commercial post-flight analyses in order to locate craters made by impacts in space of comparable dimensions to those to be investigated in the experimental programme. Furthermore, only solar cells found to be free from impacts at the resolution attained were used in the experimental programme. This scanning also made an important contribution to the definition of the solar cell flux at small sizes (Taylor *et al.*, 1999).

The author used the motorised stage and microscope of the LOSS system so that the cells could be scanned using an accurate systematic scan pattern. Using a magnification of 40 \times the estimated detection limit was 20 μm D_{co} . The LOSS system also allowed the co-ordinates of located impacts to be recorded for easy location in the SEM. The initial scanning was performed with an optical system rather than the SEM because under bright illumination the impact features show up as white dots and therefore are easier to spot than by scanning in the SEM. However, even at the highest possible optical magnification the details of the located features could not be clearly imaged so the samples were subsequently transferred to the SEM where the features were relocated from the LOSS co-ordinates and if found to be impact features, as opposed to a scratch or chip in the

surface, were imaged and measured. The author found that it was necessary to sputter-coat the cells with a few nm of gold as charging of the sample prevented clear imaging in the SEM.

The 12 craters located in this scan of 13 HST solar cells is shown in Figure 4.6. 9 of the 12 were a few tens of microns across and had a common morphology comprising a smooth, fairly circular central pit, surrounded by a concentric region of highly cracked glass in turn surrounded by several platelets bounded by radial and concentric cracks. The main difference between these smaller craters and the craters located in the primary post-flight analyses was that in most cases the material bounded by cracks had not been ejected to form the “conchoidal” zone observed for the larger craters. The conchoidal zone is observed for the larger craters found in this scan (s117.001 and s55.001) that are a few hundreds of microns across.

This disparity in morphology between large and small craters is an extremely important observation in that the definition of damage parameters such as “pit” and “conchoid” correspond to different features at different sizes. Thus comparisons between different sizes of craters and in particular crater size distributions over large ranges must take account of these changes in morphology. As will later be discussed, care must also be taken when extrapolating experimentally derived cratering equations to different sizes.

Figure 4.6 – Impacts located in scan of HST solar cells

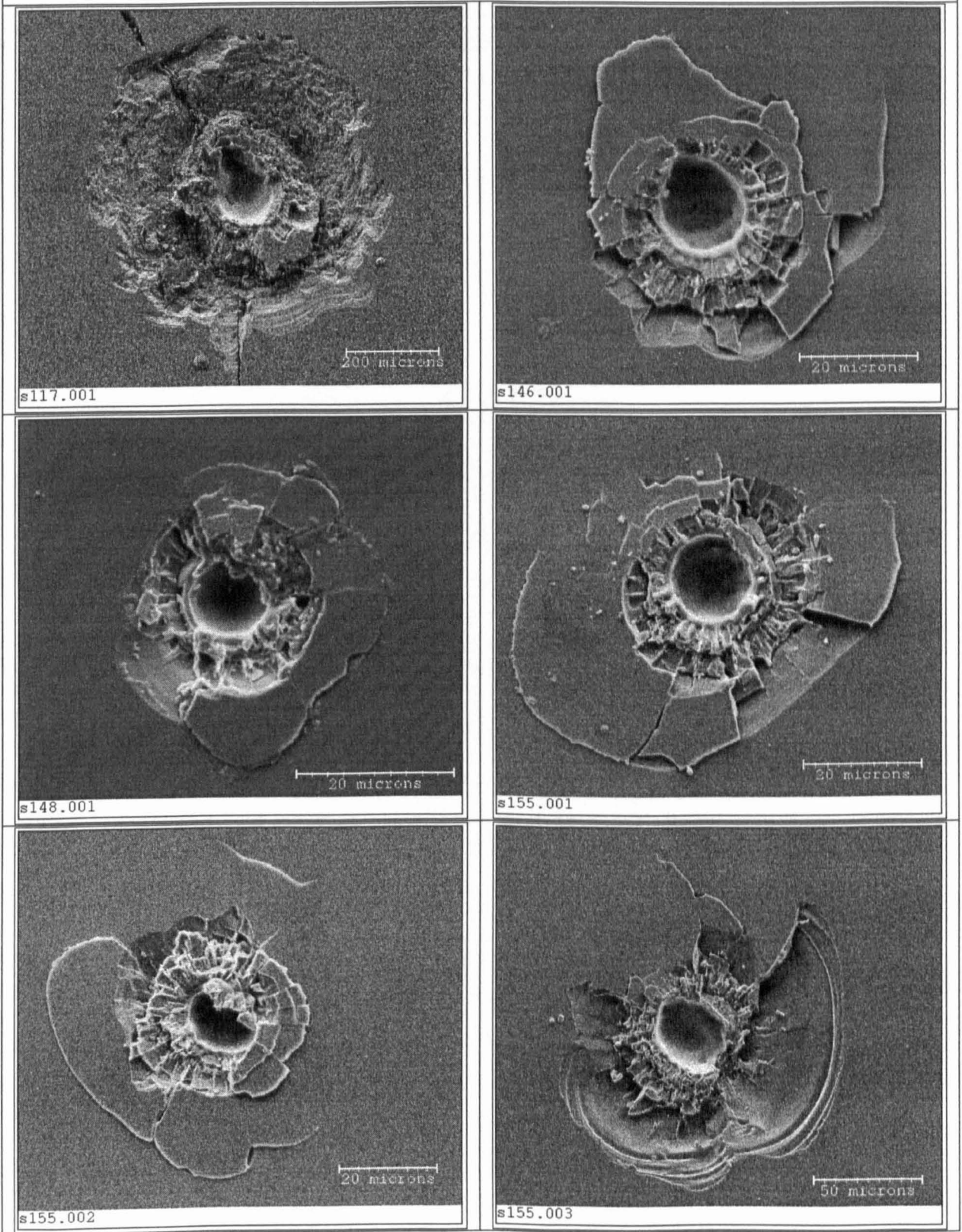
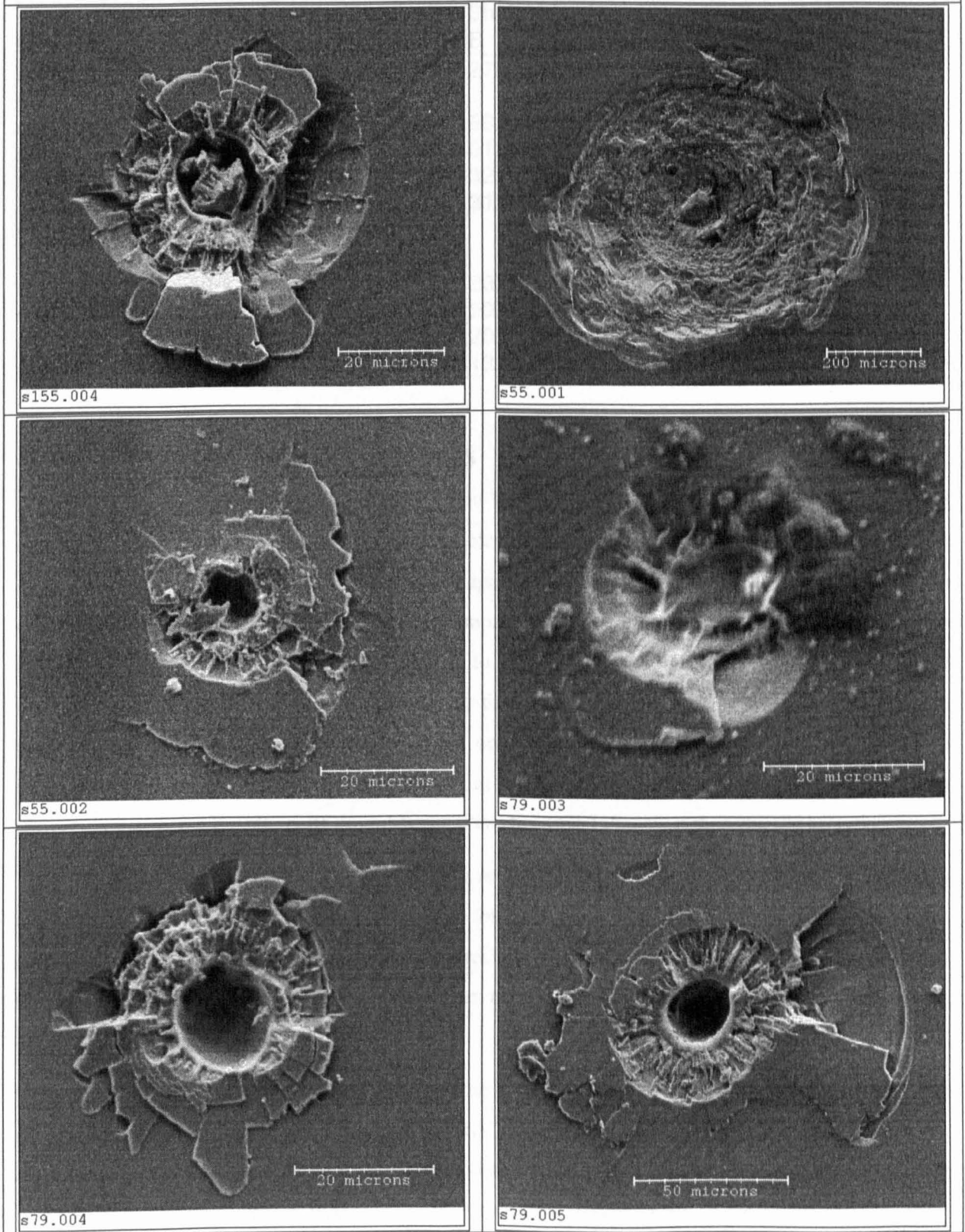


Figure 4.6 – Impacts located in scan of HST solar cells



The measurements made of each crater are given in Table 4.2, with A and B corresponding to vertical and horizontal measurements of each feature with CI being the circularity i.e. the ratio of maximum perpendicular length to minimum.

Table 4.2 – Measurements of HST craters

Crater ID	Pit (μm)				Shatter (μm)				Conchoid (μm)			
	A	B	\sqrt{AB}	CI	A	B	\sqrt{AB}	CI	A	B	\sqrt{AB}	CI
s117.001	140.0	96.0	115.9	0.828	327.9	278.5	302.2	0.922	666.0	627.8	646.6	0.971
s55.001									591.5	669.3	629.2	0.940
s155.003	33.5	32.0	32.7	0.977	64.7	56.7	60.6	0.936	146.2	139.0	142.6	0.975
s79.005	19.8	20.9	20.3	0.973	55.2	51.5	53.3	0.966	136.4	87.8	109.4	0.802
s155.002	11.6	13.0	12.3	0.945	30.0	32.6	31.3	0.959	63.2	68.0	65.6	0.964
s155.001	14.1	13.2	13.6	0.968	29.3	31.0	30.1	0.972	63.3	47.2	54.7	0.864
s155.004	16.0	15.0	15.5	0.968					56.4	49.0	52.6	0.932
s146.001	15.6	14.6	15.1	0.967					46.9	49.3	48.1	
s55.002	9.0	8.4	8.7	0.966	22.1	23.5	22.8	0.970	50.0	35.2	42.0	0.839
s79.004	14.6	13.5	14.0	0.962	31.8	29.7	30.7	0.966	37.7	36.4	37.0	
s148.001	9.2	9.6	9.4	0.979	24.1	20.2	22.1	0.916	37.6	33.4	35.4	0.942
s79.003					11.5	13.4	12.4	0.926	29.3	34.3	31.7	0.924

4.2. Oblique impact analysis

For the EURECA and HST solar cell impacts an impact direction was attributed to asymmetrical craters. It is not clear at this stage what impact elevation angle threshold is required to produce an asymmetrical crater, or to what extent the shape of the impactor affects the crater shape. An unusually high percentage (32%) of solar cell impact craters on EURECA showed signs of impact direction significantly away from the normal to the surface compared to 17% of TICCE foil perforations and 23% of TICCE mesh craters; this fraction was only 17% for HST. This high percentage of craters displaying directionality on EURECA could be a result of either: (i) an according fraction of the flux was encountered at an oblique angle by the solar arrays; (ii) crater formation processes in solar cells are more sensitive to impact direction than ductile targets.

The difference between the percentage of oblique impact signatures on EURECA and HST was attributed to the size regime of the HST data being higher than that of EURECA in the PFA reports. This assumes that response to impact direction is size dependent. However, it could equally be due to the different attitude histories of the two spacecraft giving a different proportion of oblique impact trajectories.

Due to EURECA's heliocentric stabilisation, the distribution of impact directions on EURECA may be sensitive to anisotropy of the flux. EURECA's solar panels were always sun pointing and, on average, their long axis pointed to ecliptic North and South (section 1.3.1). Consequently, the azimuth distribution of impact directions will be sensitive to anisotropy in the Earth apex-antapex-ecliptic North-South plane. Unfortunately, the crater orientation relative to the spacecraft was not preserved in the HST scanning. Although the HST solar panels were primarily solar pointing, the entire spacecraft rotated about an axis normal to the plane of the solar arrays and the telescope rotates between the solar array wings to track astronomical objects. Thus the azimuth distribution of impact directions is randomised with respect to a directional source of meteoroids. However, localised anisotropy due to spacecraft shielding and secondary production could be evident in the distribution of impact directions.

4.2.1. Impact azimuth angle

The aim of the analysis of the impact azimuth angle data is to look for any significant anisotropy. The conclusions of the author's first analysis, as presented in the contract reports and other publications, is that there was a bias of impacts coming from the +Y direction corresponding to the Earth-apex direction. This conclusion was not quantitatively justified and has not been supported by any statistical analyses in subsequent publications. The appropriate analysis is now presented here. The EURECA spacecraft axes (+X, -X, +Y, -Y) and their corresponding angle in degrees are shown with the solar array panel numbers in Figure 4.7 (compare with Figure 4.1 and Figure 1.10 on page 15).

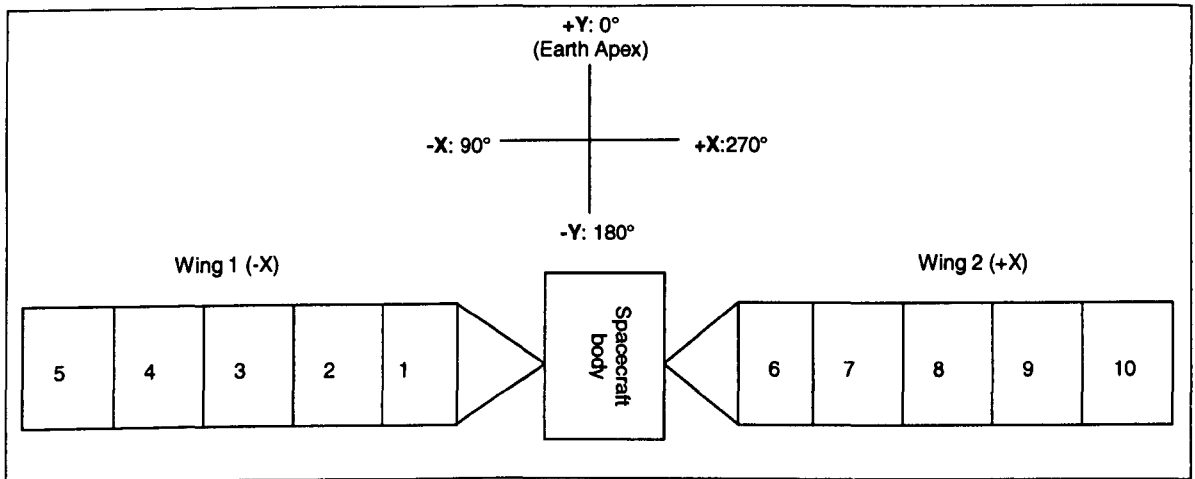


Figure 4.7 - EURECA configuration showing definition of azimuth angles and solar array panel numbers

Impact azimuth angle distributions

As we are only interested in a general bias in impact direction it was decided that binning the data at 45° intervals gave an interesting enough resolution whilst still retaining enough counts in each bin to be statistically meaningful i.e. greater than 5 (Cooper, 1969). The hypothesis to be tested is that the flux is isotropic and therefore the distribution of impact trajectories is uniform. Under this hypothesis there is an equal probability of an impact occurring in any of the impact azimuth angle bins. Therefore, the probability of an impact occurring in a bin is $1/N$, where N is the number of bins. The expected number of impacts in a bin is np , where n is the total number of impacts and p is the probability of an impact in a bin. This is the expected mean number of impacts per bin and for counting events we expect a random variation of observed frequencies about this mean described by Poisson statistics giving a variance equal to the mean.

Figure 4.8 and Figure 4.9 show histograms of the frequency distribution of impacts per angle bin for each of the EURECA solar array wings, where the angle shown is the centre of the bin. The expected mean frequency for a uniform random distribution is shown. Although, it is often the practice in the field to plot frequency distributions as x-y scatter plots with \sqrt{N} error bars the author adopts the more usual format of a histogram. Error bars are superfluous as a \sqrt{N} statistical uncertainty is implicit in any frequency distribution, hence they are not normally shown in other

disciplines. As a guide to the significance of deviations from the mean the number of standard deviations that each frequency is from the mean is shown, where the standard deviation is \sqrt{N} .

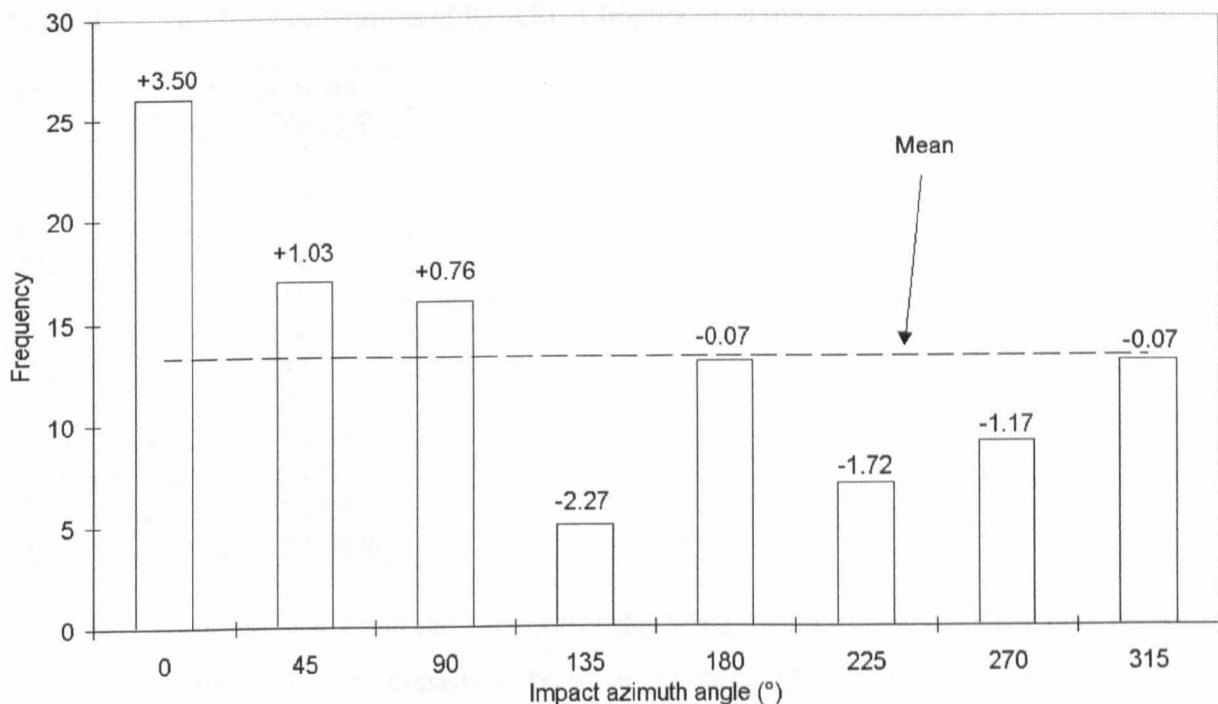


Figure 4.8 – EURECA Wing 1 impact azimuth angle distribution

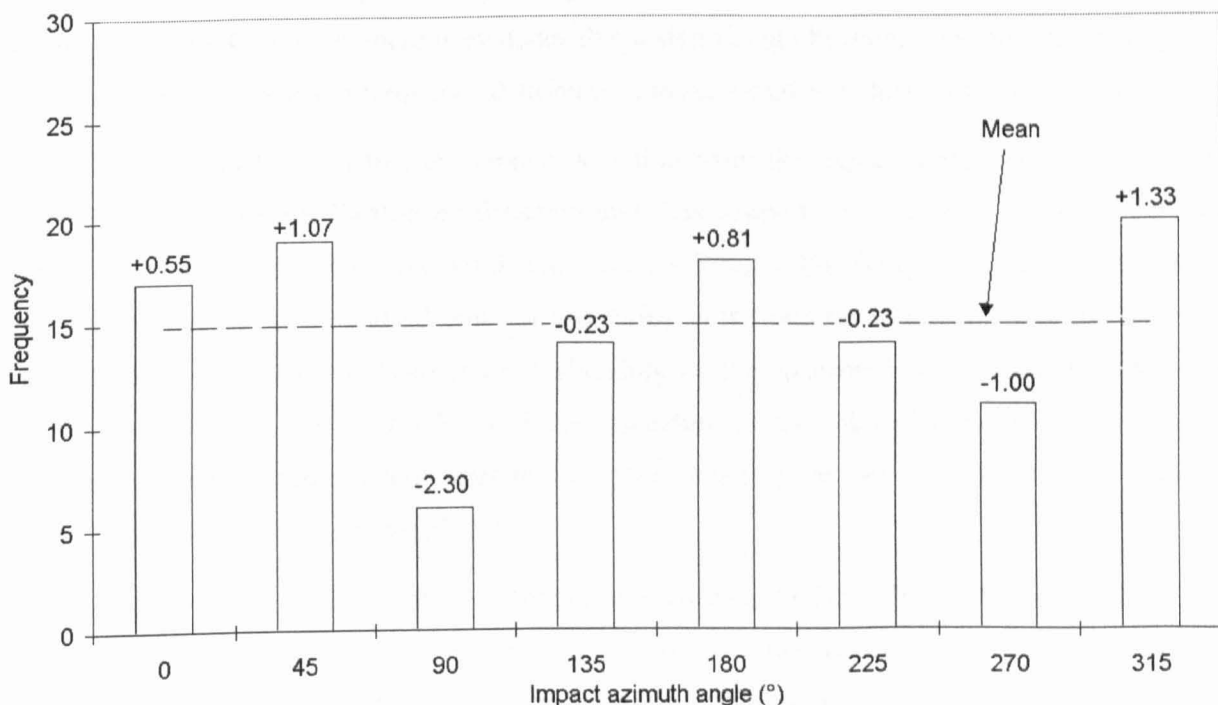


Figure 4.9 – EURECA Wing 2 impact azimuth angle distribution

Table 4.3 shows the frequency in each bin for the two wings and the mean and variance. For a random Poisson distribution the variance should equal the mean. The appropriate statistic for testing the significance of the difference between the mean (\bar{x}) and variance (s^2) is:

$$X^2 = \frac{(n-1)s^2}{\bar{x}}$$

which is χ^2 distributed with $n - 1$ degrees of freedom (Upton and Fingleton, 1985) and is equivalent to Pearson's statistic for frequency distributions (section 7.1).

Table 4.3 – Test for randomness of EURECA impact directions

Bin centre (°)	Frequencies	
	Wing 1	Wing 2
0	26	17
45	17	19
90	16	6
135	5	14
180	13	18
225	7	14
270	9	11
315	13	20
Mean	13.25	14.88
Variance	44.21	21.84
χ^2	23.36	10.28
$P(\chi^2)$	0.15%	17.34%

It can be seen in Table 4.3 that the variance of the Wing 1 frequencies is higher than the mean indicating a tendency for the impacts to be more concentrated or more sparse at certain impact azimuth angles. The χ^2 statistic indicates that there is only a 0.15% chance that this clustering could occur by chance and therefore the author deems it significant. The Wing 2 variance is also higher than expected but not as significant as Wing 1 with a 17% chance that this pattern could have arisen at random. Given that there is evidence that a significant clustering towards certain angles is occurring we can look at the frequency distributions to see where the clustering is most acute.

For Wing 1 it can be seen that the largest deviation from the expected frequency is the 0 bin corresponding to the +Y Earth-apex direction and thus supports the conclusions of the contract reports. It is puzzling that the same trend is not seen for Wing 2. For Wing 1 there are more impacts than the average in the 45 and 90 bins corresponding to the outboard direction and less from the inboard direction possibly indicating some shielding by the spacecraft body. Although there are fewer impacts in the 90 bin for Wing 2 corresponding to the inboard direction this is within expected random fluctuations and therefore the inference that spacecraft shielding is at work should not have too much weight attributed to it.

The orientation of the crater images was not preserved during the HST-PFA as the scanning rig had to be re-oriented many times to gain access to parts of the array. However, the author was able to partially reconstruct the orientation by checking the orientation of the solar cell electrodes on the photographs of the impact sites. The electrodes, which appear as white parallel lines on the images (clearly visible in Figure 4.3), are aligned in the same direction across the whole solar array wing. Consequently, it was possible to ascertain the line of flight (suggested by the crater shape) relative to the spacecraft axes, but not the direction along this line of flight as there was no way to tell if the image was upside-down.

Table 4.4 shows the distribution of HST impact directions. Due to the 180° ambiguity there are only 4 bins corresponding to the vertical, horizontal and two diagonals. The χ^2 test shows that the variance is not significantly smaller than the mean for this small number of bins. Although there is apparently no significant anisotropy it is curious that there are more impacts aligned vertically for both blankets i.e. parallel to the telescope body. This could be explained by the telescope body shielding horizontal trajectories.

Table 4.4 - Test for randomness of HST impact directions

Bin centre	Frequencies	
	Upper blanket	Lower blanket
Vertical	11	11
45° or 225°	7	6
Horizontal	6	9
135° or 315°	9	7
Mean	8.25	8.25
Variance	4.92	4.92
χ^2	1.79	1.79
$P(\chi^2)$	40.90%	40.90%

Correlation of azimuth angle with location

One of the inferences made in the post-flight analyses were that ejecta from impacts on the spacecraft body showered the solar arrays with small impacts. Accordingly, we may expect that the panels nearest the spacecraft body would witness more impacts coming from the inboard direction. The appropriate test to see if impact direction is related to location is a contingency table (described in section 2.3.1) of the frequencies of impacts on each panel and in each impact azimuth angle bin. For the χ^2 statistic to be meaningful however we require at least 5 counts per bin, therefore the two inboard panel counts and three outboard panel counts were combined

Table 4.5 shows that it is not highly unlikely that azimuth direction and location on one of the inboard or outboard panels are independent of each other. Wing 2 has an 8% probability of independence, which may indicate some correlation. The inboard panels received more impacts than expected from the spacecraft direction (90°), but this difference is not as large as other discrepancies and so does not give much weight to the conclusion that more impacts come from the spacecraft direction nearer the spacecraft.

Table 4.5 – Contingency table of impact frequencies for each panel and azimuth bin

Panels	Azimuth bins				Σ
	0	90	180	270	
<i>Wing 1 observed frequencies</i>					
Inboard	16	9	5	6	36
Outboard	26	18	15	9	68
Σ	42	27	20	15	
<i>Wing 1 expected frequencies</i>					
Inboard	14.54	9.35	6.92	5.19	
Outboard	27.46	17.65	13.08	9.81	
					$P(\chi^2)$ 74.02%
<i>Wing 2 observed frequencies</i>					
Inboard	20	12	9	11	52
Outboard	18	11	26	12	67
Σ	38	23	35	23	
<i>Wing 2 expected frequencies</i>					
Inboard	16.61	10.05	15.29	10.05	
Outboard	21.39	12.95	19.71	12.95	
					$P(\chi^2)$ 8.34%

Correlation of size with azimuth angle

In the contract reports conclusions that impacts coming from the spacecraft direction were smaller and thus constituted ejecta were unsupported by any statistics. Therefore the author now analyses the correlation between impact direction and crater pit size. For this purpose the craters were binned into 4 angle bins corresponding to the Earth-apex, inboard, Earth-antapex and outboard directions. The left hand plots of Figure 4.10 shows pit diameter plotted against impact azimuth angle and the right hand plots show the distributions of pit sizes in each bin as box charts. For the box charts the horizontal lines show the 25th, 50th (median) and 75th percentiles, the error bars show the 5th and 95th percentiles and the symbols beyond the error bars the 0th, 1st, 99th and 100th percentiles; the square symbol is the mean. A box chart is a more informative way of showing the scatter of the data and which values are more probable than others than a simple mean with 1σ error bars especially when the distribution is non-normal; the interpretation of the standard deviation is ambiguous for non-normal distributions. If the distribution of pit sizes were normal then we would test for significant difference between the sample means using one-way analysis of variance (ANOVA). However, we know that meteoroid and debris size distributions are generally described by a power law and indeed normal probability plots (Figure 4.11) show that the pit size distributions are highly non-normal. Therefore to test for a significant difference between the pit sizes in each bin we must use a non-parametric equivalent to ANOVA. One such alternative test is *Mood's median test* (Cooper, 1969), which is similar to the *Mann-Whitney test* described in section 2.3.4 but is appropriate when more than two medians are being compared.

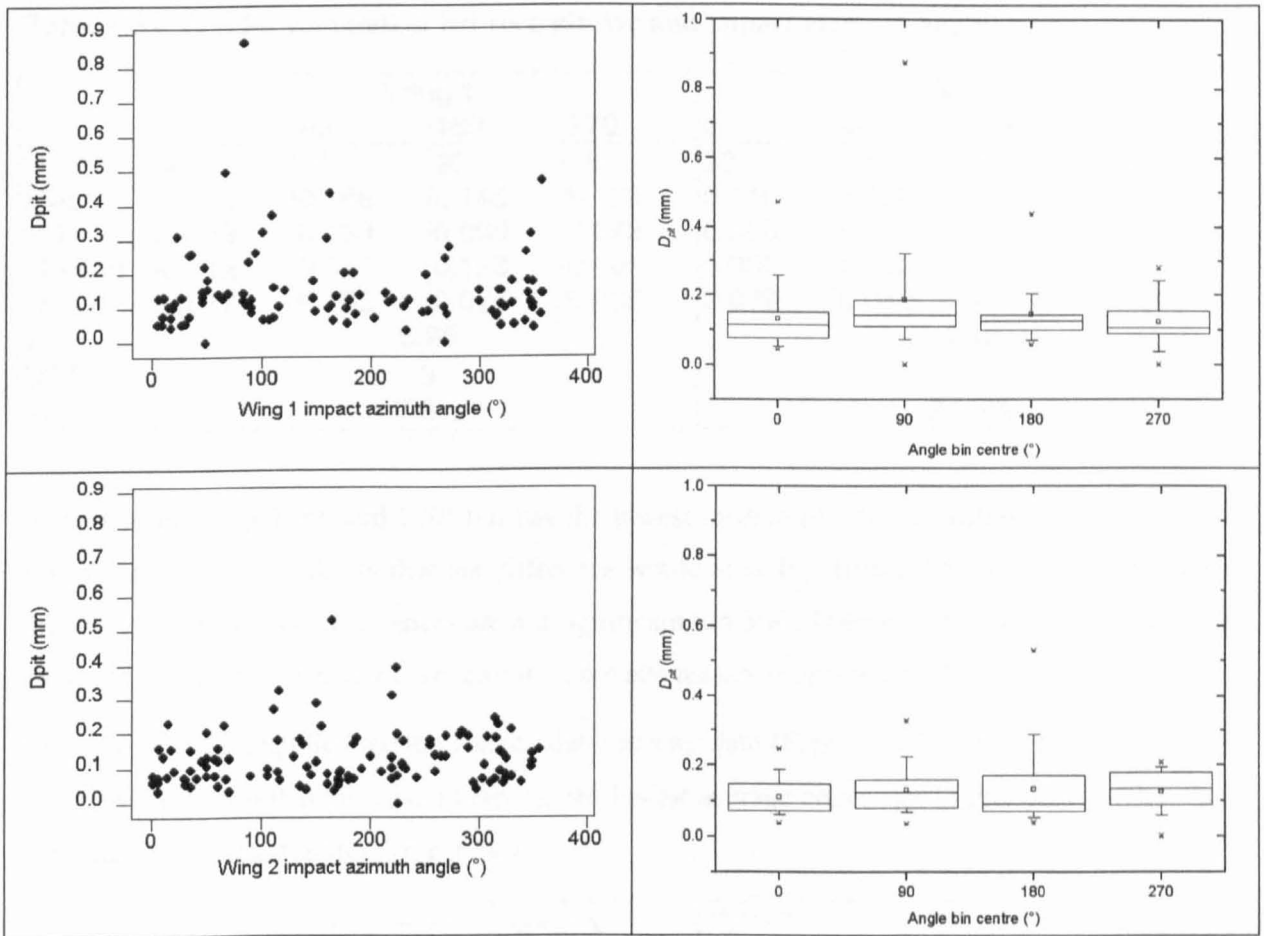


Figure 4.10 – Correlation of pit diameter with azimuth bin

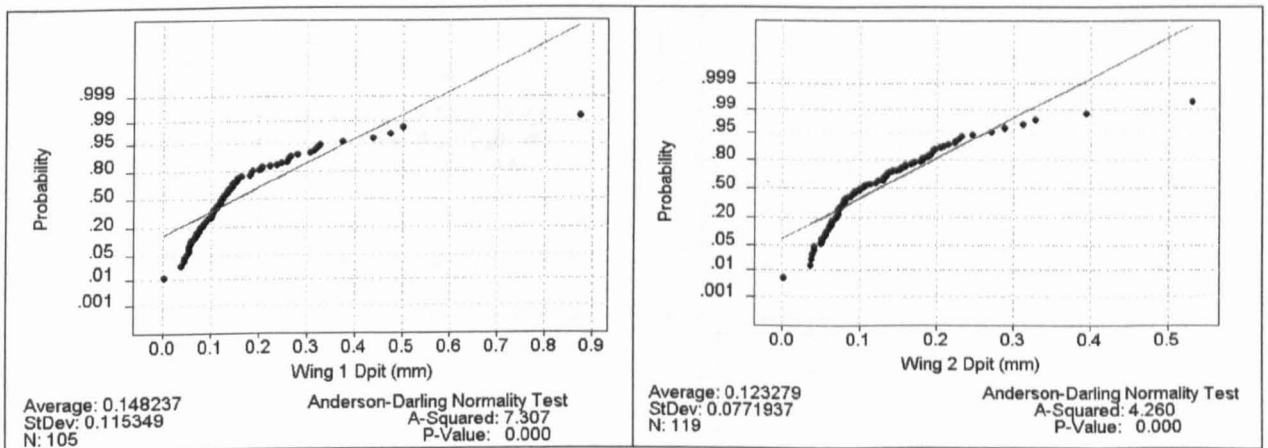


Figure 4.11 – Normal probability plots of pit diameters

Table 4.6 shows the number N of craters in each azimuth angle bin, the mean and standard deviation (SD) of the pit size and the median and inter-quartile range (Q3-Q1) between the 1st (25%) and 3rd (75%) quartiles which is an equivalent measure of spread for non-normal distributions. The χ^2 statistic from Mood's median test, the degrees of freedom (DOF) and the corresponding χ^2 probability are shown for each wing.

Table 4.6 – Test for correlation between pit size and impact azimuth angle

	Wing 1				Wing 2			
	0	90	180	270	0	90	180	270
N	42	28	20	15	38	23	35	23
Mean	0.133	0.188	0.145	0.122	0.110	0.129	0.132	0.125
SD	0.089	0.169	0.090	0.073	0.056	0.072	0.107	0.058
Median	0.112	0.141	0.123	0.106	0.088	0.122	0.090	0.134
Q3-Q1	0.077	0.105	0.077	0.065	0.079	0.080	0.103	0.108
χ^2	6.95				4.18			
DOF	3				3			
$P(\chi^2)$	7.3%				24.3%			

Although the wing 1 inboard 270° bin has the lowest median pit size the difference is not highly significant; 7.3% probability that the difference would arise by chance. There is no clear trend in the Wing 2 data and the differences are not significant (24.3%). Therefore, the conclusion that there are more small impacts near the spacecraft is not adequately supported by the statistics.

The same test was applied for the conchoidal diameter data (Figure 4.12), which concurs with the pit diameter data in that the inboard bin has the lowest average crater size (Table 4.7) but that there is no significant trend in the Wing 2 data.

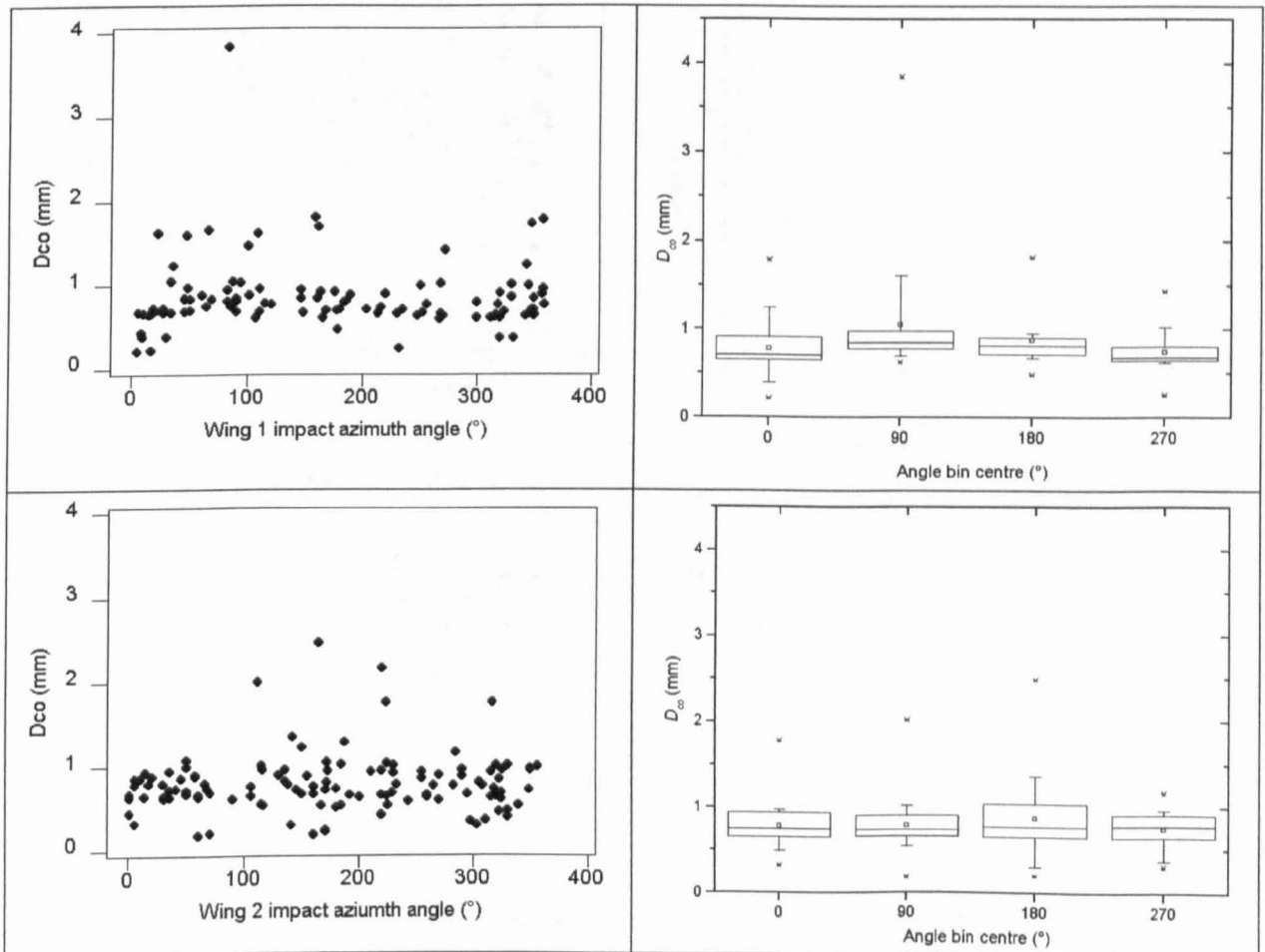
**Figure 4.12 – Correlation of conchoidal diameter with azimuth bin**

Table 4.7 – Test for correlation between conchoid size and impact azimuth angle

	Wing 1				Wing 2			
	0	90	180	270	0	90	180	270
N	42	28	20	15	38	23	35	23
Mean	0.781	1.050	0.875	0.745	0.775	0.787	0.873	0.744
SD	0.351	0.621	0.328	0.261	0.248	0.352	0.493	0.219
Median	0.694	0.850	0.813	0.671	0.744	0.739	0.768	0.784
Q3-Q1	0.266	0.265	0.220	0.182	0.300	0.262	0.397	0.308
χ^2	12.29				0.91			
DOF	3				3			
P(χ^2)	0.6%				82.3%			

Correlation of crater asymmetry with azimuth angle

The two measures of crater asymmetry used were the pit circularity and the centroid offset. It was noted by the author in the contract reports that the impacts coming from the inboard direction had a lower pit circularity and thus higher obliquities and therefore were ejecta impacts from the spacecraft body. The assumption that lower pit circularity indicates a more oblique impact will have to be tested by impact experiments. However, the correlation of pit circularity with impact direction is now tested. The data is plotted in Figure 4.13 with the test results in Table 4.8.

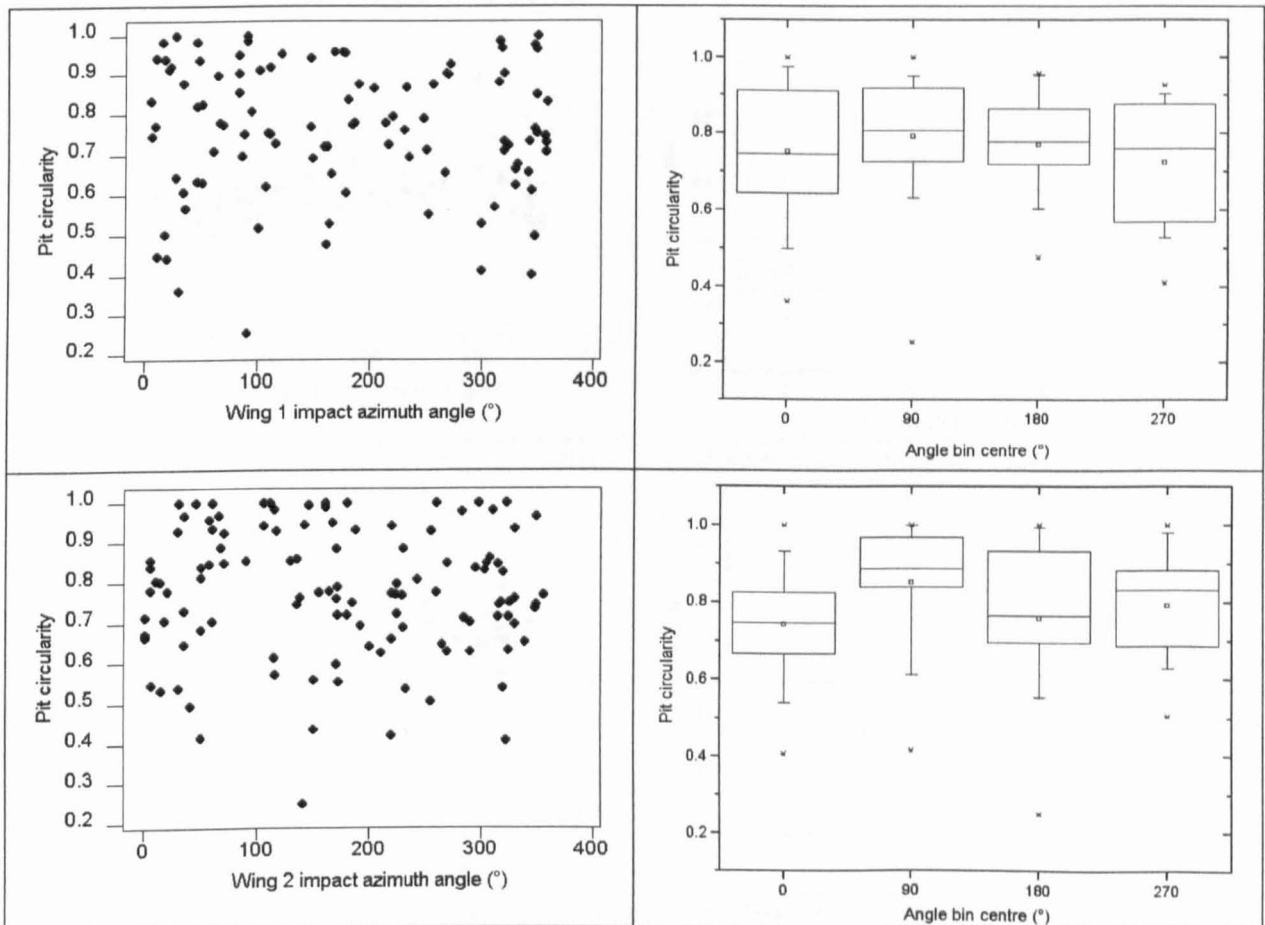
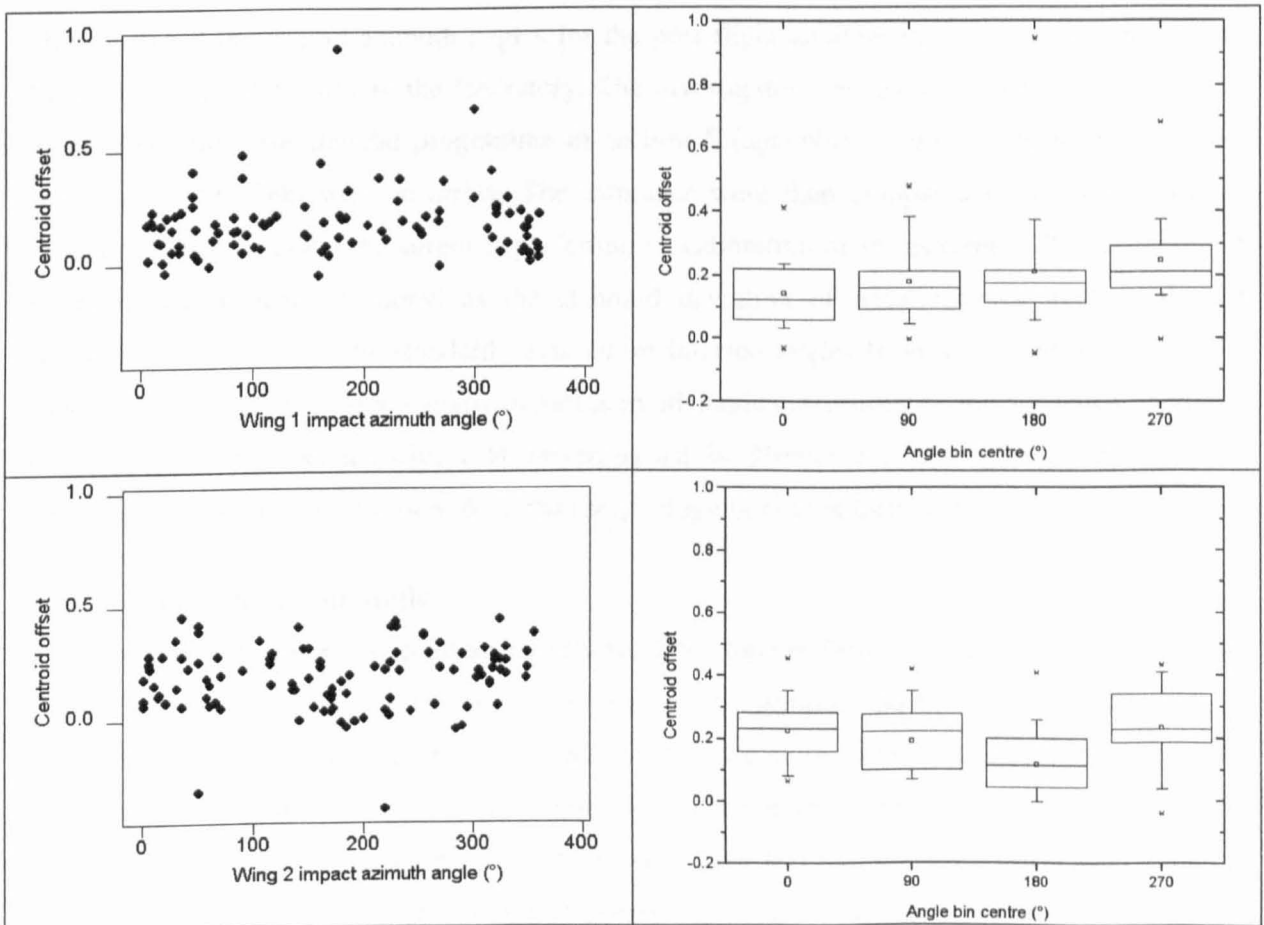
**Figure 4.13 – Correlation of pit circularity with azimuth bin**

Table 4.8 – Test for correlation between pit circularity and impact azimuth angle

	Wing 1				Wing 2			
	0	90	180	270	0	90	180	270
N	42	27	20	14	38	23	35	22
Mean	0.752	0.791	0.770	0.725	0.742	0.851	0.759	0.791
SD	0.178	0.166	0.137	0.164	0.142	0.156	0.178	0.146
Median	0.745	0.808	0.777	0.736	0.746	0.888	0.763	0.820
Q3-Q1	0.276	0.210	0.174	0.317	0.165	0.155	0.273	0.218
χ^2	2.26				12.11			
DOF	3				3			
$P(\chi^2)$	52.0%				0.7%			

The Wing 1 data shows no significant trend with impact direction. Wing 2 shows a non-random distribution of circularities over the angle bins (0.7% probability of being random) with the most circular craters being from the inboard direction. This could be due to highly oblique trajectories being shielded by the spacecraft body.

The other parameter used to infer impact elevation angle in the post-flight analyses was the centroid offset, plotted in Figure 4.14.

**Figure 4.14 – Correlation of centroid offset with azimuth bin**

The distribution of centroid offsets shows no significant trend with impact azimuth direction for Wing 1 but is non-random for Wing 2 with the lowest offsets occurring for impacts from the Earth-antapex direction (Table 4.9). An explanation for this does not intuitively present itself.

Table 4.9 – Test for correlation between centroid offset and impact azimuth angle

	Wing 1				Wing 2			
	0	90	180	270	0	90	180	270
N	41	25	20	14	34	18	33	21
Mean	0.141	0.179	0.212	0.246	0.224	0.191	0.117	0.233
SD	0.092	0.119	0.208	0.159	0.101	0.165	0.140	0.144
Median	0.123	0.161	0.163	0.203	0.232	0.211	0.113	0.229
Q3-Q1	0.160	0.125	0.144	0.157	0.129	0.186	0.168	0.231
χ^2	3.22				13.2			
DOF	3				3			
P(χ^2)	35.9%				0.4%			

Testing the reliability of the impact azimuth angle data

For the solar cell PFA analysis, the particle line of flight and the sense of the line of flight (which is the up/down-range end) was determined by essentially qualitative, subjective assessment of which way the impactor “appears” to the experimenter to have come from. This impact azimuth direction data has been used in the contract reports, several PhD theses and other publications with no check on its reliability. Therefore, to determine the accuracy of the impact azimuth angles recorded in the PFA reports the author performed a “blind” test by asking the investigator (J.A.M. McDonnell) who measured the impact azimuth angles for the post-flight analysis data to estimate the impact direction of craters formed in the laboratory. The investigator was given images of the solar cell craters from the experimental programme in section 5 (appendix C) and asked to mark on the image a line of flight with an arrow. The estimates were then compared to the actual impact directions. Thus, in effect the author is performing a calibration of an instrument. The accuracy of an instrument is usually quoted as the standard deviation of measurements made with that instrument. Accordingly, the standard deviation of inferred angles from the actual ones was 74°. Therefore, this study suggests that any impact azimuth angle determined by this investigator should have a $\pm 74^\circ$ error associated with it. However, as will be discussed later, the laboratory solar cell crater morphology is very different from the morphology of craters formed in space.

4.2.2. Impact elevation angle

A reason put forward in the contract reports for HST having fewer asymmetrical impacts than EURECA is that the scanning was performed at a lower resolution and therefore comprised larger craters. Accordingly, it is concluded that smaller craters are more sensitive to oblique impacts. The top-left plot of Figure 4.15 shows that circularity is independent of pit size, but possibly that the spread in circularity decreases with pit size. However, the fact that there are fewer data points at large sizes might be giving a misleading impression. The correlation of centroid offset with pit diameter is marginally significant (top-right in Figure 4.15) in that the appropriate *F*-statistic (appendix A) shows that there is only a 2% chance that the observed correlation could occur at random.

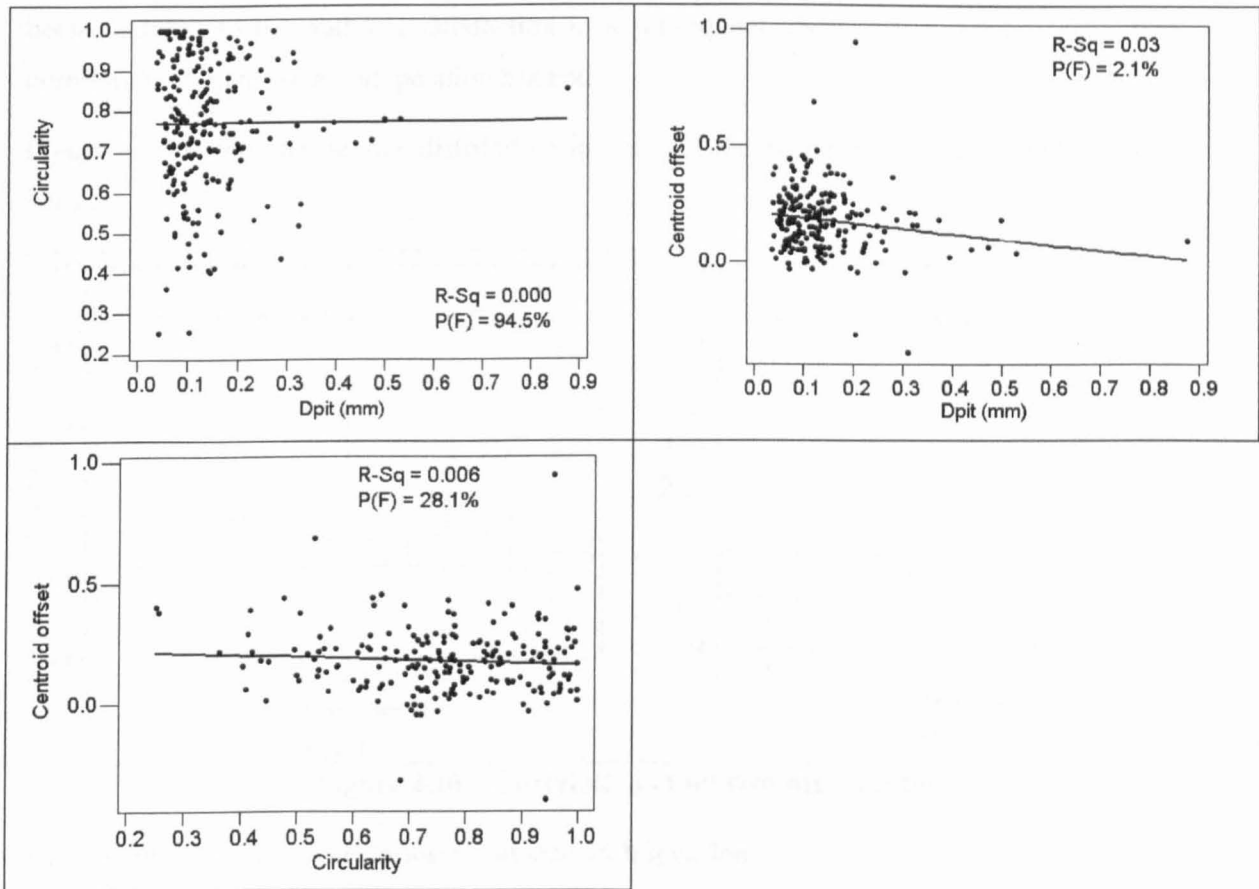


Figure 4.15 – Correlation of pit circularity, centroid offset and diameter

However, as with Figure 2.20 on page 52, the correlation of centroid offset with pit diameter could be due to outliers. Accordingly, as before, the F -test was repeated with each outlier removed in turn. The highest probability thus attained that the correlation would arise by chance, i.e. is *insignificant*, was 3.4% with the second largest crater omitted. It is not until the 5 largest craters are removed simultaneously that the probability rises above our usual 5% threshold (see section 2.3.4). Therefore, this correlation supports the hypothesis that smaller craters are more asymmetrical (larger centroid offset) than large ones. If pit circularity and centroid offset are indicators of an oblique impact we would expect them to be correlated. However, the bottom plot in Figure 4.15 shows that they are not correlated to a significant degree.

4.2.3. Correlation of crater size with location

Another analysis performed during the post-flight analysis contracts was the correlation of impactor size with location. This analysis plotted separately the flux of impacts in the low (non-fl swaths) higher resolution (fl swaths) scans against location. A linear fit of flux against distance from the spacecraft body showed that the generally larger craters found in the lower resolution scan showed no correlation with position whereas the flux of craters in the high resolution scan increased towards the spacecraft body. This is presented as further evidence of ejecta from primary impact sites on the spacecraft body. The author notes that incorrect definition of the Pearson product moment correlation coefficient R^2 in this section of the report, where it is defined as “the mean square deviation of the fit”. Although the spatial distribution of impacts across the wings has

been analysed to the author's satisfaction in a subsequent contract (Unispace *et al.*, 1998), the correlation of crater size with position has not.

Figure 4.16 shows the pit size distribution for each of the 10 panels of the EURECA solar array wing.

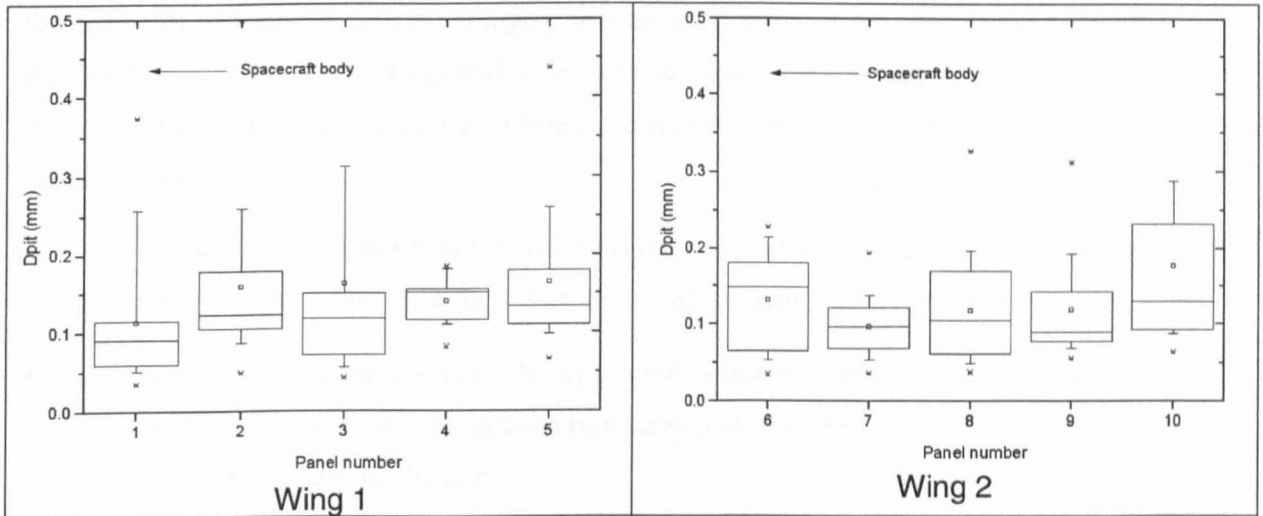


Figure 4.16 – Correlation of pit size with location

Table 4.10 – Test for correlation of pit size with location

	Wing 1					Wing 2				
	1	2	3	4	5	6	7	8	9	10
N	16	20	33	14	20	22	30	26	22	18
Mean	0.113	0.159	0.162	0.140	0.164	0.132	0.097	0.118	0.119	0.177
SD	0.088	0.103	0.161	0.031	0.089	0.065	0.038	0.071	0.065	0.125
Median	0.087	0.122	0.118	0.140	0.133	0.141	0.093	0.101	0.086	0.129
Q3-Q1	0.076	0.091	0.114	0.047	0.092	0.121	0.057	0.113	0.071	0.149
χ^2	8.81					2.88				
DOF	4					4				
$P(\chi^2)$	6.6%					57.9%				

Table 4.10 shows that the median pit sizes are not significantly different for the wing 2 impacts but that there is only a 6.6% chance that the wing 1 distribution would arise from random fluctuations. It can be seen that the inboard panel 1 median pit size is less than for the other panels, however the corresponding wing 2 inboard panel 6 does not show the same trend. There is a larger spread of sizes for panel 6 but not as large as the outboard panel 10. Therefore, there is no consistent – and certainly not persuasive - trend of pit size with location.

4.3. Discussion

During the EURECA and HST post-flight analyses the investigators identified asymmetrical craters as a separate class from symmetrical ones and deemed them to be due to oblique impacts. Accordingly, 30% and 15% of the EURECA and HST craters were inferred to be due to significantly oblique impacts. The impact azimuth angle was attributed to a crater by a subjective evaluation of the crater shape by an investigator. The circularity of the pit and the centroid offset were deemed to be indicators of impact elevation angle. The conclusions of the first analyses of the

impact azimuth angle, pit circularity and centroid offset were not supported by any statistics. The appropriate analysis has now been presented here.

4.3.1. Distributions and correlations of “oblique impact” parameters

Although there appears to be some significantly non-random clustering of some of the parameters, the degree of non-randomness is not highly supportive of many of the conclusions presented in the post-flight analysis reports. The probabilities associated with the tests are never less than 0.1% and the most striking inconsistency is that where there is evidence of non-randomness it invariably only occurs on one wing.

- The conclusion that the EURECA solar arrays received more impacts from the Earth-apex direction is supported by the wing 1 distribution of azimuth angles but not by the wing 2 data.
- The conclusion that panels near the spacecraft witnessed more or less impacts from the spacecraft direction is not evident from this study and thus there is no indication of spacecraft shielding or secondary production.
- Evidence for ejecta production is only marginally supported in that the median pit and conchoid diameters are smaller for the impacts from the inboard direction on wing 1.
- The pit circularity and centroid offset distributions show non-random distributions over azimuth angle for wing 2. However, no immediately obvious explanation can be found for the asymmetry.
- Of the supposed indicators of elevation angle, the pit circularity shows no significant correlation with size but the centroid offset shows a weak but significant decrease with size, perhaps indicating that smaller craters are more sensitive to impact angle. If these parameters indicate impact elevation angle it is puzzling that they are not significantly correlated with each other.
- The conclusion that the panels near the spacecraft received a larger proportion of smaller ejecta impacts is only marginally supported for the wing 1 data.

In summary the distributions and correlations of “oblique impact” parameters do not show any compelling evidence for any of the conclusions offered in previous publications based on this data and the author believes that most of the observed patterns can be accounted for by expected statistical fluctuations. The fact that any significant patterns are never observed simultaneously on both wings suggests that the scanning and measuring were inconsistent rather than suggesting any anisotropy of the ambient meteoroid and debris environment. The data itself is based on a subjective judgement of impact azimuth angle - shown to be highly inaccurate - and an assumption that impact elevation angle plays a primary role in determining crater asymmetry. A proportion of the asymmetrical craters could, of course, be made by impactors with a high aspect ratio.

4.3.2. Impact experiments

In order to understand better the impact data from EURECA and HST, impact experiments are required to determine the effect of impact angle on crater morphology. There have been few previous experiments addressing this issue for solar cell materials apart from a few preliminary investigations initiated by ESA in response to the findings of the post-flight analysis contracts. Accordingly, the author initiated a series of impact experiments using the Unit's light-gas gun, which are presented in the next section.

5. Oblique impact experiments on solar cells

One of the significant results of the analysis of the EURECA solar cell impact data was the unexpectedly high proportion of impacts showing signs of directionality. Therefore, either (i) the solar cells encountered particles on more highly oblique trajectories, (ii) solar cells are more sensitive to impact angle or (iii) the features interpreted as signifying an oblique impact are in fact due to something else. These questions needed to be addressed by controlled impact experiments. The experimental activity that ensued elsewhere, prompted by the analysis of retrieved solar cells, was not primarily concerned with determining the effect of impact angle and thus only a few impact tests at angles other than normal incidence were performed; usually 30°, 45° and 60° (Paul *et al.*, 1997).

Immediately after the analysis of the EURECA post flight data the author initiated a series of experiments focussed *solely* on the effect of impact angle on solar cell impact crater morphology. 12 successful shots were performed in total, firing 50 μm diameter soda-lime glass beads at solar cell samples at 5 km s^{-1} at angles of 0°, 15°, 30°, 45°, 55°, 60°, 65°, 70° and 75° from the normal. The aim of the experiments was to check that the features used for attributing impact direction to solar cell craters made in space do arise from oblique impacts. Also, it was the aim to determine preliminary empirical relationships between crater *size* and *shape* parameters and impact angle with a view to relating impact sites to projectile *size* and *trajectory*.

5.1. Introduction

5.1.1. Previous studies

Research into the effect of impact angle on craters in glass targets is scarce. Mandeville and Vedder (1971) fired polystyrene projectiles of a few microns in diameter at glass targets primarily to study the velocity dependence of crater morphology. They complemented their normal shots with some shots at 30° and 45° incidence, thus giving a mainly qualitative morphological comparison between different impact angles.

Fechtig *et al.* (1977) to the author's knowledge, present the only study whereby the shape of impact craters in brittle, glass-like materials has been monitored with changing impact angle with the aim of reconstructing the impact angle of craters made in space. The variation of crater circularity with impact angle was used to reconstruct the impact angle of lunar microcraters. However, the orientation of the samples was not preserved so no information of astrophysical significance could be extracted.

In response to the EURECA and HST post flight analyses, Paul *et al.* (1997) performed a series of impact experiments for ESA. The key objectives and rationale of the tests are vague in the contract report and subsequent publications, simply stating that "damage patterns" were investigated. The

prime output of the impact programme was a modification of Fechtig *et al.*'s, (1974) impact equation. There was no investigation into the characteristics that can be used to identify an oblique impact or how to reconstruct impact angle.

Most notably, none of the previous research reviewed by the author addresses the issue of determining the impact *azimuth* direction. It is invariably assumed that the impact direction in the plane of the target will be unambiguously identified - or it is simply not mentioned - and it is only the elevation angle that is uncertain. If the line of flight in the plane of the target is incorrectly identified then parameters such as the crater circularity and centroid offset will be inconsistently defined.

5.1.2. Experimental aims and rationale

The aim of this experimental programme is to determine the effect of impact angle on solar cell crater morphology and to determine empirical relationships between crater dimensions and impact angle. Therefore only impact angle will be varied with all other parameters held as constant as possible, thus with the 9 impact angles covered in this study we should be able to find meaningful functional forms to fit against impact angle.

The method chosen was to fire many projectiles simultaneously at the solar cell samples using the buckshot technique of firing the light-gas gun, whereby many projectiles are loaded in a single sabot. This technique was chosen for two reasons. Firstly, we want to fire projectiles that are as small as possible so as to make craters of comparable size to the ones observed on the space-flown solar cells and also ones that will not penetrate the cover glass. Firing small projectiles in the gas gun can only feasibly be achieved by the buckshot technique. Secondly, as it was pointed out in the previous experimental programme (section 3) an appropriate "error" to associate with our crater measurements is the variability between repeat shots rather than measurement errors. By firing a buckshot of projectiles at our targets we can achieve many tens to hundreds of simultaneous "repeat" shots.

The projectiles chosen were soda-lime glass beads as they were available in a suitable size range and are highly spherical (Figure 6.2, section 6.1.2). The targets available were solar cell samples from ESA's ECS satellite and from HST; all had the same type and thickness of cover glass (150 μm).

In addition to the solar cell samples, thick aluminium and glass targets were also mounted in the target area for some of the shots to give a comparison between the different materials under identical impact conditions.

5.2. Experimental procedure

The first round of shots in this experimental programme was performed in collaboration with H. Yano. Yano offered to collaborate with the author in this study with a view to a future joint publication. The author agreed to the collaboration for the first 8 shots taking the view that

assistance from a more experienced student would be helpful. Yano's contribution involved assisting with the firing procedures such as setting up the target and loading the projectiles. The author was almost entirely responsible the imaging and measuring of approximately 500 craters (appendix C). Yano (1995) presents preliminary results of the unsorted data (see section 5.3.2), only with a few qualitative observations and thus does not preclude the quantitative analysis presented here and in Shrine *et al.* (1996): the intended first publication. Also, the analysis here is based on 4 additional angles.

5.2.1. Targets and Projectiles

The targets available for impact testing were:

- Solar cells from ESA's ECS satellite: which deployed solar cells identical to EURECA.
- Solar cells from the Hubble Space Telescope solar array wing retrieved during the first servicing mission.
- Sheets of aluminium 2014-T3P alloy approximately 550 μm thick.
- Pieces of soda lime glass approximately 6 mm thick.

The projectiles used for the first 8 shots were soda-lime glass beads, approximately 50 μm (49 ± 4) in diameter. The beads were taken from a stock sieved by size by Baron (1996). The sieving process, whilst mostly grading the spherical beads to within a few microns, did allow some "shards" through, i.e. elongated, non-spherical pieces of glass of sufficiently narrow width for them to pass through the sieve mesh. These are inclusions in the stock, left over from the manufacturing process, and could be noticed amongst the beads under microscopic examination. It is not known at this stage, to what extent craters formed by shards will be different to those formed by the "proper" beads. It could be that the crater shape is indistinguishable from the ones formed by spherical impactors, in which case "weeding" them out will be difficult. The shards are only a small fraction of the total number of projectiles: visual estimate of a few shards per hundred good beads. Therefore, for a large sample of impact craters, the mean and standard deviation of the distribution of crater diameters should not be significantly influenced. The size distribution of craters was checked for normality using normal probability plots to check for any craters with significantly different sizes that might significantly alter the means and variances. The last 4 shots (9 to 12) used commercially graded soda-lime glass beads, 55 ± 1 μm in diameter (Figure 6.6, page 181).

5.2.2. Experimental procedure

Projectiles

The glass buckshot projectiles were poured into a nylon sabot and held in place by a 1 mm steel ball bearing (Figure 5.1) which also provides a good timing signal when it intersects the two laser curtains in flight. The top of the sabot was crimped to keep the projectiles in place by applying force with the tip of a scribe.

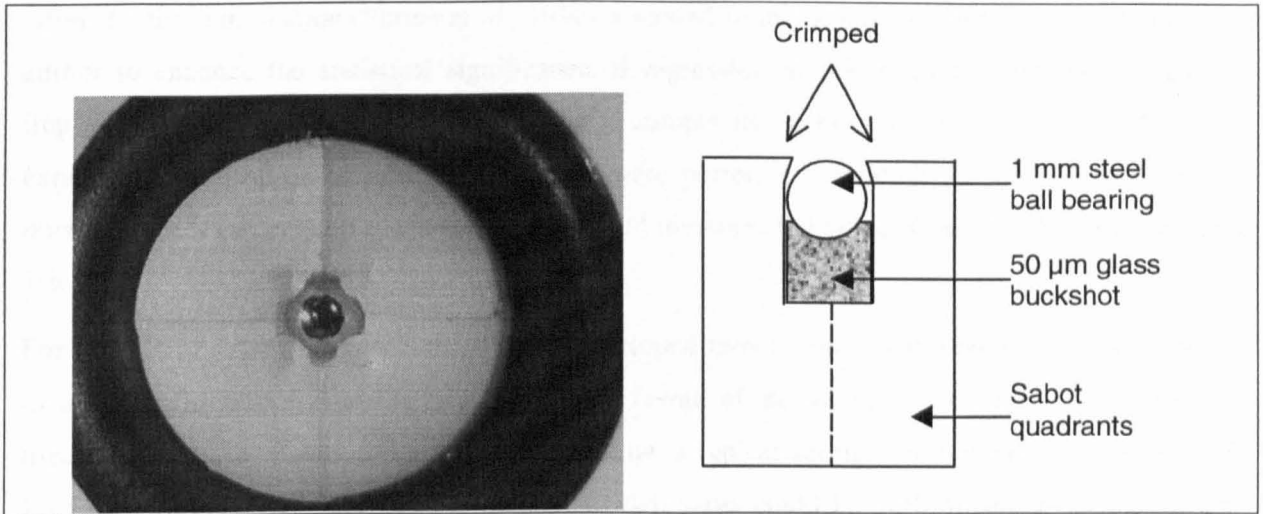


Figure 5.1 – Plan view and schematic of sabot loaded with glass buckshot

Target configurations

For shots 1-8 a target holder was required that could be mounted on the inside of the door of the experimental chamber. The holder had to allow 3 different target materials per shot to be mounted at angles from normal to 80° to the line of flight. The holder also had to allow for the passage of a 1 mm ball bearing through the assembly without impacting the targets. This was because a 1 mm steel ball bearing was used to hold the projectiles in the sabot (Figure 5.1) and was thus launched with the projectile “buckshot”. A suitable target support was designed and manufactured by the author from “off-cuts” of aluminium and is shown in Figure 5.2. A plate was mounted behind the target support to which a PZT momentum detector was attached. This plate was struck by the 1 mm ball bearing after it had passed through the gap in the target support, giving a second timing signal for velocity calculation (the first signal comes from the sabot impact on the stop plate in the blast tank).

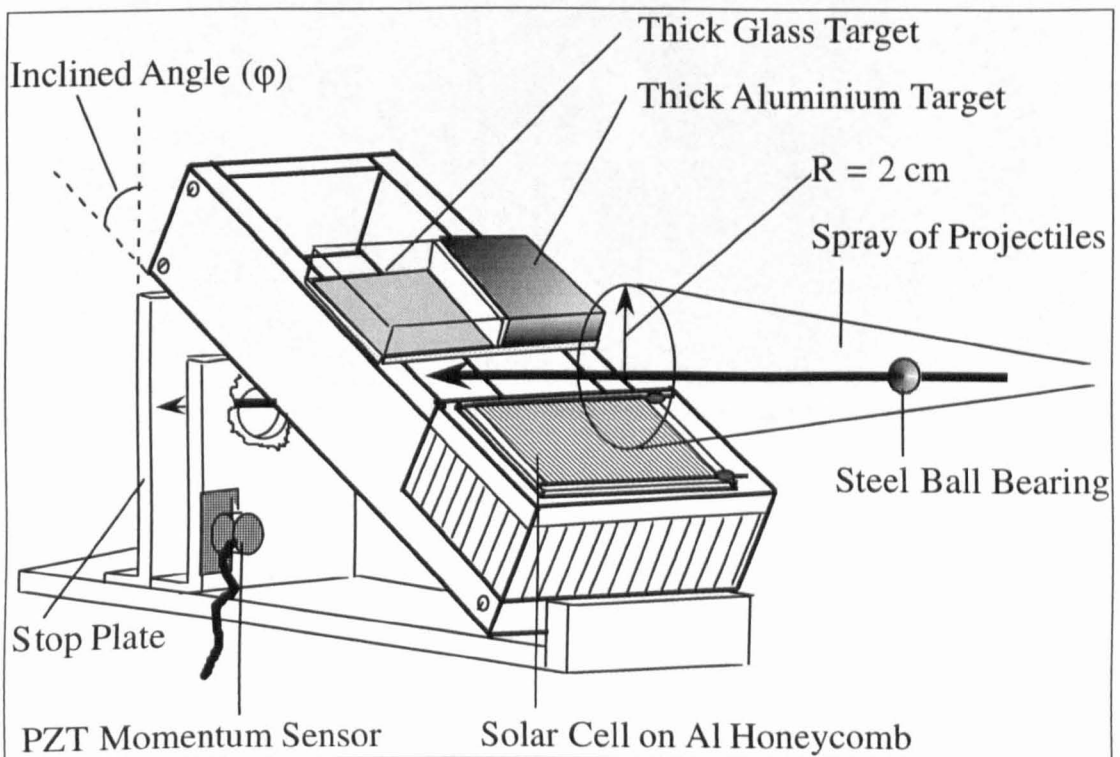


Figure 5.2 – Configuration of target support for shots 1-8

After the first publication (Shrine *et al.*, 1996) a second round of experiments was initiated by the author to enhance the statistical significance of regression of the dependent parameters against impact angle. By this time the author was a competent operator of the gas gun and so the experiments and all associated measurements were performed unaided; the experimental officer normally loads the projectile, operates the gun and measures the velocity, as was the case for shots 1-8.

For this set of experiments a commercially developed target holder was available as used for the experiments in section 3 and so this was used in favour of the author's own target holder that was used for shots 1-8. Figure 5.3 and Figure 5.4 show a typical set up that was used for shots 9-12. Half of each solar cell was masked off so that two shots could be performed for each solar cell sample. It was desirable to make maximum use of the scarce HST solar cell samples. The solar cell was positioned a few mm away from the line of flight of the projectile, far enough away so that the author was confident that it would not be hit by the ball bearing, but close enough to receive a good number of buckshot particles. Figure 5.5 shows a target after firing with a hole made by the 1 mm ball bearing and 8 or 9 visually obvious buckshot impacts on the solar cell.

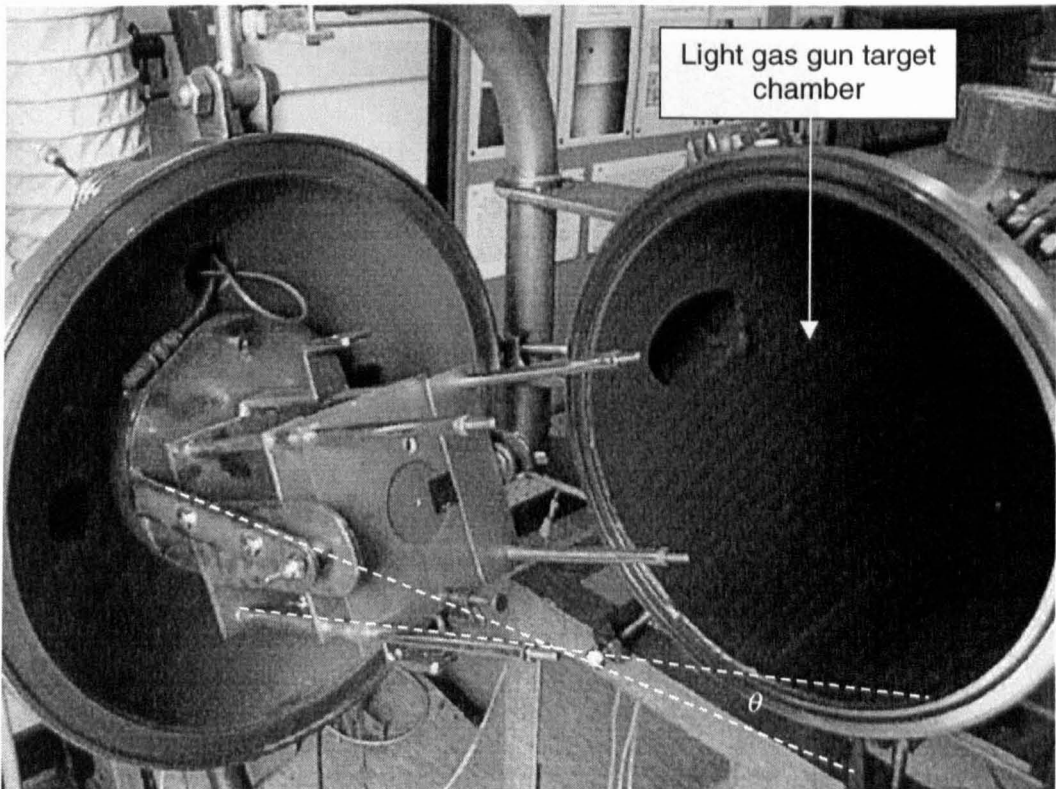


Figure 5.3 – Target set-up for shots 9-12 showing impact angle θ

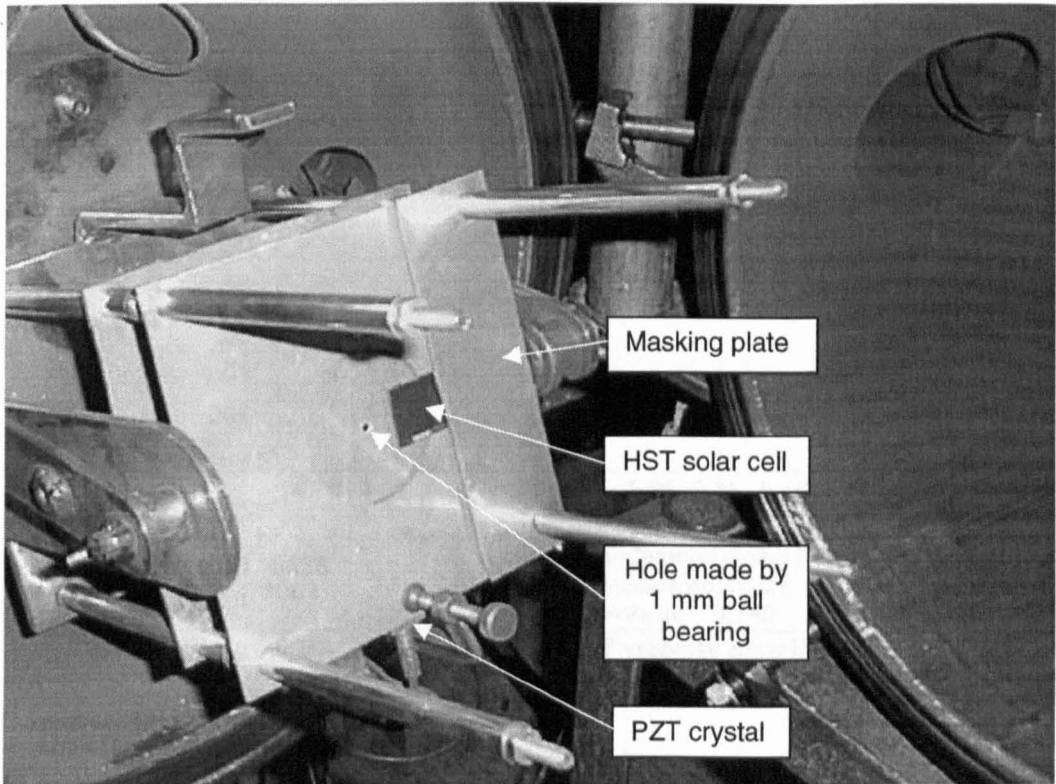


Figure 5.4 – Target configuration for shots 9-12

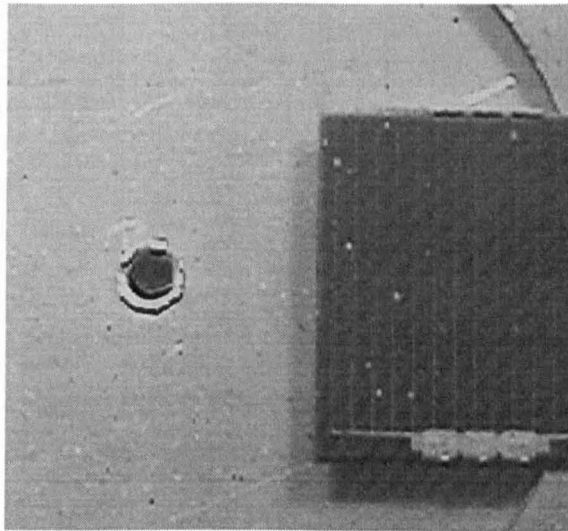


Figure 5.5 – Close-up of target after firing

5.2.3. Velocity variation

Velocity variation between shots

As with the experimental programme in section 3, velocity will not be a regressor and thus is required to be constant. It is not possible to achieve what would usually be considered “negligible” velocity variation with the light-gas gun therefore the nature of the velocity distribution attained is of relevance. It can be seen in Figure 5.6 that the velocity is approximately normally distributed. Like the previous experimental programme the velocity variation (standard deviation) is some 5% of the mean, larger than the 1% uncertainty in the measurement of any individual velocity, with a range of 860 m s^{-1} . As discussed in section 3.4.2, it is desirable also for the velocity to be uncorrelated with any other regressors. In this case we only have 1 regressor, the impact angle and Figure 5.7 shows that the velocity has negligible correlation with this.

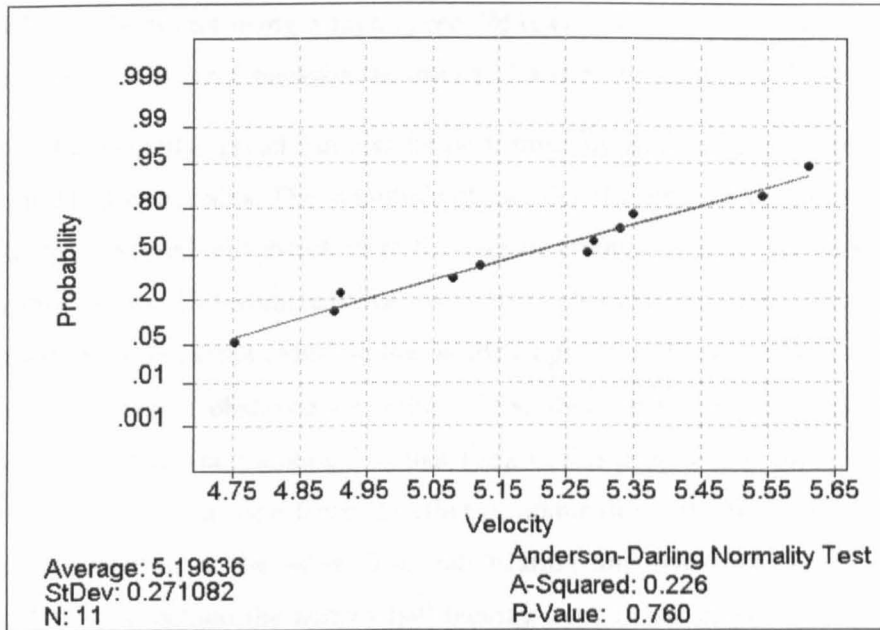


Figure 5.6 – Test for normality of velocity distribution

Table 5.1 – Summary statistics for velocities

	V (km s ⁻¹)
Mean	5.20
Standard Error	0.08
Median	5.28
Standard Deviation	0.27
Range	0.86
Minimum	4.75
Maximum	5.61
Count	11

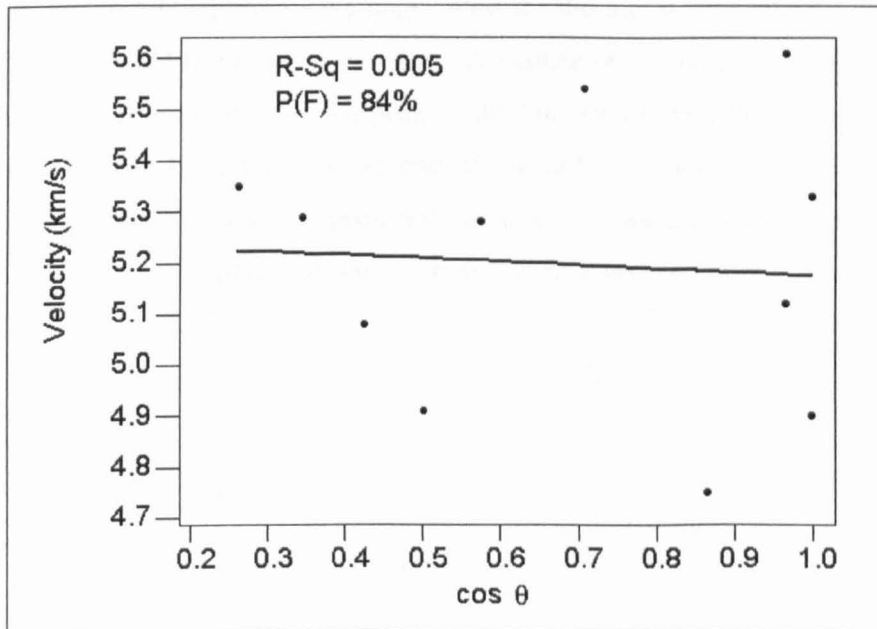


Figure 5.7 – Correlation of velocity with impact angle

Velocity variation *within* shots

With the buckshot technique of firing the gun it is necessary to assess the extent of any *spread* in the velocities within a single buckshot launch. A previous attempt has been made at calculating the

velocity spread for a buckshot using a high speed *IMACON* camera (Burchell *et al.*, 1999). This gave a velocity variation of 0.6% between the front and rear of the buckshot cloud.

A calculation of the velocity spread can also be performed by analysing the oscilloscope trace of the signals from the laser curtains. The amplitude of this signal is proportional to the amount of the laser curtain being obscured and therefore to the size or amount of material passing through the curtain at any one instant. Unfortunately, for the shots of this experimental programme there was no clear evidence of the buckshot cloud on the oscilloscope traces from the lasers. However, there was a clear buckshot signal observed for some of the shots in the experimental programme in section 6, where glass buckshot, identical to that fired in this programme, and mineral buckshots were used. Figure 5.8 shows a trace from buckshot of nominally 120-250 μm size enstatite shards loaded with a ball bearing in the sabot. The ball bearing and buckshot signals can be clearly distinguished; the signal behind the narrow ball bearing peak is not present for shots with only a ball bearing loaded. If the ball bearing is travelling with velocity V and arrives at the first laser at time t and other objects are recorded as arriving at the same point at times Δt after the ball bearing, the fractional difference in velocity between these objects and the ball bearing are given by:

$$\frac{\Delta V}{V} = \frac{\Delta t}{t}$$

The initial time interval between the buckshot and the ball bearing passing a fixed point is estimated to be around 0.4 μs based on a maximum separation of 2 mm between the rear of the buckshot and the front of the ball bearing as they are loaded in the sabot and an initial launch velocity equal to that of the ball bearing i.e. 5.4 km s^{-1} . The actual initial launch velocity will be higher than this and so this represents the upper limit for the initial time interval. This initial time interval must be subtracted from the observed Δt . The times of arrival chosen to be compared and converted to velocity differences were the peak of the buckshot cloud, the half maximum and the end of the tail. It should be noted that the end of the tail does not necessarily signify the last buckshot particles to arrive as there is invariably a cloud of soot that follows the projectiles that shows up on the lasers as a small signal. Therefore this represents the lower limit.

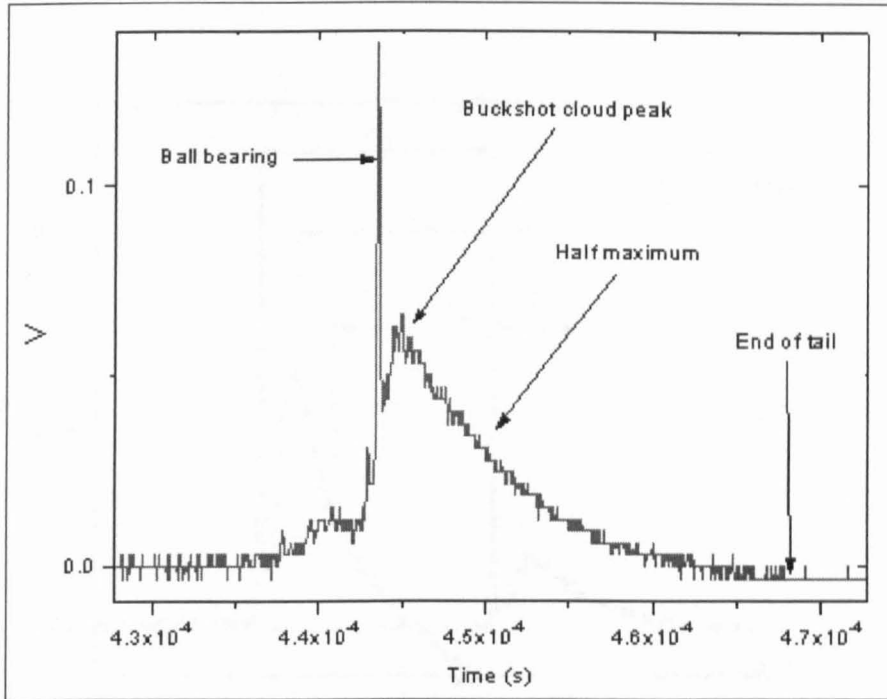


Figure 5.8 – Oscilloscope trace from section 6 shot used for velocity spread investigation

Table 5.2 shows the times of arrival at the first laser and the corresponding velocity difference from the ball bearing. The results for the enstatite buckshot in Figure 5.8 and a soda-lime glass bead buckshot from section 6 are shown.

Table 5.2 – Calculated ΔV for different regions of buckshot cloud

	Enstatite		Glass beads	
	Time (μs)	$\Delta V/V$	Time (μs)	$\Delta V/V$
Ball bearing	444	0%	387	0%
Buckshot peak	445	0.22%	388	0.18%
Half maximum	450	0.97%	393	0.98%
End of tail	468	3.98%	406	3.24%

For one buckshot firing of the light-gas gun that the author performed using a ground up ceramic (estimated size of projectiles $\sim 100\text{-}200\ \mu\text{m}$) a signal following the ball bearing one was observed on *both* lasers (Figure 5.9), believed to be due to the buckshot projectiles. Thus, with a signal on both lasers it is possible to make a time-of-flight measurement over a known distance and hence a velocity calculation for the ball bearing and the buckshot cloud.

Table 5.3 shows the velocities calculated and the corresponding $\Delta V/V$. It would appear that the velocity dispersion for this shot is greater than for the shots with the smaller enstatite and glass bead buckshots.

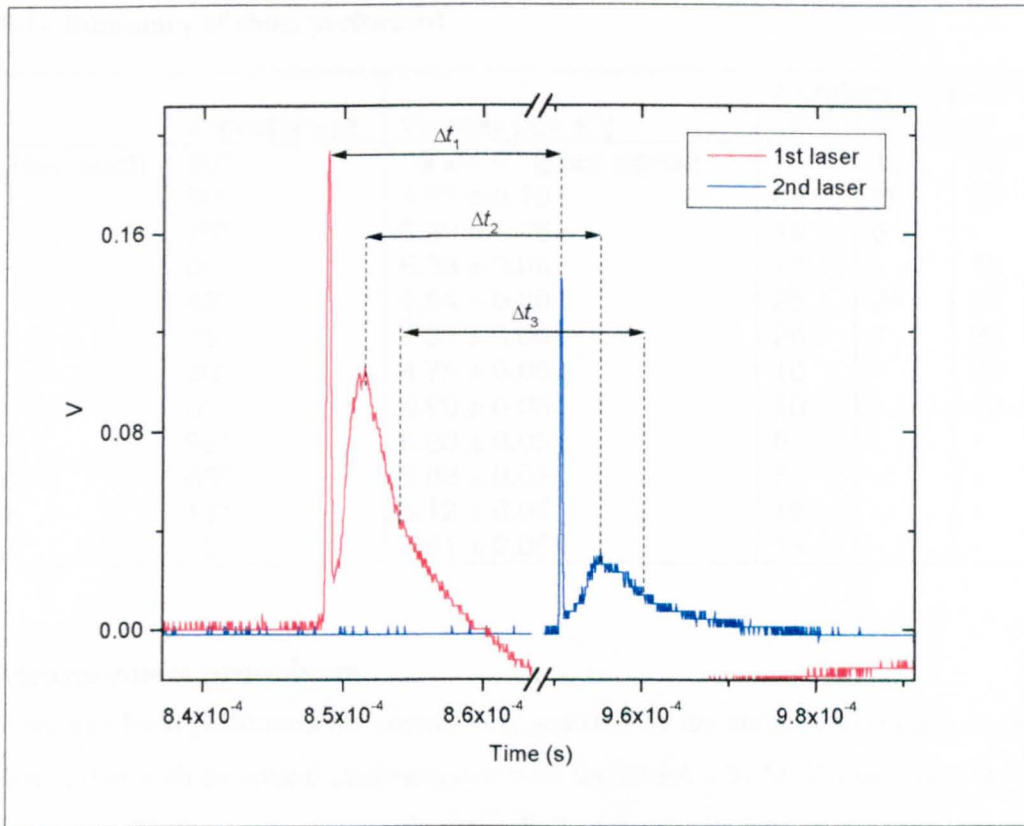


Figure 5.9 – Shot with ceramic buckshot showing a signal on both lasers

Table 5.3 – Measurement of velocity of buckshot from 2 laser signals

	1 st laser (μs)	2 nd laser (μs)	Δt (μs)	V (km s^{-1})	$\Delta V/V$
Ball bearing	849	951	102	4.90	0%
Peak	852	955	104	4.81	1.93%
Half max.	854	960	106	4.69	4.36%

The exact cause of the velocity dispersion within a buckshot is not known. Upon launch it could be that the projectiles collide with each other or there could be some drag from the residual low pressure (~ 0.2 mb) of air left in the range. The measurements made here give a larger velocity dispersion than those made by Burchell *et al.* (1999), but it is not clear if the discrepancy between this and between the ceramic and other buckshot calculations presented here could have arisen due to random variations in the gun's operation.

The relevant result from this investigation is that for the glass buckshot used here it is calculated that the *maximum* velocity spread in the buckshot is around 3.2%, larger than Burchell *et al.*'s 0.6% but still significantly smaller than the spread *between* shots. The spread at the 2σ level for the velocity distribution over the whole shot programme (Figure 5.6 and Table 5.1) is around 10% of the mean velocity. Therefore, when analysing the effect of velocity dispersion on our regression we need only be concerned with the velocity dispersion between shots.

5.3. Experimental results

The shots performed are shown in Table 5.4. The number of craters imaged and measured on each target material is shown: solar cells (ss), glass (g), aluminium (al) and the PZT plate (PZT).

Table 5.4 – Summary of shots performed

ID	Impact angle	Velocity (km s ⁻¹)	# craters on each target			
			ss	g	al	PZT
Shot 1 (test shot)	60°	~5 km s ⁻¹ (poor signal)	-	15	25	-
Shot 2	60°	4.91 ± 0.10	60	32	25	-
Shot 3	70°	5.29 ± 0.05	19	6	-	21
Shot 4	0°	5.33 ± 0.05	12	-	18	-
Shot 5	45°	5.54 ± 0.06	25	24	25	19
Shot 6	75°	5.35 ± 0.05	24	7	25	-
Shot 7	30°	4.75 ± 0.05	10	-	20	-
Shot 8	0°	4.90 ± 0.05	10	-	10	-
Shot 9	55°	5.28 ± 0.05	6	-	-	-
Shot 10	65°	5.08 ± 0.05	8	-	-	-
Shot 11	15°	5.12 ± 0.05	16	-	-	-
Shot 12	15°	5.61 ± 0.05	19	-	-	-

5.3.1. Measurement procedures

After a shot had been performed the targets were scanned by the author and images of the craters were taken, either with an optical microscope or with the USSA's SEM. For optical measurement a *Vickers* compound microscope was used with a CCD camera attached to the eyepiece to acquire digital images (Figure 5.10). A slide with a calibrated graticule was imaged which thus gave a size calibration for the images in terms of pixels, allowing rapid measurements to be made from the digitised images (section 3.3.1). Since the SEM imaging system is calibrated it was possible to make measurements directly from the images (Figure 5.11).

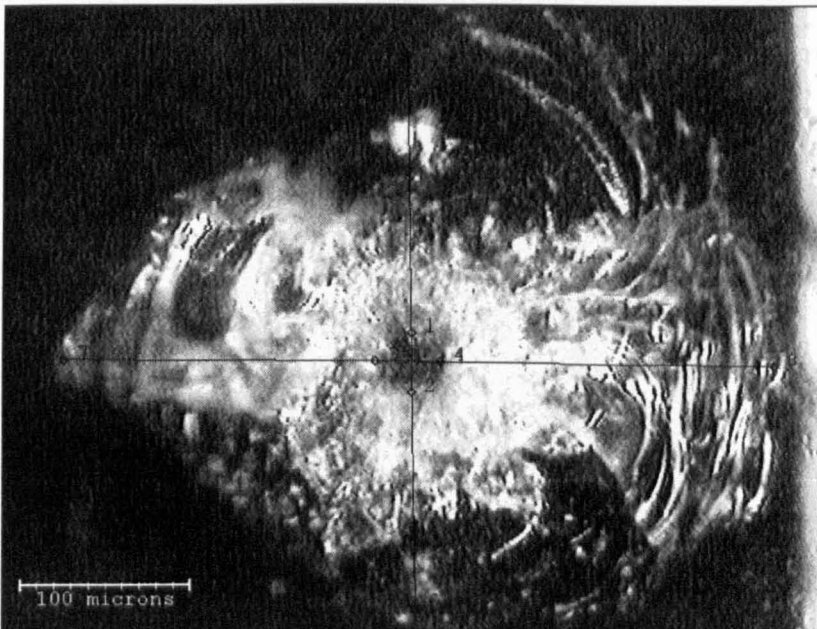


Figure 5.10 – Example solar cell crater measured using optical system

Depth measurement

For depth measurement of the optical images the graduated vertical focus of the microscope was calibrated using a digital micrometer. For depth measurement of the SEM images a second image was taken of each crater with the SEM stage tilted at 10-15° from horizontal. By measuring the horizontal displacement of a feature, which appears to be at the bottom of the crater, the depth

could be calculated. For the example images shown, with reference to Figure 5.13, length x_1 corresponds to length 1-11 in the first image (target surface normal to viewing direction) shown in Figure 5.11 and x_2 to the length 1-2 in the second image, which was taken with the stage tilted by $\theta = 10^\circ$. In Figure 5.12 x_1 and x_2 correspond to the lengths 1-5 and 1-2 in the first and second images respectively. On inspection of Figure 5.13 it can be seen that:

$$P \tan \theta = x_1 - \frac{x_2}{\cos \theta}$$

Multiplying both sides by $\cos \theta$ and rearranging gives the depth P of the point chosen inside the crater below the point placed on the surface in terms of the measured lengths x_1 and x_2 as:

$$P = \frac{x_1 \cos \theta - x_2}{\sin \theta}$$

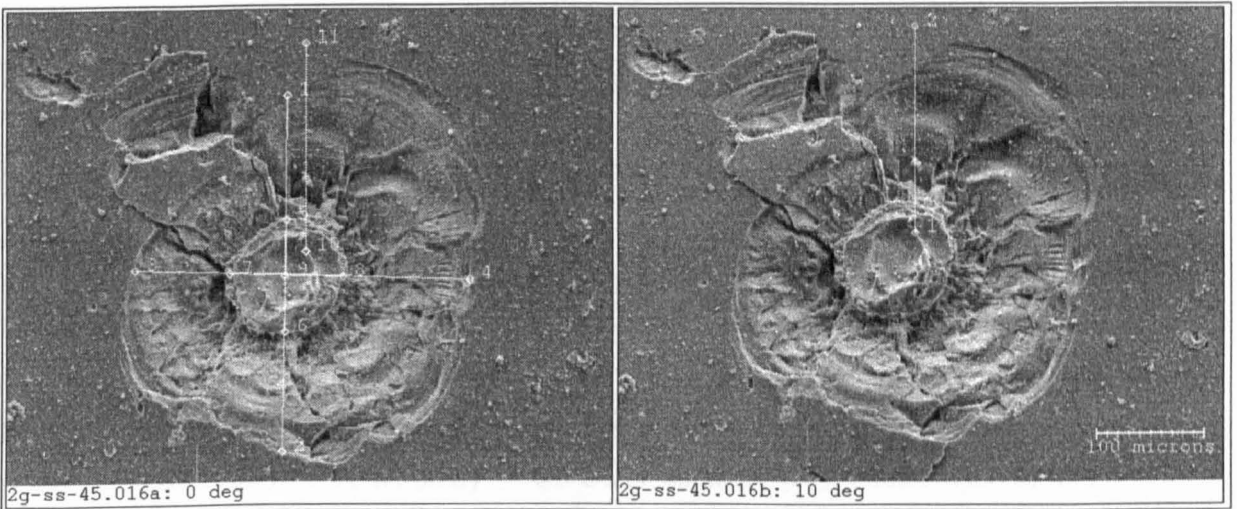


Figure 5.11 – Example solar cell SEM image pair taken for diameter and depth measurement

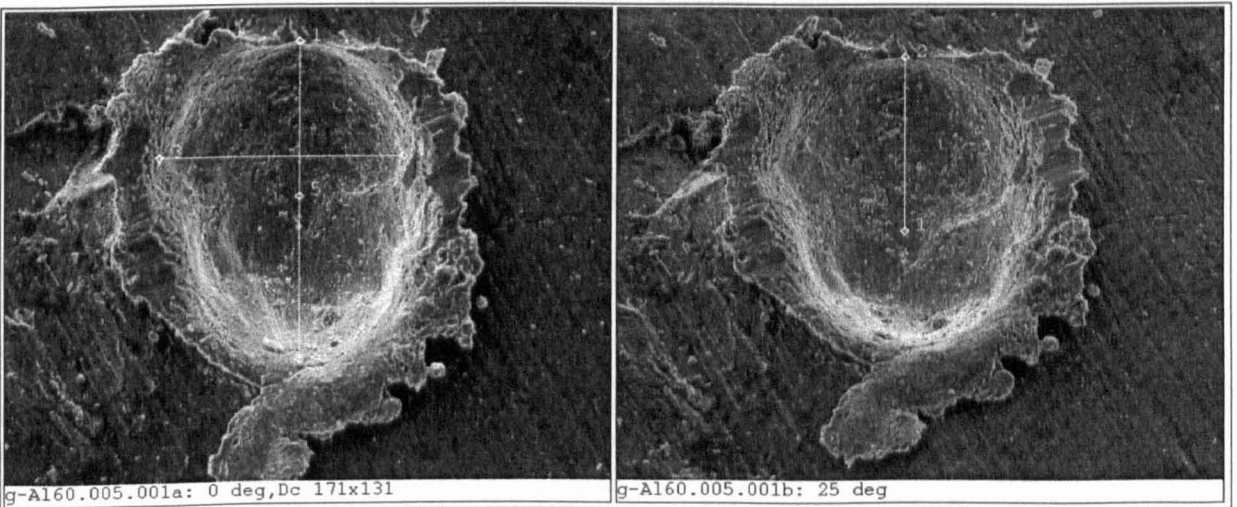


Figure 5.12 – Example aluminium SEM image pair

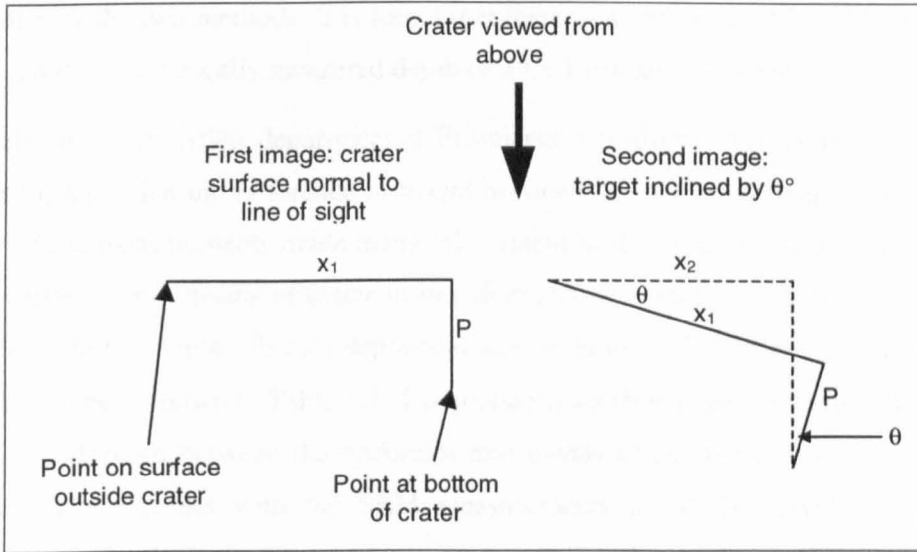


Figure 5.13 – Stereo-pair depth measurement

To the author's knowledge, this is the first time that depth calculation has been performed this way with the Unit's SEM.

5.3.2. Processing the raw data

Shot 1: 60° test shot

The first shot was performed with a glass block and an aluminium block mounted in the target holder to test the method. In particular, this was done to be sure that the target holder was mounted at the right height in the chamber such that the 1 mm ball bearing would pass through the gap between the two targets. Therefore, a solar cell was not used in the test shot for fear of destroying it if the aim wasn't correct. A summary of the crater diameter (D_c), circularity (CI) and depth (P) measurements made with the SEM (apart from the "Optical" depth measurement) are shown in Table 5.5, where A is the in-line diameter, B is the transverse diameter and P/D_c is the depth-to-diameter ratio.

Table 5.5 – Summary statistics for shot 1 aluminium data using SEM

	Dc (μm)			Circularity B/A	Depth P (μm)		P/Dc
	A	B	$\sqrt{(AB)}$		SEM	Optical	
Mean	115.6	97.7	106.1	0.848	35.1	39.2	0.335
SE	10.7	9.7	10.2	0.026	4.2	1.2	0.027
Median	138.7	120.7	130.7	0.861	38.6	40.0	0.289
SD	53.6	48.4	50.8	0.129	20.7	4.8	0.134
Range	151.0	127.3	138.2	0.591	102.7	19.1	0.597
Min	13.1	13.7	13.5	0.478	5.5	29.6	0.192
Max	164.1	141.0	151.7	1.069	108.2	48.7	0.789
Count	25	25	25	25	24	16	24
90% >	14.2	14.1	14.0	0.585	8.3	32.2	0.234
90% <	163.1	139.9	147.6	0.995	48.0	44.8	0.606

The author made both optical and SEM depth measurements (Table 5.5) of the shot 1 aluminium craters and thus a *two sample t-test* can be used to test for a significant difference between the mean

depth recorded by the two methods. It is found that there is a 36% probability that the mean SEM depth of $35 \pm 4 \mu\text{m}$ and optically measured depth of $39 \pm 1 \mu\text{m}$ are consistent.

The author also made use of the department of Bioscience's confocal laser microscope, which has a calibrated focus such that the difference in height between two focussed images can be measured. A summary of the measurements made using this system is shown in Table 5.6. A comparison of the sample variances and means of crater in-line diameter (A), transverse diameter (B), geometric mean (D_c), circularity, depth (P) and depth-to-diameter ratio (P/D_c) measured by the SEM and confocal microscope is shown in Table 5.7. The probabilities shown are the probability that there is no significant difference between the variances and means respectively. It can be seen that the confocal microscope agrees with the SEM measurements in all but depth. As the confocal microscope is specifically designed to measure depths, the confidence in our SEM measured depths is somewhat undermined by this result. As a result the depth data was not given high priority in the analysis and due to time-constraints was not analysed at this stage.

Table 5.6 – Summary statistics for shot 1 aluminium measurements using laser microscope

	A (μm)	B (μm)	D_c (μm)	CI	P (μm)	P/ D_c
Mean	127	113	120	0.860	59	0.518
SE	14	15	15	0.029	8	0.042
Median	117	100	105	0.833	58	0.544
SD	54	60	57	0.113	29	0.161
Range	211	227	220	0.338	124	0.654
Min	59	43	50	0.720	32	0.299
Max	270	270	270	1.059	156	0.953
Count	15	15	15	15	15	15
90% >	73	56	66	0.721	33	0.308
90% <	225	233	229	1.018	97	0.717

Table 5.7 – Comparison of SEM and laser microscope measurements

	A	B	D_c	CI	P	P/ D_c
Variance	48%	17%	31%	32%	7%	0%
Mean	51%	39%	44%	75%	1%	0%

Figure 5.14 shows a cumulative frequency distribution of the aluminium crater diameters for the first test shot. A cumulative distribution is used as there is not enough data to sensibly group it. D'agostino (1986) recommends the use of cumulative distribution plots for preliminary analysis as it avoids grouping difficulties, is an effective indicator of peculiarities and outliers and gives immediate and direct information of the shape of the underlying distribution (e.g. skewness or bimodality). It can clearly be seen that the distribution is bimodal comprised of two normally distributed sets of craters with sample means of 30 and 137 μm and standard deviations of 18 and 12 μm respectively. The author interprets this as the larger, narrower distribution being the craters made by the 50 μm glass beads and the smaller, wider distribution as comprising craters made by miscellaneous gun debris and/or fragmented projectiles (this issue is addressed in section 6). Thus,

the crater diameter corresponding to a 50 μm glass bead impact should be around 140 μm rather than 100 μm , which is the mean we record if we do not inspect the distribution of craters in this way. Accordingly, the author decided that it was necessary to check the distribution of craters from each shot and make a judgement about which subset of craters should be used to estimate the mean crater size corresponding to impacts by our intended projectiles. This pruning of the data was not performed for the analysis of the first 8 shots presented in Shrine *et al.* (1996) and thus the final processed data presented here – also with another 4 shots added – is a significant upgrade of that used in first analyses.

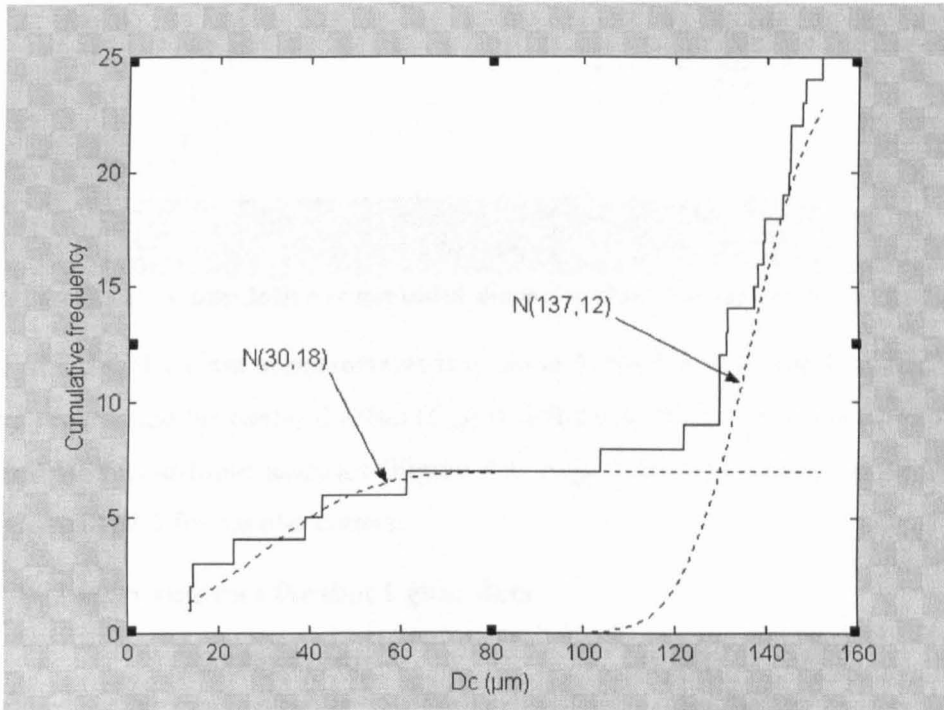


Figure 5.14 – Distribution of mean aluminium crater diameters for 60° test shot

The conchoidal diameter distribution of the glass craters from the test shot (Figure 5.15) is monomodal and normal to a good approximation. This could be interpreted as the intrinsic variability of the glass craters being larger and thus the distinction between the distribution of craters formed by projectiles and debris is lost. Alternatively, as the aluminium target was mounted further downrange than the glass target (Figure 5.2) the distribution of smaller craters observed on the aluminium target could be ejecta from the glass target.

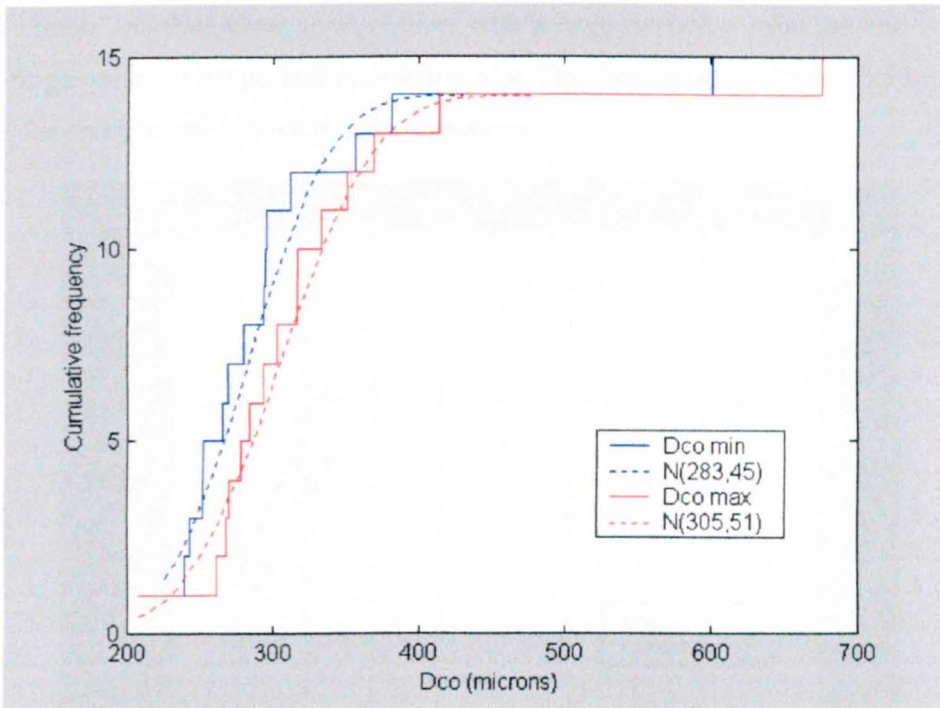


Figure 5.15 – Cumulative conchoidal diameter distribution for 60° test shot

A summary of the shot 1 glass measurements is given in Table 5.8. It should be noted that for this experimental programme the centroid offset (C_{off}) is defined as $2C/M$ rather than $1-2C/M$ as in the EURECA and HST post-flight analyses (Figure 4.4, page 114). This was done so that, like the circularity, C_{off} will be 1 for circular craters.

Table 5.8 – Summary statistics for shot 1 glass data

	Conchoid (μm)				P (μm)		C_{off}
	A	B	\sqrt{AB}	B/A	SEM	Optical	
Mean	329	304	315	0.95	18	24	0.83
SE	28	24	24	0.06	2	2	0.03
Median	303	280	290	0.82	18	25	0.86
SD	108	93	94	0.24	10	7	0.12
Range	467	375	390	0.65	30	28	0.36
Max	676	601	637	1.41	31	35	1.01
Min	209	226	248	0.75	1	7	0.64
Count	15	15	15	15	15	12	13
90% >	246	235	252	0.75	1	13	0.65
90% <	493	448	443	1.38	30	32	0.99

A different, more readily informative plot than a simple cumulative frequency plot such as Figure 5.14 and Figure 5.15 was used for studying the distribution of craters from subsequent shots. The normal probability plot is a cumulative frequency plot but with the percentile value of each datum as the y-axis. The y-axis has gaussian spacing such that a normal distribution will be linear. The author feels that it is reasonable to assume that the size and velocity variation *within* a buckshot will be random and therefore the craters formed by our intended impactors, which have a narrow size distribution, should be monomodal and approximately normally distributed. A bimodal distribution will show up as a change in gradient. Craters formed by any other miscellaneous inclusion in the buckshot reaching the target are likely to be significantly different in size from the

majority of craters and thus show up as outliers with a large deviation from the line corresponding to the best-fit gaussian on the normal probability plot. The data shown in Figure 5.15 is replotted in Figure 5.16 for comparison of the two representations.

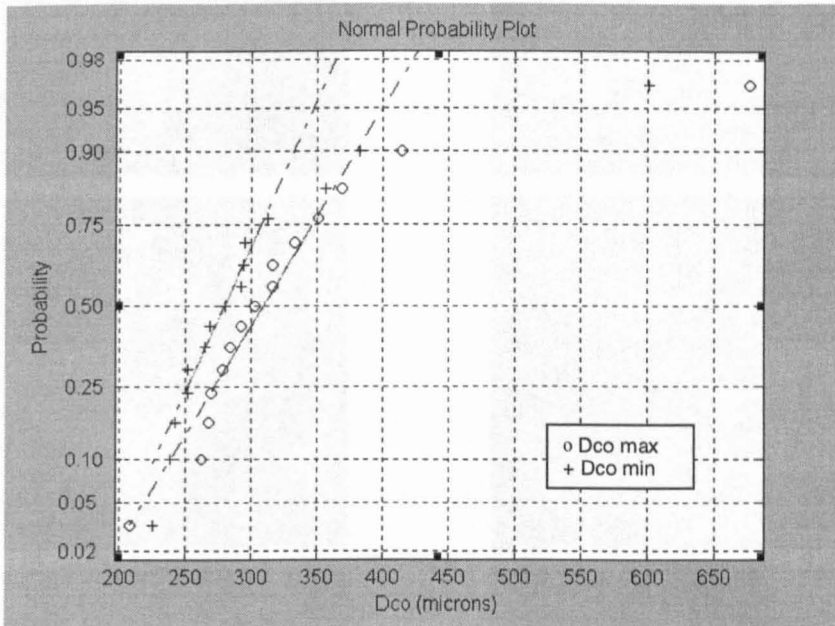


Figure 5.16 – Alternative test for normality of 60° test shot conchoidal distribution

Normal probability plots were used for initial sorting of all the craters from the shot programme. The complete set of crater images, measurements, summary statistics and normal probability plots from this experimental programme are included in appendix C. Notes on how the data from each shot was reduced using the normal probability plots are also given in appendix C.

5.4. Analysis

5.4.1. Morphological observations

Figure 5.17 shows the evolution of crater shape with impact angle for aluminium craters on the left and solar cell craters on the right. For the oblique impacts the impactor came from the top of the picture. In general, there is often a central raised plateau (sometimes with a bowl shaped indent in the centre) surrounded by a conchoidal fracture region. The 30° and 45° solar cell craters show no perceptible difference in symmetry to the normal impact. However, at 45° the plateau region is larger relative to the conchoidal zone. Not until 60° does asymmetry become apparent. The 60° crater shows little deviation from the shape of the normal impact except for a shift of the central feature, with respect to the conchoidal zone, towards the direction of approach of the impactor. The 75° crater shows no obvious conchoidal fracturing and no central feature, most likely because at this angle the normal component of the velocity is too low for conchoidal fracturing. The key changes in crater morphology with impact angle are summarised in Table 5.9.

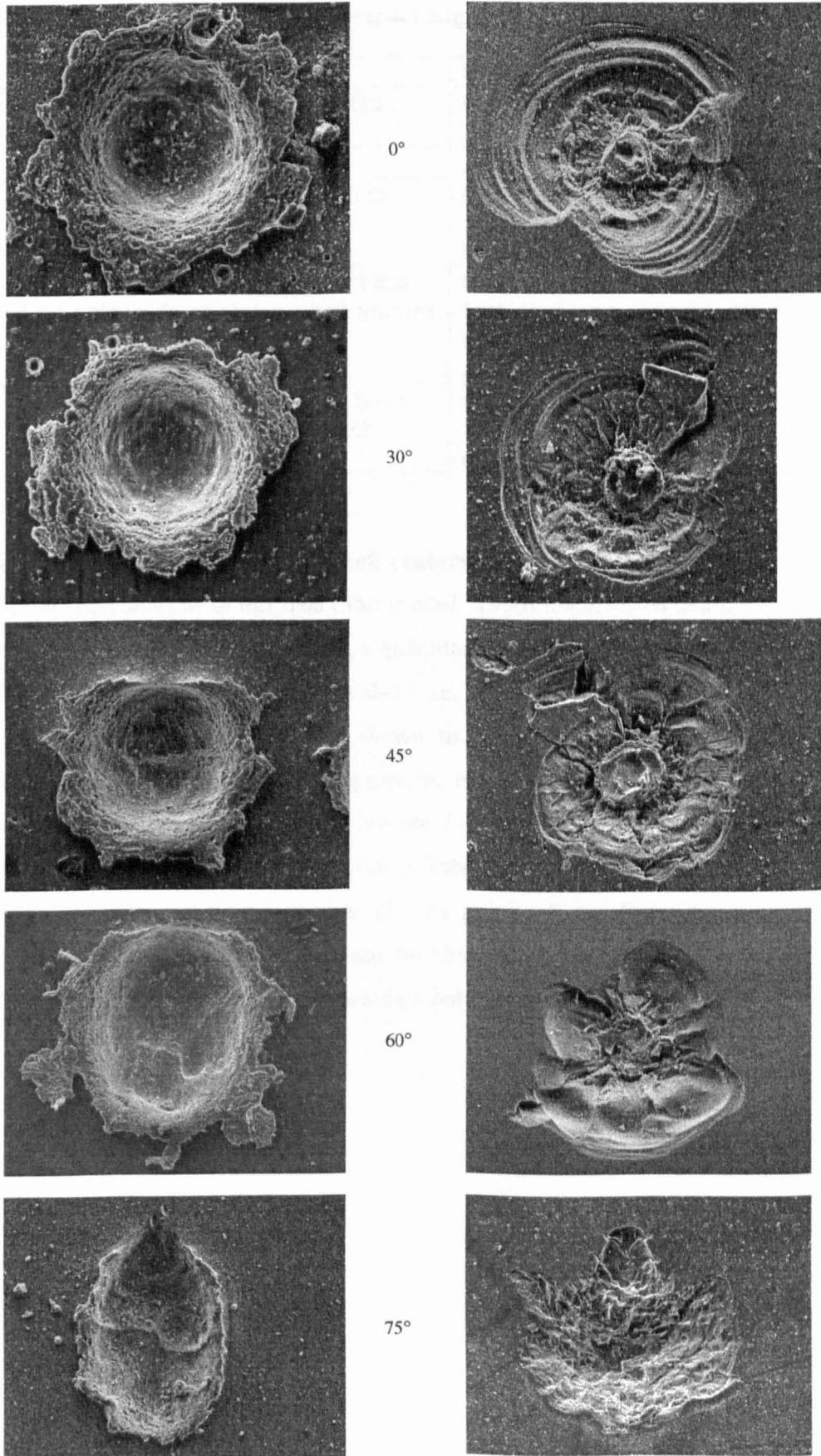


Figure 5.17 – Comparative morphologies of aluminium (left) and glass (right)

Table 5.9 – Morphological changes with impact angle

Angle	Aluminium	Solar Cell
0°	Circular crater, symmetrical lips, smooth crater bottom	Generally circularly symmetrical crater with.
30°	As for 0°	As for 0°
45°	Absence of lips on entry side of crater, rough crater bottom.	Still no significant asymmetry, but ratio of plateau to conchoidal region size is larger.
60°	Crater is elliptical, absence of lips on entry side of crater, shelf feature appearing in crater bottom.	Disappearance of central pit feature. Larger conchoidal fractures on the down-range side of shatter zone.
75°	Highly distended crater with bowl feature at point of first contact.	Different morphology to other angles, no recognizable shatter or conchoidal fracturing.

5.4.2. Comparison of glass and solar cell craters

Although in the first analysis of this data (Shrine *et al.*, 1996) it was noted that the glass craters are indistinguishable from the solar cell craters, a quantitative comparison was not made. Accordingly, the glass and solar cell data from the same shot - i.e. impacted by the same buckshot cloud – are now compared. As it has already been shown that the impact crater size distributions are approximately normally distributed the appropriate tests are the parametric tests for comparing samples from a normal population. These are the F -test for variances and the t -test for means, respectively. The results of the tests are shown in Table 5.10, where \bar{x}_n is the sample mean, s_n the sample standard deviation, n_n the number of data points, F the F -statistic and its associated probability $p(F)$, s^2 the appropriate variance for the t -test based on the outcome of the F -test (Hugill, 1985), t the t -statistic and its associated probability $p(t)$.

Table 5.10 – Test for difference between thick glass and solar cell craters

		Glass			Solar cell			Variances		Means		
		\bar{x}_1	s_1	n_1	\bar{x}_2	s_2	n_2	F	$p(F)$	s^2	t	$p(t)$
Shot 2: 60°												
Pit	A	52	11	18	55	20	55	1.76	10%	336	0.63	53%
	B	33	8	18	39	19	55	2.41	2%	299	1.15	25%
	\sqrt{AB}	41	7	18	46	19	55	2.59	2%	285	1.03	31%
	B/A	0.67	0.19	18	0.72	0.18	55	1.07	41%	0.03	1.01	31%
Shatter	A	108	5	4	130	15	29	3.23	18%	196	2.92	1%
	B	84	13	4	94	17	29	1.33	47%	283	1.08	29%
	\sqrt{AB}	95	6	4	110	13	29	2.22	28%	158	2.22	3%
	B/A	0.78	0.15	4	0.70	0.10	27	1.39	27%	0.01	1.38	18%
Conchoid	A	286	42	29	281	52	60	1.24	27%	2383	0.44	66%
	B	286	40	29	290	58	60	1.44	15%	2823	0.39	69%
	\sqrt{AB}	285	33	29	284	47	60	1.44	15%	1859	0.04	97%
	B/A	1	0	29	1.05	0.23	60	1.28	24%	0.05	0.80	42%
	P	28	6	29	25	9	61	1.60	9%	70	1.69	9%
	C_{off}	0.96	0.08	24	0.89	0.14	58	1.82	6%	0.02	2.14	4%
Shot 3: 70°												
Conchoid	A	140	53	6	195	20	18	2.67	6%	929	3.81	0%
	B	108	37	6	166	22	18	1.70	19%	683	4.78	0%
	\sqrt{AB}	122	42	6	180	17	18	2.51	7%	612	4.97	0%
	B/A	0.83	0.31	6	0.86	0.13	18	2.35	9%	0.03	0.32	75%
	P	10	4	6	20	26	18	6.04	3%	517	0.88	39%
	C_{off}	0.94	0.08	4	0.85	0.13	18	1.61	39%	0.02	1.26	22%
Shot 5: 45°												
Shatter	A	89	21	23	95	17	23	1.30	27%	367	1.09	28%
	B	85	17	23	93	14	23	1.25	30%	247	1.74	9%
	\sqrt{AB}	87	19	23	94	15	23	1.30	27%	283	1.44	16%
	B/A	0.97	0.12	23	0.98	0.09	23	1.44	20%	0.01	0.37	72%
Conchoid	A	276	58	24	280	81	25	1.39	22%	4950	0.22	83%
	B	282	61	24	283	80	25	1.31	26%	5137	0.03	98%
	\sqrt{AB}	278	53	24	281	77	25	1.44	19%	4426	0.14	89%
	B/A	1.03	0.17	24	1.02	0.16	25	1.05	45%	0.03	0.28	78%
	P (SEM)	18	10	23	23	11	24	1.10	41%	108	1.68	10%
	P (Opt)	29	6	15	20	5	11	1.16	42%	30	4.01	0%
C_{off}	1.03	0.16	22	0.99	0.17	25	1.09	42%	0.03	0.95	35%	
Shot 6: 75°												
Conchoid	A	98	21	7	137	89	24	4.26	4%	6326	1.15	26%
	B	112	21	7	132	94	24	4.41	4%	7128	0.53	60%
	\sqrt{AB}	105	20	7	134	91	24	4.54	3%	6650	0.83	41%
	B/A	1.16	0.12	7	0.97	0.23	24	1.90	22%	0.05	2.00	5%
	P	9	3	7	13	9	22	2.81	10%	67	1.33	20%
	C_{off}	1.07	0.22	6	1.06	0.23	17	1.04	53%	0.05	0.07	94%

If we take the usual 5% acceptance threshold then the samples do not generally distinguish between the thick glass and solar cell craters. There are some cases however where there appears to be a significant difference. These differences could arise for two reasons: (i) that the glass and solar cells have a different impact response due to their material properties and physical dimensions or (ii) the glass and solar cells exposed to the same buckshot received a significantly different distribution (size, shape, velocity) of impactors. For the majority of impact features where the glass is indistinguishable from the solar cells it is highly unlikely that they could have received a

significantly different portion of the buckshot and then the different response of the two materials compensated for this such that the craters produced are the same. The author suspects that for shot 3 the highly significant difference between the glass and solar cell conchoidal diameters *did* arise from the two targets receiving different impactors as for all the other shots the conchoidal diameter distributions are indistinguishable. It is generally the case that significant differences are only observed for samples of less than 10 craters, thus the author suspects that this means that the targets did not receive a sufficiently averaged buckshot thus giving rise to discrepancies. Furthermore, with such small samples the statistical tests are approaching the limits of their application being meaningful. In summary the author concludes that the glass and solar cell craters do not show a significant difference in response at the precision achieved by this experiment. This is a relevant result for experimental programmes where glass blocks are used as solar cell analogues (Taylor, 1998).

5.4.3. Regression analysis

Errors and evaluation of fit

In section 3.4.2 it was noted that the measurement errors associated with our craters are of little relevance to the regression analysis as long as they are small. It was also pointed out that what is required to determine the appropriate “error” variance was repeats of the same shot. This is the rationale adopted in this experimental programme in that many “identical” particles are fired in a single buckshot constituting “repeat” experiments. Identical repeats are, of course, a theoretical ideal and in reality what is meant by a “repeat” experiment is one where the variation in the independent variables is as small as possible from one repeat to the next. In the case of the gas gun, the minimum possible variation in the independent variables that we could achieve is to carefully select the projectiles with the closest sizes and fire the gun many times until closely matched velocities were obtained. This is impractical and unfeasible within the timescale of this research. Baron (1996) required 86 shots just to achieve 14 shots to within the required velocity tolerance. Thus, for example, if we wanted a shot at each of 10 impact angles produced by impactors with the closest possible size and velocity we would require over 60 shots. This does not include performing repeats in order to determine the intrinsic variability of crater shapes over and above simple measurement uncertainties. If we wanted 10 repeats per set of impact conditions we would require over 600 shots. However, by using the buckshot technique, we get a set of “repeats” with less variable velocities than firing the gun several times (section 5.2.3) and thus is a suitable compromise. If we do a buckshot firing for each of our chosen regressor values (impact angles in this case) and then take the mean of the independent variables measured for each as our variates such that for each regressor value X_i we have a corresponding variate Y_i given by:

$$\bar{Y}_i = \frac{1}{N_i} \sum_{j=1}^n Y_{ij} \quad (5.1)$$

The confidence associated with this value is the standard deviation of the sample mean which is the *standard error of the mean* given by $(s^2_i/N_i)^{1/2}$, where s^2_i is the sample variance given by:

$$s_i^2 = \frac{1}{N_i - 1} \sum_{j=1}^{N_i} (Y_{ij} - \bar{Y}_i)^2 \quad (5.2)$$

Any variation in projectile size and velocity within the buckshot will produce, to an unknown extent, a variation in the size of the craters formed and thus is implicitly included in our uncertainty of the \bar{Y}_i variates. Thus for our regression model:

$$Y = f(X; \beta) + \varepsilon \quad (5.3)$$

where β is the vector of coefficients, the error term ε is assumed to be normally distributed with mean 0 and standard deviation σ_ε given by:

$$\sigma_\varepsilon^2 = \sigma_m^2 + \sigma_i^2 + \sigma_v^2 + \sigma_f^2 \quad (5.4)$$

where the sources of variance identified are:

- σ_m is the accuracy of our method of measuring the craters.
- σ_i is the variability due to non-negligible variation in the independent parameters not included in the relationship $f(X; \beta)$: in this case the particle size, velocity and possibly shape.
- σ_v is the intrinsic variability of crater formation i.e. the spread in crater sizes for apparently the same initial conditions. σ_i would usually be implicitly accounted for by this variance as it arises from slight, undetectable variations in initial parameters. Conjectures have been made in this area by several researchers e.g. micro-structural flaws in the solar cells produce a varying response for the same impact conditions. In this model it is separated from σ_i to signify the variance due to unmeasurable fluctuations in the experimental parameters, such as solar cell microstructure, as opposed to those variations which we can at least estimate such as the velocity variation.
- σ_f is the lack-of-fit that is determined by our choice of model, unlike the other variances that cannot be reduced however accurate our model is.

The sample variance s_i^2 (equation 5.2) is our unbiased estimator of the residual variance after fitting accounted for by the first three terms of equation 5.4. With reference appendix A this is our $MS_{\text{pure error}}$, that is, the irreducible error. Subtracting this from our residual sum of squares after fitting our regression equation leaves us with the lack-of-fit variance, which should be significantly smaller than the error variance for a good model.

Although the effect of projectile size and velocity variation *within* shots is accounted for in the uncertainty of the mean crater size for each shot, the velocity variation *between* shots is not. The variation in *mean* projectile size for 20 or so impact craters should not be significantly different from the mean of the stock of projectiles. The velocity variation between shots will contribute to the lack-of-fit variance. Accordingly, it may be that an acceptable model with velocity omitted as a regressor may not be attainable; where by “acceptable” we mean one that gives a χ^2 probability > 5 or 1%. However, we do not really have enough data covering enough velocities *and* impact angles

in an orthogonal scheme to include both in the model and the author believes that it would be misleading to fit to both. The aim of this experiment is to find the relationship between crater parameters and impact angle at a *fixed* velocity. Therefore we hope that the velocity variation is small and does not have a significant influence, but with foreknowledge that our model is only an approximation we should be accordingly more reluctant to dismiss an improbable χ^2 statistic. The variability due to velocity will contribute to the uncertainty in our fitted impact-angle regression coefficient and so we will not be unduly overconfident in our “fixed-velocity” model given that the velocity is not *really* fixed. Any presentation of the model fitted here should, of course, explicitly state the velocity variation over the shot programme, indeed, as all uncertainties in experimental parameters should be given. However, these are frequently omitted, as are uncertainties in fitted coefficients.

Conchoidal diameter

Figure 5.18 and Figure 5.19 show summaries of all the raw data from all shots represented as the mean and standard error. For the shots where there was clearly two populations of impactors i.e. where there was a clear distinction between “big” and “small” craters the means of the data split into two corresponding sets is shown. It was then decided which subset of craters to use in the regression analysis based on which means appeared to be consistent with a general trend and which appeared to be discontinuous with the other data. It can be seen in Figure 5.18 and Figure 5.19 that the mean based on the larger set of craters from the 45° ($\cos \theta \approx 0.7$) shot 5 is more consistent with the general trend than the mean of the whole data set. Therefore, the set of larger craters was used for determining a mean and error for shot 5 rather than the whole data set based on the inference that the large craters correspond to intact glass bead impacts and the small ones to either gun debris or fragmented projectiles*. It is unlikely that the conchoidal diameter shows a sudden reverse in trend at 45° . The 15° ($\cos \theta \approx 0.97$) shots 11 and 12 were not used in the regression analysis as a bimodal distribution of projectiles occurred for both shots (see appendix C) and after splitting the data into two sets, neither set appeared to fit with the other data. It could be that the gun performance was poor for these two subsequent shots, with miscellaneous debris impacting as well as the buckshot. The data from the two normal shots 4 and 8 were amalgamated to make a single datum for 0° . Thus, the error for this datum will incorporate some variance due to the velocity variation *between* shots 4 and 8 (5.33 and 4.90 km s⁻¹ respectively) in addition to the velocity variation *within* each shot.

* This distinction between projectiles, fragments and gun debris is studied in section 6.

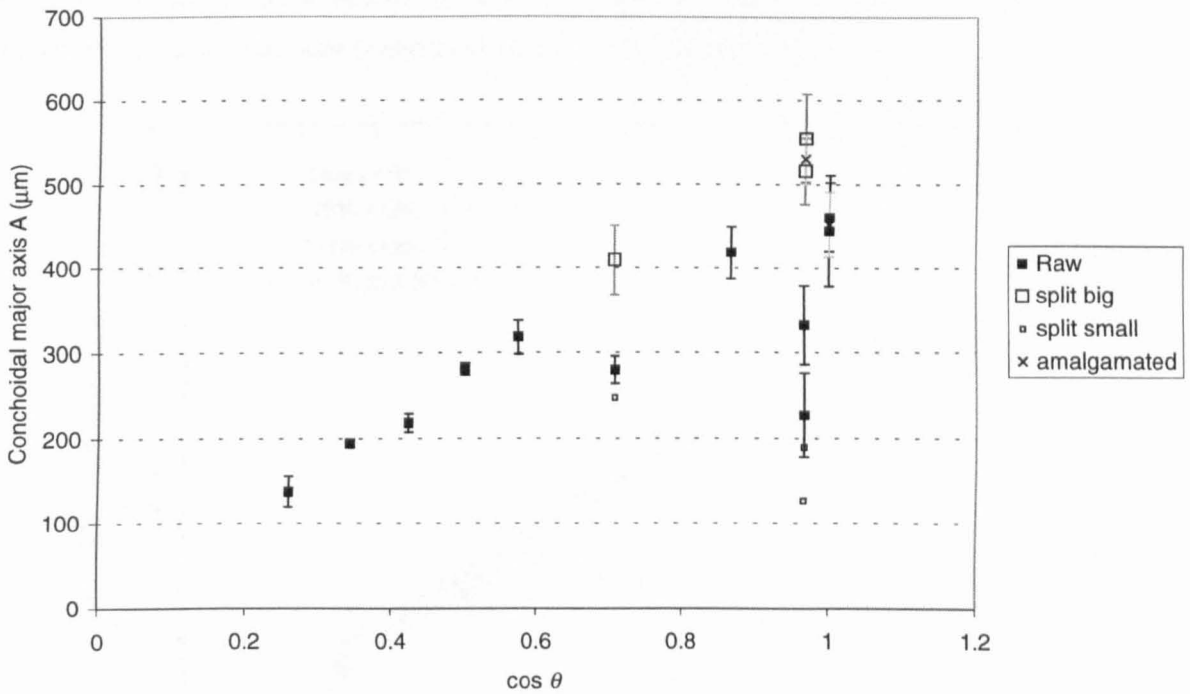


Figure 5.18 – Summary of conchoidal major axis raw data

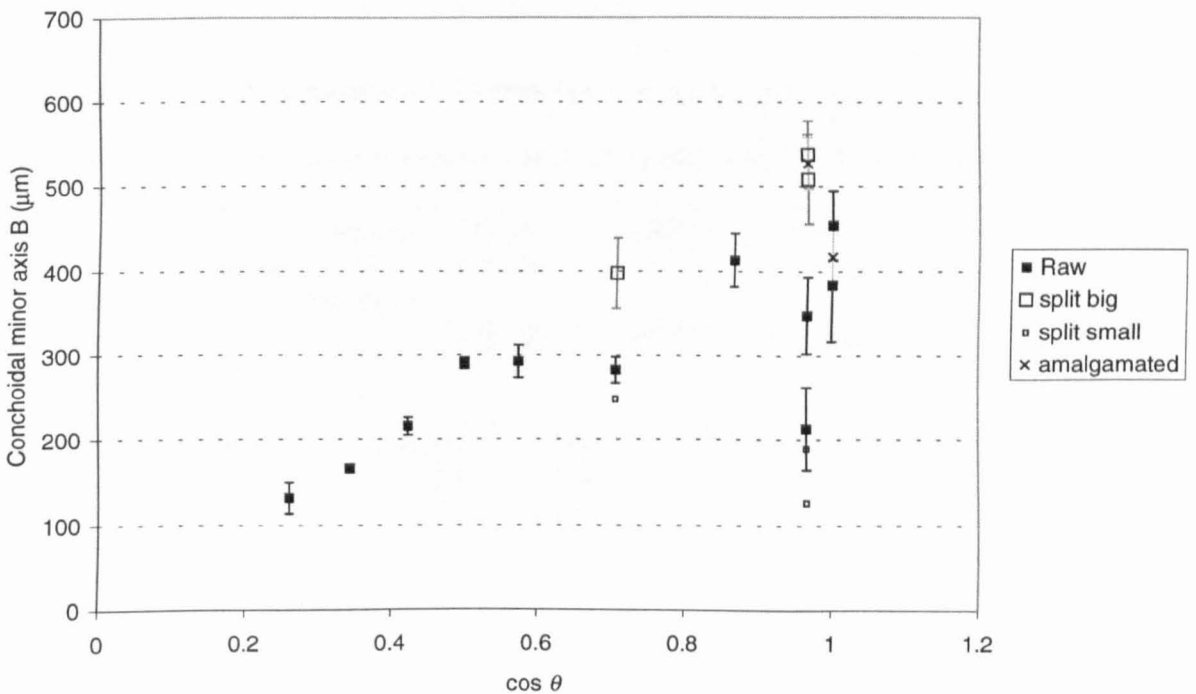


Figure 5.19 – Summary of conchoidal minor axis raw data

Despite the size difference between the shot 1-8 beads ($49 \pm 4 \mu\text{m}$) and the shot 9-12 beads ($55 \pm 1 \mu\text{m}$), the shot 9-12 beads used for the 55° (shot 9) and 65° (shot 10) shots do not appear to have resulted in a significant increase in conchoidal diameter above the fitted trend lines. These are the points at $\cos \theta$ values of 0.42 and 0.57 in Figure 5.20 and Figure 5.21.

A linear model was tried first for the conchoidal major (line-of-flight) axis A:

$$A = \beta_0 + \beta_1 \cos \theta + \varepsilon$$

The least-squares fit was weighted by the standard error of the mean and is shown in Figure 5.20, with coefficients and statistics (defined in appendix A) given in Table 5.11.

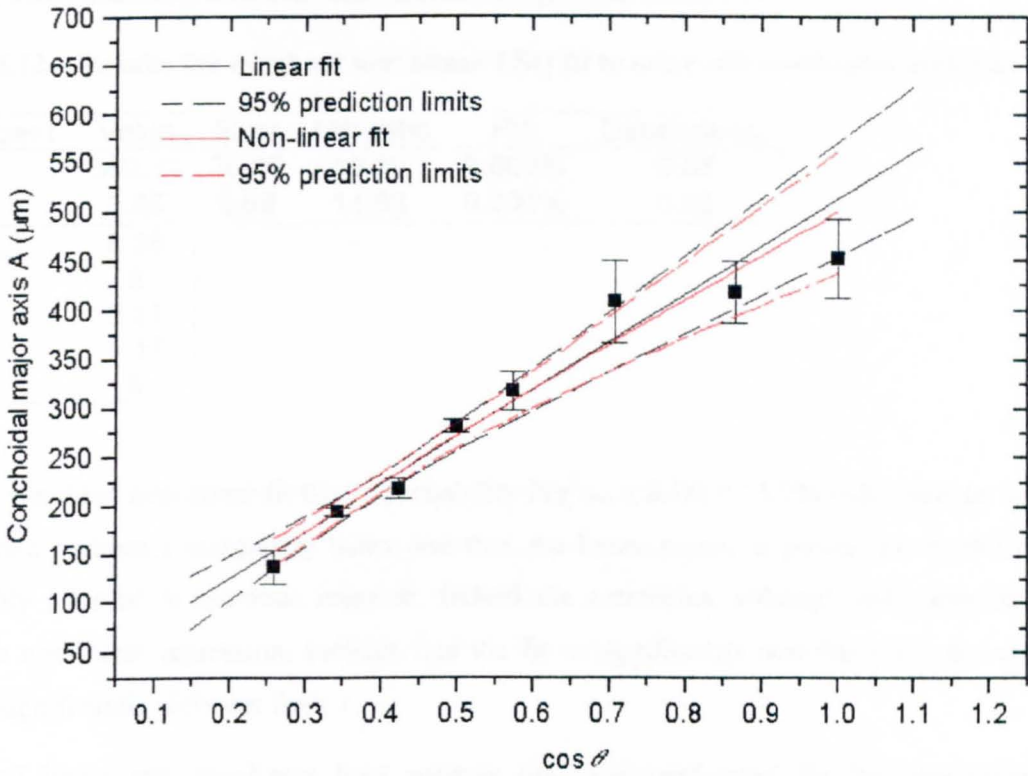


Figure 5.20 – Weighted least-squares fits to solar cell conchoidal major axis data

Table 5.11 – Results for weighted linear LSQ fit to solar cell conchoidal major axis

	Sum of squares	Degrees of freedom	Mean square	F-statistic	P(F)
Regression	242.20	1	242.20	148.37	<0.000%
Residual	9.79	6	1.63		
Total	252.00	7			

Coefficient	Value	Error	t-statistic	P(t)
Constant	29	17	1.75	13%
cos θ	484	40	12.18	<0.001%
R^2	0.96			
R^2_{adjusted}	0.95			
s	1.28			
N	8			

For a fit weighted by the error of each point the residual sum of squares will have a χ^2 distribution with $n-2$ degrees of freedom if the errors are normally distributed (Cooper, 1969) – this assumption of normality has been checked using normal probability plots. The χ^2 probability of our observed weighted $SS_{\text{residual}} = 9.79$ (Table 5.11) with 6 degrees of freedom is 13.3% indicating an acceptable model at the 5% level. However, the t -statistic indicates that the intercept (29) is not significantly different from 0 and so a model without this additional parameter or a power law model may be more appropriate. A power law model was tried:

$$A = \beta_0 \cos^{\beta_1} \theta + \varepsilon$$

The weighted non-linear least squares fit was performed using the *Levenberg-Marquadt* method (appendix A) as implemented by *Microcal Origin*. The fit is shown on the same plot as the linear fit (Figure 5.20) and the coefficients and statistics are given in Table 5.12.

Table 5.12 – Results for weighted non-linear LSQ fit to solar cell conchoidal major axis

Coefficient	Value	Error	t -statistic	$P(t)$	Dependency
β_0	500.11	25.16	19.88	0.000%	0.88
β_1	0.88	0.06	14.88	0.001%	0.88
SS_{residual}	8.28				
DF	6				
R^2	0.97				
s	1.17				
N	8				

For the weighted non-linear fit the χ^2 probability $P(\chi^2_{v=6} \geq 8.28) = 21.9\%$ indicating an acceptable model and perhaps a marginally better one than the linear model; a power law model is almost invariably adopted in previous research. Indeed the t -statistics, although only approximate for iterative non-linear regression, indicate that the fit is *significantly* non-linear i.e. the coefficient 0.88 is significantly different from 1.

Weighted linear and non-linear least squares fits were performed for the conchoidal minor (transverse) axis B, both plotted in Figure 5.21 with coefficients and statistics given in Table 5.13 and Table 5.14 respectively.

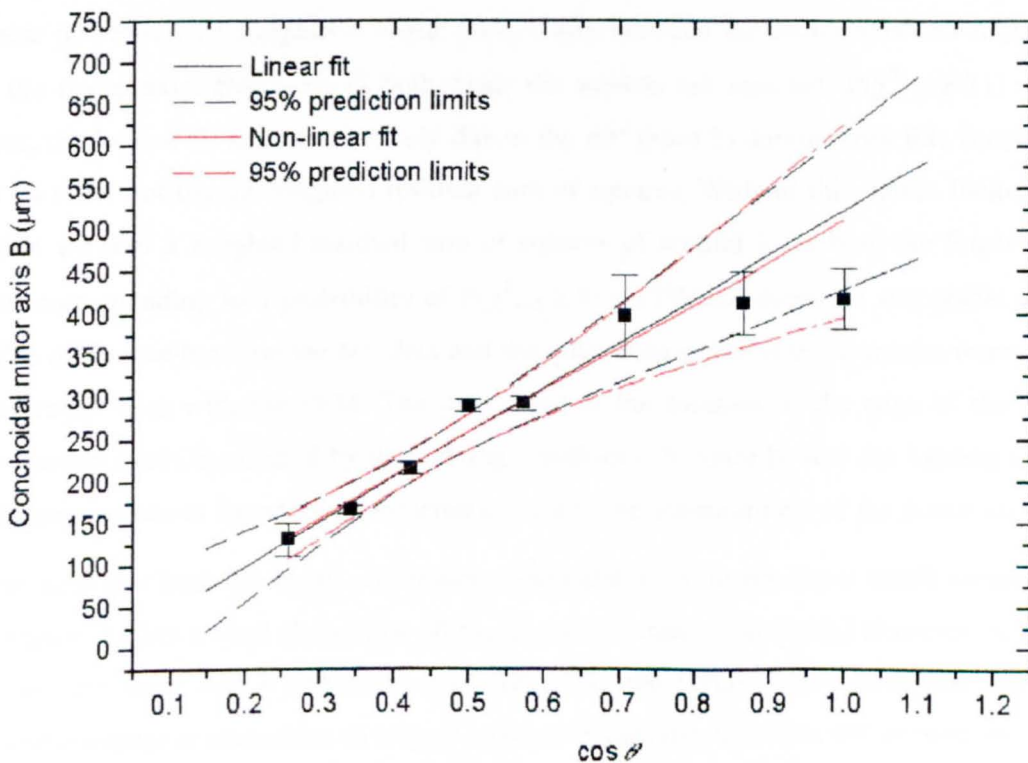


Figure 5.21 – Weighted least-squares fits to solar cell conchoidal minor axis data

Table 5.13 – Results for weighted linear LSQ fit to solar cell conchoidal minor axis

	Sum of squares	Degrees of freedom	Mean square	F-statistic	P(F)
Regression	336.36	1	336.36	64.25	<0.001%
Residual	31.41	6	5.24		
Total	367.78	7			

Coefficient	Value	Error	t-statistic	P(t)
Constant	-6	30	-0.22	84%
cosθ	531	66	8.02	<0.001%
R ²	0.91			
R ² _{adjusted}	0.90			
s	2.29			
N	8			

Table 5.14 – Results for weighted non-linear fit to solar cell conchoidal minor axis

Coefficient	Value	Error	t-statistic	P(t)	Dependency
β ₀	512.00	47.21	10.84	0.004%	0.79
β ₁	0.99	0.12	8.43	92%	0.79
SS _{residual}	31.60				
DF	6				
R ²	0.91				
s	2.29				
N	8				

Again, as with the fit to the major axis the intercept of the linear fit is indistinguishable from 0. The non-linear power-law fit suggests a linear relationship between the minor axis and impact angle, unlike the major axis. However, in both cases the models are rejected: $P(\chi^2_{v=6} \geq 31) = 0.002\%$. However, the lack-of-fit is almost entirely due to the 60° (shot 2) datum, with this accounting for around 24 (75%) of the 32 weighted residual sum of squares. Without this datum included in the regression we find a weighted residual sum of squares of around 8 for both the linear and non-linear fit corresponding to a probability of $P(\chi^2_{v=5} \geq 8) = 17\%$ and therefore acceptable at the 5% level. The difference between the 60° data and the other data is that it these craters were measured optically rather than with the SEM. The judgement of the location of the edge of the crater for optical measurements is affected by the lighting conditions. It could be that the lighting conditions for these measurements introduced a systematic error in the measurement of the minor axis.

It can be seen that both the major and minor conchoidal axes do not show much variation in the 0°-45° region. In fact a *t*-test shows that all the major and minor conchoidal diameters in the range 0°-45° are consistent with a common mean. Therefore the author infers from this data that the conchoidal diameter is insensitive to impact angle at obliquities less than 45° in both absolute size and circularity. The author has not heard of this result before as previous literature only specifies the conchoidal diameter as a power-law function of impact angle. In fact most other investigations

would not detect this behaviour as only 3 or 4 angles are investigated – so even fitting a power law is somewhat over-stretching the data. Accordingly, a linear spline* model was fitted to the data:

$$Y = \begin{cases} \beta_0 + \beta_1 X & \text{for } X < 45^\circ \\ \bar{Y} & \text{for } X \geq 45^\circ \end{cases}$$

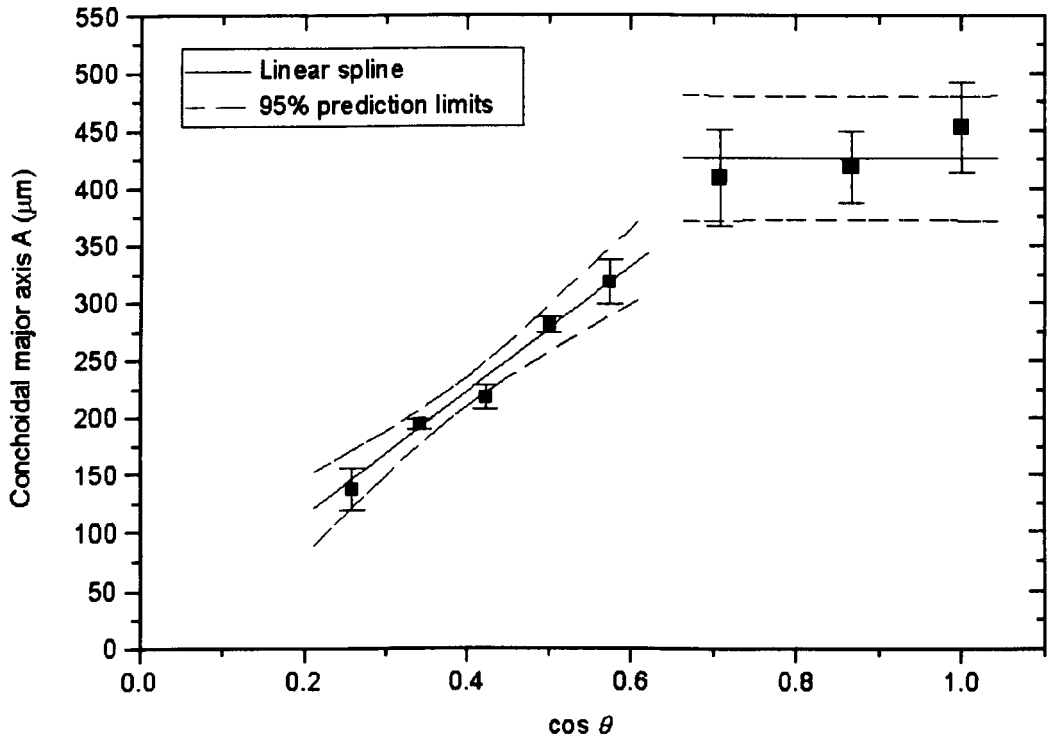


Figure 5.22 – Weighted linear spline fit to conchoidal major axis

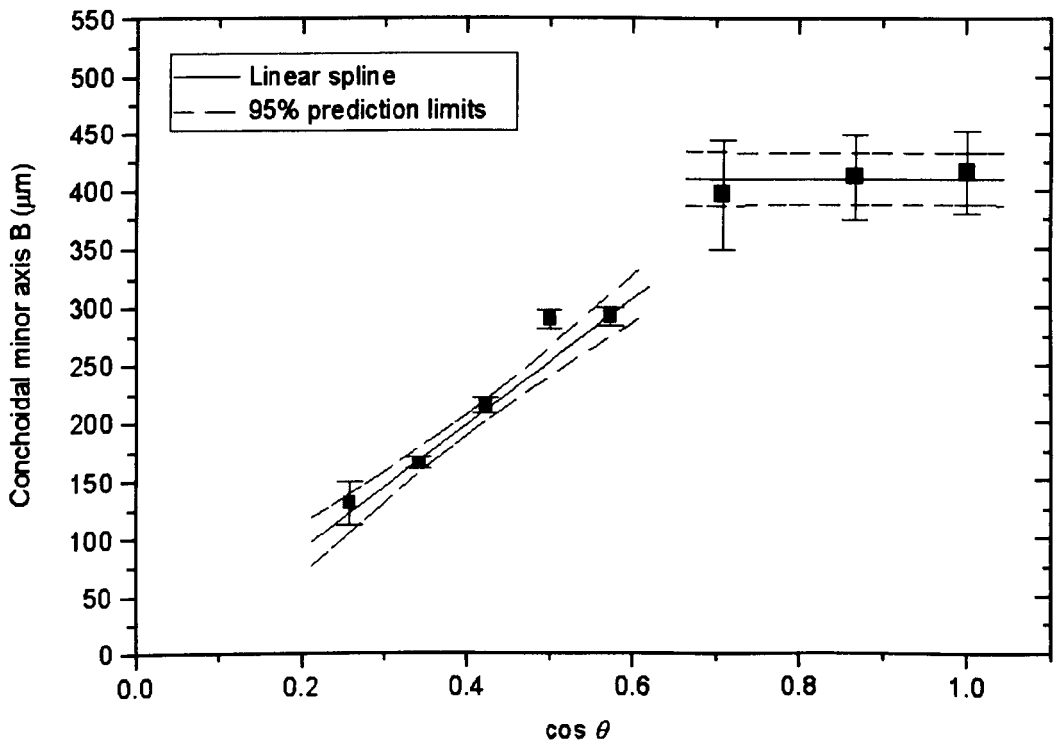


Figure 5.23 – Weighted linear spline fit to conchoidal minor axis

* The term “spline” will be used here to encompass piecewise fitting also.

The weighted linear spline fits for the major and minor conchoidal axes are shown in Figure 5.22 and Figure 5.23 with corresponding coefficients and statistics given in Table 5.15 and Table 5.16.

Table 5.15 – Results for weighted linear spline fit to conchoidal major axis

	Sum of squares	Degrees of freedom	Mean square	F-statistic	P(F)
Regression	155.37	2	77.68	89.61	0.012%
due to β_1	155.37	1			
due to \bar{Y}	0	1			
Residual	4.33	5	0.87		
due to β_1	3.65	3			
due to \bar{Y}	0.69	2			
Total	159.70	7	22.81		
Coefficient	Value	Error	t-statistic	P(t)	
β_0	5.79	19.54	0.30	78.63%	
β_1	545.15	48.22	11.31	0.15%	
\bar{Y}	426.27	12.28	34.71	0.08%	
R^2	0.973				
R^2_{adjusted}	0.962				
s	0.931				
N	8				

Table 5.16 – Results for weighted linear spline fit to conchoidal minor axis

	Sum of squares	Degrees of freedom	Mean square	F-statistic	P(F)
Regression	189.52	2	94.76	503.54	0.002%
due to β_1	189.52	1			
due to \bar{Y}	0	1			
Residual	0.75	4	0.19		
due to β_1	0.64	2			
due to \bar{Y}	0.11	2			
Total	190.27	6	31.71		
Coefficient	Value	Error	t-statistic	P(t)	
β_0	-16.37	9.30	-1.76	22.04%	
β_1	540.43	22.27	24.27	0.17%	
\bar{Y}	411.32	5.32	77.37	0.02%	
R^2	0.996				
R^2_{adjusted}	0.994				
s	0.434				
N	7				

The author could not find a published procedure for statistical evaluation of spline or piecewise regression. Therefore, it was decided to sum the weighted squared residuals from each part of the spline regression to give the total SS_{residual} in the ANOVA parts of Table 5.15 and Table 5.16. It is clear that the second part of the spline, which is simply a weighted mean, will not reduce the residual variability about the mean, by definition, and thus the contribution to $SS_{\text{regression}}$ is 0. For the fit to the minor axis the 60° shot was omitted for reasons discussed earlier. When it comes to

computing our goodness-of-fit statistic it is clear that we must lose at least 1 more degree of freedom than the 3 we lose for estimating the parameters β_0 , β_1 and \bar{Y} from the data due to the fact that we are choosing a value at which to split the data between the two functional forms. Perhaps, even the loss of another degree of freedom is appropriate in that we are imposing the constraint that the residuals for each of the two parts of the spline must sum to zero, unlike normal linear regression where this constitutes only 1 constraint applied over all the data. Thus the probabilities associated with the total (both parts of spline summed) sum of weighted square residuals are $P(\chi^2_{v=4} \geq 4.33) = 36\%$ and $P(\chi^2_{v=3} \geq 4.33) = 23\%$ for the major axis subtracting 1 and 2 additional degrees of freedom respectively and therefore signifies an appropriate model for the major axis. The corresponding minor axis probabilities are $P(\chi^2_{v=3} \geq 0.75) = 86\%$ and $P(\chi^2_{v=2} \geq 0.75) = 69\%$, which are worryingly high in that the standardised χ^2 statistics, χ^2/v , are 0.25 and 0.38. The standardised χ^2 statistic should be an estimate of unity and values significantly less than 1 suggest either overestimation of errors or an inappropriate number of degrees of freedom*.

In view of the possible ambiguity of rigorous goodness-of-fit tests the author feels that a common-sense comparison of the different functional forms is warranted. Furthermore, it would seem that the different regression equations tried here give more or less equally acceptable models. A by-eye comparison of the single linear and power law fits and the spline fits strongly suggests that the spline fits are more appropriate. The spline fits have higher adjusted correlation coefficients and smaller sums of squared residuals and thus clearly have a closer fit to the data albeit ignoring the fact that it is not clear how to evaluate the appropriateness of the added complexity of the spline model. It would appear that there is a systematic error towards over-prediction for the linear and power law models and the author suspects that such systematic errors would not be detected by simple statistical tests as they are “swamped” by the random errors associated with the data points as appears to be the case here. What is required in such cases are more diagnostic statistical tests of trends in the residuals. The author has not found a spline model applied to solar cell or brittle material oblique data in previous literature, but it has been observed that metal targets show a distinct transition in behaviour at a critical angle and thus it is not unlikely that this phenomena should be observed for solar cell targets.

Even though 45° was chosen as the switchover point between the two functions it was not possible to fit both parts of the spline through this point. The gradient of the spline at angles above 45° was significantly higher for the major axis than for the minor axis resulting in the intercepts of the two parts of the splines occurring at 40° and 35° respectively. This could signify that the minor axis starts to decrease with impact angle before the major axis, which may be due to more of the impact energy being propagated along the line of flight rather than transversely, thus enhancing the major axis.

* Values of χ^2/v less than 1 *do not* signify a “really excellent” fit; clearly your regression should not make the data significantly less variable than the variance due to random errors.

Pit diameters

Figure 5.24 shows the variation of pit major and minor axis with impact angle. There is no significant correlation.

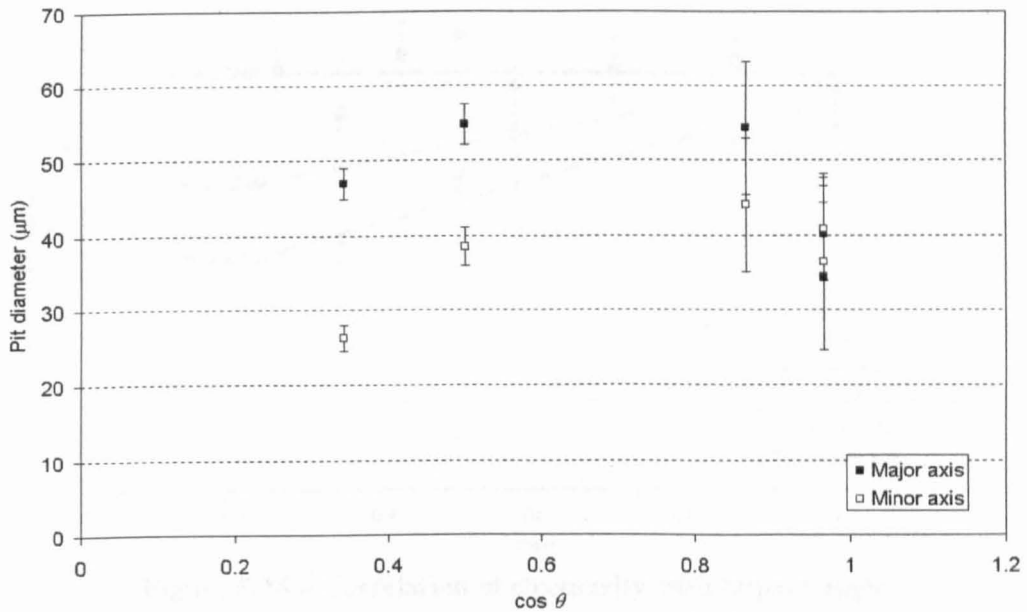


Figure 5.24 – Correlation of pit diameter with impact angle

Shatter diameter

The variation of shatter diameter with impact angle (Figure 5.25) does not show any clear correlation.

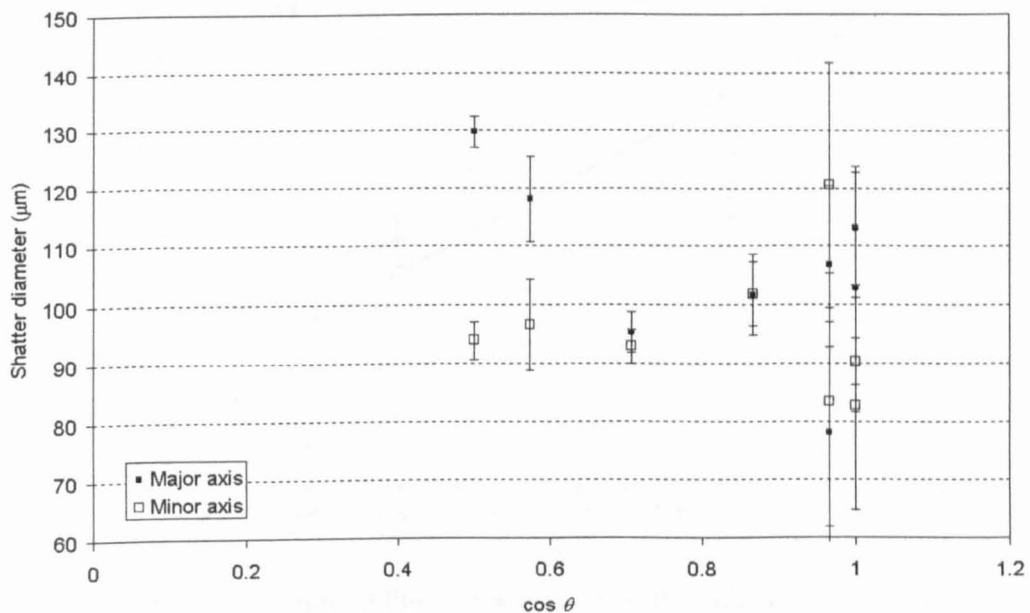


Figure 5.25 – Correlation of shatter diameter with impact angle

Circularities

Figure 5.26 shows the correlation of the circularity (B/A) of the three crater diameter parameters with impact angle. The conchoidal circularity shows no significant correlation with impact angle. The correlation of the shatter zone circularity is not highly significant for this small amount of data. The probability of this sample being observed if the population is uncorrelated with impact angle is 22%. The corresponding probability for the pit circularity is only 4% and thus it is more likely that

the pit circularity is correlated with impact angle and would be considered “significant” at the usual 5% level.

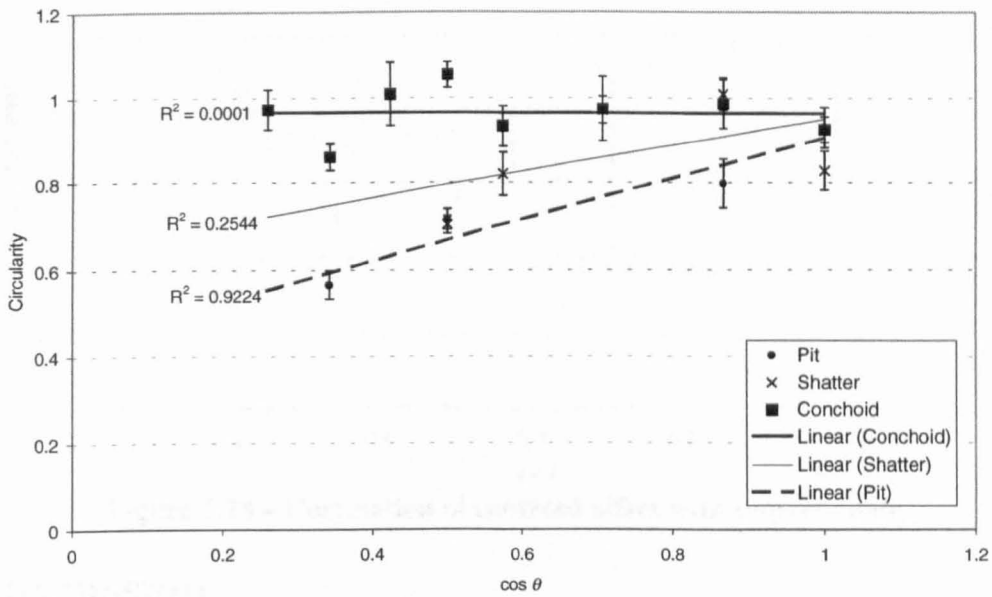


Figure 5.26 – Correlation of circularity with impact angle

A weighted least squares fit to pit circularity data (Figure 5.27) gives a linear relationship of $y = 0.44 \pm 0.07 + (0.49 \pm 0.12)\cos\theta$; alternatively a power law fit gives $y = (0.92 \pm 0.05)\cos^{(0.41 \pm 0.07)}\theta$.

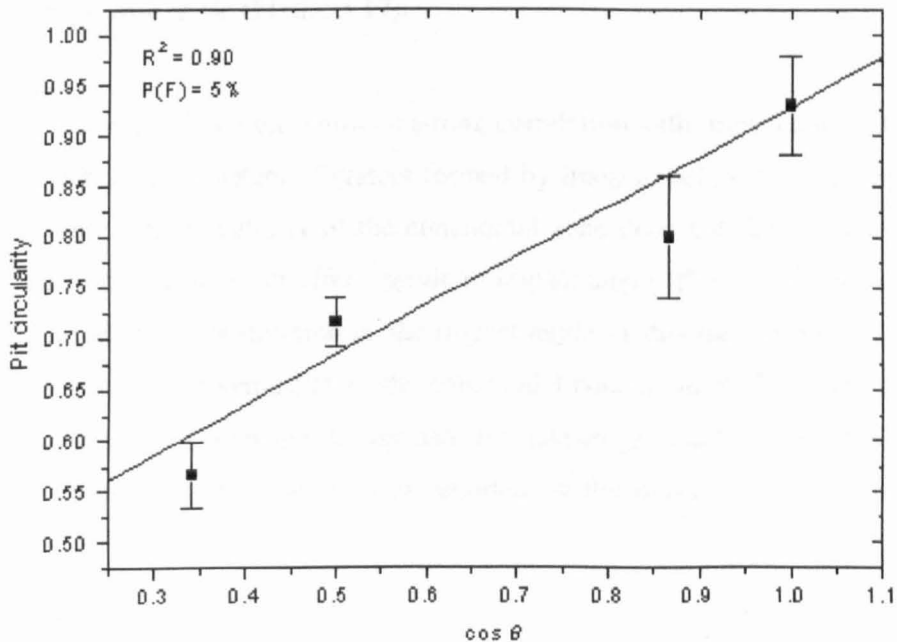


Figure 5.27 – Weighted linear least squares fit to pit circularity data

Centroid offset

Contrary to previous analysis of this data, based on fewer shots (Shrine *et al.*, 1996) the centroid offset shows no correlation with impact angle (Figure 5.28). Previous analyses did not test the significance of any correlation and the author suspects that such a test would have shown the correlation to be insignificant.

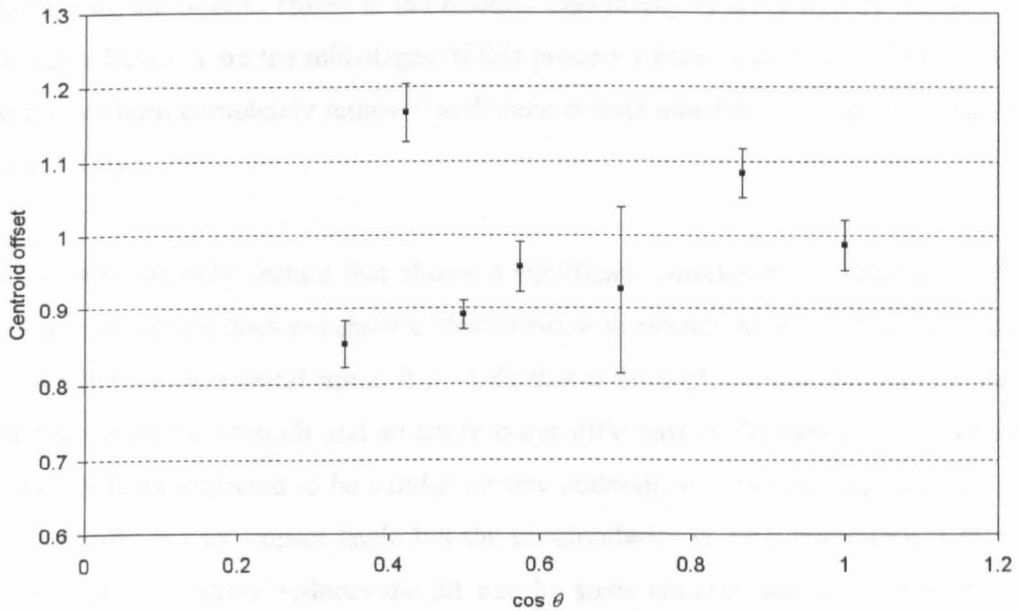


Figure 5.28 – Correlation of centroid offset with impact angle

5.5. Discussion

5.5.1. Dependence of solar cell crater parameters on impact angle

A first key observation regarding the effect of impact angle on solar cell crater morphology, shown by the results in this section, is that unlike metal craters there does not appear to be a simple progression in shape with angle (Figure 5.17).

Conchoidal zone

The diameter of the conchoidal zone shows a strong correlation with impact angle above 45° angle of incidence. Conchoidal diameters of craters formed by impacts below 45° are consistent with a common mean value. The circularity of the conchoidal zone does not show any correlation with impact angle and therefore does not offer a guide to impact angle. The size of the conchoidal zone of course does not allow reconstruction of the impact angle as this has a primary dependence on projectile size. The sustained symmetry of the conchoidal zone at all angles is consistent with the theory that this region of damage is formed by late-stage cracking of the target as the hydrodynamic expansion of the central pit is retarded by the material further from the point of impact.

Shatter or “plateau” zone

The next concentric damage feature in from the conchoidal zone is the shatter zone, which on SEM images of some space craters and on most of the craters from these experiments appears to form a raised plateau. The shatter zone does not show any significant correlation in size or symmetry with impact angle. The author does not agree with Yano’s (1995) interpretation of these plateau regions as being “flattened projectiles stuck at the bottom of the crater”. We do not see any flattened soda-lime glass projectiles in the aluminium craters from the corresponding buckshot. The author suspects that the plateau region is the base of the transient crater formed early in the impact process. At later stages of the impact surrounding material bounded by radial and concentric cracks

is ejected leaving the plateau region in the middle. This theory is supported by the observation of what the author believes are the mid-stages of this process where platelets have been lifted but not all of them have been completely removed and some remain attached to the plateau region (Figure 4.6, section 4.1.3).

Central pit

The central pit is the only feature that shows a significant correlation in circularity with impact angle. The size of the pit does not show a clear trend with impact angle. It is believed that the pit forms in a similar way to a metal crater. It is likely that at the high energies achieved at the point of impact that the material strength and structure plays little part in the initial crater formation and thus craters would be expected to be similar for any material. It is not obvious why the pit size is apparently not affected by impact angle but the pit circularity is. One conjecture is that the late-stage ejection of the material reduces the pit size by some amount that is independent of impact angle whilst still retaining the overall shape of the pit.

5.5.2. Comparison with aluminium craters

Crater size

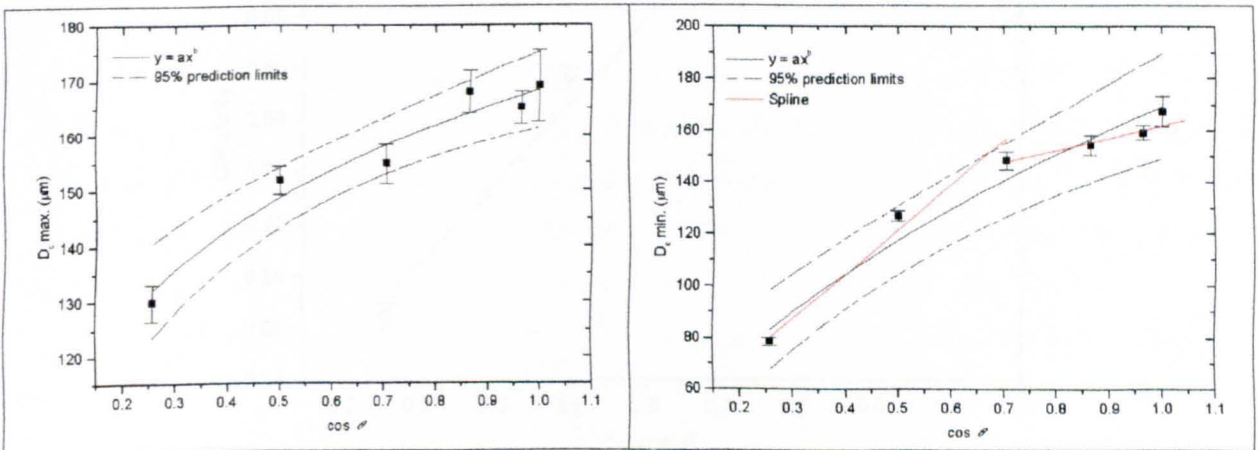


Figure 5.29 – Weighted least-squares fits to aluminium crater diameters: in-line (left); transverse (right)

Figure 5.29 shows weighted non-linear least squares fits to the aluminium crater major (in-line) and minor (transverse) axes for the craters in aluminium targets for this experimental programme; a linear fit gave a significantly poorer fit.

Table 5.17 – Coefficients for fits to aluminium data

Axis	a	b	R^2	χ^2/ν
Major	168 ± 2	0.18 ± 0.02	0.95	1.13
Minor	169 ± 6	0.53 ± 0.06	0.96	10.5

The coefficients, correlation coefficients and standardised χ^2 statistics given in Table 5.17 indicate that a power law model is appropriate for the major axis (for this data), but that another model may be more appropriate for the minor axis. Consequently, a linear spline with a *knot* point at 45° is also shown for the minor axis.

When compared to the solar cell conchoidal diameter $\cos\theta$ coefficients of 0.88 ± 0.06 and 0.99 ± 0.12 (Table 5.12 and Table 5.14) for the major and minor axes respectively, the aluminium craters show a significantly smaller dependence on impact angle. The two materials show similar behaviour in that the minor axes of both is more sensitive to impact angle and decreases in size with impact angle more rapidly than the major axis.

Crater circularity

Figure 5.30 shows a weighted linear spline fit to the aluminium crater circularity data with the gradient above 45° being 0.1 ± 0.1 and below 45° 0.7 ± 0.1 . This is compatible with a previous study by Gardner and Burchell (1997) who fired cellulose acetate (density 1.4 g cm^{-3}) 1.5 mm spheres at aluminium targets (single impacts only as opposed to buckshot) at 12 angles from 0 to 80° inclination. They found that above 44° the circularity is linear with $\cos\theta$ with a gradient of 0.091 and 0.742 below 44° (no uncertainties provided on these values quoted to 3 decimal places).

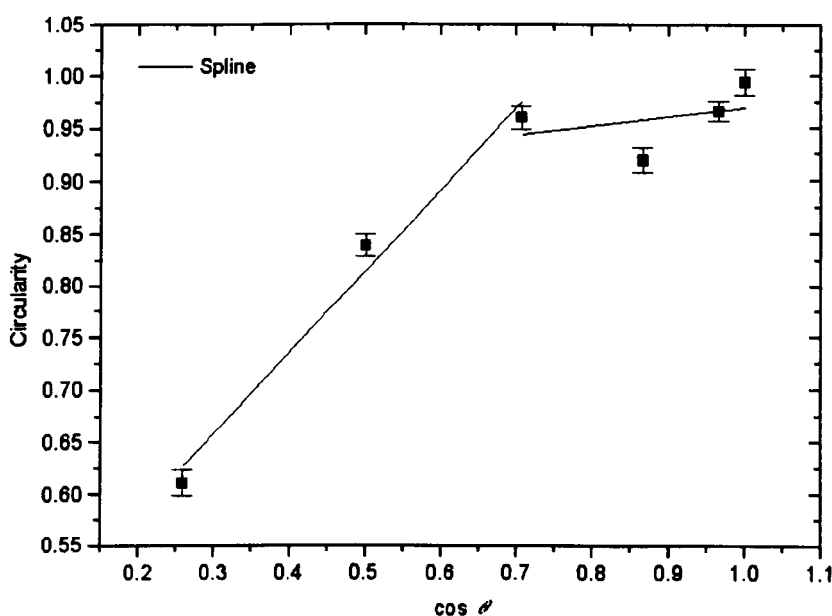


Figure 5.30 – Spline fit to aluminium crater circularity

Despite the conchoidal minor axis decreasing in size at a faster rate than the major axis the difference is not enough to produce a significant correlation of conchoidal circularity with impact angle. This exposes the limitations of the precision of this experiment in that although the coefficient for the major axis of 0.88 is significantly different from 1 , the coefficient for the minor axis of 0.99 is not significantly different from 1 or 0.88 . The aluminium circularity gives a better guide to impact angle than the conchoidal zone above 45° at these speeds. The slope of the pit circularity linear relationship with impact angle is 0.49 ± 0.12 , but as pits were only observed for 4 impact angles we cannot tell if there is a transition from a shallow slope below a certain angle to a steep one and therefore whether the observed gradient is an average of these.

5.5.3. Comparison with space impacts

The immediately obvious difference between the space craters and the ones from this experimental programme is the absence of clearly defined smooth round pits in the laboratory craters. The space

craters display a prominent central pit as seen on lunar microcraters (Hörz *et al.*, 1971), surrounded by a highly fractured zone. However, the morphology of crater s117.001 and s155.003 (Figure 4.6, section 4.1.3) observed on the space retrieved HST solar cells show some degree of similarity with the laboratory impacts in that they have a distinct raised plateau region. These similar space craters are roughly the same size (few 100s of μm) as the laboratory craters with the other space craters generally being 50 μm or less. Thus, it seems that morphology is dependent on absolute size, unlike aluminium craters which look the same whatever size they are. It is most likely that the difference in morphology between the space impacts and the laboratory ones is due to the difference in impact velocity; Hörz *et al.*, (1971) quote a velocity of 10 km s^{-1} as being necessary for formation of a smooth, glass-lined pit. This could provide a significant clue to discerning meteoroid and space debris impacts as space debris has normal encounter velocities below 10 km s^{-1} . Furthermore, it could be that at the high energies associated with space impacts the temperature achieved is higher making the pit and surrounding material more molten than for slower impacts. If this is the case then the material close to the point of impact in a slow laboratory impact will be less molten and therefore more brittle and more susceptible to being dislocated by cracking. This would explain the general absence of well-defined pits for the laboratory impacts.

5.5.4. Comparison with previous work

The most widely published and referenced previous study of oblique impact on solar cells is that of Paul *et al.* (1997). However, they only cover 4 impact angles of 0° , 30° , 45° and 60° . Their data was not taken at a constant particle size and velocity for each impact angle. Particle size, velocity and impact angle are all varied over the 36 shots and a power law is fitted in against these three regressors for both conchoidal and pit *geometric mean* diameters, where the geometric mean of the in-line and transverse diameters. They find that the conchoidal diameter scales as $\cos^{0.601}\theta$ and the pit diameter as $\cos^{0.150}\theta$. No uncertainties in any parameters are discussed, either in the experimental data or the fitted coefficients quoted to 3 decimal places. The author suspects that with only 4 angles the pit diameter exponent is probably not significant and that no significant correlation with impact angle can be ascribed to the pit diameter.

5.5.5. Summary

This experimental programme has covered more impact angles for laboratory based oblique hypervelocity impacts on solar cells than any previous study to the author's knowledge. The issues involved with using the buckshot technique have been identified and discussed, namely velocity and size dispersion *within* and *between* shots and the choice of the appropriate variates and associated uncertainties. The author also presents – for the first time to his knowledge – an instructive variance model for the light-gas gun buckshot experiment. In the author's opinion this model should be refined and the appropriate formal statistical analysis of the model be identified. Some type of analysis of variance (ANOVA) method is called for. ANOVA specifically addresses comparison of variances *within* and *between* samples. This is also the first study to the author's

knowledge where the variation of both the in-line and transverse diameters of oblique hypervelocity solar cell craters has been *separately* analysed. Previous studies (Paul *et al.*, 1997 and Shrine *et al.*, 1996) invariably only study the geometric mean diameter and the circularity.

One of the primary aims of these experiments was to find a parameter that could be used for decoding impact angle. It has been confirmed that the parameter most closely *primarily* related to impact angle is the pit circularity. Other parameters such as the conchoidal diameter show a strong correlation with impact angle but as diameters are *also* related to other projectile parameters do not offer a guide to impact angle. Although the post-flight analyses of the EURECA and HST solar arrays identified the centroid offset as a candidate for a guide to impact angle, no significant correlation was observed in these experiments.

The fact that pits were not consistently observed for all angles in this experimental programme means that light-gas gun simulations at these velocities and projectiles sizes are inappropriate for determining the relationship between pit circularity and impact angle, but nevertheless we had to do the experiment to learn this. With the current development of the Unit's light-gas gun velocities upward of 6 km s^{-1} are now attainable and efforts continue to further enhance the velocity to approach 7 km s^{-1} . Impacts at 6 km s^{-1} and 7 km s^{-1} give us an energy enhancement of 44% and 96% respectively, which may be sufficient to produce pit features more closely resembling the ones observed in space impacts.

The result of primary interest from this study is that the conchoidal diameter appears to show two distinct regimes of dependence on impact angle in a similar manner as has been observed for metal craters. This has not been reported previously to the author's knowledge in that previous studies based on, at most, 4 impact angles employ a monotonic power law over the whole range of impact angles. Previous modelling of solar cell impact fluxes based on these empirical equations (Paul *et al.*, 1997 and Taylor *et al.*, 1999) will most likely have a systematic error*. The conchoidal diameter shows a higher sensitivity to impact angle than aluminium crater diameters, which implies that the size distribution of solar cell impacts may have a different *shape* to the corresponding distribution of aluminium craters for surfaces that encountered a statistically identical flux of impacting meteoroids and space debris.

5.5.6. Follow-up experiments

High velocity experiments

The author initiated a second series of experiments using the Unit's 2 MV *Van de graaff* electrostatic accelerator, which is capable of accelerating micron sized projectiles to several tens of km s^{-1} . The first part of this experimental programme was aimed at studying oblique impacts by placing a cylindrical glass rod in the beam line, such that many impact angles could be attained in a single run (Figure 5.31).

* Not to mention, for the time being, the questionable application of gas-gun speed relationships to space impacts.

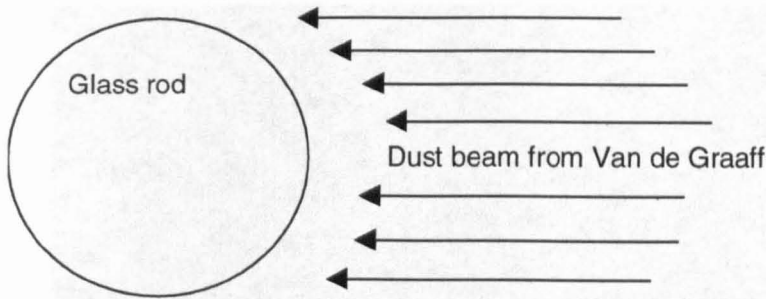


Figure 5.31 – Oblique glass impacts using the Van de Graaff

The projectiles used were boron carbide dust grains of around 1 μm in size (Figure 5.32). It can be seen that the projectiles are highly irregular. Furthermore, the velocity of each impact is unknown and could range from $\sim 1\text{-}10 \text{ km s}^{-1}$. Thus the quantitative analysis of this data will be complicated by these two factors. At this time this experimental programme is still in the trial stages but some initial qualitative observations can be made of the first impacts located. The Van de Graaff operator estimates that there were $\sim 18,000$ impacts on a 20 mm length of the approximately 10 mm diameter glass rod.

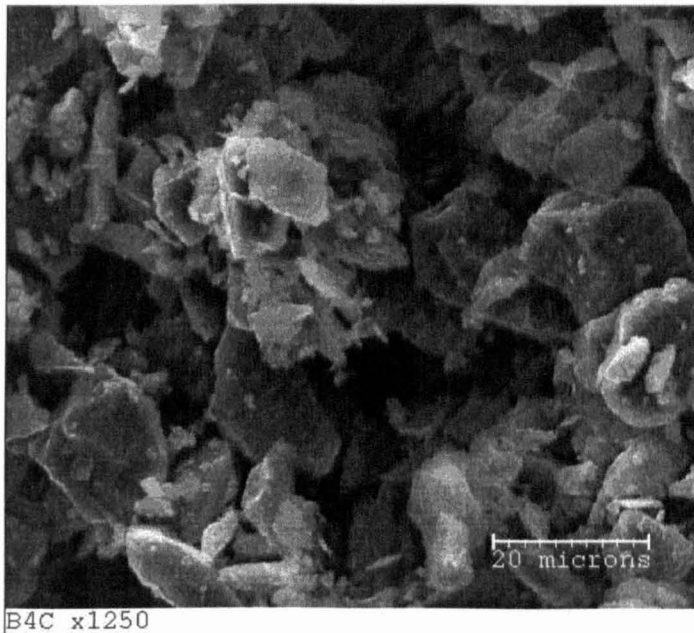


Figure 5.32 – Boron carbide dust grains used for Van de Graaff experiments

The author scanned the glass rod in the SEM and was able to locate ~ 20 impacts. These are shown in appendix D. It can be seen that no clear pits are produced mimicking the space morphology (Figure 4.6, section 4.1.3). A typical impact is shown in Figure 5.33 showing a highly cracked region in the centre with a surrounding conchoidal zone. This impact and some of the others (appendix D) resemble to some extent the butterfly morphology observed for space impacts (Figure 4.5, page 115). It is still not known if these are due to the impact angle or due to high aspect ratio projectiles. As this morphology was not observed for the impacts using spherical projectiles in the light gas gun, but is observed for the irregular projectiles used here, weight is added to the case for projectile shape being responsible for this morphology.

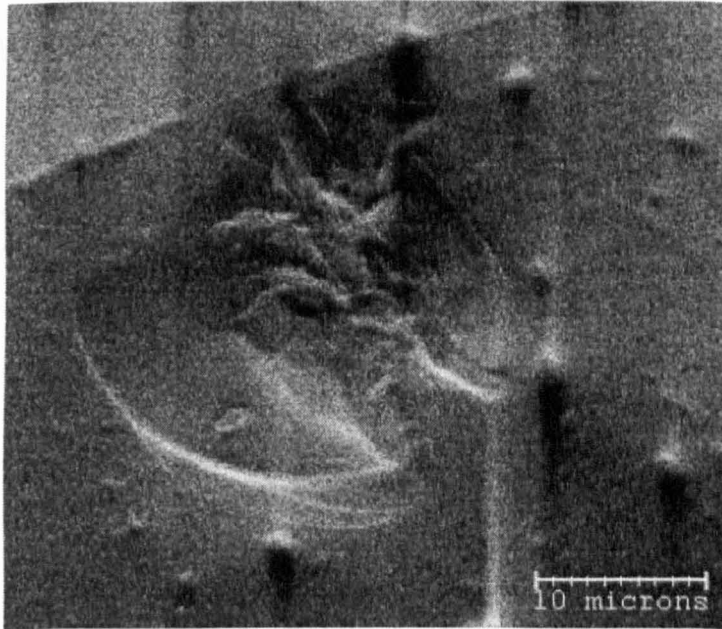


Figure 5.33 – Boron carbide impact on glass rod in Van de Graaff

Crushing of buckshot projectiles in the light-gas gun

The question has been raised on several occasions of whether buckshot projectiles survive launch in the light-gas gun or are fragmented by the forces at launch (Barrett *et al.*, 1992). The results of this experimental programme are dependent on whether the projectiles survive launch and hence how closely that which arrives at the target is matched with what was loaded in the gun in terms of size and shape. This has only been indirectly investigated to the author's knowledge and thus an experimental programme was performed to specifically address this issue presented in the next section.

6. Survivability of buckshot projectiles upon launch in the light-gas gun

The aim of this study is to determine if buckshot projectiles survive launch in a light-gas gun, specifically the UKC facility. This is done experimentally by firing various typical buckshots in the light-gas gun and comparing the size and shape of the projectiles arriving at the target to the buckshot that was initially loaded in the sabot. To determine the size and shape of the projectiles arriving in the target chamber thin foils are mounted perpendicular to the line of flight to intercept the projectiles such that they punch out their cross-section. Various complications need to be considered in this approach.

Firstly, the assumption that a particle will punch out its cross section is only valid for a sufficiently thin foil. It is well known that hypervelocity impact craters are generally circular in an infinitely thick target and do not generally reflect the shape of the impactor unless it has a high aspect ratio and impacts with its long axis parallel to the target surface. There is a transition - considered gradual - between this behaviour and thin target behaviour where the perforation in the target is highly correlated in size and shape with the cross section of the impacting projectile. Although the behaviour as regards the relationship between hole *size* and projectile size, for spherical projectiles *only*, has been mapped out over a wide range of target thicknesses (Gardner *et al.*, 1997a), the behaviour of hole *shapes* has not. In particular the author has not found any literature that tells us what we can infer about the shape of the impacting particle from the shape of a thin target perforation for a given hole-size-to-target-thickness ratio. Therefore, by using different thickness foils and projectiles with markedly different shapes this study may also produce some preliminary indications of the effect of relative target thickness on hole *shape*. If highly irregular holes are observed then it is clear that this is a reflection of the particle shape. The ambiguity arises when holes are approximately circular. Was the projectile circular or was it irregular but its shape was obliterated in the impact process?

Another complication in this study is that we cannot be sure that all the material arriving at the target originated in the sabot. When the light-gas gun is fired there is invariably a layer of soot coating the target after the shot. Additionally, a few smaller impacts around the target area are often visible when a single projectile - a 1 mm ball bearing for example - is launched indicating that some other material is also in flight with the primary projectile. The consensus among experimenters who use the gun is that this miscellaneous material comprises such things as pieces of the sabot, burst disk and piston. Therefore, there is the problem of discerning between holes made by projectile material loaded in the sabot and a general background of shot debris. However, the majority of this debris is micron scale soot with a rapid fall off in number with increasing size. The amount of debris will by no means be as abundant as the projectiles at the sizes of buckshot used. Consideration of a debris inclusion will still need to be made however and is expected to

show up as a population of small holes that may or may not vary between shots depending on the operation of the gun.

The projectiles first chosen for this study were “50 μm ” glass beads as used for the experimental programme in section 5. The question to be answered of primary importance to this thesis - and many other experimental programmes that use these projectiles - is do the soda-lime glass projectiles reach the target intact? As already mentioned, the presence of circular holes in the foil is not entirely conclusive that the projectiles did not fragment. Admittedly a narrow size distribution of circular holes would be fairly compelling evidence on its own that fragmentation did not occur, nevertheless other projectiles with highly irregular shapes were also used to contrast with the circular glass beads. As well as testing the degree to which projectile shape is reflected in hole shape, using these irregular projectiles will also test for their survivability upon launch. The irregular projectiles chosen were samples of the minerals enstatite and kamacite, which were suitable not only because of their high aspect ratio but also because these are materials that are frequently used as meteorite analogues in impact experiments. Thus, the survivability of these projectiles to launch is of direct concern to previous and ongoing experimental programmes.

6.1. Experimental method

6.1.1. Targets

The targets were chosen from the Unit’s stock of aluminium foils. 3 of the thinnest foils were chosen having measured thicknesses of 30.9 μm , 12 μm and 5 μm to around 5% accuracy. The author decided that it was not necessary to re-check the thickness of the foils as the uncertainty of the existing measurement was small enough for the purposes of this experiment where the primary analysis is concerned with the distribution of hole shapes and sizes. The parameters of these distributions are not regressed against foil thickness in this study.

The target arrangement is shown in Figure 6.1. Two foils were used for each shot mounted parallel to each other and perpendicular to the line of flight of the projectile. The foils were separated by a distance “x” shown in Figure 6.1 that was maintained at 49 mm to within about 1 mm tolerance, given that the spacing was achieved by flexible rubber tubes. Again, this accuracy was acceptable in that the spacing is not a critical parameter of the analysis. Two aluminium stop plates, each around 1 mm thick and separated by an estimated 30 mm, were placed 130 mm behind the second foil to stop the projectiles after exiting the rear face of the foil. It was decided to mount the two foils as far away from the stop plate as was feasible to minimise any ejecta from the ball bearing impact on the stop plate coming back through the foils and thus giving ambiguous results. However, as the same arrangement was used for all the shots, any *variation* in ejecta inclusion should be statistically small-to-negligible over the entire programme and thus not greatly complicate the interpretation of *comparisons between* the hole distributions.

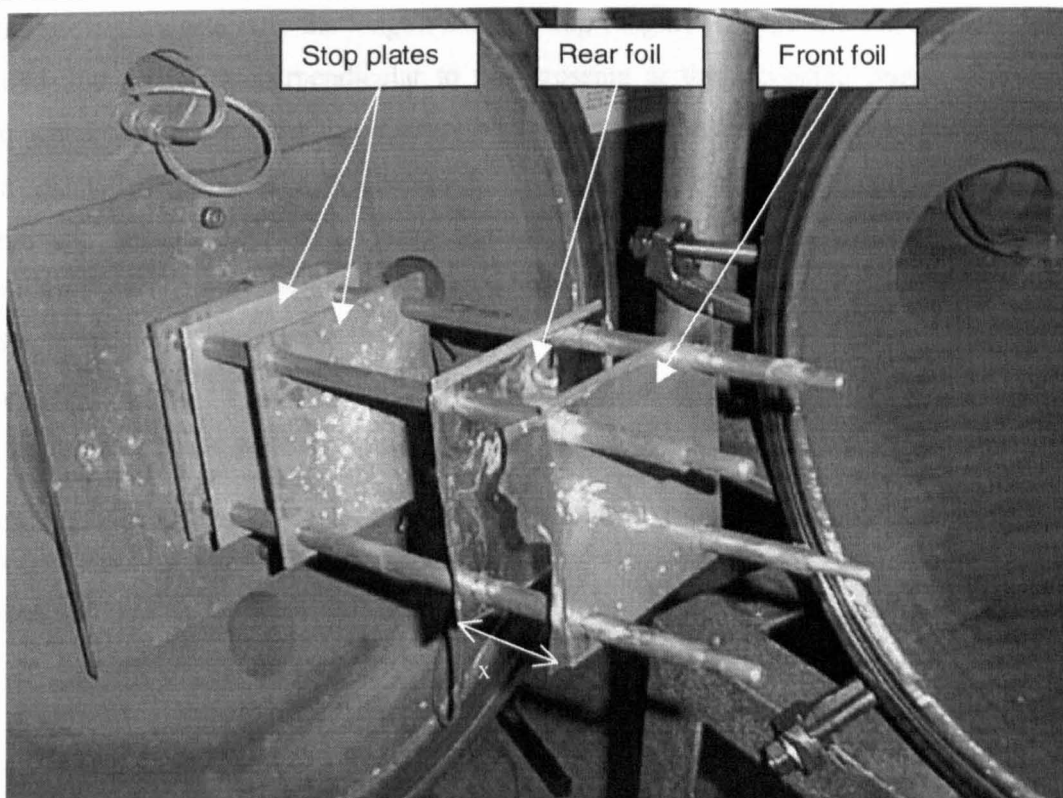


Figure 6.1 – Target configuration

6.1.2. Projectiles

The first set of projectiles used were nominally “ $53 \pm 1.5\% \mu\text{m}$ ” soda-lime glass beads as used for the experimental programme in section 5. The author decided to measure a sample of these in the SEM to check their size and shape. If the beads are indeed highly circular then one would expect them to make highly circular holes, if they remain intact. For comparison irregular projectiles were chosen from a stock of meteorite mineral analogues kindly donated by D. Wallis. The minerals with the highest length-to-width ratio were chosen to give the highest contrast to the glass spheres. *Enstatite* was chosen first, as the sample appeared to consist of long shards. Based on preliminary inspection of the enstatite shot results the author decided that projectiles with a higher aspect ratio were required and thus *kamacite* was chosen. A summary of the projectiles’ material properties* is given:

- *Soda-lime glass beads*: Density 2.56 g cm^{-3} ; highly spherical; hardness unknown.
- *Enstatite* (MgSiO_3): Density $\sim 3.5 \text{ g cm}^{-3}$; hard (Vickers 600) but brittle; has 1 cleavage along which it often breaks.
- *Kamacite* (*Fe* 94%, *Ni* 6% by weight): Density $\sim 8 \text{ g cm}^{-3}$; heat treated to harden to around Vickers 500; ductile with no important cleavage planes.

The soda-lime glass beads were imaged and measured in the Unit’s SEM by the author. Both had to be sputter-coated with a few nm (~ 25) of gold for this. Figure 6.2 and Figure 6.3 show some sample SEM images showing the measurements made for the glass and enstatite projectiles. For the

* Description of properties in e-mail from supplier checked against information at <http://minerals.net/>

enstatite projectiles generally the longest axis passing roughly through the centre of the shard was measured and the width perpendicular to this crossing at the estimated centre. The SEM was broken when the author came to measure the kamacite projectiles and so had to use the optical system discussed previously (section 3.3.1). Because kamacite is mostly iron and hence ferromagnetic the shards tended to clump together making identification of discrete pieces difficult. It was found that the best definition of the outline of the kamacite projectiles was achieved when the sample was back lit. Figure 6.4 shows an image of the kamacite shards under normal top lighting and also back lit with measurements shown. Outlines that could not be clearly identified as a single discrete particle were not measured.

Size and aspect distributions

For the size distributions the *arithmetic* mean of the perpendicular length and width measurements was used rather than the often-favoured *geometric* mean as a linear combination of two similarly (functional form) distributed variables will result in a similar combined distribution, whereas a non-linear combination will alter the shape. The author observed this effect in that for all the projectiles the lengths and widths were separately closely normally distributed, however the distribution of geometric means was not as closely normal as the distribution of arithmetic means. The author decided that it was desirable to preserve normality such that the approximation of significance tests associated with a normal distribution would be improved.

Figure 6.5 shows the distributions of the major (A) and minor (B) axes of the projectiles, with summary statistics given in Table 6.1. Figure 6.6 shows the output of the “Descriptive statistics” function in the software package *Minitab*[®] for the *mean-size* and *aspect-ratio* distributions for the soda-lime glass, enstatite and kamacite projectiles respectively. As this type of output is employed frequently in this section the information displayed will be described:

- **Histogram**: In the top-left is the frequency distribution of the variable plotted as a histogram with the best-fit gaussian also shown.
- **Box plot**: Below the histogram is a box plot showing the median, 1st (Q1) and 3rd (Q3) quartiles and the “maximum” and “minimum”, defined as the 0th and 100th percentiles calculated by an extrapolation based on the location of the 1st (25%) and 3rd (75%) quartiles. Thus the 100th percentile is given by $Q3 + 1.5(Q3 - Q1)$. Values lying beyond the maximum and minimum (stalks on the box plot) are likely to be outliers and are represented by dots.
- **Mean, median and confidence intervals**: Below the box plot are graphical representations of the location of the mean and median and their associated 95% confidence intervals. Confidence intervals for the mean and standard deviation are simply looked up from the *student's-t* and *F* distributions respectively (the sampling distributions of the mean and standard deviation of a gaussian) and are relevant if the distribution is approximately normal. Confidence intervals for the median are calculated using the *sign test for a median* discussed in section 2.3.4.

- Moments about the mean: In addition to the variance, the 3rd and 4th moments about the mean, the *skewness* and *kurtosis* are shown: statistics based on the mean of the cube and 4th powers of the deviations about the mean – the variance being the second moment as it is the mean *square* deviation. The skewness is negative for distributions skewed towards the right (greater than the mean), positive for distributions skewed to the left and should be close to 0 for approximately normal distributions. The kurtosis is a measure of the “peakedness” of the distribution and is positive for distributions with a sharp, narrow peak with wide tails and negative if the peak is broad; again this should be close to 0 for a normal distribution.
- Normality test: Also shown is a test for normality: the Anderson-Darling statistic and its associated probability. This statistic is based on the maximum difference between the data’s cumulative distribution and the normal cumulative distribution function. The rationale and detailed formulation of this test is covered by Press (1992), suffice to say that it is a formal alternative to the normal probability plots used in section 5.3.2 and appears to give probabilities above 5% for distributions that appear normal and <0.0% for ones that clearly do not.

It can be seen in Figure 6.6 that all the size distributions are approximately normal, with the soda-lime glass having a tightly constrained size range, the standard deviation being some 2% of the mean. The enstatite and kamacite both have wider size ranges $\sigma = 23\%$ and 24% respectively. The aspect ratio distributions are all non-normal, although not highly so for the soda-lime glass ($P = 1.4\%$). The soda-lime glass beads are highly circular with a small variation in circularity ($\sigma = 2\%$) and tail of lower circularity, “defective” beads. The enstatite and kamacite projectiles have on average (mean or median) an aspect ratio of just over 2:1 with a large variation ($\sigma = 41\%$ for both). In both cases there is a tail of lower aspect ratio particles that the author believes cannot be attributed to long, thin projectiles being viewed end-on.

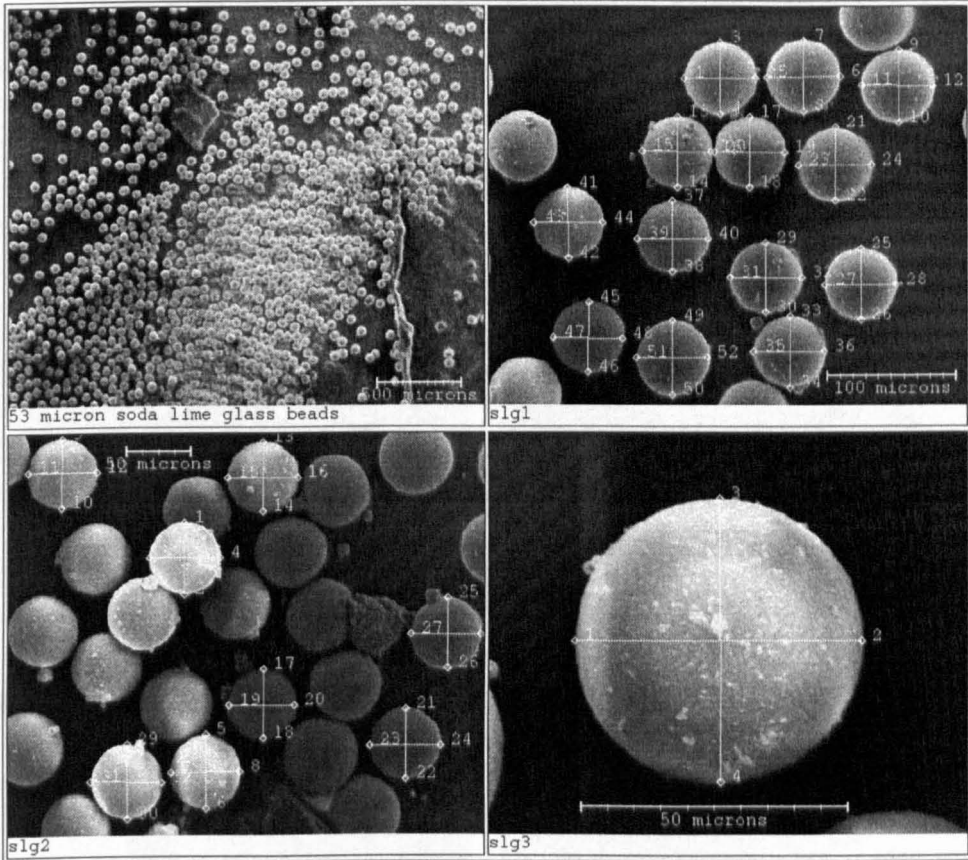


Figure 6.2 – Measurement of soda-lime glass projectiles

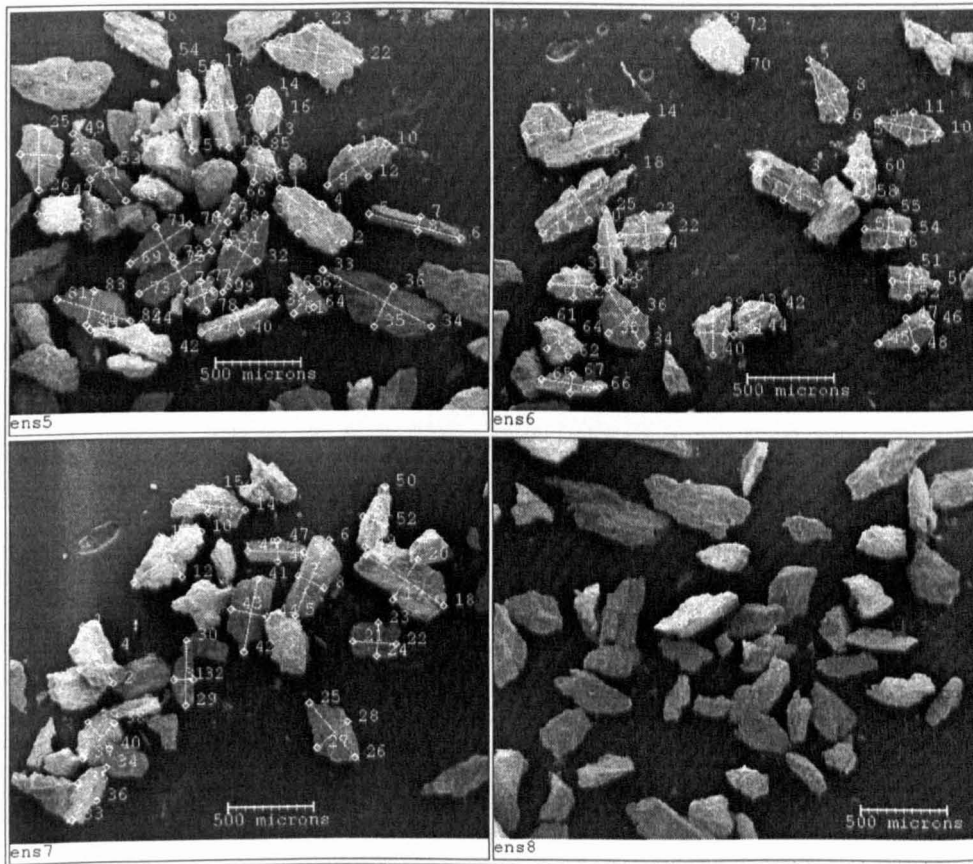


Figure 6.3 – Measurement of enstatite projectiles

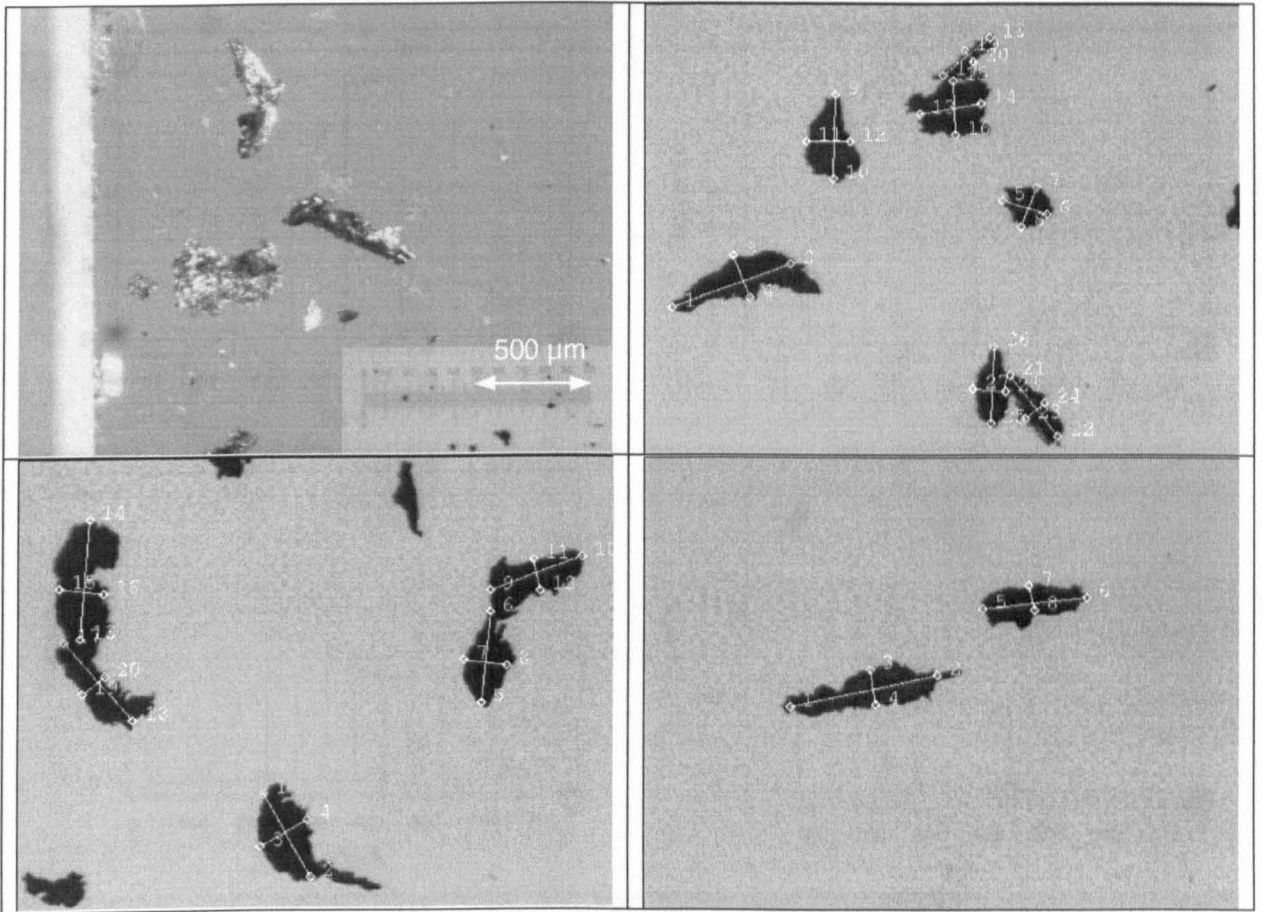


Figure 6.4 – Measurement of Kamacite projectiles

6. Survivability of buckshot projectiles upon launch in the light-gas gun

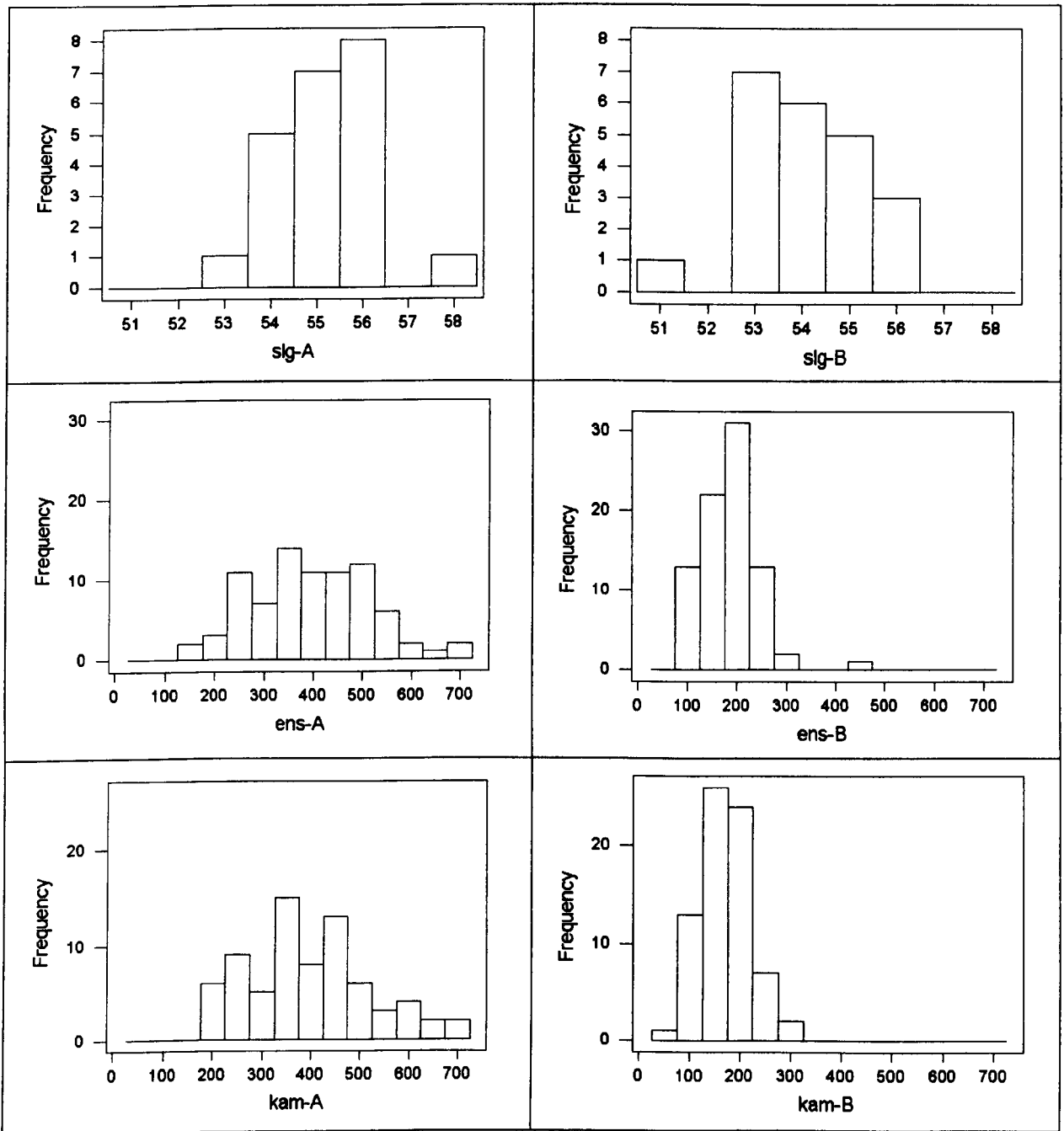
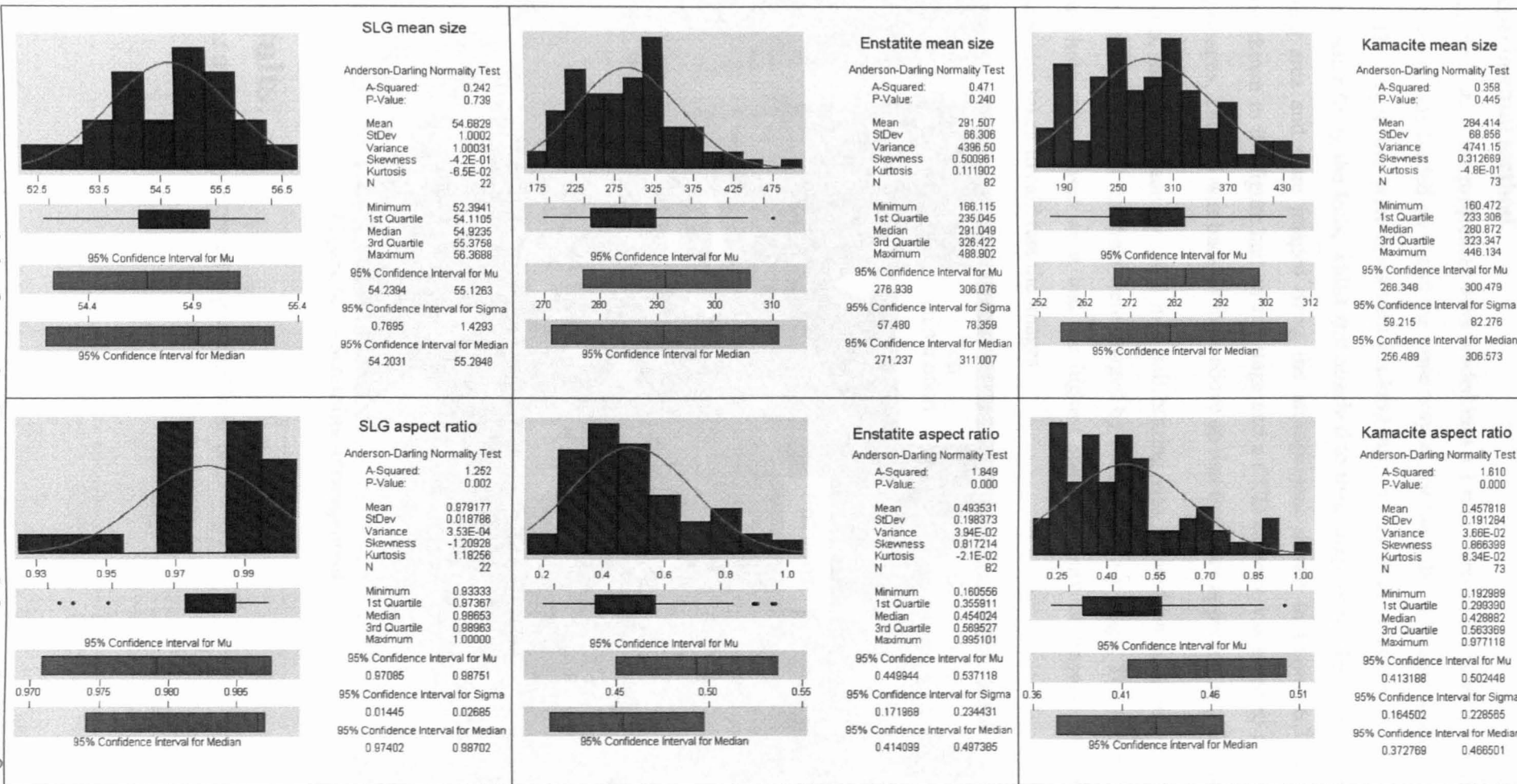


Figure 6.5 – Size (μm) distributions of projectile lengths (A) and widths (B)

Table 6.1 – Summary statistics for projectile measurements

All in μm	Glass beads		Enstatite		Kamacite	
	A	B	A	B	A	B
Mean	55.23	54.14	397.16	185.86	400.86	167.97
Standard Error	0.23	0.26	13.41	6.28	14.52	5.63
Median	54.93	54.20	387.14	180.33	391.88	160.21
Standard Deviation	1.07	1.22	121.39	56.84	124.08	48.07
Kurtosis	0.04	2.38	-0.13	5.57	-0.29	0.19
Skewness	0.48	-0.89	0.32	1.36	0.45	0.47
Range	4.33	5.78	553.24	379.57	506.40	230.53
Minimum	53.48	50.59	163.66	81.78	199.16	60.52
Maximum	57.81	56.37	716.90	461.35	705.56	291.05
Count	22	22	82	82	73	73

Figure 6.6 – Descriptive statistics for projectile sizes (μm) and shapes (*Minitab*® output)



6.1.3. Experimental method

For each of the 7 shots the projectiles were loaded into a 1 mm internal diameter sabot and a 1 mm steel ball bearing was loaded on top in the same way as for the solar cell experiments (Figure 5.1, page 137). The target foils were fixed with masking tape to aluminium plates with a hole or notch cut in them. After firing the foils, whilst still attached to their supporting plate, were transferred to the scanning area and were imaged using the arrangement shown in Figure 6.7. The inverted microscope shown in the figure had an x-y stage and a CCD camera was taped to the eyepiece to record the images. The foil was back-lit from above so that the holes appeared as points of light.

To start with, the hole made by the 1 mm ball bearing was located on each foil and then non-overlapping frames around this hole were imaged by moving the x-y stage. The region nearest the ball-bearing hole was chosen as it had the highest spatial density of impacts. An image of a graticule was also taken to calibrate the images.

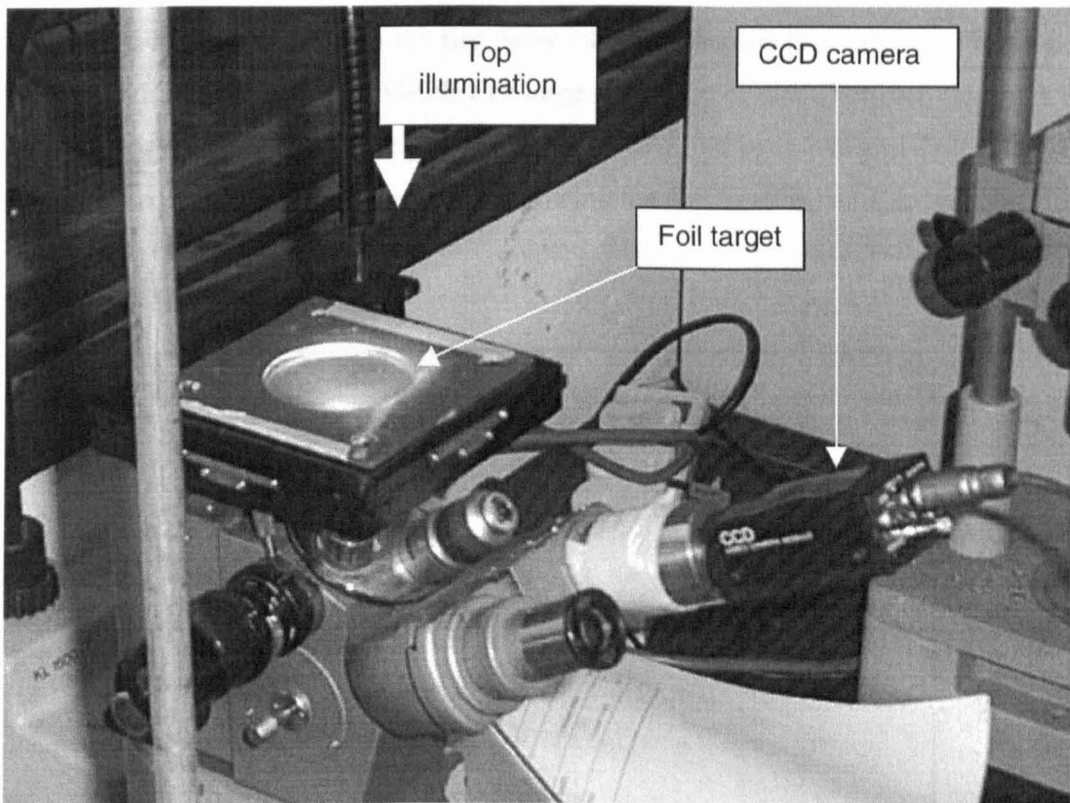


Figure 6.7 – Scanning arrangement

6.2. Results

A summary of the 7 shots performed is given in Table 6.2.

Table 6.2 – Summary of shots performed

ID	Projectiles	Target	Velocity (km s ⁻¹)
Shot 1	Enstatite	30.9 μm Al foil	5.40 \pm 0.05
Shot 2	Glass beads	5 μm Al foil	5.23 \pm 0.05
Shot 3	Glass beads	30.9 μm Al foil	5.51 \pm 0.05
Shot 4	Kamacite	12 μm Al foil	5.25 \pm 0.05
Shot 5	Glass beads	12 μm Al foil	5.14 \pm 0.05
Shot 6	Kamacite	30.9 μm Al foil	5.08 \pm 0.05
Shot 7	Enstatite	30.9 μm Al foil	5.21 \pm 0.05

Shot 1

Projectiles	“120-250 μm ” enstatite buckshot + 1 mm steel ball bearing
Target	30.9 μm Al foil
Velocity	5.40 \pm 0.05 km s ⁻¹
Range pressure	0.21 mb

An example oscilloscope trace from the first laser curtain is shown for shot 1 in Figure 6.8. The passage of the ball bearing is clearly visible as a large peak. The distance between this peak and the corresponding one on the second laser provides the time-of-flight over a known distance and thus a velocity measurement. The cloud of buckshot following the ball bearing can also be seen.

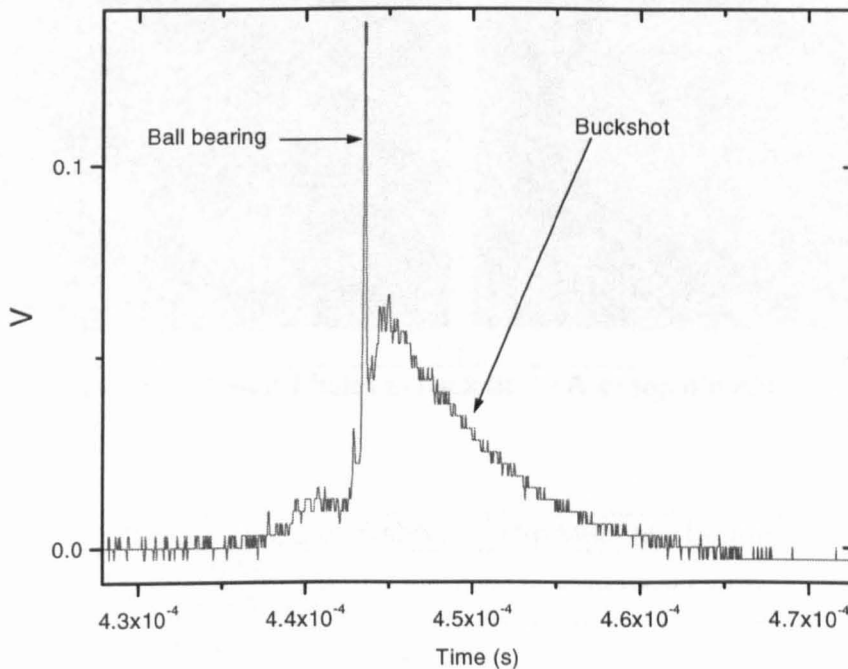
**Figure 6.8 – Shot 1 oscilloscope trace for first laser**

Figure 6.9 shows a negative image of the light visible through the holes in the shot 1 front foil. Note the large (~ 1 mm) hole made by the ball bearing. There was no rear foil used for shot 1.

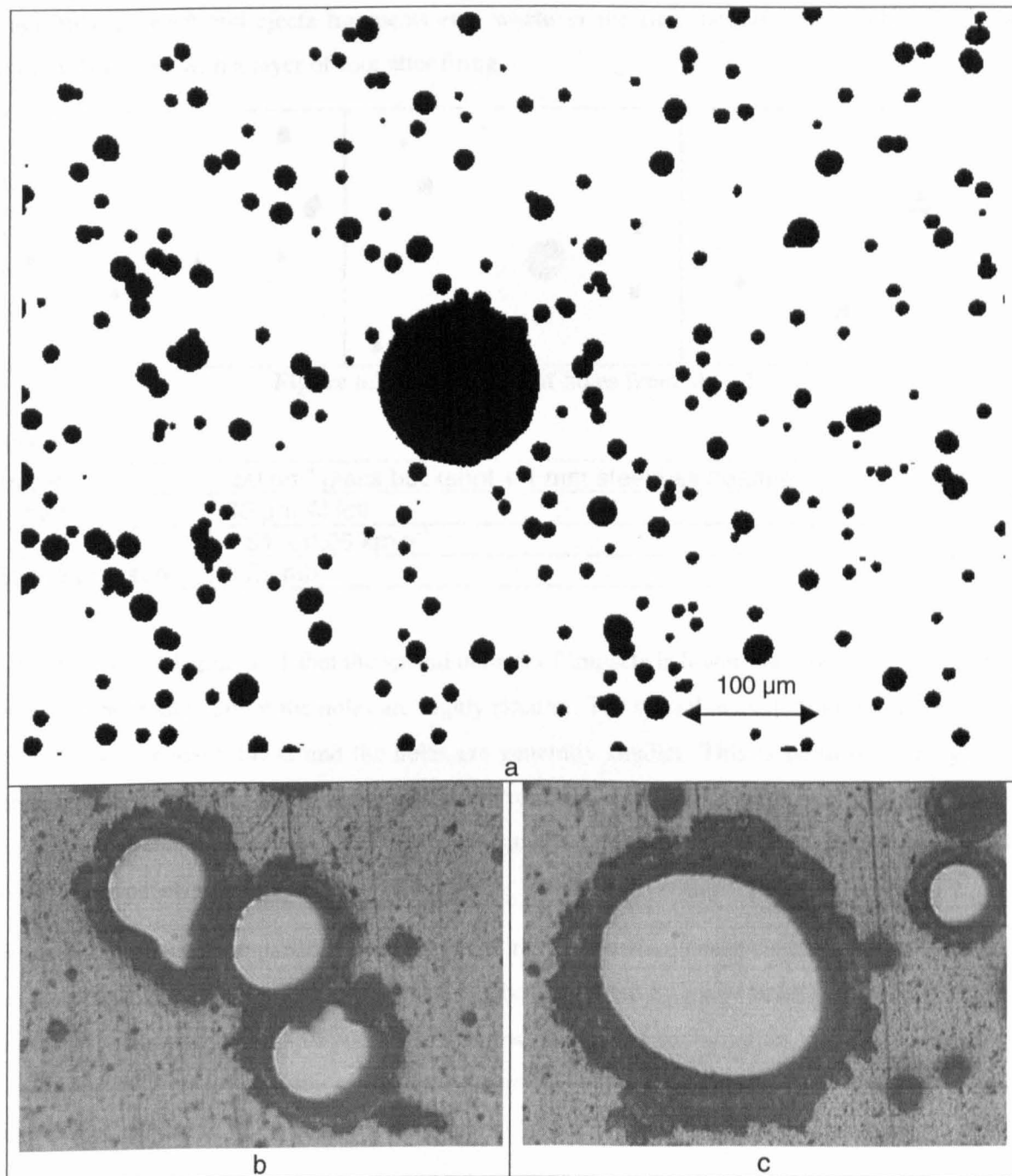


Figure 6.9 Shot 1 holes a) back lit; b) & c) top illumination

Shot 2

Projectiles	"50 μm " glass buckshot + 1 mm steel ball bearing
Target	5 μm Al foil
Velocity	$5.23 \pm 0.05 \text{ km s}^{-1}$
Range pressure	0.33 mb

For shot 2 it was found that the 5 μm foil was much more highly perforated than expected, with many (tens of?) thousands of holes such that the foil was almost transparent when held up to the light. Thus the author decided that a 5 μm foil was too thin for the purposes of this experiment in that it appears that every microscopic piece of debris that enters the target chamber upon firing makes a hole. Note the wide variety of hole sizes and shapes in Figure 6.10. This debris is suspected to comprise burnt powder, the frictionally burnt outer surface of the sabot, piston

fragments, ricochet and ejecta fragments etc.; whatever the shot, targets in the light-gas gun are invariably coated with a layer of soot after firing.

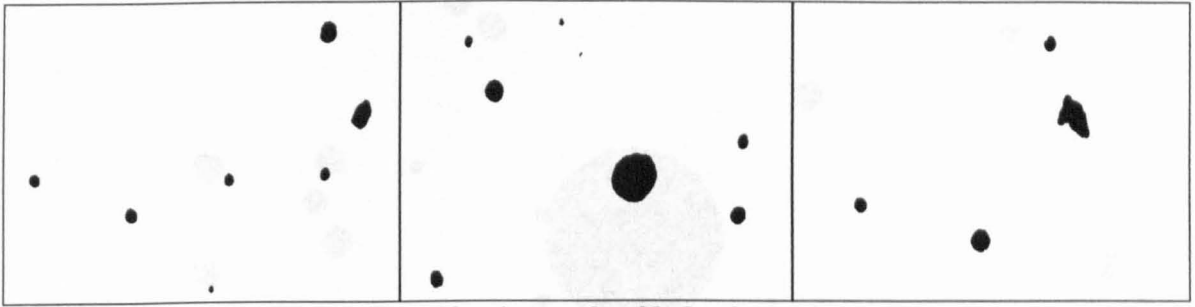


Figure 6.10 – A sample of holes from shot 2

Shot 3

Projectiles	"50 μm " glass buckshot + 1 mm steel ball bearing
Target	30 μm Al foil
Velocity	$5.51 \pm 0.05 \text{ km s}^{-1}$
Range pressure	0.25 mb

It can be seen in Figure 6.11 that the spatial density of impacts is lower than for the shot 1 enstatite buckshot, but that many of the holes are highly circular. The spatial density of holes in the rear foil (Figure 6.12) is much lower and the holes are generally smaller. This is because at the particle-diameter-to-foil thickness ratio used (~ 1.7), the front foil will act as a bumper shield and break up the projectiles upon impact such that the fragments impacting the second foil are smaller such that some do not penetrate.

Figure 6.13 shows a comparison of the front and rear foil surfaces near the ball bearing hole and it can be clearly seen that the rear foil surface has been abraded by many small impacts. With this in mind it was decided to try a thinner foil for subsequent shots such that the particle might survive penetrating the first foil, but thicker than the 5 μm foil so that only the projectile material loaded in the sabot penetrates.

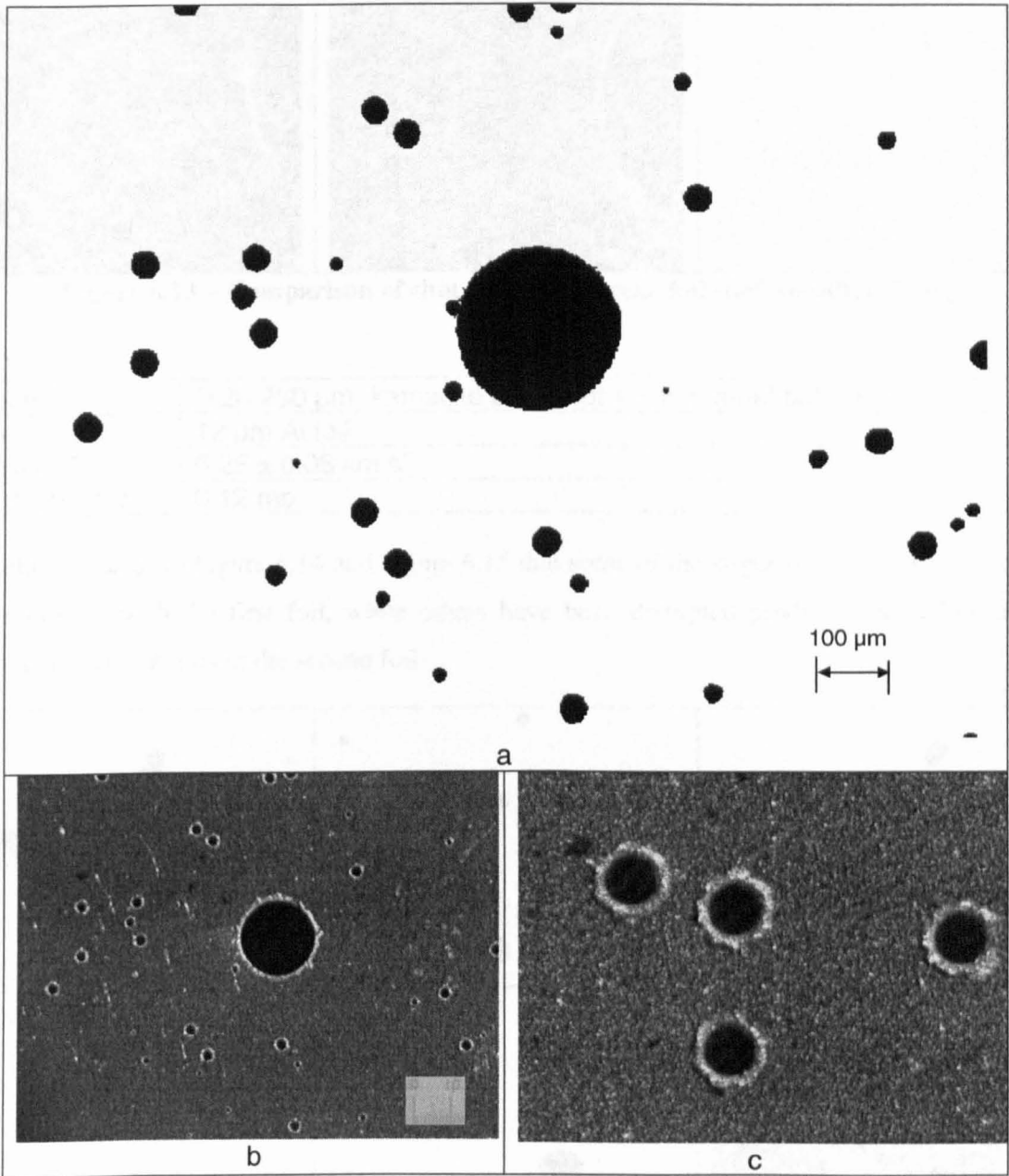


Figure 6.11 – Holes in shot 3 front foil

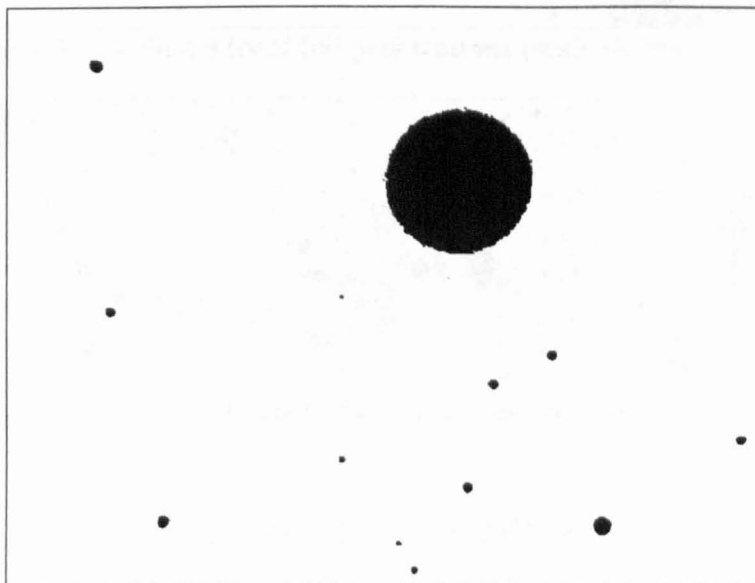


Figure 6.12 – Holes in shot 3 rear foil

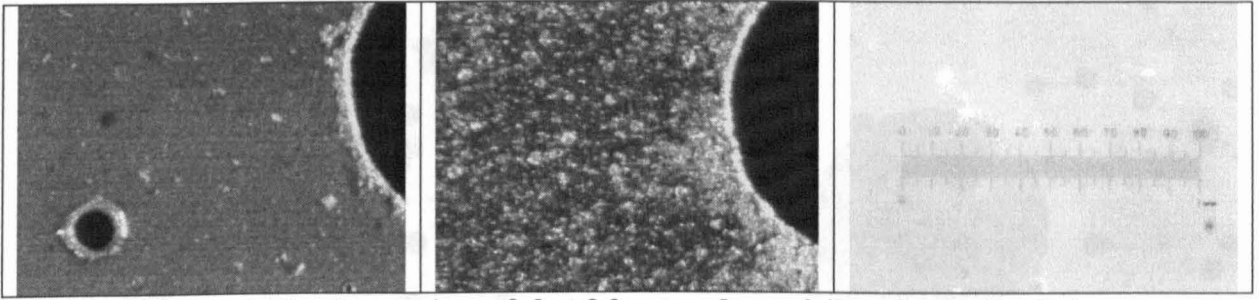


Figure 6.13 – Comparison of shot 3 front and rear foil surfaces after firing

Shot 4

Projectiles	“120-250 μm ” kamacite buckshot + 1 mm steel ball bearing
Target	12 μm Al foil
Velocity	$5.25 \pm 0.05 \text{ km s}^{-1}$
Range pressure	0.12 mb

It would appear from Figure 6.14 and Figure 6.15 that some of the larger projectiles have survived penetration through the first foil, while others have been disrupted producing a background of many small perforations in the second foil.

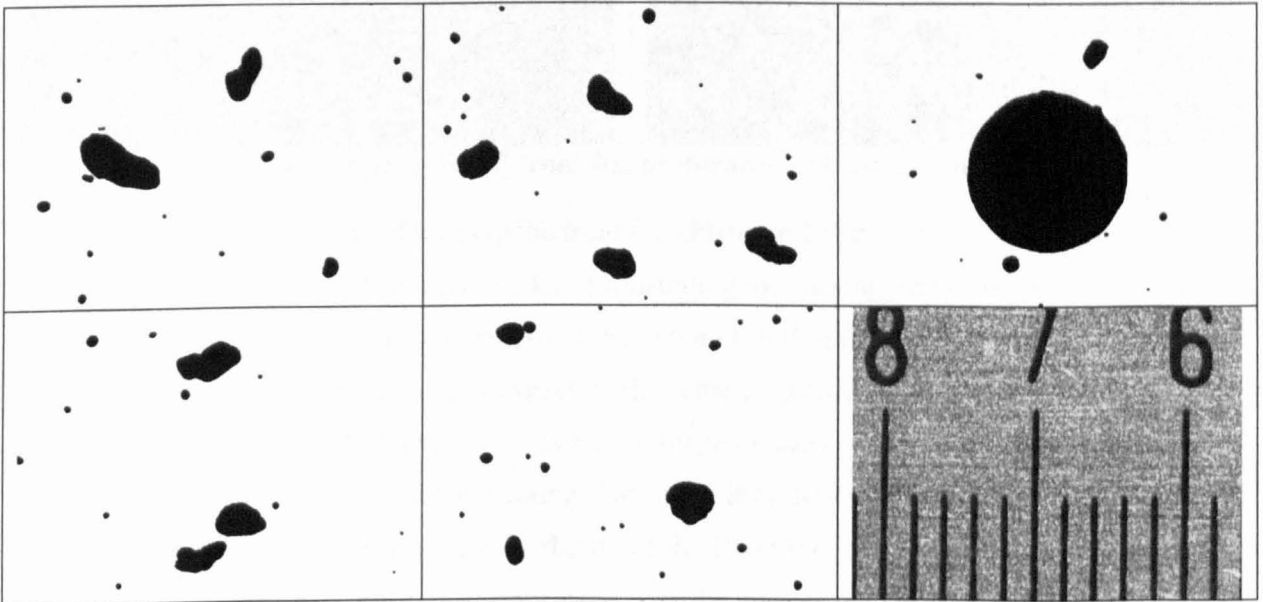


Figure 6.14 – Shot 4 front foil penetrations (scale shown is in mm)

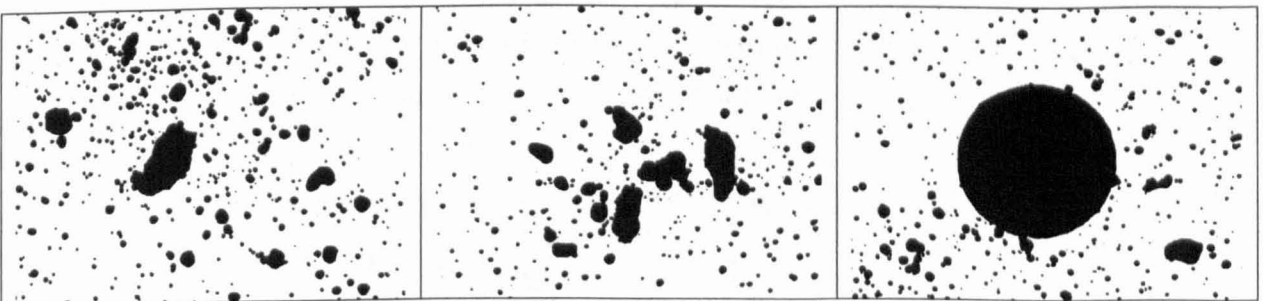


Figure 6.15 – Shot 4 rear foil penetrations (same scale as above)

Shot 5

Projectiles	“50 μm ” glass buckshot + 1 mm steel ball bearing
Target	12 μm Al foil
Velocity	$5.14 \pm 0.05 \text{ km s}^{-1}$
Range pressure	0.10 mb

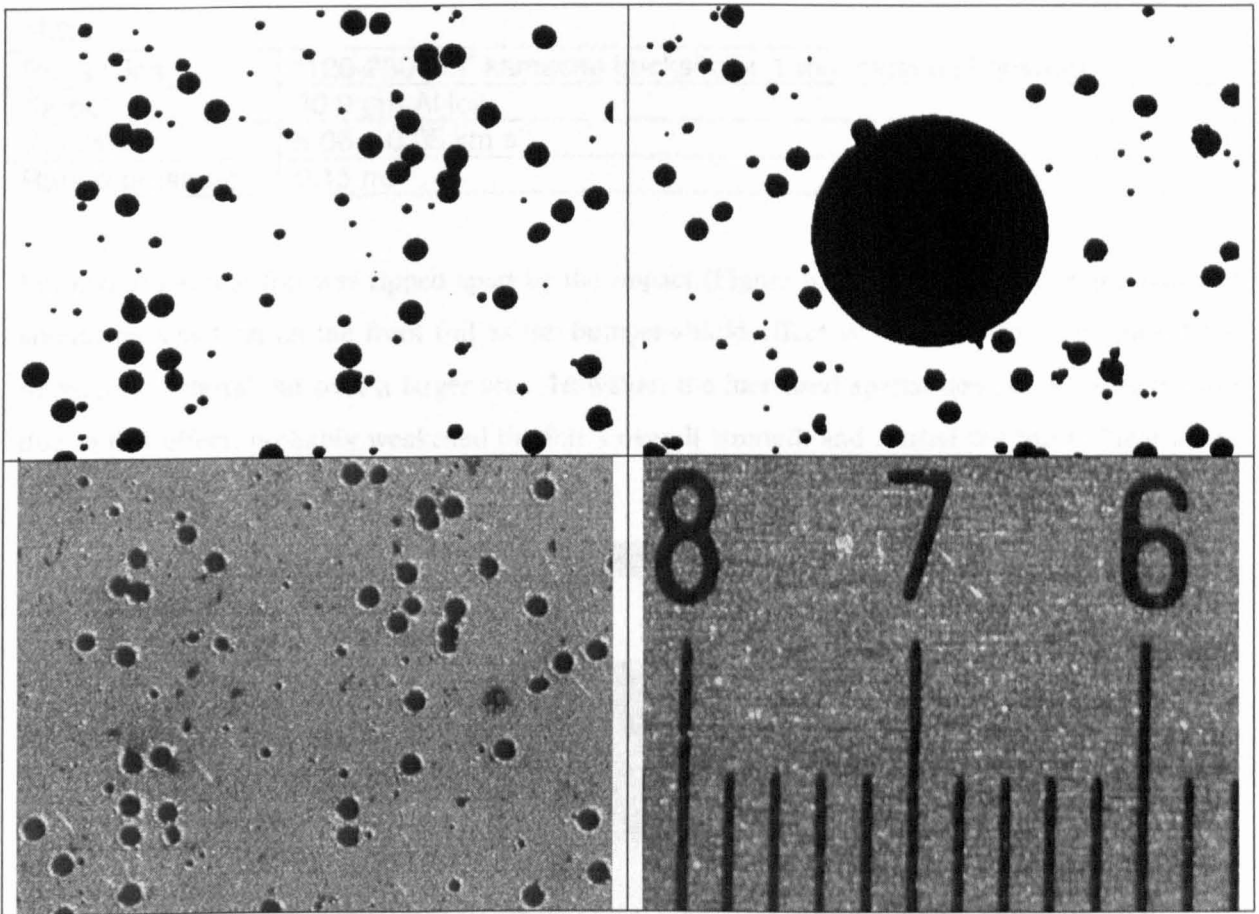


Figure 6.16 – Shot 5 front foil perforations (scale is in mm)

For shot 5 the spatial density of holes in the front foil (Figure 6.16) is higher than for shot 3 (Figure 6.11), which also used the same glass buckshot illustrating the varying performance of the buckshot technique. There are also more perforations of the second foil (Figure 6.17) than for shot 3 and they are generally larger indicating that, as expected, the same projectiles have a higher survivability in penetrating a thinner foil. However, there is a wide range of sizes and shapes of hole with a higher spatial density in the second foil indicating that some projectiles – be they the beads or other unwanted debris – are being disrupted by the first foil. Therefore, a balance between having a foil thick enough so that it is not too heavily perforated by miscellaneous shot debris and one thin enough so that the projectiles are not fragmented by the first foil has not been achieved in this programme of shots. It is likely that such a balance is not possible for beads as small as $\sim 50\ \mu\text{m}$ and that the technique of having two foils to determine the survivability of buckshot projectiles is only feasible for larger particles.

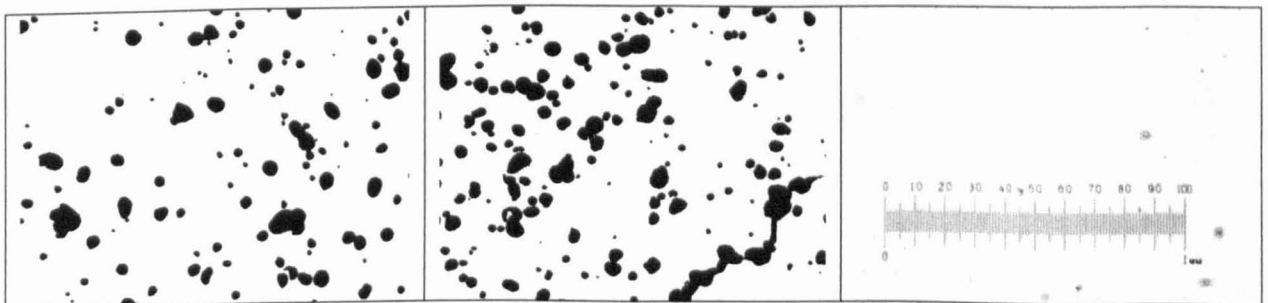


Figure 6.17 – Shot 5 rear foil perforations (scale is 1 mm full scale)

Shot 6

Projectiles	"120-250 μm " kamacite buckshot + 1 mm steel ball bearing
Target	30.9 μm Al foil
Velocity	$5.08 \pm 0.05 \text{ km s}^{-1}$
Range pressure	0.15 mb

For shot 6 the rear foil was ripped apart by the impact (Figure 6.18). The pressure on the rear foil should be less than on the front foil as the bumper-shield effect of the front foil will spread the impacting material out over a larger area. However, the increased spatial density of impacts, also due to this effect, probably weakened the foil's overall strength and caused the foil to "tear along the dotted line".

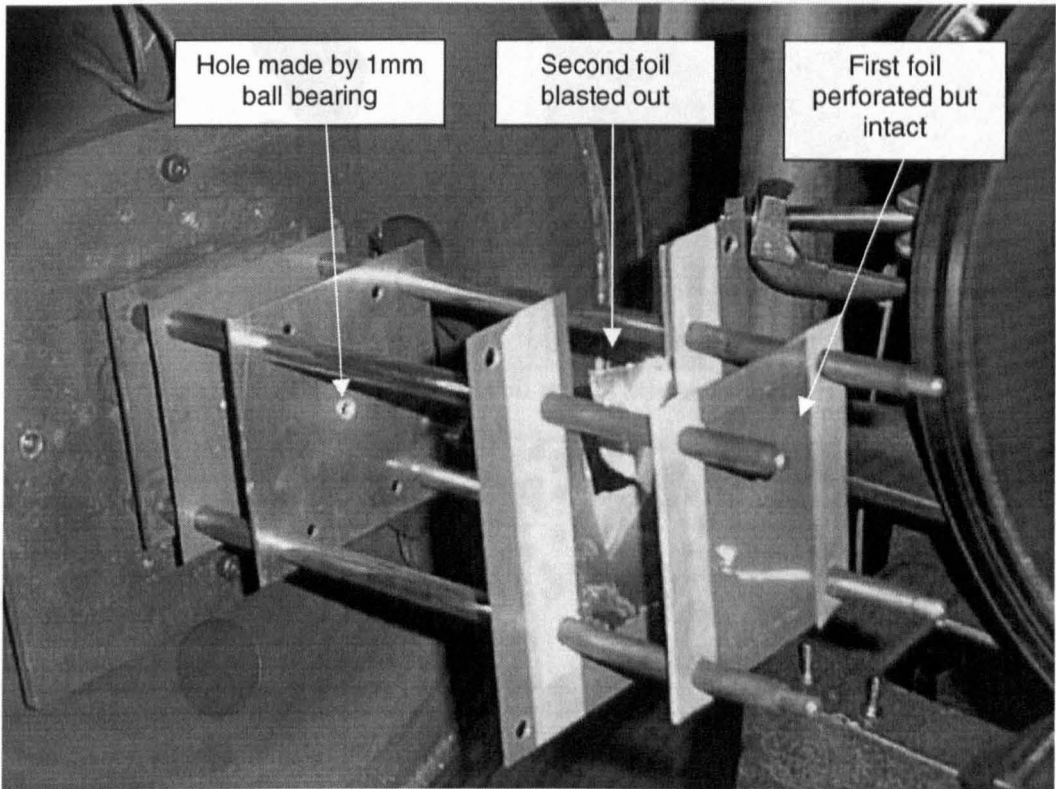


Figure 6.18 – Shot 6 targets after firing

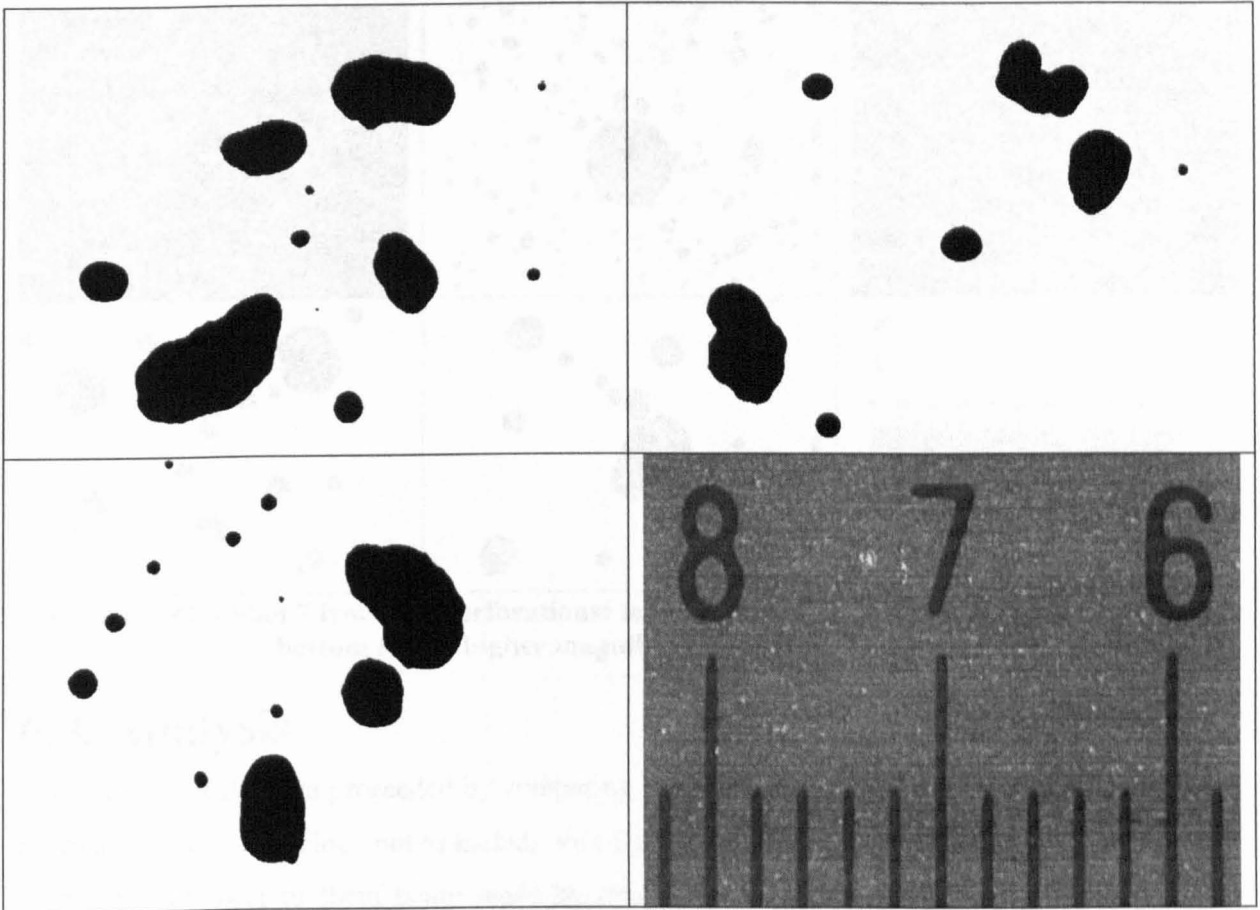


Figure 6.19 – Shot 6 front foil perforations (scale is in mm)

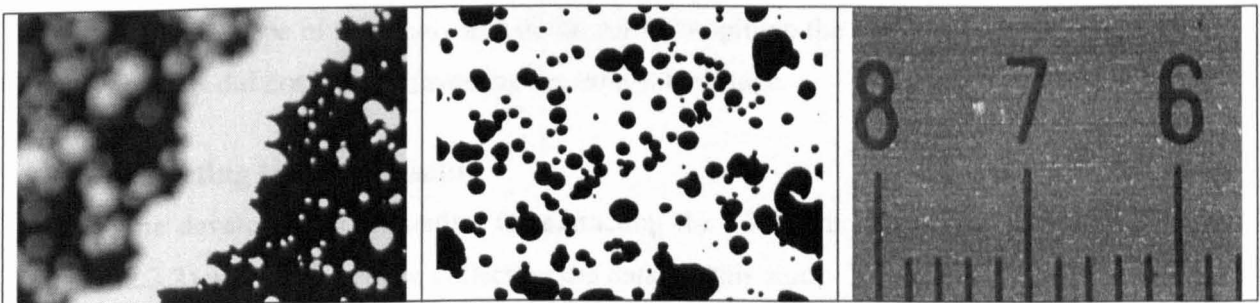


Figure 6.20 – Shot 6 rear foil perforations (scale is in mm)

Shot 7

Projectiles	“120-250 μm ” enstatite buckshot + 1 mm steel ball bearing
Target	30.9 μm Al foil
Velocity	$5.21 \pm 0.05 \text{ km s}^{-1}$
Range pressure	0.16 mb

Shot 7 was essentially a repeat of shot 1 but with 2 foils this time.

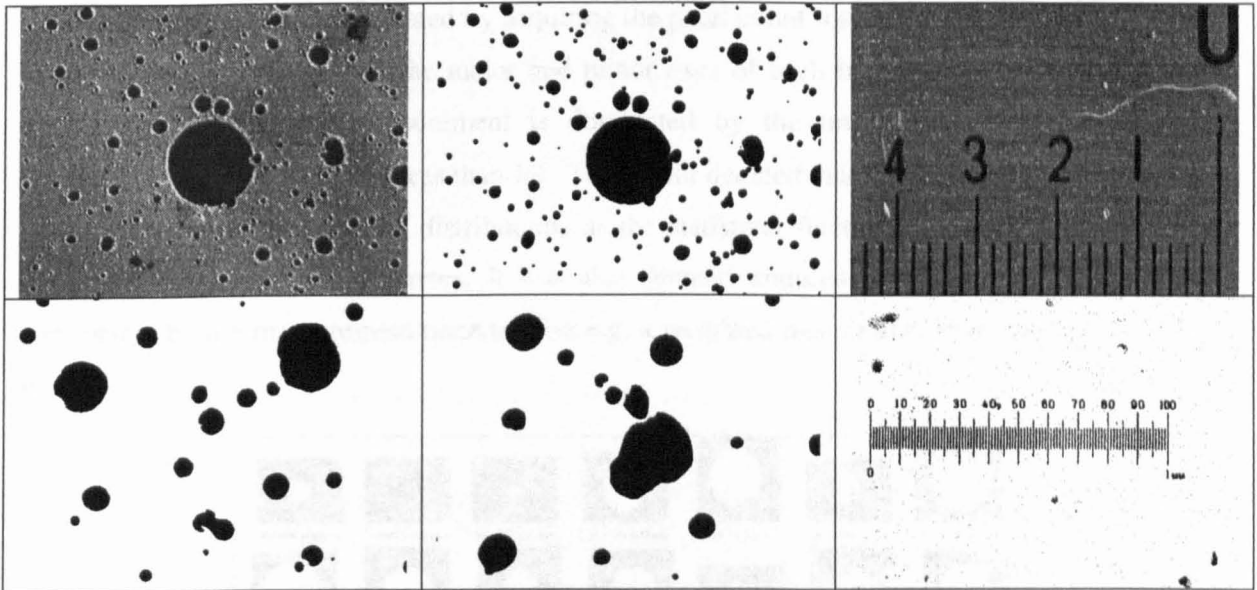


Figure 6.21 – Shot 7 front foil perforations: top row is low magnification (scale is in mm); bottom row is higher magnification (full scale is 1 mm)

6.3. Analysis

The analysis of the data proceeded by comparing the size and aspect ratio distributions of the foil perforations. It was decided not to include shot 2 as the foil had too many perforations with a low probability of most of them being made by the buckshot particles. It was also decided to not include the rear foil distributions in the analysis as the complication due to fragmentation effects was outside the scope of this study and in the author's opinion the convoluted information offered by this analysis did not warrant investing the time at this stage.

6.3.1. Collecting the shape data

The routine developed by the author for extracting the TICCE hole size and shape distributions (section 2.3.2) was employed for collecting the data for this study. The procedure involved loading each image of hole profiles into an image processing package and cutting out the individual holes from the image and saving each one as an input file for the ellipse fitting routine. With more time available the author would have attempted modifying the software such that a single image containing many holes could be input, however it was decided it would be quicker to separate the images into ones containing an individual hole. The holes were selected, as far as possible, without bias in that every hole in an image was included, until a statistically significant sample (around 80-100) for each foil had been obtained. However, for shot 4 where there is a clear distinction between “large” and “small” holes (Figure 6.14), only the large holes were included otherwise a sample taken by including all holes in the image would clearly be dominated by non-buckshot projectiles; it is reasonable to assume that the debris in a shot is smaller than the buckshot loaded in the sabot. Thus, only 56 perforations were recorded for shot 4. Examples of subsets of hole images acquired are shown for shot 1 (Figure 6.22) and shot 3 (Figure 6.23).

The hole images were fed into the ellipse fitting routine, which output the semi-major and semi-minor axis of the best-fit ellipse and the mean square residual of points about the fit, all in pixel

counts. The images were calibrated by acquiring the pixel count for lengths on the graticule images as per section 3.3.1 and thus the major and minor axes of each hole in μm was calculated. The uncertainty in the axes measurement is dominated by the uncertainty in the fitted ellipse parameters, which was mostly less than 1%. The author decided that these uncertainties need not be included in the analysis of the distributions as the statistical fluctuations would almost certainly dominate over measurement errors. It was also deemed unnecessary to weight the distribution parameters by the measurement uncertainties e.g. a weighted mean rather than a simple arithmetic mean.

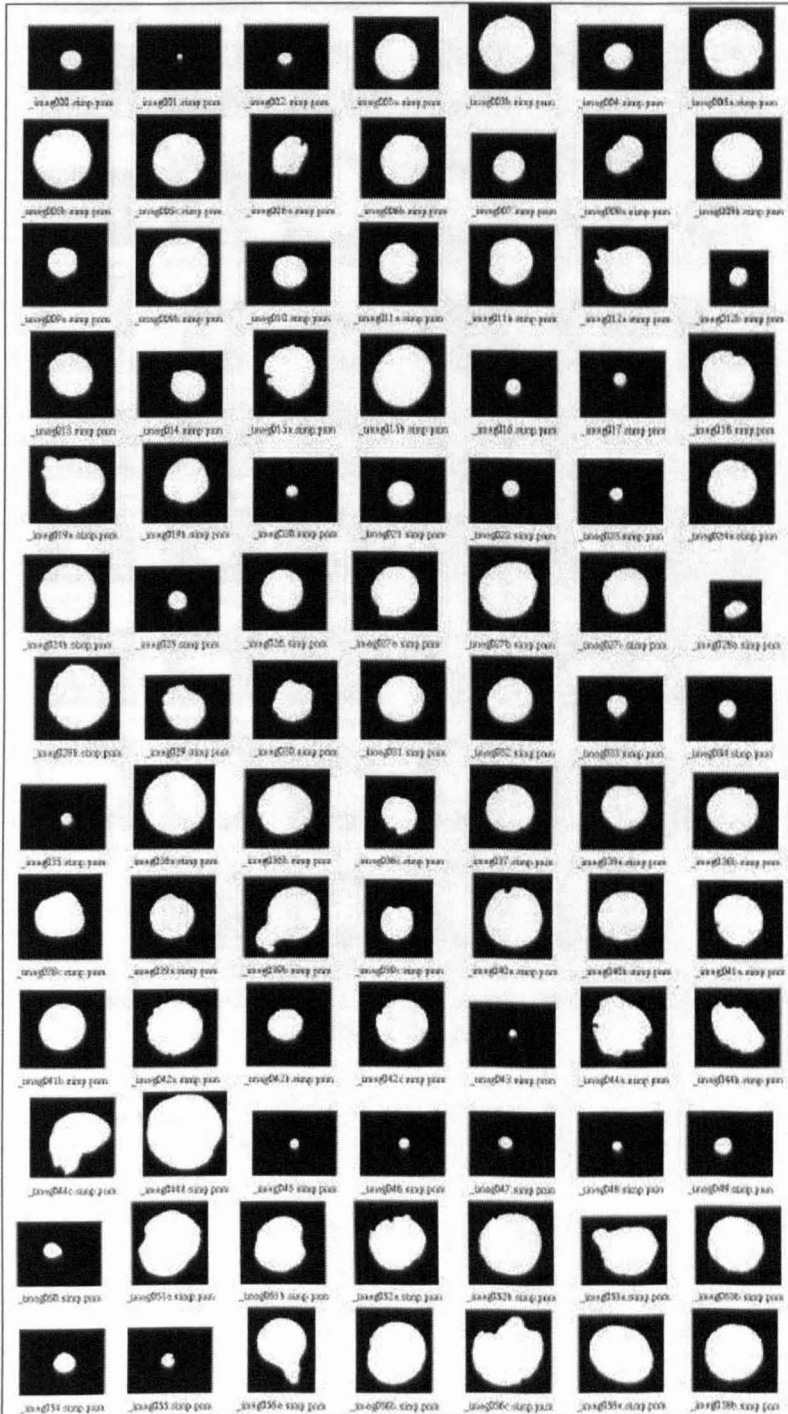


Figure 6.22 – Shot 1 (enstatite projectiles) holes separated into individual images for ellipse fitting

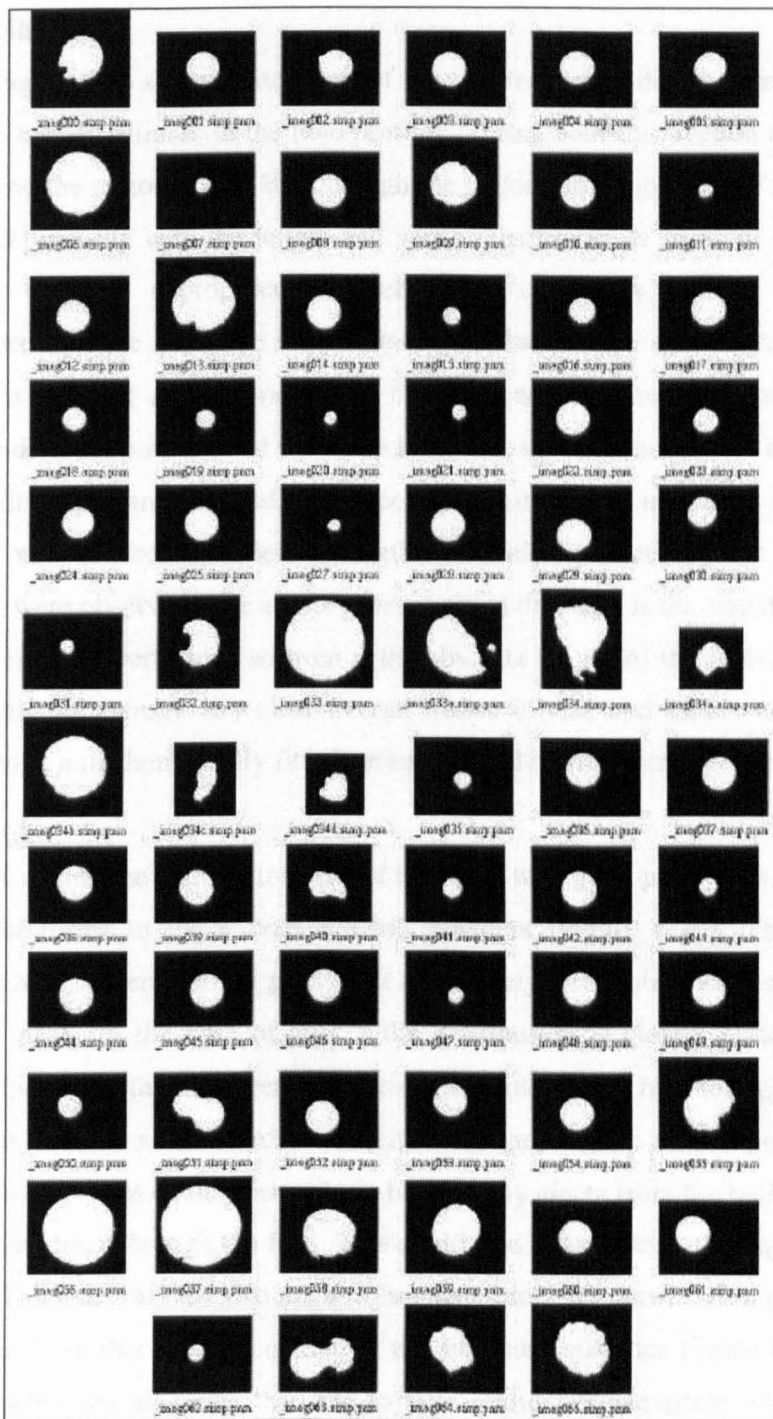


Figure 6.23 – Shot 3 holes (soda-lime glass projectiles) separated into individual images for ellipse fitting

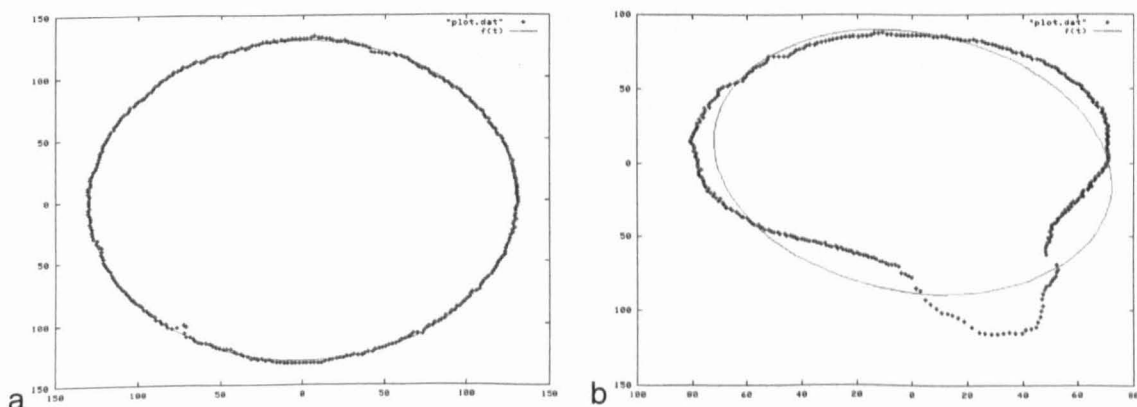


Figure 6.24 – Ellipses fitted to profiles for a hole from a) shot 3 (glass beads); b) shot 1 (enstatite shards)

6.3.2. Size distributions

Figure 6.25 and Figure 6.26 shows histograms of the size frequency distributions of the major and minor axes of the best-fit ellipses to the hole profiles. Throughout this section the major axis will be denoted as A and the minor axis as B. Although the major and minor axes of the best fit ellipses do not correspond precisely with the length and width measurements made of the projectiles, the author feels that they are appropriate parameters to use. Firstly, we do not expect a 1:1 correspondence between the hole size distributions and the particle size distribution even if the projectiles are not crushed as the orientation upon impact will be randomised. Additionally, measuring each individual hole (500 of them) by hand was unfeasible with the time available. The axes of the best fit ellipse are believed to be acceptable surrogates in that in most cases will be highly correlated with a carefully selected length and width, particularly for the approximately circular holes that were observed. The author stresses again that as it is the statistical comparison of *distributions* that is being performed so even if the absolute values of the individual hole axes are perhaps ambiguous, on *average* any clear overall trends in size and aspect ratio should still be evident. Furthermore, a mathematically fitted parameter will be free from operator bias.

Glass bead projectiles

A first observation of the size distributions is that the shots with glass projectiles (Figure 6.25) have markedly different forms to those with mineral powders (Figure 6.26). The glass-bead shot distributions have a prominent narrow peak with a relatively wider size range of particles smaller than those in the peak. In the case of shot 5 the distribution is clearly bimodal. The intuitive interpretation of this is that the large peak comprises the holes made by intact glass beads and that the distribution at smaller sizes corresponds either to gun debris and/or possibly fragmented projectiles. The smaller holes could alternatively be made by ejecta from the ball bearing impact on the stop plate coming back through the foils. This could also contribute to the higher density of rear foil perforations. The rear foil will also act as a bumper shield for small ejecta protecting the front foil to some extent from this debris. Looking at the summary statistics (Table 6.3) it can be seen that the hole diameters are all larger than the particles, which is consistent with them remaining intact.

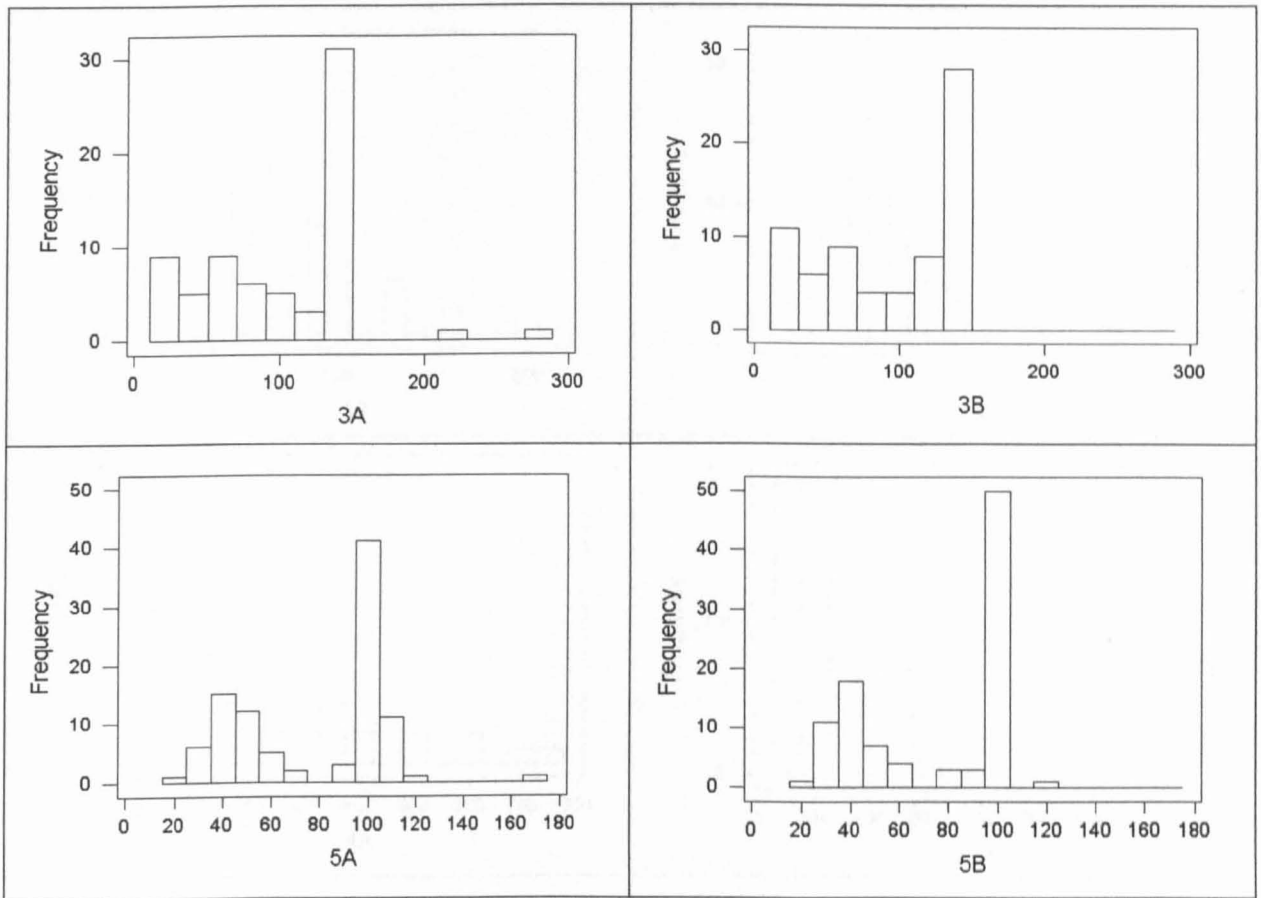


Figure 6.25 – Size (μm) frequency distributions of shots using glass beads

Table 6.3 – Summary statistics for glass shots

(μm)	3A	3B	5A	5B
Mean	98.85	91.63	79.21	74.49
SE	6.03	5.34	3.14	2.97
Median	124.61	112.27	100.11	96.04
SD	50.41	44.69	31.08	29.38
Kurtosis	0.86	-1.38	-1.04	-1.65
Skewness	0.36	-0.49	-0.18	-0.36
Range	257.90	126.17	145.68	101.78
Min	16.63	10.32	23.37	22.54
Max	274.53	136.49	169.06	124.32
N	70	70	98	98

Mineral powder projectiles

The distributions of holes for the mineral-powder shots (Figure 6.26) are positively skewed, almost exponential in form for shots 4, 6 and 7. Shot 6 is perhaps bimodal, but as a rule-of-thumb (Cooper, 1969) frequencies less than 5 are not considered to be highly significant. Looking at the summary statistics (Table 6.4) it can be seen that the hole sizes of the enstatite shots (1 and 7) are considerably smaller than the projectile dimensions of approximately $400 \times 200 \mu\text{m}$ (Table 6.1). However, kamacite hole dimensions are only slightly smaller than the projectile dimensions and overlap the size range of the projectiles. Therefore, it would appear at this stage that the enstatite projectiles have suffered greater fragmentation than the ductile, less brittle kamacite projectiles. A more detailed investigation of these distributions follows.

6. Survivability of buckshot projectiles upon launch in the light-gas gun

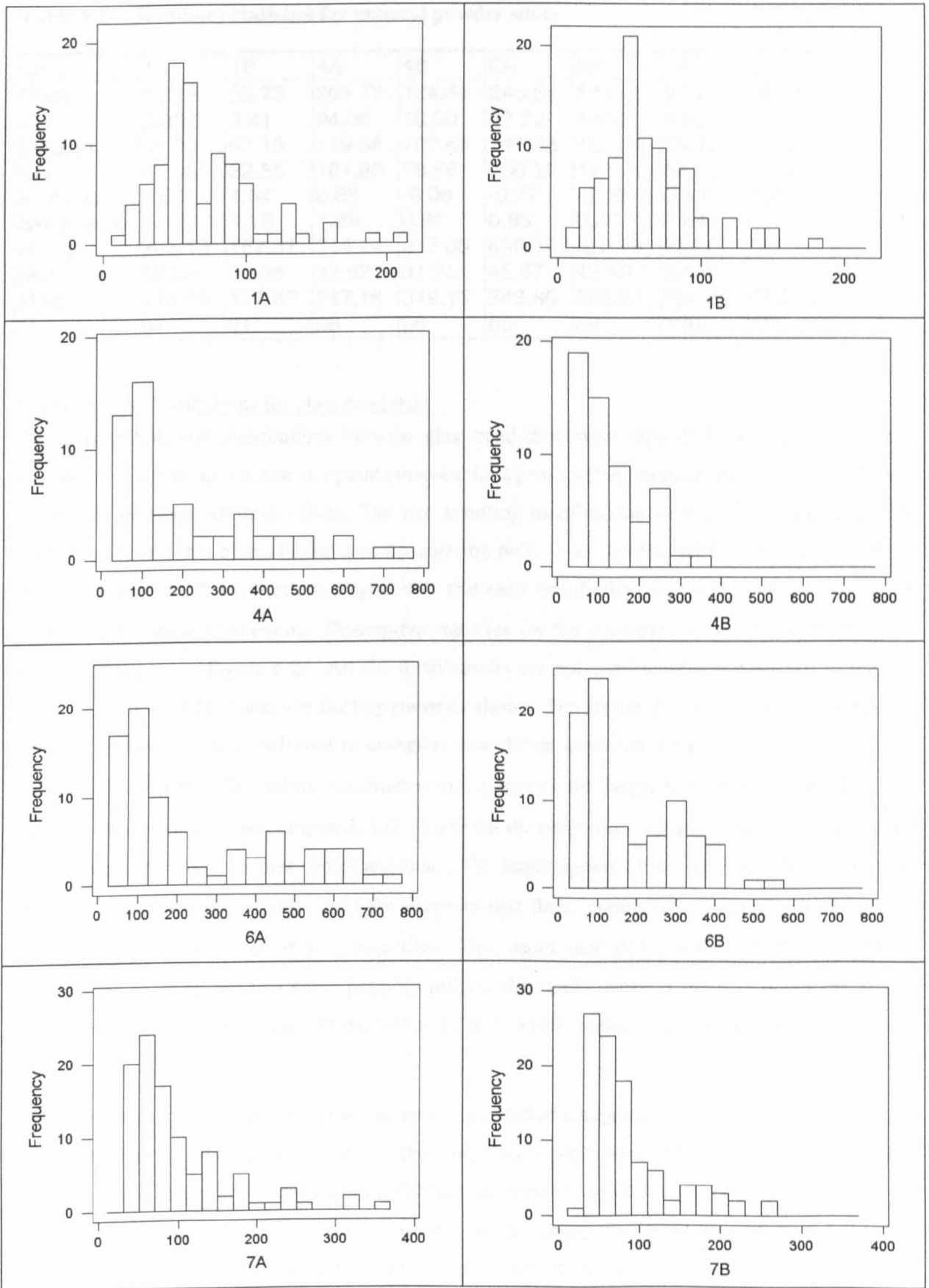


Figure 6.26 – Size (µm) frequency distributions of shots using mineral powders

Table 6.4 – Summary statistics for mineral powder shots

(μm)	1A	1B	4A	4B	6A	6B	7A	7B
Mean	70.19	63.73	206.73	124.67	248.64	177.63	97.78	86.58
SE	3.88	3.41	24.30	10.50	22.39	13.53	6.60	5.30
Median	61.03	57.15	119.38	100.66	141.88	123.24	78.12	69.15
SD	37.05	32.55	181.86	78.56	206.39	124.71	66.02	52.95
Kurtosis	2.66	1.64	0.88	-0.08	-0.77	-0.20	3.49	1.41
Skewness	1.42	1.16	1.29	0.91	0.83	0.88	1.84	1.43
Range	201.13	167.31	714.24	317.80	698.17	520.48	322.07	225.55
Min	12.88	10.36	32.92	31.35	45.67	43.49	32.46	29.08
Max	214.00	177.67	747.16	349.15	743.85	563.97	354.52	254.63
N	91	91	56	56	85	85	100	100

Separation of distributions for glass bead data

The 2 mean hole size distributions from the glass bead shots were separated into 2 data sets either side of a threshold size chosen at a point between the 2 peaks where there appeared to be the largest separation between adjacent values. The two resulting distributions were analysed for normality and it was found that by excluding 3 and 6 outlying points - as determined from a box plot - from the shot 3 and shot 5 distributions respectively that each distribution appeared to be a sample from two distinct normal populations. Descriptive statistics for the 2 distributions from each of shot 3 and 5 are shown in Figure 6.27. All the distributions are not significantly non-normal at the 5% level, according to the Anderson-Darling statistics shown. The second population at smaller sizes is labelled “debris”, as it is believed to comprise gun debris launched with the main population of buckshot projectiles. The tightly constrained size range of the larger-hole distribution, $\sigma = 1.6\%$ and 2% respectively, when compared to $\sigma = 1.8\%$ for the projectiles, supports the assertion that the projectiles responsible for these holes are intact. The larger spread of the smaller-hole distribution, $\sigma = 50\%$ and 20% respectively, strongly suggests that these populations comprise debris and/or fragments rather than our intact projectiles. The significant difference in σ for the debris populations between the two shots possibly reflects the randomness of the gun operation in that some shots are “cleaner” than others, although it is worth noting that the means are the same between these two shots.

A further check on the conclusion that the larger population comprises the unfragmented soda-lime glass beads is to compare the sizes of the holes with predictions from established empirical equations. The equation of Gardner *et al.* (1997a), referred to as GMC within the Unit, predicts the projectile diameter for a given hole diameter for a variety of projectile and metallic target combinations. If the relevant parameters (velocity, target and projectile densities) for shot 3 and 5 are input into the GMC equation along with the mean hole diameters for the larger-size distributions, GMC predicts that the impacting particles were 66 and $70 \mu\text{m}$ respectively. Our 5% uncertainty in velocity corresponds to a $\pm 0.5 \mu\text{m}$ fluctuation in predicted particle diameter; a 10% error in projectile density corresponds to $\pm 2 \mu\text{m}$; 10% error in foil thickness to $\pm 3 \mu\text{m}$ and the standard deviation of our hole distribution to $\pm 1.3 \mu\text{m}$. Thus the actual projectile diameters are not

within the uncertainties due to the experimental parameters. However, the form of GMC employed was that using the coefficients derived from impacts of aluminium on aluminium at 1.2 to 6.0 km s⁻¹, as this was the closest target-projectile density combination to the ones used in this work available in the given table of coefficients.

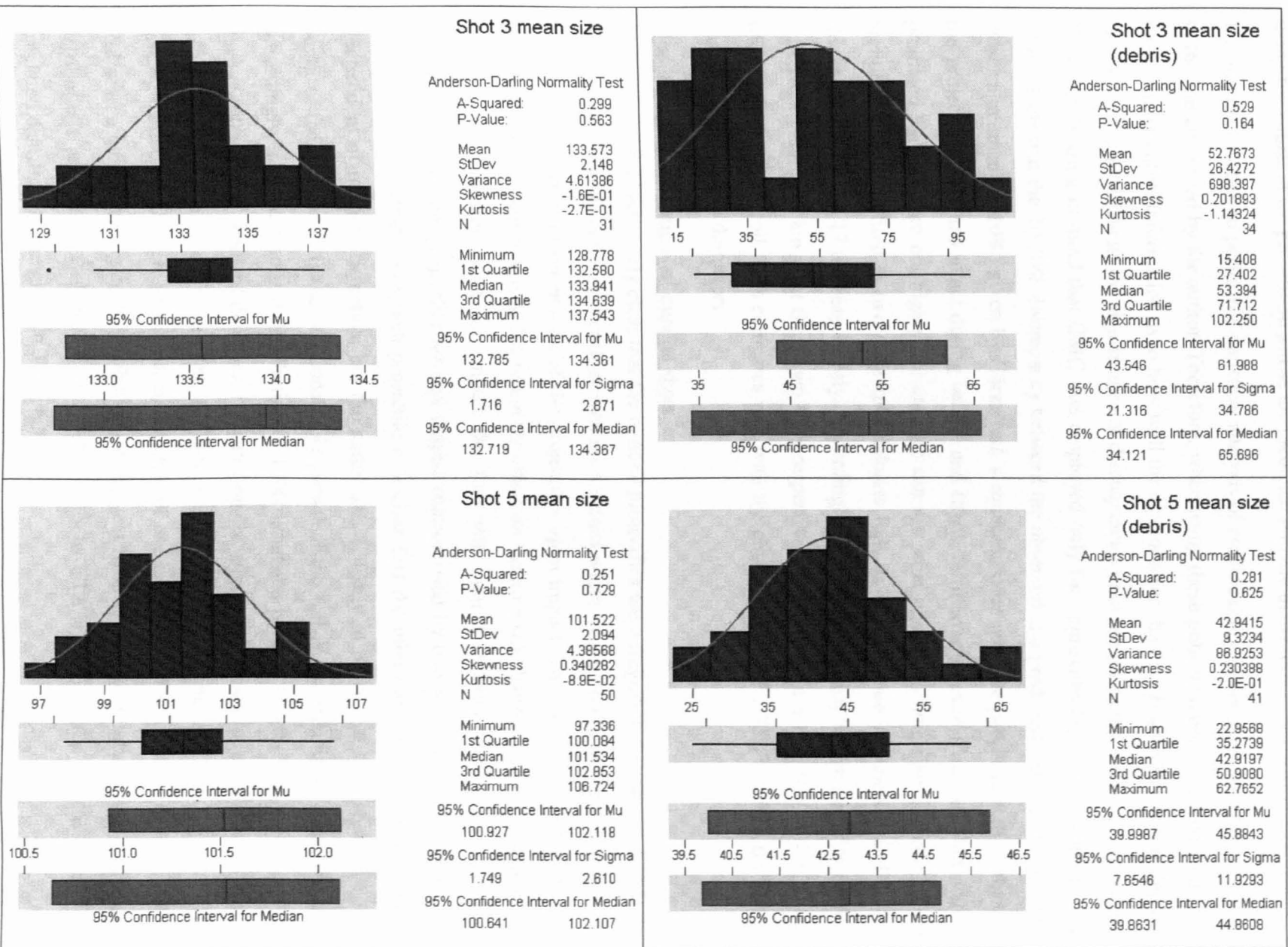


Figure 6.27 – Glass bead shots 3 and 5 separated into 2 normal populations; sizes in μm .

A possibly more appropriate empirical relationship is that of Hörz *et al.* (1993), who fired soda-lime glass beads in the size range 50 to 3000 μm at aluminium foils at $\sim 6 \text{ km s}^{-1}$. This equation predicts 46.3 μm for shot 3, but 101 μm for shot 5. Curiously, the values given by Hörz *et al.*'s equation do not match up with the function plotted in their paper. If we read off the plot instead of using the equation we get $\sim 40\text{-}50 \mu\text{m}$ as the predicted particle diameter.

It is not the practice to perform a statistical analysis of empirical regression equations (appendix A) in the literature read by the author. Therefore, when using these published empirical equations one has no quantitative information as to how well the equation fits the data from which it was derived and so we cannot evaluate the significance of discrepancies between predicted and observed values. However, bearing in mind that GMC was employed only for approximately similar materials the author feels that the 20-30% discrepancy between the observed and predicted values, and the even closer agreement (5-10%) given by Hörz *et al.*'s equation, does not give good cause to doubt that the projectiles remained intact during launch and flight. Furthermore, even if the absolute values predicted by GMC are not highly accurate we can see what *change* in hole size is predicted for identical projectiles fired at two different thickness foils as was the case for shots 3 and 5: foil thicknesses 30.9 and 12 μm respectively. Accordingly, GMC predicts that 55 μm particles fired at 5.51 km s^{-1} and 5.14 km s^{-1} at these two foils respectively will result in a hole that is 1.31 times wider in the thicker foil. This compares well with the observed ratio of 1.32:1 between the shot 3 and shot 5 mean hole diameters.

Modelling of distributions of mineral shots

Although, it is already fairly clear that the mineral projectiles were fragmented in launch in that the hole sizes are significantly smaller than even the smallest width measured (B) the author decided to investigate the effect of orientation of the projectiles upon impact. This is of interest both to this and future studies. The aim is to determine the effect on the hole size distribution if we assume that the projectiles remain intact but impact the foil with their orientation randomised. Another assumption is that the projectiles are rod shaped characterised by two variables only, namely the diameter and the length. For such projectile it is clear that the minor axis of a hole (B) will be independent of impact orientation, but the major axis is likely to be $A \cos\theta + C$, where A is the length of the rod and C is the additional hole growth if the foil is not effectively infinitely thin. Accordingly, a random normal distribution of 1000 simulated particle lengths was produced with mean = 400 μm and standard deviation 120 μm (top-left Figure 6.28), approximately the same as the enstatite and kamacite projectiles. 6 random uniform distributions of 1000 impact angles ranging from 0 to 90° were produced, an example of one is shown in the top-right pane of Figure 6.28 with a corresponding $\cos\theta$ distribution on the next row. 3 of the 6 simulated hole major axis distributions are shown in Figure 6.28 labelled C15 to C17. The summary statistics for the 6 simulated distributions are given in Table 6.5.

6. Survivability of buckshot projectiles upon launch in the light-gas gun

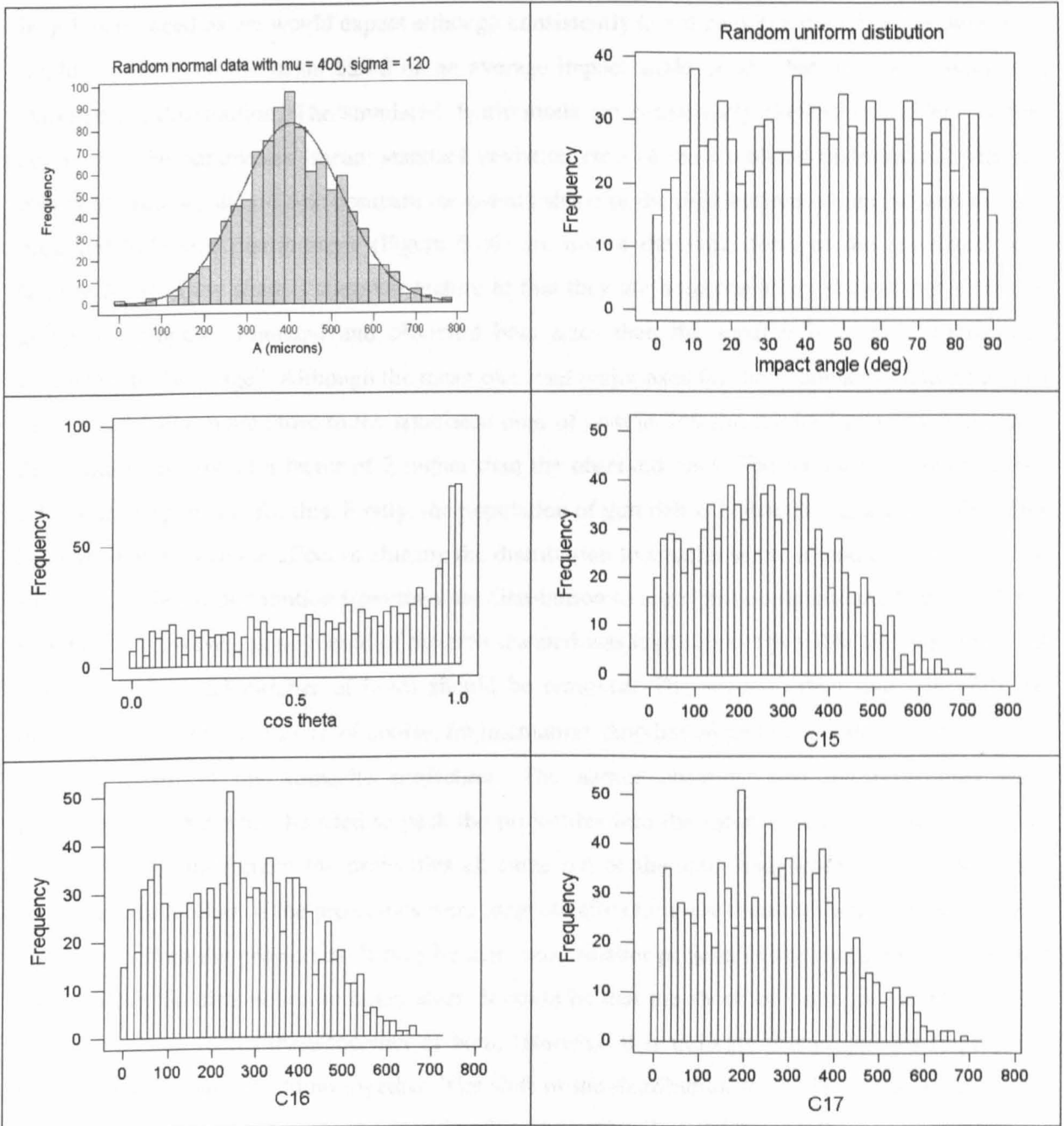


Figure 6.28 – Simulations to study effect of projectile orientation upon impact

Table 6.5 – Summary statistics for simulations

	C15	C16	C17	C18	C19	C20
Mean	256.45	261.34	261.32	255.56	254.83	263.70
Standard Error	4.66	4.78	4.71	4.83	4.83	4.85
Median	253.50	255.68	261.74	246.75	242.25	255.44
Standard Deviation	147.21	151.15	148.91	152.77	152.64	153.32
Kurtosis	-0.64	-0.80	-0.67	-0.69	-0.65	-0.62
Skewness	0.25	0.17	0.20	0.28	0.33	0.29
Range	687.38	666.51	687.30	693.49	673.67	717.25
Minimum	-1.19	-1.44	-1.48	-1.14	-0.13	-0.84
Maximum	686.19	665.07	685.81	692.35	673.54	716.41
Count	1000	1000	1000	1000	1000	1000

Randomly sampled distributions were used rather than ideal distributions to illustrate the effect of random fluctuations. It can be seen that the distribution of simulated hole lengths that the mean

length is reduced as we would expect although consistently less than $400 \times \cos 45 = 283$, which we might expect to be the mean based on an average impact angle of 45° , but this mean assumes a symmetrical distribution. The simulated distributions are consistently skewed to the left. Before comparing the parameters (mean, standard deviation etc.) of the simulated distributions with the observed ones we should first compare the overall shape of the distributions. It can be seen that the observed hole size distributions (Figure 6.26) are not of the same form as the simulated ones (Figure 6.28). They share a common feature in that they are both positively skewed but if we are going to compare simulated and observed hole sizes then the median is a more appropriate characteristic “average”. Although the mean observed major axes for the 2 kamacite shots (4 and 6) of 207 and 249 μm are close to the simulated ones of around 260 μm the median of the simulated distributions is around a factor of 2 higher than the observed ones. The author proposes that two effects are responsible for this. Firstly, the population of gun debris isolated by analysis of the glass bead shots will have the effect of shifting the distribution to smaller sizes. It would seem logical to subtract the debris distribution from the total distribution to see if this compares any better with the simulation. However, as no record of the area scanned was kept it is not possible to determine what fraction of the total number of holes should be removed. The second effect that will shift the distribution to smaller sizes is, of course, fragmentation. Another effect that should be considered is the magnetism of the kamacite projectiles. The author observed that the projectiles were magnetised in that when he tried to pack the projectiles into the sabot with a metal scribe tip, on removal of the instrument the projectiles all came out of the sabot magnetically attracted to the scribe and each other. If the projectiles were magnetically clumping together then we would expect larger holes than the projectiles. It may be that some smaller projectiles are clumping together and thus shifting the distribution to larger sizes. It could be that the shock of launch separates them or the compression forces them together or both. However, it is unlikely that projectiles fragmented by launch subsequently clump together. The shift of the distribution to smaller sizes suggests that the dominant process is fragmentation rather than the projectiles sticking together.

In summary there are four factors that transform the projectile size distribution to the hole size distribution.

1. *Orientation*: The randomised orientation of the projectiles upon impact will decrease the major axis in the manner illustrated by the simulation. It will not effect the minor axis distribution for cylindrical projectiles.
2. *Fragmentation* will decrease both the average major and minor axis.
3. *Debris inclusion*: An inclusion of small miscellaneous fragments with the buckshot will skew the distribution to small sizes.
4. *Hole growth*: The growth of the hole due to hydrodynamic after-flow will increase the diameter of the hole an amount that is related primarily to the target thickness and the velocity. This will increase both the average major and minor axes.

It is highly likely for the enstatite shots that fragmentation is occurring in that the decrease in size from the projectiles to the corresponding holes cannot be accounted for by random orientation or a debris inclusion. However, the kamacite hole distribution suggests that a proportion of the projectiles survived impact.

A further investigation of the enstatite size distribution can be made based on the fact that fragmentation processes are usually characterised by a power law distribution of fragments. Hence, a power law often describes the mass distribution of the meteoritic complex, as meteoroids are products of fragmentation processes such as asteroid grinding and mutual collisions. The author decided to see if a power law was an appropriate description of the distribution of hole sizes. It can be seen in Figure 6.29, a fit to the shot 7 enstatite distribution, that a power law is an appropriate model: $\chi^2/\nu = 0.87$ corresponding to a probability of 58%.

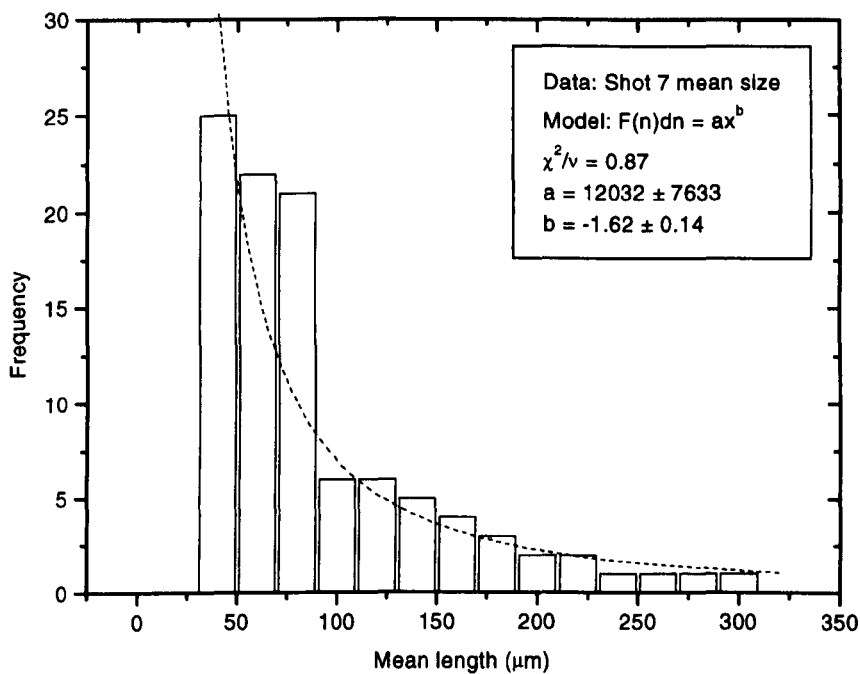


Figure 6.29 – Power law fit to shot 7 enstatite data

6.3.3. Aspect-ratio distributions

Glass beads

Figure 6.30 shows the frequency distributions of the aspect ratio of the glass-bead shot holes, divided into the larger size distribution on the left and the smaller “debris” distribution on the right. As expected the distribution attributed to intact glass bead impacts is more highly circular (1:1 aspect ratio) than the debris distribution although the contrast is not so marked for shot 5. In the table of summary statistics (Table 6.6) the median and associated confidence intervals are the appropriate characteristic parameters for non-normal distributions such as these; the mean and standard deviation are shown merely for comparison.

6. Survivability of buckshot projectiles upon launch in the light-gas gun

It is not immediately clear if the shot 5 distributions are significantly different. A Mann-Whitney test (section 2.3.4) gives a probability of 3% that they are samples from a common population and thus are significantly different at the 5% level. It is clear however that the shot 3 holes are more circular than the shot 5 holes (note the 95% confidence intervals for the median; Mann-Whitney test for shot 5 population median \geq shot 3 population median returns $<0.00\%$ probability). The author attributes this to passage through a thicker foil (shot 3 foil $30.9 \mu\text{m}$) tending to circularise the hole more than a thinner foil (shot 5 foil $12 \mu\text{m}$). In the limit of an infinitely thick target craters are generally circular regardless of projectile shape.

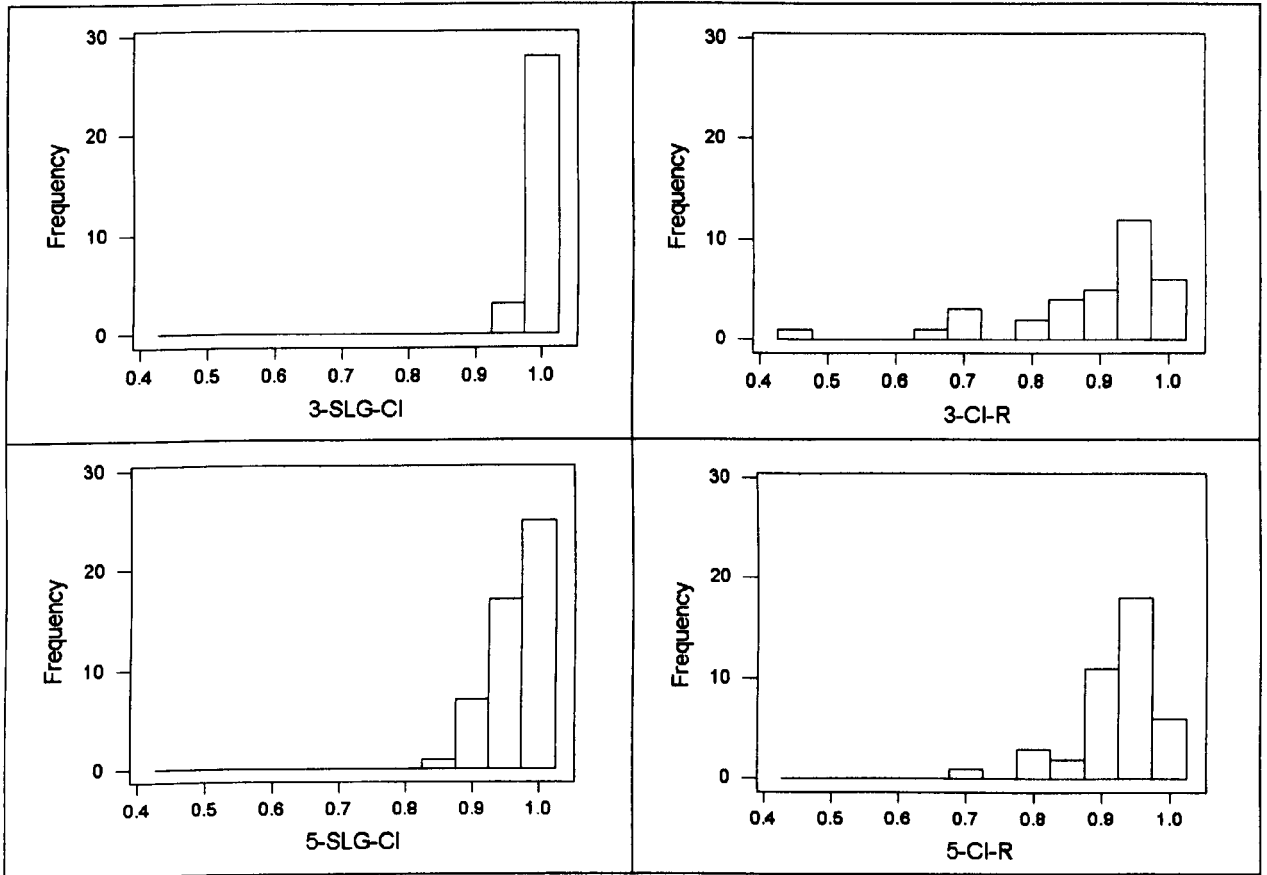


Figure 6.30 – Circularity distributions for glass bead shots

Table 6.6 – Summary statistics for circularities of glass bead shot holes

	3SLG	3R	5SLG	5R
Mean	0.988	0.882	0.961	0.924
SD	0.007	0.121	0.033	0.062
Median	0.989	0.933	0.972	0.951
95% conf. for median	0.987 – 0.991	0.880 – 0.943	0.959 – 0.981	0.920 – 0.960
N	31	34	50	41

Mineral powders

There is a clear distinction between the enstatite (shots 1 and 7) and the kamacite (shots 4 and 6) aspect ratio distributions (Figure 6.31). The enstatite holes have aspect ratios close to 1 and a smaller variation than the kamacite projectiles. This indicates that the kamacite projectiles retain their shape better than the enstatite ones. A Mann-Whitney test gives a 32% probability that the

6. Survivability of buckshot projectiles upon launch in the light-gas gun

shot 1 and 7 samples come from a common population. Thus, although the 2 shots appeared to contain a sample of different size projectiles, it appears that they did not contain significantly different shape projectiles. Once again the impacts in the thicker 30.9 μm foil of the 2 kamacite shots (shot 6) results in more symmetrical holes than in the thinner 12 μm foil (shot 4); Mann-Whitney $P(\text{shot 4} \geq \text{shot 6}) = 1\%$.

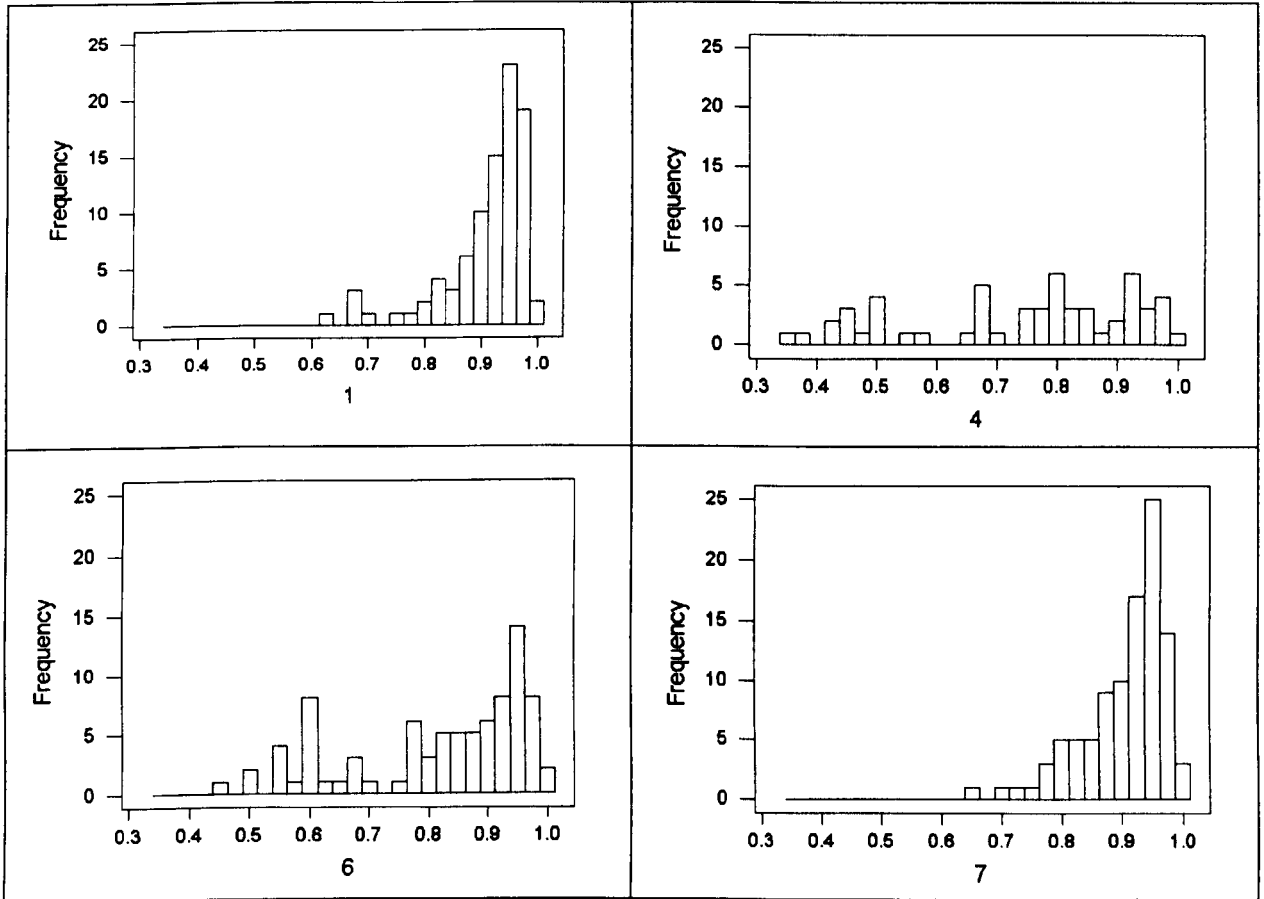


Figure 6.31 – Aspect ratio distributions for shots using mineral powders

Table 6.7 – Summary statistics for mineral powder aspect ratios

	1	4	6	7
Mean	0.911	0.742	0.817	0.906
SD	0.077	0.187	0.149	0.070
Median	0.935	0.790	0.870	0.929
95% conf. for median	0.925 – 0.946	0.707 – 0.831	0.819 – 0.900	0.905 – 0.938
N	91	56	85	100

6.3.4. Shape distributions

Glass beads

Figure 6.32 shows the shape factor (defined in section 2.3.2) distributions of the glass bead shots. The “debris” distributions both have significantly higher shape factors (more irregular) than for the “intact-bead” distributions; note the 95% confidence intervals for the medians in Table 6.8. Also, the holes in the thicker shot 3 foil are significantly more regular than for the thinner shot 5 foil, which is consistent with the conclusions of the aspect ratio analysis.

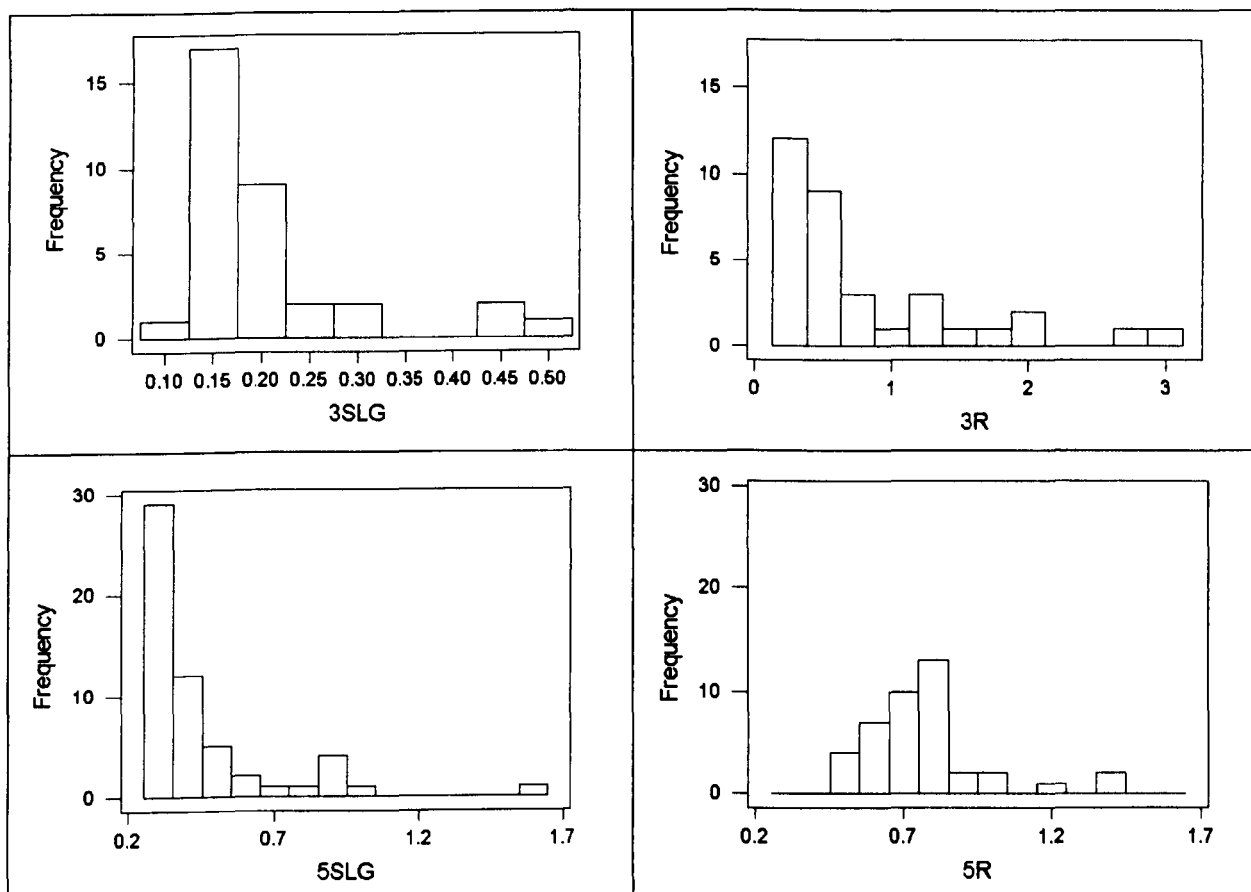


Figure 6.32 – Shape factor distributions for glass bead shots

Table 6.8 – Summary statistics for glass bead shape factors

	3SLG	3R	5SLG	5R
Mean	0.205	0.794	0.446	0.759
SD	0.096	0.732	0.251	0.212
Median	0.165	0.468	0.345	0.713
95% conf. for median	0.152 – 0.206	0.341 – 0.726	0.320 – 0.392	0.666 – 0.776
N	34	34	56	41

Mineral powders

The distributions of the mineral powder shot shape factors (Figure 6.33) does not show any obvious differences between the shots other than perhaps the kamacite projectiles producing a wider variety of shapes. Comparison of the means leads to a contradictory conclusion to a comparison of the medians (Table 6.9) and since the shape factor is based on how well the shape is described by an ellipse, only marginally significant differences are not particularly conclusive considering that the projectiles are not elliptical.

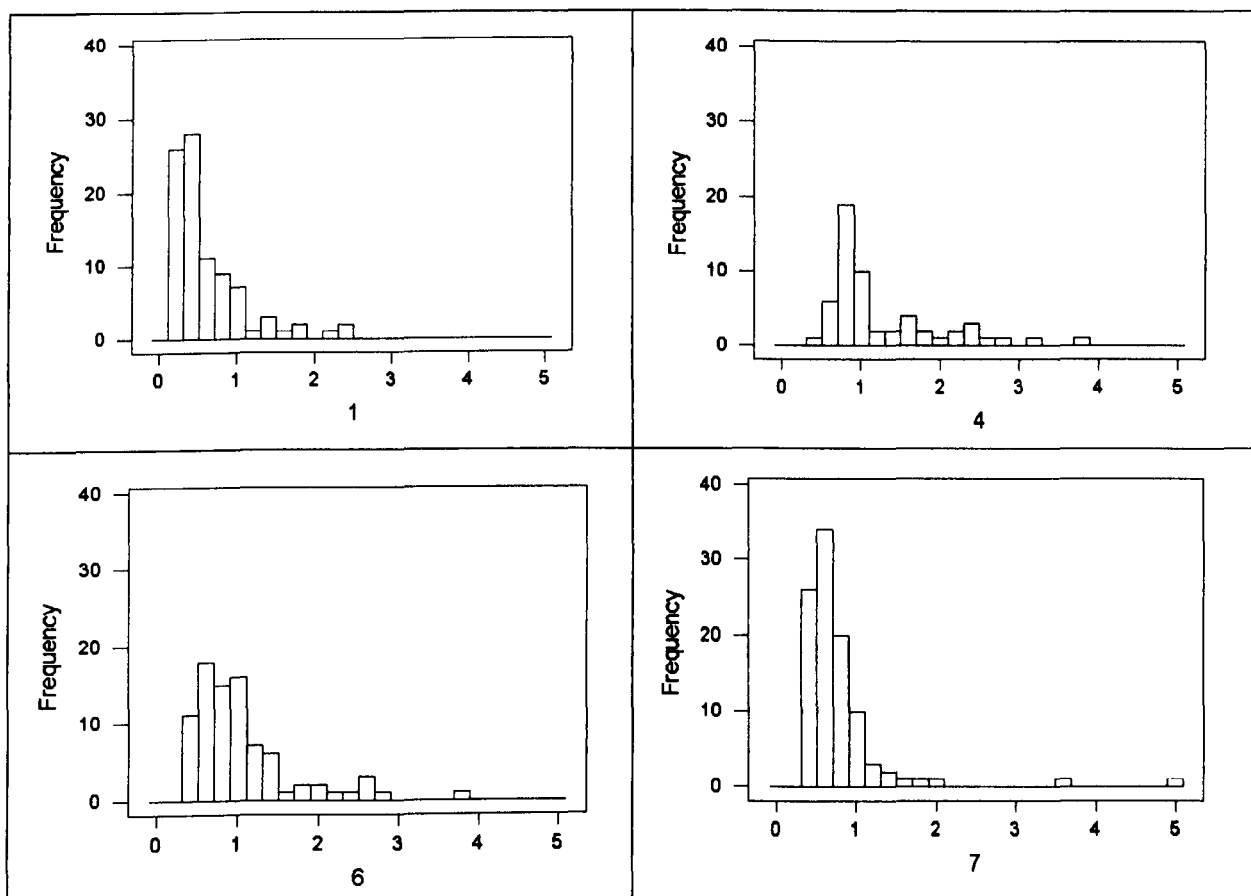


Figure 6.33 – Shape factor distributions for mineral powder shots

Table 6.9 – Summary statistics for mineral powder shape factors

	1	4	6	7
Mean	0.597	1.271	1.045	0.756
SD	0.489	0.737	0.628	0.593
Median	0.935	0.790	0.870	0.929
95% conf. for median	0.925 – 0.946	0.707 – 0.831	0.819 – 0.900	0.905 – 0.938
N	91	56	85	100

6.4. Discussion

6.4.1. Summary of main results

It would appear that under the condition of the light-gas gun being fired at 5 km s^{-1} with a sabot loaded with buckshot and a 1 mm steel ball bearing that for the 3 buckshots tried in this study:

1. *50 μm soda-lime glass spheres*: many reach the target intact with an inclusion of smaller impactors that is comprised of gun-debris and possibly some fragmented projectiles
2. *400 \times 185 μm enstatite shards*: likely that none remain intact.
3. *400 \times 168 μm kamacite shards*: likely that some survive.

Additionally, it is found that holes in a 30.9 μm foil are significantly more symmetrical (lower aspect ratio) and more regular (better fit to an ellipse) than holes in a 12 μm foil made by impacts

of the same projectile type. Therefore, an accurate signature of projectile shape is diminished over this increase in foil thickness.

6.4.2. Comparison with previous similar studies

Barrett *et al.* (1992) note that when firing 100 μm diameter soda-lime glass buckshot through 1 μm foils that there are many circular holes with sizes approximating that of the glass beads. They also note that there is an accompanying set of smaller irregular holes that they attribute to being caused by fragmented projectiles. They do not mention the possibility of inclusion of any gun debris however.

Baron (1996) fired soda-lime glass spheres at a variety of metals to determine their ballistic limit. Although he does not comment himself on the survivability of the projectiles the fact that he observed circular holes has been cited by others as evidence of intact projectiles. However, as Baron's study was focussed on achieving marginal penetration as close to the ballistic limit as possible, the author believes that irregular projectiles may still have produced highly circular holes as the phenomena will be more akin to cratering than non-destructive penetration.

6.4.3. Implications for previous, current and future studies

The buckshot technique has been applied in many previous hypervelocity impact programmes both within the Unit and elsewhere and yet it is often taken for granted that what is loaded in the sabot is what will arrive at the target.

Yano (1995) performed an impact experiment firing a buckshot comprising enstatite and albite shards at a HST solar cell. In this study the crater sizes are compared to craters from the experimental programme of section 5, which used soda-lime glass beads, by normalising by the projectile diameter. The normalised enstatite/albite projectile diameters are almost certainly wrong, as this study has shown that it is highly likely that enstatite disintegrates upon launch.

Burchell *et al.* (1999a) performed impact experiments with the Unit's light-gas gun firing soda-lime glass spheres and buckshot containing the mineral olivine. Although, they present a case for the soda-lime glass remaining intact (citing Baron, 1996), they do not discuss the survivability of the olivine. Olivine, although harder (Vickers 750) than enstatite is brittle, has 2 cleavage planes and often occurs in dense aggregates of grainy crystals (<http://minerals.net>). Thus, it is possible, but as of yet untested to the author's knowledge, that olivine is susceptible to fragmentation upon launch. If the olivine projectiles reaching the target were smaller than their original size then Burchell *et al.*'s linear regression against projectile diameter will have too shallow a slope.

The primary aim of this study was to determine the survivability of the glass buckshot used for the experimental programme in section 5. As it appears that the glass buckshot does have a good survival rate, the analysis of this experimental data is validated in this respect. Thus the previously unsupported conclusions of publications (e.g. Shrine, Taylor *et al.*, 1996 and Taylor, Shrine *et al.* 1999) using this data are fortunately not undermined; these publications do not identify the

survivability of the buckshot as a potential problem. However, there is the problem of the inclusion of the smaller debris particles. The author suspects that, as this debris inclusion forms a clearly separate distribution from the glass projectiles, the pruning of the data using normal probability plots (section 5.3.2) will have excluded the craters belonging to this small-size population of impactors or at least the ones that would have a significant effect on the location and width of the overall distribution.

There are ongoing studies within the Unit modelling crater shapes (Kay *et al.*, 1997) that are currently being extended to studying mineral impacts. It is thus vital that any regression of whatever “shape” variates against impactor dimensions should take into account the survivability of the projectiles. In particular for the case of the analysis of historical enstatite buckshot data it would be more appropriate to use the distribution of thin foil holes presented here rather than the dimensions of the original enstatite shards.

6.4.4. Future recommendations

The author recommends that all buckshot projectiles should be tested for survivability by firing them through as thin a foil is as feasible. If high-speed photography of projectiles in flight becomes available again in the Unit, it would be extremely useful to attempt photography of commonly used buckshot materials in flight. The Unit also possesses apparatus for determining the ultimate compressive strength of materials and use of this to determine the strength of projectile materials would aid in theoretical considerations of this problem. It would also allow comparative inferences to be made in that if the projectile being used is measured to be stronger than one that we are confident survives launch then it is reasonable to assume that it will also survive in the absence of more rigorous testing.

7. Discussion: Interpreting space data

Before an interpretation of space data in the light of the work in this thesis is made it is necessary to describe how a measure of significance will be determined.

7.1. Statistical analysis of flux distributions

As mentioned in the introduction to this thesis, statistical analyses of *in situ* measurements of meteoroid and debris fluxes are hard to find. The usual presentation of such data is a plot of the *cumulative flux* (number $\text{m}^{-2} \text{s}^{-1}$) of impacts *above* a certain measurement e.g. hole size, penetration depth with the error of each point being the square root of the number of counts divided by the area-time product. It should be noted that for small counts these error bars will not correspond to the same confidence interval for the upper and lower error bar as the distribution function (binomial or Poisson) is not symmetrical. Comments regarding the significance of discrepancies between fluxes are usually based on whether these error bars are seen to overlap. Publications where an actual significance level is or probability is calculated are the exception.

There are two aspects in comparing distributions of impacts. Firstly, we can see if the overall numbers of impacts registered are compatible between two experiments. Secondly, we can see if the distribution of impacts has the same functional form. In the first case we are seeing whether the absolute rate of impacts has changed; in the second case we are seeing of the relative rates between different size particles, for example, has changed. It could be that although the first experiment witnessed 10 times more impacts $\text{m}^{-2}\text{s}^{-1}$ than the second one, the *size distribution indices* between the experiments are identical. Conversely, two exposures could witness very different shaped size distribution but still register the same *total* number of impacts.

Since, impact events are assumed to be random, the expected total number of impacts is directly proportional to the area-time product. Therefore, if we had two identical detectors, one having twice the area-time product of the other, receiving n_1 and n_2 impacts respectively, we would expect one detector to receive $1/3(n_1 + n_2)$ impacts and the second to receive $2/3(n_1 + n_2)$ impacts if the impact rate is the same for the two exposures. Therefore, the probability of observing n_1 impacts on one detector is given by the binomial probability for n_1 successes of $n_1 + n_2$ trials with a probability of a success of $1/3$. Often the Poisson approximation to the binomial distribution is used – mostly quoted rather than actually *used* – but Maclay *et al.* (1996) recommend use of the binomial distribution, where feasible, as it is a “physical model” rather than an approximation. They show that the Poisson approximation can lead to as much as a 13% error in calculated impact probability for a large area-time product experiment such as LDEF.

Figure 7.1 shows the pit size distribution of impacts on the EURECA and HST solar arrays as would normally be plotted. Without careful thought it may be tempting to conclude that “the fluxes show good agreement” at 0.4 mm D_{pit} and that HST was more heavily impacted above this size.

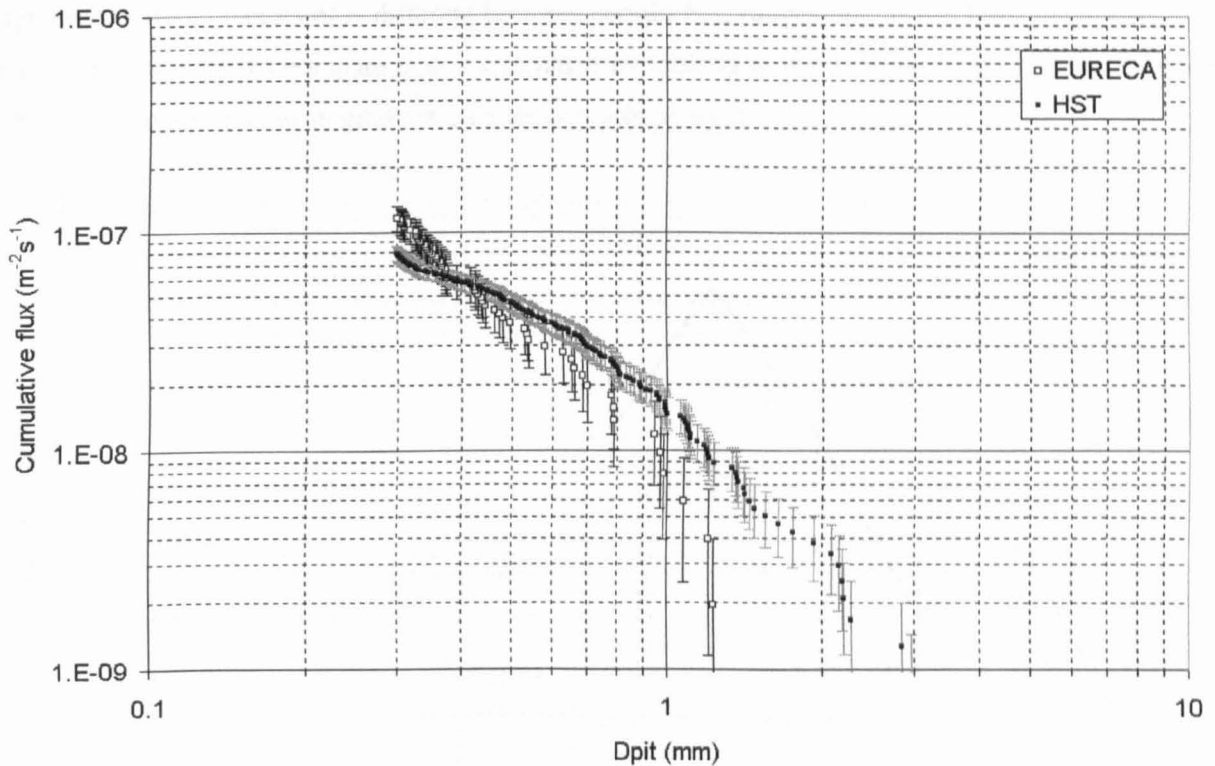


Figure 7.1 – Cumulative size distribution of solar cell pit diameters

However, for the differential distribution Figure 7.2 with the flux of impacts plotted in equally logarithmically spaced bins* shows that EURECA witnessed a higher flux between 0.3 and 0.5 mm D_{pit} and roughly the same flux between 0.5 and 1 mm. The cumulative distribution only allows comparison between the *accumulated* number of impacts, by definition; the vertical distance between points does not signify the relative flux at that particular size. This may seem a trivial point but the author believes that cumulative flux plots have been thoughtlessly misinterpreted in this way in the past. This is symptomatic of relying solely on a graphical method for comparing fluxes rather than a formal numerical technique. D’agostino (1986) notes that “...sole reliance on them [cumulative distribution plots] can lead to spurious conclusions”.

7.1.1. Previous analyses of flux distributions

Griffiths’ 1997 thesis, which compared impact data collected in the Unit to meteoroid and space debris modelling by ESA, NASA and McBride *et al.* (1999), would presumably require statistical analyses to say quantitatively how “well” the data is modelled. However, no quantitative measures of significance are calculated and all comparisons of data and models are performed by inspection of cumulative flux plots. The analysis uses phrases such as “...they [the data and model fluxes] become almost identical at $f_{max} \geq 600 \mu\text{m}$ ” and “The model fluxes are seen to be in approximate agreement with the measured data”. What constitutes “almost identical” and “approximate agreement” is not quantified, except in terms of percentage differences, but what percentage difference is significant or to be expected by statistical uncertainties? Griffiths talks about fluxes

* As the bins are of different widths, the flux in each bin must be divided by the bin width so that they are in meaningful relative proportions; hence the ordinate in Figure 7.2 is the *flux density* i.e. the flux per pit diameter interval $d(D_{pit})$ in $\text{m}^2 \text{s}^{-1} \text{mm}^{-1}$.

agreeing or being factors of N different between certain F_{\max} ranges but, as has been illustrated, you cannot tell how fluxes compare over a size range by looking at the cumulative flux (unless you are able to judge differences in gradient on a log-log plot by eye).

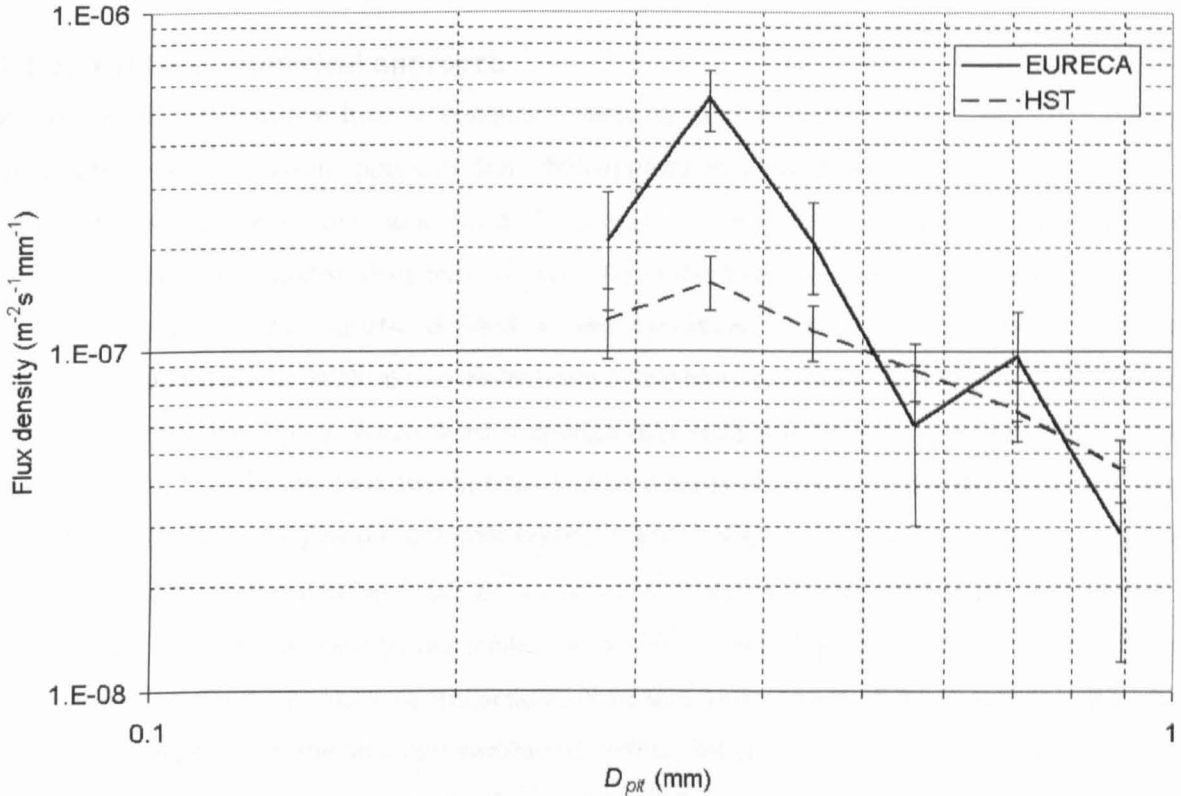


Figure 7.2 – Differential size distribution of solar cell pit diameters

Yano (1995) similarly comments on the apparent by-eye agreement or disagreement of fluxes over certain size ranges; at one point he notes that “*The brass data agreed perfectly with the Al foil data*”. The author does not believe that the data did agree “perfectly”, as the probability of perfect agreement between continuous variables is 0. He also notes that “...*the data is in very good agreement with the model values in the 10-100 μm size range due to abundant data points to have reduced statistical uncertainty.*” By “agreement” Yano most probably means numerically close to some subjective degree rather than the performance of the model being any better as determined by a statistic that takes into account the number of degrees of freedom and thus does not favour models compared against more data.

Taylor (1998) also talks of “good agreement” over f_{\max} ranges, again “good agreement” simply refers to points that look vertically close on a log-log cumulative flux plot.

This type of analysis could be defended on the grounds that “good agreement” refers to when the error bars overlap. But when comparing the flux over a certain size range, rather than the total cumulative flux, even when the lines cross does not signify agreement of the fluxes, merely that the accumulated number of impacts at that point is the same, the actual impact *rate* (i.e. the gradient of the cumulative plot) could be highly different. Even if fully aware of the proper interpretation of a cumulative flux plot, conclusions are often not unambiguous. What does it mean that “the flux is 20% higher in the range 20-100 μm particle diameter”? That a particle in this size range arrives

20% more often on one detector than the other (the wrong conclusion) or that the total number of impacts larger than 20, 30, 40...100 μm is 20% more for one detector than the other (the correct interpretation)? In summary the author feels that there is a lack of formality in previous comparisons of impact flux data.

7.1.2. A formal numerical approach

It has already been shown how to compare counts between two experiments using the binomial distribution (or the Poisson approximation when appropriate). What we want to know now is if the two distributions are of the same form. It is easier to test the similarity of two differential distributions than cumulative distributions. Tests for cumulative distributions are more obscure, but most are based on the statistic defined as the *maximum* vertical distance between the two cumulative distributions such as the *Kolmogorov-Smirnov* and *Anderson-Darling tests* (Press, *et al.*, 1992 or Cooper, 1969). When there is enough data such that binning is feasible the counts in corresponding bins for the two distributions can be compared. When comparing frequency data – not cumulative frequency as these do not represent *independent* trials - to a model the appropriate χ^2 statistic is Pearson's statistic $\Sigma(O - E)^2/E$, where O is the observed number of impacts in a bin and E is the number predicted by the model. It should be noted that this statistic can *only* be used for frequencies, not for normalised frequencies or fluxes, as the shape of the underlying probability distribution depends on the absolute number of events. When comparing two data sets, each of n bins, a contingency table (demonstrated in section 2.3.4) is required. In this way the expected number of impacts E_{pq} in the p th bin for the q th detector is given by:

$$E_{pq} = \frac{\sum_{i=1}^2 O_{pi} \sum_{j=1}^n O_{jq}}{\sum_{i=1}^2 \sum_{j=1}^n O_{ij}} \quad (7.1)$$

Simply put, in each bin the ratio of impacts on each detector should equal the ratio of the total number of impacts.

The procedure is demonstrated for a comparison of the EURECA and HST solar cell pit diameter fluxes. An initial inspection of the EURECA and HST cumulative distributions indicates that the HST data rolls off below 300 μm and thus only data above this size is used. Since HST had an area-time product 4.66 times greater than EURECA, under the hypothesis that the fluxes were the same we would expect HST to receive 4.66 times more impacts larger 300 μm than EURECA. The probability of the actual ratio of 188:59 being observed under this hypothesis is 0.3% and so we would conclude that the impact rates were different for the two exposures. To see if the size distribution of impactors has the same form Table 7.1 shows the contingency table for the EURECA and HST $\log D_{\text{pit}}$ data binned in equal width bins. Logs are taken so, that for an approximately power law distribution such as these, there are more balanced frequencies in each bin. Just to clarify with an example, the expected frequency for the -0.55 bin for EURECA with

reference to equation 7.1 is $(26 \times 59)/247 = 6.21$. It can be seen that the probability of these samples being observed if there is a common parent probability distribution is 0.25% and therefore we would conclude that it is highly unlikely that the same population is being sampled.

Table 7.1 – Contingency table for EURECA and HST D_{pit} data above 300 μm

Log D_{pit} bin upper limit	-0.55	-0.45	-0.35	-0.25	-0.15	-0.05	+	
<i>Observed frequencies</i>								$\Sigma \downarrow$
EURECA	7	23	11	4	8	3	3	59
HST	19	31	28	27	26	22	35	188
$\Sigma \rightarrow$	26	54	39	31	34	25	38	247
<i>Expected frequencies</i>								
EURECA	6.21	12.90	9.32	7.40	8.12	5.97	9.08	
HST	19.79	41.10	29.68	23.60	25.88	19.03	28.92	
								0.25%

7.1.3. Parametric tests

The contingency table is a non-parametric test in that it does not assume anything about the shape of the parent distribution. The most prolific parametric model for meteoroid and space debris fluxes is a power law model of the form:

$$N = kx^{-a} \quad (7.2)$$

where N is the number of events occurring $\geq x$, where x is some detector parameter such as hole diameter, plasma signal, foil thickness penetrated etc. The author has not found any literature in the field that addresses how this model should be applied to meteoroid and space debris data in terms of fitting and hypothesis testing. Fortunately, the statistical distribution theory for this model has received much attention in the social sciences as equation 7.2 is the model used in economics to model the distribution of income over a population and is called the *Pareto distribution* (Johnson *et al.*, 1994). In the author's opinion, the most useful results for this field from advances made in the social sciences in distribution theory associated with the Pareto distribution are the techniques for parameter estimation and measuring inequality.

The most common way to estimate the parameter a in previous literature in the field is linear least-squares fitting between the logged N and x data. However, least-squares fitting assumes that the data are uncorrelated and that positive and negative uncertainties are equal; neither of these assumptions are met for the log cumulative distribution. Additionally, a fit in log space will be biased towards smaller values. For comparison, a linear least squares fit to the TICCE ti4t log cumulative hole size distribution gives $a = 2.05 \pm 0.09$, whereas a non-linear fit with statistical weighting gives 1.91 ± 0.06 .

Johnson *et al.* (1994) describe the method of *Maximum likelihood* for unbiased estimation of the parameters of a Pareto distribution. That is the calculation of the values of a and k that give the maximum probability of the observed data arising.

The estimator of k is simply:

$$\hat{k} = \min_i X_i$$

i.e. the smallest value observed and the estimator of a is:

$$\hat{a} = \left[\ln \left(\frac{\hat{g}}{\hat{k}} \right) \right]^{-1}$$

where g is the geometric mean of the data $(\prod_{i=1}^n X_i)^{1/n}$. A $100(1 - \alpha)\%$ confidence interval for a is:

$$\left(\frac{\hat{a}\chi_{2(n-1),\alpha/2}^2}{2n}, \frac{\hat{a}\chi_{2(n-1),1-\alpha/2}^2}{2n} \right)$$

where $\chi_{2(n-1),\alpha/2}^2$ is the value of the χ^2 distribution with $2(n - 1)$ degrees of freedom corresponding to a probability of $\alpha/2$. Thus, we can make a quantitative comparison between different cumulative distribution coefficients. For the TICCE data the maximum likelihood method gives $a = 1.91$ with a 68.3% confidence interval of (1.70, 2.00) and a 95% confidence interval of (1.38, 2.41). Although this is in agreement with the non-linear least-squares result, the confidence intervals are more relevant than the ± 0.06 uncertainty returned by the least-squares method; note also that they are asymmetrical.

7.2. Thin metal target penetrations

It was shown in section 3 that the equation (called GMC; first published in Gardner *et al.*, 1997a) routinely used for processing the Unit's perforation data from thin metal foils flown in space does not perform well for oblique impacts at light-gas gun velocities ($\sim 5 \text{ km s}^{-1}$). It was found that it performed best for predicting the minimum hole diameter using the velocity of the projectile as the parameter V in the equation rather than the way it is applied to space data using the geometric mean diameter and the normal component of velocity $V\cos\theta$. To determine the effect on the inferred particle size distribution of using GMC in the usual way compared to the way that the author's experiments suggest is more appropriate, the TICCE hole size distribution is converted to a particle size distribution. This has been done using GMC by Gardner *et al.*, (1997b). Therefore, the same parameters are used to perform the conversion i.e. a mean particle density of 2200 kg m^{-3} , a mean velocity of 25 km s^{-1} and a mean impact elevation angle of 45° . Figure 7.3 shows the TICCE flux converted to particle diameters in 3 ways: (i) Using the geometric mean hole diameter and the normal component of velocity; (ii) using the minimum hole diameter instead of the geometric mean; (iii) using V instead of $V\cos\theta$. The hole diameter data set used is the one corrected for astigmatism with diameters determined by ellipse fitting (section 2.3.3). The cumulative plot is shown more correctly as steps rather than the usual linear interpolation of points. Error bars are not shown as statistical uncertainties are implicit for frequency distributions and, in the author's opinion, are not particularly instructive and make the plot too cluttered. The author has only ever

seen error bars used on a cumulative frequency distribution in this field. In more other disciplines they are not shown as numerical methods are employed for evaluating significance.

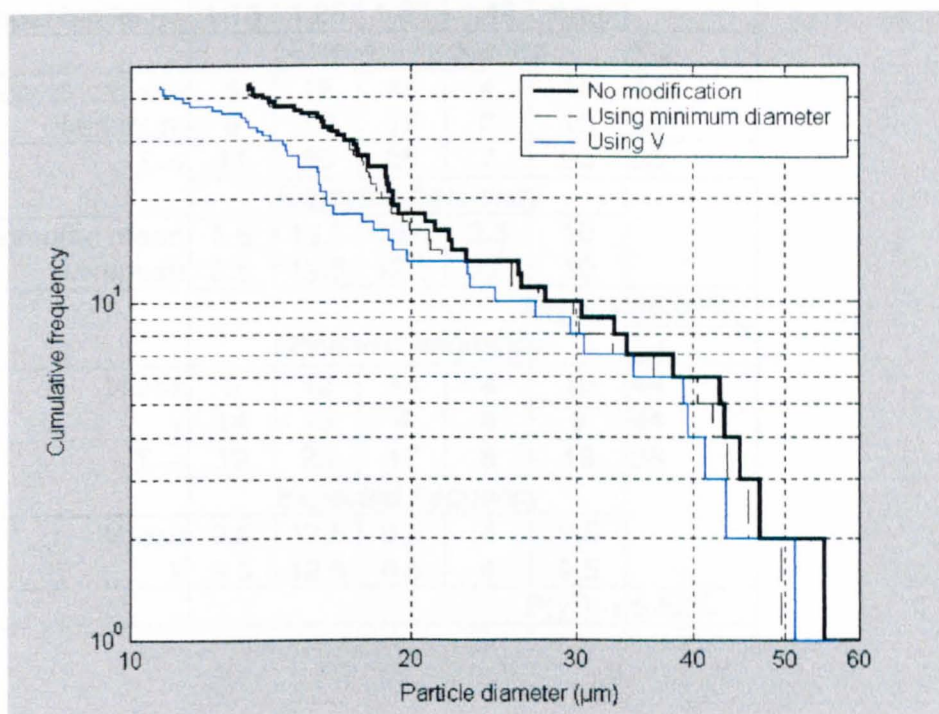


Figure 7.3 – TICCE flux converted to particle diameters using GMC

It can be seen that using the minimum diameter has a small effect. This is because most of the TICCE holes were highly circular (mean circularity 0.93). Not all the significantly non-circular holes will be due to oblique impacts; some will be due to irregularly shaped particles. Therefore this represents the maximum error from using the geometric mean instead of the minimum diameter. A possible reason why the TICCE holes were highly circular could be that the circularity has a significant dependence on velocity. The effect of using the velocity instead of its normal component has a clearly larger effect. To determine if the resulting difference in the particle diameter distribution is significant the distributions were binned and a contingency table was used (Table 7.2).

It can be seen in Table 7.2 that there is a high probability (99%) that the underlying distributions of the data converted using the geometric mean and the minimum diameter are no different, but there is only a 6% probability that the observed difference between the data converted using V and $V\cos\theta$ is insignificant. These tests are only approximate for the small number of counts observed, note that some bins have less than 5 counts. The *Kolmogorov-Smirnov* test for cumulative distributions (Cooper, 1969) is implemented in the statistical package *SPSS* and returns probabilities of 93.9% and 2.3% for the comparisons made above, respectively.

Cumulative size distribution indices for the three methods (geometric mean using $V\cos\theta$, minimum diameter using $V\cos\theta$, geometric mean using V) and 68.3% confidence intervals are 2.07 (1.87, 2.16), 2.15 (1.94, 2.24) and 1.83 (1.65, 1.91), respectively. Therefore, the *shape* of the distributions is altered significantly by using V instead of $V\cos\theta$, as well as the location, due to the non-linear dependence on V in GMC.

Table 7.2 – Contingency table for comparison between different methods of applying GMC

Log D_p upper bin limit	1.15	1.25	1.35	1.45	more	
	<i>Observed frequency</i>					$\Sigma \downarrow$
Geometric mean	5	12	13	4	10	44
Minimum	6	13	12	3	10	44
$\Sigma \rightarrow$	11	25	25	7	20	88
	<i>Expected frequency</i>					
Geometric mean	5.5	12.5	12.5	3.5	10	
Minimum	5.5	12.5	12.5	3.5	10	
	$P(\chi^2) \rightarrow$					98.89%
	<i>Observed frequency</i>					$\Sigma \downarrow$
$V \cos \theta$	5	12	13	4	10	44
V	14	13	4	4	9	44
$\Sigma \rightarrow$	19	25	17	8	19	88
	<i>Expected frequency</i>					
$V \cos \theta$	9.5	12.5	8.5	4	9.5	
V	9.5	12.5	8.5	4	9.5	
	$P(\chi^2) \rightarrow$					5.82%

7.3. Solar cells

7.3.1. Applying laboratory calibration to space data

It is clear that the results of the impact experiments in this thesis cannot be applied to space-deployed solar cells with any confidence, as the morphology of the laboratory impacts is vastly different from the space morphology (compare appendix C to Figure 4.6, page 117). Nevertheless, this has not deterred others from employing laboratory derived empirical relationships to decode solar cell space impacts. When Paul *et al.*, (1997) presented the results of their solar cell impact experiments and its application to space data at the 1996 COSPAR assembly in Birmingham, the author posed the question “Do your laboratory impacts look like your space impacts?” They answered in the affirmative, but despite showing many images of space impacts, did not show any images of laboratory impacts so that we could make our own judgement. Paul *et al.* (1997) plot the cumulative flux of impacts on EURECA and HST converted to particle diameters using their empirical equation. They make the observation: “*It can be seen that the particle environment encountered by the two satellites was very similar despite the differences in their orbits*”. No uncertainties are presented such as those arising from measurement errors, uncertainties in the particle diameters arising from the residual variability about the fitted equation or statistical uncertainties in the count rate of impacts. Therefore, “very similar” is an entirely subjective assessment. Their final conclusion that any expected difference due to orbital dissimilarities may have been compensated for by “*variations in the solar activity and the resulting variation in man-made debris presence*” is premature and should be disregarded, in the author’s opinion, until some quantitative consideration of the *significance* of the results of their analysis is made.

The current status is that impact morphology observed on space-flown solar cells cannot be reproduced in the laboratory and although extrapolations of metal-target empirical equations to space velocities may be defensible, doing so for solar cell impacts is highly questionable. An alternative, however, to laboratory calibration is “space” calibration performed by equating fluxes on identically exposed surfaces.

7.3.2. Space calibration

Gardner *et al.*, (1996) equated the flux between thick and thin targets exposed on the same face of LDEF to calibrate foil perforations to an equivalent depth that would be penetrated in a thick target. With this in mind the author decided to see if a similar approach could be employed to find a conversion from solar cell crater diameters to the equivalent aluminium target parameter, thus permitting a comparison between solar cell and aluminium crater distributions from space-flown experiments. It was discovered that NASA’s *Goddard Space Flight Center* (GSFC) flew a test plate on LDEF, upon which solar cells were mounted to evaluate the degradation in performance due to prolonged exposure to the near Earth micro-particle environment (Hill and Rose, 1994). The cells were mounted on row 8 of LDEF: 35° from the ram direction. We also have impact data from aluminium targets on row 8 of LDEF, from the *Meteoroids and Debris Special Investigation Group* (M & D SIG: Zolensky *et al.*, 1995). The cumulative conchoidal diameter (D_{co}) flux and ballistic limit (F_{max}) fluxes from each experiment are plotted on the same axis in Figure 7.4.

As these surfaces have been identically exposed to the space environment (same exposure time, pointing direction etc.), the difference between the solar cell crater diameters and the F_{max} measured by the aluminium targets, at the *same flux* (the horizontal arrow in Figure 7.4), gives a calibration for solar cell damage that is applicable to this impact regime for space impactors. This calibration will be better than any laboratory calibration in that we are effectively doing the reverse of what we are trying to achieve by laboratory calibration. With laboratory calibration we are trying to determine how D_{co} and F_{max} are related so that we can convert one to the other and compare impact fluxes. Thus, the comparison is only as accurate as our calibration, which for solar cells has been shown to be poor in that we are extrapolating far beyond the parameter range of the calibration data. By this alternative method we are starting with fluxes that are the same (statistically) and thus the difference between the two distributions corresponds to the relationship between the two parameters for that environment (particle size, density, velocity). Thus the calibration is being performed at a closer proximity, if not within, the parameter range that we want to apply it. The values of F_{max} at a corresponding flux to each value of D_{co} are plotted in Figure 7.5. This is an important new calibration curve that has not been previously identified.

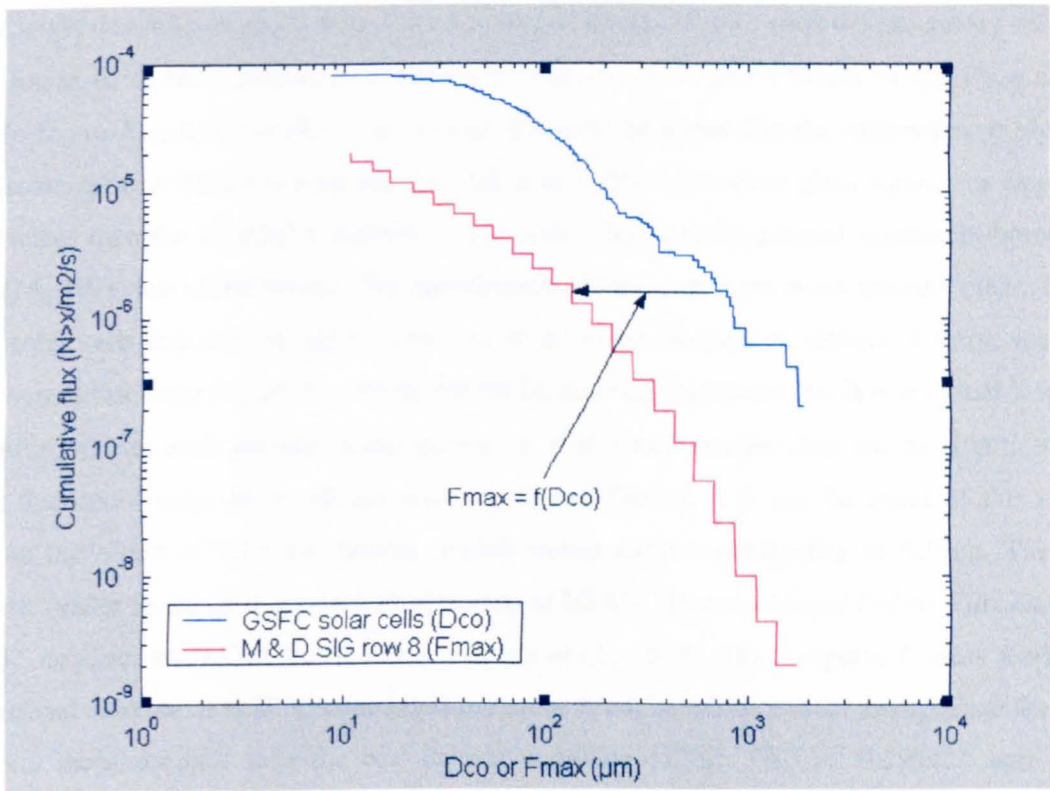


Figure 7.4 – Fluxes measured on LDEF row 8

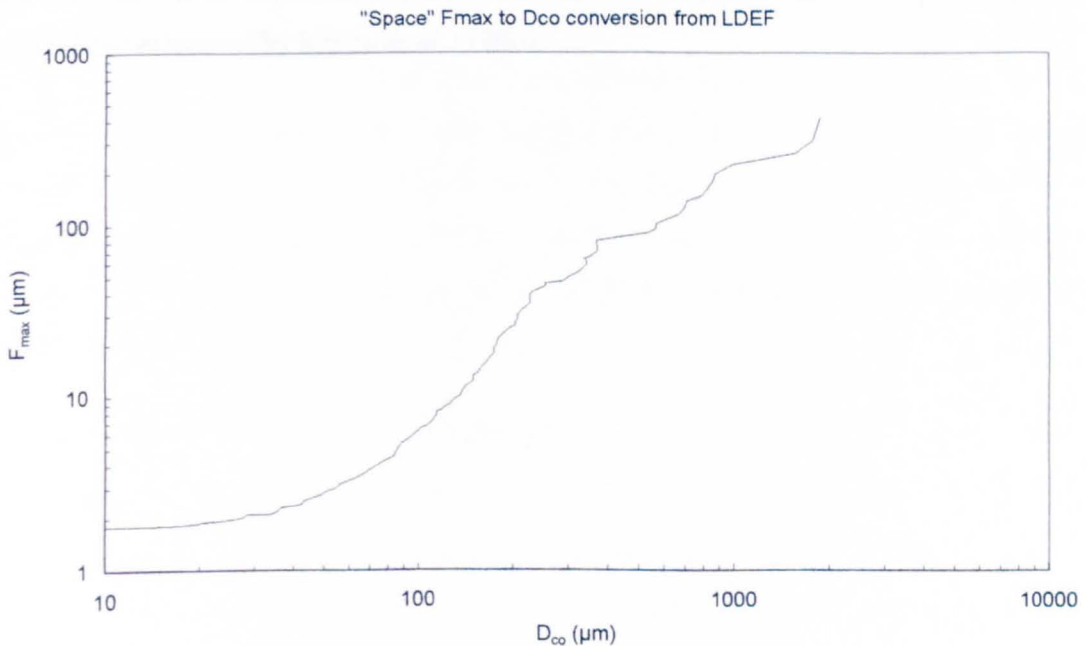


Figure 7.5 - D_{co} to F_{max} conversion derived from identically exposed GSFC solar cell samples and metal targets on row 8 of LDEF

The kinks in the curve most likely correspond to penetration of successive layers of the solar cells. The decrease in gradient at around $200 \mu\text{m}$ D_{co} probably corresponds to penetration of the cover glass with the accompanying loss of energy slowing the increase in the conchoidal diameter with increasing impact energy. The other turning points in the curve at larger sizes probably correspond to penetration of successive layers.

Taylor (1998) compares this calibration, identified by the author, to her D_{co} -to- F_{max} conversion derived from laboratory impacts, which incorporates an earlier version (Shrine *et al.*, 1996) of the

impact angle dependence study in section 5 as its $\cos \theta$ term. Taylor uses the laboratory calibration and a linear fit to the calibration in Figure 7.5 between 136 and 170 μm to specify a range of possible $D_{\text{co-to-}F_{\text{max}}}$ ratios in that size bracket. It should be noted that the calibration in Figure 7.5 is for solar cells of different construction and with a different cover glass (quartz as opposed to borosilicate) than the EURECA and HST solar cells. Taylor notes general agreement between the EURECA, HST and LDEF fluxes. The significance of this agreement is not entirely clear. The flux on the solar cells depends on many factors, such as orbital inclination, attitude history, shadowing by the spacecraft body (which is variable for HST), secondary impacts etc. It is not clear if the wide calibration bracket even permits disagreement i.e. if it is any smaller than the maximum variation in flux that could arise due to all the afore-mentioned factors. It is not the remit of this thesis to calculate the effect of all these factors, which would require substantial modelling. The author refers the reader to the final and technical reports of ESA's "*Meteoroid and Debris Flux and Ejecta Models*" contract no. 11887/96/NL/JG (Unispace *et al.*, 1998) which reports 2 years work by an international team of around 30 contracted researchers whose remit was to amalgamate the results of *in situ* measurements over the past decade including LDEF, TICCE, EURECA and HST to improve current models of the near-Earth environment. The contract also amalgamated the results of solar cell calibration experiments performed since the EURECA and HST post-flight analyses including those presented by Shrine *et al.* (1996).

8. Summary

This thesis reports observations of hypervelocity impact features on space-flown materials that are suspected to be due to oblique impacts. Interpretation of oblique impacts requires an understanding of the effect impact angle has on the final crater morphology. It was found that, for the types of space-flown targets studied, namely thin foils and solar cells, laboratory investigation of oblique impacts was lacking in adequate coverage of the parameter range. Accordingly, impact experiments were performed to investigate the oblique impact response of these two types of “detector”.

It was found that the method by which the GMC thin foil penetration equation is applied to space data, using an assumed impact angle dependence, does not model laboratory impacts well. Accordingly a new method of applying GMC, that more closely matches the laboratory impacts, was used for space data and was shown - using an appropriate statistical analysis - to produce a *significantly* different interpretation of the meteoroid and debris size distribution.

An important factor that required clarification for solar cell hypervelocity impacts is which features indicate impact angle. It was found that, of the features used to interpret impact elevation angle in the EURECA and HST post-flight analyses, only pit circularity showed a significant correlation with impact angle, circularity of any other damage parameter (conchoidal and shatter zones) or the centroid offset did not. It was found that the conchoidal diameter, the most commonly used parameter for decoding particle parameters, shows a change in response at 45°. Previous studies based on less data use a single power law for all angles. The author withholds application to space data as it is not felt that it is justified given the disparity in morphology between the laboratory and space impacts, but offers an alternative approach based on comparing identically exposed solar cell and metal targets.

8.1. Oblique impacts in space

8.1.1. TICCE

In order to study the shape of perforations in the space-flown foils of the TICCE experiment an extension to the capabilities of the Unit's LOSS optical scanning system was implemented by the author whereby the polar co-ordinates of hole perimeters could be automatically recorded. The distribution of circularities for the different thicknesses of foil used on TICCE suggested that circularity is correlated with foil thickness.

The data acquired by the new technique also facilitated the correction of the TICCE data for a previously unknown astigmatism of the SEM system.

8.1.2. EURECA and HST

The author's first analysis (Drolshagen *et al.*, 1996) identified some trends in the distribution of *inferred* impact azimuth directions, which were interpreted as evidence of anisotropy of the meteoroid environment. The distributions were analysed in this thesis using the appropriate

statistical techniques and it was found that there did appear to be a bias of impacts from the Earth-apex direction, assuming the correct azimuth angle was attributed to craters, but for one wing only. The other, weaker correlations between azimuth angle, impact location and crater circularity and centroid offset were shown to be insignificant and to be expected by random fluctuations. The first check on the accuracy of the azimuth angle that has been performed on this data set - all other use of this data makes no check of its validity - shows that the inferred impact directions could be highly inaccurate.

8.2. Oblique impacts in the laboratory

8.2.1. Oblique penetration of metal targets

The experiments presented in this thesis to study the effect on crater shape of *both* impact angle and relative target thickness give a more complete coverage of the parameter space than any previous study that the author was able to find. The regression analysis shows that a simple power law is an appropriate model for the major and minor axes of the holes. The author feels that the discussion of regression analysis presented in this section is necessary to clarify the rationale and exactly how the regression should be evaluated in the context of the experimental errors and the undesirable velocity variation; such considerations are lacking in previous literature reviewed in this section.

It is found that the GMC thin target penetration equation (Gardner *et al.*, 1997a) is best suited for predicting the minor axis using the velocity as a parameter rather than the more often used normal component. It may be, however, that although a $\cos\theta$ exponent of 0 is more appropriate than 1, that a weaker modification of the velocity dependence is appropriate for oblique impacts. This question will have to be addressed by experiments where the velocity is varied in a methodical way.

8.2.2. Oblique impacts on solar cells

The experimental programme in section 5 covered more impact angles than any previous study to the author's knowledge. The data obtained was different from other similar experiments in that many craters were produced for a single angle by use of the buckshot technique of firing the light-gas gun. In this way the variability craters could be studied for each angle thus permitting the appropriate confidence limits to be placed on the regression based on the repeatability of the phenomena rather than less relevant (in the author's opinion) measurement uncertainties.

It was found that the morphology of the craters observed on the EURECA and HST solar cells could not be reproduced in the light-gas gun experiments. The key difference was the absence of smooth bowl shaped pits in the laboratory impacts.

Checks were made on the correlation of features used in the EURECA and HST post-flight analyses to infer impact direction. It was found that the circularity of the conchoidal zone and shatter zones shows no significant correlation with impact angle, neither does the centroid offset. It was found that the pit circularity is the only parameter that is *primarily* dependent on impact angle.

However, it could be that at space velocities correlations not observed here might arise. The size, rather than the circularity, of the conchoidal zone shows a strong dependence on impact angle above an angle of 45° from the normal. Below this, the conchoidal zone does not show a significant correlation with impact angle. This result is relevant for empirical equations used for decoding space data that previously used a power law $\cos\theta$ term for all angles.

8.2.3. The light-gas gun buckshot technique

The most in-depth study to date of the commonly used buckshot technique of firing the light-gas gun has been presented in this thesis. In the experimental programme in section 5 it was shown how normal probability plots can be used for initial appraisal of the crater size distribution. The different sources of variance in a buckshot firing were identified and the role they play in the analysis of any regression equations. The velocity variation within a buckshot was calculated and shown to be generally smaller than the variation between shots and thus the craters produced in a single buckshot are a closer approximation to ideal repeat experiments than a series of individual shots.

The important issue of the survivability of buckshot projectiles upon launch was addressed in section 6 and it was found that it is highly likely that soda-lime glass spheres survive launch, but that mineral powders do not.

8.3. Other work by the author

8.3.1. 3D stereo analysis: a new technique for measuring craters

Whilst scanning the TICCE meshes and targets from the experimental programmes in this thesis the author discovered that the SEM measuring software had the facility to process stereo images and determine the heights of sample features as well as the dimensions in a plane perpendicular to the viewing direction. Accordingly, the author imaged craters with the SEM stage tilted at an equal angle either side of normal. An example of the first output of this analysis is shown in Figure 8.1. The top row shows a crater and the mesh that is overlaid at which heights are calculated. The bottom-left image shows the heights interpolated with a surface, which can then be rotated, as shown, so that the crater can be viewed from any angle. The bottom-right image shows the data plotted in a mathematical package with contours also shown. The author produced crater profiles using this technique which were subsequently incorporated into a study whereby crater shapes are described by orthogonal polynomials (Kay *et al.*, 1997). Previous to this the crater profiles were obtained by a coherence radar technique outside the group. This new technique, identified by the author, allowed this sort of data to be collected within the group and now forms the basis of a current student's PhD project.

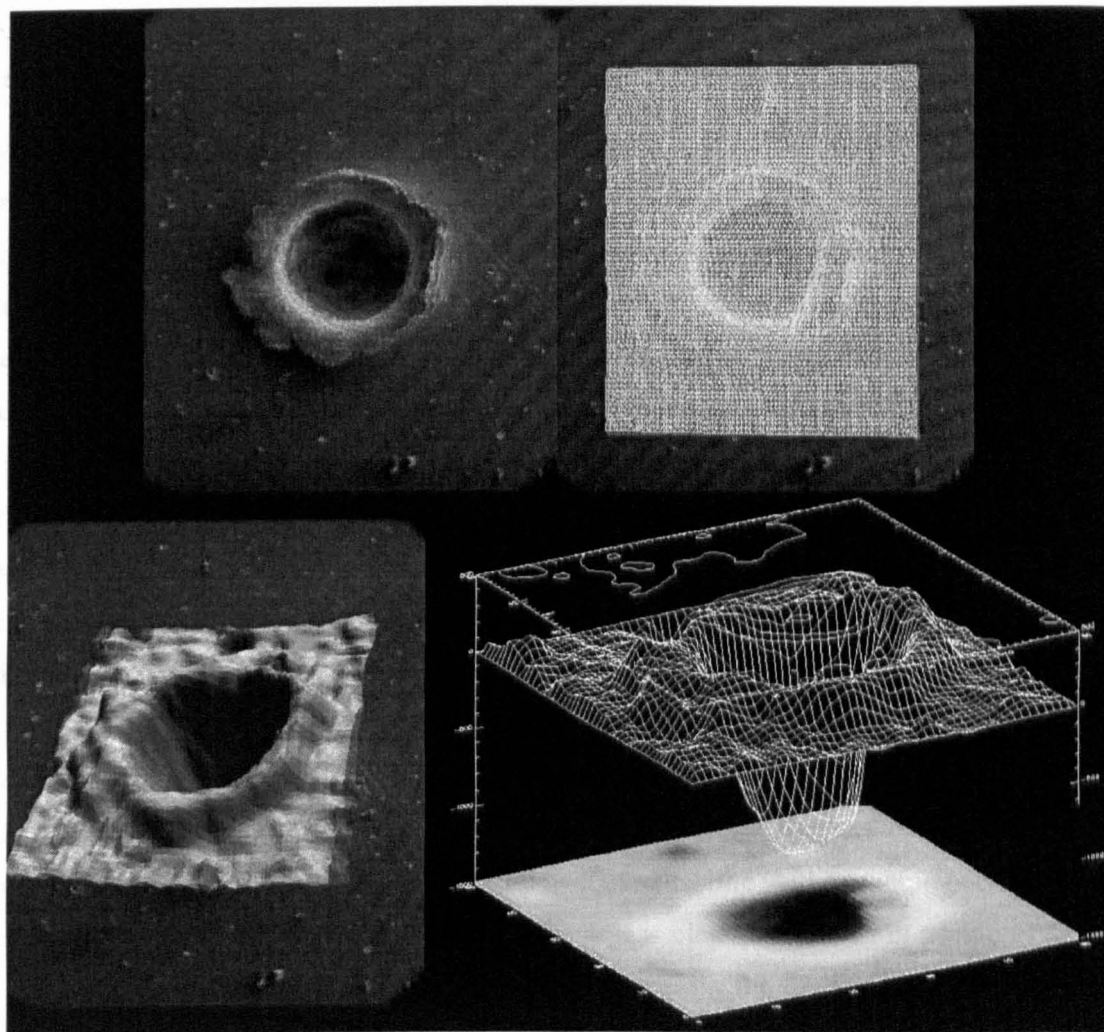


Figure 8.1 – 3D profiling of crater shapes

8.3.2. ESEF-Euromir '95: Dustwatch-P

The Unit's Dustwatch-P experiment was one of a suite of experiments housed in the *European Space Exposure Facility* (ESEF). ESEF was flown on the Russian *Mir* space station during late 1995/early 1996 as part of the *Euromir '95* mission. The original concept of ESEF was to sample a meteor stream by selective exposure. However in the context of *Euromir '95*, a precursor mission to operations on-board the forthcoming Columbus platform, its purpose is broadened to monitoring the meteoroid *and* debris environment in the vicinity of a large space facility. Dustwatch-P comprised and a passive capture cell unit and an aerogel collector. This two-fold approach is thus intended to measure a penetration flux and additionally capture particles for microscopic and chemical analysis on retrieval.

Dustwatch-P was an important experiment for the Unit in terms of showing that our detector design was viable in such an exposure facility (ESEF) and thus paving the way for future experimental opportunities on-board the international space station. The author was given sole responsibility for the post-flight analysis of the Dustwatch-P detectors in view of his experience with the TICCE scanning. The author presented the results at 2 international conferences (*Asteroids, Comets, Meteors* in Versailles, 1996 and *COSPAR '96* in Birmingham) and at the *Euromir '95* science working group meeting at the ESA astronaut centre at *DLR* in Cologne attended by *Euromir '95*

ESA astronaut Thomas Reiter. The author's presentation at COSPAR '96 (Shrine *et al.*, 1997) led to a telephone interview with the science editor of the *Daily Telegraph*.

However, the author's analysis was hampered by factors beyond his control and thus limited the scientific output of this experiment. Firstly, the *exact* exposure time of the detectors was not clearly specified by the ESEF principle investigator and all publications of ESEF results are vague in this respect as the cassettes were opened and closed at various times, usually when the shuttle came close to *Mir*. Furthermore, the project paid for the attitude telemetry so that the pointing history of the detectors over the duration of the exposure could be recorded. However, the co-ordinates did not specify what the direction 0,0,0 corresponded to. The author spent many weeks trying to interpret the attitude data and corresponding with the other institutes involved with the Euromir '95 mission, but no-one could offer sufficient information and to this date the most complete description of ESEF's attitude is that it was primarily Earth pointing due to the gravity gradient stabilisation of *Mir*. Another obstacle to the author's analysis was that the cassette in which Dustwatch was housed was not available for analysis. The author requested that the cassette be made available for analysis at the Unit because it was inferred that it received an unexpectedly large impact by analysis of the distribution of secondary ejecta impacts on the Dustwatch foil holder (Shrine *et al.*, 1997). However, without consulting the author, shipment of the wrong cassette (cassette 1) from Orsay was arranged, when it is clearly specified in Shrine *et al.* (1997) that cassette 2 is believed to have received a large impact. By the time the cassette arrived at the Unit and the author identified it as the wrong one, the correct one had been allocated to further experiments at Orsay and was thus, unfortunately, unavailable. Taking all these factors into consideration, along with the fact that so many instruments were packed into such a small area on a curiously Earth-pointing meteoroid detector, the author feels that the primary results of the ESEF-Dustwatch experiment were design-validation and publicity rather than scientific.

8.3.3. The Van de Graaff top-terminal monitor

On arrival at the Unit the author was assigned the task of writing the software for a new piece of monitoring equipment for the Van de Graaff accelerator. The author spent around 3 months writing the low level control code for the device's microprocessor and a graphical user interface in C++ for the computer that communicates with the monitoring device when it is *in situ*. The top-terminal monitor is still in the process of installation in the Van de Graaff at the time of writing. When the system finally comes into use it is hoped that a publication in the Journal of Scientific Instruments will follow.

8.4. Future recommendations

The author believes that the experimental programmes initiated in for this thesis should be taken forward and the effect of parameters not studied in this thesis be investigated. In particular, now that the UKC light-gas gun velocity can be varied in a controlled manner, the effect of velocity on oblique impact phenomena can be studied.

Application of the GMC thin foil penetration equation (Gardner *et al.*, 1997a) for modelling oblique impacts on spacecraft surfaces should now use the method presented in this thesis rather than the previously employed $\cos \theta$ modification.

The author believes that the relatively straightforward (in that all the tests presented are “off the peg” rather than being specifically designed) statistical analyses demonstrated in this thesis have shown the way towards a more rigorous and quantitative interpretation of impact flux data and empirical regression equations. In particular the author recommends that, in future, regression equations from laboratory hypervelocity impact studies should have the appropriate uncertainties quoted for their fitted coefficients so that quantitative comparisons between their predictions and new data can be made. The adoption of formal numerical methods for comparing flux distributions is clearly overdue.

References

- Ari, N. and Wilbeck, J.S.**, Debris Fragment Characterisation in Oblique Hypervelocity Impacts, *Int. J. Impact Engng.* Vol. 14, pp. 37-48 (1993).
- Ashworth, D.G.**, Lunar and Planetary Impact Erosion in *Cosmic Dust*, Ed. J.A.M.McDonnell, John Wiley & Sons (1978).
- Baker, J.R. and Persechino, M.A.**, An Analytical Model of Hole Size in Finite Plates for both Normal and Oblique Hypervelocity Impact for all Target Thicknesses up to the Ballistic Limit, *Int. J. Impact Engng.* Vol. 14, pp. 73-84 (1993).
- Baron, M.J.**, *Microparticle Hypervelocity Impacts on Satellites in Low-Earth Orbit*, PhD Thesis, University of Kent (1996).
- Barret, R.A., Zolensky, M.E., Hörz, F., Lindstrom, D.J. and Gibson, E.K.**, Suitability of silica aerogel as a capture medium for interplanetary dust, *Proc. Lun. Planet. Sci.* Vol. 22, pp. 203-212, Lunar and Planetary Institute, Houston (1992).
- Bevington, P.R.**, *Data reduction and error analysis for the physical sciences*, McGraw-Hill (1969).
- Burchell, M.J., Cole, M.J., McDonnell, J.A.M. and Zarnecki, J.C.**, Hypervelocity Impact Studies Using the 2 MV Van de Graaff Accelerator and Two-stage Light Gas Gun of the University of Kent at Canterbury, *Meas. Sci. Technol.* **10**, pp. 41-50 (1999).
- Burchell, M.J., Thomson, R. and Yano, H.**, Capture of hypervelocity particles in aerogel: in ground laboratory and low earth orbit, *Planet. Space Sci.*, **47**, pp. 189-204 (1999a).
- Christiansen, E.L., Cykowski, E. and Ortega, J.**, Highly Oblique Impacts into Thick and Thin Targets, *Int. J. Impact Engng.* **14**, pp. 157-168 (1993).
- Collier, I.**, *Hypervelocity Impacts and Perforations: A First Examination of Eureka, TiCCE*, MSc Thesis, University of Kent (1995).
- Cooper, B.E.**, *Statistics for Experimentalists*, Pergamon Press (1969).
- Cour-Palais, B.G.**, Hypervelocity Impact in Metals, Glass and Composites, *Int. J. Impact Engng.* **5**, pp 221-237 (1987).
- D'Agostino, R.B.** Graphical Analysis in *Goodness-of-fit Techniques* Ed. D'Agostino and Stephens, Marcel Dekker Inc. (1986).
- Drolshagen, G., McDonnell, J.A.M., Stevenson, T.J., Deshpande, S., Kay, L., Tanner, W.G., Mandeville, J.C., Carey, W.C., Maag, C.R., Griffiths, A.D., Shrine, N.G. and R.Aceti.**, Optical Survey of Micrometeoroid and Space Debris Impact Failures on EURECA, *Planet. Space Sci.*, **44(4)**, pp 317-340 (1996).
- Farenthold, E.P.**, Oblique hypervelocity impact simulations for Whipple shield-protected structures, *Int. J. Impact Engng.* **17**, pp. 291-302 (1995).
- Fechtig, H., Gentner, J.B., Hartung, K., Nagel, G., Neukum, G., Schneider, E. and Storzer, D.**, Microcraters on Lunar Samples, *NASA SP-370* (1974).
- Fechtig, H., Nagel, K., Stähle, V., Grögler, N., Schneider, E. and Neukum, G.**, Impact Phenomena on an Apollo 12 Sample, *Proc. Lunar Sci. Conf 8th*, pp 889-899 (1977).
- Fechtig, H., Grün, E. and Kissel, J.**, Laboratory Simulation in *Cosmic Dust*, Ed. J.A.M.McDonnell, John Wiley & Sons (1978).
- Gardner, D.J.**, *Hypervelocity Impact Morphology*, PhD Thesis, University of Kent (1995).
- Gardner, D.J., Collier, I., Shrine, N.R.G., Griffiths, A.D. and McDonnell, J.A.M.**, Micro-particle Impact Flux on the Timeband Capture Cell Experiment of the EURECA Spacecraft, *Adv. Space. Res.* **17**, No. 12, pp. (12)193-(12)199 (1996).
- Gardner, D.J. and Burchell, M.J.**, Thick Target Hypervelocity Impact Crater Morphology: The Influence of Impact Angle, Speed and Density Ratio, *Proc. Second European Conf. On Space Debris*, *ESA SP-393*, pp. 481-486 (1997).

- Gardner, D.J., McDonnell, J.A.M. and Collier, I.**, Hole Growth Characterisation for Hypervelocity Impacts in Thin Targets, *Int. J. Impact Engng.* Vol. 19, No. 7, pp. 589-602 (1997a).
- Gardner, D.J., Shrine, N.R.G. and McDonnell, J.A.M.**, Determination of Hypervelocity Impactor Size from Thin Target Spacecraft Penetrations, *Proc. Second European Conf. on Space Debris, ESA SP-393*, p. 493 (1997b)
- Glassner, A.S.**, *Graphics Gems, Ed. A.S. Glassner*, Academic Press (1990).
- Grady, D.E. and Kipp, M.E.**, Experimental and Computational Simulation of the High Velocity Impact of Copper Spheres on Steel Plates, *Int. J. Impact Engng.* Vol. 15, No. 5, pp. 645-660 (1994).
- Griffiths, A.D.**, *Modelling of Meteoroid and Debris Impacts on Recently Retrieved Near Earth Spacecraft*, PhD Thesis, University of Kent (1997).
- Grün, E., Zook, H.A., Fechtig, H. and Geise, R.H.**, Collisional Balance of the Meteoritic Complex, *Icarus*, 62, 244-272 (1985).
- Herrmann, W. and Wilbeck, J.S.**, Review of Hypervelocity Penetration Theories, *Int. J. Impact Engng.* Vol. 5, pp. 307-322 (1987).
- Hill D.C. and Rose M.F.**, Analysis of Space Environment Damage to Solar Cell Assemblies from LDEF Experiment A0171-GSFC Test Plate, *NASA Contract NAS8-39131 Final Report* (1994).
- Hörz, F., Hartung, J.B. and Gault, D.E.**, Micrometeorite Craters on Lunar Rock Surfaces, *J. Geophysical Res.* Vol. 76, No. 23, p. 5770 (1971).
- Hörz, F., Cintala, M.J., Bernhard, R.P. and See, T.H.**, Dimensionally Scaled Penetration Experiments to Extract Projectile Sizes from Space Exposed Surfaces, *Int. J. Impact Engng.* Vol. 14, pp. 347-358 (1993).
- Hugill M.**, *Advanced Statistics*, Bell and Hyman (1985).
- Johnson, N.L., Kotz, S. and Balakrishnan, N.**, *Continuous Univariate Distributions*, John Wiley & Sons, (1994).
- Kay, L., Podoleanu, A., Seeger M. and Solomon, C.J.**, A new approach to the measurement and analysis of impact craters, *Int. J. Impact Engng.* Vol. 19, No. 8, pp. 739-753 (1997).
- Lyons, L.**, *A Practical Guide to Data Analysis for Physical Science Students*, Cambridge University Press (1991).
- Maag, C.R., Tanner, W.G., Stevenson, T.J., Borg, J., Bibring, J-P., Alexander, W.M. and Maag, A.J.**, Intact Capture of Hypervelocity Impact Particles and Ejecta, *Proc. First European Conf. on Space Debris, ESA SD-01*, p. 125 (1993).
- Maclay, T.D., Fudge, M.L. and Harris, C.M.**, The validity of the Poisson distribution for orbital debris impact problems, *SPIE Proceedings series 2813: 'Characteristics and Consequences of Orbital Debris and Natural Space Impactors'*, SPIE - The International Society for Optical Engineering, Bellingham, WA. USA (1996).
- Maiden, C.J., Gehring, J.W. and McMillan, A.R.**, Investigation of fundamental mechanism of damage to thin targets by hypervelocity projectiles, *NASA TR 63-225* (1963).
- Mandeville, J.C.**, Aragatz Mission Dust Collection Experiment, *Adv. Space Res.* Vol. 10, No. 3, p. 397 (1990).
- Mandeville, J.C. and Vedder, J.F.**, Microcraters formed in glass by low density projectiles, *Earth. Planet. Sci. Letters*, 11, pp. 297-306 (1971).
- Mandeville, J.C. and Berthoud, L.**, From LDEF to EURECA: Orbital Debris and Meteoroids in Low Earth Orbit, *Adv. Space Res.* Vol. 16, No. 11, pp. 67-72 (1995).
- McBride, N., Green, S.F. and McDonnell, J.A.M.**, Meteoroids and small sized debris in low Earth orbit and at 1 AU: results of recent modelling, *Adv. Space. Res.* Vol. 23, No. 1, pp. 73-82 (1999).

- McDonnell, J.A.M.**, Microparticle Studies by Space Instrumentation in *Cosmic Dust*, Ed. J.A.M. McDonnell, John Wiley & Sons (1978).
- McDonnell, J.A.M.**, HVI Phenomena: Applications to Space Missions, *Int. J. Impact Engng., Proc. Hypervelocity Impact Symposium, Huntsville, Alabama, 1998*, in press (1999).
- McDonnell, J.A.M., Carey, W.C. and Dixon, D.G.**, Cosmic dust collection by the capture cell technique on the Space Shuttle, *Nature*, Vol. 309, No. 5965, pp. 237-240 (1984).
- McDonnell, J.A.M., McBride, N., Ratcliff, P.R., Gardner, D.J., Griffiths, A.D. and Green, S.F.**, Near Earth Environment in *Cosmic Dust Ed. E. Grün et al.* University of Arizona press, in preparation (1998).
- Melosh, H.J.**, *Impact Cratering A Geologic Process*, Oxford University Press (1989).
- Mog, R.A., Helba, M.J. and Robinson, J.H.**, Development and optimization of a multibumper design-model for spacecraft protective structures, *Int. J. Impact Engng.* Vol. 14, No. 1-4, pp. 519-530 (1993).
- Mullin, S.A., Littlefield, D.L., Anderson, C.E. and Chhabildas, L.C.**, An Examination of Velocity Scaling, *Int. J. Impact Engng.* Vol. 17, pp. 571-581 (1995).
- National Research Council**, *Orbital Debris – A Technical Assessment*, National Academy Press (1995).
- Nysmith, C.R. and Denardo, B.P.**, Experimental investigation of the momentum transfer associated with impact into aluminium targets, *NASA TND 5492* (1969).
- O’Neal, R.L. and Lightner, E.B.**, Long Duration Exposure Facility – A General Overview, *LDEF – 69 Months in Space, First Post-Retrieval Symp.* Part 1, p. 3 NASA CP-3134 (1991).
- Paley, M.T.**, *The development of an automated optical scanning system and studies of the earth orbital dust environment by means of the LDEF micro abrasion package*, PhD Thesis, University of Kent (1995).
- Paul, K. G., Igenbergs, E.B. and Berthoud, L.**, Hypervelocity Impacts on Solar Cells – Observations, Experiments and Empirical Scaling Laws, *Int. J. Impact Engng.* Vol. 20, pp. 627-638 (1997).
- Press, W.H., Teukolsky, S.A., Vetterling, W.T. and Flannery, B.P.**, *Numerical Recipes in C*, Cambridge University Press (1992).
- Ryan, T.P.**, *Modern Regression Methods*, John Wiley & Sons (1997).
- Sawle, D.R.**, Hypervelocity impact in thin sheets and semi-infinite targets at 15 km/sec, *Proc. AIAA Hypervelocity Impact Conference, Cincinnati, Ohio* (1969).
- Schonberg, W.P. and Taylor, R.A.**, Penetration and Ricochet Phenomena in Oblique Hypervelocity Impact, *AIAA Journal*, Vol. 27, No. 5, pp. 639-646 (1989).
- Shrine, N.R.G., Taylor, E.A., Yano, H. Griffiths, A.D. and McDonnell, J.A.M.**, Using Solar Cells as Microparticle Detectors in Low Earth Orbit, *SPIE Proceedings series 2813: ‘Characteristics and Consequences of Orbital Debris and Natural Space Impactors’*, SPIE - The International Society for Optical Engineering, Bellingham, WA. USA (1996).
- Shrine N.R.G., McDonnell, J.A.M., Burchell, M.J, D.J. Gardner, H.S. Jolly, P.R. Ratcliff, R. Thomson**, Euromir '95: First Results from the Dustwatch-P detectors of the European Space Exposure Facility, *Adv. Space Res.* Vol. 20, No. 8, pp. 1481-1484 (1997).
- Space Applications Services, Mare Crisium, CERT-ONERA, Unispace Kent, Hubble Space Telescope Micrometeoroid and Debris Post Flight Analysis - Technical Report**, ESA ESTEC contract number 10830/94/NL/JG (1995).
- Stevenson, T.J.**, EURECA TICCE – A Nine Month Survey of Cosmic Dust and Space Debris at 500 km Altitude, *J. Brit. Interplanetary Soc.* 41, pp. 429-432 (1988).
- Taylor, A.D.**, The Harvard Radio Meteor Project meteor velocity distribution reappraised, *Icarus*, 116, pp. 154-158 (1995).

- Taylor, E.A., Shrine, N.R.G., and Kay, L.,** Hypervelocity Impact on Semi-infinite Brittle Materials: Fracture Morphology Related to Projectile Diameter, *Adv. Space Res.* Vol. 20, No. 8, pp. 1437-1440 (1997).
- Taylor, E.A.,** *Experimental and Computational Study of Hypervelocity Impact on Brittle Materials and Composites*, PhD Thesis, University of Kent (1998).
- Taylor, E.A., Shrine, N.R.G., McBride, N., Green, S.F., McDonnell, J.A.M. and Drolshagen, G.,** Impacts on HST and EURECA solar arrays compared with LDEF using a new glass-to-aluminium conversion, *Adv. Space Res.*, Vol. 23, No.1, pp. 83-87 (1999).
- Unispace Kent, Space Applications Services, C.R.Maag, Mare Crisium and CERT-ONERA,** *EuReCa Micrometeoroid and Debris Post Flight Investigation - Technical Report*, ESA ESTEC Contract No. 10522/93/NL/JG (1994).
- Unispace Kent, HTS, Century Dynamics, MMS, Open University/Oxford Brookes, ONERA, TUBS, SAS, TUM.,** *Meteoroids and Debris Flux and Ejecta Models*, ESA Contract No. 11887/96/NL/JG (1998).
- Upton, G. and Fingleton, B.,** *Spatial Data Analysis by Example*, John Wiley & Sons (1985).
- Warren, J.L., Zook, H.A., Allton, J.H., Clanton, U.S., Dardano, C.B., Holder, J.A., Marlow, R.R., Schultz, R.A., Watts, L.A. and Wentworth, S.J.,** The Detection and Observation of Meteoroid and Space Debris Impact Features on the Solar Max Satellite, *Proc. 19th Lun. Planet. Sci. Conf.* pp. 641-657 (1989).
- Yano, H.,** *The Physics and Chemistry of Hypervelocity Impact Signatures on Spacecraft: Meteoroids and Space Debris*, PhD Thesis, University of Kent (1995).
- Yano, H., Collier, I., Shrine, N.R.G. and McDonnell, J.A.M.,** Microscopic and chemical analyses of major impact sites on timeband capture cell experiment of the EURECA spacecraft, *Adv. Space. Res.* 17, No. 12, pp. (12)189-(12)192 (1996).
- Zolensky, M.E., See, T.H., Bernhard, R.P., Barrett, R., Hörz, F., Warren, J.L., Dardano, C., Leago, K.S., Kessler, D. and Foster, T.R.,** Final Activities of the Long Duration Exposure Facility Meteoroid and Debris Special Investigation Group, *Adv. Space. Res.* 16, No. 11, pp 53-65 (1995).

A - Regression theory

Multiple regression

The simple *linear* multiple regression model is:

$$Y = \beta_0 + \beta_1 X_1 + \beta_2 X_2 + \dots + \beta_m X_m + \varepsilon \quad (\text{A.1})$$

Where Y is the dependent variable, X_m are the independent variables, β_m the coefficients and ε is the error term, which is assumed to be normally distributed with mean 0 and standard deviation σ_ε given by:

$$\sigma_\varepsilon^2 = \sigma_m^2 + \sigma_f^2$$

where σ_m is the measurement error of Y and σ_f is the residual variability about the function or “lack of fit” due to factors such as choosing the wrong functional form or selecting the wrong regressors. Minimising $\sum \varepsilon_i^2$ - or to be more precise its unbiased estimator e^2 - is the well-known method of *least squares*.

Statistical texts agree (e.g. Cooper, 1969 and Ryan, 1997) that a choosing a linear model is always preferable to a non-linear model whenever appropriate, due to the inherent complexity of non-linear regression. A linear model does not mean one that can be plotted as a straight line, just one that is linear in its terms, so in equation A.1 above, Y and X_m could be logarithmic or trigonometric terms for example.

In multiple regression the most commonly used approach is to *centre* the data (Cooper, 1969 and Ryan, 1997) such that the simple regression model (equation A.1) becomes:

$$Y - \bar{Y} = \beta_1 (X_1 - \bar{X}_1) + \beta_2 (X_2 - \bar{X}_2) + \varepsilon \quad (\text{A.2})$$

This form is desirable in that it involves one less parameter and also expresses the regression relative to the “centre” of the data rather than to a possibly less meaningful origin (β_0), which may lie beyond the range of the data itself. The coefficients are estimated by minimising S given by:

$$S = \sum_{i=1}^n \varepsilon_i^2 = \sum_{i=1}^n [Y_i - \bar{Y} - \beta_1 (X_{1i} - \bar{X}_1) - \beta_2 (X_{2i} - \bar{X}_2)]^2$$

taking partial derivatives of S with respect to β_1 and β_2 gives simultaneous equations which can be solved using standard matrix techniques. Expressed in matrix form the above equation A.2 becomes:

$$\mathbf{Y}^+ = \mathbf{X}^+ \boldsymbol{\beta} + \boldsymbol{\varepsilon}$$

where

$$\mathbf{Y}^+ = \begin{bmatrix} Y_1 - \bar{Y} \\ Y_2 - \bar{Y} \\ \vdots \\ Y_n - \bar{Y} \end{bmatrix} \quad \mathbf{X}^+ = \begin{bmatrix} X_{11} - \bar{X}_1 & X_{21} - \bar{X}_2 \\ X_{12} - \bar{X}_1 & X_{22} - \bar{X}_2 \\ \vdots & \vdots \\ X_{1n} - \bar{X}_1 & X_{2n} - \bar{X}_2 \end{bmatrix} \quad \boldsymbol{\beta} = \begin{bmatrix} \beta_1 \\ \beta_2 \end{bmatrix} \quad \boldsymbol{\varepsilon} = \begin{bmatrix} \varepsilon_1 \\ \varepsilon_2 \\ \vdots \\ \varepsilon_n \end{bmatrix}$$

It can be shown (Ryan, 1997) that the vector containing the estimated values of the coefficients is given by:

$$\hat{\beta} = \left[(\mathbf{X}^+)' \mathbf{X}^+ \right]^{-1} (\mathbf{X}^+)' \mathbf{Y}^+ = \begin{bmatrix} \hat{\beta}_1 \\ \hat{\beta}_2 \end{bmatrix}$$

where the hats above the coefficients signify that they are the values estimated by a fit to the data as opposed to the “true” values. The first part of the above equation:

$$(\mathbf{X}^+)' \mathbf{X}^+ = \begin{bmatrix} \sum (X_1 - \bar{X}_1)^2 & \sum (X_1 - \bar{X}_1)(X_2 - \bar{X}_2) \\ \sum (X_1 - \bar{X}_1)(X_2 - \bar{X}_2) & \sum (X_2 - \bar{X}_2)^2 \end{bmatrix}$$

has special significance in that it is the variance-covariance matrix of the regressors. It is desirable for this matrix to be *orthogonal*; that is, the off-diagonal elements (covariances) should be 0. Thus, the *covariance* of X_1 and X_2 is zero i.e. the regressors are uncorrelated and consequently the coefficients β_i can be unambiguously interpreted as the rates of change due to each regressor with the other held constant.

Statistics for the regression and analysis of variance (ANOVA)

Once the coefficients for the fit have been obtained, we need to find out what inferences can be drawn from the regression. Accordingly, we must first find out how well the model fits the data, what the confidence intervals for the coefficients are and if the residual variance of the data about the model supports the model or suggests that we use a better one. The most common starting point in analysing a regression is the *analysis of variance* (ANOVA) table, where the variances accounted for by different sources are calculated and compared (Table A.1). Many other useful statistics can be derived by simple combination of the elements in the ANOVA table.

Table A.1 – ANOVA table for multiple regression

Source	Sum of squares (SS)	Degrees of freedom (DF)	Mean square (MS)	F statistic (F)	p-value
Regression	$\sum(\text{Due to } X_1 \text{ \& } X_2)$	2	$\frac{SS_{regression}}{DF_{regression}}$	$\frac{MS_{regression}}{MS_{residual}}$	$F_{2,n-2,1-\alpha}$
Due to X_1	$\hat{\beta}_1 \sum (X_1 - \bar{X}_1)^2$	1			
Due to X_2	$\hat{\beta}_2 \sum (X_2 - \bar{X}_2)^2$	1			
Residual	$\sum (y - \hat{y})^2$	$n - 3$	$\frac{SS_{residual}}{DF_{residual}}$		
Total	$\sum (y - \bar{y})^2$	$n - 1$			

The first source of variance in the table labelled “Regression” is that accounted for by the fitted function and is sometimes alternatively referred to as the “due to slope” variance for obvious reasons: the “slope” i.e. the fitted coefficient determines this variance. For multiple regression the $SS_{regression}$ has a component due to each regressor: X_1 and X_2 in this case. $SS_{regression}$ can be thought of

as the reduction in the total variance of the data (the last row in the table) in using X to predict Y and thus the variance remaining after this reduction is called the “Residual” variance, in summary:

$$SS_{total} = SS_{regression} + SS_{residual}$$

The first column of the ANOVA table can be calculated by matrices thus:

$$\begin{aligned} SS_{regression} &= \hat{\beta}'(\mathbf{X}^+)' \mathbf{Y}^+ \\ SS_{total} &= (\mathbf{Y}^+)' \mathbf{Y}^+ \\ \therefore SS_{residual} &= \hat{\beta}'(\mathbf{X}^+)' \mathbf{Y}^+ - (\mathbf{Y}^+)' \mathbf{Y}^+ \end{aligned} \quad (\text{A.3})$$

For the regression to be of any use it is clear that the reduction in variance due to the regression must be significantly larger than the residual variance. A simple illustration of this is to think of a scatter plot with the points randomly distributed, it is clear that whatever the slope of a line through the data, the variance of the data about the line will not be reduced. The formal test for significantly different variances is based on the F -distribution, which is the sampling distribution of the statistic defined as the ratio of two variances of samples from normal populations and gives probabilities that the ratio is 1. Thus if the probability in the far right column of the ANOVA table is greater than our chosen confidence level then we would conclude that $MS_{regression}$ is not significantly different enough from $MS_{residual}$ for the regression to be useful. In other words for any value of X we would not be any better off using the regression to predict Y than if we just picked a value of Y at random. The F statistic is, of course, related to the commonly used *correlation coefficient*, R^2 , and the formal test for the significance of R^2 gives the same result as the F test in the ANOVA table.

Goodness/lack of fit

It was mentioned that σ_e has two components, one being the experimental error, the other being the variance due to “lack of fit”. Accordingly, the residual sum of squares has two components:

$$SS_{residual} = SS_{pure\ error} + SS_{lack\ of\ fit}$$

The $SS_{pure\ error}$ can be evaluated by taking repeat measurements of Y for identical values of the regressors X_n , but in the absence of such is usually based on an estimated accuracy of the measurement. A formal lack of fit test discussed by Ryan (1997) is performed using the F statistic defined as $MS_{lack\ of\ fit}/MS_{pure\ error}$ i.e. if the lack of fit is significantly larger than the experimental error it indicates either that there are missing regressors or that the model is wrong. However, a more widely used statistic – certainly in the physical sciences – not mentioned by Ryan, is the χ^2 statistic defined as:

$$\chi^2 = \sum_i \left(\frac{Y_i - \hat{Y}}{\sigma_i} \right)^2 \quad (\text{A.4})$$

where σ_i is the error of the Y_i^{th} value. This gives a measure of the observed variance as a proportion of the expected variance and its sampling distribution is χ^{2*} with degrees of freedom $\nu = n-p$, where n is the number of data points and p is the number of parameters estimated from the data. It can be seen that this statistic is $SS_{\text{residual}}/MS_{\text{pure error}}$ and is more convenient than the F -test proposed by Ryan in that we don't need to know the number of degrees of freedom associated with the calculation of the experimental error. The author found that the χ^2 goodness-of-fit test gave probabilities to within 2% of the F lack-of-fit test when applied to the same data; Bevington (1969) highlights some of the deeper insights that can be gained using the F -test over the χ^2 test. Rather than consulting the actual values of the χ^2 distribution a often used rule-of-thumb is that if $\chi^2/\nu \approx 1$, that is < 1.5 then the probability of the observed value of the χ^2 statistic occurring is close to 50% (Bevington, 1969) and therefore signifies an appropriate model.

We now have an estimate of the *standard error* variance σ_ϵ^2 given by MS_{residual} , it can be seen from Table A.1 and equation A.3 that this is specifically:

$$\hat{\sigma}_\epsilon^2 = \frac{\hat{\beta}'(\mathbf{X}^+)' \mathbf{Y}^+ - (\mathbf{Y}^+)' \mathbf{Y}^+}{n - 3}$$

We can also compute the correlation coefficient R^2 and its adjusted value R^2_{adjusted} by:

$$R^2 = 1 - \frac{SS_{\text{residual}}}{SS_{\text{total}}} \quad R^2_{\text{adjusted}} = 1 - \frac{MS_{\text{residual}}}{MS_{\text{total}}}$$

Since the *mean square* values depend on the degrees of freedom (Table A.1), R^2_{adjusted} will not be artificially large if there is a small amount of data or too many parameters in the regression. We can also compute the contribution each regressor makes to R^2 , and these are given by $(SS_{\text{regression due to } X_i})/SS_{\text{total}}$ and also do a partial F test for each regressor to see if the inclusion of each regressor significantly improves the model.

After analysing our “goodness of fit” and deciding whether or not we have the appropriate model and have included all the necessary regressors we want to find confidence intervals for our regression coefficients and for values predicted by the regression equation. This requires estimators of the variance of the coefficients and of predicted Y values. It can be shown (Cooper, 1969; Press, 1992 or Ryan, 1997) that:

$$\hat{\sigma}_\epsilon^2 \left[(\mathbf{X}^+)' \mathbf{X}^+ \right]^{-1} = \mathbf{C} = \begin{bmatrix} \text{var}(\hat{\beta}_1) & \text{covar}(\hat{\beta}_1, \hat{\beta}_2) \\ \text{covar}(\hat{\beta}_1, \hat{\beta}_2) & \text{var}(\hat{\beta}_2) \end{bmatrix}$$

* There is ambiguity here between the χ^2 *statistic* and the χ^2 *distribution*. Often a statistic is given the same name as its sampling distribution, some texts make the distinction clear but it can be confusing. For example in this case to say χ^2 has a χ^2 distribution sounds like a truism but in the first instance we are referring to the *statistic* defined as equation A.4 and in the second case the *probability distribution* referred to as χ^2 ; there are many other statistics apart from equation A.4 whose sampling distributions are also χ^2 .

and thus the estimators of the variances of the coefficients β_i are given by the diagonal elements of the matrix C_{ii} . As previously discussed, it is desirable for the off-diagonal covariances to be 0 indicating that our fitted coefficients are independent of each other. Now that we have an estimate of the standard error (s_{β}) of the coefficients given by the square root of the variance we can test the hypothesis that the coefficient is significantly different from 0 and accordingly decide whether the regressor should be included. The usual t statistic is used, defined as:

$$t = \frac{\hat{\beta}_i - 0}{s_{\hat{\beta}_i}}$$

with a $(1-\alpha)\%$ confidence limit of the statistic being defined by the two-tailed value of the *Student's t*-distribution with $n-1-p$ degrees of freedom, where p is the number of parameters in the model.

The variance of predicted Y values is given by:

$$\text{var}(\hat{Y}) = 1 + \frac{\hat{\sigma}_\epsilon^2}{n} + (\mathbf{x}^+)' \mathbf{C} \mathbf{x}^+ \quad (\text{A.5})$$

where \mathbf{x}^+ is the vector containing the *centred* values of the independent variables for which you want to predict the dependent variable, so for values of X_1 and X_2 equal to x_1 and x_2 we have:

$$\mathbf{x}^+ = \begin{bmatrix} x_1 - \bar{X}_1 \\ x_2 - \bar{X}_2 \end{bmatrix}$$

so as we might expect the uncertainty in any predicted Y value increases the further the independent variables are from the centre of the data used to derive the prediction equation. Thus to accurately compute confidence intervals we require not only the regression coefficients and their uncertainties, but the mean values of the regressors from with the equation was derived. However, in the absence of such, if the data in question is believed to be within the domain of the original data and the variances of the coefficients are small then the third term in equation A.5 will be small so that $1 + \frac{\sigma_\epsilon^2}{n}$ will be a good approximation for $\text{var}(Y)$.

Finally, $(1-\alpha)\%$ confidence intervals for the coefficients β_i and for predicted Y values are given by:

$$\hat{\beta}_i \text{ or } \hat{Y} \pm t_{\alpha/2, \nu} s_{\hat{\beta}_i \text{ or } \hat{Y}}$$

where $t_{\alpha/2, \nu}$ is the value of the *student's t*-distribution corresponding to a confidence of $\alpha/2$ with $\nu = n-1-p$ degrees of freedom and $s = [\text{var}(\beta_i \text{ or } Y)]^{1/2}$ is the standard error.

Non-linear regression

The previous discussion of linear multiple regression provides a good introductory framework to non-linear regression. As for linear least squares we wish to minimise:

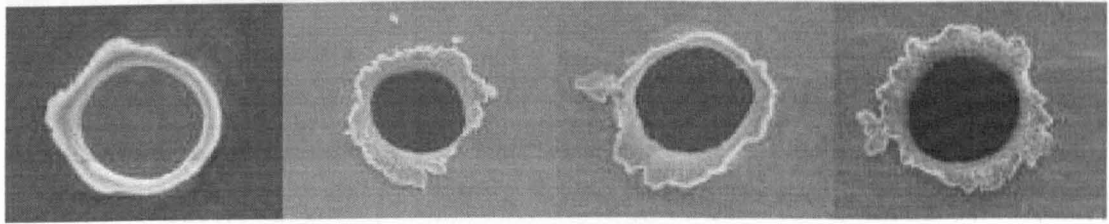
$$S = \sum_{i=1}^n [y_i - f(x_i, \beta)]^2$$

where β is the vector of coefficients. The minimisation can only be done iteratively; a common formulation of the algorithm is (Press, 1992):

$$\hat{\beta}_{next} = \hat{\beta}_{current} - \text{constant} \times \nabla S(\hat{\beta}_{current})$$

where initial values of the parameters need to be chosen and the residual sum of squares is calculated and the matrix of second partial derivatives of S with respect to each combination of two regressors. The matrix is evaluated for the current coefficients then a step down the gradient is taken. The size of the step determined by a constant that is chosen small enough so as not to exhaust the downhill direction (Press, 1992). That is to say, if the sum of squares increases then the constant is decremented until a decrease in S results. Next, the current values of the coefficients ($\beta_{current}$) are replaced with the ones just calculated (β_{next}) and the process is repeated until the last change in S is not significantly any smaller than the one previous. The mathematical formulation of this in terms of matrices of partial derivatives will not be given here as the details of the algorithm vary between texts and the author does not actually implement these computations, but relies on established computer implementations.

There are various algorithms for performing this procedure and for determining the convergence criterion, but the most widely used non-linear least-squares implementation is that of Marquardt (1963), which is an extension of earlier work by Levenberg and is thus named the *Levenberg-Marquardt method*. The author used the *Levenberg-Marquardt* non-linear regression tool in *Microcal Origin* to perform the non-linear fitting in this thesis, the results of which were checked against another implementation of *Levenberg-Marquardt* in the package *Gnuplot*. Ryan (1997) notes that distribution theory cannot be applied exactly to iterative non-linear regression and tests such as F and t tests will only asymptotically approach a good approximation for large data sets; it should also be noted that SS_{total} will not necessarily equal $SS_{regression} + SS_{residual}$. Furthermore, Ryan does not cover *multiple* non-linear regression in his comprehensive book on regression methods, stating that “*Multiple nonlinear regression presents considerable additional complexities.*” At this point it was decided to take on good faith – based on the high reliability so far - the output from regression software and to draw inferences from the fits by intuitive interpretation of the available statistics rather than continue the search for rigorous, quantitative quality factors; a case of diminishing returns in the author’s opinion.

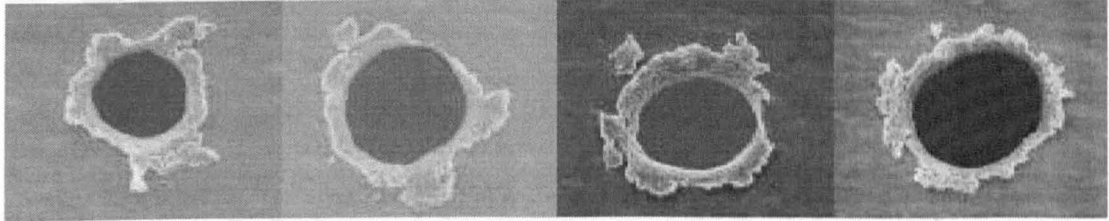
B - TICCE perforationsTi4t - 9.2 μm foil

ti4t1-12.005a

ti4t1-24.001a

ti4t1-58.001a

ti4t1-66.001a

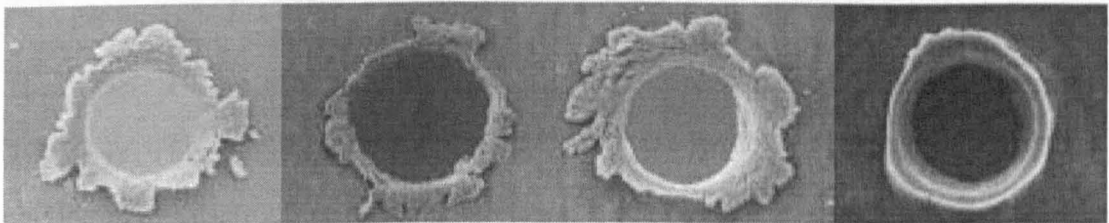


ti4t1-67.001a

ti4t1-73.002a

ti4t1-82.001a

ti4t1-83.001a

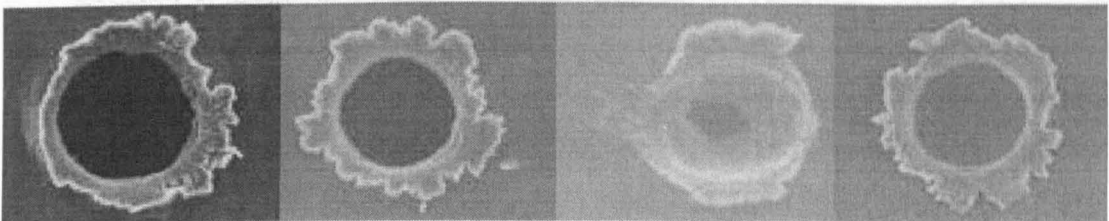


ti4t2-12.001a

ti4t2-56.001a

ti4t2-67.001a

ti4t2-73.001a

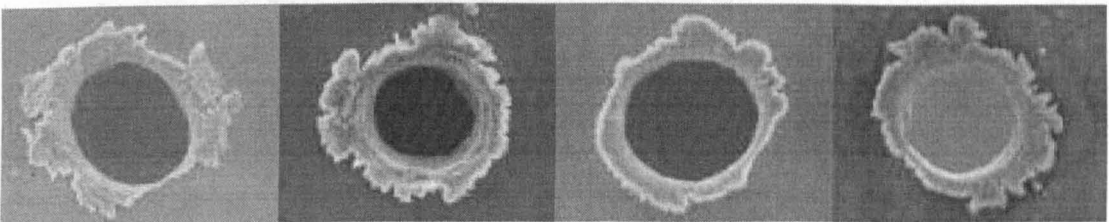


ti4t2-73.002a

ti4t3-16.001a

ti4t3-27.001a

ti4t3-27.002a

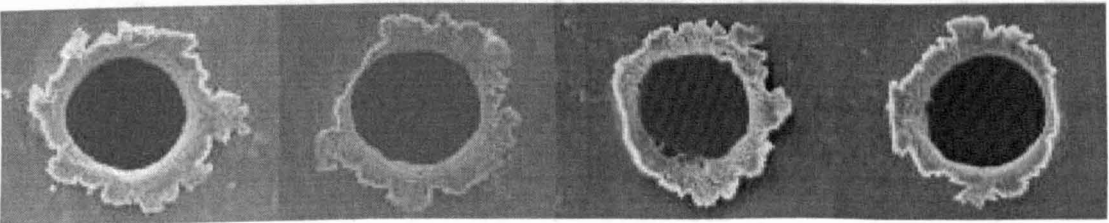


ti4t3-35.001a

ti4t3-36.001a

ti4t3-51.001a

ti4t3-63.001a

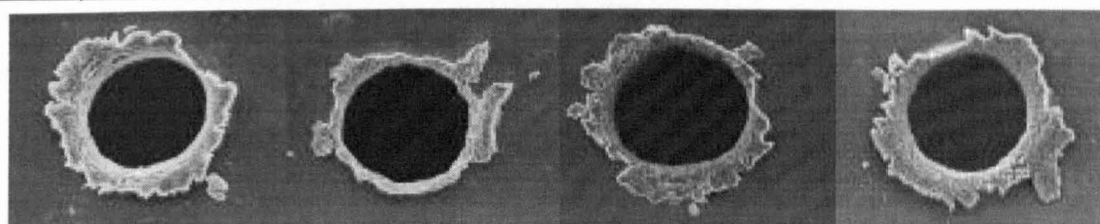


ti4t3-72.001a

ti4t3-86.001a

ti4t4-11.001a

ti4t4-12.001a

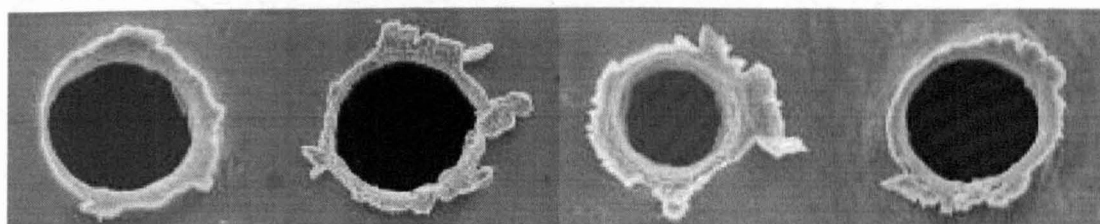
Ti4t - 9.2 μ m foil (continued)

ti4t-16.001 a

ti4t-17.001 a

ti4t-18.001 a

ti4t-28.001 a

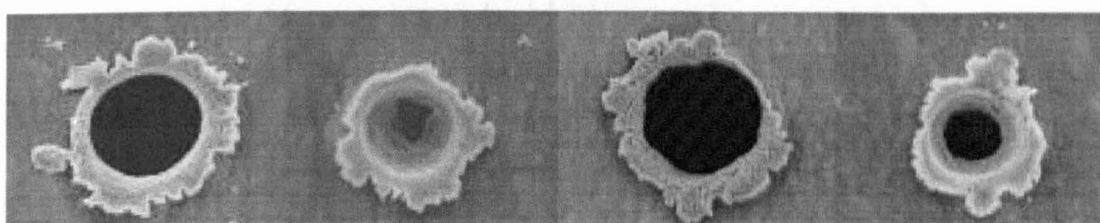


ti4t-31.001 a

ti4t-36.001 a

ti4t-42.001 a

ti4t-57.001 a

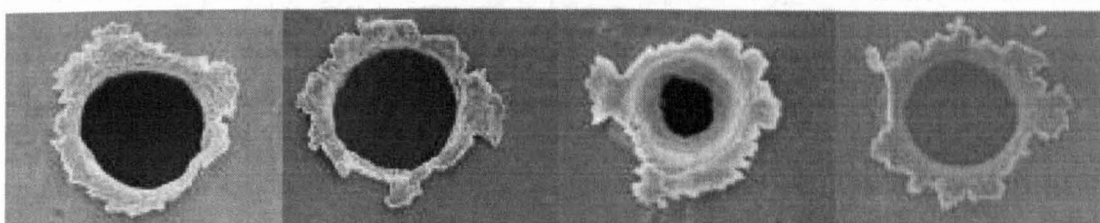


ti4t-61.001 a

ti4t-62.001 a

ti4t-65.001 a

ti4t-87.001 a

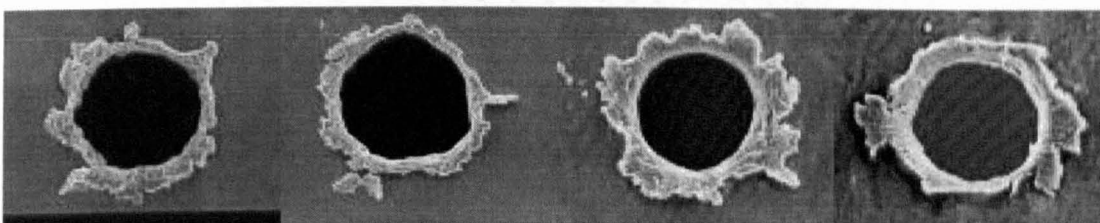


ti4t-88.001 a

ti4t5-22.001 a

ti4t5-35.001 a

ti4t5-36.001 a

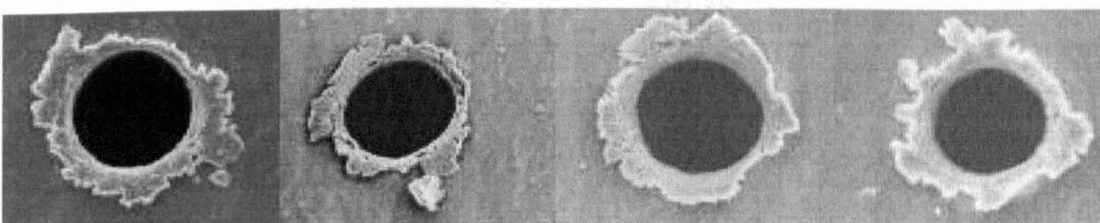


ti4t5-39.001 a

ti4t5-41.001 a

ti4t5-51.001 a

ti4t5-62.001 a



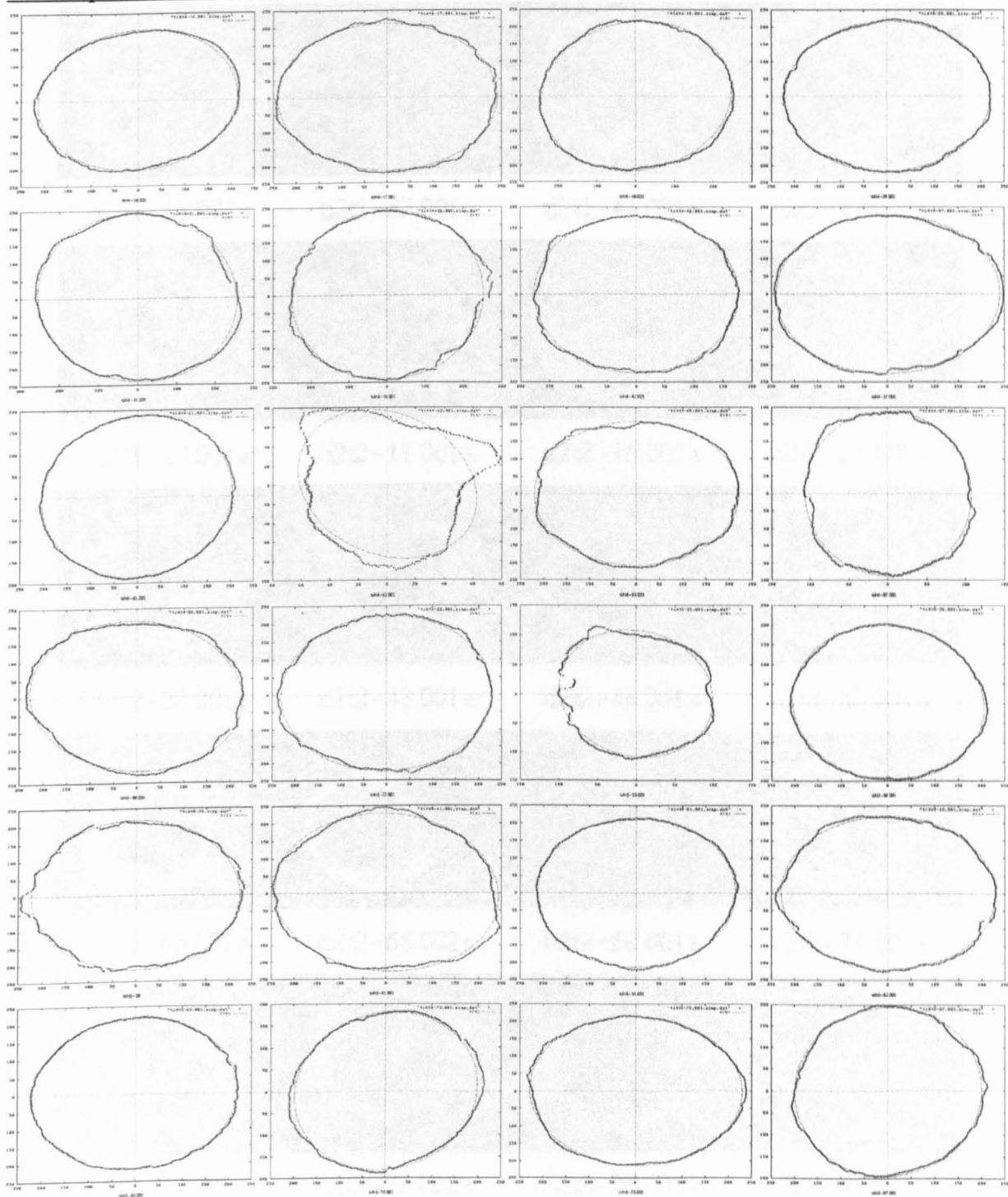
ti4t5-63.001 a

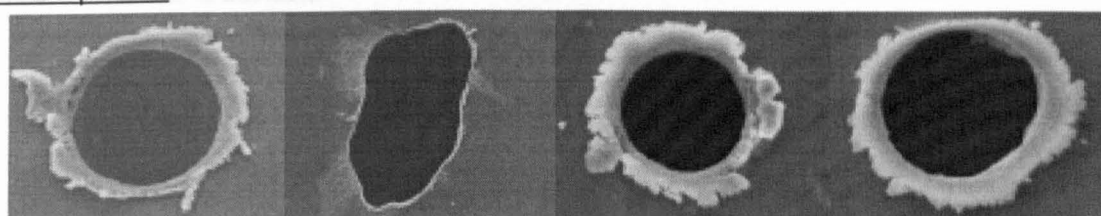
ti4t5-73.001 a

ti4t5-75.001 a

ti4t5-87.001 a

Ti4t ellipse fits (continued)



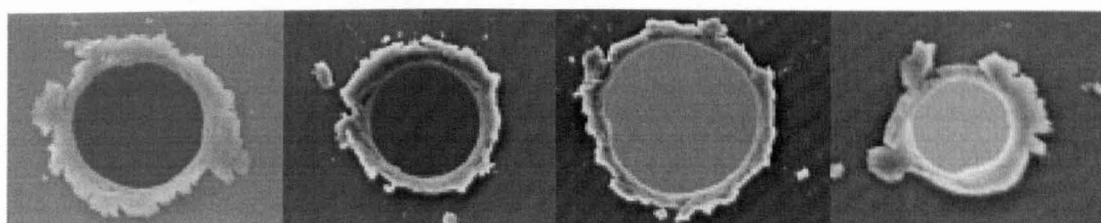
Ti2t - 2.1 μm foil

ti2t1-18.001 a

ti2t1-37.001 a

ti2t1-41.001 a

ti2t1-42.001 a

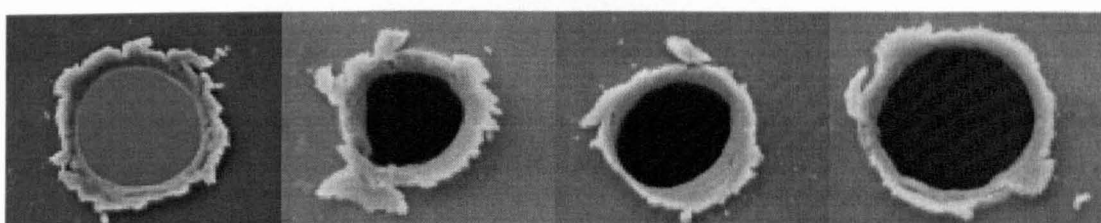


ti2t1-43.001 a

ti2t2-11.001 a

ti2t2-16.001 a

ti2t2-23.001 a

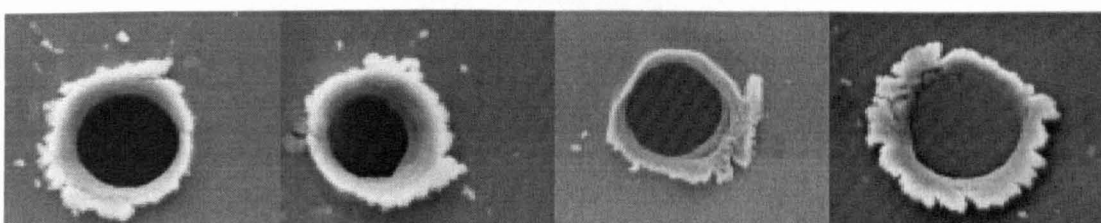


ti2t2-27.001 a

ti2t2-43.001 a

ti2t2-44.001 a

ti2t2-53.001 a

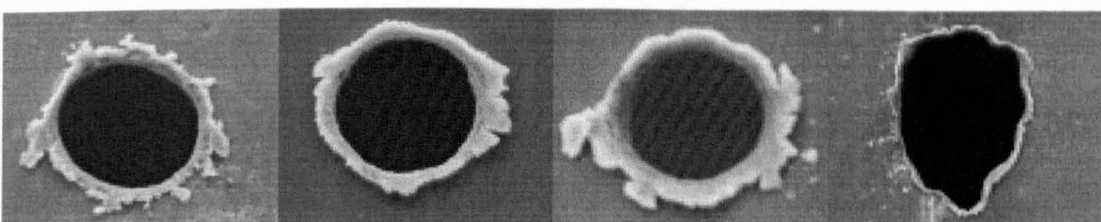


ti2t2-66.001 a

ti2t2-66.002 a

ti2t2-68.001 a

ti2t2-74.001 a

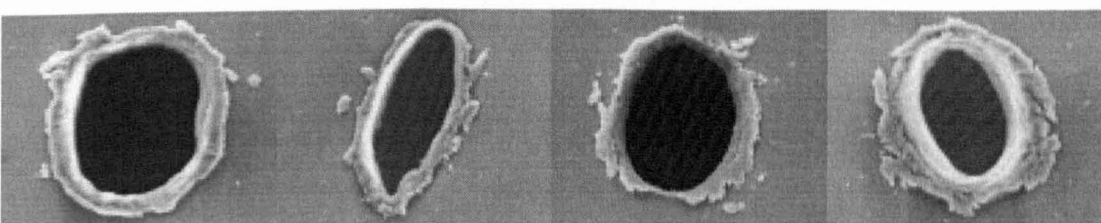


ti2t2-77.001 a

ti2t2-77.002 a

ti2t3-33.001 a

ti2t3-44.001 a



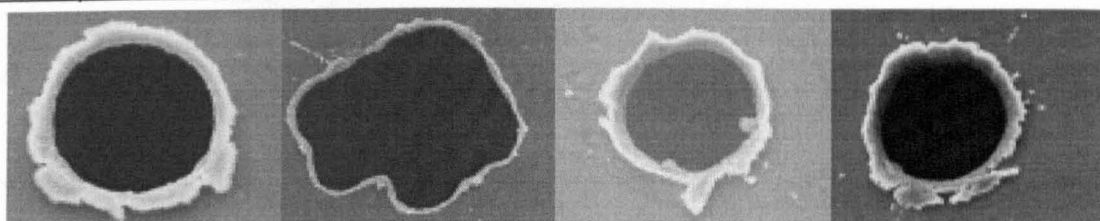
ti2t3-54.001 a

ti2t3-66.001 a

ti2t3-77.001 a

ti2t3-82.001 a

Ti2t - 2.1 μ m foil (continued)

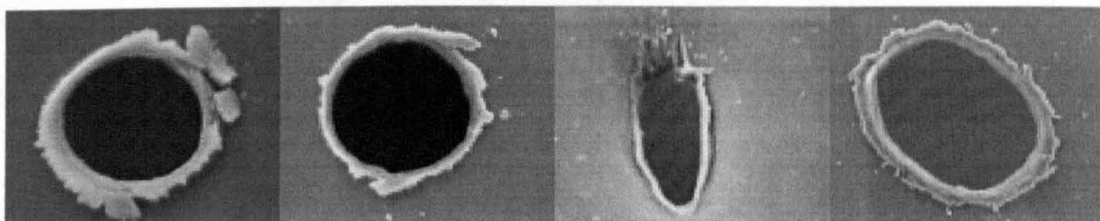


ti2t4-33.001 a

ti2t4-56.001 a

ti2t4-57.002 a

ti2t4-63.001 a

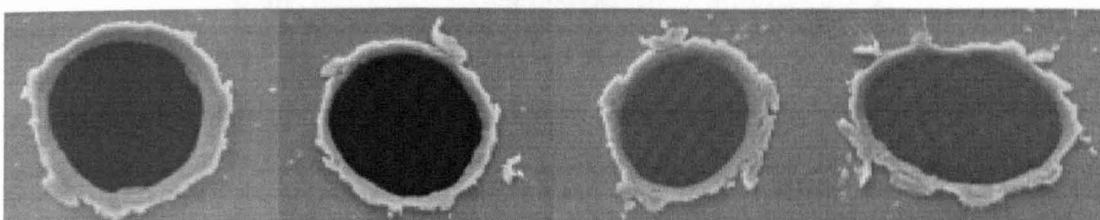


ti2t4-65.001 a

ti2t4-71.001 a

ti2t4-73.001 a

ti2t5-64.001 a

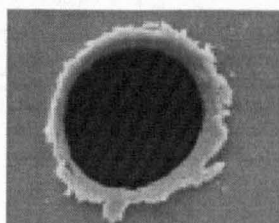


ti2t5-82.001 a

ti2t5-93.001 a

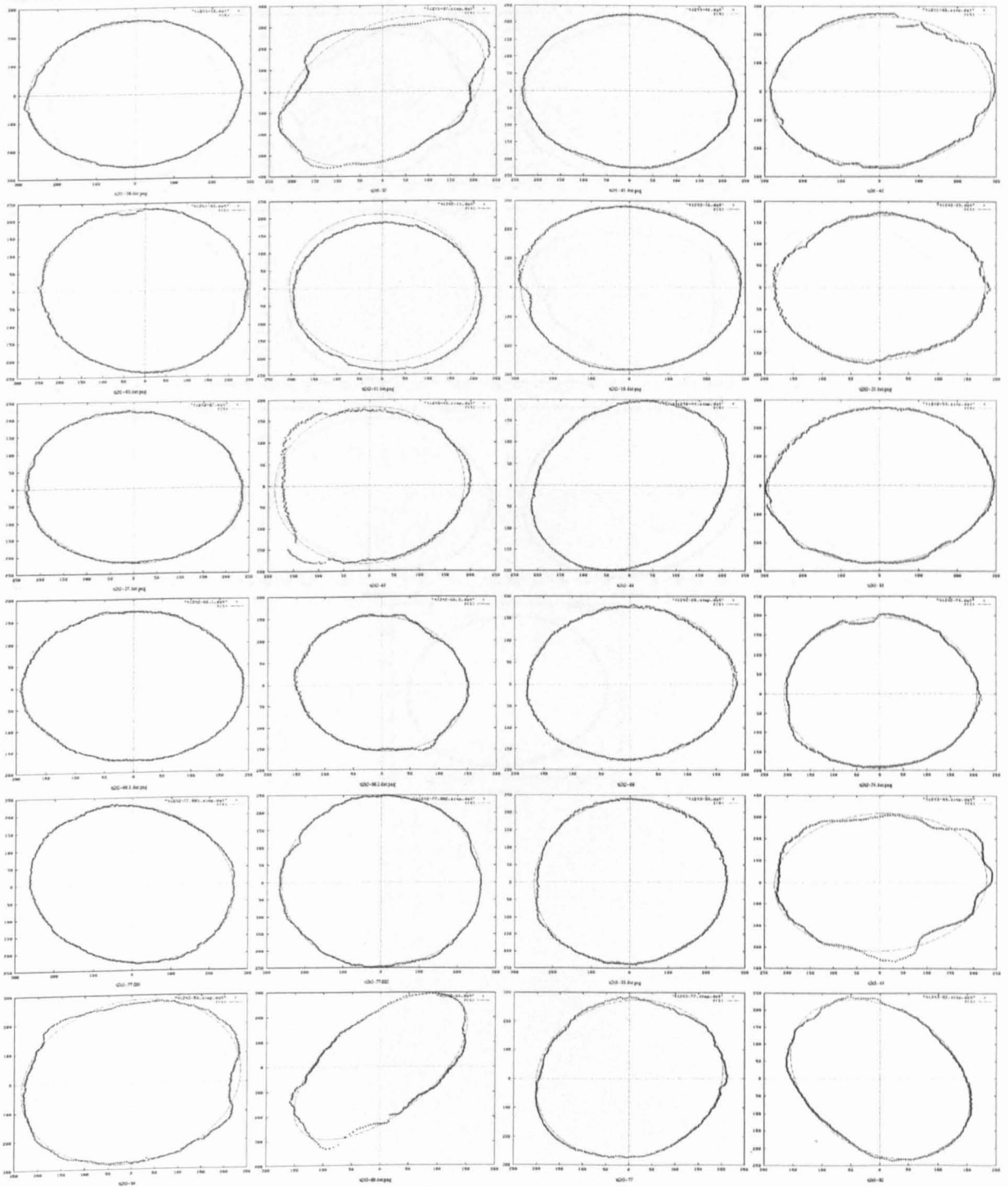
ti2t5-B4.001 a

ti2t5-B5.001 a

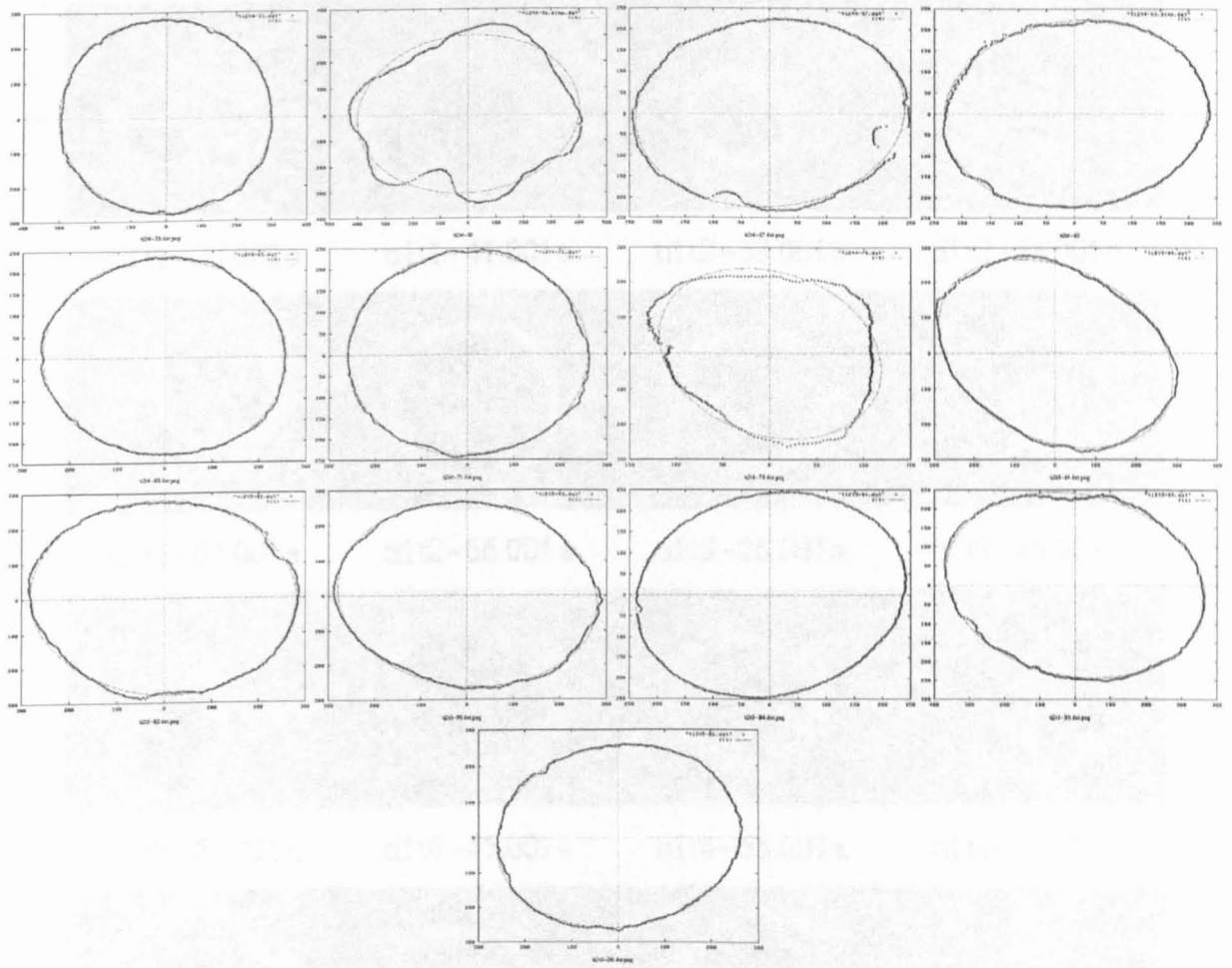


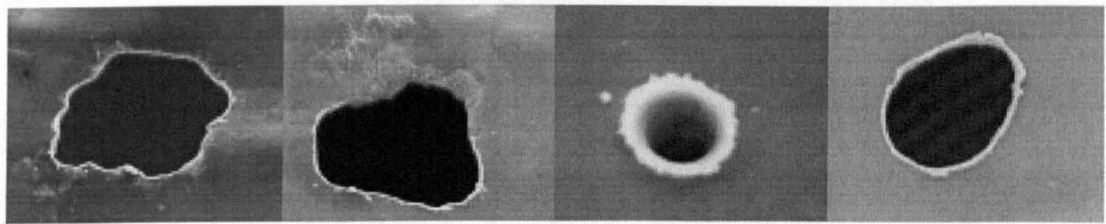
ti2t5-B6.001 a

Ti2t ellipse fits



Ti2t ellipse fits (continued)



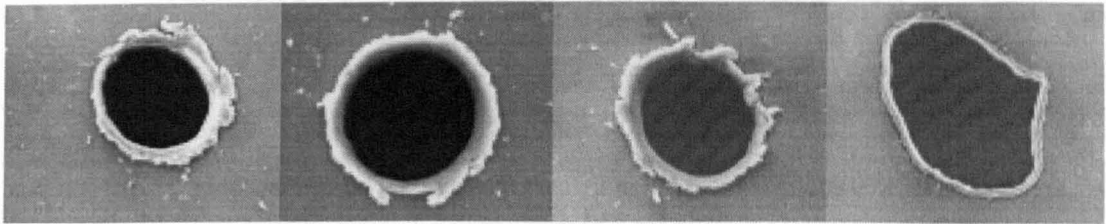
Tilt - 1.7 μ m foil

ti1t1-23.001 a

ti1t1-41.001 a

ti1t2-53.001 a

ti1t2-55.001 a

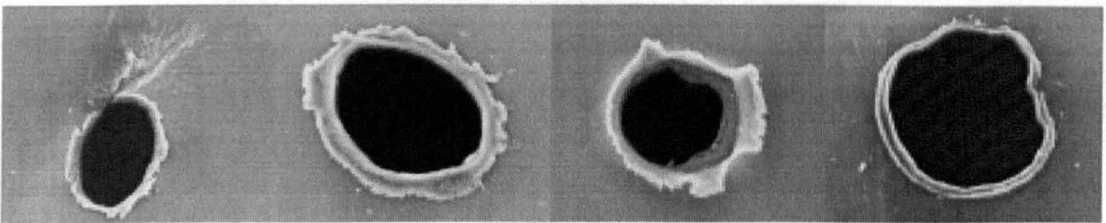


ti1t2-64.001 a

ti1t2-66.001 a

ti1t3-16.001 a

ti1t3-46.001 a

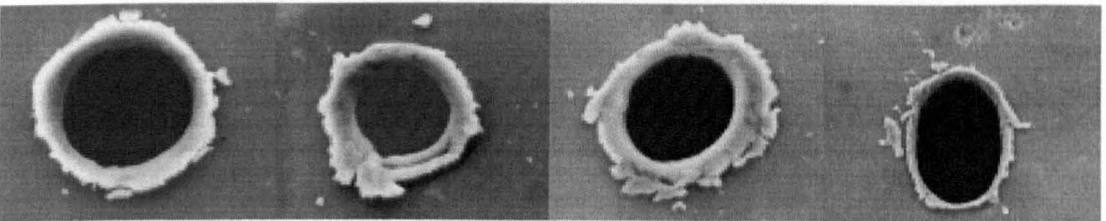


ti1t3-64.001 a

ti1t4-45.001 a

ti1t4-55.001 a

ti1t4-86.001 a

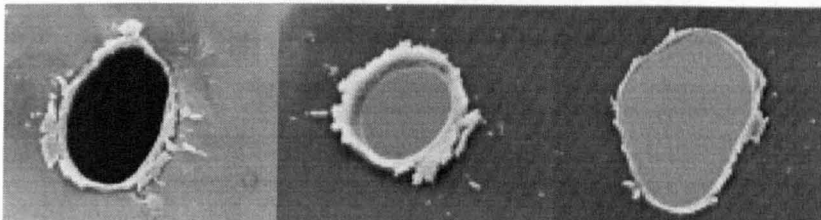


ti1t5-24.001 a

ti1t5-33.001 a

ti1t5-44.001 a

ti1t5-54.001 a

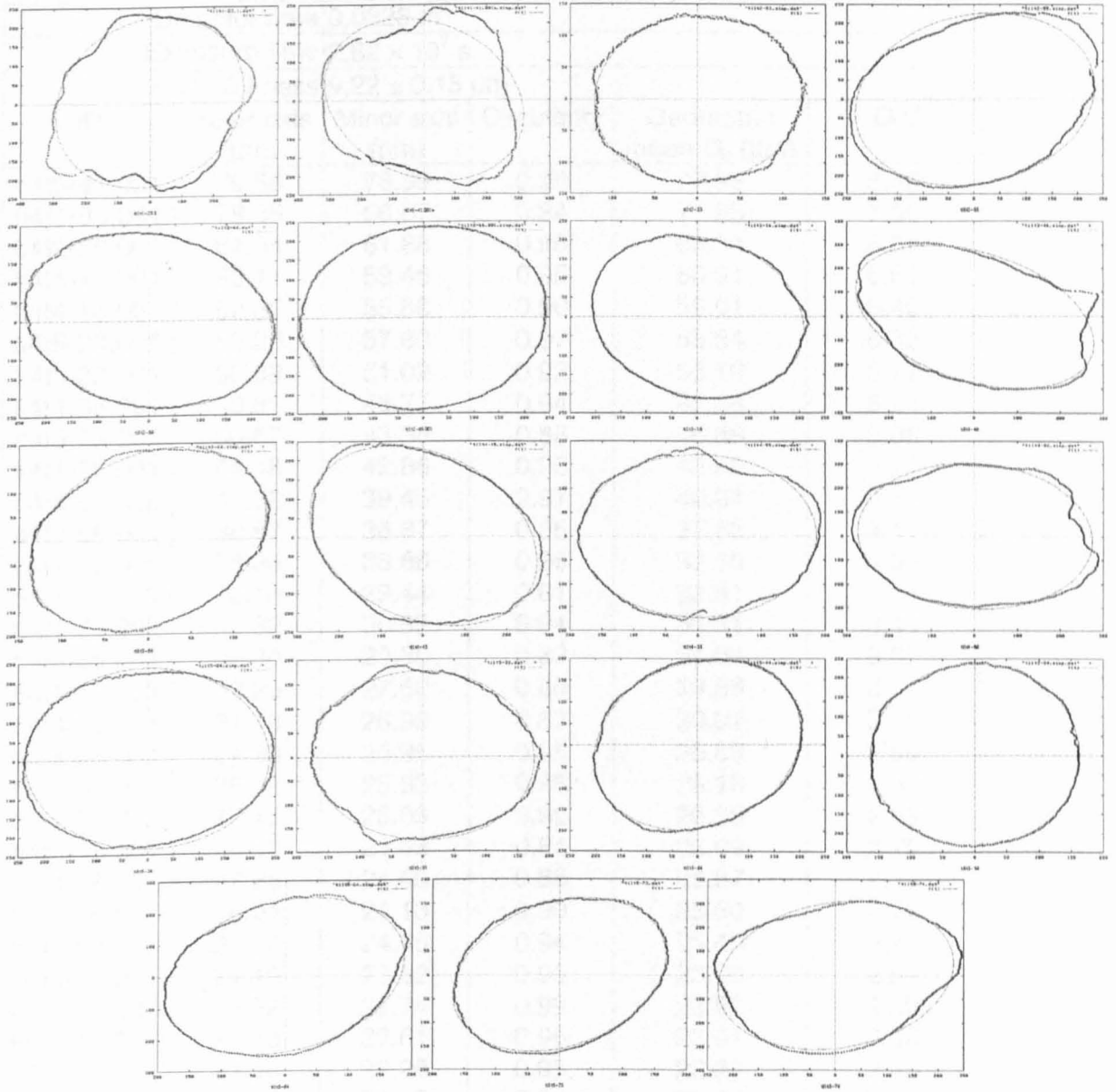


ti1t5-64.001 a

ti1t5-73.001 a

ti1t5-74.001 a

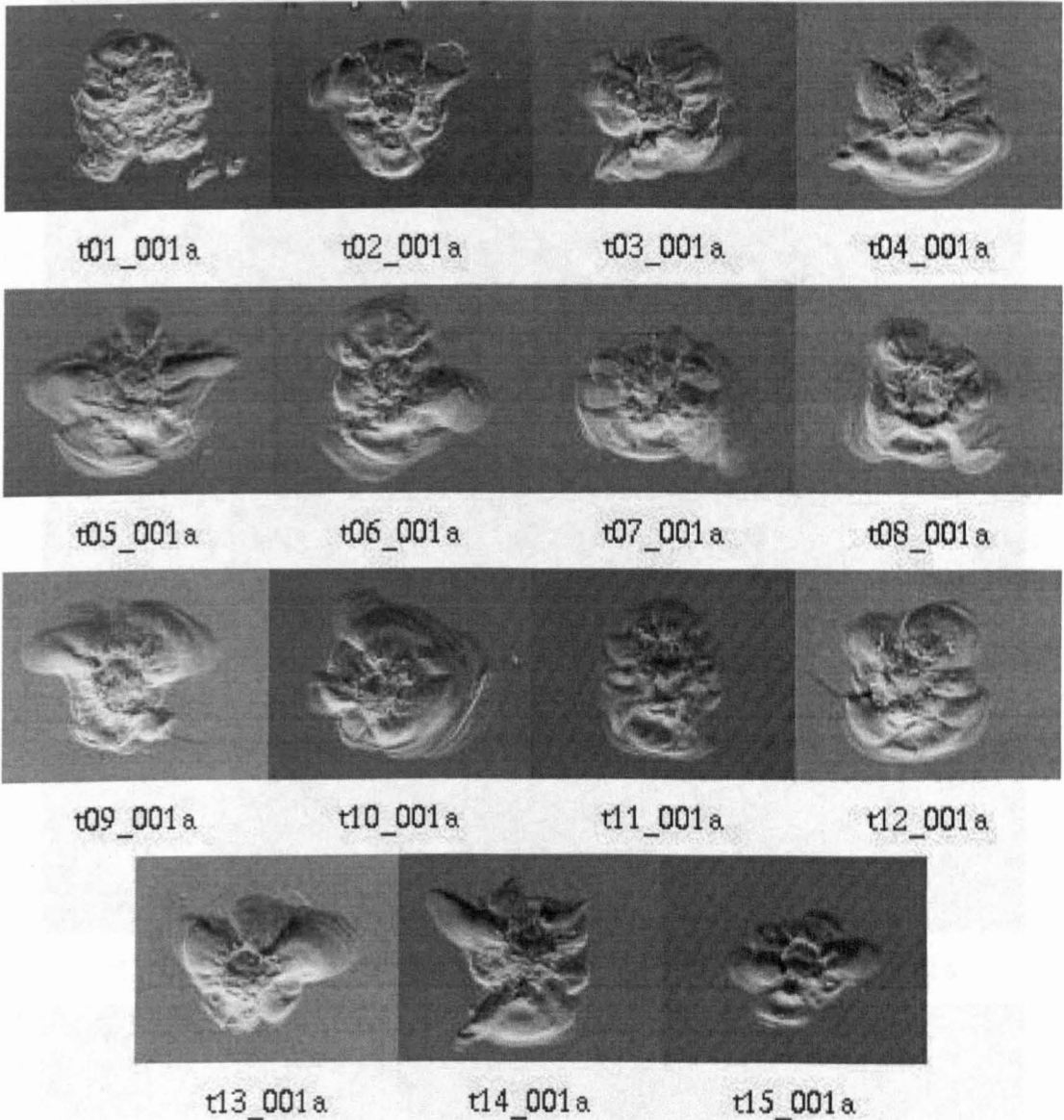
Tilt ellipse fits



Appendix B - TICCE perforations

Corrected TICCE ti4t foil data

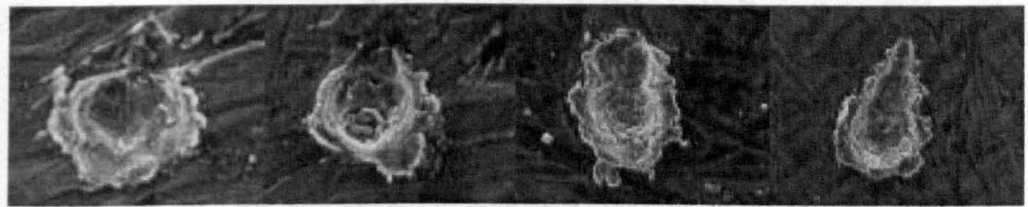
Detector area		0.0328 m ²			
Exposure time		2.82 × 10 ⁷ s			
Foil thickness		9.22 ± 0.15 μm			
ID	Major axis (μm)	Minor axis (μm)	Circularity	Geometric mean D _h (μm)	D _h /f
ti4t5-41.001	79.56	76.39	0.96	77.96	8.46
ti4t1-83.001	78.35	66.07	0.84	71.95	7.80
ti4t2-56.001	64.84	61.88	0.95	63.34	6.87
ti4t4-17.001	62.41	59.46	0.95	60.91	6.61
ti4t4-18.001	62.32	55.88	0.90	59.01	6.40
ti4t5-39.001	59.29	57.80	0.97	58.54	6.35
ti4t5-22.001	55.39	51.02	0.92	53.16	5.77
ti4t4-36.001	49.83	46.77	0.94	48.28	5.24
ti4t5-73.001	50.67	43.36	0.86	46.88	5.08
ti4t1-66.001	44.48	42.86	0.96	43.66	4.74
ti4t4-88.001	40.58	39.45	0.97	40.01	4.34
ti4t3-86.001	38.87	36.87	0.95	37.86	4.11
ti4t1-67.001	38.36	36.86	0.96	37.60	4.08
ti4t1-82.001	36.13	29.44	0.81	32.61	3.54
ti4t1-73.002	32.32	30.53	0.94	31.41	3.41
ti4t4-65.001	32.90	29.36	0.89	31.08	3.37
ti4t1-58.001	32.28	27.62	0.86	29.86	3.24
ti4t4-11.001	31.18	26.99	0.87	29.01	3.15
ti4t4-28.001	27.33	25.95	0.95	26.63	2.89
ti4t5-51.001	26.33	25.93	0.98	26.13	2.83
ti4t2-73.002	27.13	25.09	0.92	26.09	2.83
ti4t3-35.001	28.10	23.48	0.84	25.69	2.79
ti4t4-16.001	27.25	24.00	0.88	25.57	2.77
ti4t1-24.001	26.94	24.13	0.90	25.50	2.77
ti4t5-63.001	26.28	24.65	0.94	25.45	2.76
ti4t4-57.001	24.49	23.32	0.95	23.90	2.59
ti4t3-72.001	23.92	23.74	0.99	23.83	2.58
ti4t4-12.001	23.48	22.61	0.96	23.04	2.50
ti4t3-51.001	23.50	22.28	0.95	22.88	2.48
ti4t5-75.001	23.13	22.19	0.96	22.66	2.46
ti4t5-36.001	21.86	21.46	0.98	21.66	2.35
ti4t5-62.001	21.16	20.87	0.99	21.02	2.28
ti4t3-27.002	20.95	20.16	0.96	20.55	2.23
ti4t1-12.005	19.91	19.74	0.99	19.83	2.15
ti4t4-31.001	20.29	19.02	0.94	19.64	2.13
ti4t4-61.001	20.05	18.47	0.92	19.24	2.09
ti4t3-16.001	17.79	17.56	0.99	17.68	1.92
ti4t2-12.001	17.04	16.75	0.98	16.89	1.83
ti4t2-67.001	15.43	14.32	0.93	14.87	1.61
ti4t5-87.001	14.37	14.26	0.99	14.31	1.55
ti4t3-63.001	14.09	12.89	0.91	13.48	1.46
ti4t2-73.001	13.01	11.74	0.90	12.36	1.34
ti4t4-42.001	12.77	11.91	0.93	12.33	1.34
ti4t3-36.001	12.68	11.65	0.92	12.16	1.32
ti4t4-87.001	7.67	7.03	0.92	7.35	0.80
ti4t5-35.001	7.19	6.03	0.84	6.59	0.71
ti4t3-27.001	6.66	3.98	0.60	5.15	0.56
ti4t4-62.001	5.78	4.07	0.70	4.85	0.53

C - Oblique solar cell impact programme: images and data*Shot 1 glass

ID g-g60T	Pit (μm)	Shatter (μm)	Conchoid (μm)				P	P	Centroid C
			A	B	Dc	Cl			
1	26		676	601	637	0.889	18.1	6.96	0.896
2		93	316	295	305	0.934	24.7	20.88	1.006
3		91	270	280	275	1.037	1.4	27.84	0.704
4		87	316	252	282	0.797	21.6	34.8	0.943
5		79	414	312	359	0.754	26.7	26.1	0.652
6		94	351	265	305	0.755	14.6	20.88	0.912
7		80	333	252	290	0.757	29.3	24.36	0.643
8		88	268	269	268	1.004	3.6	27.84	0.881
9		95	278	382	326	1.374	26.3	29.58	0.971
10		72	369	293	329	0.794	15.7	24.36	
11		86	303	243	271	0.802	1.4	17.4	0.858
12		75	284	226	253	0.796	31.0	29.58	0.789
13		58	262	357	306	1.363	17.1		
14		98	293	239	265	0.816	23.1		0.689
15		71	209	294	248	1.407	18.3		0.813

* The greyed-out rows in the tables indicate data that was excluded from the final analysis.

Shot 1 aluminium

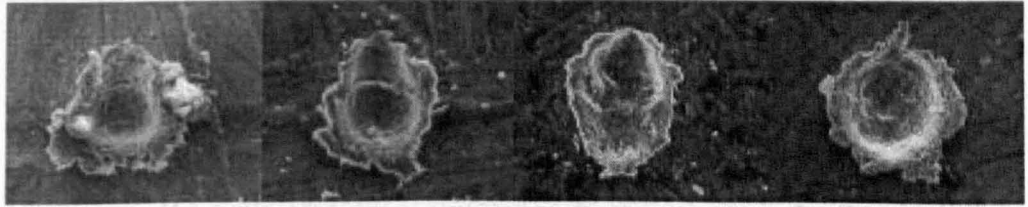


t01_001a

t02_001a

t03_001a

t04_001a

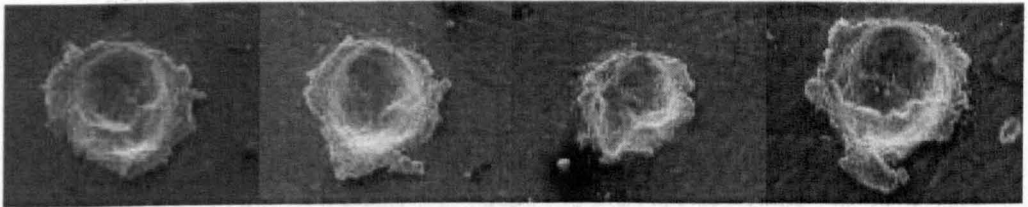


t05_001a

t06_001a

t07_001a

t08_001a

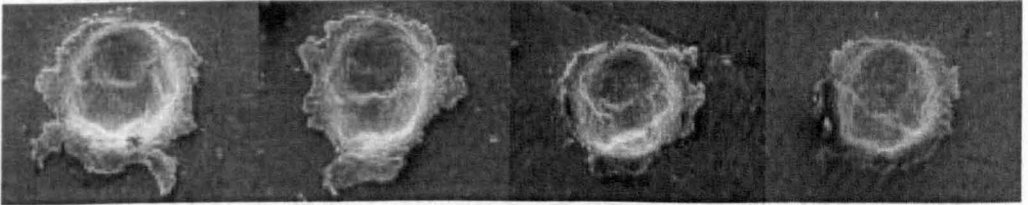


t09_001a

t10_001a

t11_001a

t12_001a

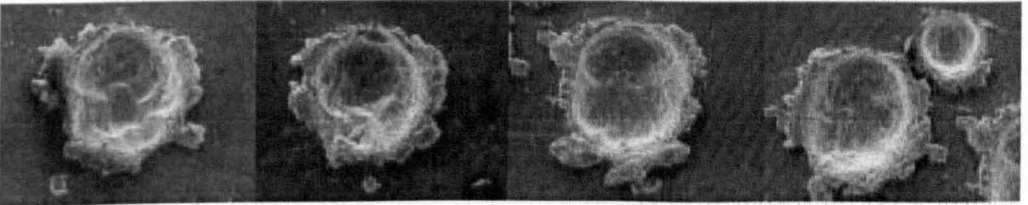


t13_001a

t14_001a

t15_001a

t16_001a

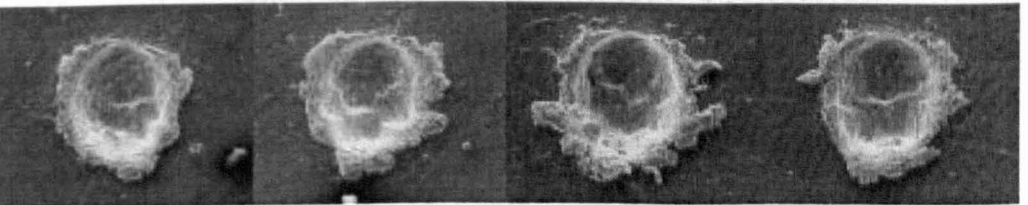


t17_001a

t18_001a

t19_001a

t20_001a

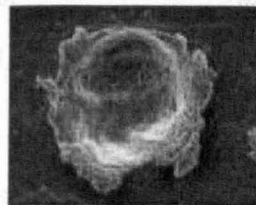


t21_001a

t22_001a

t23_001a

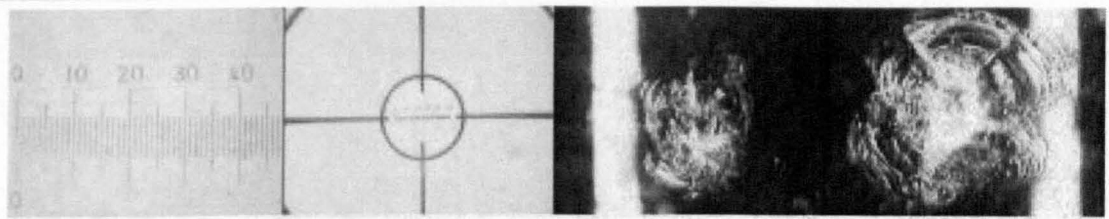
t24_001a



t25_001a

ID g-Al60T	Dc (μm)			CI	Depth P (μm)	optical P (μm)	P/Dc
	A	B	Dc				
1	13.1	14	13.5	1.07			
2	14.2	13.7	13.9	0.96	5.5		0.396
3	49.8	28.4	37.6	0.57	10.7		0.284
4	82.7	39.5	57.2	0.48	10.9		0.192
5	24.4	22.5	23.4	0.92	14.4		0.615
6	14.4	14.3	14.3	0.99	8.0		0.557
7	52.1	33.5	41.8	0.64	9.7		0.233
8	130.5	113.4	121.6	0.87	41.0	33.06	0.337
9	137.5	136.8	137.1	0.99	108.2	43.5	0.789
10	138.1	120.7	129.1	0.87	35.9	38.28	0.278
11	111.6	95.6	103.3	0.86	31.5	40.02	0.305
12	154.1	141	147.4	0.91	42.7	43.5	0.290
13	156.9	133.6	144.8	0.85	43.8	36.54	0.303
14	164.1	126.1	143.9	0.77	41.1	36.54	0.286
15	138.7	124.2	131.2	0.90	42.6	48.72	0.324
16	138.7	120.1	129.1	0.87	37.2	33.06	0.288
17	154.2	135.4	144.5	0.88	38.2	29.58	0.264
18	143.9	135.6	139.7	0.94	44.7	41.76	0.320
19	160.9	135.6	147.7	0.84	40.7	36.54	0.276
20	152.8	126.1	138.8	0.83	36.1	40.02	0.260
21	142.5	119.8	130.7	0.84	31.3	43.5	0.240
22	145.3	113.9	128.6	0.78	39.2	41.76	0.305
23	154.3	132.9	143.2	0.86	41.2	40.02	0.287
24	151.4	124.8	137.5	0.82	39.1		0.284
25	163.6	140.7	151.7	0.86	48.6		0.320

Shot 2 solar cells

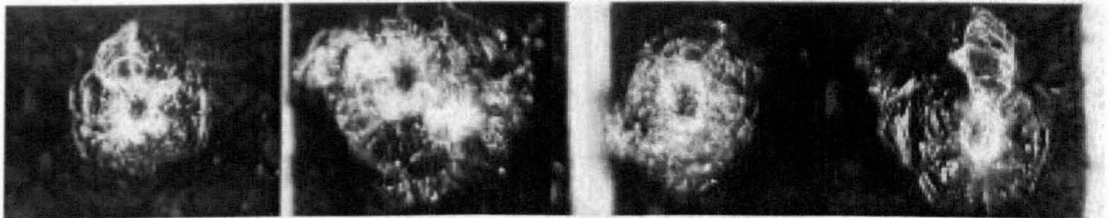


_imag000

_imag001

_imag002

_imag003

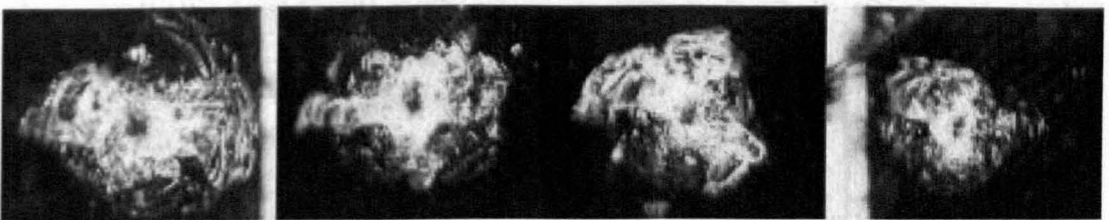


_imag004

_imag005

_imag006

_imag007

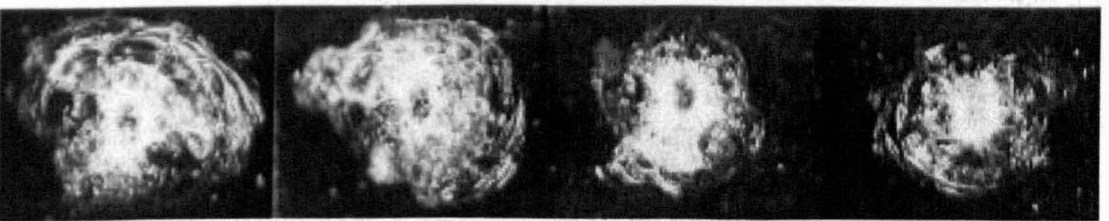


_imag008

_imag009

_imag010

_imag011

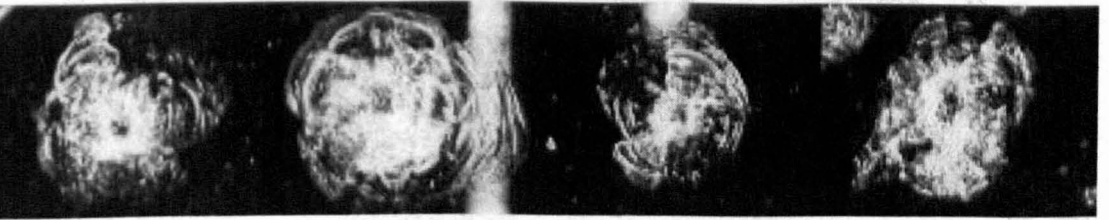


_imag012

_imag013

_imag014

_imag015

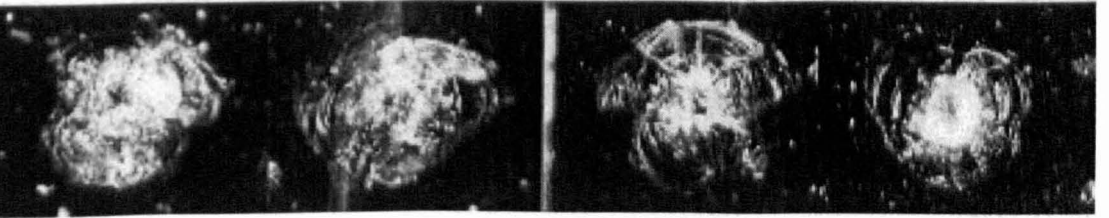


_imag016

_imag017

_imag018

_imag019



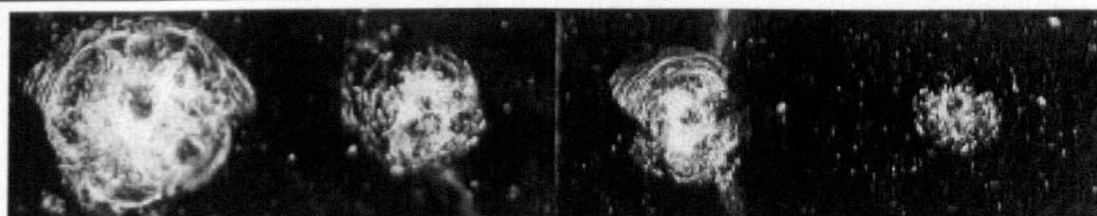
_imag020

_imag021

_imag022

_imag023

Shot 2 solar cells (continued)



_imag024

_imag025

_imag026

_imag027

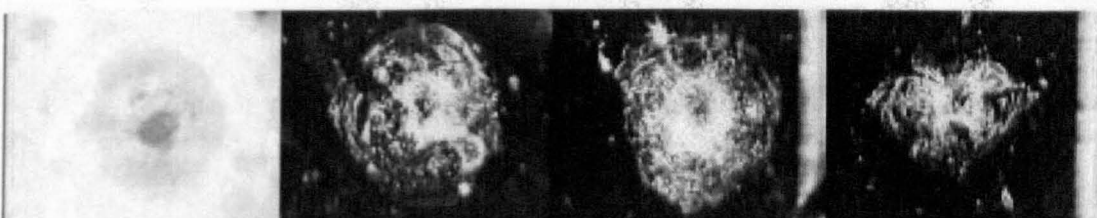


_imag028

_imag029

_imag030

_imag031



_imag032

_imag033

_imag034

_imag035



_imag036

_imag037

_imag038

_imag039

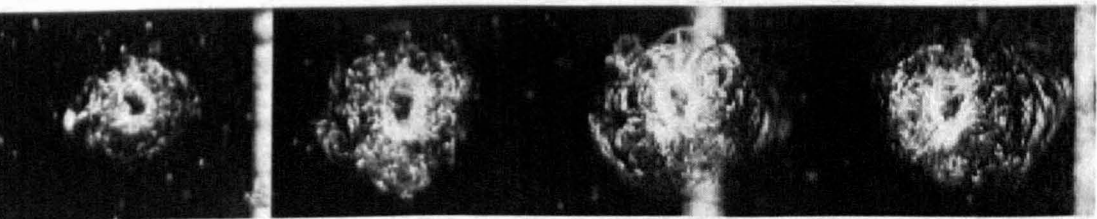


_imag040

_imag041

_imag042

_imag043



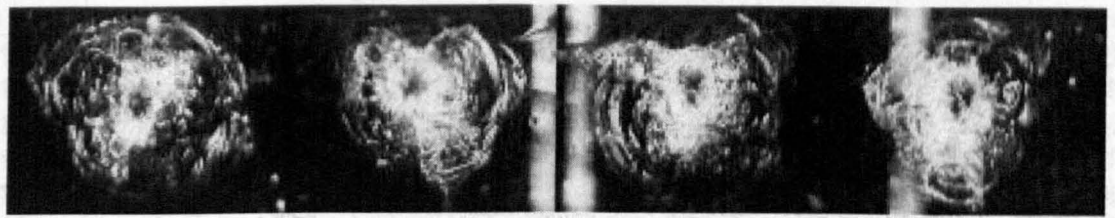
_imag045

_imag046

_imag047

_imag048

Shot 2 solar cells (continued)

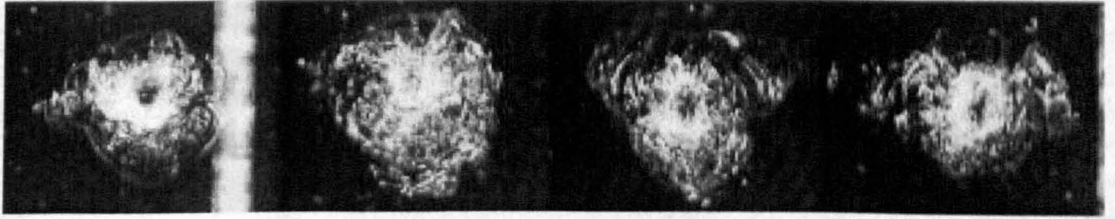


_imag049

_imag050

_imag051

_imag052

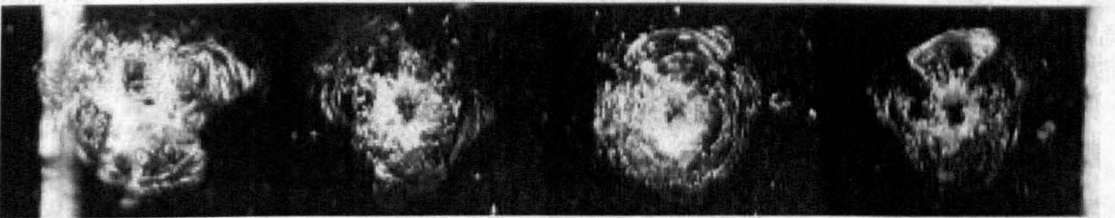


_imag053

_imag054

_imag055

_imag056

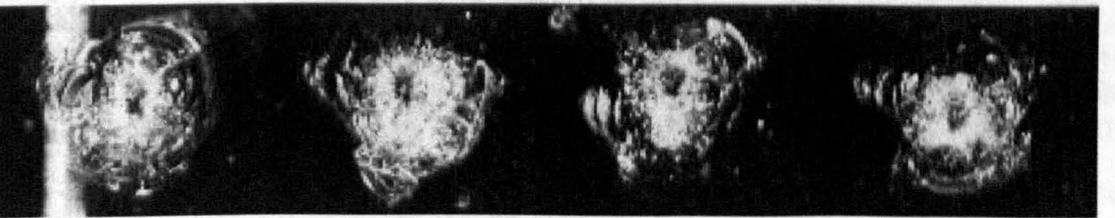


_imag057

_imag058

_imag059

_imag060

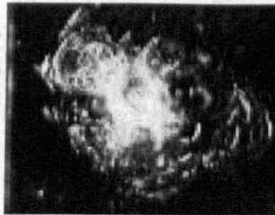


_imag061

_imag062

_imag063

_imag064



_imag065

IMAGE ID No.	Pit (μm)		Shatter (μm)		Conchoid (μm)		P (μm)	Centroid offset
	A	B	A	B	A	B		
2	39	28			242	178	20.88	
3	50	45	148	97	356	299	36.54	0.955
4	37	33	117	74	249	220	24.36	1.068
5	53	35	130	108	280	389	41.76	0.693
6	55	41	125	85	295	231	17.4	0.976
7			111	72	347	272	24.36	1.239
8								
9	63	34	151	109	229	310	36.54	0.672
10	56	35			273	256	40.02	1.048
11	48	20	116	68	212	216	26.1	1.000
12	53	37	131	104	297	395	17.4	1.185

Appendix C - Oblique solar cell impact programme: images and data

IMAGE ID No.	Pit (μm)		Shatter (μm)		Conchoid (μm)		P (μm)	Centroid offset
	A	B	A	B	A	B		
13	52	32	151	86	305	354	22.62	0.964
14	61	33			279	258	34.8	0.817
15			116	83	242	272	24.36	0.769
16	36	30	126	108	297	306	33.06	0.519
17	50	37			344	353	8.7	0.942
18	36	32			262	237	19.14	1.137
19	71	38	139	87	316	235	24.36	1.000
20	47	28			284	246	29.58	0.873
21					268	326	24.36	0.925
22	45	28	110	61	311	324	12.18	0.920
23					237	277	13.92	0.835
24	61	40			341	371	22.62	0.880
25	22	16			203	222	24.36	0.887
26	30	34			235	182	12.18	0.996
27	21	23			111	144	10.44	0.577
28					191	270	13.92	0.827
29	50	36	149	101	332	330	31.32	1.012
30	57	26			354	295	24.36	0.960
31	172	167					69.6	
32	50	66						
33	63	39	126	90	326	303	19.14	0.914
34	72	40	143	120	320	278	24.36	0.850
35	51	34			169	292	8.7	0.533
36	38	38	99	100	288	380	27.84	0.826
37	70	32	143	96	330	307	17.4	0.764
38	78	43	127	147	357	351	20.88	0.846
39	55	32			286	222	24.36	0.860
40	61	39	137	94	324	379	19.14	0.809
41					230	228	26.1	
42	55	36	140	94	250	304	19.14	0.776
43	42	36			301	290	27.84	0.850
44								
45	41	34			181	221	13.92	0.906
46	50	31	134	84	323	258	26.1	0.978
47	50	30	109	95	295	291	20.88	0.969
48	52	28			270	291	22.62	1.074
49	62	45	140	83	328	406	33.06	0.970
50	49	46	111	108	248	327	26.1	0.871
51	59	34	153	96	330	316	33.06	0.752
52	75	47			334	304	26.1	0.886
53	48	42			267	306	27.84	0.787
54	56	33			330	309	26.1	0.794
55	68	40	126	83	343	293	29.58	0.980
56	66	42			191	351	26.1	0.880
57	57	51			315	380	26.1	0.711
58	51	38	134	111	252	287	24.36	0.929
59	63	41			282	279	29.58	1.121
60	48	42	122	81	292	238	19.14	1.021
61	41	28			293	288	31.32	1.024
62	60	43			316	331	31.32	0.759
63	55	39			299	230	27.84	0.749
64	60	41			268	230	31.32	0.963
65					253	388	20.88	0.870

Shot 2 glass



_imag000 _imag001 _imag002 _imag003



_imag004 _imag005 _imag006 _imag007



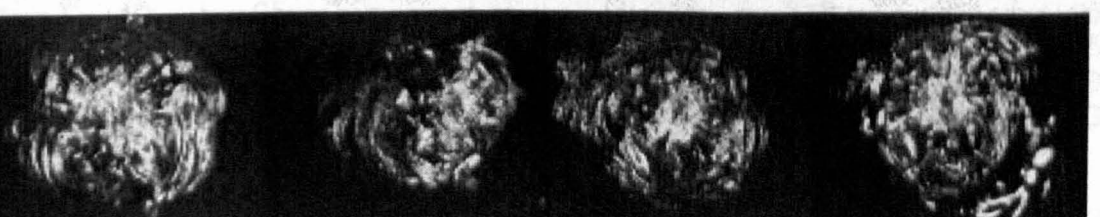
_imag008 _imag009 _imag010 _imag011



_imag012 _imag013 _imag014 _imag015

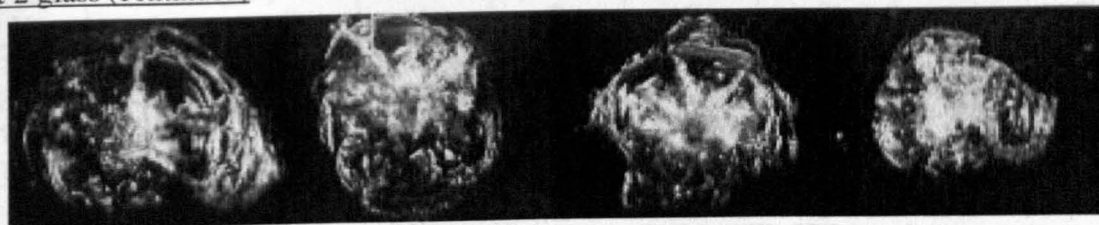


_imag016 _imag017 _imag018 _imag019



_imag020 _imag021 _imag022 _imag023

Shot 2 glass (continued)



_imag024

_imag025

_imag026

_imag027

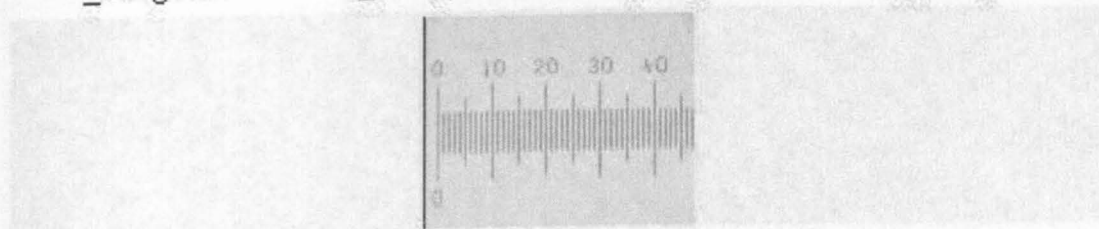


_imag028

_imag029

_imag030

_imag031



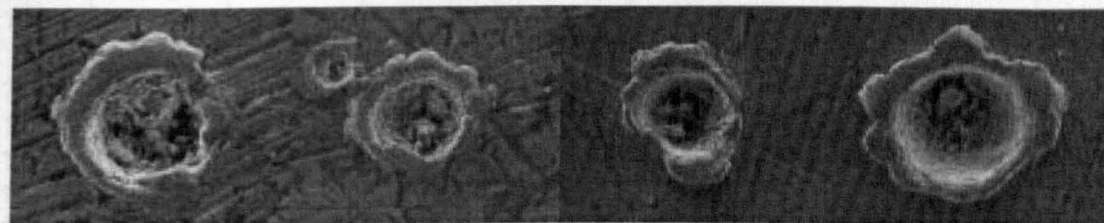
_imag032

IMAGE ID No.	Pit (μm)		Shatter (μm)		Conchoid (μm)		P μm	C offset
	A	B	A	B	A	B		
18					243	425	33	
24					299	416	37	1.104
29	61	34			288	401	33	0.944
10	56	43			251	359	35	0.892
31	58	37			314	347	28	0.924
8	42	24			301	345	31	0.877
4					318	331	37	0.925
20					345	318	28	1.020
28	33	30			268	318	17	1.112
26	54	42			294	317	31	1.068
0					298	313	35	
25	75	42			371	312	28	0.927
11	40	35			244	312	30	0.959
12	37	30			269	301	30	0.952
22			105	82	300	299	19	0.887
5	41	22			341	294	42	0.933
2					364	292	26	
21					225	286	19	
1	66	34	109	74	263	283	33	0.928
27					257	278	30	0.934
3	60	30			316	274	31	0.741
6					254	273	31	
7					205	268	23	0.917
23	69	19			315	267	28	0.971
14	55	26			309	263	26	0.984
17	49	28			273	257	37	1.004
16	47	49	104	103	302	255	28	0.934
9	44	37			236	246	28	1.110

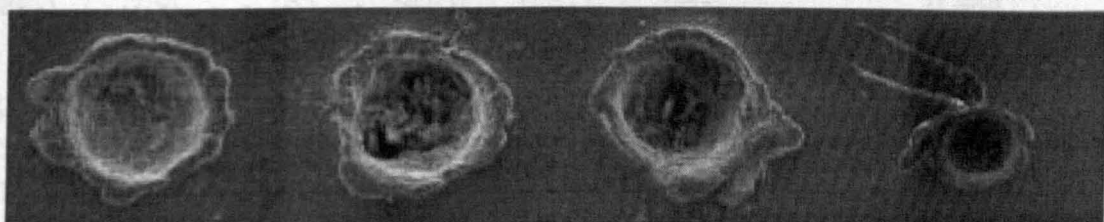
Appendix C - Oblique solar cell impact programme: images and data

IMAGE ID No.	Pit (μm)		Shatter (μm)		Conchoid (μm)		P μm	C offset
	A	B	A	B	A	B		
15	48	30			224	246	26	1.036
30	55	38			276	245	23	0.964
13					310	203	23	
19			114	78	257	183	19	1.004

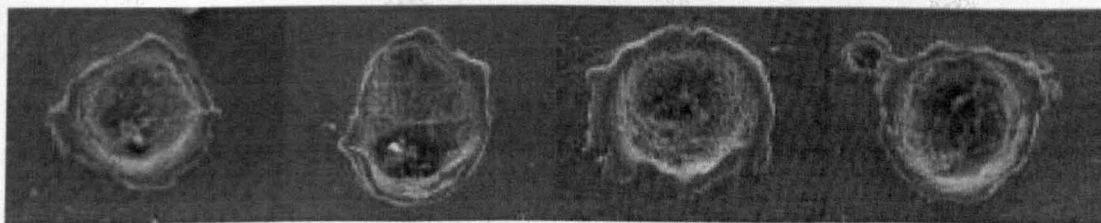
Shot 2 aluminium



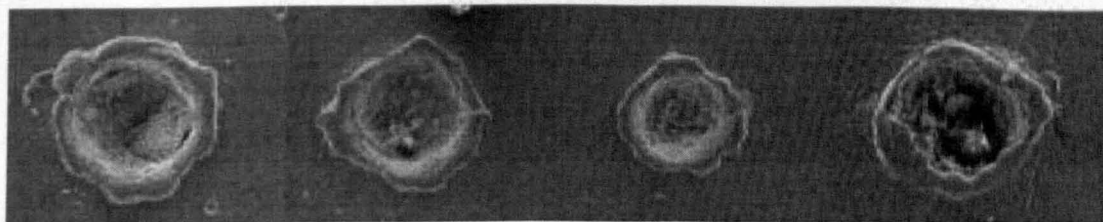
01_001a 02_001a 03_001a 04_001a



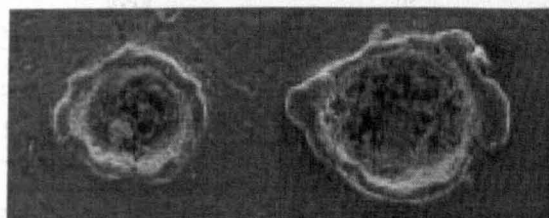
05_001a 06_001a 07_001a 08_001a



09_001a 10_001a 11_001a 12_001a



13_001a 14_001a 15_001a 16_001a



17_001a 18_001a

ID g-Al60	Dc (μm)			CI	P (μm)		P/Dc
	A	B	\sqrt{AB}		SEM	Optical	
9	90.5	64.4	76.3	0.712	16.7	19.1	0.219
6	98.8	76.6	87.0	0.775	26.3	20.9	0.302

Appendix C - Oblique solar cell impact programme: images and data

ID g-Al60	Dc (μm)			CI	P (μm)		P/Dc
	A	B	\sqrt{AB}		SEM	Optical	
10	102.2	80.8	90.9	0.791	34.4	34.8	0.379
8	111.5	106.4	108.9	0.954	32.9	45.2	0.302
16	122.9	104.5	113.3	0.850	39.6	43.5	0.349
23	130.8	112.1	121.1	0.857	40.7		0.336
20	144.4	111.3	126.8	0.771	44.8		0.354
3	136.2	118.4	127.0	0.869	41.3	34.8	0.325
25	140.6	117.8	128.7	0.838	48.3		0.375
13	141.9	117.8	129.3	0.830	40.0	36.5	0.310
1	144.9	121.2	132.5	0.836	49.7	22.6	0.375
15	159.9	116.7	136.6	0.730	51.1	31.3	0.374
11	161.6	116.6	137.3	0.722	43.0	40.0	0.313
14	157.1	125.4	140.4	0.798	45.8	38.3	0.326
19	162.1	121.6	140.4	0.750	44.1		0.314
12	139.3	146.8	143.0	1.054	53.5	27.8	0.374
22	158.3	132.4	144.8	0.836	46.8		0.323
24	164	133	147.7	0.811	53.8		0.364
5	171	130.5	149.4	0.763	42.4	10.4	0.284
2	166	135.3	149.9	0.815	50.0	15.7	0.334
21	166.7	135.2	150.1	0.811	44.2		0.295
18	174	134.4	152.9	0.772	47.7		0.312
17	183	141.9	161.1	0.775	57.5		0.357
7	174.2	151.4	162.4	0.869	59.3	47.0	0.365
4	184.9	151.4	167.3	0.819	60.9	13.9	0.364

Shot 3 solar cells

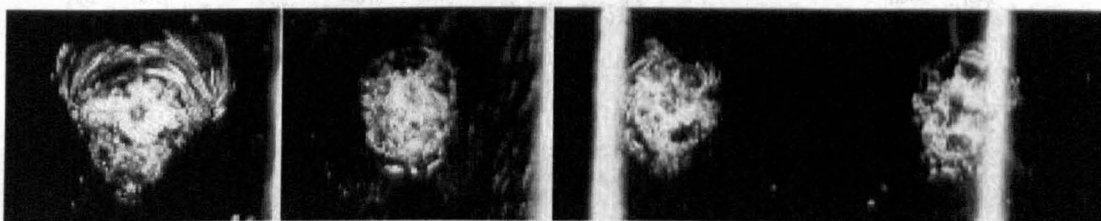


_imag000

_imag001

_imag002

_imag003



_imag004

_imag005

_imag006

_imag007



_imag008

_imag009

_imag010

_imag011



_imag012

_imag013

_imag014

_imag015



_imag016

_imag017

_imag018

_imag019

IMAGE ID No.	Pit (μm)		Conchoid (μm)		P μm	Centroid offset
	A	B	A	B		
4	36	31	263	240	22.62	0.95057
0	52	32	226	207	19.14	0.823009
17	50	27	213	181	8.7	0.816901
15	34	17	212	155	12.18	0.745283
5	41	30	211	167	12.18	0.815166
2			209	197	17.4	0.937799
16	37	24	208	118	121.8	0.653846
13	56	40	207	197	19.14	0.801932
7	39	24	203	152	12.18	0.995074
11	39	18	200	165	15.66	0.85
10	55	27	199	151	12.18	0.974874

Appendix C - Oblique solar cell impact programme: images and data

IMAGE ID No.	Pit (μm)		Conchoid (μm)		P μm	Centroid offset
	A	B	A	B		
6	44	37	197	166	13.92	0.751269
1	41	18	193	141	5.22	0.632124
9	53	31	188	159	12.18	0.702128
8	51	26	180	182	10.44	0.933333
18	64	19	178	151	22.62	0.966292
3	38	20	171	175	15.66	1.087719
12	52	22	162	175	15.66	1.024691
14	51	35	151	155	12.18	0.847682

Shot 3 glass

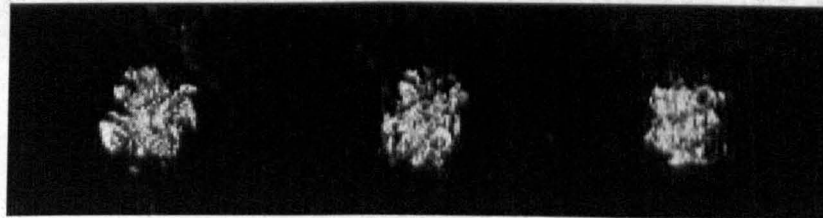


_imag000

_imag001

_imag002

_imag003



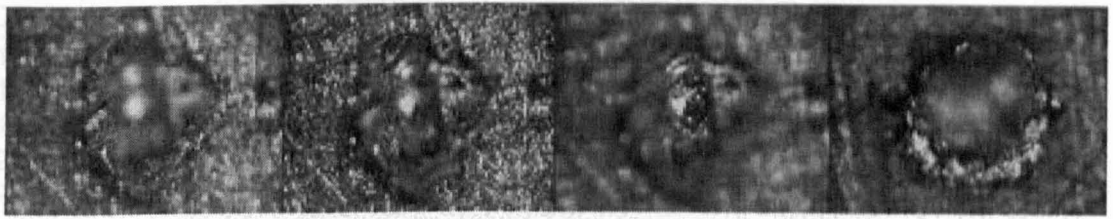
_imag004

_imag005

_imag006

IMAGE ID No.	Conchoid (μm)				P μm	Centroid offset
	A	B	\sqrt{AB}	CI		
1	210	147	175.6986	0.7	19.14	1.009524
2	126	66	91.1921	0.52381	8.7	0.920635
3	52	71	60.76183	1.365385	8.7	
4	154	155	154.4992	1.006494	8.7	
5	167	103	131.1526	0.616766	8.7	0.994012
6	132	103	116.6019	0.780303	8.7	0.833333

Shot 3 aluminium

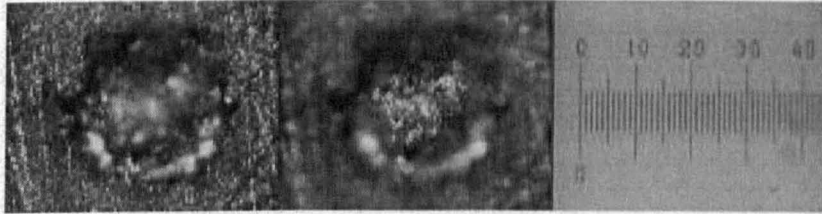


_imag000

_imag001

_imag002

_imag003

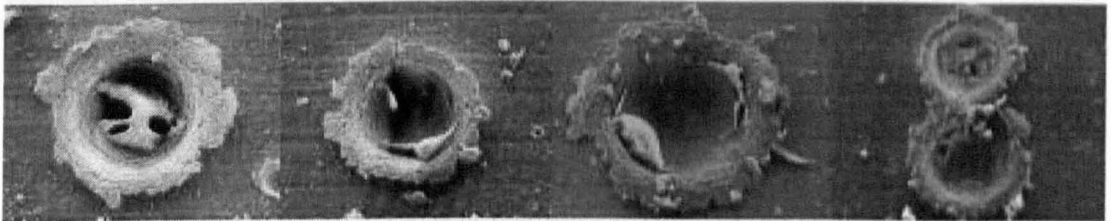


_imag004

_imag005

_imag006

Shot 3 PZT plate



001a

002a

003a

004&5a



006a

007a

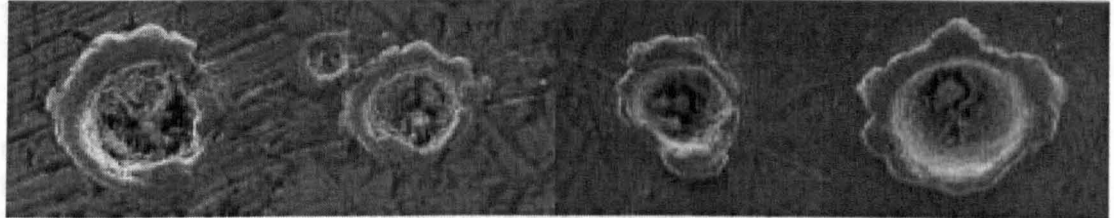
019a

ID g-PZT70	Dc (μm)			CI	SEM P (μm)	Optical P (μm)
	A	B	\sqrt{AB}			
1	171	168	169.49	0.98	64.25	80.04
2	150	141	145.43	0.94	68.13	87.00
3	208	193	200.36	0.93	75.68	76.56
4	101	99	99.99	0.98	42.69	95.70
5	120	104	111.71	0.87		83.52
6	111	128	119.20	1.15	50.83	81.78
7	162	184	172.65	1.14	91.30	76.56
8	168	160	163.95	0.95		74.82
9	132	113	122.13	0.86		81.78
10	141	122	131.16	0.87		85.26
11	116	113	114.49	0.97		69.60
12	162	160	161.00	0.99		71.34
13	73	69	70.97	0.95		81.78
14	159	143	150.79	0.90		
15	147	120	132.82	0.82		
16	139	128	133.39	0.92		

Appendix C - Oblique solar cell impact programme: images and data

ID g-PZT70	Dc (μm)			CI	SEM P (μm)	Optical P (μm)
	A	B	\sqrt{AB}			
17	103	88	95.21	0.85		
18	134	132	133.00	0.99		
19	126	118	121.93	0.94		
20	130	120	124.90	0.92		
21	141	136	138.48	0.96		

Shot 4 aluminium

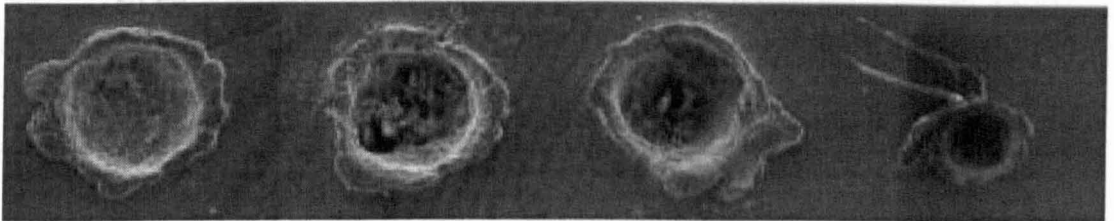


01_001a

02_001a

03_001a

04_001a

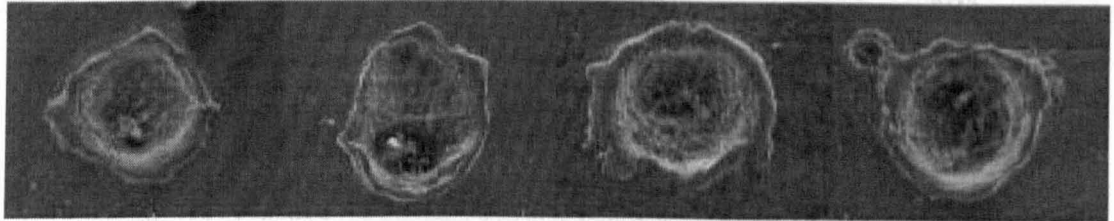


05_001a

06_001a

07_001a

08_001a



09_001a

10_001a

11_001a

12_001a

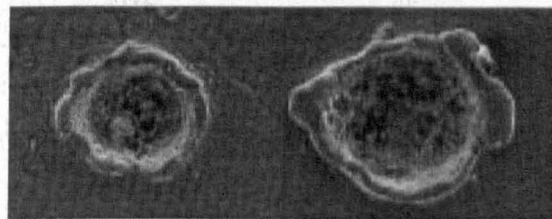


13_001a

14_001a

15_001a

16_001a



17_001a

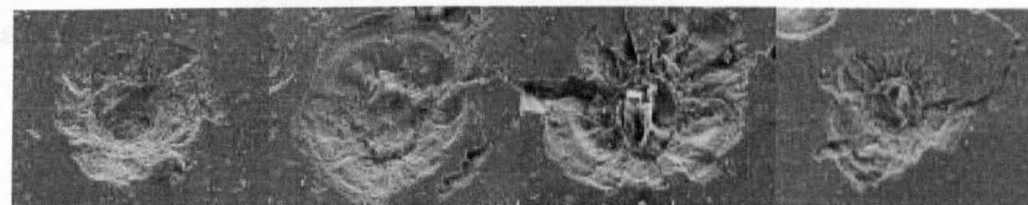
18_001a

Appendix C - Oblique solar cell impact programme: images and data

ID g-AIN	Dc (μm)			CI	P (μm)	
	A	B	\sqrt{AB}		SEM	Optical
7	233.10	238.30	235.69	1.02	100.54	
8	220.40	234.60	227.39	1.06		
10	236.50	184.90	209.11	0.78	51.83	20.88
6	145.90	165.30	155.30	1.13	46.75	
12	144.30	135.80	139.99	0.94	41.30	120.06
14	135.60	134.90	135.25	0.99	33.57	22.62
9	131.90	129.40	130.64	0.98	31.07	
11	103.10	110.72	106.84	1.07	37.26	64.38
18	101.90	108.30	105.05	1.06	43.51	120.06
15	100.70	103.90	102.29	1.03	19.40	109.62
5	92.30	98.20	95.20	1.06	36.20	
4	83.90	95.90	89.70	1.14	36.35	
13	88.30	89.50	88.90	1.01	38.90	31.32
16	65.80	72.60	69.12	1.10	21.57	137.46
17	56.80	60.80	58.77	1.07	25.49	78.30
3	51.20	57.90	54.45	1.13	27.79	
1	33.90	37.40	35.61	1.10	9.55	
2	29.80	27.00	28.37	0.91	11.41	

Shot 5 solar cells

ID 2g-ss-45	Shatter (μm)		Conchoid (μm)			SEM P (μm)	Optical P (μm)	Centroid offset	
	A	B	A	B	\sqrt{AB}				CI
1			566.00	520.00	542.51	0.92	48.57		0.63
2	130.00	115.00	407.00	510.00	455.60	1.25	16.38		1.27
3	99.00	95.00	391.00	310.00	348.15	0.79	13.58		0.99
4	95.00	98.00	350.00	335.00	342.42	0.96	20.72	17.40	0.74
5	105.00	106.00	332.00	314.00	322.87	0.95	11.21		1.01
6	100.00	96.00	291.00	275.00	282.89	0.95	22.10		0.95
7	118.00	117.00	289.00	278.00	283.45	0.96	3.79		1.27
8	85.00	93.00	283.00	198.00	236.72	0.70	29.61		0.96
9	90.00	88.00	280.00	287.00	283.48	1.03	30.66	26.10	1.00
10	93.00	89.00	278.00	273.00	275.49	0.98	18.62		0.99
11	100.00	84.00	268.00	252.00	259.88	0.94	25.34	19.14	1.18
12	93.00	98.00	267.00	287.00	276.82	1.07	31.97	22.62	1.26
13	70.00	76.00	266.00	266.00	266.00	1.00	33.88	12.18	0.98
14	72.00	73.00	252.00	267.00	259.39	1.06	29.00		1.01
15	91.00	92.00	250.00	245.00	247.49	0.98	21.07		1.13
16	97.00	90.00	249.00	282.00	264.99	1.13	33.88	29.58	0.74
17	102.00	104.00	248.00	200.00	222.71	0.81	15.56		1.03
18	87.00	101.00	241.00	266.00	253.19	1.10	15.82		1.06
19	119.00	111.00	235.00	317.00	272.94	1.35	21.58		0.93
20	98.00	103.00	222.00	250.00	235.58	1.13	27.51	13.92	0.60
21	85.00	77.00	220.00	209.00	214.43	0.95	28.21	20.88	1.00
22	64.00	61.00	214.00	211.00	212.49	0.99	9.36		0.98
23			212.00	226.00	218.89	1.07	6.05	19.14	1.08
24	122.00	94.00	202.00	298.00	245.35	1.48	40.95	17.40	0.95
25	78.00	78.00	192.00	189.00	190.49	0.98		20.88	0.92



ss45-01a

ss45-02a

ss45-03a

ss45-04a



ss45-05a

ss45-06a

ss45-07a

ss45-08a

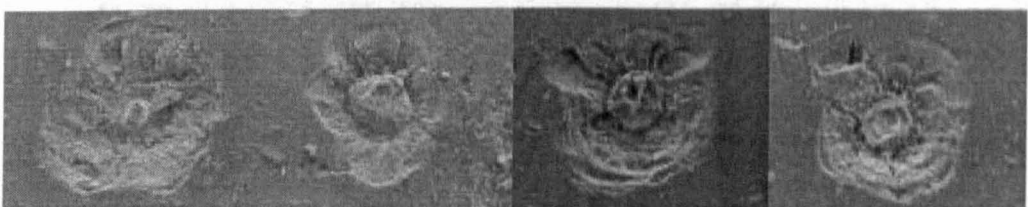


ss45-09a

ss45-10a

ss45-11a

ss45-12a



ss45-13a

ss45-14a

ss45-15a

ss45-16a



ss45-17a

ss45-18a

ss45-19a

ss45-20a



ss45-21a

ss45-22a

ss45-23a

ss45-24a



ss45-25a

Shot 5 glass

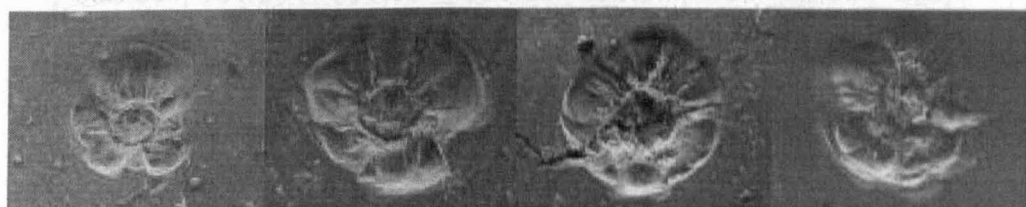


g45-01a

g45-02a

g45-03a

g45-04a



g45-05a

g45-06a

g45-07a

g45-08a

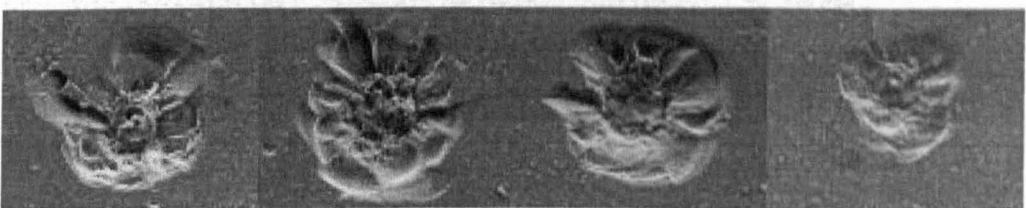


g45-09a

g45-10a

g45-11a

g45-12a

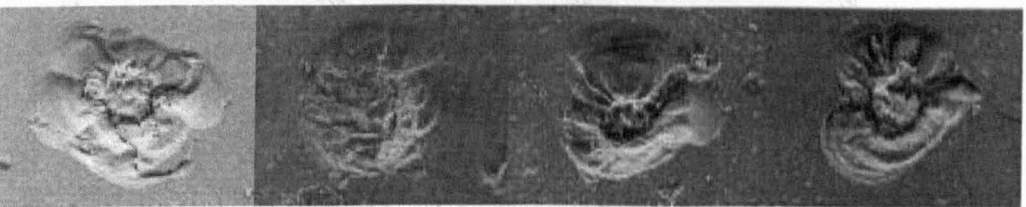


g45-13a

g45-14a

g45-15a

g45-16a

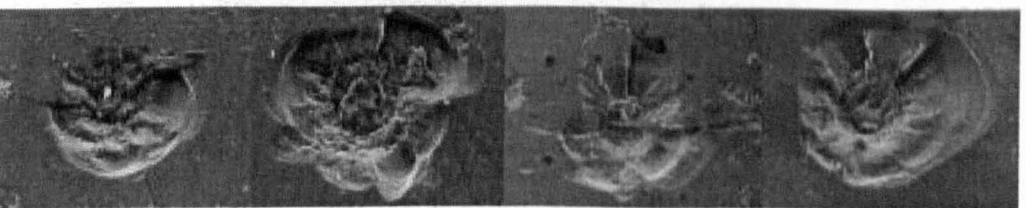


g45-17a

g45-18a

g45-19a

g45-20a

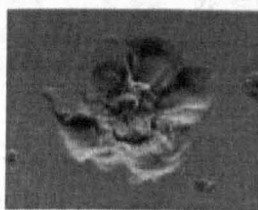


g45-21a

g45-22a

g45-23a

g45-24a



g45-25a

Appendix C - Oblique solar cell impact programme: images and data

ID 2g-ss-75	Splatter (μm)		Conchoid (μm)			CI	SEM P (μm)	Optical P (μm)	Centroid offset
	A	B	A	B	\sqrt{AB}				
1							29.58		
2	105.00	97.00	253.00	330.00	288.95	1.30	13.29	31.32	1.15
3	108.00	109.00	267.00	332.00	297.73	1.24	22.78	24.36	
4	108.00	111.00	376.00	308.00	340.31	0.82	25.15	24.36	1.07
5	93.00	100.00	299.00	243.00	269.55	0.81	20.18	33.06	1.32
6	82.00	86.00	255.00	308.00	280.25	1.21	28.92	34.80	0.97
7	108.00	101.00	301.00	293.00	296.97	0.97	22.64	36.54	1.09
8	109.00	77.00	330.00	303.00	316.21	0.92	14.70	26.10	0.88
9	75.00	66.00	230.00	232.00	231.00	1.01	19.40	26.10	1.06
10	52.00	56.00	192.00	200.00	195.96	1.04	5.57	26.10	0.92
11	84.00	77.00	252.00	244.00	247.97	0.97	11.76	20.88	1.14
12	39.00	52.00	193.00	194.00	193.50	1.01	25.33	17.40	1.08
13	105.00	96.00	365.00	343.00	353.83	0.94	31.55	36.54	1.19
14	85.00	87.00	252.00	215.00	232.77	0.85	8.47	27.84	0.87
15	96.00	92.00	239.00	282.00	259.61	1.18	39.24	34.80	1.00
16	62.00	68.00	175.00	177.00	176.00	1.01	12.64		0.75
17	119.00	96.00	345.00	430.00	385.16	1.25	7.24		0.79
18			346.00	309.00	326.98	0.89	33.53		
19	64.00	66.00	238.00	239.00	238.50	1.00	18.14		1.30
20	74.00	67.00	234.00	202.00	217.41	0.86	20.79		0.99
21	95.00	97.00	284.00	349.00	314.83	1.23	1.36		0.77
22	82.00	70.00	245.00	338.00	287.77	1.38	9.80		0.99
23	123.00	106.00	375.00	274.00	320.55	0.73	18.00		1.17
24	82.00	78.00	261.00	300.00	279.82	1.15			1.06
25	102.00	99.00	313.00	324.00	318.45	1.04	4.61		1.14

Shot 5 aluminium

ID 2g-Al-45	Dc (μm)			CI	SEM P (μm)	Optical P (μm)
	A	B	\sqrt{AB}			
1	143	127	134.76	0.89	36.13	46.98
2	116	103	109.31	0.89	34.64	10.44
3	150	158	153.95	1.05	44.25	29.58
4	128	134	130.97	1.05	49.74	46.98
5	163	151	156.89	0.93	47.41	36.54
6	161	152	156.44	0.94	25.02	46.98
7	131	124	127.45	0.95	48.91	64.38
8	143	149	145.97	1.04	49.39	46.98
9	128	118	122.90	0.92	36.26	19.14
10	160	146	152.84	0.91	57.29	45.24
11	169	154	161.33	0.91		38.28
12	155	146	150.43	0.94	37.58	46.98
13	169	175	171.97	1.04	49.65	57.42
14	137	138	137.50	1.01	46.62	52.20
15	160	164	161.99	1.03	70.55	43.50
16	175	166	170.44	0.95	61.24	50.46
17	150	140	144.91	0.93	37.31	38.28
18	155	143	148.88	0.92	47.41	34.80
19	172	152	161.69	0.88	57.03	46.98
20	175	162	168.37	0.93	41.84	36.54
21	181	175	177.97	0.97	42.19	53.94
22	141	144	142.49	1.02	58.21	59.16
23	163	167	164.99	1.02	42.71	43.50
24	179	161	169.76	0.90	38.10	55.68
25	167	162	164.48	0.97	52.46	67.86

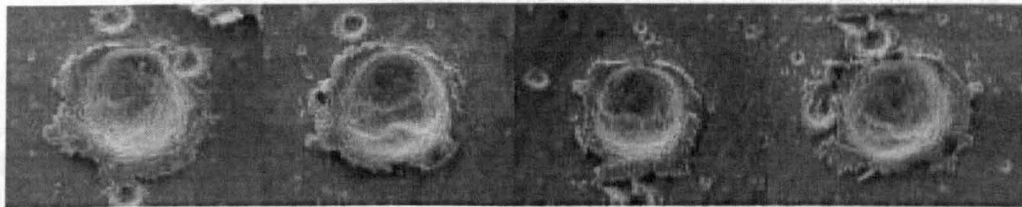


al45-01a

al45-02a

al45-03a

al45-04a

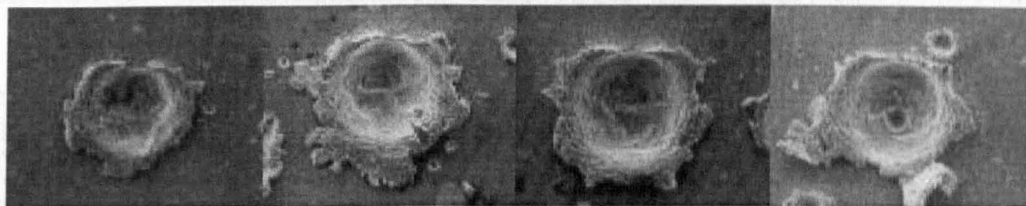


al45-05a

al45-06a

al45-07a

al45-08a



al45-09a

al45-10a

al45-11a

al45-12a

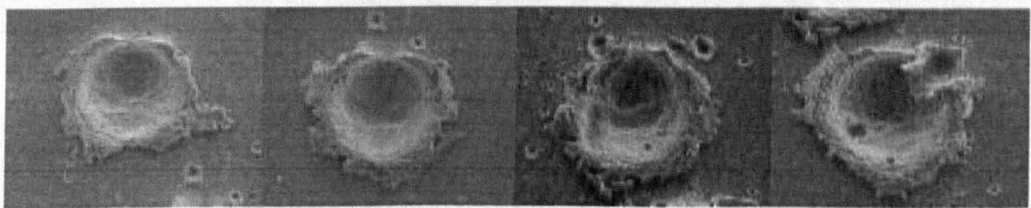


al45-13a

al45-14a

al45-15a

al45-16a



al45-17a

al45-18a

al45-19a

al45-20a

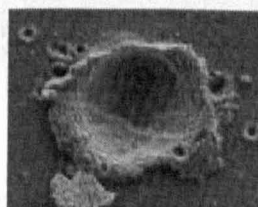


al45-21a

al45-22a

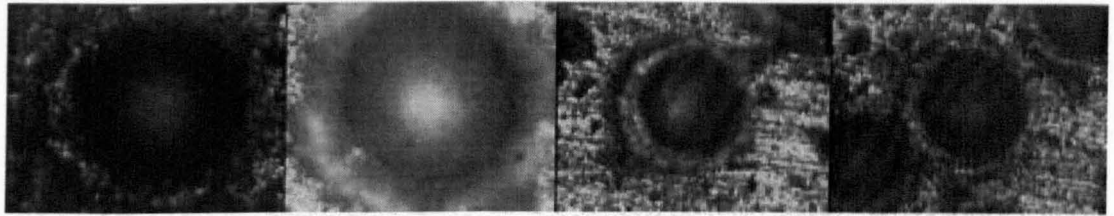
al45-23a

al45-24a



al45-25a

Shot 5 PZT plate

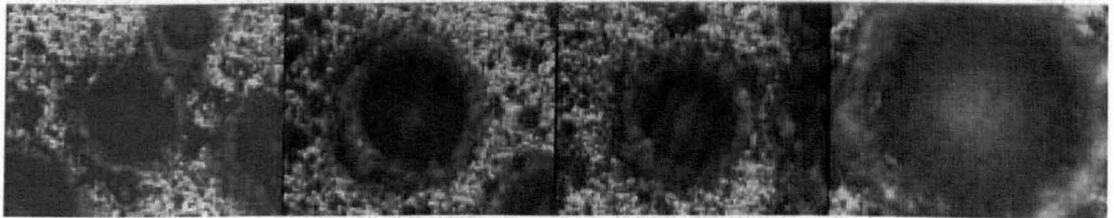


_imag000

_imag001

_imag003

_imag004

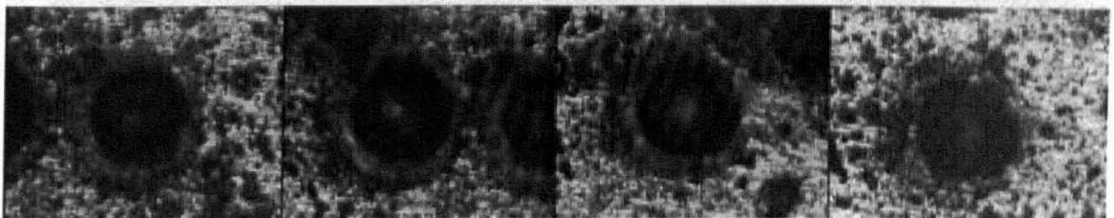


_imag005

_imag006

_imag007

_imag008

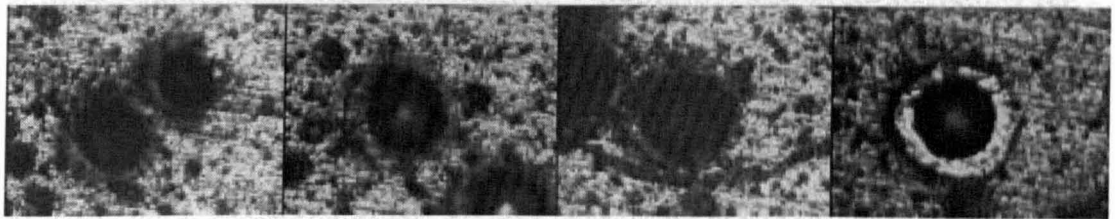


_imag009

_imag010

_imag011

_imag012

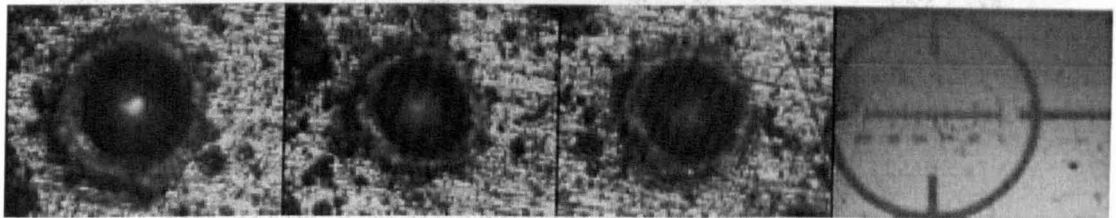


_imag013

_imag014

_imag015

_imag016

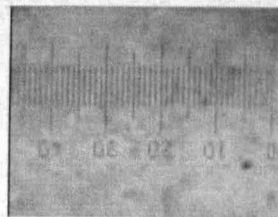


_imag017

_imag018

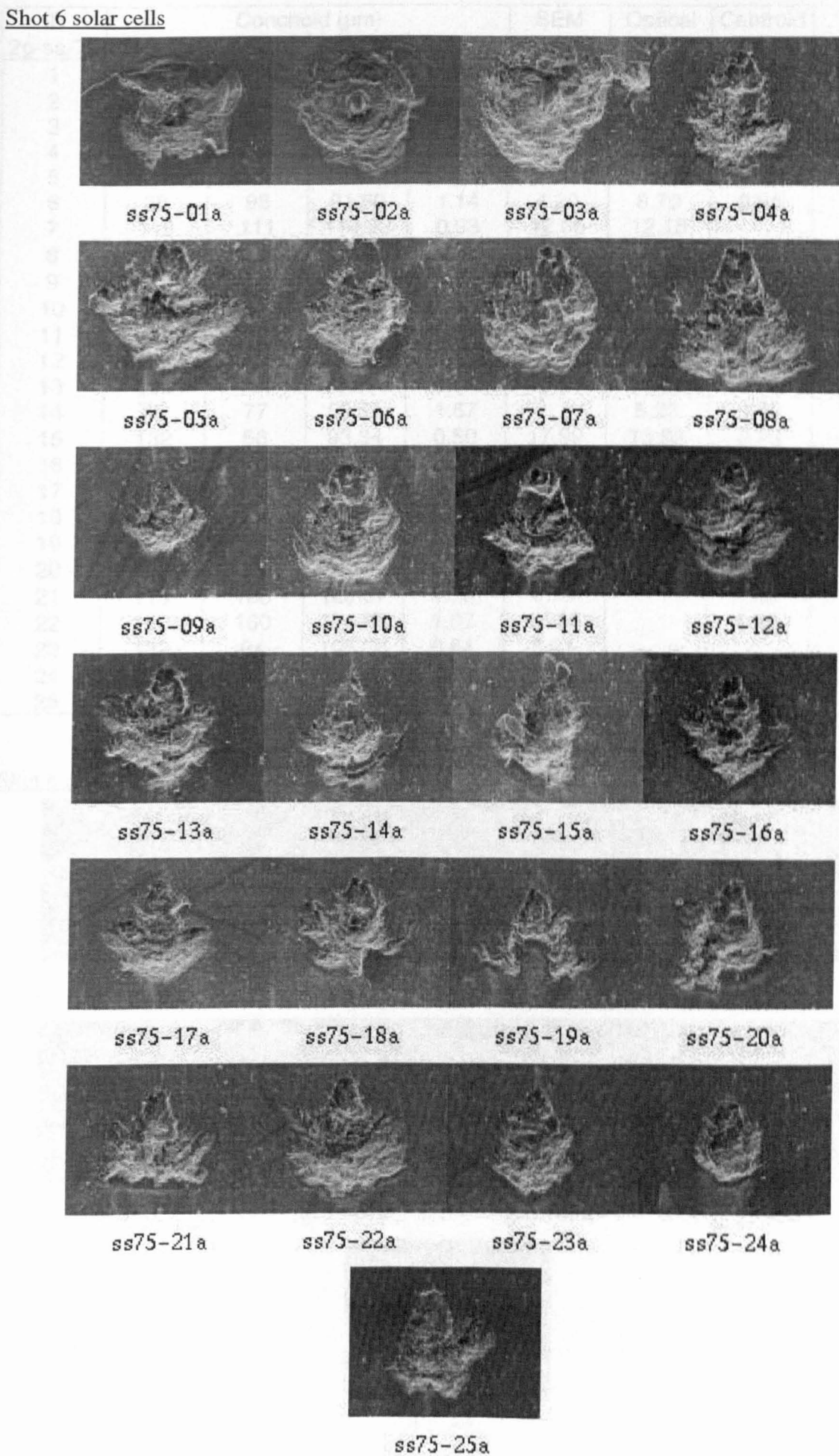
_imag019

_imag020



_imag021

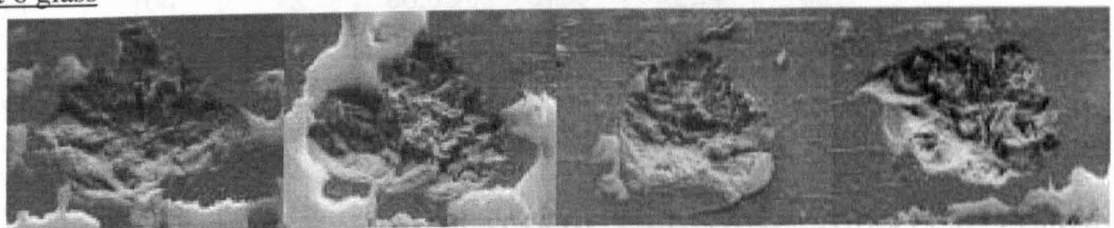
Shot 6 solar cells



Appendix C - Oblique solar cell impact programme: images and data

ID 2g-ss-75	Conchoid (μm)				SEM P (μm)	Optical P (μm)	Centroid offset
	A	B	Dco	CI			
1	189	209	198.75	1.11	15.99	15.66	1.14
2	530	546	537.94	1.03	43.26	6.96	0.91
3	129	122	125.45	0.95	17.47	8.70	
4	117	98	107.08	0.84	13.11	10.44	1.23
5	118	135	126.21	1.14	12.15	13.92	0.97
6	86	98	91.80	1.14	4.20	8.70	0.84
7	119	111	114.93	0.93	12.06	12.18	
8	128	121	124.45	0.95	7.52	10.44	1.31
9	64	77	70.20	1.20	4.11	10.44	
10	120	92	105.07	0.77	6.39	168.78	1.13
11	93	98	95.47	1.05	13.37	17.40	1.48
12	169	151	159.75	0.89	31.08	5.22	1.16
13	130	131	130.50	1.01	18.95	13.92	0.94
14	46	77	59.51	1.67		5.22	0.65
15	132	66	93.34	0.50	17.99	13.92	0.73
16	136	129	132.45	0.95	14.07	13.92	1.13
17	132	145	138.35	1.10	8.40	15.66	1.03
18	126	108	116.65	0.86	10.57	6.96	0.78
19						8.70	
20	108	73	88.79	0.68	7.17	12.18	
21	115	133	123.67	1.16	6.74		1.32
22	150	160	154.92	1.07	14.68		1.25
23	132	84	105.30	0.64	8.31		
24	103	81	91.34	0.79	5.69		
25	126	117	121.42	0.93			

Shot 6 glass

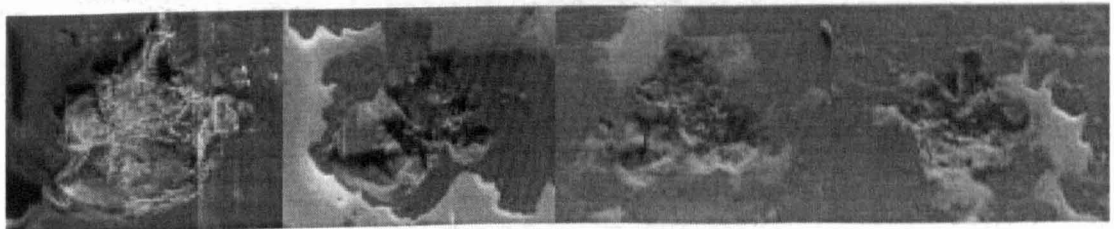


g75-01a

g75-02a

g75-03a

g75-04a



g75-05a

g75-06a

g75-07a

g75-08a

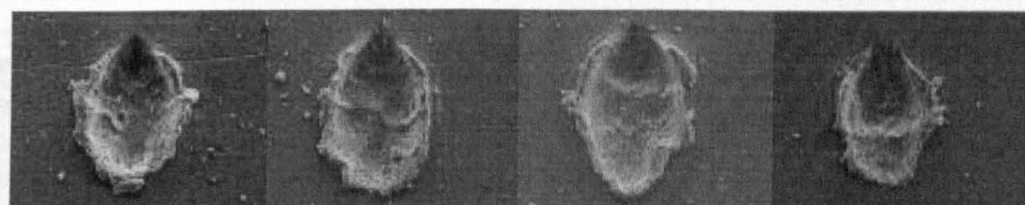


g75-09a

ID 2g-g-75	Shatter (μm)		Conchoid (μm)			CI	SEM P (μm)	Centroid Offset	
	A	B	A	B	\sqrt{AB}				
1	36	42	119	136	127.22	1.14	4.16	0.96	
2			106	137	120.51	1.29	12.02	1.09	
3			82	93	87.33	1.13	12.02	1.17	
4			88	116	101.03	1.32	10.25	0.70	
5			131	125	127.96	0.95	8.08		
6	28	24	81	93	86.79	1.15	4.54	1.11	
7			79	87	82.90	1.10	9.30	1.37	
8									
9									

Shot 6 aluminium

ID 2g-Al-75	Dc (μm)			CI	SEM P (μm)	Optical P (μm)
	A	B	\sqrt{AB}			
1	124	78	98.35	0.63		20.88
2	138	76	102.41	0.55	5.22	13.92
3	142	83	108.56	0.58	22.56	10.44
4	119	73	93.20	0.61	9.08	12.18
5	127	84	103.29	0.66	17.78	10.44
6	129	74	97.70	0.57	16.33	13.92
7	126	74	96.56	0.59	11.76	12.18
8	116	82	97.53	0.71	12.55	10.44
9	129	79	100.95	0.61	20.81	15.66
10	111	71	88.77	0.64	6.85	12.18
11	104	72	86.53	0.69	12.82	5.22
12	120	72	92.95	0.60	10.53	5.22
13	110	68	86.49	0.62	9.08	10.44
14	156	83	113.79	0.53	17.78	13.92
15	128	87	105.53	0.68	20.28	13.92
16	167	74	111.17	0.44	15.49	13.92
17	145	101	121.02	0.70	13.47	12.18
18	138	78	103.75	0.57	26.25	
19	123	81	99.81	0.66	12.82	
20	121	81	99.00	0.67	13.34	
21	138	76	102.41	0.55	13.34	
22	144	92	115.10	0.64	8.95	
23	102	68	83.28	0.67	4.30	
24	160	89	119.33	0.56	19.23	
25	129	72	96.37	0.56	16.28	



al75-01a

al75-02a

al75-03a

al75-04a

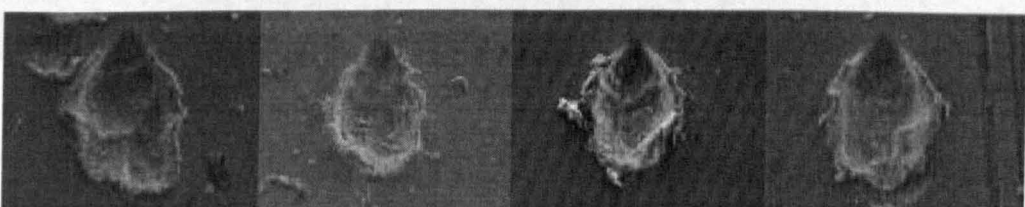


al75-05a

al75-06a

al75-07a

al75-08a

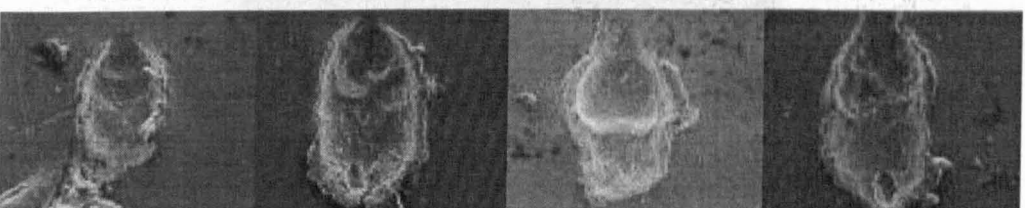


al75-09a

al75-10a

al75-11a

al75-12a

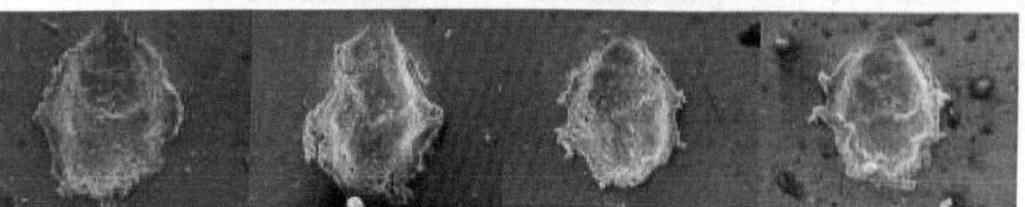


al75-13a

al75-14a

al75-15a

al75-16a



al75-17a

al75-18a

al75-19a

al75-20a



al75-21a

al75-22a

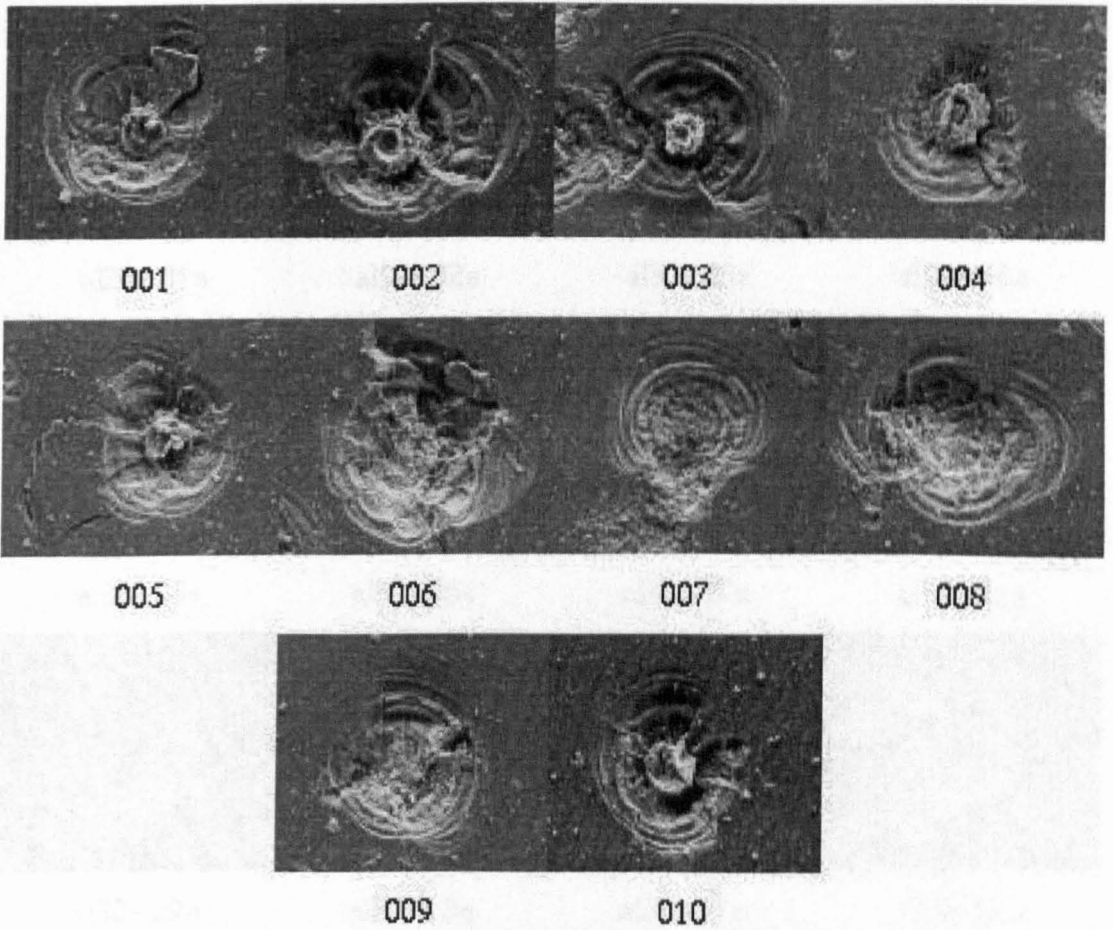
al75-23a

al75-24a



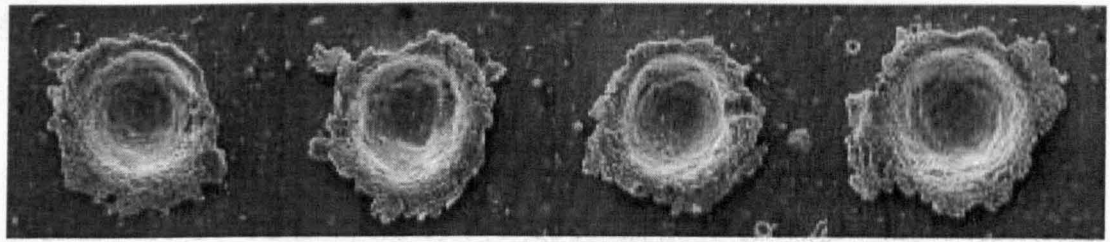
al75-25a

Shot 7 solar cells



ID No.	Pit (μm)		Shatter (μm)		Conchoid (μm)			CI	P (μm)	Centroid Offset
	A	B	A	B	A	B	\sqrt{AB}			
1					651	583	616.06	0.90	55	0.96
2	54.00	48.00	111.00	105.00	491	490	490.50	1.00		1.25
3					447	526	484.89	1.18	64	1.15
4					441	441	441.00	1.00	54	1.17
5	70.00	57.00	111.00	116.00	365	504	428.91	1.38	33	1.16
6					422	435	428.45	1.03	64	0.99
7			91.00	97.00	373	309	339.50	0.83	64	1.08
8	39.00	27.00	92.00	84.00	318	312	314.99	0.98		1.08
9			80.00	92.00	347	266	303.81	0.77	38	1.08
10			125.00	117.00	331	265	296.17	0.80	42	0.92

Shot 7 aluminium

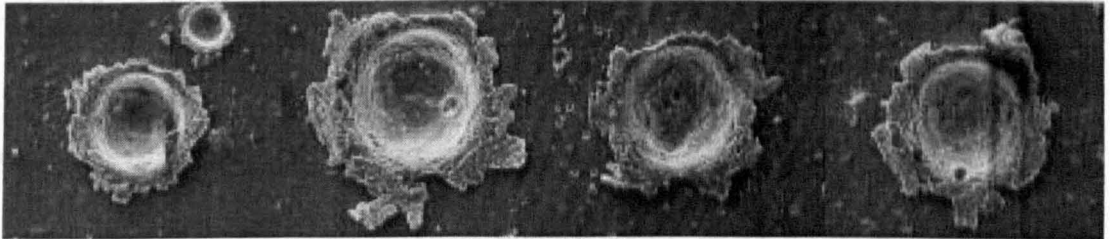


a130-01a

a130-02a

a130-03a

a130-04a

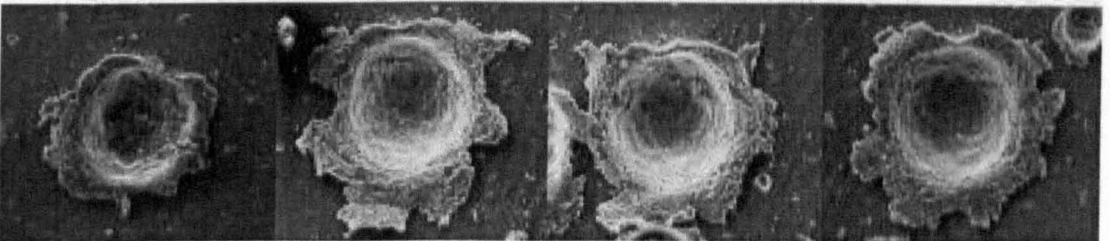


a130-05a

a130-06a

a130-07a

a130-08a

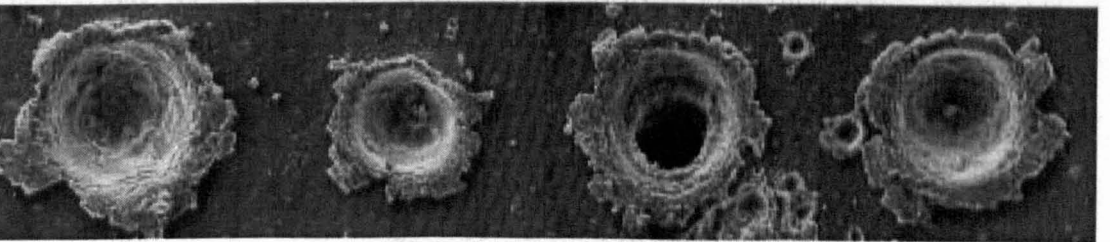


a130-09a

a130-10a

a130-11a

a130-12a

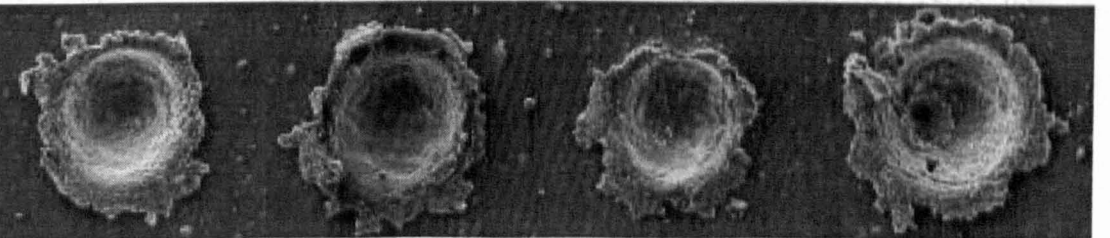


a130-13a

a130-14a

a130-15a

a130-16a



a130-17a

a130-18a

a130-19a

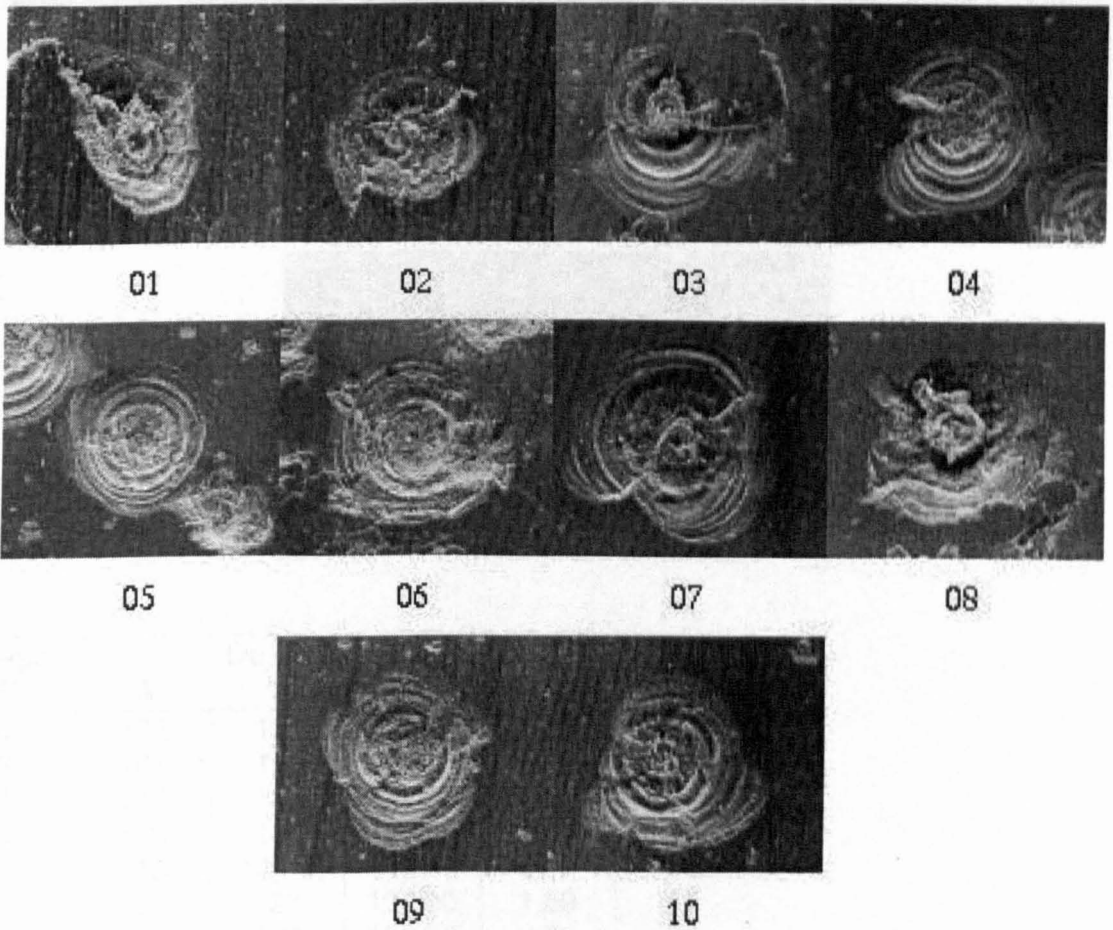
a130-20a

Image g-al30	Dc (μm)			CI
	A	B	\sqrt{AB}	
1	173	146	158.93	0.84
1	168	154	160.85	0.92
1	163	137	149.44	0.84
1	179	177	178.00	0.99
1	129	117	122.85	0.91
1	179	163	170.81	0.91
1	158	143	150.31	0.91

Appendix C - Oblique solar cell impact programme: images and data

Image g-al30	Dc (µm)			
	A	B	\sqrt{AB}	CI
1	153	137	144.78	0.90
1	148	138	142.91	0.93
1	173	163	167.93	0.94
1	181	164	172.29	0.91
2	181	158	169.11	0.87
3	185	192	188.47	1.04
4	130	132	131.00	1.02
5	191	168	179.13	0.88
6	171	163	166.95	0.95
7	167	150	158.27	0.90
8	176	165	170.41	0.94
9	165	143	153.61	0.87
10	189	178	183.42	0.94

Shot 8 solar cells

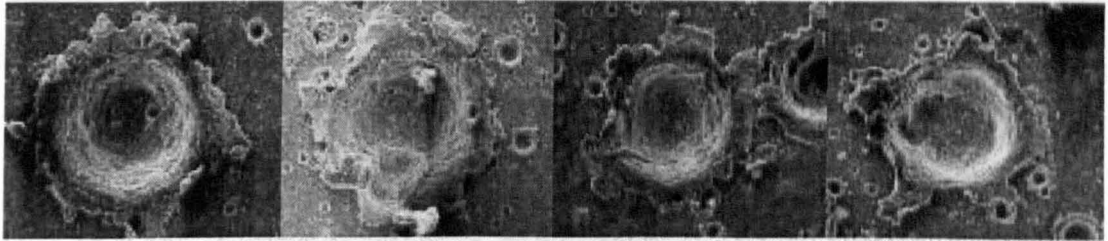


Shatter (µm)			Conchoid (µm)				
A	B	P	A	B	\sqrt{AB}	CI	P
			642	518	576.68	0.81	74
			565	584	574.42	1.03	196
			606	506	553.75	0.83	67
			519	524	521.49	1.01	135
115	75	28	564	468	513.76	0.83	49
112	89	24	498	490	493.98	0.98	75
100	89	37	404	386	394.90	0.96	68
129	105	33	324	345	334.34	1.06	105

Appendix C - Oblique solar cell impact programme: images and data

Shatter (μm)			Conchoid (μm)				
A	B	P	A	B	\sqrt{AB}	CI	P
76	90	74	257	326	289.45	1.27	101
146	94	28	320	230	271.29	0.72	59

Shot 8 aluminium

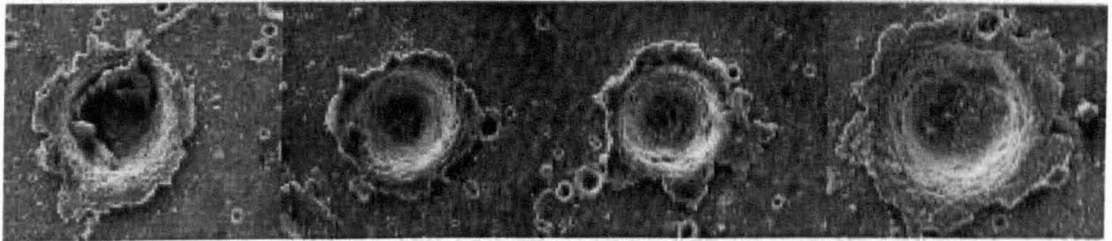


01a

02a

03a

04a

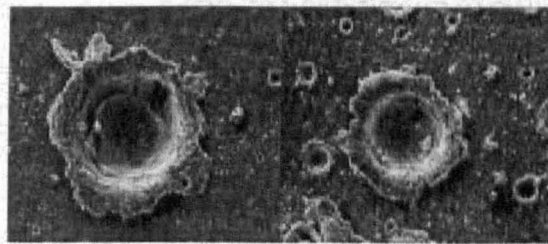


05a

06a

07a

08a

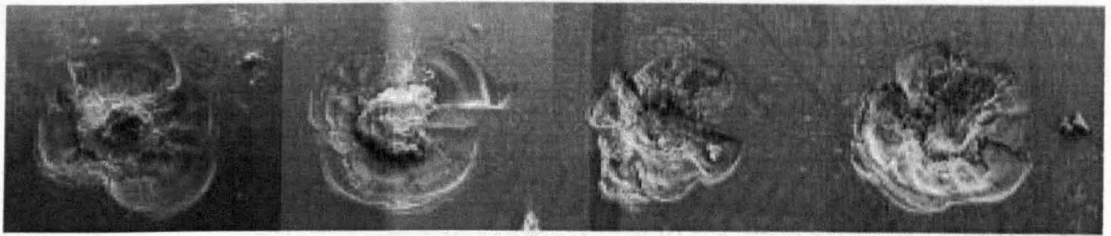


09a

10a

Image ID	Dc (μm)		\sqrt{AB}	CI	Depth P
	A	B			
1	172	161	166.41	0.94	94
2	161	155	157.97	0.96	76
3	143	138	140.48	0.97	68
4	138	160	148.59	1.16	96
5	146	141.5	143.73	0.97	63
6	127	127	127.00	1.00	57
7	127	126	126.50	0.99	78
8	185	176	180.44	0.95	76
9	144	135	139.43	0.94	62
10	107	100	103.44	0.93	45

Shot 9 solar cells

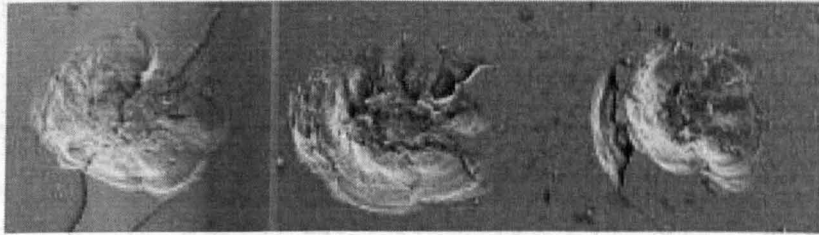


250299-1b

250299-1c

250299-1d

250299-1e



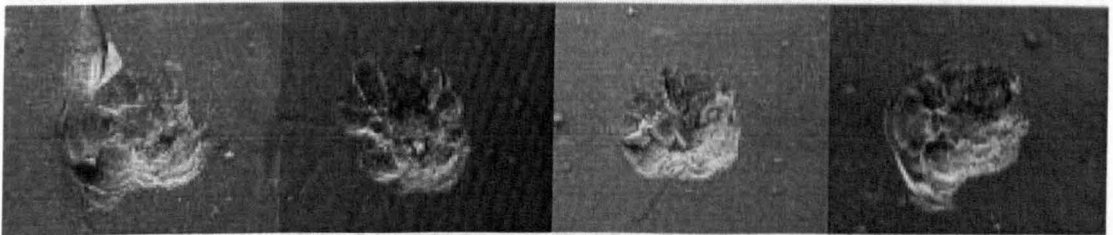
250299-1f

250299-1g

250299-1h

ID	Shatter (μm)				Conchoid (μm)				
	A	B	Dsh	B/A	A	B	Dco	B/A	Coff
b	103.28	88.73	95.73	0.86	324.87	303.52	314.01	0.93	1.00
c	127.03	112.00	119.28	0.88	328.74	291.42	309.52	0.89	1.00
d					230.79	260.87	245.37	1.13	0.87
e					305.46	302.09	303.77	0.99	0.91
f					353.47	279.77	314.46	0.79	1.08
g	124.12	89.22	105.23	0.72	366.07	316.64	340.46	0.86	0.88

Shot 10 solar cells

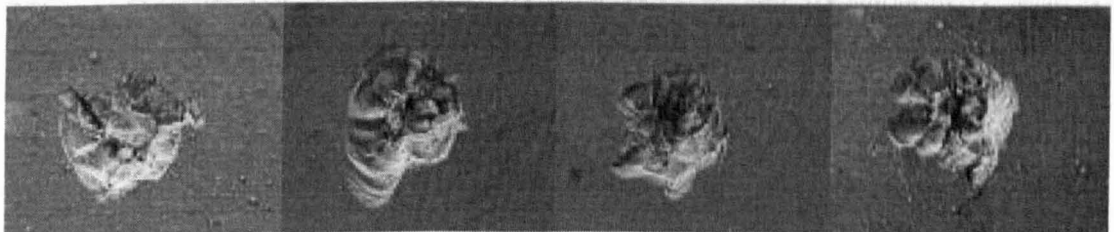


250299-1j

250299-1k

250299-1l

250299-1m



250299-1n

250299-1o

250299-1p

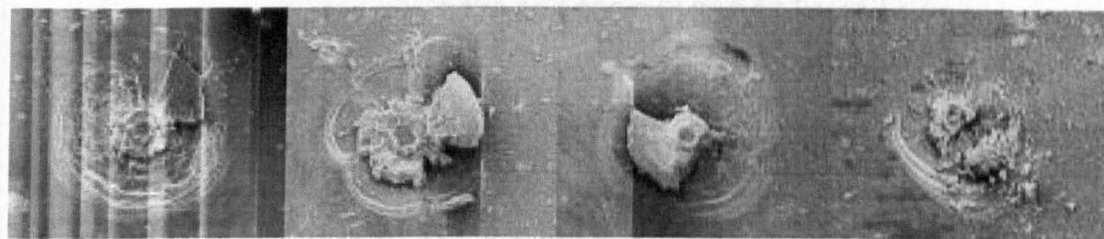
250299-1q

ID	Conchoid (μm)			B/A	Coff
	A	B	Dco		
j	235.16	198.84	216.24	0.85	1.20
k	221.58	240.49	230.84	1.09	1.22
l	213.34	186.68	199.57	0.88	
m	257.96	212.86	234.32	0.83	1.18

Appendix C - Oblique solar cell impact programme: images and data

ID	Conchoid (μm)				Coff
	A	B	Dco	B/A	
n	249.22	218.19	233.19	0.88	1.02
o	207.04	204.13	205.58	0.99	1.30
p	165.34	239.55	199.01	1.45	1.04
q	197.86	223.04	210.08	1.13	1.21

Shot 11 solar cells



15deg-a

15deg-b

15deg-c

15deg-d

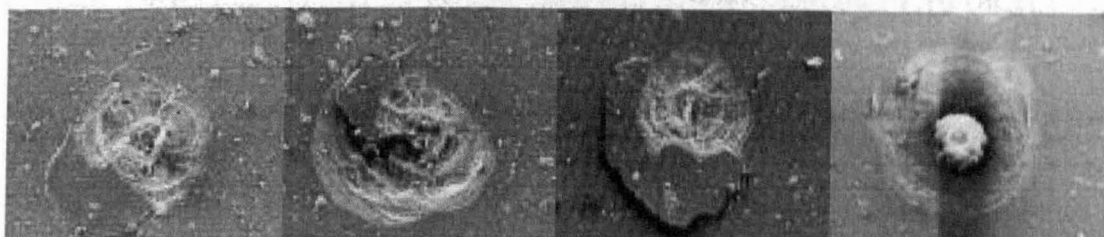


15deg-e

15deg-f

15deg-g

15deg-h

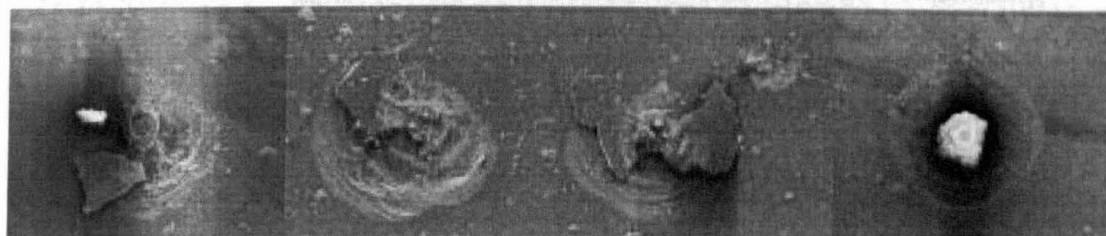


15deg-i

15deg-j

15deg-k

15deg-l

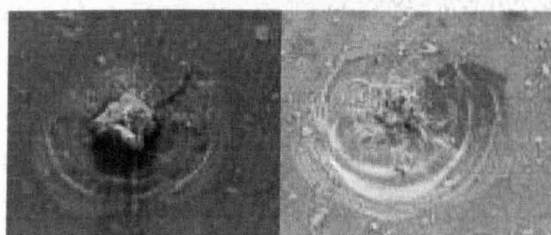


15deg-m

15deg-n

15deg-o

15deg-p



15deg-q

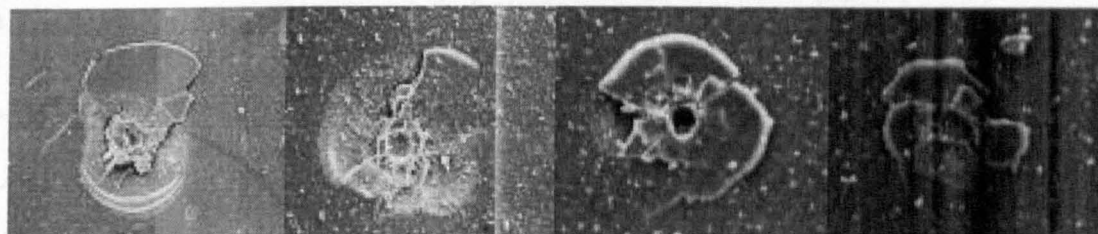
15deg-r

Appendix C - Oblique solar cell impact programme: images and data

ID	Pit (μm)		Shatter (μm)		Conchoid (μm)				
	A	B	A	B	A	B	Dco	B/A	C
c	67.69	70.45	185.38	340.16	672.92	626.57	649.33	0.93	0.91
i	81.56	88.10	189.08	182.59	591.35	566.32	578.70	0.96	0.94
a	53.50	58.58	151.98	157.08	561.22	559.53	560.37	1.00	1.01
o	64.81	66.74	147.98	151.85	467.14	597.73	528.42	1.28	1.40
q			168.06	180.23	444.11	566.68	501.67	1.28	1.21
k			95.67	91.00	520.36	419.26	467.08	0.81	1.30
j	36.24	38.89	90.96	89.60	358.46	430.88	393.01	1.20	1.17
r					273.89	300.04	286.67	1.10	1.21
l	31.03	27.16	67.44	65.46	238.65	248.25	243.40	1.04	1.10
g	38.46	28.37	97.07	115.00	205.34	244.92	224.26	1.19	1.03
m			66.75	53.88	213.56	187.35	200.03	0.88	1.29
b	27.92	27.89	83.68	96.76	180.73	194.10	187.30	1.07	0.97
d	26.63	23.52	42.20	46.00	190.91	178.10	184.39	0.93	1.26
f	19.18	21.79	67.12	72.93	167.08	197.00	181.42	1.18	1.25
e	22.80	25.27	40.54	45.54	117.74	140.78	128.75	1.20	1.33
h	12.79	12.79			120.60	113.47	116.98	0.94	1.10

Shot 12 solar cells

	Pit (μm)		Shatter (μm)		Dco (μm)			B/A	Coff
	A	B	A	B	A	B	Dco		
1	16.98	14.81	64.68	68.29	234.52	136.23	178.74	0.58	0.89
2	36.86	19.52	78.79	70.82	231.29	169.83	198.19	0.73	1.19
3	70.45	61.17	171.47	198.36	486.61	579.31	530.94	1.19	1.31
4	12.56	15.41	32.71	31.52	66.37	92.68	78.43	1.40	1.15
5			50.76	59.54	140.58	162.03	150.92	1.15	1.04
6			58.87	76.12	448.03	272.86	349.64	0.61	1.10
7	145.62	171.90	excavated		669.37	615.78	642.02	0.92	0.97
8	58.42	77.86	252.13	274.37	618.29	565.41	591.26	0.91	1.00
9	12.96	12.16			52.42	58.20	55.24	1.11	0.86
10	14.01	13.23	24.91	23.09	73.95	72.39	73.16	0.98	0.91
11	7.91	6.75			40.22	45.15	42.61	1.12	0.94
16	21.74	26.22	55.14	58.73	123.72	164.52	142.67	1.33	0.86
17	14.62	14.07			67.41	63.34	65.34	0.94	1.29
18			56.40	50.59	232.08	178.86	203.74	0.77	1.12
19	26.76	31.40			134.57	217.63	171.13	1.62	1.25
20	20.10	18.27	39.10	35.08	118.76	108.16	113.34	0.91	0.84
21	23.16	27.13	52.16	57.55	127.96	123.27	125.59	0.96	1.00



15deg-1

15deg-10

15deg-11

15deg-12

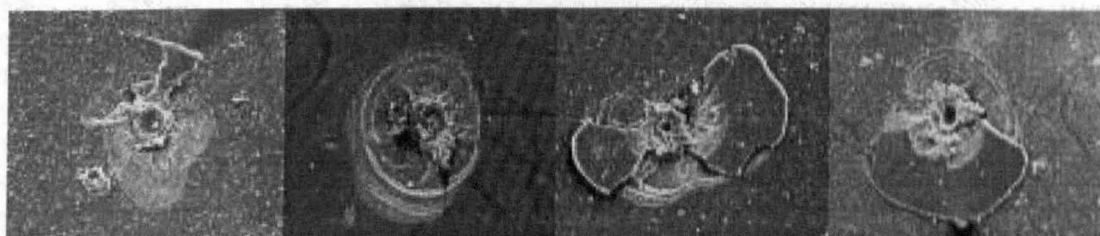


15deg-13

15deg-14

15deg-15

15deg-16

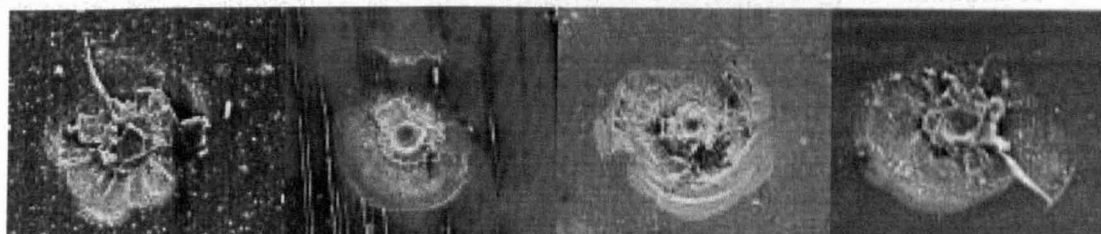


15deg-17

15deg-18

15deg-19

15deg-2

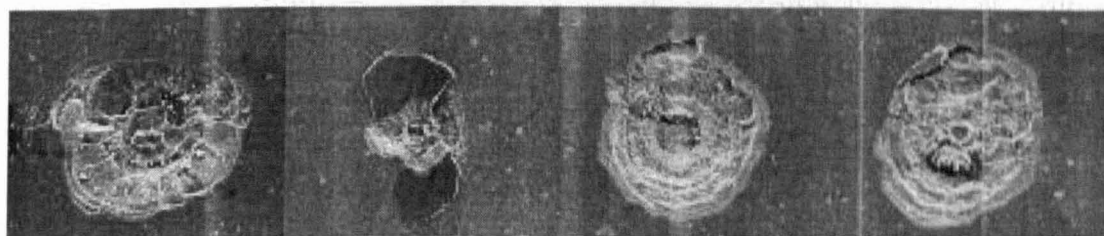


15deg-20

15deg-21

15deg-3

15deg-4



15deg-5

15deg-6

15deg-7

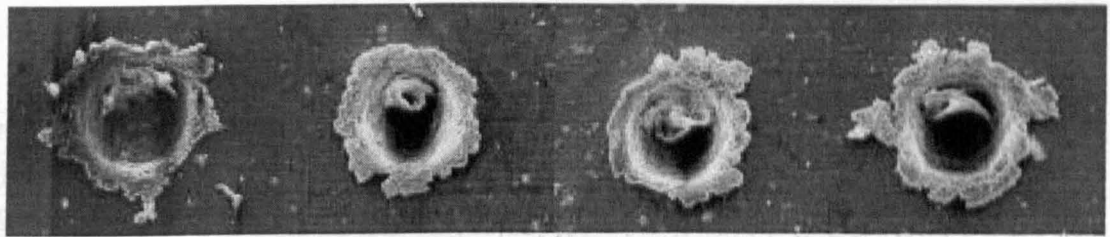
15deg-8



15deg-9

Shot 12 aluminium

	Dc (μm)			Cl
	A	B	Dc	
1	180.32	179.39	179.86	0.99
2	162.66	151.51	156.98	0.93
3	143.14	145.93	144.53	1.02
4	164.52	158.02	161.23	0.96
5	174.74	167.31	170.98	0.96
6	162.66	145.01	153.58	0.89
7	159.87	160.80	160.34	1.01
8	172.88	163.59	168.17	0.95
9	177.53	164.52	170.90	0.93
10	171.03	166.38	168.69	0.97
11	162.68	157.08	159.86	0.97
12	181.25	174.74	177.97	0.96
13	171.96	167.31	169.62	0.97
14	135.72	138.49	137.10	1.02
15	97.60	105.03	101.25	1.08
16	105.05	112.47	108.69	1.07
17	158.95	149.66	154.24	0.94
18	159.87	165.45	162.64	1.03
19	166.38	152.44	159.25	0.92

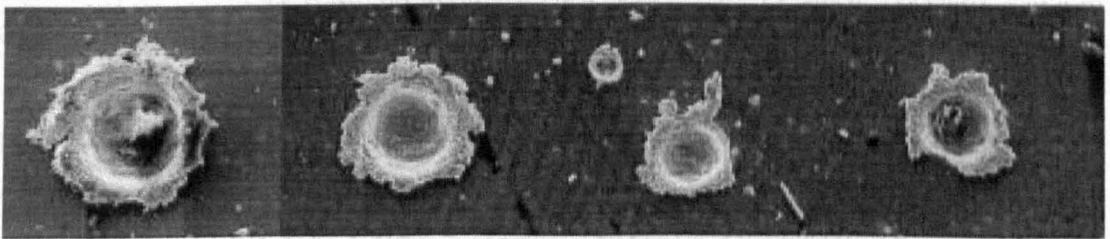


15Al-1

15Al-10

15Al-11

15Al-12

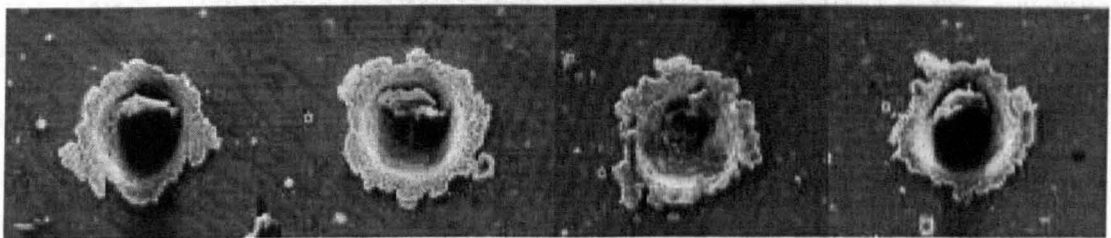


15Al-13

15Al-14

15Al-15

15Al-16

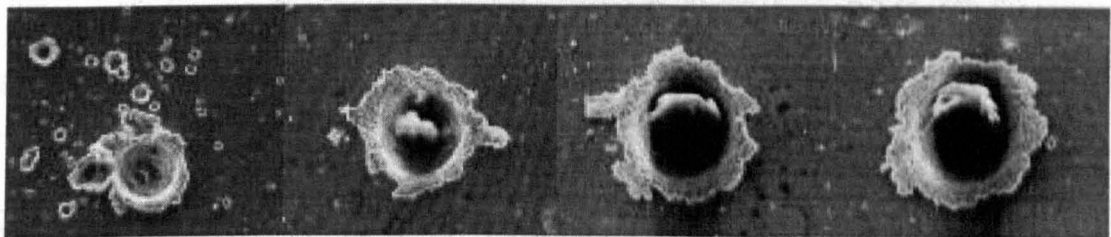


15Al-17

15Al-18

15Al-19

15Al-2

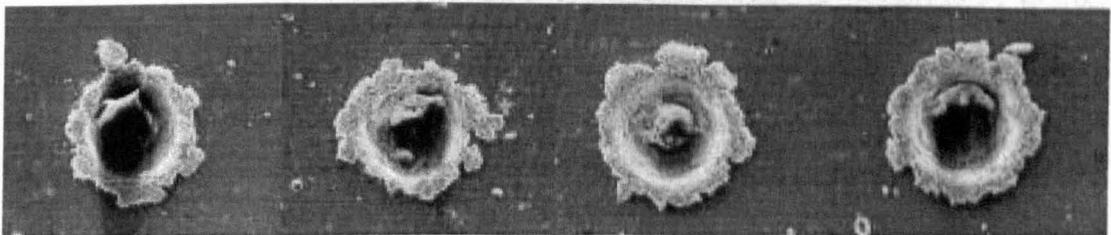


15Al-20

15Al-3

15Al-4

15Al-5



15Al-6

15Al-7

15Al-8

15Al-9

Summary statistics and normal probability plots used for sorting raw data

Title	Shot 1 (test shot)
Projectile	50 μm glass beads
Target	Glass plate and Al plate
Angle	60°
Pressure	0.22 mb
Velocity	~5 km s ⁻¹ (poor target PZT signal)

Table C.1 – Summary statistics for shot 1 aluminium data

	Dc (μm)			Circularity B/A	Depth P (μm)		P/Dc
	A	B	$\sqrt{(AB)}$		SEM	Optical	
Mean	115.6	97.7	106.1	0.848	35.1	39.2	0.335
SE	10.7	9.7	10.2	0.026	4.2	1.2	0.027
Median	138.7	120.7	130.7	0.861	38.6	40.0	0.289
SD	53.6	48.4	50.8	0.129	20.7	4.8	0.134
Range	151.0	127.3	138.2	0.591	102.7	19.1	0.597
Min	13.1	13.7	13.5	0.478	5.5	29.6	0.192
Max	164.1	141.0	151.7	1.069	108.2	48.7	0.789
Count	25	25	25	25	24	16	24
90% >	14.2	14.1	14.0	0.585	8.3	32.2	0.234
90% <	163.1	139.9	147.6	0.995	48.0	44.8	0.606

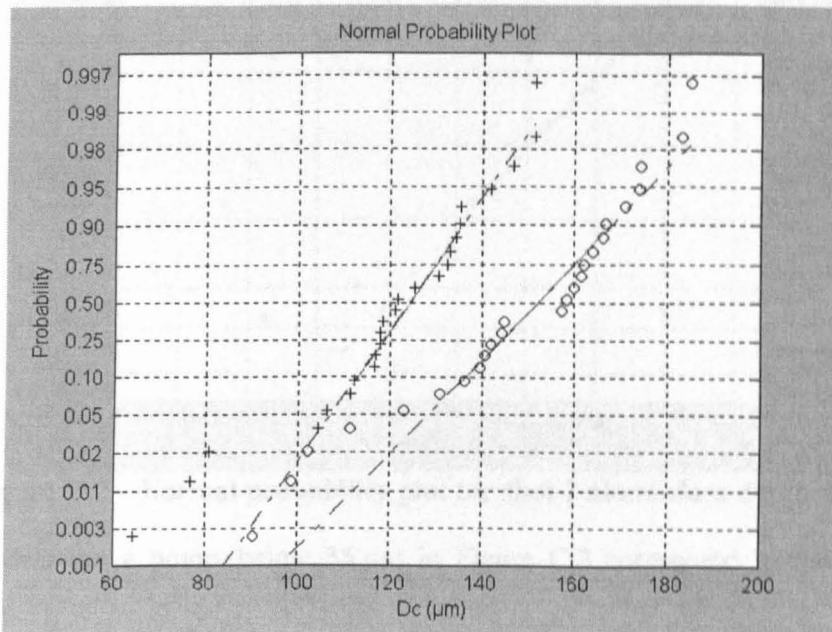
Table C.2 – Summary statistics for shot 1 glass data

	Conchoid (μm)				P (μm)		C _{off}
	A	B	$\sqrt{(AB)}$	B/A	SEM	Optical	
Mean	329	304	315	0.95	18	24	0.83
SE	28	24	24	0.06	2	2	0.03
Median	303	280	290	0.82	18	25	0.86
SD	108	93	94	0.24	10	7	0.12
Range	467	375	390	0.65	30	28	0.36
Max	676	601	637	1.41	31	35	1.01
Min	209	226	248	0.75	1	7	0.64
Count	15	15	15	15	15	12	13
90% >	246	235	252	0.75	1	13	0.65
90% <	493	448	443	1.38	30	32	0.99

Title	Shot 2
Projectile	50 μm glass beads
Target	Glass plate, Al plate & ECS solar cell
Angle	60°
Pressure	0.23 mb
Velocity	4.91 \pm 0.10 km s ⁻¹

Table C.3 – Summary statistics for shot 2 aluminium data

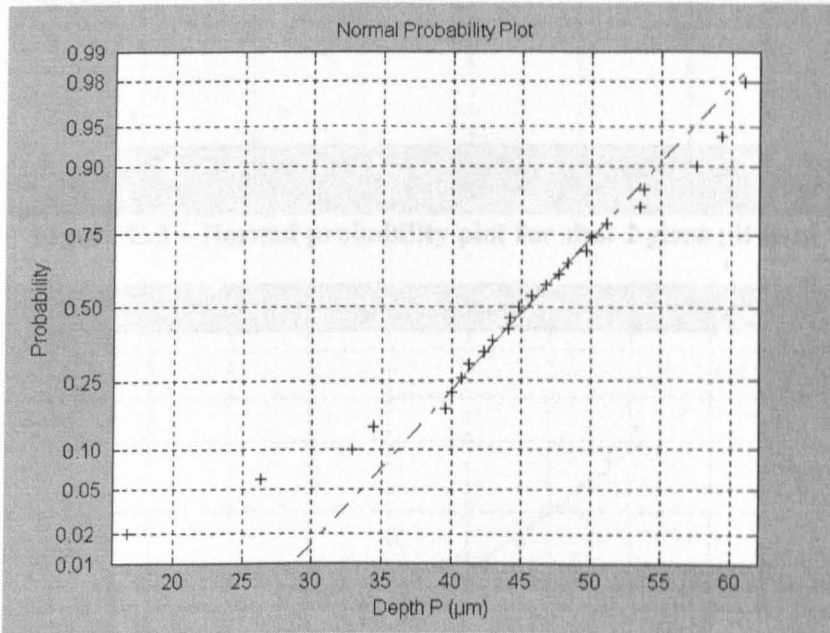
	Dc (μm)			Circularity B/A	Depth P (μm)		P/Dc
	A	B	$\sqrt{(AB)}$		SEM	Optical	
Mean	147.5	120.2	133.0	0.816	44.6	30.1	0.333
SE	5.2	4.4	4.7	0.015	2.0	2.9	0.008
Median	157.1	121.2	137.3	0.811	44.8	33.1	0.334
SD	26.2	21.8	23.3	0.073	9.9	11.7	0.038
Range	94.4	87	91.0	0.342	44.1	36.5	0.160
Min	90.5	64.4	76.3	0.712	16.7	10.4	0.219
Max	184.9	151.4	167.3	1.054	60.9	47.0	0.379
Count	25	25	25	25	25	16	25
90% >	9.45	7.85	8.37	0.127	3.58	2.15	0.014
90% <	172.54	140.56	152.36	1.034	53.73	43.94	0.375

**Figure C.1 – Normal probability plot for shot 2 aluminium data**

It can be seen in Figure C.1 that, as with the test shot (section 6), there appears to be an inclusion of smaller impactors. Consequently, the author decided to exclude the data below the 5% probability level, which corresponds to below around 120 μm for the major axis and 100 μm for the minor axis. This gives a new characteristic set of statistics for the shot in Table C.4. The reduced data set has generally closer means and medians and so is more symmetric. The author considered retaining *all* the circularity data, based on the assumption that circularity (the ratio B/A) would be insensitive to small fluctuations in overall crater size. However, if it is assumed that the smaller impacts are due to ejecta then this material may be impacting the target at angles very different from the intended 60° and so was excluded.

Table C.4 – Revised shot 2 aluminium data

	D _c (μm)				P (μm) SEM	P/D _c
	A	B	√(AB)	B/A		
Mean	156	127	141	0.82	47.8	0.34
SE	4	3	3	0.02	1.4	0.01
Median	160	125	140	0.82	46.8	0.34
SD	17	13	14	0.07	6.3	0.03
Count	21	21	21	21	21	21


Figure C.2 – Normal probability plot for shot 2 aluminium depth data

For the depth data the 4 points below 35 μm in Figure C.2 correspond to the craters already excluded.

Table C.5 – Summary statistics for shot 2 glass data

	Pit				Shatter				Conchoid				P	C _{off}
	A	B	√AB	B/A	A	B	√AB	B/A	A	B	√AB	B/A		
Mean	52	33	41	0.660	108	84	95	0.784	285	298	290	1.061	29	0.963
SE	3	2	2	0.043	2	6	3	0.073	7	10	6	0.041	1	0.016
Median	54	34	40	0.625	107	80	94	0.733	291	293	291	1.063	29	0.948
SD	11	8	7	0.185	5	13	6	0.146	41	54	35	0.234	6	0.081
Range	42	30	26	0.767	10	29	14	0.311	166	242	136	1.094	24	0.371
Max	75	49	56	1.043	114	103	103	0.990	371	425	353	1.749	42	1.112
Min	33	19	30	0.275	104	74	90	0.679	205	183	217	0.655	17	0.741
Count	19	19	19	19	4	4	4	4	32	32	32	32	32	26
90% >	37	22	31	0.453	104	75	90	0.680	225	226	235	0.762	19	0.879
90% <	70	44	50	0.922	113	100	102	0.959	354	408	340	1.409	37	1.109

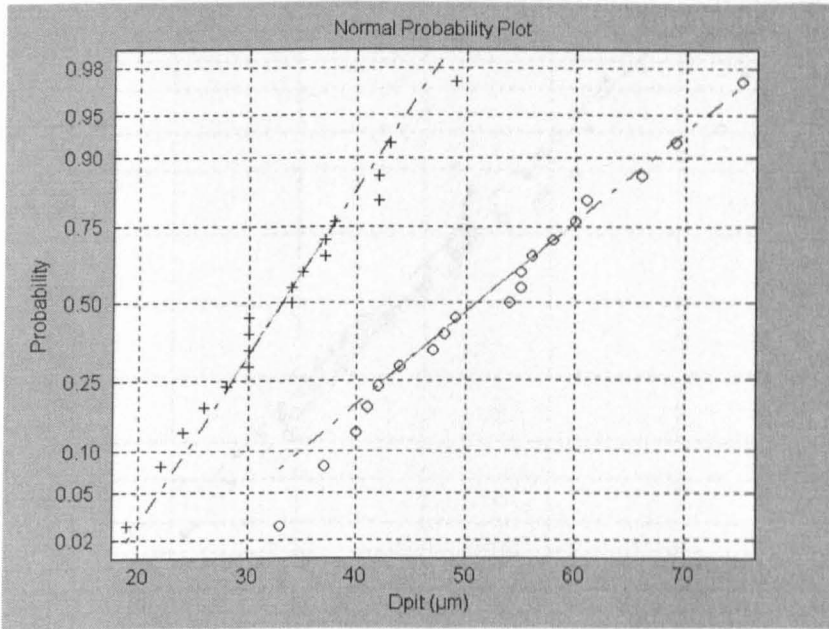


Figure C.3 – Normal probability plot for shot 2 glass pit data

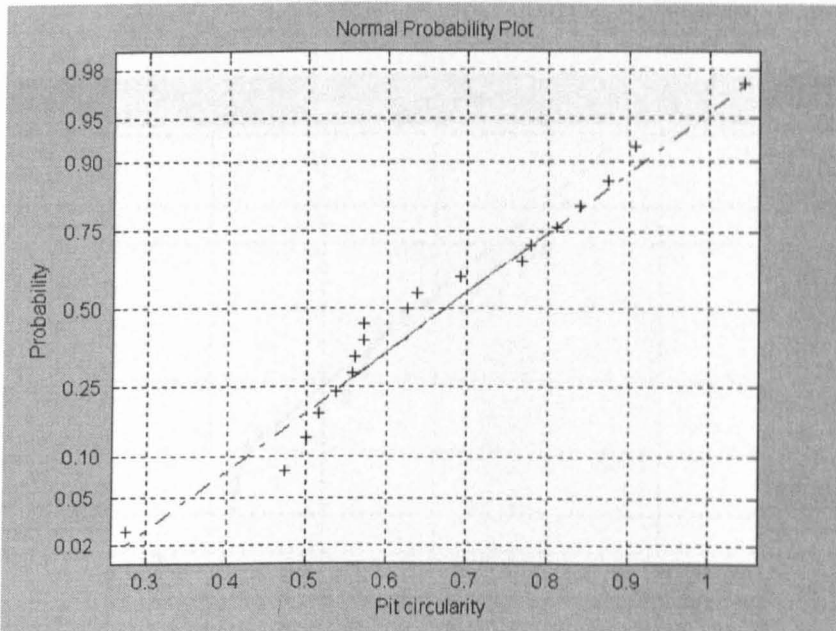


Figure C.4 – Normal probability plot for shot 2 glass pit circularity

Figure C.3 indicates that the pit major and minor axes are normally distributed to a good approximation, suggesting that the impactors were from a common population. In Figure C.4 the circularity of the pit also appears to be approximately normally distributed.

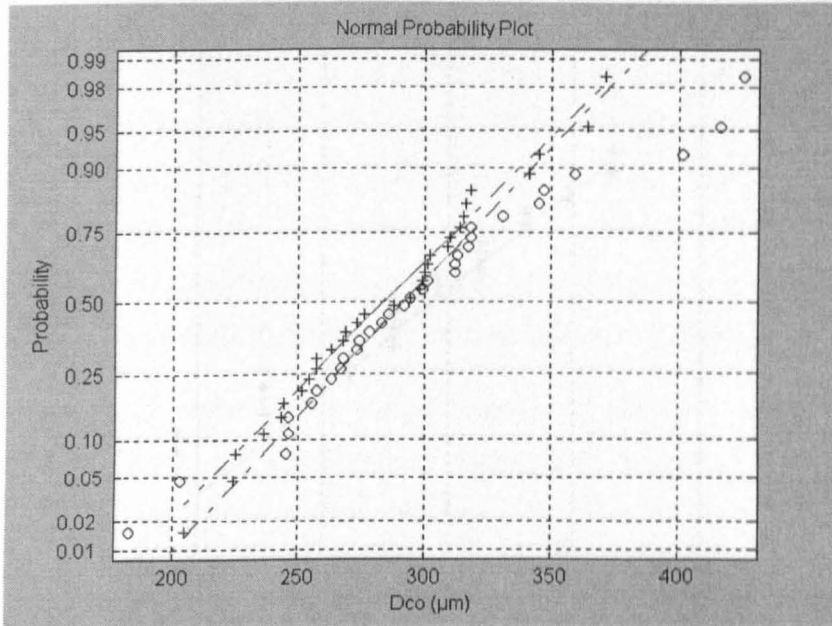


Figure C.5 – Normal probability plot for shot 2 glass conchoidal diameter

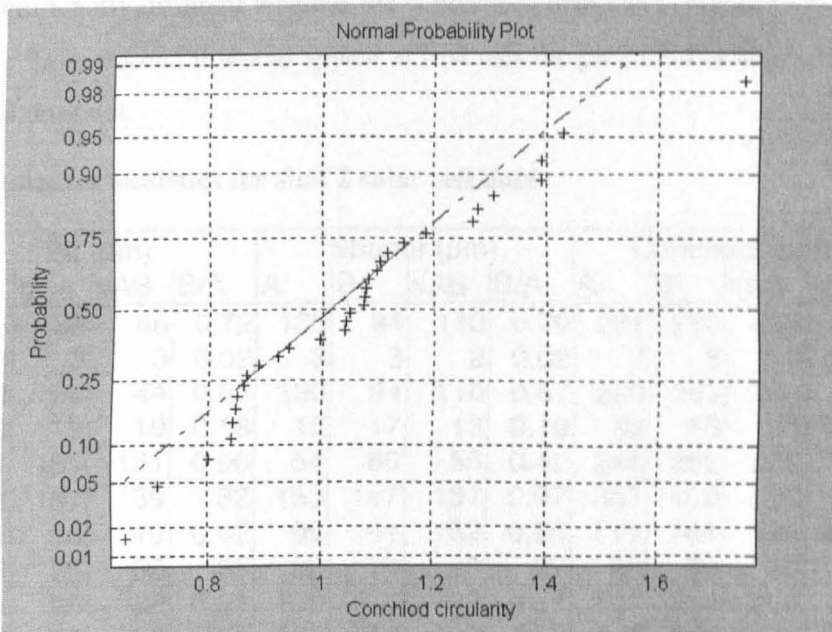


Figure C.6 – Normal probability plot for shot 2 glass conchoidal circularity

Figure C.5 suggests that the conchoidal diameters are generally normally distributed, but there appears to be 3 outliers above $D_{co} = 400 \mu\text{m}$. It is not clear whether these could have arisen due to an inclusion of some unwanted large or irregular impactors in the buckshot or whether it is a reflection of the inherent variability of the crater shape. Since the other parameters do not show a large deviation from normality it was decided to include all the data in later analyses at the expense of some uncertainty (increased σ). Since the mean and median of the conchoidal data are close (Table C.5) this should not significantly effect analyses based on the assumption of normality or symmetry around the mean/median.

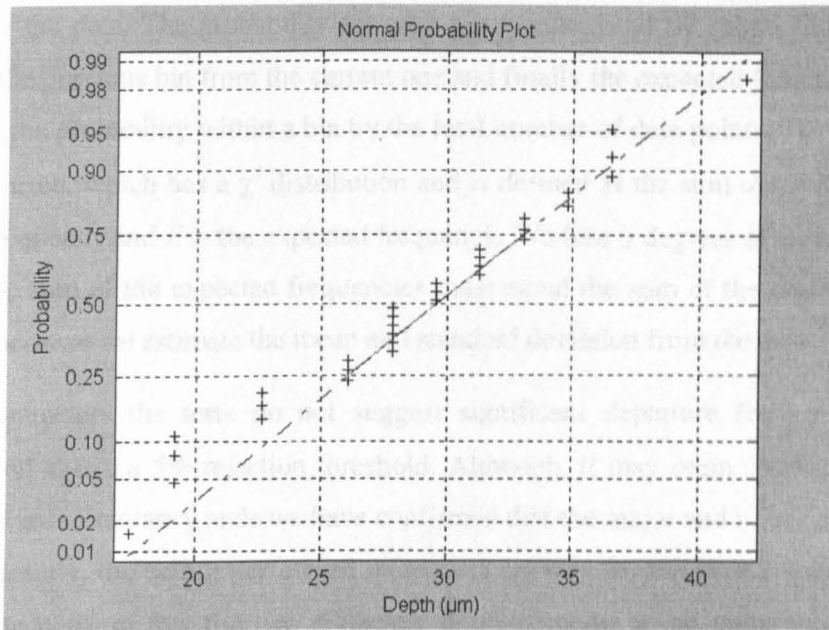


Figure C.7 – Normal probability plot for shot 2 glass depth data

A first observation from the shot 2 glass data is that the 2 perpendicular pit diameters (Figure C.3) appear to be significantly different whereas the conchoidal diameters (Figure C.5) do not. Thus for an impact at 60° from normal it would appear at first that the pit becomes asymmetric whereas the conchoidal zone does not.

Table C.6 – Summary statistics for shot 2 solar cell data

	Pit (μm)				Shatter (μm)				Conchoid (μm)				P	C_{off}
	A	B	\sqrt{AB}	B/A	A	B	\sqrt{AB}	B/A	A	B	\sqrt{AB}	B/A		
Mean	55	39	46	0.72	130	94	110	0.70	281	290	284	1.05	25	0.89
SE	3	3	3	0.02	3	3	2	0.02	7	8	6	0.03	1	0.02
Median	53	36	44	0.67	130	94	110	0.67	290	292	287	0.99	24	0.89
SD	20	19	19	0.18	15	17	13	0.10	52	58	47	0.23	9	0.14
Range	151	151	151	0.90	54	86	55	0.42	246	262	238	1.10	61	0.72
Max	172	167	169	1.32	153	147	137	0.97	357	406	365	1.84	70	1.24
Min	21	16	19	0.42	99	61	82	0.55	111	144	126	0.74	9	0.52
Count	55	55	55	55	29	29	29	27	60	60	60	60	61	58
90% >	34	25	32	0.51	109	70	89	0.57	191	214	208	0.77	12	0.66
90% <	73	48	58	1.03	151	116	130	0.87	347	388	351	1.42	37	1.12

For the shot 2 the solar cell received many impacts and the author recorded enough of them (60) so that we can perform a quantitative assessment of the normality of the distribution of impact feature parameters. Figure C.8 and Figure C.9 show the binned *differential* distributions of the pit and conchoidal perpendicular diameters respectively for the shot 2 solar cell data. The dotted line shows the normal distribution function with the same mean and standard deviation as the data.

Although the histograms have equal-width bins the data is binned in unequal-width bins for the χ^2 tests (Table C.7 - Table C.12) such that there are never less than 5 counts in each bin. This value of 5 is a long established (circa. 1930s) rule-of-thumb for significance testing of frequency distributions to be meaningful (Cooper, 1969). For the χ^2 tests the cumulative normal probability is looked up at each bin upper limit from the normal distribution with mean and standard deviation

equal to that of the data. The probability for each bin is calculated by subtracting the cumulative probability of the previous bin from the current one and finally the expected frequency is calculated by multiplying the probability within a bin by the total number of data points. The usual *Pearson's* statistic (χ^2) is used, which has a χ^2 distribution and is defined as the sum of $(O-E)^2/E$, where O is the observed frequency and E is the expected frequency. We lose 3 degrees of freedom in this case: one because the sum of the expected frequencies must equal the sum of the observed frequencies and two more because we estimate the mean and standard deviation from the data.

For all the parameters the tests do not suggest significant departure from normality: all χ^2 probabilities well above a 5% rejection threshold. Although, it may seem unnecessary to test the geometric mean and circularity once we have confirmed that the major and minor axis are normally distributed separately, the author performed these tests anyway for the shot 2 solar cell data. This was done just to confirm that the two diameters don't combine in an unexpected way so as to produce non-normal distributions; the major and minor diameters from corresponding craters to not always have the same *rank* in the data. As with the glass data it appears that the pits are asymmetric ($\bar{A} > \bar{B}$) and that the conchoidal zone is not. In summary, as the data appears to be normally distributed there are no apparent grounds for rejecting any of it. If there were any impactors in the buckshot that do not correspond to our intended 50 μm projectiles there is no obvious way of telling by inspection of this distribution of impact features.

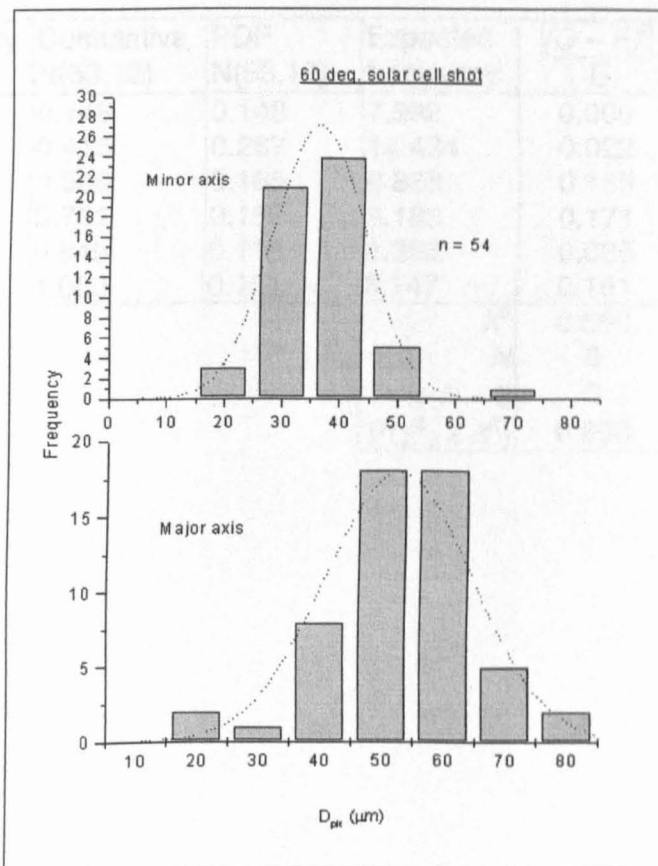


Figure C.8 – Differential distribution of shot 2 solar cell pit diameters

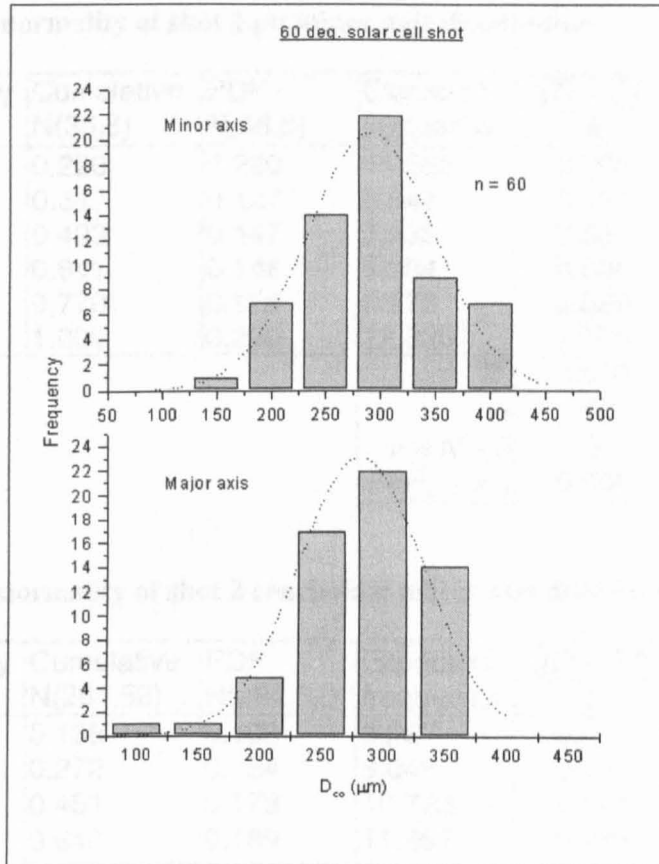


Figure C.9 – Differential distribution of shot 2 solar cell conchoidal diameters

Table C.7 – Test for normality of shot 2 pit major axis distribution

Bin	Frequency	Cumulative N(53,12)	PDF N(53,12)	Expected frequency	$\frac{(O - E)^2}{E}$
< 40	8	0.148	0.148	7.992	0.000
< 50	15	0.415	0.267	14.434	0.022
< 55	10	0.580	0.165	8.888	0.139
< 60	7	0.731	0.152	8.183	0.171
< 65	7	0.849	0.118	6.355	0.065
more	7	1.000	0.151	8.147	0.161
				χ^2	0.559
				N	6
				$\nu = N - 3$	3
				$P(\chi^2_{\nu} \geq \chi^2)$	0.906

Table C.8 – Test for normality of shot 2 pit minor axis distribution

Bin	Frequency	Cumulative N(36,8)	PDF N(36,8)	Expected frequency	$\frac{(O - E)^2}{E}$	
< 30	11	0.220	0.220	11.866	0.063	
< 33	8	0.347	0.127	6.847	0.194	
< 36	10	0.493	0.147	7.935	0.537	
< 39	8	0.641	0.148	7.984	0.000	
< 42	9	0.770	0.129	6.973	0.589	
more	8	1.000	0.230	12.395	1.558	
					χ^2	0.559
					N	6
					$\nu = N - 3$	3
					$P(\chi^2_{\nu} \geq \chi^2)$	0.906

Table C.9 – Test for normality of shot 2 conchoidal major axis distribution

Bin	Frequency	Cumulative N(281,52)	PDF N(281,52)	Expected frequency	$\frac{(O - E)^2}{E}$	
< 225	7	0.138	0.138	8.287	0.200	
< 250	9	0.272	0.134	8.048	0.113	
< 275	8	0.451	0.179	10.723	0.691	
< 300	13	0.640	0.189	11.367	0.235	
< 325	9	0.800	0.160	9.588	0.036	
more	14	1.000	0.200	11.988	0.338	
					χ^2	1.612
					N	6
					$\nu = N - 3$	3
					$P(\chi^2_{\nu} \geq \chi^2)$	0.657

Table C.10 – Test for normality of shot 2 conchoidal minor axis distribution

Bin	Frequency	Cumulative N(290,59)	PDF N(290,59)	Expected frequency	$\frac{(O - E)^2}{E}$	
< 225	8	0.130	0.130	7.821	0.004	
< 250	8	0.244	0.113	6.790	0.215	
< 275	6	0.395	0.152	9.112	1.063	
< 300	12	0.565	0.170	10.195	0.320	
< 325	10	0.724	0.158	9.509	0.025	
more	16	1.000	0.276	16.572	0.020	
					χ^2	1.647
					N	6
					$\nu = N - 3$	3
					$P(\chi^2_{\nu} \geq \chi^2)$	0.649

Table C.11 – Test for normality of shot 2 conchoidal geometric mean axis distribution

Bin	Frequency	Cumulative N(284,47)	PDF N(284,47)	Expected frequency	$\frac{(O-E)^2}{E}$
< 225	7	0.104	0.104	6.245	0.091
< 250	5	0.233	0.129	7.732	0.965
< 275	13	0.421	0.188	11.274	0.264
< 300	11	0.629	0.208	12.501	0.180
< 325	12	0.805	0.176	10.541	0.202
more	12	1.000	0.195	11.708	0.007
χ^2					1.710
N					6
$\nu = N - 3$					3
$P(\chi^2_{\nu} \geq \chi^2)$					0.635

Table C.12 – Test for normality of shot 2 conchoidal circularity distribution

Bin	Frequency	Cumulative N(1.05,0.23)	PDF N(1.05,0.23)	Expected frequency	$\frac{(O-E)^2}{E}$
< 0.8	8	0.139	0.139	8.345	0.014
< 0.95	15	0.328	0.189	11.351	1.173
< 1.05	13	0.493	0.164	9.868	0.994
< 1.15	6	0.658	0.166	9.944	1.564
< 1.3	9	0.853	0.194	11.653	0.604
more	9	1.000	0.147	8.839	0.003
χ^2					4.352
N					6
$\nu = N - 3$					3
$P(\chi^2_{\nu} \geq \chi^2)$					0.226

Title	Shot 3
Projectile	50 μm glass beads
Target	Glass plate & ECS solar cell
Angle	70°
Pressure	0.07 mb
Velocity	5.29 \pm 0.05 km s ⁻¹

Table C.13 – Summary statistics for shot 3 glass data

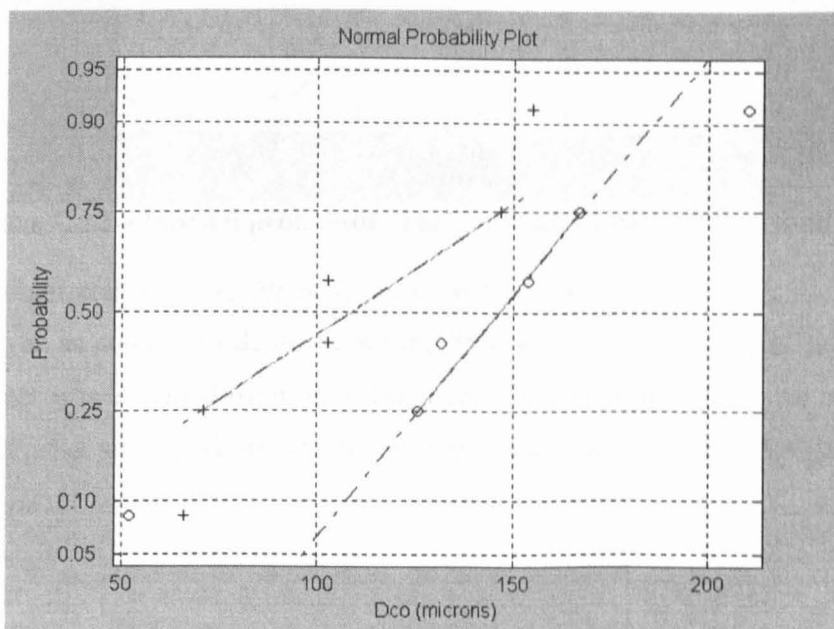
	Conchoid (μm)				P (μm)	C _{off}
	A	B	\sqrt{AB}	B/A		
Mean	140	108	122	0.832	10.4	0.939
SE	21	15	17	0.126	1.7	0.040
Median	143	103	124	0.740	8.7	0.957
SD	53	37	42	0.309	4.3	0.081
Range	158	89	115	0.842	10.4	0.176
Max	210	155	176	1.365	19.1	1.010
Min	52	66	61	0.524	8.7	0.833
Count	6	6	6	6	6	4
90% >	71	67	68	0.547	8.7	0.846
90% <	199	153	170	1.276	16.5	1.007

Table C.14 – Summary statistics for shot 3 solar cell data

	Pit (μm)				Conchoid (μm)				P (μm)	C _{off}
	A	B	\sqrt{AB}	B/A	A	B	\sqrt{AB}	B/A		
Mean	46	27	35	0.583	198	170	183	0.863	20.06	0.858
SE	2	2	1	0.035	6	6	5	0.029	5.74	0.029
Median	47	27	35	0.562	200	166	181	0.848	13.92	0.848
SD	9	7	6	0.147	25	27	23	0.128	25.04	0.128
Range	30	23	23	0.564	112	122	98	0.513	116.58	0.456
Max	64	40	47	0.861	263	240	251	1.080	121.80	1.088
Min	34	17	24	0.297	151	118	153	0.567	5.22	0.632
Count	18	18	18	18	19	19	19	19	19	19
90% >	36	18	26	0.404	161	139	156	0.714	8.35	0.652
90% <	57	37	43	0.844	230	210	220	1.032	32.54	1.031

Table C.15 – Summary statistics for shot 3 aluminium PZT plate data

	D _c (μm)				P (μm)	
	A	B	\sqrt{AB}	B/A	SEM	Optical
Mean	138	130	134	0.946	65.48	80.44
SE	6	7	6	0.018	7.10	1.92
Median	139	128	133	0.940	66.19	81.78
SD	29	30	29	0.082	17.40	6.93
Range	135	124	129	0.337	48.61	26.10
Max	208	193	200	1.153	91.30	95.70
Min	73	69	71	0.816	42.69	69.60
Count	21	21	21	21	6	13
90% >	101	88	95	0.854	44.73	70.64
90% <	171	184	173	1.136	87.39	90.48

**Figure C.10 – Normal probability plot for shot 3 glass conchoid data**

There were no clearly identifiable pits observed for the shot 3 glass impacts. There is barely enough data to draw even a tentative assessment of the normality of the distribution, but since the mean and median conchoidal diameter values are “close” (at least to well within the standard error of the means) the data is at least symmetric to some extent.

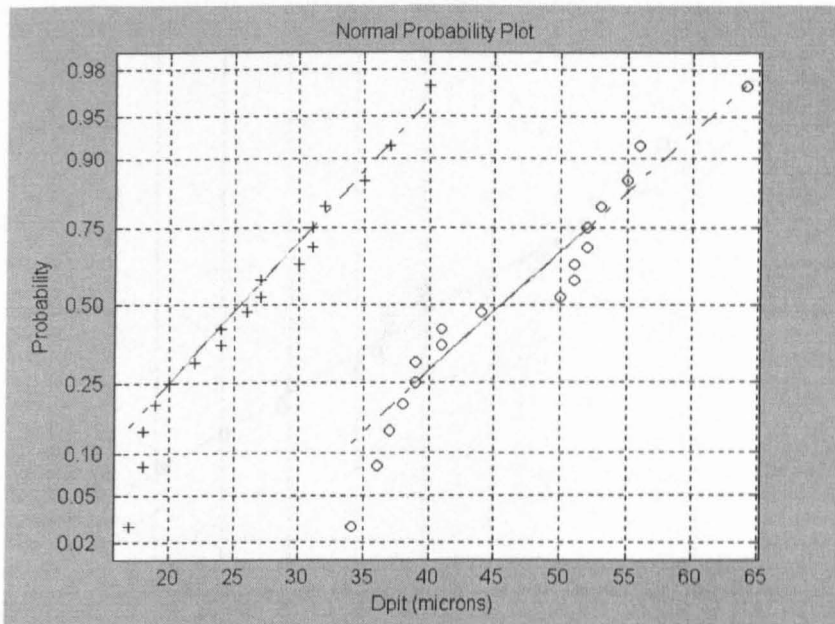


Figure C.11 – Normal probability plot for shot 3 solar cell pit data

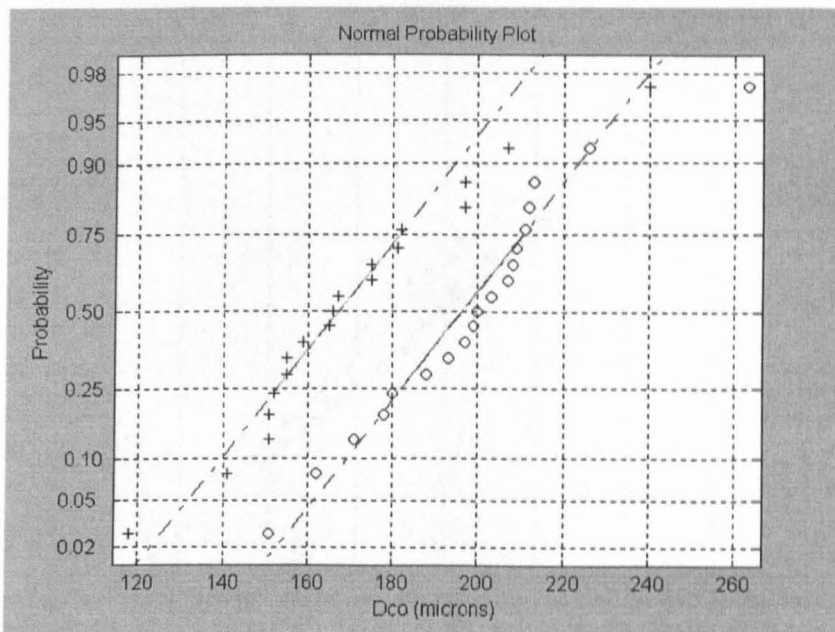


Figure C.12 – Normal probability plot for shot 3 solar cell conchoid data

For the shot 3 solar cell impacts, although the pit data (Figure C.11) shows no obvious outliers, there appears to be an anomalous datum above the 95% level in the conchoidal data (Figure C.12). This largest crater was excluded from the subsequent analyses, although the pit of this crater was smaller than the mean pit size. However, the pit size is not expected to be strongly correlated with the impactor size.

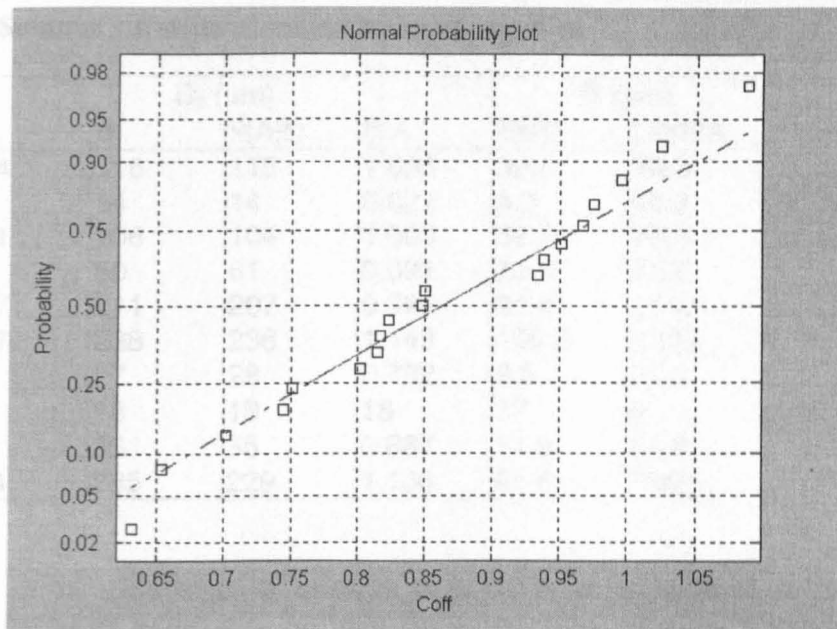


Figure C.13 – Normal probability plot for shot 3 solar cell centroid offset data

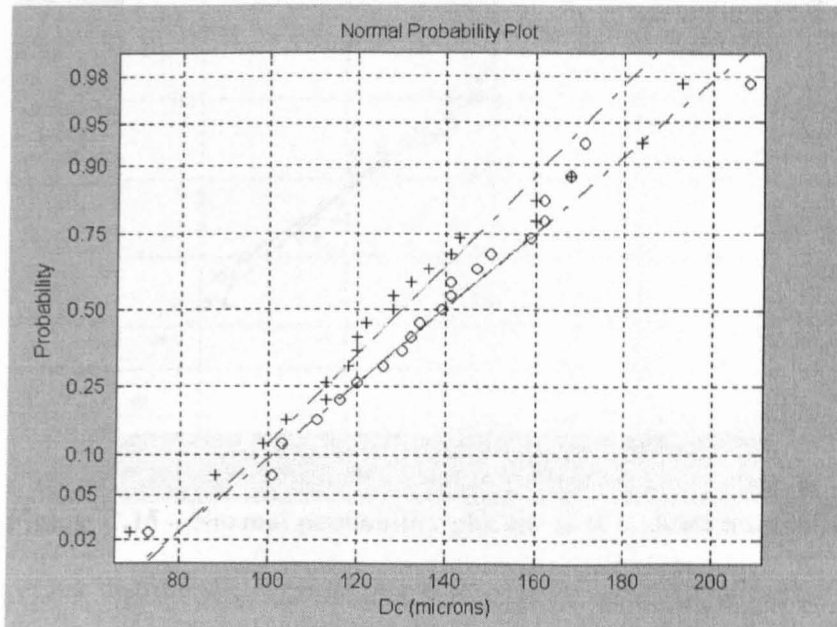


Figure C.14 – Normal probability plot for shot 3 PZT plate craters

The centroid offset and PZT crater normal probability plots (Figure C.13 and Figure C.14) do not strongly suggest that any further pruning of the data is required.

Title	Shot 4
Projectile	50 μm glass beads
Target	Al plate & ECS solar cell
Angle	0°
Pressure	0.2 mb
Velocity	5.33 \pm 0.05 km s ⁻¹

Table C.16 – Summary statistics for shot 4 aluminium data

	D _c (µm)				P (µm)	
	A	B	√(AB)	B/A	SEM	Optical
Mean	114	116	115	1.035	36.0	78.3
SE	15	14	14	0.021	4.9	15.3
Median	101	106	104	1.063	36.2	78.3
SD	64	60	61	0.091	20.3	45.8
Range	207	211	207	0.361	91.0	116.6
Max	237	238	236	1.143	100.5	137.5
Min	30	27	28	0.782	9.5	20.9
Count	18	18	18	18	17	9
90% >	33	36	35	0.887	11.0	21.6
90% <	234	235	229	1.134	61.6	130.5

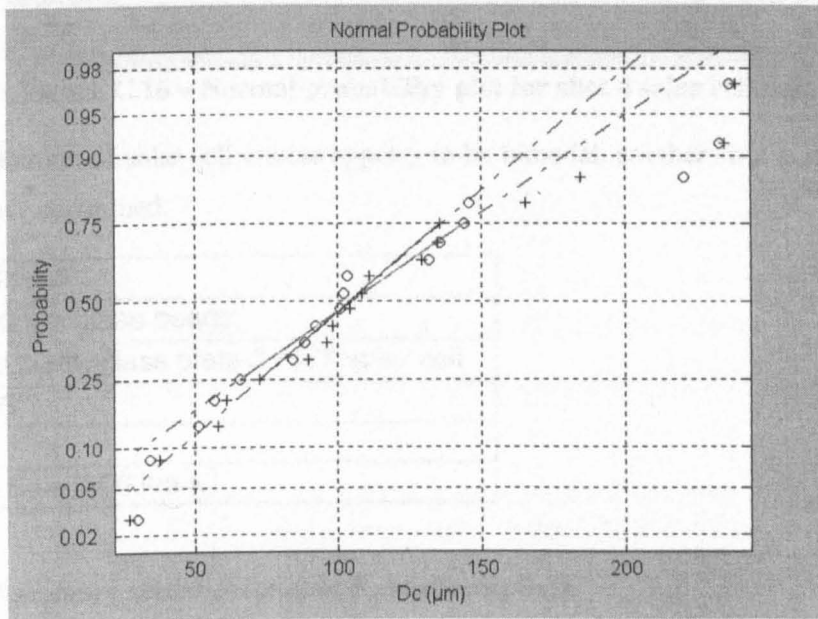
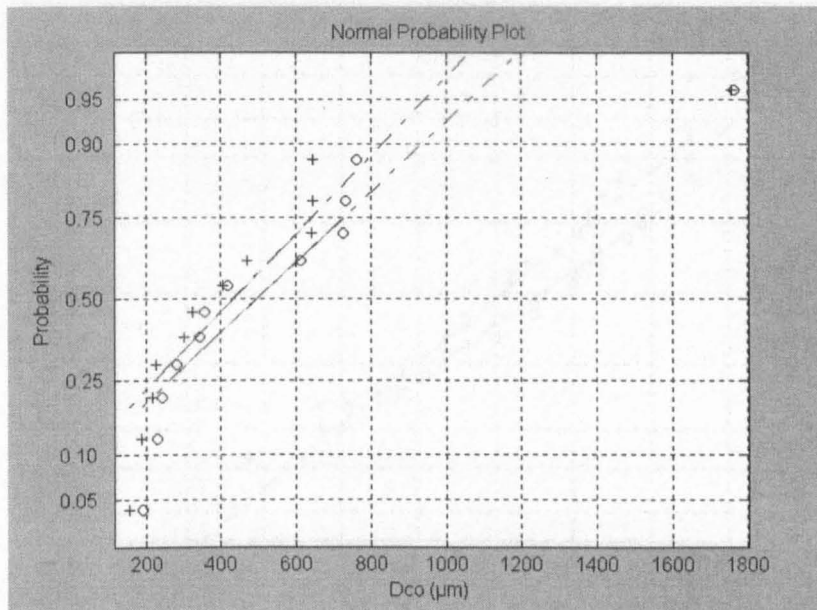


Figure C.15 – Normal probability plot for shot 4 aluminium data

The aluminium crater distribution suggests that there was an inclusion of impactors significantly larger than the main population of smaller projectiles.

Table C.17 – Summary statistics for shot 4 solar cell data

	Pit (µm)				Shatter (µm)				Conchoid (µm)				P (µm)	
	A	B	√AB	B/A	A	B	√AB	B/A	A	B	√AB	B/A	SEM	Opt.
Mean	66	60	63	0.934	183	161	171	0.841	555	498	525	0.875	21.5	8.7
SE	25	23	24	0.040	82	80	81	0.051	125	126	126	0.026	6.7	2.4
Median	52	52	52	1.000	91	68	79	0.841	388	365	376	0.887	15.8	7.0
SD	65	60	62	0.107	247	239	243	0.154	434	436	435	0.091	19.0	4.7
Range	178	169	173	0.278	784	753	768	0.509	1571	1600	1570	0.316	49.1	10.4
Max	185	176	180	1.000	825	786	805	1.091	1762	1756	1759	0.997	52.6	15.7
Min	7	7	7	0.722	41	33	37	0.582	191	157	189	0.681	3.5	5.2
Count	7	7	7	7	9	9	9	9	12	12	12	12	8	4
90% >	7	7	7	0.763	41	38	39	0.629	213	174	190	0.730	4.3	5.5
90% <	162	151	156	1.000	575	549	562	1.039	1212	1146	1176	0.987	50.9	14.4


Figure C.16 – Normal probability plot for shot 4 solar cell data

Since the distribution of solar cell craters appears to be bimodal, another shot at normal incidence (shot 8) was later performed.

Title	Shot 5
Projectile	50 µm glass beads
Target	Al plate, glass plate & HST solar cell
Angle	45°
Pressure	?
Velocity	5.54 ± 0.06 km s ⁻¹

Table C.18 – Summary statistics for shot 5 aluminium data

	D _c (µm)				P (µm)	
	A	B	√(AB)	B/A	SEM	Optical
Mean	155	148	152	0.96	46	45
SE	4	4	3	0.01	2	3
Median	160	151	154	0.94	47	47
SD	18	18	17	0.06	10	13
Range	65	72	69	0.17	46	57
Max	181	175	178	1.05	71	68
Min	116	103	109	0.88	25	10
Count	25	25	25	25	24	25
90% >	128	119	124	0.89	35	21
90% <	178	173	172	1.05	61	63

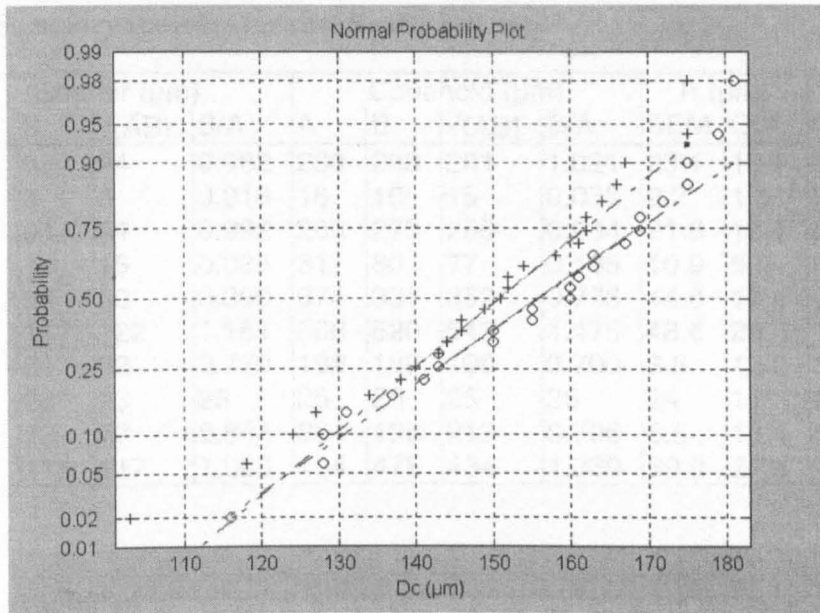


Figure C.17 – Normal probability plot for shot 5 aluminium D_c

Table C.19 – Summary statistics for shot 5 glass data

	Shatter (μm)				Conchoid (μm)				P (μm)		C_{off}
	A	B	$\sqrt{(AB)}$	B/A	A	B	$\sqrt{(AB)}$	B/A	SEM	Opt.	
Mean	89	85	87	0.97	276	282	278	1.03	18.0	28.7	1.03
SE	4	4	4	0.03	12	13	11	0.04	2.1	1.5	0.03
Median	93	87	92	0.96	258	297	284	1.01	18.1	27.8	1.06
SD	21	17	19	0.12	58	61	53	0.17	9.9	5.8	0.16
Range	84	59	69	0.63	201	253	209	0.65	37.9	19.1	0.57
Max	123	111	114	1.33	376	430	385	1.38	39.2	36.5	1.32
Min	39	52	45	0.71	175	177	176	0.73	1.4	17.4	0.75
Count	23	23	23	23	24	24	24	24	23	15	22
90% >	53	57	55	0.81	192	195	194	0.81	4.7	19.8	0.77
90% <	118	109	109	1.09	374	348	352	1.30	33.3	36.5	1.30

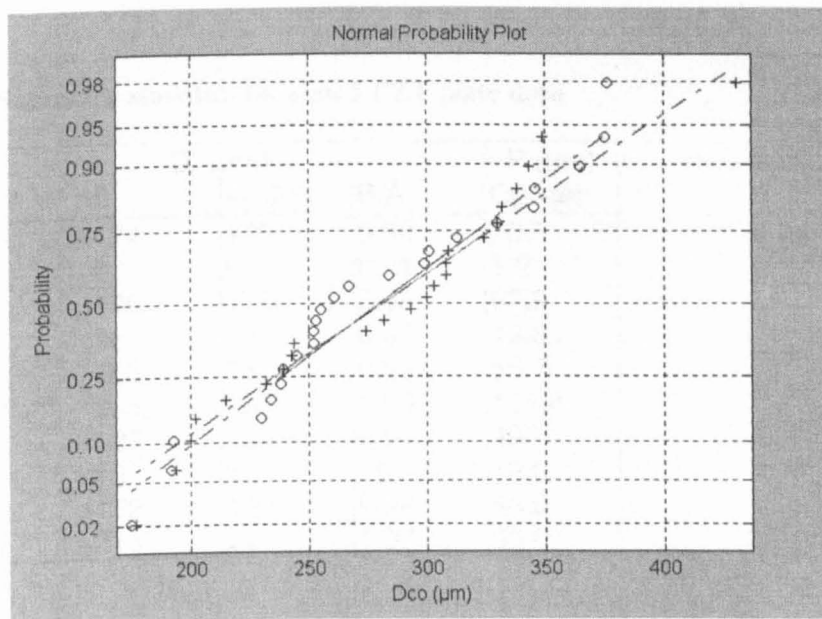


Figure C.18 – Normal probability plot for shot 5 glass D_{co}

Table C.20 – Summary statistics for shot 5 solar cell data

	Shatter (μm)				Conchoid (μm)				P (μm)		C_{off}
	A	B	$\sqrt{(AB)}$	B/A	A	B	$\sqrt{(AB)}$	B/A	SEM	Opt.	
Mean	95	93	94	0.982	280	283	281	1.021	23.1	19.9	0.986
SE	3	3	3	0.018	16	16	15	0.033	2.2	1.5	0.034
Median	95	94	94	0.992	266	273	265	0.984	21.8	19.1	0.993
SD	17	14	15	0.085	81	80	77	0.165	10.9	5.0	0.172
Range	66	56	60	0.390	374	331	352	0.776	44.8	17.4	0.664
Max	130	117	122	1.161	566	520	543	1.475	48.6	29.6	1.268
Min	64	61	62	0.770	192	189	190	0.700	3.8	12.2	0.604
Count	23	23	23	23	25	25	25	25	24	11	25
90% >	70	73	73	0.844	204	198	213	0.796	6.5	13.1	0.651
90% <	122	115	117	1.093	404	475	434	1.330	39.9	27.8	1.265

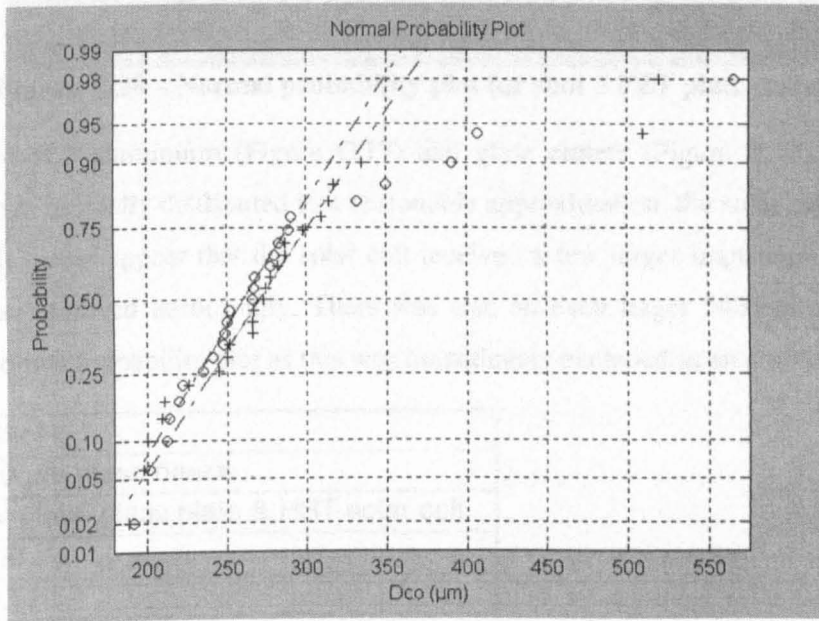


Figure C.19 – Normal probability plot for shot 5 solar cell D_{co}

Table C.21 – Summary statistics for shot 5 PZT plate data

	D_c (μm)				P (μm)
	A	B	$\sqrt{(AB)}$	B/A	Optical
Mean	176	174	175	0.99	70.5
SE	9	8	9	0.01	3.2
Median	176	179	178	0.99	67.9
SD	39	36	37	0.05	13.8
Range	165	158	159	0.22	55.7
Max	292	285	288	1.13	104.4
Min	127	127	130	0.91	48.7
Count	19	19	19	19	19.0
90% >	132	132	131	0.94	55.0
90% <	224	214	219	1.07	95.0

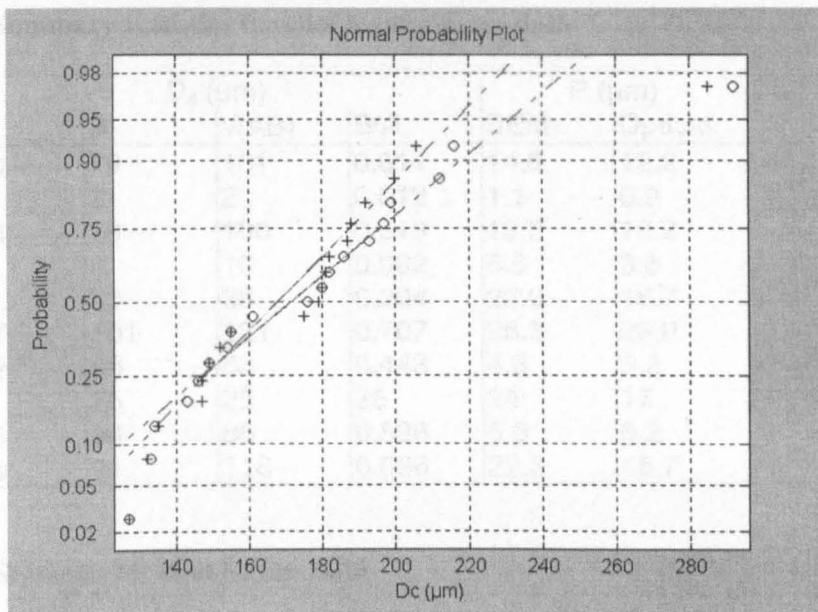


Figure C.20 – Normal probability plot for shot 5 PZT plate craters

Although the shot 5 aluminium (Figure C.17) and glass craters (Figure C.18) appear to have diameters that are normally distributed to a reasonable approximation, the solar cell craters (Figure C.19) do not. It would appear that the solar cell received a few larger impactors. The data above 350 µm D_{co} was removed accordingly. There was also an even larger 540 µm crater that is not shown in the normal probability plot as this was immediately excluded as an anomalous impactor.

Title	Shot 6
Projectile	50 µm glass beads
Target	Al plate, glass plate & HST solar cell
Angle	75°
Pressure	0.11
Velocity	5.35 ± 0.05 km s ⁻¹

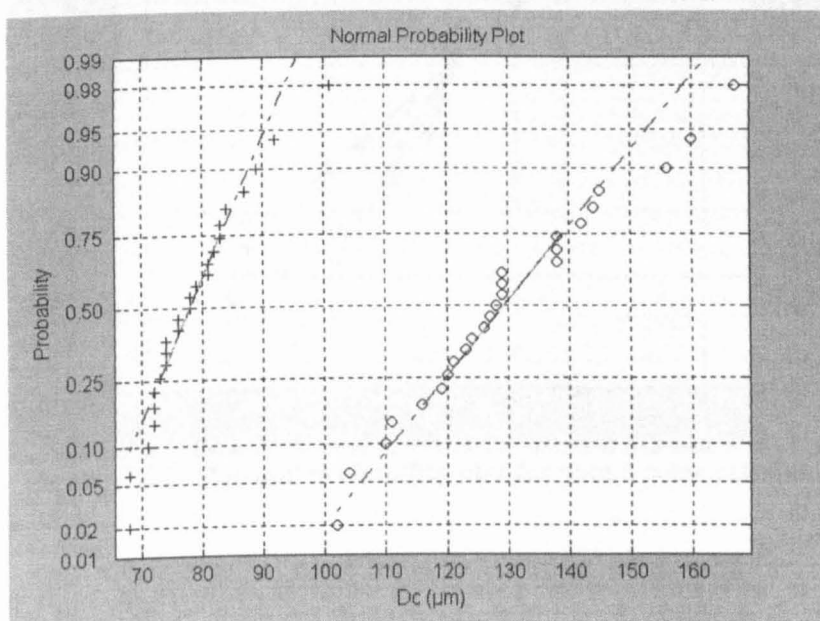


Figure C.21 – Normal probability plot for shot 6 aluminium data

Table C.22 – Summary statistics for shot 6 aluminium data

	D _c (µm)				P (µm)	
	A	B	√(AB)	B/A	SEM	Optical
Mean	130	79	101	0.611	14.0	12.2
SE	3	2	2	0.012	1.1	0.9
Median	128	78	100	0.613	13.3	12.2
SD	17	8	10	0.062	5.5	3.6
Range	65	33	38	0.264	22.0	15.7
Max	167	101	121	0.707	26.3	20.9
Min	102	68	83	0.443	4.3	5.2
Count	25	25	25	25	24	17
90% >	105	69	86	0.536	5.5	5.2
90% <	159	91	118	0.696	22.3	16.7

Table C.23 – Statistics for shot 6 glass data

	Shatter (µm)				Conchoid (µm)				P(µm)	C _{off}
	A	B	√(AB)	B/A	A	B	√(AB)	B/A		
Mean	32	33	32	1.01	98	112	105	1.16	8.6	1.07
SE	4	9	6	0.15	8	8	8	0.05	1.2	0.09
Median	32	33	32	1.01	88	116	101	1.14	9.3	1.10
SD	6	13	9	0.22	21	21	20	0.12	3.2	0.22
Range	8	18	13	0.31	52	50	45	0.36	7.9	0.66
Max	36	42	39	1.17	131	137	128	1.32	12.0	1.37
Min	28	24	26	0.86	79	87	83	0.95	4.2	0.70
Count	2	2	2	2	7	7	7	7	7	6
90% >	28	25	27	0.87	80	89	84	1.00	4.3	0.77
90% <	36	41	38	1.15	127	137	128	1.31	12.0	1.32

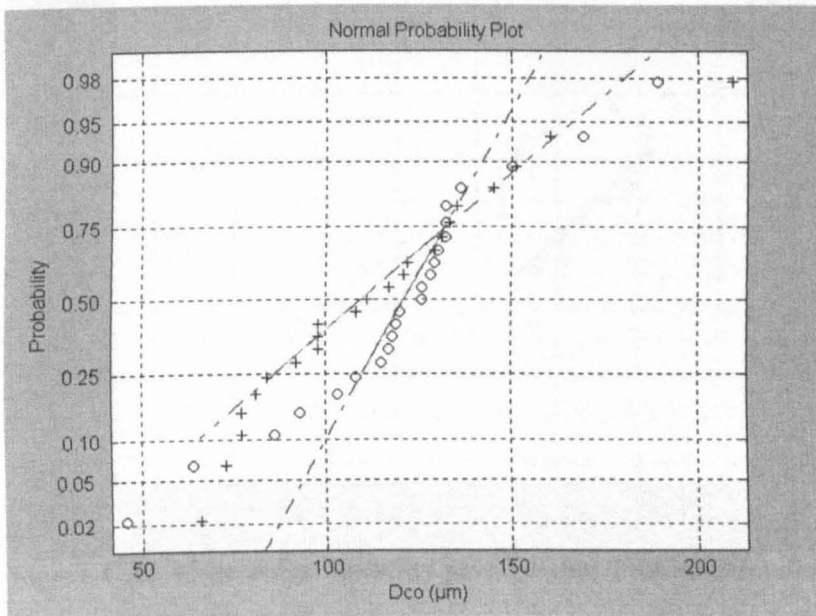


Figure C.22 – Normal probability plot for shot 6 solar cell data

Table C.24 – Summary statistics for shot 6 solar cell data

	Conchoid (μm)				P(μm)		C _{off}
	A	B	$\sqrt{(AB)}$	B/A	SEM	Optical	
Mean	137	132	134	0.97	13.3	19.0	1.06
SE	18	19	19	0.05	1.9	7.9	0.06
Median	126	114	119	0.95	12.1	11.3	1.13
SD	89	94	91	0.23	9.1	35.4	0.23
Range	484	480	478	1.17	39.1	163.6	0.83
Max	530	546	538	1.67	43.3	168.8	1.48
Min	46	66	60	0.50	4.1	5.2	0.65
Count	24	24	24	24	22	20	17
90% >	67	74	73	0.64	4.3	5.2	0.71
90% <	186	202	193	1.20	30.5	25.0	1.35

Although the aluminium crater diameters (Figure C.21) appear to be normally distributed the solar cell craters (Figure C.22) appear to have an unusual distribution of major axes. This is not surprising considering the unusual morphology of the craters at 75° incidence.

Title	Shot 7
Projectile	50 μm glass beads
Target	Al plate & HST solar cell
Angle	30°
Pressure	?
Velocity	4.75 \pm 0.05 km s ⁻¹

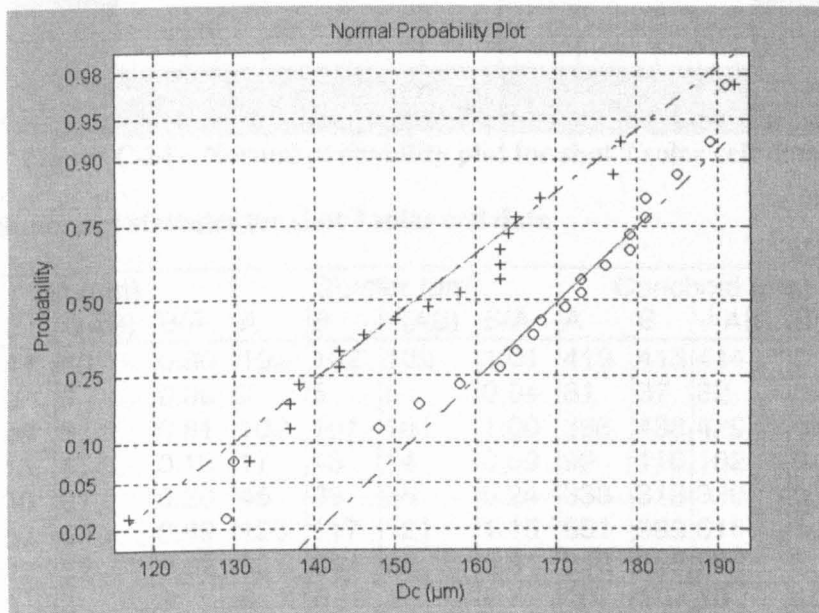


Figure C.23 – Normal probability plot for shot 7 aluminium data

Table C.25 – Statistics for shot 7 aluminium data

	D _c (µm)			
	A	B	√(AB)	B/A
Mean	168	154	161	0.92
SE	4	4	4	0.01
Median	172	156	164	0.91
SD	17	18	17	0.05
Range	62	75	66	0.20
Max	191	192	188	1.04
Min	129	117	123	0.84
Count	20	20	20	20
90% >	130	131	131	0.84
90% <	189	179	184	1.02

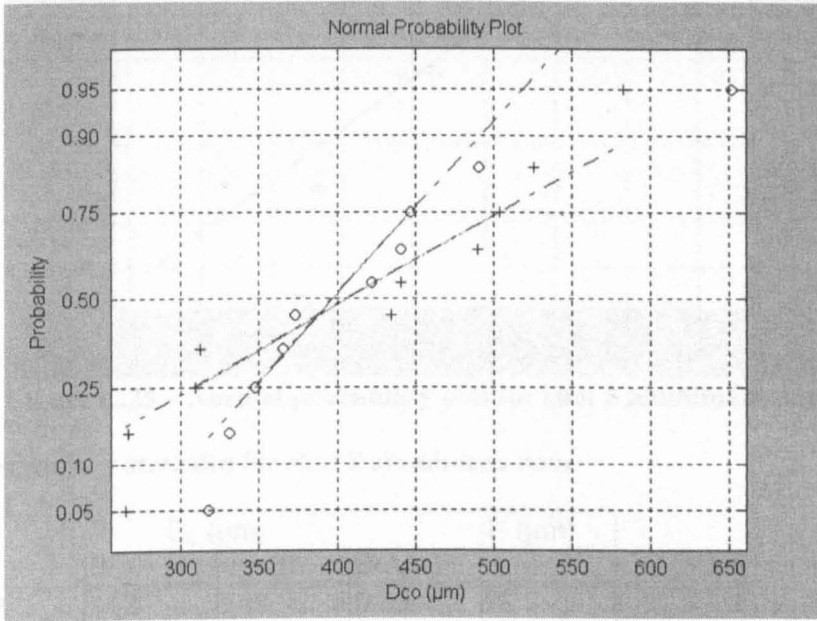


Figure C.24 – Normal probability plot for shot 7 solar cell data

Table C.26 – Summary statistics for shot 7 solar cell data

	Pit (µm)				Shatter (µm)				Conchoid (µm)				P (µm)	C _{off}
	A	B	√(AB)	B/A	A	B	√(AB)	B/A	A	B	√(AB)	B/A		
Mean	54	44	49	0.80	102	102	102	1.01	419	413	414	0.99	52	1.08
SE	9	9	9	0.06	7	5	6	0.04	31	37	32	0.06	4	0.03
Median	54	48	51	0.81	102	101	101	1.00	398	438	429	0.99	55	1.08
SD	16	15	15	0.10	17	13	14	0.09	99	116	102	0.19	13	0.10
Range	31	30	31	0.20	45	33	35	0.24	333	318	320	0.61	31	0.33
Max	70	57	63	0.89	125	117	121	1.15	651	583	616	1.38	64	1.25
Min	39	27	32	0.69	80	84	86	0.91	318	265	296	0.77	33	0.92
Count	3	3	3	3	6	6	6	6	10	10	10	10	8	10
90% >	41	29	34	0.70	83	86	86	0.92	324	265	300	0.78	35	0.94
90% <	68	56	62	0.88	122	117	119	1.13	579	557	560	1.29	64	1.21

The shot 7 aluminium data appears to be normally distributed, however, it is hard to tell for the few solar cell impacts that there are. Thus, the large standard deviation (~25%) will diminish the weight of the data from this shot in the regression analysis.

Title	Shot 8
Projectile	50 μm glass beads
Target	Al plate & HST solar cell
Angle	0°
Pressure	?
Velocity	4.90 \pm 0.05 km s ⁻¹

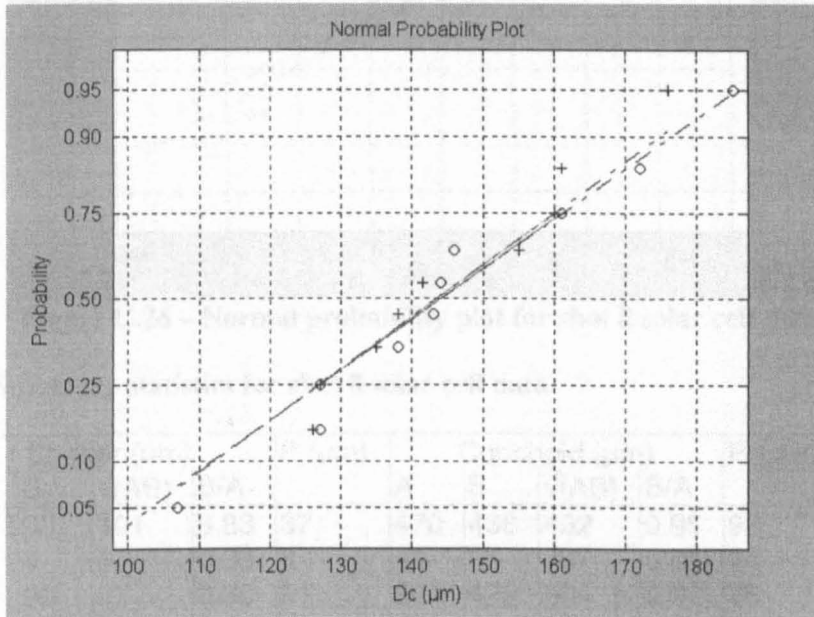


Figure C.25 – Normal probability plot for shot 8 aluminium data

Table C.27 – Summary statistics for shot 8 aluminium data

	D _c (μm)				P (μm)
	A	B	$\sqrt{(AB)}$	B/A	
Mean	145	142	143	0.98	72
SE	7	7	7	0.02	5
Median	144	140	142	0.96	72
SD	23	22	22	0.07	16
Range	78	76	77	0.22	51
Max	185	176	180	1.16	96
Min	107	100	103	0.93	45
Count	10	10	10	10	10
90% >	116	112	114	0.94	50
90% <	179	169	174	1.09	95

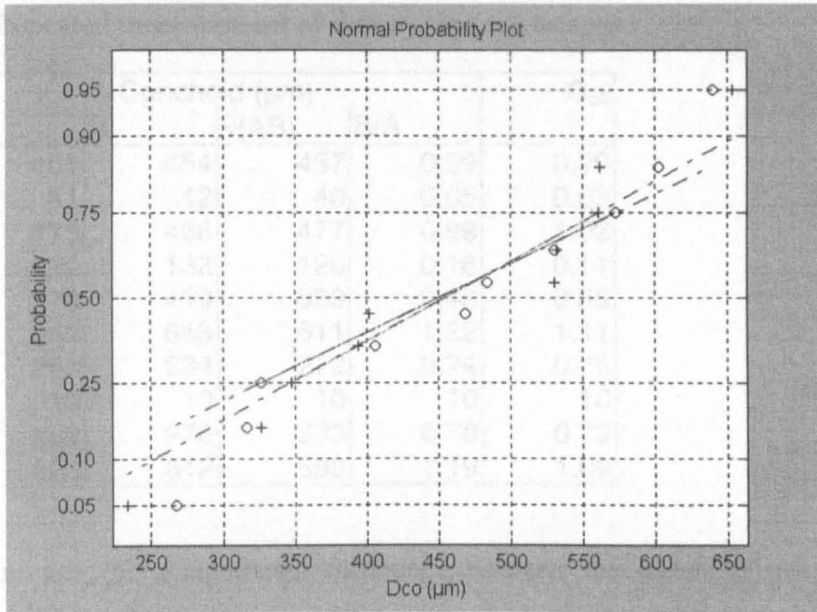


Figure C.26 – Normal probability plot for shot 8 solar cell data

Table C.28 – Summary statistics for shot 8 solar cell data

	Shatter (µm)				P (µm)	Conchoid (µm)				P (µm)
	A	B	$\sqrt{(AB)}$	B/A		A	B	$\sqrt{(AB)}$	B/A	
Mean	113	90	101	0.83	37	470	438	452	0.95	93
SE	10	4	6	0.08	8	43	35	38	0.05	14
Median	114	90	97	0.80	31	509	479	504	0.97	75
SD	24	10	14	0.20	19	134	111	119	0.16	44
Range	70	30	34	0.54	50	385	354	305	0.55	147
Max	146	105	117	1.18	74	642	584	577	1.27	196
Min	76	75	83	0.64	24	257	230	271	0.72	49
Count	6	6	6	6	6	10	10	10	10	10
90% >	82	79	85	0.65	25	285	273	279	0.76	54
90% <	142	102	117	1.11	65	626	557	576	1.18	169

The shot 8 aluminium and solar cell data appear to be roughly normally distributed. The author neglected to measure the centroid offset for shot 8 in the first round of experiments and so subsequently reloaded the images and measured this. Whilst measuring the centroid offsets the author decided to remeasure the conchoidal diameters to check the variability due to operator influences; perhaps the author’s judgement/accuracy had changed in the intervening time between subsequent measurements?

Table C.29 – Repeated measurement of shot 8 solar cell images

	Conchoid (μm)				C_{off}
	A	B	$\sqrt{(AB)}$	B/A	
Mean	461	454	457	0.99	0.99
SE	41	42	40	0.05	0.03
Median	476	466	477	0.99	1.02
SD	129	132	126	0.16	0.11
Range	373	419	339	0.48	0.35
Max	640	653	611	1.22	1.11
Min	267	234	272	0.74	0.76
Count	10	10	10	10	10
90% >	289	276	283	0.78	0.79
90% <	623	612	598	1.19	1.09

The appropriate test for a significant difference between the means of the two rounds of measurement is the *paired sample t-test*. This test is a variation on the standard *t-test* for sample means relevant to repeated measurements of the *same* sample from a population. It is usually used to test for difference arising from two measurements of the same sample made either by two different instruments or two different experimenters. The results of the test along with an *F-test* for variances (Table C.30) shows that there is no significant difference between the means and variances of the data from the two rounds of measurements if we choose the usual 5% level.

Table C.30 – Test for consistency between repeated measurement

	A	B	$\sqrt{(AB)}$	B/A
<i>F-test</i> for variances	45%	31%	43%	48%
<i>Paired sample t-test</i> for means	55%	44%	61%	48%

Title	Shot 9 (failed)
Projectile	50 μm glass beads
Target	Al plate & HST solar cell
Angle	15°
Pressure	0.4 mb
Velocity	~5.3 km s ⁻¹

The first attempt at shot 9 resulted in only 1 impact on the solar cell and thus a shot at 15° was later repeated.

Title	Shot 9
Projectile	50 μm glass beads
Target	Al plate & HST solar cell
Angle	55°
Pressure	0.4 mb
Velocity	5.28 ± 0.05 km s ⁻¹

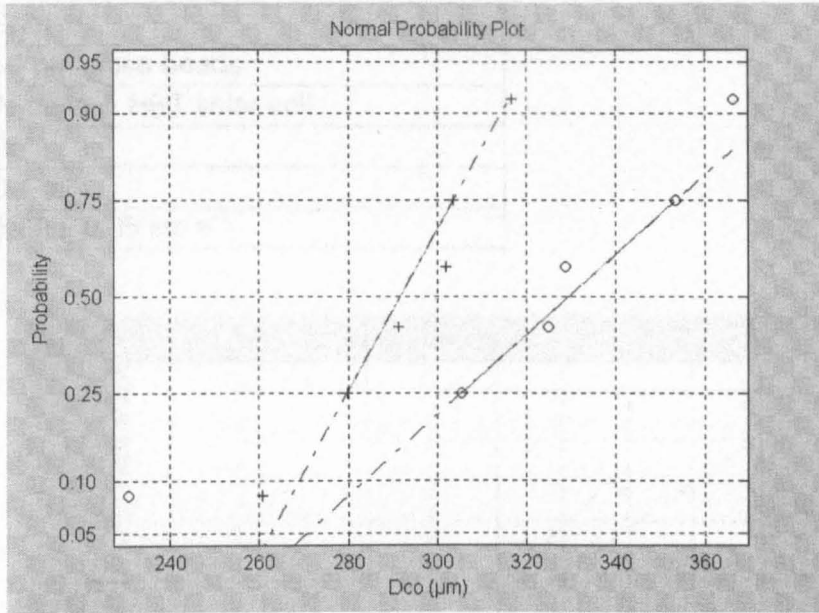


Figure C.27 – Normal probability plot for shot 9 solar cell data

Table C.31 – Summary statistics for shot 9 solar cell data

	Shatter (µm)				Conchoid (µm)				C _{off}
	A	B	√(AB)	B/A	A	B	√(AB)	B/A	
Mean	118	97	107	0.82	318	292	305	0.93	0.96
SE	7	8	7	0.05	20	8	13	0.05	0.03
Median	124	89	105	0.86	327	297	312	0.91	0.95
SD	13	13	12	0.09	48	20	32	0.12	0.08
Range	24	23	24	0.16	135	56	95	0.34	0.21
Max	127	112	119	0.88	366	317	340	1.13	1.08
Min	103	89	96	0.72	231	261	245	0.79	0.87
Count	3	3	3	3	6	6	6	6	6
90% >	105	89	97	0.73	249	266	260	0.81	0.87
90% <	127	110	118	0.88	363	313	334	1.09	1.06

Although there were only 6 solar cell impacts for shot 9 the craters have a small standard deviation (~10% of the mean) and close mean and median values. Thus it is reasonable to assume that they were made by our intended impactors.

Title	Shot 10 (failed)
Projectile	50 µm glass beads
Target	Al plate & HST solar cell
Angle	65°
Pressure	0.33 mb
Velocity	?

The first attempt at a 65° shot failed in that no projectiles reached the target.

Title	Shot 10
Projectile	50 μm glass beads
Target	Al plate & HST solar cell
Angle	65°
Pressure	0.4 mb
Velocity	5.08 \pm 0.05 km s ⁻¹

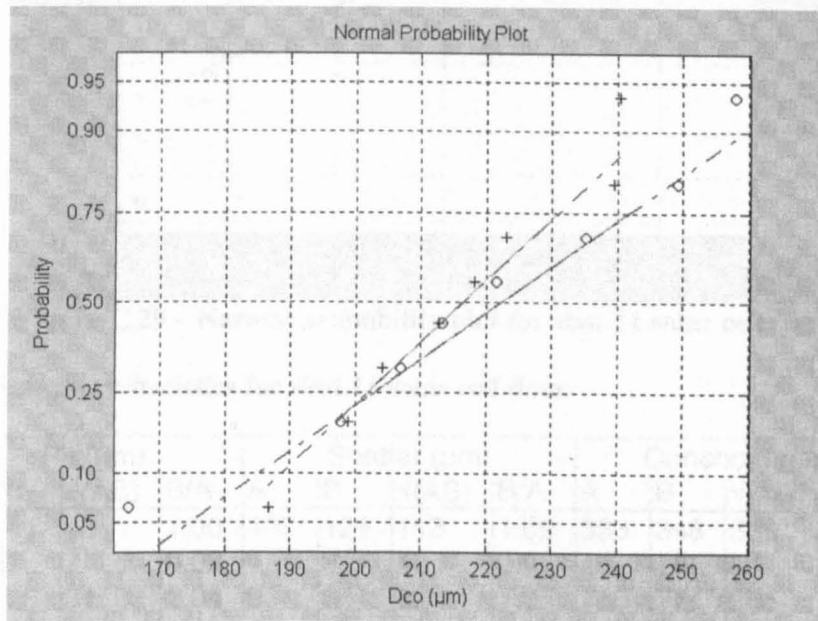


Figure C.28 – Normal probability plot for shot 10 solar cell data

Table C.32 – Summary statistics for shot 10 solar cell data

	Conchoid (μm)				C_{off}
	A	B	$\sqrt{(AB)}$	B/A	
Mean	218	215	216	1.01	1.17
SE	11	7	5	0.07	0.04
Median	217	216	213	0.93	1.20
SD	30	19	15	0.21	0.10
Range	93	54	35	0.62	0.28
Max	258	240	234	1.45	1.30
Min	165	187	199	0.83	1.02
Count	8	8	8	8	7
90% >	177	191	199	0.83	1.02
90% <	255	240	234	1.34	1.27

The normal probability plot, closeness of the mean and median values and the relatively small standard deviation of the shot 10 data does not suggest that any modifications are required.

Title	Shot 11
Projectile	50 μm glass beads
Target	Al plate & HST solar cell
Angle	15°
Pressure	0.24 mb
Velocity	5.12 \pm 0.05

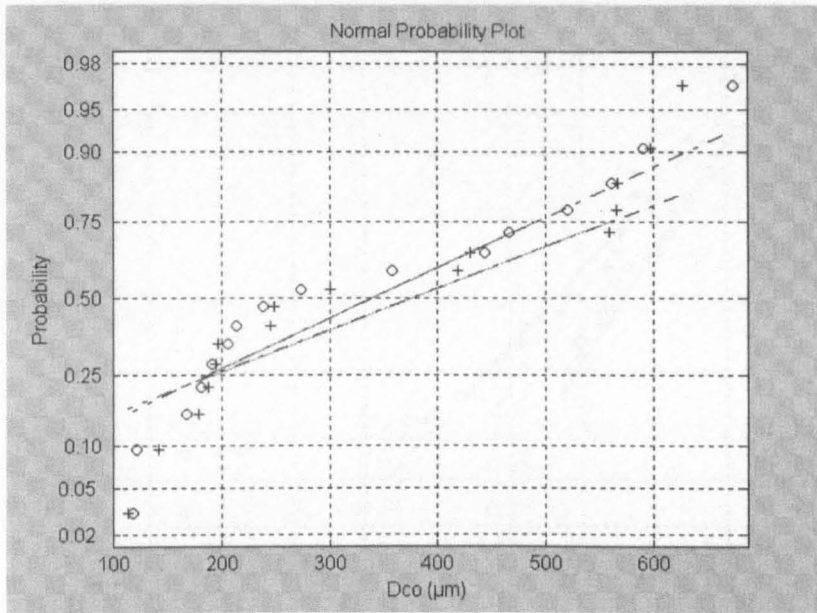


Figure C.29 – Normal probability plot for shot 11 solar cell data

Table C.33 – Summary statistics for shot 11 solar cell data

	Pit (µm)				Shatter (µm)				Conchoid (µm)				C _{off}
	A	B	$\sqrt{(AB)}$	B/A	A	B	$\sqrt{(AB)}$	B/A	A	B	$\sqrt{(AB)}$	B/A	
Mean	40	41	40	1.00	107	121	113	1.09	333	348	339	1.06	1.15
SE	6	7	7	0.03	14	21	16	0.06	46	46	45	0.04	0.04
Median	34	28	31	1.04	93	94	92	1.05	256	274	265	1.06	1.19
SD	22	24	23	0.12	52	79	61	0.23	184	185	181	0.15	0.15
Range	69	75	72	0.40	149	295	208	1.03	555	513	532	0.47	0.49
Max	82	88	85	1.14	189	340	251	1.83	673	627	649	1.28	1.40
Min	13	13	13	0.74	41	46	43	0.81	118	113	117	0.81	0.91
Count	12	12	12	12	14	14	14	14	16	16	16	16	16
90% >	16	18	17	0.81	42	46	44	0.90	120	134	126	0.86	0.93
90% <	74	78	76	1.12	187	238	209	1.41	612	605	596	1.28	1.34

The shot 11 data appears to be rather anomalous in that it appears from the normal probability plot that 2 populations of particles reached the target: note the 2 distinct gradients above and below the 50% level. The mean and medians are markedly different indicating a skewed distribution. Furthermore, the standard deviations are relatively large. Consequently shot 11 was repeated to try and obtain a buckshot with a size range closer to that of the intended projectiles.

Title	Shot 12
Projectile	50 µm glass beads
Target	Al plate & HST solar cell
Angle	15°
Pressure	0.27 mb
Velocity	5.61

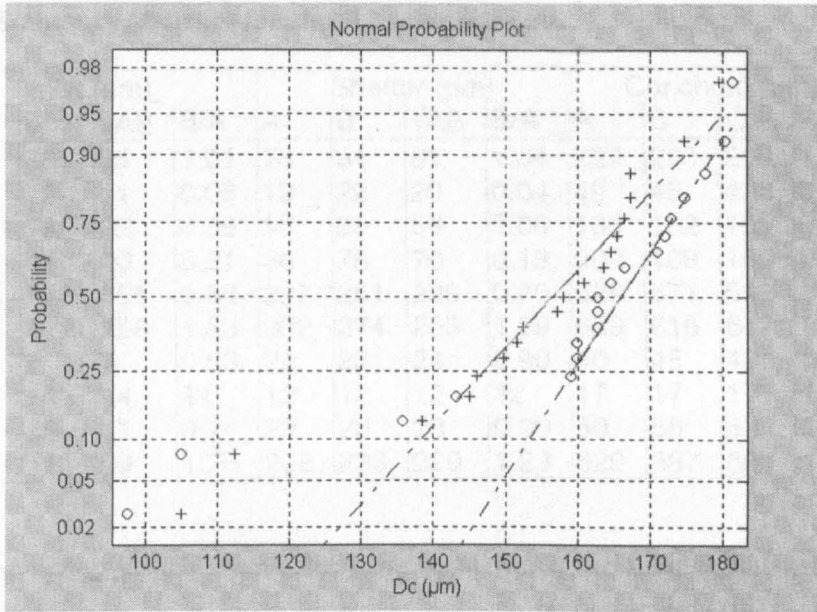


Figure C.30 – Normal probability plot for shot 12 aluminium data

Table C.34 – Summary statistics for shot 12 aluminium data

	D _c (µm)			
	A	B	\sqrt{AB}	B/A
Mean	158	154	156	0.98
SE	5	4	5	0.01
Median	163	158	160	0.97
SD	23	19	21	0.05
Range	84	74	79	0.18
Max	181	179	180	1.08
Min	98	105	101	0.89
Count	19	19	19	19
90% >	104	112	108	0.91
90% <	180	175	178	1.07

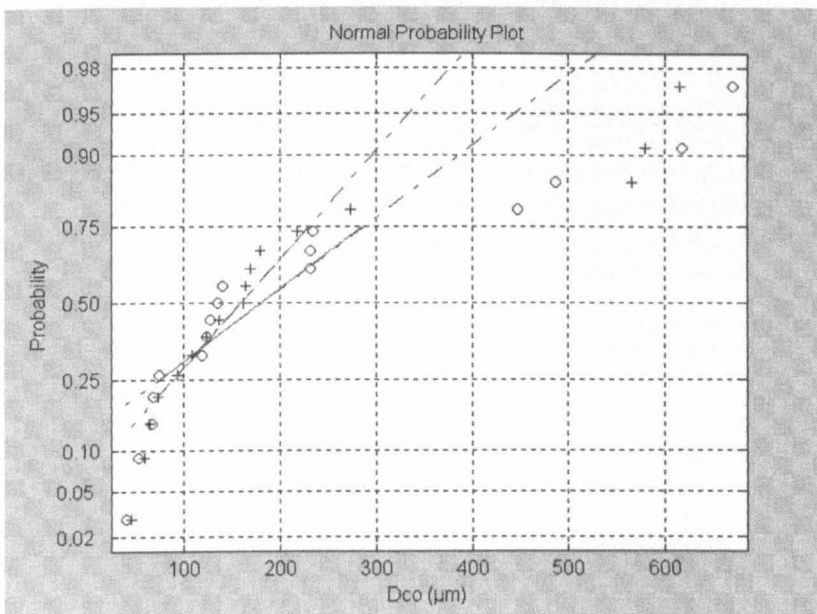


Figure C.31 – Normal probability plot for shot 12 solar cell data

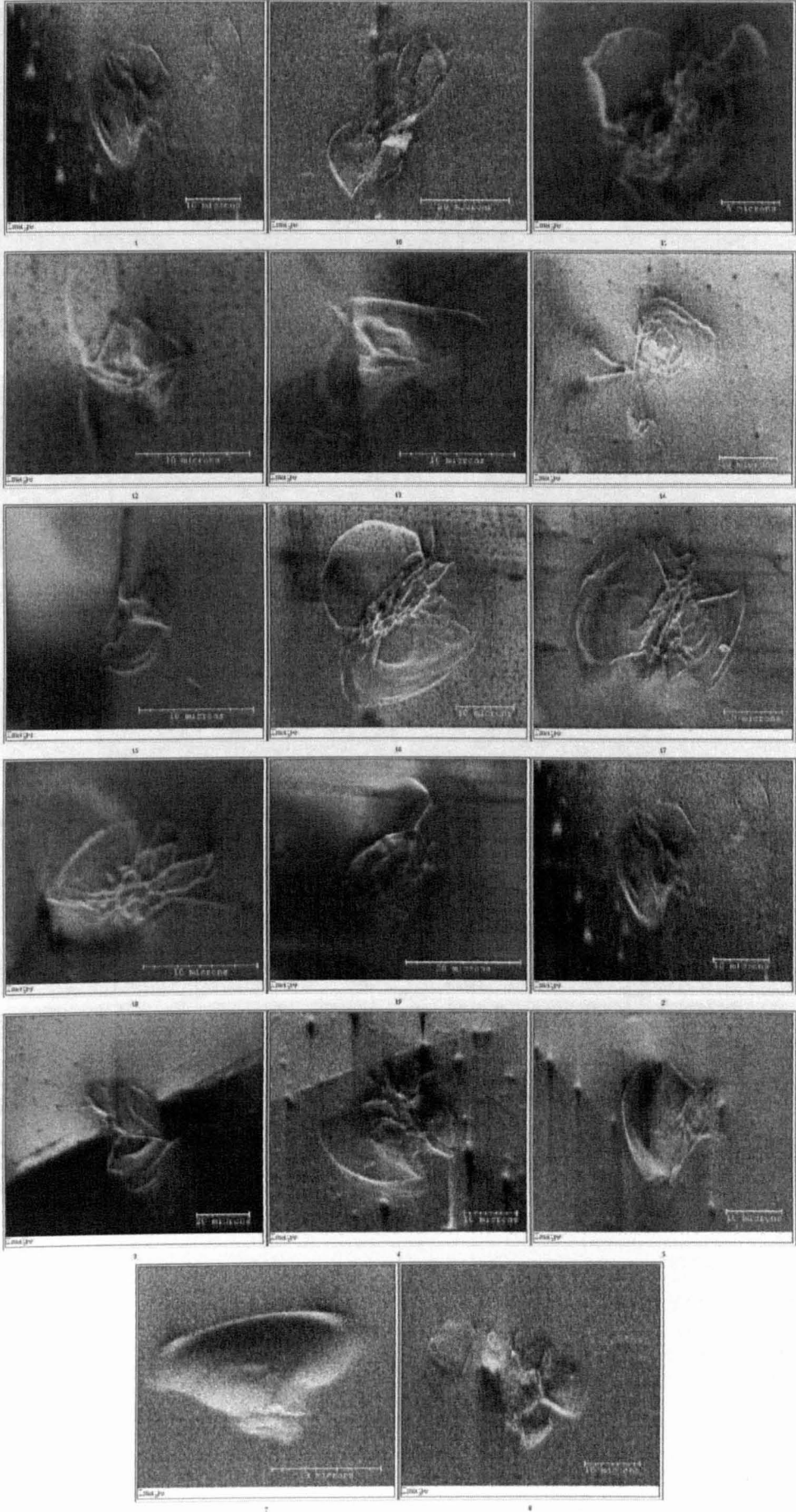
Table C.35 – Summary statistics for shot 12 solar cell data

	Pit (μm)				Shatter (μm)				Conchoid (μm)				C_{off}
	A	B	\sqrt{AB}	B/A	A	B	\sqrt{AB}	B/A	A	B	\sqrt{AB}	B/A	
Mean	34	36	35	1.01	78	84	81	1.04	227	213	218	1.01	1.04
SE	10	12	11	0.06	19	22	20	0.04	49	46	47	0.07	0.04
Median	21	19	22	0.95	56	59	56	1.06	135	162	151	0.96	1.00
SD	37	44	40	0.21	66	75	70	0.13	202	188	192	0.27	0.16
Range	138	165	151	0.80	227	251	239	0.40	629	571	599	1.04	0.47
Max	146	172	158	1.33	252	274	263	1.29	669	616	642	1.62	1.31
Min	8	7	7	0.53	25	23	24	0.90	40	45	43	0.58	0.84
Count	14	14	14	14	12	12	12	12	17	17	17	17	17
90% >	11	10	11	0.74	29	28	28	0.90	50	56	53	0.60	0.85
90% <	97	111	99	1.26	208	233	220	1.23	629	587	601	1.44	1.30

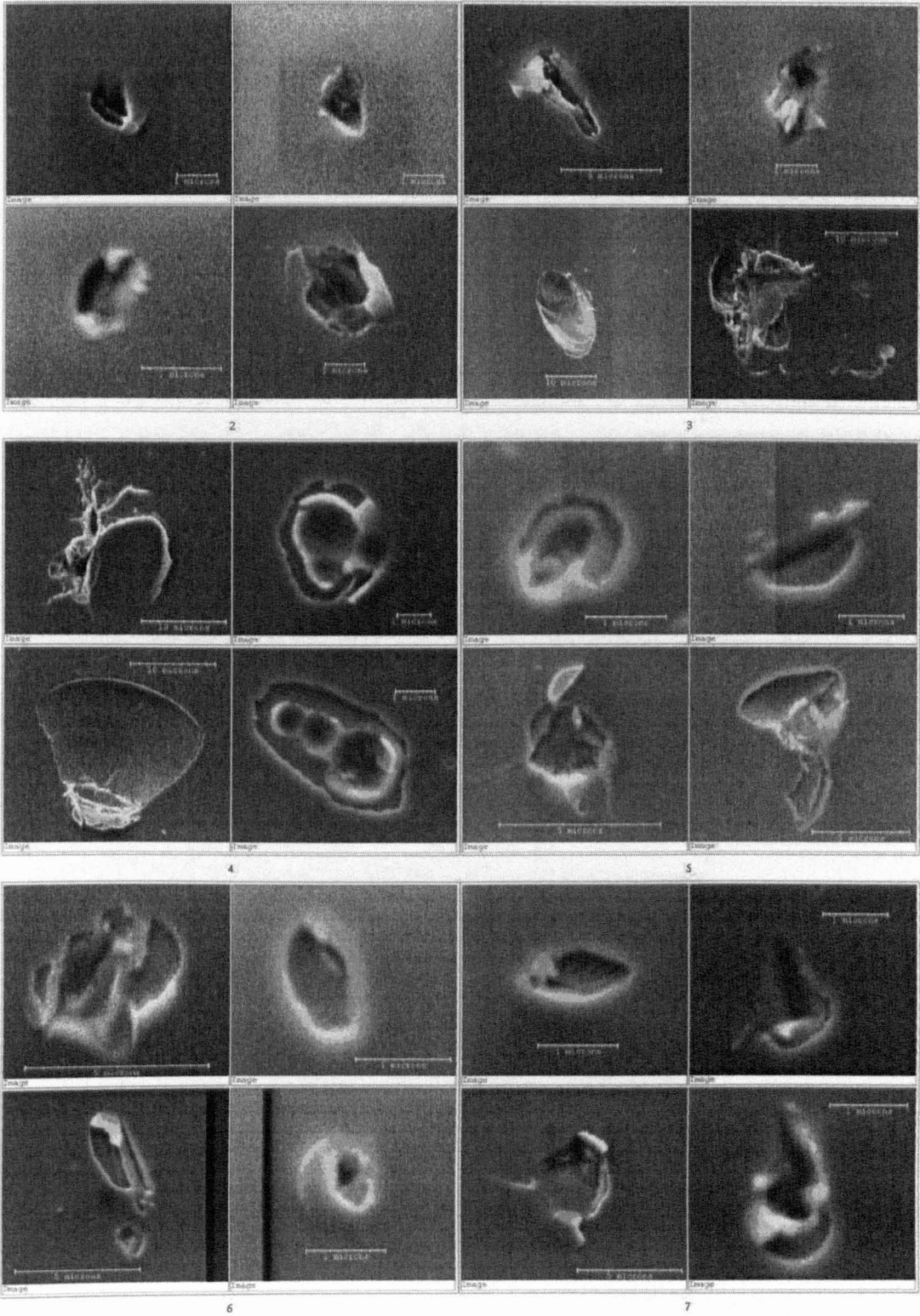
For shot 12 the craters in the aluminium plate upon which the solar cell is mounted were also measured and show an approximately normal distribution (Figure C.30). Once again the solar cell craters show evidence of impact by at least 2 different types of impactor. However, this time the distinction between the 2 populations is clearer (Figure C.31) with several particles above 400 μm , the rest below 300 μm .

D - Images of Van de Graaff glass impacts

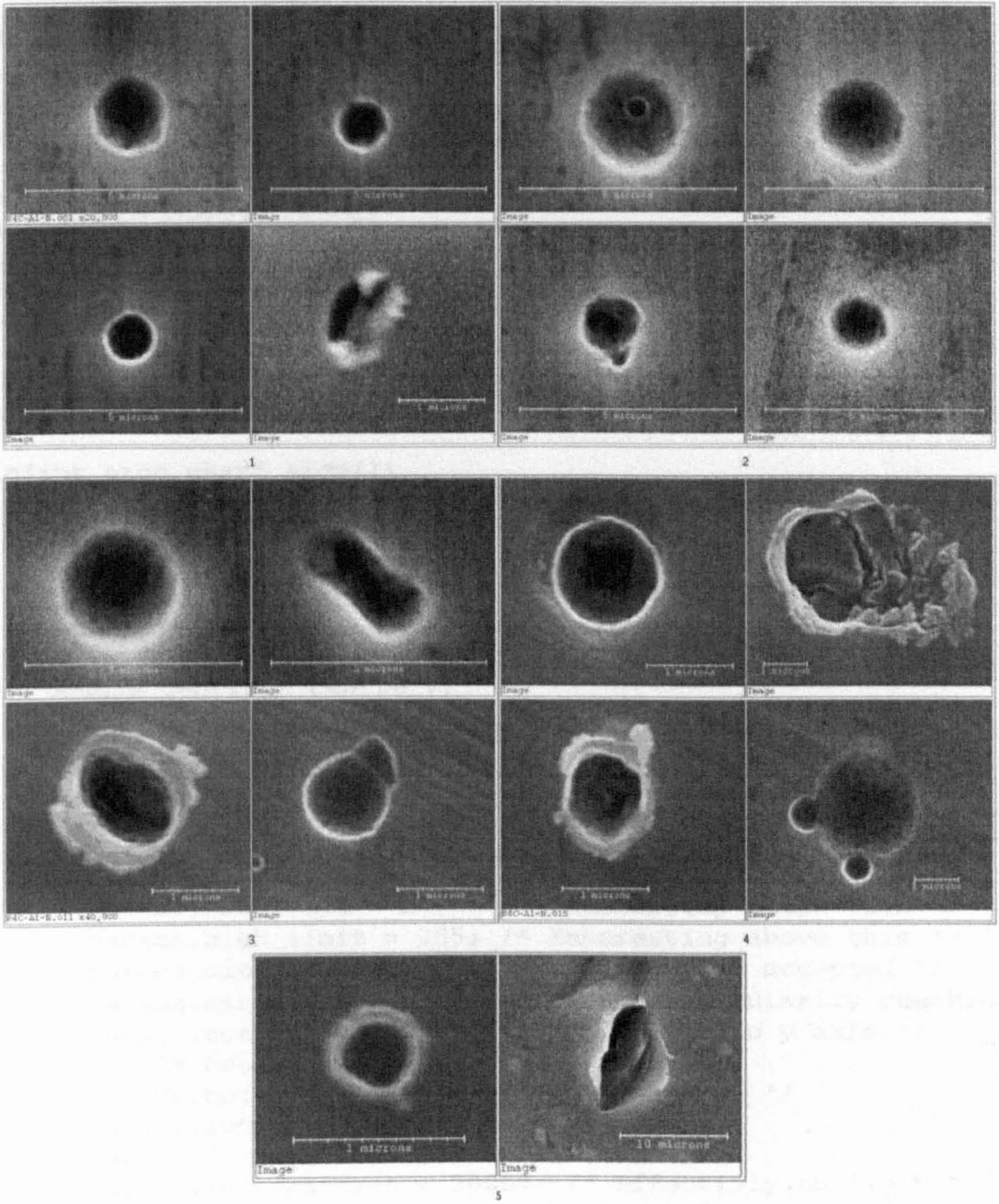
Boron carbide impacts on glass cylinder



Boron carbide impacts on CMX cover slide



Boron carbide impacts on aluminium



E - Program listingsListing of simplify.c

```

#include <stdio.h>
#include <math.h>
#include <pip/typedefs.h>
#include <pip/rasterfile.h>
#include <pip/pip.h>
#include <pip/findlight.h>
#include <pip/globdefs.h>
#include <pip/records.h>
#include <pip/stage.h>

void read_rasterfile(fl_params*,struct rasterfile*,struct
pallete*,const char*,byte*);

main(int argc,char* argv[])
{
    struct rasterfile header;
    struct pallete pallete;
    fl_params params;
    byte* image;
    FILE* fp;
    double centre_x,centre_y;
    int size,junk,i,steps,averaging;
    float* r;

    steps=50;
    averaging=0;
    /* Set some defaults (from mtp's getcoord.c) */
    params.low_limit = 20; /* Interesting below this */
    params.high_limit = 255; /* Interesting above this */
    params.sizelim = 0; /* Minimum size accepted */
    params.circlim = 2.0; /* Disable circularity checking*/
    params.scaling = 1.41; /* Ratio of x to y axis */
    params.header = &header;
    params.object_id = ""; /* Do not label */
    params.output = stdout;
    params.flags = AUTO_FEATURE;
    params.max_features = 20000; /* Effectivly no limit */
    /*scan_file = FALSE; Do not take input from an image file */

    if (argc>3)
        params.low_limit = atoi(argv[3]);
    if (argc>4)
        params.high_limit = atoi(argv[4]);
    read_rasterfile(&params, &header, &pallete, argv[1], image);
    image=params.image;
    simplify_image(image,header.ras_length,params.low_limit,param
s.high_limit);
    fp=fopen(argv[2], "w");
    write_header(&header, fp);
    write_pallete(&pallete, fp);
    fwrite(image,header.ras_length,1, fp);
}

```

Listing of shape.c

```
#include <stdio.h>
#include <math.h>
#include <pip/typedefs.h>
#include <pip/rasterfile.h>
#include <pip/pip.h>
#include <pip/findlight.h>
#include <pip/globdefs.h>
#include <pip/records.h>
#include <pip/stage.h>

void read_rasterfile(fl_params*,struct rasterfile*,struct
palette*,const char*,byte*);
int radar(byte*, struct rasterfile, float, float, float, float*);
int smooth(float*, int, int);

main(int argc,char* argv[])
{
    struct rasterfile header;
    struct palette palette;
    fl_params params;
    byte* image;
    FILE* fp;
    double centre_x,centre_y;
    int size,junk,i,steps,averaging;
    float* r;

    steps=50;
    averaging=0;
    if (argc>2)
        steps=atoi(argv[2]);
    r=(float*)calloc(steps,sizeof(float));
    if (argc>3)
        averaging=atoi(argv[3]);
    read_rasterfile(&params, &header, &palette, argv[1], image);
    image=params.image;
    mapout_feature(image,&header,header.ras_width/2,header.ras_he
ight/2,&junk,&junk,&junk,&junk,&centre_x,&centre_y,&size);
    radar(image,header,centre_x,centre_y,(2*M_PI)/steps,r);
    if(averaging>0)
        smooth(r,averaging,steps);
    for(i=0; i<steps; i++)
        printf("%f %f\n",i*((2*M_PI)/steps),r[i]);
}
```

Listing of radar.c

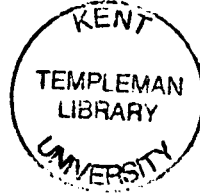
```

#include <stdio.h>
#include <math.h>
#include <pip/rasterfile.h>
#include <pip/findlight.h>

int radar(byte* image, struct rasterfile header, float centre_x,
float centre_y, float incr, float* r)
{
    int i;
    float theta;

    theta=0;
    for(i=0; theta<6.283; i++)
    {
        int pix_x,pix_y;
        float pos_x,pos_y;
        pos_x=centre_x;
        pos_y=centre_y;
        do
        {
            pos_x+=cos(theta);
            pos_y-=sin(theta);
            pix_x=(int)(pos_x+0.5);
            pix_y=(int)(pos_y+0.5);
            r[i]=hypot(pos_x-centre_x,pos_y-centre_y);
            if(pix_x<0 || pix_x>header.ras_width ||
                pix_y<0 || pix_y>header.ras_height)
                return(1);
        }
        while(*(image+(header.ras_width*pix_y)+pix_x)==50);
        theta+=incr;
    }
    return(0);
}

```

Listing of smooth.c

```

int smooth(float* r, int averaging, int steps)
{
    int i;

    for(i=averaging; i<(steps-averaging); i++)
    {
        int j;
        float sum;

        sum=0;
        for(j=(i-averaging); j<=(i+averaging); j++)
            sum+=r[j];
        r[i]=sum/((2*averaging)+1);
    }
    return(0);
}

```